UVSOR

# Users Reports

# Estimation of the FEL gain for the Helical Optical Klystron

Hiroyuki HAMA, Masahito HOSAKA, Jun-ichiro YAMAZAKI, Toshio KINOSHITA
and Kazuhiko KIMURA*)

*UVSOR Facility, Institute for Molecular Science, Okazaki 444 Japan*
*)*The Graduate University for Advanced Studies, Okazaki 444 Japan*

Free electron laser (FEL) oscillation at wavelengths from visible down to 239 nm has been obtained at the UVSOR-FEL facility using a helical optical klystron (UNKO-3). One of big advantages of UNKO-3, namely less degradation of the cavity mirror was demonstrated in experiments. For further development of the UV-FEL, the FEL gain has been compared with a theoretical one calculated by employing a numerical evaluation of an 1-D model with actual helical magnetic fields. On the way to develop a 3-D simulation code for the storage ring FEL, an instantaneous peak gain was brought by a simple model of electromagnetic interaction between the optical field and the relativistic electrons.

Even for the $\mathrm{TEM}_{00}$ cavity mode, a complete simulation of the FEL interaction taking a finite size of cross section and a longitudinal distribution of the electron beam into account is very complicate. Prior to such irritating calculation, a simple model is applied to estimate the gain. Electric field of circular polarized electromagnetic wave with a power density $P\,[W/m^2] = \sqrt{\varepsilon/\mu}\,E^2$ is expressed as $E_x = E\cos(\omega t - kz + \phi)$ and $E_y = E\cos(\omega t - kz + \phi - \pi/2)$ (here elliptical polarization is able to be considered). The magnetic field of the optical klystron is analytically given to the simulation with following parameters. A period length is 0.11 m and a period number of undulator sections is 9. A length of one-period dispersive section is just 3 times of the period length of the undulator section. For the resonant wavelength of 270 nm, the peak magnetic field is 0.234 T at the beam energy of 600 MeV. The magnetic field at the dispersive section is chosen to produce $N_d$ =120 which is almost same as that of UNKO-3. Equivalent conditions are applied to another calculation of the gain of a planar optical klystron.

A well-known theorem of Madey can predict the FEL gain in the small signal

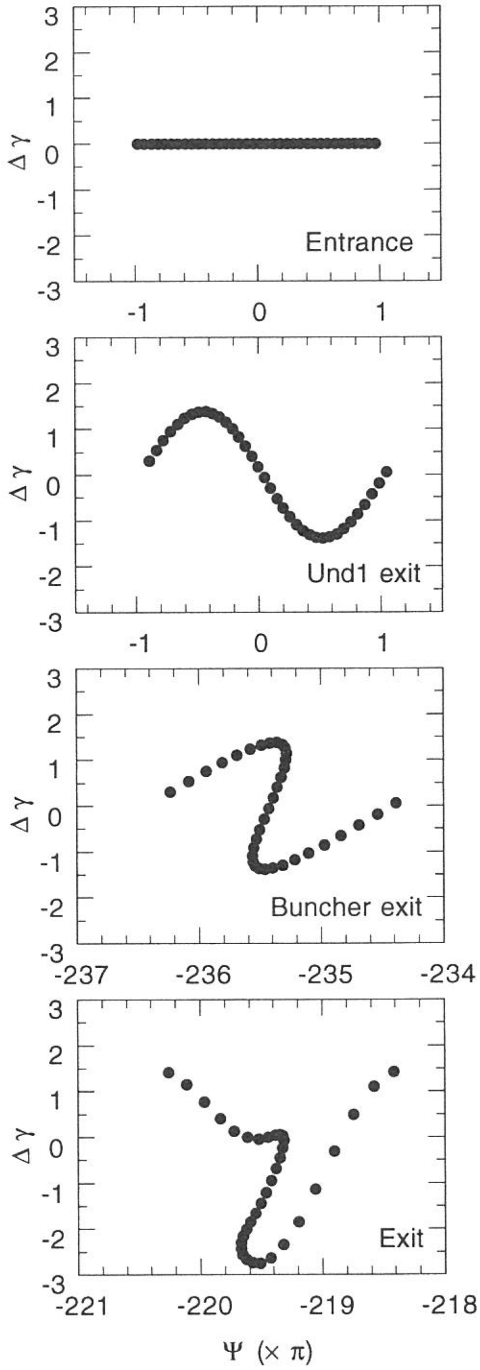

Fig.1 Phase space evolution in the helical optical klystron.

regime. Accordingly the FEL gain is proportional to the brilliance factor of the spontaneous radiation, which is expressed using Bessel functions and is unity for the complete helical beam trajectory. Deduced FEL gains using the analytical expression of the magnetic fields consequently agreed with Madey's theorem as shown in Fig. 2. For the resonant wavelength of 270 nm, the gain with the helical optical klystron is approximately 2 times higher than that with the planar optical klystron.

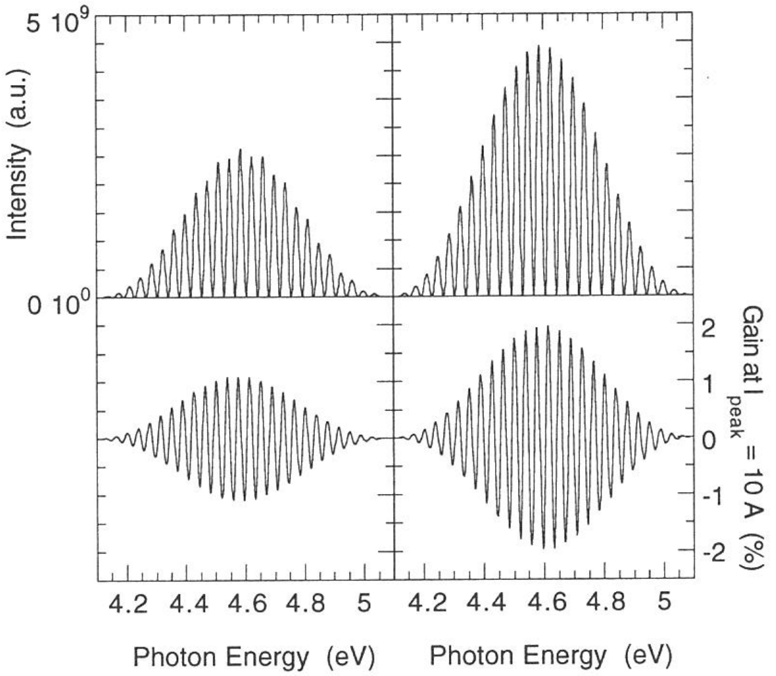

Fig. 2 Calculated intensity distributions and the FEL gains at a peak current of 10 A for a planar optical klystron (left) and a helical optical klystron (right).

As a matter of fact, the actual magnetic field of UNKO-3 is not expressed by complete trigonometric functions. Figure 3 shows calculated magnetic fields using an equivalent current method applied for actual configurations of the permanent magnet arrays of UNKO-3. At the gap of 50 mm, strengths of peak magnetic field in the vertical and the horizontal directions are almost identical with each other, and the resonant wavelength at the beam energy of 600 MeV is 248 nm (5 eV), which is not so far from the above model case.

A result of the gain calculation by the 1-D simulation using the magnetic fields shown in Fig. 3 was essentially in good agreement with that of the ideal case (right hand in Fig. 2). The deduced peak gain is 1.88 % at the peak current of 10 A. Figure 4 shows the spectrum of spontaneous radiation and the gain variation against the photon energy. Unfortunately the strength of magnetic field at the dispersive section is not able to be changed due to a mechanical constrain, it is

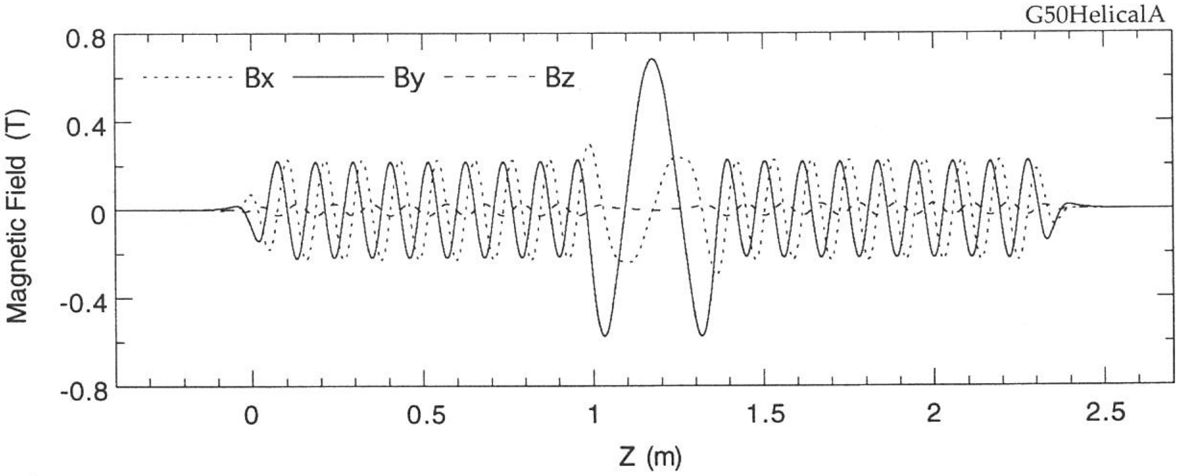

Fig. 3 Magnetic fields of UNKO-3 at the gap of 50 mm.

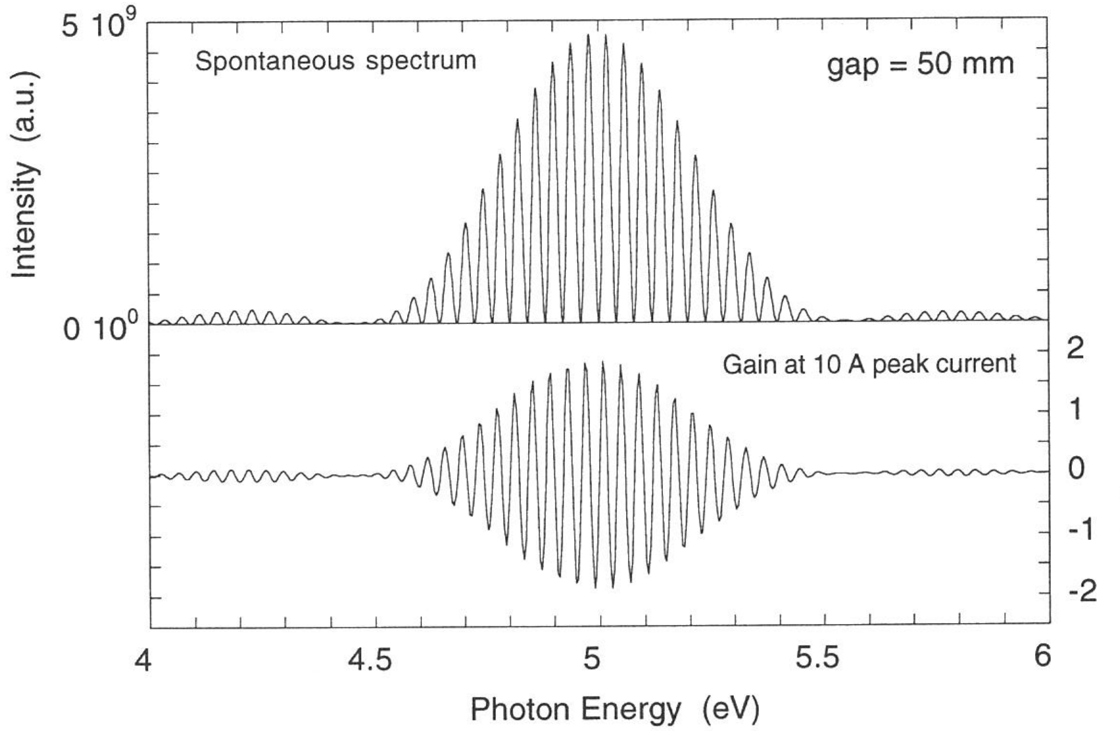

Fig. 4 Spectrum of spontaneous radiation calculated based on Lienard-Wiechert potential and the gain variation against the photon energy obtained from an 1-D simulation.

difficult to optimize $N_d$ to produce the maximum gain (optimized $N_d$ may be ~ 200 but strongly depends on the beam energy spread in an equilibrium state of the gain and the laser power). The FEL gain is indeed reduced by other parameters so-called "filling factor" and "modulation factor", then it can be estimated that the calculated FEL gain would be reduced to 40 % approximately. An experimental value of the effective gain at the 270 nm lasing was obtained to be 0.8 % at the peak current of ~ 10 A, which agreed well with the estimated gain.

Saturation of the FEL gain in the undulator is one of major issues of the linac-based FEL (high gain regime) and SASE (self amplification spontaneous emission) mode. For the storage ring FEL, the laser power saturation is, however, normally coming from a different mechanism. As shown in Fig. 4, the single path gain saturation arises with the laser power of more than 10 $W/m^2$, which may correspond to ~ 1 W average output power in case of the UVSOR-FEL. The gain reduction due to the bunch-heating resulted from the energy exchange and the phase space oscillation of the electrons in the storage ring is much more quicker, and then a nominal output power of the UVSOR-FEL does not exceed a couple of mW (here the mirror transmission is about 50 ppm).

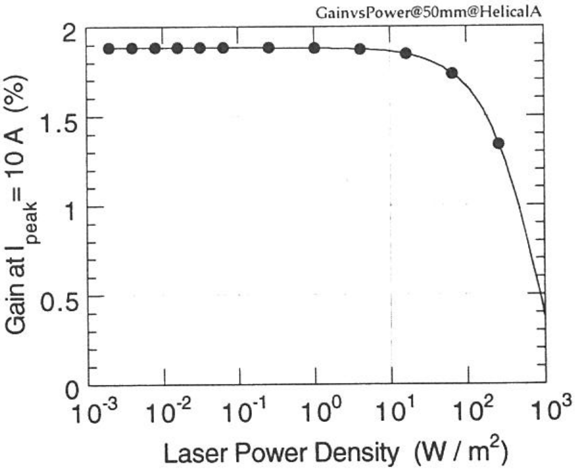

Fig. 5 Laser power density dependence of the FEL gain.

# Free Electron Laser Oscillation Using a Helical Optical Klystron

Kazuhiko Kimura[a], Hiroyuki Hama[a,b], Masahito Hosaka[b],
Jun-ichiro Yamazaki[b] and Toshio Kinoshita[b]

[a] *The Graduate University for Advanced Studies, Myodaiji, Okazaki 444, Japan*
[b] *UVSOR Facility, Institute for Molecular Science, Myodaiji, Okazaki 444, Japan*

The storage ring FEL (SRFEL) looks precious because combination of synchrotron radiation (SR) and the SRFEL gives possibility of challenging many-color experiments such as a pump-probe spectroscopy without complicate system for synchronization. Among a couple of facilities where the SRFELs have been operated, only the Super-ACO FEL, Orsay, is providing a UV FEL to users. There are some requirements for such experiments. Particularly, duration of lasing time should be reasonably long. Beside the beam lifetime, degradation of mirrors in the optical cavity is an impending problem.

An optical klystron employing helical undulators has been considered to be a promising candidate to qualify minimum requirement for use of the SRFEL. Because on-axis photon intensity of higher harmonic radiation is expected to be significantly reduced, the degradation rate of mirrors might be hopefully suppressed. Moreover the FEL gain of the helical optical klystron should be higher than a planar one with identical period length and period number. Advantage of the helical optical klystron numerically evaluated and compared with a planar type optical klystron was already reported [1].

Basic description of the helical optical klystron (UNKO-3) is found in ref. 1. The permanent magnet array is consisted with three lanes. The vertical and the horizontal magnetic fields are provided by the center lane array and the side lane arrays, respectively. Phase between the center lane and the side lanes can be changed mechanically, so that complete helical with both helicities, ellipsoidal and planar modes of magnetic field are able to be produced. Measurement and correction of magnetic fields of the UNKO-3 using a hole probe had been initially done for the vertical and horizontal directions independently. By putting a couple of small tip magnets into the magnet cubes, residual 1st integral of magnetic field were reduced to be less than 100 G•cm at various gaps and phases.

A region of uniform field of UNKO-3 is very narrow so that control of the beam orbit is critical to obtain a good spontaneous radiation. Figure 1 shows measured vertical and horizontal focusing power of the UNKO-3 and predicted ones deduced from the calculation of the magnetic field. By using additional windings of the quadrupoles, the lattice function can be completely corrected in a gap range down to 55 mm for the beam energy of 600 MeV. The field errors of the UNKO-3 have been compensated by additional steering magnets.

The beam orbit was carefully placed on the center of the magnetic field. Because there is the strong focusing power in the UNKO-3, the beam would be kicked considerably if the beam is not going though the center of the field. We measured orbit displacements as a function of the off-set position of the beam by changing the gap a bit. A modulation factor of the spontaneous

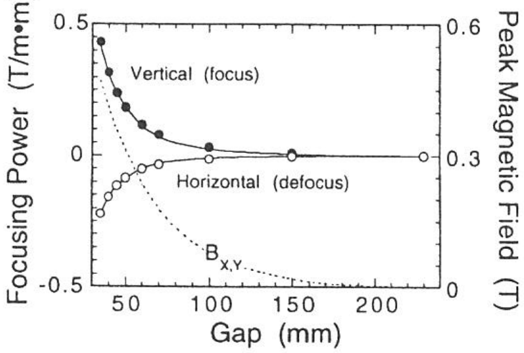

Fig. 1 Measured focusing powers (circles) and calculated ones (solid lines) against the gap length. Peak magnetic field of undulator is also shown.

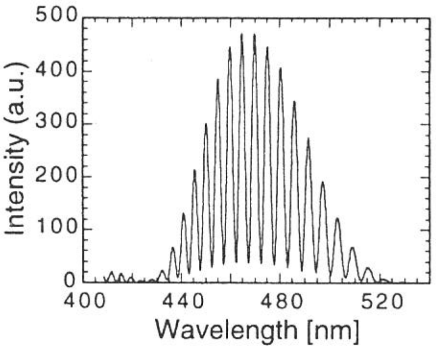

Fig. 2 A spontaneous spectrum from the UNKO-3 obtained after alignment of the beam orbit.

radiation $f_{mod}$ was found to be sensitive to the beam orbit, and then it was a good indication of the beam orbit. Finally we obtained the best $f_{mod}$ of 0.86 at the 470 nm (see Fig. 2), which is in agreement with a calculation including the energy spread and the angular spread of the beam.

In the lasing experiments, we have used dielectric $HfO_2/SiO_2$ multilayers fabricated by an ion-beam sputtering for the cavity mirrors. Although photon absorption rate of $HfO_2$ increases rapidly as the wavelength becomes shorter than ~ 260 nm, we have obtained an FEL oscillation around the shortest wavelength of 240 nm as shown in Fig. 3. Because the band width of the mirror reflectance is very narrow, a region which the FEL wavelength was able to be varied was only from 239 nm to 243 nm.

Since the electron beam energy is increased up to 600 MeV from 500 MeV of the former FEL experiment, some changes have occurred on the laser property along with the improvement of the beam lifetime. In lasings of the former UVSOR-FEL, a CW-like macrotemporal structure of the laser was seen in a large detuning region, and the macropulse arisen at the top of the detuning curve. Meanwhile, another region of CW-like laser structure appeared around the best synchronism. This continuous macrotemporal structure has been confirmed by measuring with a dual-sweep streak camera. However this CW-like laser is not so stable, and sometimes laser pulsation interrupted the continuum lasing. We have presumed that the laser macrotemporal structure is strongly affected by the beam properties such as the bunch length and the synchrotron damping time. In the present experiment, the bunch length become approximately 2 times longer than that at previous experiment. In the case of the long bunch length, longitudinal distribution of the electron density is rather flat, so that effects of perturbation for the synchronism like a mechanical vibration and collective instabilities of the beam may be relatively suppressed. Moreover fast energy damping (synchrotron damping time $\tau_s$ = 19 ms and 33 ms for E = 600 MeV and 500 MeV, respectively) may regain the laser intensity quickly.

To demonstrate the reduction of the mirror degradation rate, the mirrors for the wavelengths of 460 nm and 270 nm were partly irradiated by the radiation from the UNKO-3 of a planar mode with a same set-up of the lasing experiment. Variation of mirror reflectivity against a dose of the beam current are plotted in Fig. 4. It is quite impressive result that the degradation rate with the planar mode was more than 50 times faster than that with the helical mode. Another fact seen in Fig. 4 is that the degradation rate gets fast as the resonant wavelength became shorter even the mirror was mostly irradiated by the fundamental radiation from the helical mode of the optical klystron. We have thought another coating material which has a high band gap energy is required for the high index of the multilayer to operate the FEL with the laser wavelength less than 250 nm. In a sense, $Al_2O_3$ is one of the candidate for the high index material. Because the refraction index of $Al_2O_3$ is very close to the low index material $SiO_2$ and then huge number of layers may be required to obtain a reasonable high reflectance, improvement of the deposition technique is necessary.

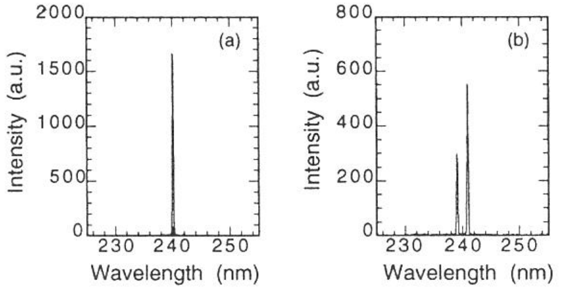

Fig. 3 Measured FEL spectra around the wavelength region of 240 nm at two different undulator gaps.

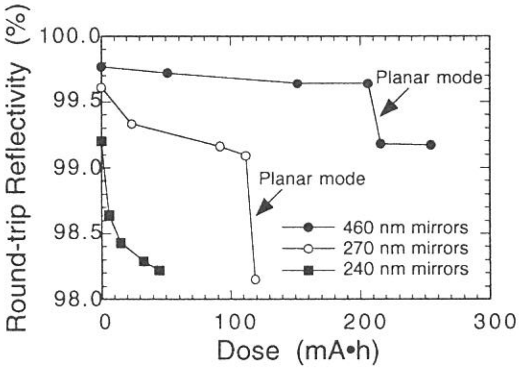

Fig. 4 Measured round-trip reflectivities for three different mirrors plotted as a function of the irradiation dose of the electron beam.

*Reference*

[1] H. Hama, Nucl. Instr. and Meth. A375 (1996) 57.

# High Energy Gamma-Beam from Intracavity Compton Backscattering of the UVSOR-FEL

Masahito Hosaka[a], Hiroyuki Hama[a, b], Kazuhiko Kimura[b], Jun-ichiro Yamazaki[a] and Toshio Kinoshita[a]

[a]*UVSOR Facility, Institute for Molecular Science, Myodaiji, Okazaki 444, Japan*
[b]*The Graduate University for Advanced Studies, Myodaiji, Okazaki 444, Japan*

High energy gamma ray beam produced by intracavity Compton backscattering of a free electron laser(FEL) has been observed for the first time on the UVSOR storage ring. Compton backscattering of laser photons on high energy electron beam is well known method of producing gamma ray beam. Conventionally, lights from an external laser is used and arranged to collide "head-to-head" with electron beam in a storage ring. An attractive new way to increase the intensity of the gamma ray beam is to use a storage ring FEL instead of an external laser. The electron beam can interact directly with high intracavity peak power of the FEL that is naturally synchronized and aligned with it, so that the production rate of gamma rays will be greatly enhanced.

In the experiment, the storage ring was operated at an electron energy of 600 MeV. Recent development of UVSOR-FEL experiment is fully reported elsewhere [1]. For the usual FEL oscillation, the storage ring is operated in a two-bunch mode with equal spacing because the length of the optical cavity is a quarter of the storage ring circumference. For the Compton backscattering experiment, another bunch of electron beam (Compton bunch) for collision with the FEL photons is added between the two bunches (FEL bunch). Possible points for photon-electron collision are shown in fig. 1. There are totally 4 points expected. To produce gamma ray beam with well defined energy, a small angular dispersion of electron beam is necessary. Therefore we decided a point (D) where angular dispersion of the electron beam is the smallest, as the colliding point

In this experiment, the FEL was operated with wavelength of 451 nm and 264 nm and then maximum gamma ray energies were calculated to be 15.0 MeV and 25.2 MeV, respectively. For monochromatization of the gamma ray, leads collimators which limit the angle of the gamma rays within 0.16 and 0.43 mrad were used. The gamma ray spectra were measured with a 5"×5" NaI scintillation detector placed 9.4 m downstream from an electron-photon colliding point. The measured gamma ray spectra are shown in Fig. 2. Dotted lines in the figure are calculations obtained by a simulation including the angular dispersion of the electron beam. As shown in the figure, the measured spectra are much broader than calculated ones. It is because the detector's response functions for high energy gamma rays are broad. The detector's response functions for high energy gamma rays have been calculated using the Monte Carlo simulation code EGS4 [2]. High energy gamma rays

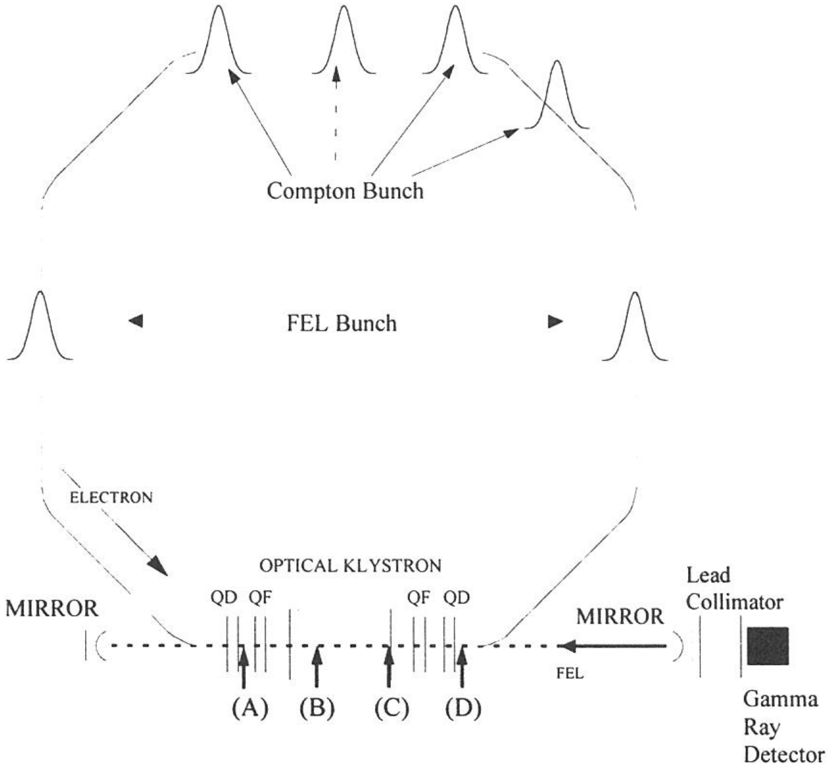

Figure 1. Schematic layout of the experimental set up for intracavity Compton backscattering. Possible points for photon-electron collision areindicated as (A) ~(D).

shower in a matter and do not deposit all of its energy in the detector lead relatively broad response functions. Spectra taking account of the detector response are also plotted as dashed line in the figure and agree with experimental ones except for low energy region which is probably affected by scattered gamma rays in a collimator. However the measured absolute intensities of the gamma ray beam were about one-half and 1.1 times of the calculated ones. We supposed that the difference comes from overestimation and underestimation of intracavity power.

During the preliminary experiment, we kept the intensity of the Compton bunch low to prevent too much counting rate of gamma rays for the detector. Furthermore the intensity of the FEL was also kept low by reducing the electrons of the FEL bunches near the threshold for lasing. In the UVSOR storage ring, the electron beam can be stored up to 50 mA/bunch. At this beam intensity, an average intracavity power is estimated to be 80 W for a wavelength of 460 nm, and the total production rate of gamma ray of $1.6\times10^8$/sec is therefore expected. By collimating the beam, an intensity of the monochromatic gamma ray with an energy resolution of 2% is estimated to be about $2\times10^6$/sec. These values are more than two order higher than those available in the existing facility using a conventional external laser in this energy region [3]. To utilize such intense gamma ray beam for applications, further development of the whole system will be necessary for radiation protection.

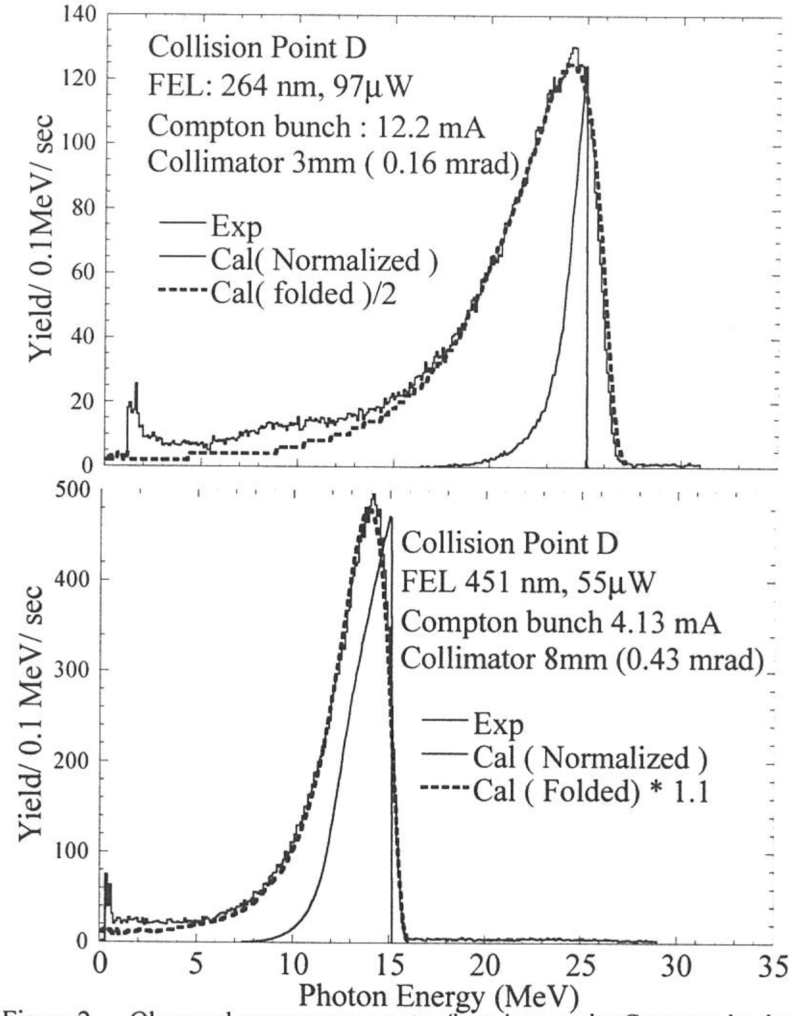

Figure 2. Observed gamma ray spectra from intracavity Compton backscattering under conditions, (a) FEL: 264 nm, 97 μW Compton bunch : 12.2 mA Collimator: 0.16 mrad (b) FEL: 451 nm, 55 μW Compton bunch: 4.13 mA Collimator: 0.43 mrad

References

[1] H. Hama et. al., Nucl. Instr. and Meth. A (in press).
[2] Nelson, H. Hirayama, and D. W. O. Rogers, "The EGS4 Code System", Stanford Linear Accelerator Report no. 265 (1985).
[3] H. Ohgaki et. al., Nucl. Instr. and Meth. A 375 (1996) 602.

(BL1A)

# Polarization Dependence of Ni 2*p* Photoabsorption of $K_2Ni(CN)_4{\cdot}H_2O$ and Ni Dimethylglyoxime

Takaki HATSUI, Yasutaka TAKATA*, Nobuhiro KOSUGI*,
Kaoru YAMAMOTO**, Toshihiko YOKOYAMA** and Toshiaki OHTA**

*The Graduate University for Advanced Studies, Myodaiji, Okazaki 444*
**Institute for Molecular Science, Myodaiji, Okazaki 444*
***The University of Tokyo, Bunkyo-ku, Tokyo 113*

Transition metal complexes with planar geometry have been extensively studied in order to elucidate their bonding nature. The metal *2p* photoabsorption is an electronic transition from 2p core electron to unoccupied orbital and gives the information on the low-lying unoccupied states. In the present study, we have measured polarized Ni 2p photoabsorption spectra of $K_2Ni(CN)_4{\cdot}H_2O$ and nickel dimethylglyoxime [ $Ni(Hdmg)_2$ ], which are both typical complexes with $\pi$-bonding. The observed polarization dependence was interpreted in terms of the symmetry and the character of unoccupied molecular orbitals (MO).

The crystal structure of $K_2Ni(CN)_4{\cdot}H_2O$ was determined by the X-ray diffraction analysis[2]. The planar $Ni(CN)_4^{2-}$ ions were roughly stacked within a dihedral angle of 25.6°. The molecular plane in a single crystal of $K_2Ni(CN)_4{\cdot}H_2O$ (10 mm x 10 mm x 2 mm) was determined by examining anisotropy of photoabsorption in the visible light region [1]. The needle-like crystals of $Ni(Hdmg)_2$ were aligned with each *c* axis to be parallel. The planar $Ni(Hdmg)_2$ complexes are stacked and the molecular plane is perpendicular to the *c* axis [3].The Ni 2p photoabsorption spectra were measured at the soft x-ray beamline BL1A by monitoring total electron yields. A pair of beryl crystals was used in a double crystal monochromator.

The polarized Ni 2p photoabsorption spectra of $K_2Ni(CN)_4{\cdot}H_2O$ are shown in Figure 1. The spectra have strong two bands in the Ni $2p_{3/2}$ region, which are characteristic of this sample. Other nickel compounds show only weak structures above the most intense peak [4-6]. Each unoccupied MO of $Ni(CN)_4^{2-}$ ion with $D_{4h}$ symmetry was characterized by examining whether the associated transition is allowed or not (Table 1). The x and y axes were defined as shown in the inset of Figure 1. Since the $b_{1g}$ orbital with the Ni $3d_{x2-y2}$ component has the lowest energy among the unoccupied MOs, we can assign peak **a** to the excitation to the $b_{1g}$ orbital. Peak **a** was not completely eliminated in **E // z** spectrum though the excitation to $b_{1g}$ orbital is a forbidden transition in this orientation. This is due to the incompleteness of molecular orientations. The second peak **b**, which showed the same polarization dependence as peak **a**, can be ascribed to the excitation to $b_{2g}$ orbital. Peak **c** is assigned to the excitation not to the $a_{1g}$ orbital but to the $e_g$ orbital from the following reasons. Firstly, the energy of the $e_g$ orbital would be close to that of $b_{2g}$. Secondly, the transition probability of the excitation to the $a_{1g}$ orbital is largely dependent on Ni $3d_{z2}$ component; therefore the intensity should be larger in **E // z** orientation.

The polarized Ni 2p photoabsorption spectra of $Ni(Hdmg)_2$ are shown in Figure 2. The spectra shows weak structures (peaks **c**, **d**) above the most intense peak. Distinct difference in the polarization dependence can be seen between this structure and the corresponding one observed for $K_2Ni(CN)_4{\cdot}H_2O$. Table 2 shows the allowed transitions to unoccupied MOs. $Ni(Hdmg)_2$ is supposed to have $D_{2h}$ symmetry and the coordinates are chosen as shown in the inset of Figure 2. Peak **a** is ascribed to the excitation to the $b_{1g}$ orbital because the polarization dependence of this transition is uniquely consistent with peak **a**. For this sample, there are two kinds of $b_{1g}$ orbitals. Since the Hdmg ligand does not have $\pi^*$ orbitals in the molecular plane, peak **a** is assigned to the $b_{1g}$ orbital with Ni $3d_{xy}$* and ligand $\sigma$ character. Peak **d** can not be assigned to the transition to the $b_{2g}$ orbital because the intensity of this transition would not be stronger in **E // z** orientation. On the contrary, the excitation to $a_g$ orbital would be stronger in the **E // z** orientation as discussed in the excitation to the $a_{1g}$ orbital for $Ni(CN)_4^{2-}$. Consequently, peak **d** can be ascribed to the transition to the $a_g$ orbital.

Finally, we would like to thank Dr. Masaaki Tomura for analyzing the structure of $K_2Ni(CN)_4{\cdot}H_2O$.

## References

[1] C. J. Ballhousen, N.Bjerrum, R. Dingle, Klaas Eriks, and C. R. Hare, *Inorg. Chem.* **4**, 514 (1965)
[2] The crystal structure was determined by R-AXIS-4 (Rigaku, Co.) spectrometer and obtained parameters were as follows: $P2_1/a$ Z=20, R=0.118, a=15.493(3) Å, b=15.919(4) Å, c=18.636(3) Å, b=107.26(1)°, V=4389(1)$Å^3$
[3] D.E.Williams, G. Wohlauer, and R. E. Rundle, *J. Am. Chem. Soc.*, **81**, 755 (1959)
[4] G. van der Laan, B. T. Thole, and G. A. Sawatzky, M. Verdaguaer, *Phys. Rev. B*, **37**, 6587 (1988)
[5] J. van Elp et. al. *J. Am. Chem. Soc.* **116**, 1918, (1994)
[6] G van der Laan, J. Zaanen, G. A. Sawatzky, R. Karnatak, and J.-M. Esteva, *Phys. Rev. B*, **33**, 4253 (1986)

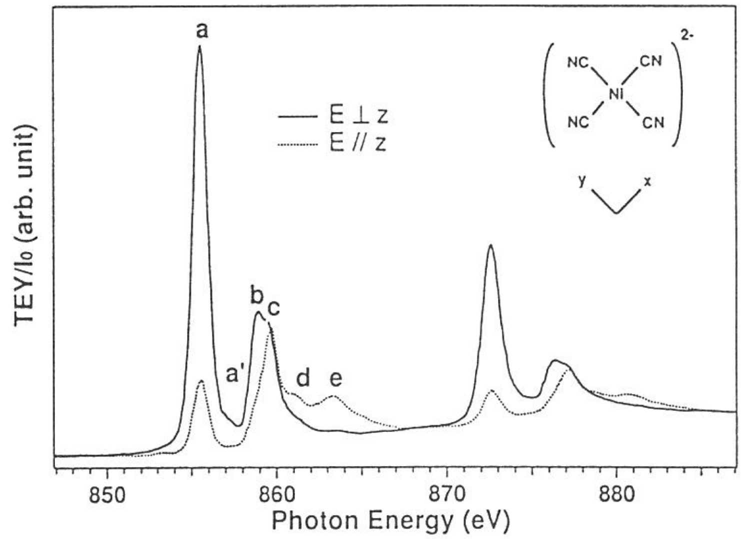

Figure 1. Polarized Ni 2p photoabsorption spectra of $K_2Ni(CN)_4 \cdot H_2O$

Table 1 Polarization dependence of the excitations to unoccupied MO in $K_2Ni(CN)_4 \cdot H_2O$ ($D_{4h}$)

| Symmetry of unoccupied MO | Character | Transition<br>**E⊥z** | <br>**E // z** | Assignment |
|---|---|---|---|---|
| $b_{1g}$ | Ni $3d_{x2-y2}$* ligand σ | allowed ($2p_{x,y}$)[a] | forbidden | a |
| $b_{2g}$ | Ni $3d_{xy}$ ligand π* | allowed ($2p_{x,y}$) | forbidden | b |
| $e_g$ | Ni $3d_{xz}$ ligand π* | allowed ($2p_z$) | allowed ($2p_x$) | c |
|  | Ni $3d_{yz}$ ligand π* | allowed ($2p_z$) | allowed ($2p_y$) | c |
| $a_{1g}$ | Ni 4s* $3d_{z2}$ ligand σ | allowed ($2p_z$) | allowed ($2p_{x,y}$) | ? |

a) The orbital noted in ( ) indicates the electron excited by Ni 2p photoabsorption.

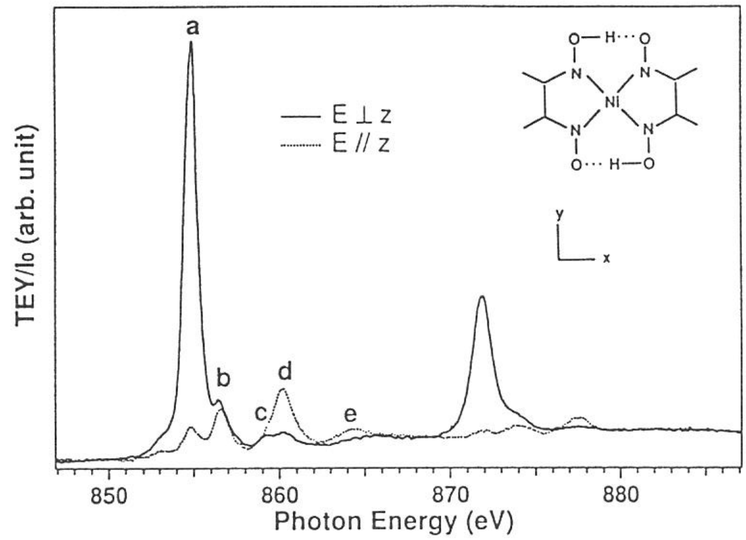

Figure 2. Polarized Ni 2p photoabsorption spectra of $Ni(Hdmg)_2$

Table 2 Polarization dependence of the excitations to unoccupied MO in $Ni(Hdmg)_2$ ($D_{2h}$)

| Symmetry of unoccupied MO | Character | Transition<br>**E⊥z** | <br>**E // z** | Assignment |
|---|---|---|---|---|
| $b_{1g}$ | Ni $3d_{xy}$* ligand σ | allowed ($2p_{x,y}$) | forbidden | a |
| $a_g$ | Ni $3d_{x2-y2}$ ligand π* | allowed ($2p_{x,y}$) | forbidden | –[a] |
| $b_{2g}$ | Ni $3d_{xz}$ ligand π* | allowed ($2p_z$) | allowed ($2p_x$) | b |
| $b_{3g}$ | Ni $3d_{yz}$ ligand π* | allowed ($2p_z$) | allowed ($2p_y$) | ? |
| $a_g$ | Ni 4s* $3d_{z2}$ ligand σ | allowed ($2p_z$) | allowed ($2p_{x,y}$) | d |

a) This transition would not be observed because Hdmg ligand does not have the π* orbital with $a_g$ symmetry.

(BL1A)

# Resonant Photoelectron Spectra of Nickel Dimethylglyoxime Following the Ni 2p Photoabsorption

Yasutaka TAKATA, Takaki HATSUI*, Kaoru YAMAMOTO**, Toshihiko YOKOYAMA**,
Toshiaki OHTA**, and Nobuhiro KOSUGI

*Institute for Molecular Science, Myodaiji, Okazaki 444*
**The Graduate University for Advanced Studies, Myodaiji, Okazaki 444*
***The University of Tokyo, Bunkyo-ku, Tokyo 113*

Recently, resonant photoelectron spectroscopic studies have been performed for various systems to investigate electronic structure of core-excited states and their deexcitation mechanism. We have reported the Ni 3s and 3p photoelectron spectra of NiO [1] and $K_2Ni(CN)_4$ [2] in the photon energy region of the Ni 2p absorption. For $K_2Ni(CN)_4$, all the peaks enhanced by resonant excitation are attributable to the spectator Auger transitions, where the final ionic states are correlation satellite states with a Ni 3s or 3p hole and are weakly allowed or forbidden in the non-resonant spectra. The kinetic energies shift to the lower energy linearly with increase of the excitation energy. In the present study we have measured resonant photoelectron spectra of nickel dimethylglyoxime [$Ni(Hdmg)_2$].

The experiments were performed at the soft x-ray beam line BL1A. A pair of beryl ($10\bar{1}0$) crystal was used as a crystal monochromator and the band pass energy was 0.6 eV at the Ni 2p edge. $Ni(Hdmg)_2$ was evaporated on a Au plate about 1000 Å. The Ni 2p photoabsorption spectra were measured by monitoring the total electron yield. A hemispherical electron energy analyzer (SCIENTA, SES-200) was used for the photoelectron measurement. The pass energy of the analyzer was set to 300 eV and the energy resolution was about 0.3 eV. The total energy resolution of photoelectron spectra was about 0.7 eV.

Figure 1 shows the Ni 2p photoabsorption spectrum of the evaporated $Ni(Hdmg)_2$ samples. Figure 2 shows the resonant photoelectron spectra in the Ni 3p and 3s region measured at the photon energy marked in the photoabsorption spectrum (Fig. 1). The intensity of the resonant photoelectron spectra is normalized using the C 1s photoelectron peak. The normal Auger spectrum was measured at the photon energy of 1387 eV. The Ni 3p and 3s photoelectron peaks labeled as (*), whose binding energies are constant, show no resonance enhancement. On the other hand, the peaks (a, b), (c), and (d, e) enhanced by resonant photoabsorption have higher kinetic energy in comparison with the normal Auger spectrum and their final ionic states correspond to the $\underline{3p}\underline{3d}e$, $\underline{3s}\underline{3d}e$ and $\underline{3p}\underline{3p}e$ shake-up like states, respectively, where the under bar denotes single hole and the symbols $e$ represents the excited electron.

The kinetic energies of the most intense peak (b) and $\underline{3p}\underline{3d}$ normal Auger peak are plotted in Fig. 3 as a function of photon energy. In the case of $K_2Ni(CN)_4$, the data points can be fitted by a line with the slope of -0.55±0.05 indicating the photoexcited electron behaves like a hydrogenic exciton. In the present case, the data points can not be fitted by a line and the shift can not be interpreted by the simple hydrogenic model. This indicate that $Ni(Hdmg)_2$ is not so ionic as $K_2Ni(CN)_4$. $Ni(Hdmg)_2$ is a square-planer complex as same as $K_2Ni(CN)_4$, but has different metal-ligand and intermolecular interaction.

Figure 4 shows the resonant photoelectron spectra in the valence region. In contrast to the Ni 3p and 3s core spectra, the peak labeled as (#) observed in the off-resonant spectrum (0) is enhanced by the resonant excitation and is attributable to the $\underline{3d}$ ionic state. Peak (f) is also enhanced and the kinetic energy shift to the lower energy as converging to the $\underline{3d}\underline{3d}$ normal Auger final state and is ascribed to the $\underline{3d}\underline{3d}e$ shake-up like state. This peak shows nearly the same kinetic energy shift as that of peak (b) shown in Fig. 3.

## References

[1]M. Nakamura, Y. Takata, and N. Kosugi, J.Electron.Spectrosc. **78** (1996) 115.

[2]Y. Takata, M. Nakamura, and N.Kosugi, UVSOR Active. Rep. (1995) 50. Y. Takata, M. Nakamura, and N.Kosugi, to be published in J. de Physique IV.

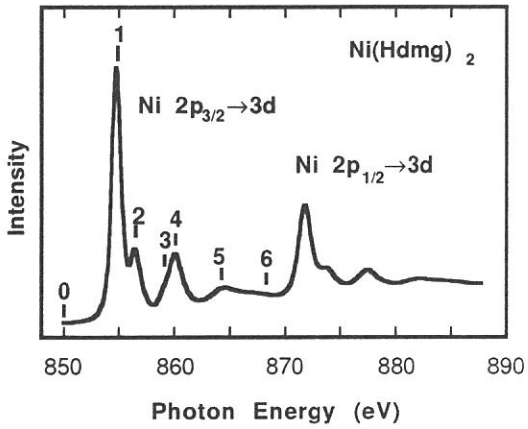

Fig. 1. Ni 2p→3d absorption spectrum of Ni(Hdmg)$_2$.

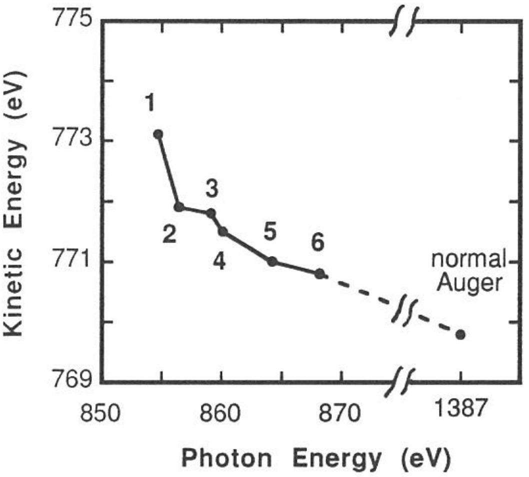

Fig. 3. Kinetic energy variation of peak (b) as a function of the excitation energy.

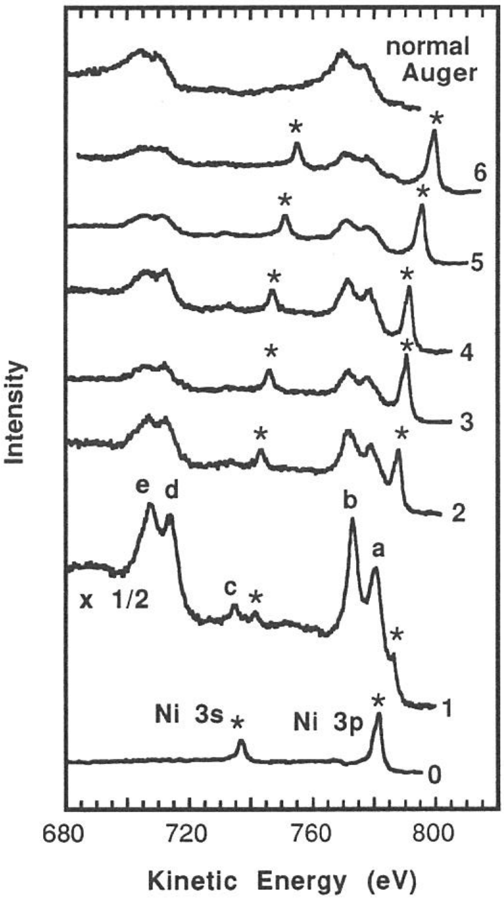

Fig. 2. Resonant photoelectron spectra of Ni(Hdmg)$_2$ in the Ni 3p, 3s region measured at the photon energies marked in Fig. 1.

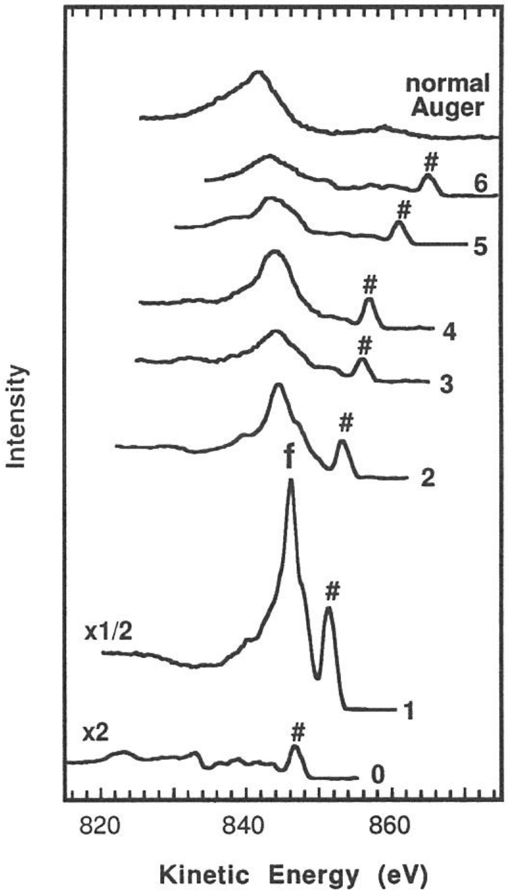

Fig. 4. Resonant photoelectron spectra of Ni(Hdmg)$_2$ in the valence region measured at the photon energies marked in Fig. 1.

(BL1B)

# Vacuum UV Photoluminescence of CsCl and CsBr at the RoomTemperature and 80K.

Arisato Ejiri, Kunihiro Arakaki, and Theeraphong Inthanonte

Science Education Devision, College of Education, University of the Ryukyus, Nishihara, Okinawa 903-01.

Recently, a complemental relation ¹⁾ between the vacuum UV-excited-luminescence and the photoelectric total yield in alkali halides ²⁾ and alkali earth fluorides ³⁾ have been attracted some interests as a photoelectron dynamics including Auger free luminescence ( cross luminescence) related to the decay process of the outer most core hole. Auger free luminescence (AFL) in CsCl and CsBr has been studied by Itoh et al ⁴⁾ but the temperature dependences of the excitation spectra for the luminescence have not well known yet.

In the present work, AFL as well as its excitation spectra in CsCl and CsBr is studied at the room temperature and 80 K in connection with the photoelectric yield in these halides. ⁵⁾

A 1m Seya-Namioka monochromator and a Spex spectrometer (Jobin Ybon) were used at BL-1B. Measurements were performed in the photon energy range of 8-40 eV for the excitation and 2-6. 8 eV for the luminescence. Samples used were single crystal slabs of these halides. ⁶⁾ The luminescence spectra were not corrected for the spectral efficiency of the spectrometer and the excitaion spectra were normalized by the spectral output of the monochromator .

In Fig. 1, observed luminescence spectra in CsCl and CsBr excited at 20 eV for the room temperature are shown. On the CsCl spectrum, three bands at 3. 2 eV, 4. 5 eV and 5. 2 eV are appeared. The 4. 5 and 5. 2 eV bands are known as AFL. ⁴⁾ Whereas, on the CsBr, a 3. 2 eV band and a weak 4. 9 eV band are observed. The 4. 9 eV band is known as AFL. ⁴⁾

In Fig. 2, observed excitation spectra of the CsCl 4. 5 eV AFL band at the room temperature and 80 K are shown. The abrupt rise at 14. 2 eV indicates the threshold energy corresponding to the transition from the Cs $^{+}$5p core level to the conduction band and agrees well with Itoh et al s data at the room temperature. ⁴⁾ The intensities near the threshold are common in the both spectra, however, strong increasing of the intensity is observed in the photon energy range of 17-28 eV upon the cooling. This increasing can be explained in terms of increasing of STE component upon the cooling. This temperature effect has not observed so far but corresponds to the decreasing of photoelectric emission. ⁵⁾

In Fig. 3 are shown the observed excitation spectra of the 4. 9 eV CsBr AFL band at the room temperature and 80 K. In the case of CsBr, situations are much different from the CsCl case. The excitation spectrum for the room temperature does not show the abrupt rise at the threshold and is weak, however, that for 80 K clearly shows the threshold rise and is intense. The behavior of the excitation spectrum at the room temperature is different from Itoh et al s results. They have obtained the excitation spectrum with the clear threshold rise. ⁴⁾

However, the present results reveal that the probability of AFL in CsBr much increases at the low temperature, because the band gap energy should overcome the energy between the top of valece band and the top of the core band at the low temperature. This situation can be seen in the decrease of Auger enhancement in photoelectric emission [2-3] at the low temperature in a sence of the complemental relation. [5]

## References

1) A. Ejiri, S. Kubota, A. Hatano, and K. Arakaki; J. Elec. Spec. Rel. Phen. 79 (1996) 151.
2) A. Ejiri, A. Hatano, and K. Nakagawa; J. Phys. Soc. Jpn. 63 (1994) 314.
3) A. Ejiri, S. Kubota, A. Hatano, and K. Yahagi; J. Phys. Soc. Jpn. 64 (1995) 1484.
4) M. Itoh, S. Kubota, J. Ruan, and S. Hashimoto; Rev. Solid State Science 4 (1990) 467.
5) A. Ejiri, K. Arakaki, S. Kobota; Abst. Meet. Phys. Soc. Jpn. 2 (1996. Oct.) 244.
6) Supplied by Profs. Kubota and Hashimoto, made from Merk Super Grade.

Fig. 1 Luminescence spectra in CsCl and CsBr excited at 20 eV for the room temperature.

Fig. 2 Excitatin spectra of 4.5 eV band in CsCl at the room temperature and 80 K.

Fig. 3 Excitation spectra of 4.9 eV band in CsBr at the room temperature and 80 K.

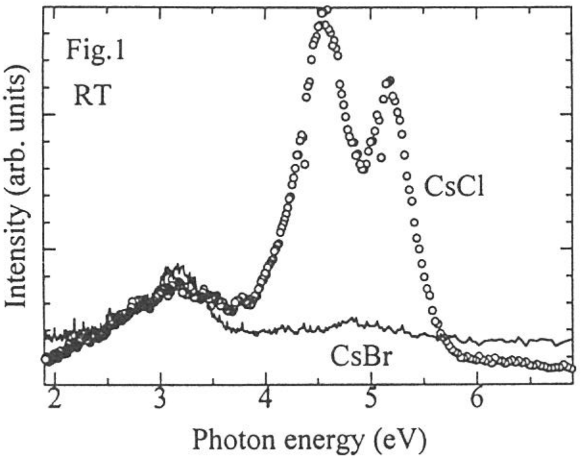

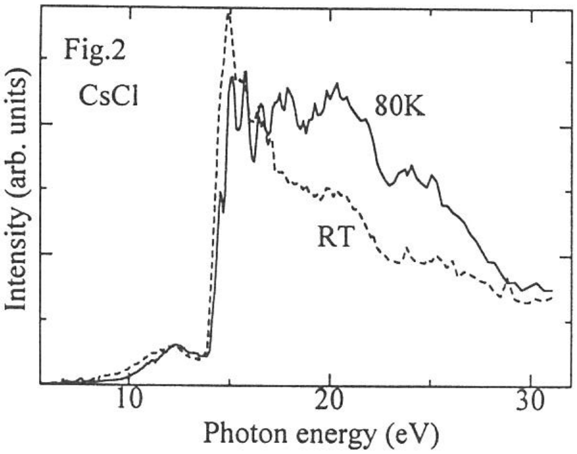

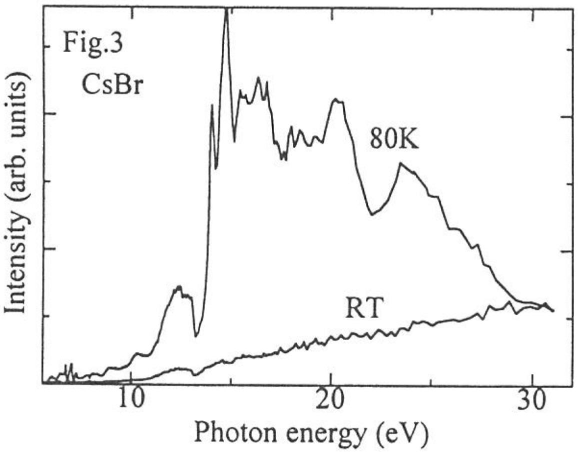

(BL1B)

# Synchrotron Radiation and Laser Combined Two-Photon Spectroscopy of $BaF_2$

Toru TSUJIBAYASHI[a], Masayuki WATANABE[b], Osamu ARIMOTO[c], Shigeki FUJIWARA[c], Minoru ITOH[d],
Syunsuke NAKANISHI[e], Hiroshi ITOH[e], Shuji ASAKA[f], and Masao KAMADA[g]

[a]*Department of Physics, Osaka Dental University, Hirakata 573*
[b]*Department of Fundamental Sciences, Kyoto University, Kyoto 606-01*
[c]*Department of Physics, Okayama University, Okayama 700*
[d]*Department of Electrical & Electronic Engineering, Shinshu University, Nagano 380*
[e]*Department of Physics, Kagawa University, Takamatsu 760*
[f]*Equipment Development Center, Institute for Molecular Science, Okazaki 444*
[g]*UVSOR Facility, Institute for Molecular Science, Okazaki 444*

We report a novel technique of two-photon spectroscopy using synchrotron radiation (SR) and lasers in this paper. Two-photon spectroscopy is a powerful tool of optical measurements because the parity selection rule is different from that for one-photon absorption. In addition, the polarization selection rule is available to identify the symmetry of the relevant states experimentally [1]. However, the two-photon spectroscopy has been utilized by using intense lights from high-power lasers, since the probability of the two-photon absorption is much lower than that of one-photon absorption. Consequently, the application of the two-photon spectroscopy has been limited in narrow spectral range due to the restriction of laser wavelengths. On the other hand, SR is a fascinating light source because of its wide photon energy distribution ranging from X-ray region to infrared region. If we use SR for the two-photon spectroscopy, we can get fruitful information of the electronic structures of many materials. However, SR has not been used for two-photon spectroscopy because of its weak intensity. We should mention the pioneering work of an Italian group [2]. They studied two-photon absorption of excitons in alkali bromides and chlorides measuring the transmission difference of SR beam under irradiation of strong pulses of a Nd:YAG laser operating at ~10Hz. We have conducted two-photon experiments by using another technique which enables the detection of a weak signal in combination with high-repetition SR pulses (90 MHz at UVSOR) and low-repetition laser pulses (~10 Hz). Our technique is a kind of zero-methods and is expected to be more reliable and sensitive than the Italian group's method.

In the following we report for the first time the two-photon spectroscopy of the valence exciton in $BaF_2$ measured by our new technique. The band-gap of $BaF_2$ is about 10.5 eV which corresponds to the transition from the 2p state of $F^-$ to the 6s and 5d states of $Ba^{2+}$ [3]. The luminescence due to self-trapped excitons (STE's) is observed at 4.1 eV. We detected the STE luminescence to monitor the two-photon absorption. The decay time of the luminescence is about 0.6μs. Detecting the luminescence in place of the transmission difference is the main feature of our experiment. A single crystal of $BaF_2$ was obtained from Horiba Ltd. A cleaved specimen was polished on a water-impregnated cloth. Figure 1 shows the experimental configuration. The SR beam, dispersed through a 1-m Seya-Namioka-type monochromator, irradiated the sample under the normal incidence. The second harmonic light of a Nd:YAG laser (2.33 eV) irradiated the sample in the direction opposite to that of the SR beam. The energy of the laser pulse was attenuated down to 5.2 mJ to avoid the damage of the sample. The polarization direction of the laser beam was perpendicular to that of the SR beam. The luminescence was detected by a MCP photomultiplier in the direction perpendicular to the both beams. The signal pulse was led to a counter. We

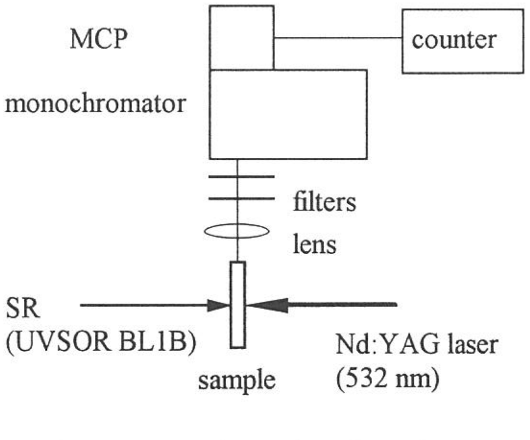

Fig. 1. Experimental configuration.

used filters and a monochromator to eliminate the scattering of the excitation lights. The sample was kept at 295 K. For the simultaneous incidence of the laser pulse and the SR pulse to the sample, the laser was triggered by the master oscillator of the SR with a divider which lowered the frequency of the pulses down to 14 Hz. The time duration of the laser pulse was 5 ns.

We show two-photon excitation spectrum by circles in Fig. 2. That is, the intensity of the STE luminescence is depicted as a function of the sum of the photon energy of the SR beam and that of the laser beam. The signal was accumulated for 10 minutes to obtain each data point. The luminescence was not observed when either of the beams was missing. The intensity of the luminescence arises at 9.2 eV to reach a plateau at 9.5 eV. Then it rises again at 10.0 eV and continues to increase toward 10.5 eV. The scanning range is limited to 11 eV because one-photon absorption obscures the two-photon absorption process. The one-photon excitation spectrum of the STE luminescence is shown by a solid line in the figure for comparison. Each spectrum is normalized at the maximum. The band around 9.5 eV in the one-photon spectrum is attributed to the 1S valence exciton. The two-photon excitation spectrum is quite different from the one-photon excitation spectrum. The rise at 10 eV may be due to the 2P valence exciton since the rise locates on the high-energy side of the 1S exciton band and the 2P exciton state is the lowest one among the states allowed by the parity selection rule. The location of the plateau coincides with that of the 1S exciton band in the one-photon excitation spectrum. According to the parity selection rule, the transition to the 1S exciton state is forbidden for two-photon absorption. Some phonon effects or contribution of other electronic states should be considered to explain the plateau at 9.5 eV.

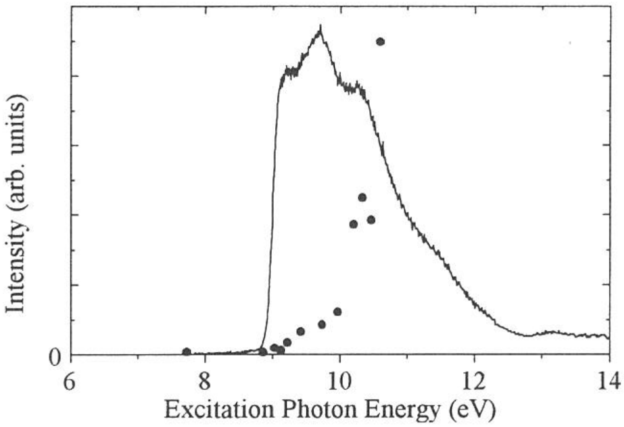

Fig. 2. Two-photon excitation spectrum of $BaF_2$ at 295 K is shown by circles. One-photon excitation spectrum is also shown for comparison by a solid line.

## References

[1] M. Inoue and Y. Toyozawa: J. Phys. Soc. Jpn. **20** (1965) 363.

[2] R. Pizzoferrato, M. Casalboni, R. Francini, U. M. Grassano, F. Antonangeli, M. Piacentini, N. Zema, and F. Bassani: Europhys. Lett. **2** (1986) 571; M. Casalboni, C. Cianci, R. Francini, U. M. Grassano, M. Piacentini, and N. Zema: Phys. Rev. B **44** (1991) 6504.

[3] T. Tomiki and T. Miyata: J. Phys. Soc. Jpn. **27** (1969) 658.

(BL1B)

# Reflection spectra of $Ca_{1-x}Y_xTiO_3$ single crystals

K.Ueda, H.Yanagi, M.Mizuguchi and H.Kawazoe
Materials and Structures Laboratory, Tokyo Institute of Technology
4259 Nagatsuta, Midori-ku, Yokohama 226, Japan

N.Ueda and H.Hosono
Institute for Molecular Science
Myodaiji, Okazaki 444, Japan

Reflection measurements in the UV region and photoemission measurements are the effective methods for experimental estimation of the electronic structure of materials. In contrast to photoemission measurements, reflection measurements are relatively easy due to the insensitivity to the surface state of the samples. Dielectric functions can be calculated from the reflection spectra by the K-K transformation technique and the spectra give some pieces of information on electronic transitions in materials.

In order to observe the electronic structure and its changes upon doping, reflection spectra of $Ca_{1-x}Y_xTiO_3$ ( x=0, $10^{-4}$, $10^{-3}$, $10^{-2}$ ) crystals were measured at room temperature and liquid nitrogen temperature at BL1B in UVSOR. Single crystals were grown by the FZ method using an infrared radiation furnace. The crystals were cut in the shape of a plate and the surfaces were polished using diamond slurry. The plate shaped single crystals were set so that the incident angle of light was about 10 degrees in order to simulate the normal incident reflection. The direction of the incident light to $Ca_{1-x}Y_xTiO_3$ crystals was normal to (100) planes. The photon energy was scanned from 2.0 to 40eV with the resolution smaller than 0. 1eV using the two gratings. Some corrections were introduced to the as-measured spectra because those spectra included the reflection from the back surface of the crystal in the transparent region. The corrections were done in the way that the spectra were smoothly connected at about 4eV to the reflection spectra which were carefully measured by the conventional spectrometer.

Reflection spectra of $Ca_{1-x}Y_xTiO_3$ are shown in figure 1. The crystal structure of $CaTiO_3$ is known as $GdFeO_3$ type derived by distorting the ideal cubic perovskite structure. Accordingly, anisotropy in the crystal structure is small and no marked difference in the spectra was observed within the two polarized directions of the incident light, (i) and (ii). Moreover, Y substitution in $CaTiO_3$ did not have any notable influence on the spectra probably due to the small concentration of the dopant.

Each of the spectra was roughly divided into three parts, from 3.0 to 6.0-7.0eV, from 6.0-7.0 to 15.0eV and higher than 15.0eV. Considering the orbitals of the component elements, it is supposed that the first part is related to an electronic transition from O2p band to Ti3d band and the second one from O2p band to Ti4s or Ca4s band and the last one from shallow-core bands to the conduction bands. The shallow-core bands mean O2s and Ca3p bands whose binding energies are about 22eV and 25eV, respectively. These assignments here are similar to the one reported for $SrTiO_3$1) and $BaTiO_3$2)

The results of the K-K transformation in $CaTiO_3$ are shown in figure 2. Several methods in the K-K transformation were tried to approximate the extrapolation of the spectra. All transformed spectra were slightly different in the ordinate scale in higher energy region but they were quite different in the lower energy region than the fundamental absorption edge. The Roessler's method3) was adopted for the K-K transformation to obtain reasonable results in the lower energy region. Since the structure of the extinction coefficient spectrum is very similar to the reflectance spectrum, the rough assignments of the structure in the spectra would be the same as described above. The theoretical support such as energy band calculation will be needed for more detailed discussions.

Reference

1)D. Bauerle, W.Braun, V. Saile, G. Sprussel and E.E. Koch, Z. Physik B, 29 (1978) 179

2)M. Cardona, Phys.Rev., 140 (1965) A651

3)D.M. Roessler, Brit. J. Appl. Phys., 17 (1966) 1313

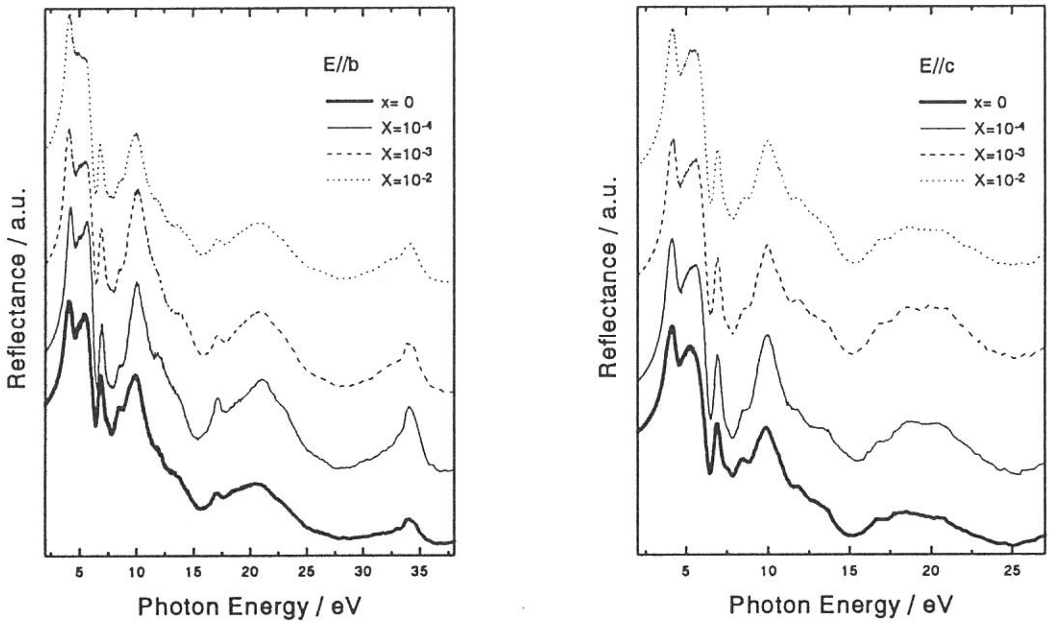

(i) (ii)

Fig. 1. Reflectance spectra of $Ca_{1-x}Y_x TiO_3$ at liquid $N_2$ temperature under an electric field parallel to (i) b axis and (ii) c axis.

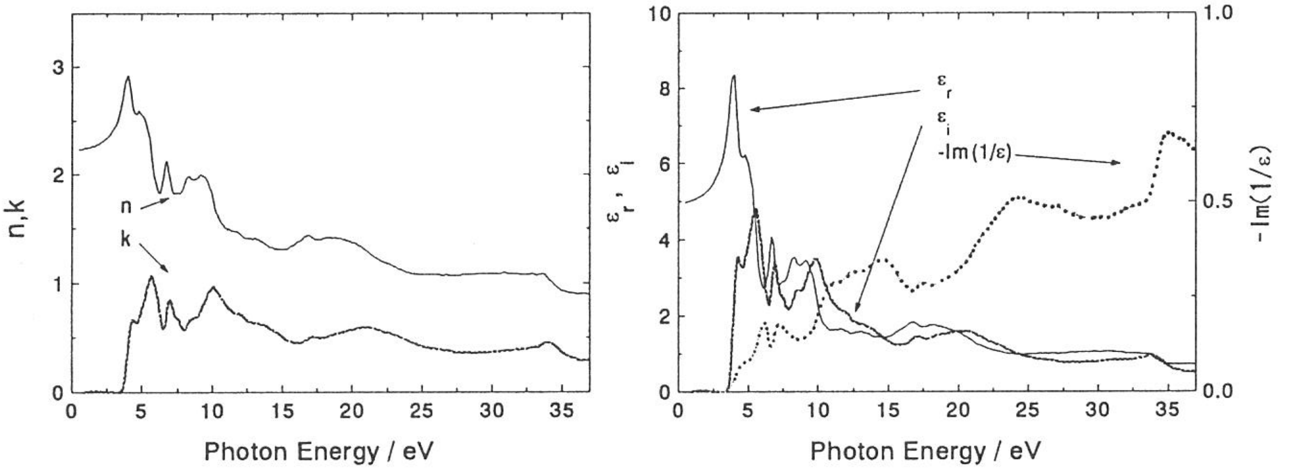

Fig. 2. n, k, $\varepsilon_r$, $\varepsilon_i$, $-\mathrm{Im}(1/\varepsilon)$ vs. photon energy in $CaTiO_3$ calculated by the K-K transformation technique.

**(BL 1B)**

# Luminescence Study in $PbCl_{2(1-x)}$-$PbBr_{2x}$ Mixed Crystals

Mamoru KITAURA and Hideyuki NAKAGAWA

*Department of Electronics Engineering, Faculty of Engineering, Fukui University, Fukui, 910*

The excitonic absorption structures in lead halides crystals have been connected to intra-ionic transitions in a $Pb^{2+}$ ion (cationic exciton model) [1]. Self-trapped excitons (STE's) in these systems have been, therefore, attributed to the relaxed excited states of the $Pb^{2+}$ ion (cationic STE) [2]. Recently, we reported that two kinds of STE's coexist in $PbCl_2$ and $PbBr_2$ crystals; the one is the monomer type-STE localized at the $Pb^{2+}$ ion, which is responsible for the UV ($PbCl_2$) and B ($PbBr_2$) emission, and the other is the dimer type-STE associated with the $(Pb_2)^{3+}$ self-trapped electron (STEL) center, giving rise to the BG emission [3][4].

In the previous studies based on the cationic STE model, the roles of halogen ions were not taken into consideration. In the present study, the STE luminescence in $PbCl_2$-$PbBr_2$ mixed crystals has been investigated in order to make it clear how the halogen ions contribute to the self-trapping processes of the excitons. Excitation was made with SR light pulses dispersed by a 1m Seya-Namioka type monochromator.

Figure 1 and 2 represent emission and excitation spectra of $PbCl_{2(1-x)}$-$PbBr_{2x}$ mixed crystals at 10 K, where $x$ indicates the mole fraction of $PbBr_2$ in the solid solution. Intensity of each spectrum shown in Fig. 1 and 2 is normalized to unity at the maximum. Excitation was made in the low energy part of the lowest exciton absorption band, whose energy positions are indicated in the right hand side of Fig. 1. The emission spectrum of (a) $PbCl_2$ and (g) $PbBr_2$ exhibits a prominent band, namely, the UV and B emission band, the peak positions and halfwidths of which are in good agreement with those reported previously [5][6]. The features of the UV and B emission are summarized as follows: they are excited in the exciton absorption band and decrease their intensity rapidly above 20 K. In the $PbCl_2$:Br (0.01mol%) crystal, an intense emission band is observed at 3.20 eV under the excitation with 4.28 eV light. The 3.20 eV emission band is excited only in the energy region around 4.28 eV, which locates below the exciton absorption band of the host $PbCl_2$ crystal. It is supposed that a localized exciton absorption band due to a $Br^-$ ion is hidden in the energy region around 4.28 eV. As $x$ increases, the 3.20 eV emission band disappears rapidly and is replaced by the 2.95 eV emission band which is observed in the $x < 0.5$ region. In the $x$=0.3 crystal, a new emission band is observed around 2.75 eV as the photon energy of excitation light is shifted to the lower energy side. The 2.75 eV emission band is observed dominantly in the $x > 0.5$ crystals. The peak position of the 2.75 eV band is just the same as that of the B emission band in $PbBr_2$. The excitation spectrum for the 2.75eV emission exhibits a prominent peak at 4.01 eV in the $x$=0.3 crystal, which turns to the dip of the excitation spectrum for the B-emission in $PbBr_2$ with increase in $x$. On the other hand, we can see a broad emission band around 2 eV in the mixed crystals, the origin of which is not clear at present.

Beside the UV emission band (at 3.76eV) originating from STE in $PbCl_2$, three emission bands are found to appear at 3.20 eV ($0.01< x< 0.1$), 2.95 eV ($0.01< x < 0.5$) and 2.75 eV ($0.1< x$) in the $PbCl_{2(1-x)}$-$PbBr_{2x}$ mixed crystals. It should be noted that these four emission bands coexist one other in the region of $x < 0.5$; the relative intensities are changed with $x$ and with the excitation energy as depicted in Fig.1(d). These results indicate that these emission bands are related not only to the $Pb^{2+}$ ion but also halogen ions. Consequently, it is obvious that the relevant electronic states of the STE in $PbCl_2$ and $PbBr_2$ are not equivalent to the relaxed excited states of a $Pb^{2+}$ ion.

Optically created excitons in lead halides correspond to an excited $Pb^{2+}$ ion having the $(6s)(6p)$ electronic configuration. A hole created on the $Pb^{2+}$ 6s orbital may remove into the nearest neighbor halogen sites, and the $(6s)(6p)$ electronic configuration would easily passes into the $(6s)^2(6p)$ one. This configuration is expected to be stabilized by making bonds through $(sp^2)$ hybridization, which form a nearly coplanar molecule comprising a central $Pb^+$ ion and three ligand halogen ions, namely, the $Pb^+(X^-)_3$ center. In the $PbCl_2$ crystal structure, there are two non-equivalent halogen sites which possess 4 or 5 $Pb^{2+}$ ions as ligands. Here, we call them site 4- or 5-halogens. It has been already known that only the site 5-halogens are selectively substituted by $Br^-$ ions as $x$ increases from 0 to 0.5 [7]. As shown in Fig. 1, prototype of the B emission band in $PbBr_2$ is formed in the $x$=0.3 crystal, indicating that only the $Br^-$ ion substituting the site 5-$Cl^-$ ion are related to the STE's in $PbBr_2$. Therefore, we propose the $[Pb^+(5\ \text{site-}X^-)_3 + \text{hole}]$ structural model for the STE in $PbX_2$ (X=Cl, Br).

## [REFERENCES]

[1] K. Wada: Sci. of Light **26** (1977) 77.
[2] W.C. De Gruijter: J. Solid State Chem. **6** (1973) 151.
[3] M. Kitaura et al.: UVSOR Activity Report 1994, p.32.
[4] M. Kitaura and H. Nakagawa: J. Electron Spectrosc. and Relat. Phenom. **79** (1996) 171.
[5] G.G. Liidya and V.G. Plekhanov: Opt. Spectrosk. **36** (1974) 945.
[6] V.G. Plekhanov: Opt. Spectrosk. **39** (1975) 980.
[7] M. Lumbreras et al.: Soli State Ionics **16** (1985) 195.

## [Figure captions]

Fig.1: Emission spectra of $PbCl_{2(1-x)}$-$PbBr_{2x}$ mixed crystals observed at 10 K, where $x$ indicates the mole fraction of $PbBr_2$ in the solid solution. Excitation was made in the low energy part of the lowest exciton absorption band.

Fig. 2: Excitation spectra of $PbCl_{2(1-x)}$-$PbBr_{2x}$ mixed crystals observed at 10 K.

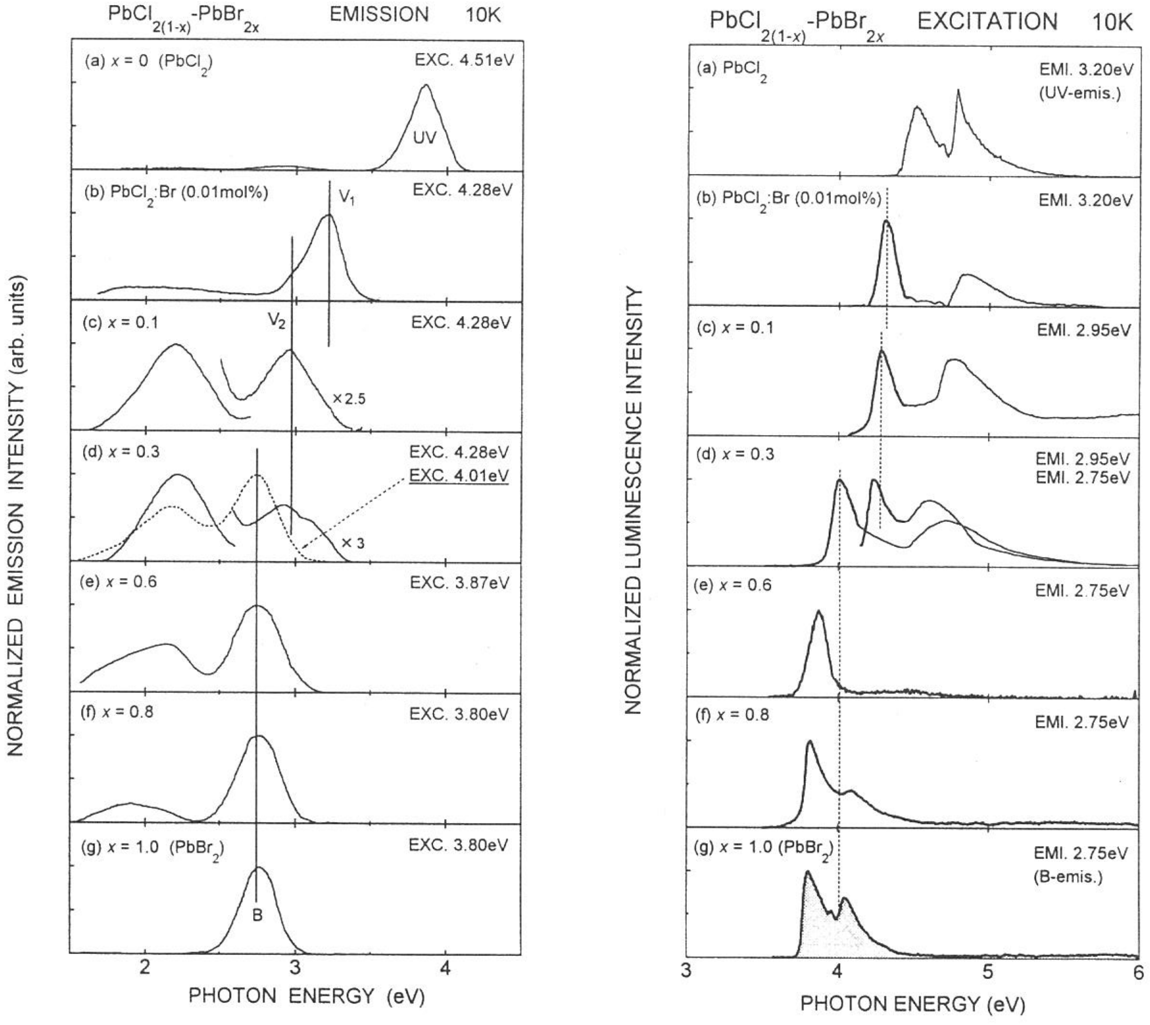

Figure 1

(BL1B)

# Photoluminescence from fluorinated fullerene $C_{60}F_x$ ($x \leq 48$) thin films

I. AKIMOTO[a], J. AZUMA[a], M. SHIRAI[a], K. KAN'NO[a], F. OKINO[b], H. TOUHARA[b], M. KAMADA[c]

[a] Department of Physics, Kyoto University, Sakyo, Kyoto 606, Japan
[b] Department of Chemistry, Faculty of Textile Science and Engineering, Shinshu University, Ueda 386, Japan
[c] Institute for Molecular Science, Myodaiji, Okazaki 444, Japan

Fluorinated fullerenes $C_{60}F_x$ ($x \leq 48$) are attractive compounds of a novel wide-band-gap insulator with high symmetric carbon-based molecules. Synthesis and characterization of fluorinated fullerenes $C_{60}F_x$ ($x \leq 48$) have been performed by several groups [1]. Various compositions $x$ of carbon-fluorine (C-F) bonds can be created by reacting C=C $\pi$ bonds of $C_{60}$ with $F_2$ molecules [2,3,4,5]. Very little, however, has been known about optical properties and photo-induced phenomena of these materials. In the present work, optical absorption, luminescence and excitation spectra of $C_{60}F_x$ ($x$=42, 48) films have been observed with vacuum ultra-violet light from BL1B of UVSOR. Films were prepared on quartz substrates by evaporating and spin-coating from the powder solved into $C_6F_6$ solvent.

Optical spectra of the $C_{60}F_{42}$ spin-coated film at 6K are shown in Fig. 1. A maximum of absorption is located at 6.4 eV with shoulders at ~ 5.8 eV and ~ 5 eV. Features of the emission spectra were essentially the same for different excitations, as far as excitation energy was larger than 6 eV. A typical emission spectrum consists of two broad bands peaked at 2.4 eV and 3.4 eV. Excitation spectra for these bands are also shown. The spectrum for the 2.4 eV emission reproduces fairly well the overall features of the absorption spectrum. Absorption and luminescence spectra of $C_{60}F_{48}$ films were similar to those of $C_{60}F_{42}$ films.

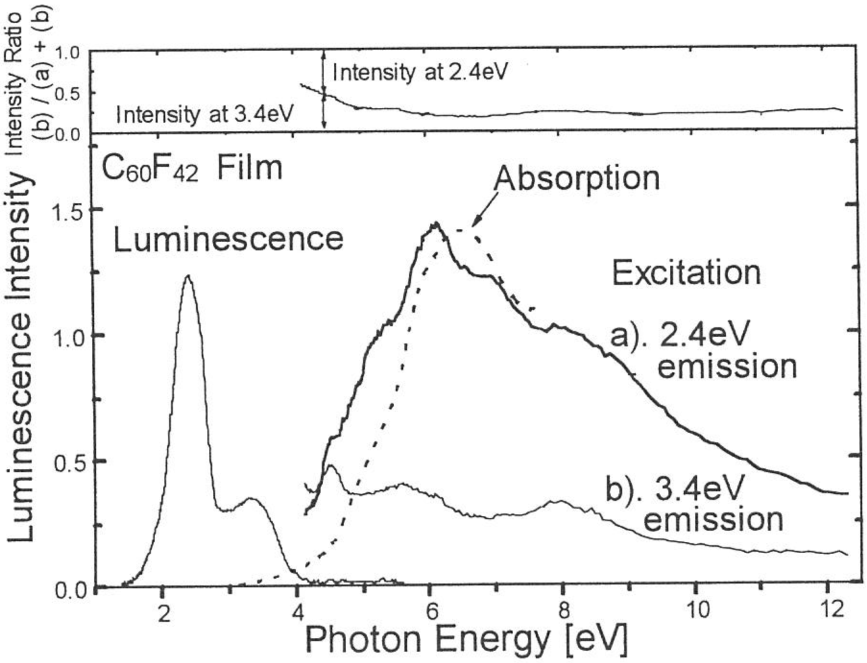

Fig. 1 Absorption spectrum (dot), luminescence spectrum (solid, left) stimulated by 6.4eV light and excitation spectra (solid, right) for the 2.4eV and 3.4eV bands at 6K. The ratio of the intensity of 3.4eV band to total intensity is also plotted in upper side.

Contrasted with the narrow band gap at ~1.8 eV of the starting $C_{60}$ material [6], the fundamental absorption edge in solid $C_{60}F_x$ is shifted to energy larger than 5 eV. The $C_{60}F_x$ absorption maximum at 6.4 eV is rather close to that of CF molecule; $X^2\Pi \rightarrow B^2\Delta$ (6.1 eV)[7]. It is tentatively assigned that the electronic excitation is concentrated on the C-F bonds of $C_{60}F_x$. The 2.4 eV emission band which is certainly stimulated in the fundamental absorption range is supposed to be intrinsic, while the origin of the 3.4 eV band somewhat ambiguous, because the relative intensity of the band to that of the 2.4 eV band is dependent on sample-to-sample, and sometime stimulated more efficiently by low energy excitaiton below 5 eV. One can intuitively see such a situation in Fig.2 where a contour-map of the luminescence intensity is depicted in the two-dimensional plane; the emission energy vs. excitation energy.

The Stokes shift of the broad 2.4 eV band is larger than 2 eV. The very low quantum yield of the luminescence is also noteworthy. Degradation of the luminescence intensity and the photo-induced desorption of C, HF, CF and $C_2F$ under prolonged irradiation with UV light have also been reported [8]. These facts remind us of the characteristics of *"strong electron-lattice coupling systems"*. The electronic excitation, which is probably concentrated on the C-F bonds, destroys the C-F bonds or detaches the C-F bonds via non-radiative relaxation process. The luminescence could be stimulated from certain atomic and/or molecular relaxed states following the electronic excitation of C-F bonds.

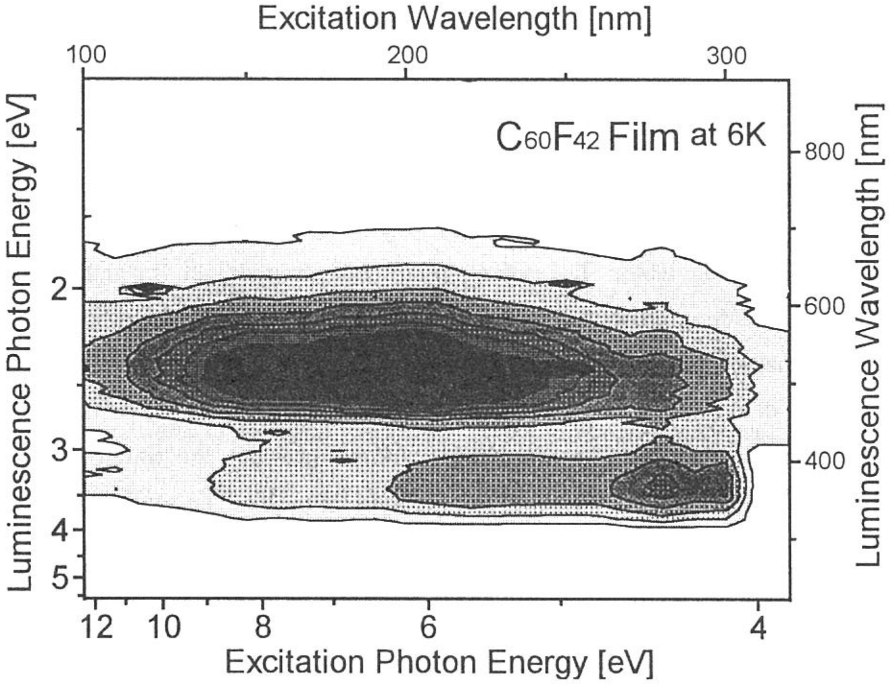

Fig. 2 Contour-map representation of the luminescence energy vs. excitation energy in $C_{60}F_{42}$ film at 6 K.

## References

[1] J.H. Holloway: *"Fluorine-Carbon and Fluoride-Carbon Materials"*, ed. by T. Nakajima, (Marcel, Dekker, Inc., New York, 1995) p.239-249; references therein.

[2] A.A.Tuinman, P.Mukherjee, J.L.Adcock, R.L.Hettich and R.N.Compton: J.Phys. Chem. 96 (1992) 7584

[3] K.Kniaz, J.E.Fischer, H.Selig, G.B.M.Vaughan, W.J.Romanow, D.M.Cox, S.K.Chowdhury, J.P.McCauley, R.M.Strongin and A.B.Smith III: J.Am.Chem.Soc. 115 (1993) 6060.

[4] A.A.Gakh, A.A.Tuinman, J.L.Adcock, R.A.Sachleben and R.N.Compton: J. Am.Chem.Soc. 116 (1994) 819.

[5] F.Okino, H.Touhara, K.Seki, R.Mitsumoto, K.Shigematsu and Y.Achiba: Fullerene Science & Technology 1(3) (1993) 425

[6] M.S.Dresselhaus, G.Dresselhaus and P.C.Eklund: *"Science of Fullerenes and Carbon Nanotubes"*, (Academic Press, 1995)

[7] P.K.Carroll and T.P.grennan : J.Phys.B ; Atom.Molec.Phys. 3(1970) 865

[8] A.Kolmakov, V.Stankevitch, V.Bezmelnitsin, A.Rizkov, V.Sokolov, N.Svechnikov, I.Akimoto, T.Matsumoto, K.Kan'no, S.Hirose and M.Kamada: UVSOR Activity Report 1994 (1995) 88.

(BL1B)

# Reflection Spectra in $(CH_3NH_3)_3Bi_2X_9$ (X:Cl,Br,I) Single Crystals

Taketoshi KAWAI, Kaori RISAI and Shigetaka SHIMANUKI

*Department of Natural Science, Osaka Women's University, Daisen-cho, Sakai 590*

Alkylammonium halogenometallates have attracted much interest because of a variety of their physical properties. Not only phase transitions, magnetic and dielectric properties but also optical properties have been extensively investigated on these crystals[1−4]. We have investigated the optical properties of alkylammonium halogenobismuthate crystals which contain the $Bi^{3+}$ ion as the constituent metal cation.

Single crystals of $(CH_3NH_3)_3Bi_2X_9$ (X: Cl, Br, I) were grown by slow evaporation of the HX solution containing the stoichiometric molar ratio of $Bi_2O_3$ and $CH_3NH_3X$. The chloride, bromide and iodide crystals were transparent, yellowish and deep red, respectively. The measurement of reflection spectra was performed at the beam line BL1B of UVSOR.

Figure 1 shows the reflection spectra of the $(CH_3NH_3)_3Bi_2X_9$ single crystals at normal incidence in the energy region of 2.0∼13 eV. As seen in this figure, several remarkable structures were observed in this energy region. The reflection structures shift to the high energy side as a whole, as the halogen proceeds upper in the periodic table. The reflection structure around 3.45, 3.1 and 2.5 eV in the order of chloride, bromide and iodide is attributed to the band-edge exciton state. In iodide, the vaule of 2.5 eV is almost equal to that of the intrinsic exciton band as reported previously[5]. In the spectrum of bromide measured in detail, the structures having the splitting energy of 0.15 eV were observed in the band-edge region. In chloride, the Kramers-Kronig analysis provides the transverse exciton energy of 3.43 eV and the longitudinal−transverse splitting energy of 90 meV. The origins of the electronic states around the band edge may be interpreted on the basis of electronic states in the $Bi^{3+}$ ion, because the $CH_3NH_3X$ solution does not exhibit any optical absorption band in the energy region below 6.0 eV.

Figure 2 shows the oblique-incidence reflection spectra for *p*-polarized light. Incident angle is about

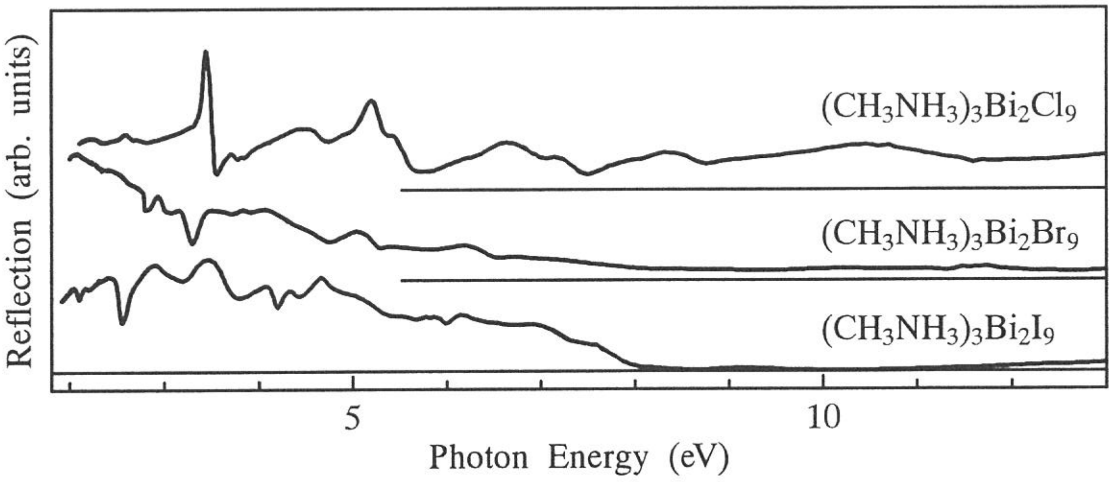

Figure 1 Reflection spectra of $(CH_3NH_3)_3Bi_2X_9$(X:Cl,Br,I) single crystals at normal incidence.

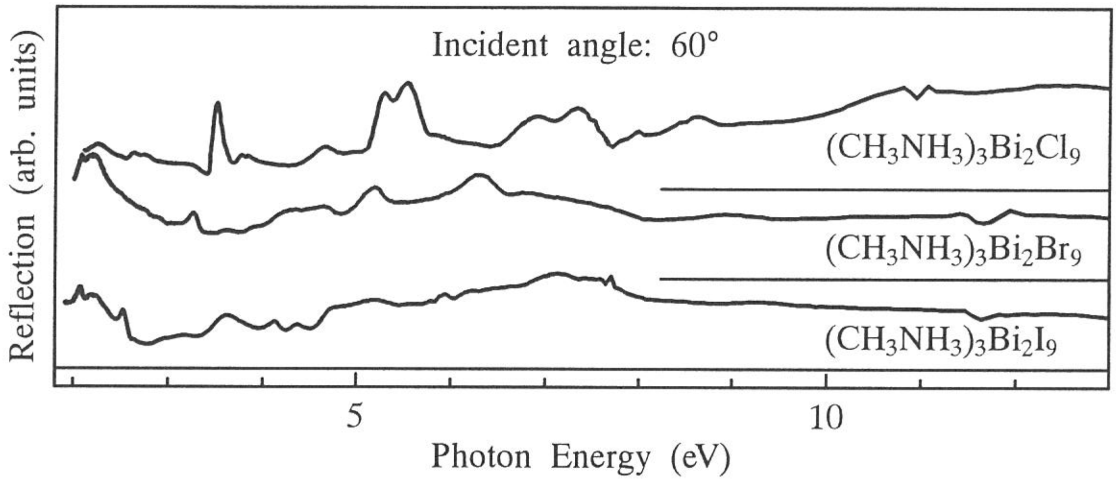

Figure 2 Oblique- incidence reflection spectra of $(CH_3NH_3)_3Bi_2X_9$(X:Cl,Br,I) single crystals.

60˚. The oblique-incidence reflection spectra are quite different from those at normal incidence. In the band-edge region, particularly, the dip at normal incidence disappears and the new peaks appear in the lower energy side. On the basis of the simple oscillator model of an isolated exciton resonance, we can reproduce the characteristics of the oblique-incidence reflection spectra as follows..

Assuming the simple oscillator model of an isolated exciton resonance, dielectric function $\varepsilon(\omega)$ is represented by the formula,

$$\varepsilon(\omega) = \varepsilon_r + \varepsilon_i = \frac{4\pi\alpha_0\omega_{ex}^2}{\omega_{ex}^2 - \omega^2 - i\omega\Gamma}$$

where $\varepsilon_r$ and $\varepsilon_i$ are the real and imaginary parts of the dielectric constant $\varepsilon$, respectively, $\omega_{ex}$ is the resonance frequency of the exciton, $4\pi\alpha_0$ the exciton polarizability, $\varepsilon_b$ the background dielectric constant, and $\Gamma$ the damping constant. The reflectance $R_p$ for $p$-polarized light at incident angle of $\theta$ is given by

$$R_p = \frac{(a-\cos\theta)^2+b^2}{(a+\cos\theta)^2+b^2} \times \frac{(a-\sin\theta\cdot\tan\theta)^2+b^2}{(a+\sin\theta\cdot\tan\theta)^2+b^2}$$

where $a$ and $b$ are real numbers satisfying the equations: $a^2-b^2=\varepsilon_r-\sin^2\theta$ and $ab=\varepsilon_i/2$. The calculated oblique-incidence reflection spectra are qualitatively consistent with the experimental results. Thus, the band-edge exciton state can be explained by the simple oscillator model. The detailed line-shape analysis is now in progress.

## References

[1] R.Jakubas and L.Sobczyk: Phase Transitions **20** (1990) 163.

[2] T.Yoshinari: Phase Transitions **36** (1991) 89.

[3] G.C.Papavassiliou and I.B.Koutselas: Synthetic Metals **71** (1995) 1713.

[4] T.Ishihara: Optical Properties of Low-Dimensional Materials, edited by T.Ogawa and Y.Kanemitsu, (World Scientific, Singapore, 1995), Chap. 6, p.288.

[5] T.Kawai, A.Ishii, T.Kitamura, S.Shimanuki, M.Iwata and Y.Ishibashi: J. Phys. Soc. Jpn **65** (1996) 1464.

(BL1B)

# Phonon broadening of Auger-free luminescence measured by time-resolved spectroscopy

T. Shiokawa,[a] M. Itoh,[a] K. Sawada,[a] N. Ohno[b] and M. Kamada[c]

[a] *Faculity of Engineering, Shinshu University, Nagano 380*
[b] *Faculity of Engineering, Osaka Electro-Communication University, Neyagawa 572*
[c] *Institute for Molecular Science, Okazaki 444*

Auger-free luminescence (AFL) is known to originate from radiative transition of valence electrons into outermost-core holes, in which the Auger decay process is energetically forbidden [1]. For AFL spectra one can expect the phonon-relaxation effects because the core-hole lifetime is much longer than the phonon-relaxation time. However, there has been no clear evidence for such effects. With this in mind, the present work has been undertaken on the temperature dependence of AFL line shapes for $BaF_2$, CsF, CsBr, CsCl and RbF in the range from 10 to 300 K.

In the crystals investigated here, the low-energy tail of AFL considerably overlaps with intense luminescence bands originating from valence-band excitation. Since such luminescence bands due to valence excitation have a long lifetime compared to the AFL, we can eliminate the contribution from valence excitation by time-resolved measurements of luminescence spectra. Decay behavior of the luminescence was observed using a time-correlated single-photon counting technique. Time-resolved spectra were obtained using a system capable of detecting two signals simultaneously through independent time windows. The time windows corresponding to the fast- and slow-decay components were suitably decided by taking the decay behavior into account. The spectra (S) of the slow component were measured during an appropriate time window in which the fast AFL component was negligible. For the spectra (F) of the fast component measured during the time window of 0-5 ns, however, we could not neglect any contribution of the slow component. The spectra proper to AFL were thus obtained by eliminating the contribution of the slow component from the spectra (F). This was done by subtracting the spectra (S) multiplied by an appropriate constant from the spectra (F). To take advantage of time-resolved technique, we used SR light pulses from UVSOR under single-bunch operation. The samples were mounted on the copper holder in a variable-temperature cryostat of He-flow type.

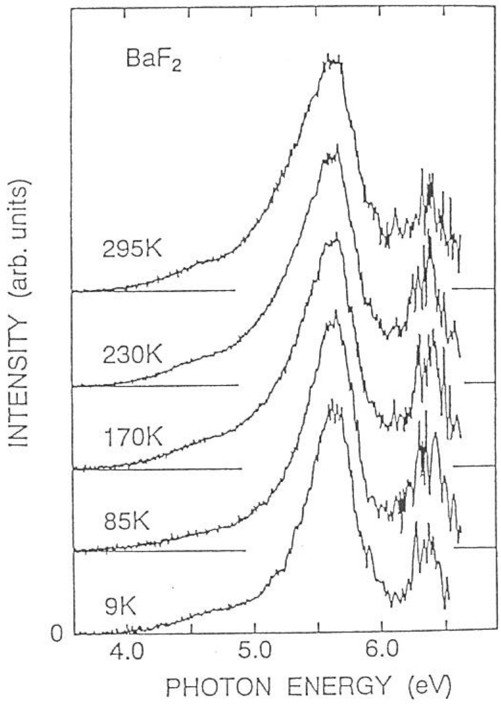

Fig.1 Time-resolved AFL spectra of $BaF_2$ measured at 9, 85, 170, 230 and 295 K under the core-band excitation with 21.4-eV photons.

Figure 1 shows AFL spectra of $BaF_2$ measured at several different temperatures under the core-band excitation at 21.4 eV. Each curve has been normalized at the maximum. The spectra consist of two intense bands peaking at 5.6 and 6.4 eV, with a hump on the low-energy side.

Figure 2 shows decay behaviors of the 4.6-, 5.6- and 6.4-eV bands in $BaF_2$ at 9 K. It is evident that the decay time does not change throughout the spectrum. This indicates that the overall structure of Fig. 1 originates from the same initial state with a core hole. The same conclusion has been obtained for all the AFL spectra in CsF, CsCl, CsBr and RbF.

From Fig. 1 we can recognize the thermal broadening of the main band at 5.6 eV in $BaF_2$. Figure 3 shows the full width at half-maximum plotted as a function of temperature. The experimental data can be expressed by the well-known formula [2]:

$$W(T) = W(0)\left[\coth(\hbar\omega/2kT)\right]^{1/2}, \tag{1}$$

where $\omega$ is the effective angular frequency of the photons involved in the relaxation process. From this fit we get $\omega=4.4\times10^{13}$ $sec^{-1}$ for $BaF_2$. Thermal variation of the AFL linewidth in other systems is also expressed by Eq. (1). These results strongly suggest that some lattice relaxation is induced around a core hole generated on metal ions before the radiative transition takes place. As in the case of the photoluminescence from localized electronic states, the configuration coordinate model may be valid for understanding of the emitting process of AFL.

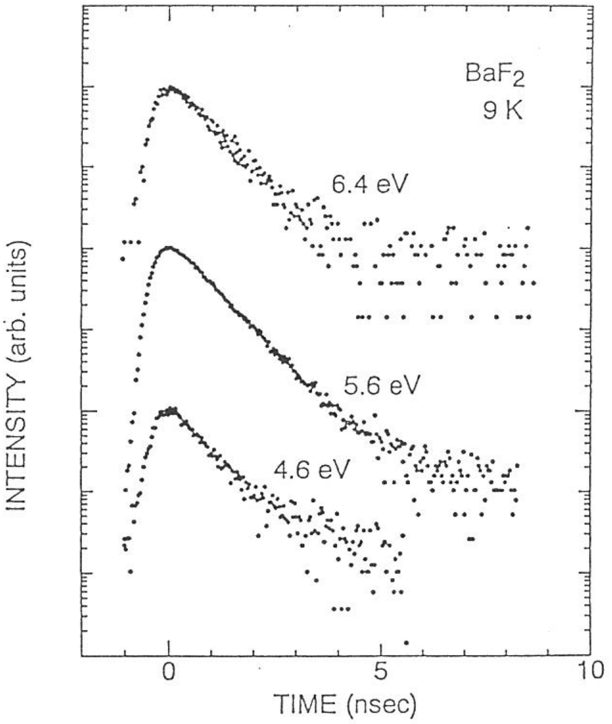

Fig.2 Decay curves of the 4.6-, 5.6- and 6.4-eV bands in $BaF_2$ excited with 21.4-eV photon pulses.

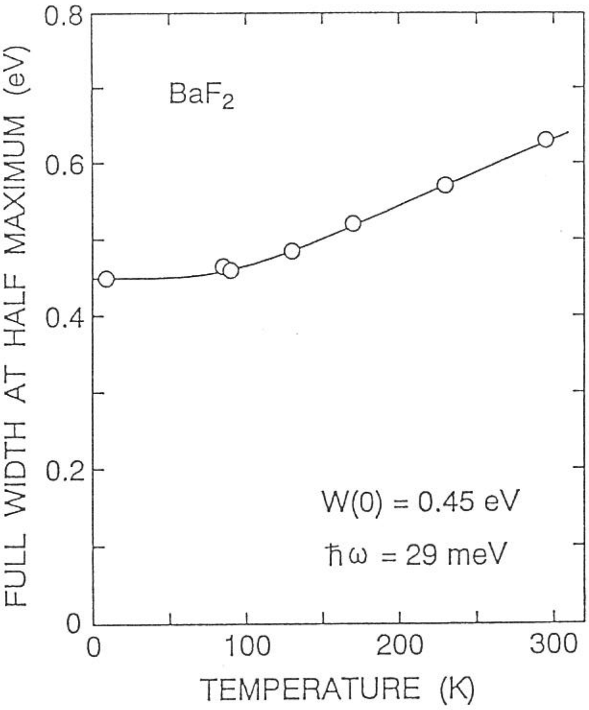

Fig.3 Temperature dependence of the full width at half-maximum of the 5.6-eV band in $BaF_2$. Solid curve is the best fit of Eq. (1) to the experimental data indicated by open circles.

[1] M. Itoh, S. Kubota, J. Ruan(Gen) and S. Hashimoto: Rev. Solid State Sci. 4 (1990) 497.
[2] W. B. Fowler, *Physics of Color Centers*, edited by W. B. Fowler (Academic Press, New York, 1968) Chap. 2.

(BL1B)

# Suppression of Self-Trapped Exciton Luminescence in Polished $BaF_2$ Crystals

M. Itoh,[a] M. Kamada,[b] T. Tsujibayashi,[c] O. Arimoto,[d] M. Watanabe,[e] S. Nakanishi[f] and H. Itoh[f]

[a]*Department of Electrical & Electronic Engineering, Shinshu University, Nagano 380*
[b]*UVSOR Facility, Institute for Molecular Science, Okazaki 444*
[c]*Department of Physics, Osaka Dental University, Hirakata 573*
[d]*Department of Physics, Okayama University, Okayama 700*
[e]*Department of Fundamental Sciences, Kyoto University, Kyoto 606*
[f]*Department of Physics, Kagawa University, Takamatsu 760*

Auger-free (AF) luminescence was first found in $BaF_2$ crystals in the course of searching fast scintillator. This luminescence is due to radiative transition of electrons from the $F^-$ $2p$ valence band to the $Ba^{2+}$ $5p$ outermost-core band, in which the Auger decay process is energetically impossible [1]. The AF bands of $BaF_2$ are centered at 5.6 and 6.4 eV with a low-energy tail extending down to 3.5 eV, and exhibit a very short decay time of sub-nanosecond. $BaF_2$ has another intrinsic emission band at 4.1 eV with a slow decay time of 0.6 μs at room temperature. This band arises from radiative annihilation of a self-trapped exciton (STE).

The $BaF_2$ crystals are now used as scintillation materials in many fields, *e.g.*, high-energy physics or nuclear medicine, because of the fast time response of the AF luminescence. However, the slow STE component causes serious pile-up problems in the use where high count rates are expected. The suppression of the STE luminescence is therefore a key issue for further application of this material to detectors. Dorenbos *et al.* [2] have reported that the STE component can be suppressed by $La^{3+}$ or $Nd^{3+}$ doping. In the present paper we report the observation of a suppression of the STE luminescence in polished $BaF_2$ crystals.

Crystal ingots of $BaF_2$ used here were grown from the melt by a vertical Bridgman method in the Horiba Ltd. A specimen with a size of $2\times10\times15$ $mm^3$ was cleaved in the air. The cleaved surface was carefully polished with distilled water on a soft sheet of silk cloth. The measurements were done at room temperature.

Figure 1 shows luminescence spectra of (a) cleaved and (b) polished $BaF_2$ crystals. Solid and broken curves were taken under the core-band excitation at 21.4 eV and the exciton-band excitation at 9.9 eV, respectively. The spectra were not corrected for the spectral response of the detection system. The vertical scale in nA is equivalent for (a) and (b). The STE band is observable with the same intensity in (a) and (b), when excited in the region of the first exciton band peaking at 9.8 eV. In the case of the core-band excitation, the STE component is considerably suppressed in polished crystal, while the intensity of the AF component is much less dependent on the surface treatment. This result was also confirmed by time-resolved lumines-

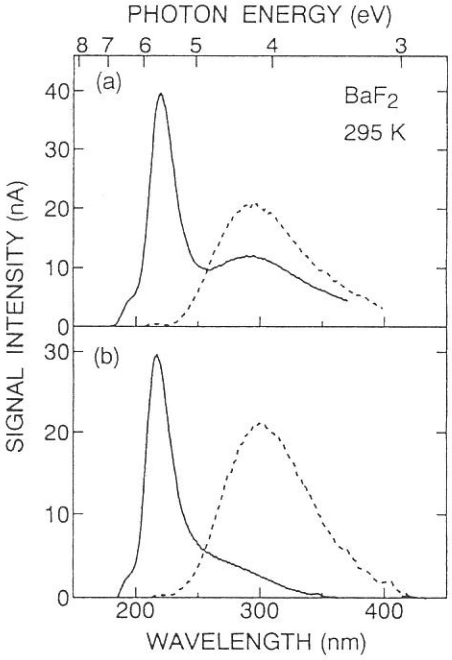

Fig. 1. Luminescence spectra of (a) cleaved and (b) polished $BaF_2$ crystals at 295 K. Solid and broken curves were obtained under photo-excitation at 21.4 and 9.9 eV, respectively.

cence spectroscopy, in which the slow STE component was nicely separated from the fast AF component.

Figure 2 represents excitation spectra for the AF band (solid curve) and the STE band (broken curve) measured in (a) cleaved and (b) polished $BaF_2$ crystals. These spectra were normalized to the intensity of the incident light. The AF band has the excitation threshold at 18.1 eV, which corresponds to the onset of interband transitions from the $Ba^{2+}$ $5p$ core band to the conduction band. The STE band in (a) can be excited in the whole region of the fundamental absorption. On the other hand, that in (b) is stimulated in the exciton-band region, but hardly excited in the high-energy region above the band-gap edge (~ 10.5 eV).

From the results mentioned above, we propose a possible mechanism to explain the suppression of STE luminescence. Upon excitation of the crystal with ionizing irradiation, electrons are excited to the conduction band and holes are created in the valence (and core) band. The conduction electrons and/or valence holes are efficiently trapped at some surface center of a polished crystal, thus preventing the formation of excitons followed by the relaxation into STE's. There is another plausible explanation that the polished surface increases the non-radiative decay rate of an STE itself. This is, however, ruled out in the present case, because the quantum efficiency of STE luminescence is almost the same in Fig. 2 (a) and (b) when excitons are directly created to form STE's.

Recently it was shown that the decay kinetics of the AF luminescence in $BaF_2$ is influenced by the surface conditions [3]. In Fig. 3 are presented decay behaviors of the AF luminescence in our samples, observed under the single-bunch operation of SR at 21.4 eV. One may see a shortening of the decay time in a polished crystal. This is probably due to the migration of core holes to the surface centers at which they annihilate through a non-radiative process. In fact, the quantum efficiency of AF luminescence is somewhat smaller in Fig. 2(b) than in Fig. 2(a).

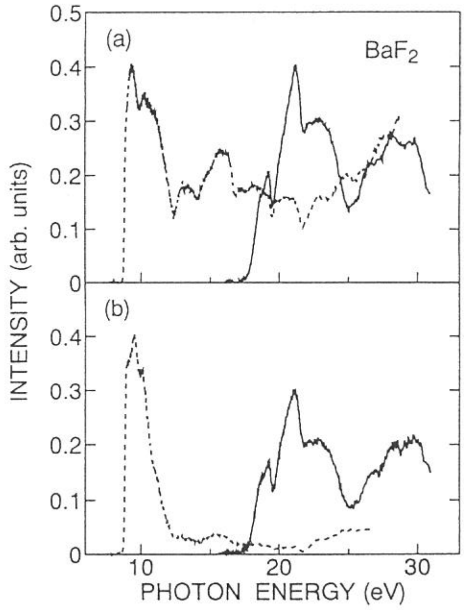

**Fig. 2.** Luminescence excitation spectra detected at 5.6 eV (solid curve) and at 4.1 eV (broken curve) in (a) cleaved and (b) polished $BaF_2$ crystals at 295 K.

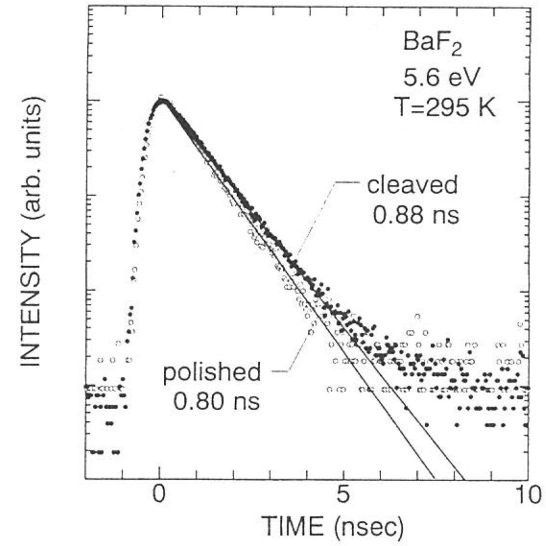

**Fig. 3.** Decay behaviors of the 5.6-eV luminescence in $BaF_2$ measured at 295 K by using SR light pulses at 21.4 eV.

[1] M. Itoh, S. Kubota, J. Ruan(Gen) and S. Hashimoto; Rev. Solid State Sci., **4** (1990) 467.

[2] P. Dorenbos, R. Visser, R. Dool, J. Andriessen and C.W.E. van Eijk; J. Phys.: Condens. Matter 4 (1992) 5281.

[3] M.A. Terekhin, A.N. Vasil'ev, M. Kamada, E. Nakamura and S. Kubota; Phys. Rev. B **52** (1995) 3117.

(BL1B)

# Time-Resolved Measurements of Self-Trapped Exciton Luminescence in Cesium Halides

Minoru Itoh
*Department of Electrical & Electronic Engineering, Faculty of Engineering,*
*Shinshu University, Wakasato, Nagano 380*

Two kinds of intrinsic luminescence bands with seemingly different characteristics are observed in alkali halide crystals. These bands have been confirmed to originate from radiative annihilation of a self-trapped exciton (STE). The one is fluorescence with a lifetime shorter than 5 ns and is $\sigma$-polarized with respect to the molecular axis of the STE. The other is phosphorescence with a much longer lifetime and is $\pi$–polarized. The $\sigma$ and $\pi$ bands are assigned to an allowed transition from a spin-singlet STE state and a partially allowed transition from a spin-triplet STE state, respectively.

In the last several years, a new classification of the STE luminescence bands in alkali halides has been introduced in order to understand their material dependence. The type-I band is characterized by a small Stokes shift, and the type-III band shows an extremely large Stokes shift. The type II is an intermediate between these two. It has been believed that the type-I STE is on-centered and the type-III (and/or type-II) STE is off-centered. These conclusions have been drawn from many experimental and theoretical studies of the STE luminescence in alkali halides with NaCl-type structure. There are, however, only a few investigations for the STE luminescence in the cesium halide crystals which have a CsCl-type structure at low temperatures [1].

Time-resolved spectroscopic study on the STE's in NaCl-type alkali halides has been undertaken in detail by Kyoto group [2]. In the present work we have measured the time-resolved emission spectra arising from the STE's in cesium halides. In CsCl, an intense band is observed at 2.92 eV, which is assigned to the off-centered STE's [3]. There appear two emission bands at 3.54 and 4.68 eV in CsBr. The former is due to the off-centered STE's and the latter to the on-centered STE's [3].

Figure 1 shows decay behavior of the 4.68-eV band in CsBr, excited at 9 K by 7.29-eV photons in the region of the band-to-band transition. The measurement was made with use of SR light pulses

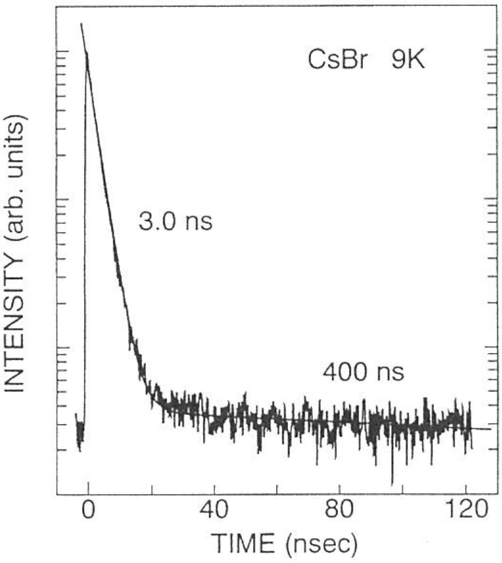

**Fig. 1.** Decay behavior of the 4.68-eV band in CsBr obtained at 9 K under the single-bunch operation of synchrotron radiation (SR) at 7.29 eV.

from UVSOR under single-bunch operation. It is clear that the 4.68-eV band consists of two decay components; a lifetime of the fast component is estimated to be 3.0±0.2 ns, while the slow component has a lifetime of 0.4±0.2 μs. Time-integrated intensity of the slow component is about 10 % of that of the fast component. The 3.54-eV band of CsBr exhibits only the slow decay component with a lifetime longer than 1 μs, resulting in piling-up of the luminescence intensity. No appreciable fast component was also found for the 2.92-eV band in CsCl.

In Fig. 2 is shown time-resolved emission spectra of CsBr at 9 K. Solid curve represents the counts of photons measured through the time window of 50-100 ns after the excitation pulse. Since the fast component is negligible in this time range, the solid curve corresponds to the spectrum of the slow component. The counts of photons measured for the time range of 0-10 ns include not only the fast component but also the slow component. Dotted curve was obtained by eliminating the contribution of the slow component from the counts of the 0-10 ns range, and therefore, it corresponds to the spectrum of the fast component. One can recognize the coexistence of the fast and slow decay components for the type-I band in CsBr. This result indicates that the type-I luminescence in alkali halide with the CsCl structure comes from a pair of singlet and triplet levels in the lowest electronic state of the on-centered STE's, similarly to the case of NaCl-type alkali halides [2].

Figure 3 shows time-resolved emission spectra of CsBr in an expanded scale, in which both components are normalized at their maxima. There are no significant differences in peak position and spectral width of the luminescence between the fast (dotted) and slow (solid) components. For CsBr, a well-defined local minimum of the adiabatic potential energy surface is expected not only for the singlet state but also for the triplet state in the on-center configuration. The present result suggests that the minima of both potential surfaces are located at the same position on the configuration coordinate, if the exchange energy of the on-centered STE's in CsBr is negligibly small.

The author would like to thank Mr. H. Yoshida for his assistance on this experiment.

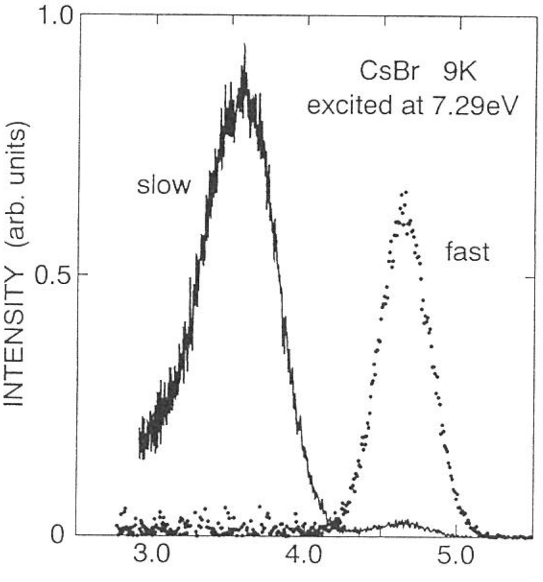

Fig.2. Time-resolved emission spectra of CsBr excited with 7.29-eV photons at 9 K.

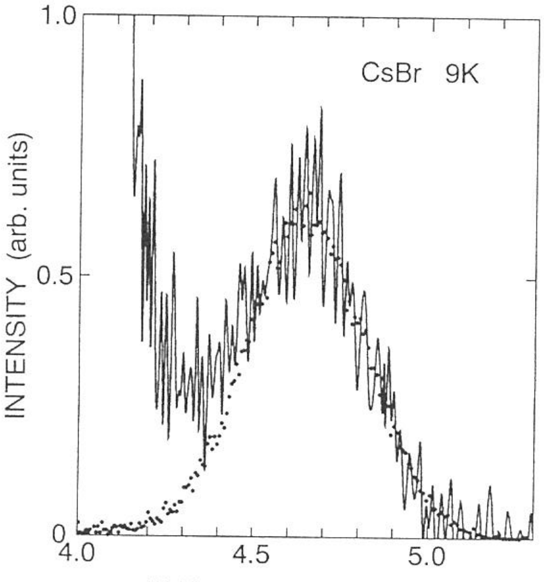

Fig.3. Expansion of Fig.2. Both components are normalized at their maxima.

[1] M. Itoh, K. Tanimura and N. Itoh; J. Phys. Soc. Jpn., **62** (1993) 2904.
[2] T. Matsumoto, T. Kawata, A. Miyamoto and K. Kan'no; J. Phys. Soc. Jpn., **61** (1992) 4229.
[3] H. Yoshida, N. Ohno and M. Itoh; *Proc. 2nd Int. Conf. on Excitonic Processes in Condensed Matter*, Kurort Gohrisch, edited by M. Schreiber (August 1996) p.231.

# (BL1B)

# Polarized Absorption and Reflection studies of Poly(tetrafluoroetylene) and Its Model Compound in the Vacuum Ultraviolet Region.

T.Miyamae[a,c], K.Mogi[a], K.Nagayama[b], I.Mori[b], R.Mistumoto[b], Y.Sakurai[b], H.Ishii[a,b], Y.Ouchi[b], M.Tsutsui[c], N.Ueno[d], and K.Seki[b]

[a]*Institute for Molecular Science, Myodaiji, Okazaki 444*
[b]*Department of Chemistry, Faculty of Science, Nagoya University, Nagoya 464-01*
[c]*Graduate School of Science and Technology, Chiba University, Chiba 263*
[d]*Department of Materials Science, Faculty of Engineering, Chiba University, Chiba 263*

Poly(tetrafluoroetylene) (PTFE) $(CF_2)_n$, is one of the most fundamental organic polymers, with unique properties such as chemical stability, small surface energy, and good electrical insulation. Its electronic structure for occupied states has been studied by photoemission spectroscopy[1-3]. The results of occupied state structures have been rather well understood. As for the unoccupied states, however, there is still some ambiguity about the character of the lower-lying vacant states and low energy excitations due to the low reliability of theoretical calculations.

A useful way of obtaining more detailed information is the study of anisotropic properties using oriented samples. In this work, we report polarized vacuum ultraviolet absorption and reflection spectra of such specimen using well polarized synchrotron radiation, and discuss the structure of the unoccupied states.

As the sample for reflection measurements, we used a PTFE sealing tape after uniaxial elongation. The absorption samples were evaporated self-standing films of perfluorotetracosane (PFT) $n$-$C_{24}F_{50}$ with thickness of 0.5 μm. For PFT, X-ray diffraction [3,4] and NEXAFS [3,4] revealed that the molecules in the evaporated film are well oriented with the axis vertical to the substrate surface. These absorption and reflection spectra were measured at the beamline 1B at UVSOR using 1m-Seya-Namioka type monochromator.

In Fig. 1, we show the reflection spectra in the region from 3 to 37 eV at normal incidence for PTFE sealing tape with the electric vector $\boldsymbol{E}$ of light parallel and vertical to the oriented direction. We see a sharp peak at 7.64 eV, with its intensity being stronger for $\boldsymbol{E}$ parallel to the oriented direction. This observation suggests that the lowest excitation of PTFE is polarized parallel to the PTFE molecular chain.

More definite information can be obtained from the absorption spectra of PFT, where the molecular axes are almost perfectly aligned. In Fig. 2, the spectra of PFT for various incident angle $\theta$ are shown. For normal incidence ($\theta = 0°$), where $\boldsymbol{E}$ is perpendicular to the molecular chain, absorption is almost absent at 8.0 eV. When $\theta$ is changed from 0°, we see a peak grows up at 8.0 eV, with shoulders at 8.3 and 8.8 eV, respectively. These results indicate that the lowest energy excitation is precisely polarized parallel to the molecular chain.

Figure 3 shows the absorption spectra of PTFE which were converted by Kramers-Kronig transformation of the reflection data. The absolute intensity of the absorption coefficient of the lowest excitation peak at 7.64 eV was found to be $1.8 \times 10^5$ cm$^{-1}$ for the better oriented PTFE tape. The data of corresponding peak in the vapor spectra of oligomer of $n = 6$ gives ca. $1.5 \times 10^5$ cm$^{-1}$, which is of the same order as the present result.

For interpreting these results, theoretical calculations are helpful. The results of *ab initio* band calculation predict that the transition from the highest occupied band to the lowest vacant level is allowed for $\boldsymbol{E}$ parallel to the chain direction [3]. From the CI calculation of perfluoroalkanes, the main configuration of the lowest energy excitation is predicted to be a transition from the HOMO to the LUMO. The band calculation also indicates that both the topmost occupied and the lowest unoccupied orbitals show strong dispersion, *i.e.* there should be a significant carbon number $n$ dependence of the orbital energies. For examining this point, in Fig. 4 we plot the reported and presently observed excitation energies, and the CI results as a function of $\cos(\pi/(n+1))$, where $n$ is the carbon number. We see a fairly good linear relationship. This can be explained by assuming a simple one-dimensional band predicted for units interacting through nearest-neighbor interactions.

The rapid lowering of the LUMO with increasing chain length was demonstrated by electron transmission experiments on perfluoroalkanes up to $n$-$C_6F_{14}$ [5]. The extrapolation of the observed value to PTFE gives a value of -0.2 eV as the electron affinity of an isolated PTFE chain. The threshold ionization energy of an isolated PTFE gives 11.7 eV, which is deduced from the extrapolation of the values of oligomers. The energy of absorption is much smaller than the energy difference of 11.9 eV between the HOMO and LUMO in an isolated chain. This is due to the electron-hole interaction (excitonic effect), which is estimated to be 4.3 eV.

[1] J.J.Pireaux, J.Riga, R.Caudano, J.J.Verbist, J.M.Andre, J.Delhalle, and S.Delhalle, *J. Electron Spectrosc.*,

**5**, 531 (1974).

[2] J.Delhalle, S.Delhalle, J.M.Andre, J.J.Pireaux, J.Riga, R.Caudano, and J.J.Verbist, *J. Electron Spectrosc.*, **12**, 293 (1977).

[3] K.Seki, H.Tanaka, T.Ohta, Y.Aoki, A.Imamura, H.Fujimoto, H.Yamamoto, and H.Inokuchi, *Phys. Scripta*, **41**, 167 (1990).

[4] K.Nagayama, R,Mitsumoto, T.Araki, Y.Ouchi, and K.Seki, *Physica* **B208/209**, 419 (1995).

[5] I.Ishii, R.McLaren, A.P.Hichcock, K.D.Jordan, Y.Choi, and M.B.Robin, *Can. J. Chem.*, **66**, 2104 (1988).

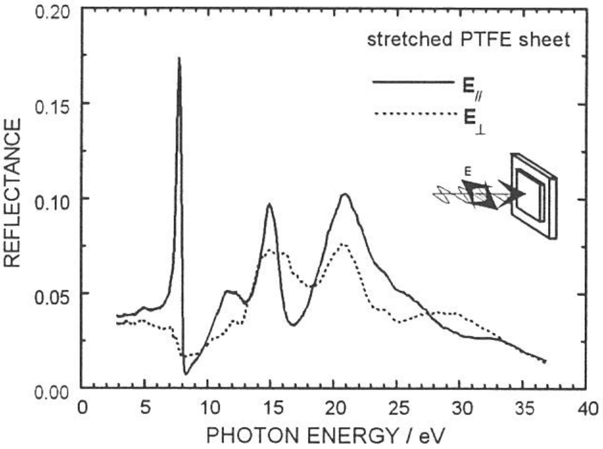

Fig. 1 Polarized reflection spectra of elongated PTFE sealing tape.

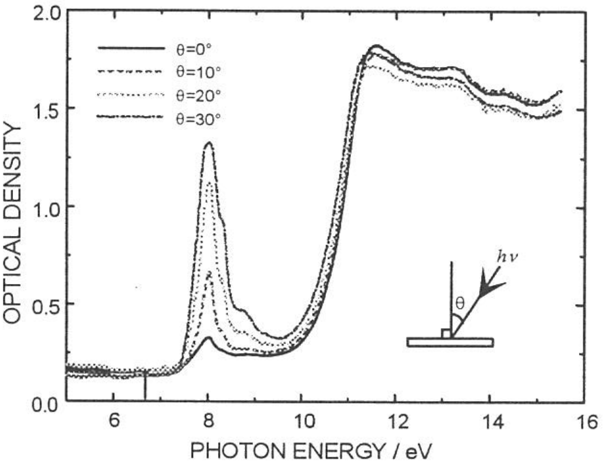

Fig. 2 Absorption spectra of perfluorotetracosane (PFT) of 0.5μm thickness at various incident angle $\theta$ of photons.

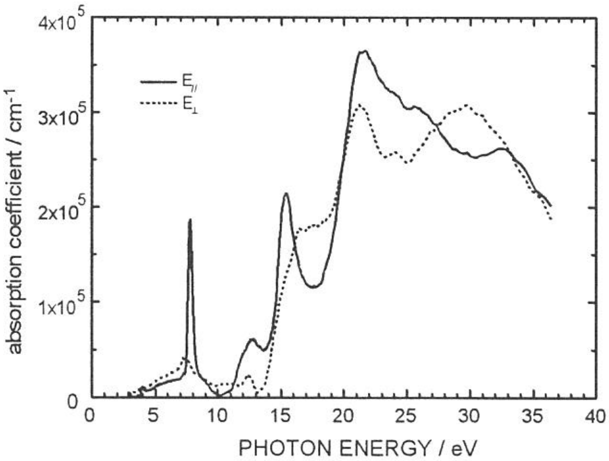

Fig. 3 Polarized absorption spectra of elongated PTFE tape obtained by Kramers-Kronig transformation of the reflection spectra.

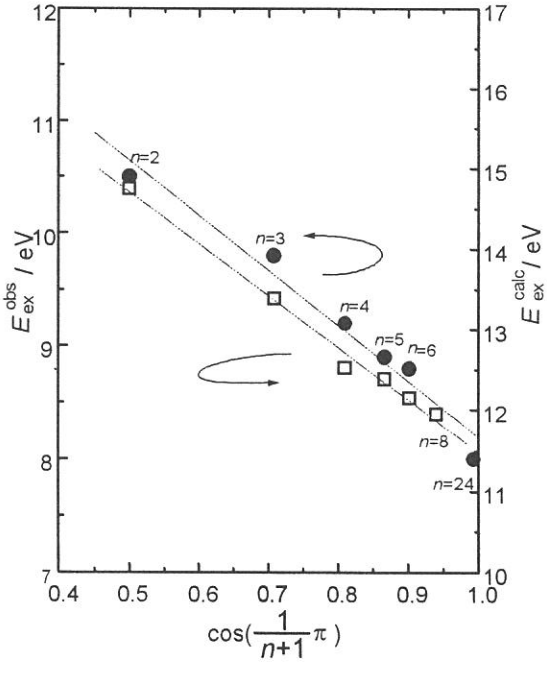

Fig. 4 Carbon number ($n$) dependence of the lowest excitation energy $E_{ex}$ and calculated excited energy of perfluoroalkanes.

(BL1B)

# Correlation between Ge E' Centers and Optical Absorption Bands in $SiO_2$:$GeO_2$ Glasses

Hideo HOSONO [1,2], Naoyuki UEDA [2], Masafumi MIZUGUCHI [1], and Hiroshi KAWAZOE [1]
[1]Tokyo Institute of Technology, Research Laboratory of Engineering Materials,
Nagatsuta, Midori-ku, Yokohama 226
[2] Institute for Molecular Science, Myodaiji, Okazaki 444

Recently, novel photonic properties of germanosilica glasses have attracted much attention, in particular Bragg gratings and second harmonic generation.It is now established that the buildup of both properties is closely related to the formation of Ge E' centers. Although identification of ESR signals of Ge E' centers was made by Weeks and Purcell in 1965, no definite correlation between Ge E' centers and optical absorption bands has been established, to our knowledge. The location and oscillator strength of the Ge E' optical absorption band are essential quantities in considering the mechanism of the above properties. So far,we reported that ArF (photon energy: 6.3 eV) or KrF ( 5.0 eV ) excimer laser irradiation induces a pair of a Ge-electron centers (GEC) and a self-trapped hole via band-to-band excitation by 2-photon absorption processes and that the resulting GEC is photochemically converted into Ge E' centers by prolonged irradiation. It may be understood that this relaxation occurs in order to reserve local electroneutrality around Ge ions, i.e., the local electroneutrality around a Ge ion is restored by detaching a non-bridging oxygen with a negative charge from its coordination sphere. As a consequence, the remaining defect in long-irradiated specimens is primarily the Ge E' center. Here, we undertake to establish the correlation between Ge E' centers and optical absorption band by examining isochronal annealing experiments using the prolonged ArF laser irradiated $SiO_2$:$GeO_2$ glasses.

Samples used were germanosilica glasses which were prepared by the vapor-phase axial deposition method and had a nominal chemical composition of $1GeO_2$-$9SiO_2$ (in a molar ratio) glasses.Vacuum ultraviolet (vuv) absorption spectra were measured using SR light at BL1B. Isochronal annealing was performed in an ambient atmosphere at temperatures from ~250 °C to ~ 750 °C. The holding time was 10 min at each temperature.

Figure 1 shows induced uv-vuv absorptions in the specimens after irradiation of $1.5 \times 10^3$ and $6.6 \times 10^4$ pulses along with Gaussian-deconvoluted spectra. Each spectrum was obtained by subtracting the spectrum of the specimen before irradiation from that after irradiation. A primary band and a shoulder are seen at ~ 6.3 eV and ~ 5.7 eV, respectively, and a subband is noted at ~ 4.7 eV. A dent appearing at ~ 5 eV results from uv bleaching of neutral oxygen vacancies associated with Ge ions. Thus, the induced absorptions were decomposed into 4 Gaussian bands, i.e., bands peaking at ~6.3 eV, ~ 5.6 eV, ~5.0 eV and ~4.6 eV. The synthesized line shape reproduces well the observed absorption shape in each spectrum. GECs are known to give two bands peaking at ~ 4.6 and ~ 5.6 eV. 7) It is therefore suggested that the remaining band peaking at ~6.3 eV is due to Ge E' centers. The intensity ratios of the 6.3 eV band to the 4.6 eV band in the spectra of the specimens after irradiation of $6.6 \times 10^4$ pulses and of $1.5 \times 10^3$ pulses are ~12 and ~3, respectively. This difference in the ratios is compatible with the difference in the ratios of the contribution of Ge E' centers to GEC in the induced ESR spectra of the corresponding specimens.

Figure 2 shows changes in induced uv-vuv absorptions in the specimen irradiated with $6.6 \times 10^4$ pulses with isochronal annealing. It is evident that intensities of the peak at 6.3 eV decrease with increasing annealing temperature. ESR intensities of corresponding Ge E' centers were also reduced monotonically with temperature. Figure 3 shows correlation between the concentrations of Ge E' centers versus the absorption coefficients of the 6.3 eV band. The absorption coefficients of the 6.3 eV band increase linearly with Ge E' center concentrations. Therefore, it is now evident that correspondence between the Ge E' centers and the 6.3 eV absorption band.

Provided this correlation is valid, we calculate the oscillator strength (f) of the 6.3 eV band using Smakula's formula

$$f = 0.87 \times 10^{17}\, n \cdot \alpha \cdot w \, / \, ( n^2 + 1 )^2 N, \qquad (1)$$

where n is the refractive index of glass, $\alpha$( $cm^{-1}$) the absorption coefficient at the peak of the absorption band, w(eV) the full-width at the half maximum(FWHM) and N( $cm^{-3}$ ) the defect concentration. Substantiating n of 1.6, w of 1.1 eV, and $\alpha$ / N ( the value of the slope of the least-square-fitted line in fig.4 ) of 7.2 x$10^7$ as into eq.(1), we obtain f of ~0.5.

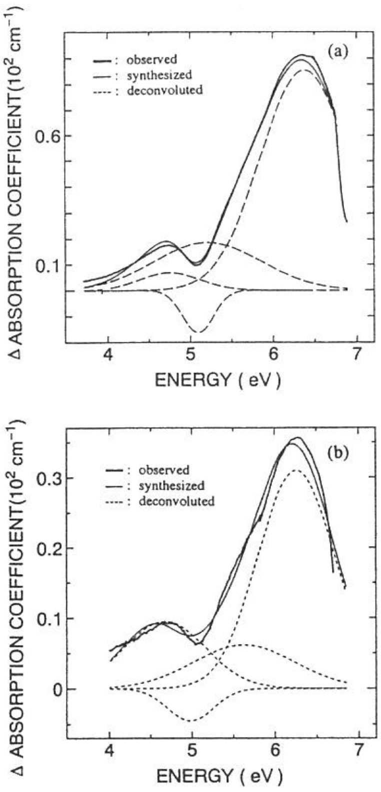

Fig.1. Ultraviolet - vacuum ultraviolet absorptions induced by ArF excimer light irradiation.
(a) 6.6x$10^4$ pulses, (b) 1.5x$10^3$ pulses.
Induced absorptions were obtained by subtracting the spectrum of the specimen after irradiation from that before irradiation.

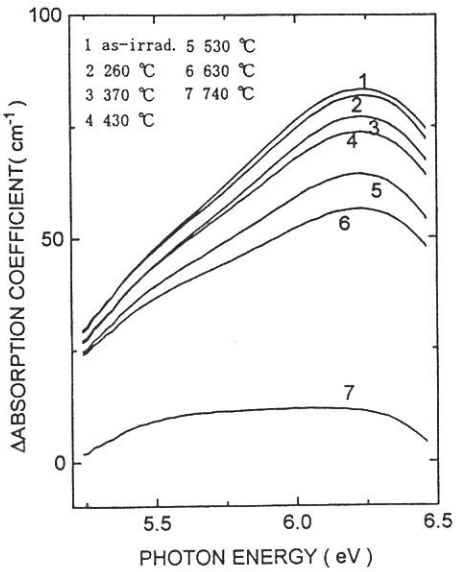

Fig.2. Changes in uv-vuv absorptions induced by ArF laser irradiation with isochronal annealing. Irradiation:40 mJ /$cm^2$ /pulses x 6.6x$10^4$ pulses at ~ 300 K. Holding time: 10 min at each temperature.

Fig.3. Correlation between concentrations of laser-induced Ge E' centers and absorption coefficients($\alpha$) of the 6.3 eV band. The data were taken from isochronal annealing experiments. Numbers in the figure denote the annealing temperature. The curve is least square fit of the data to a linear function, $\Delta\alpha$=k(Ge E' center concentrations), where k is a constant.

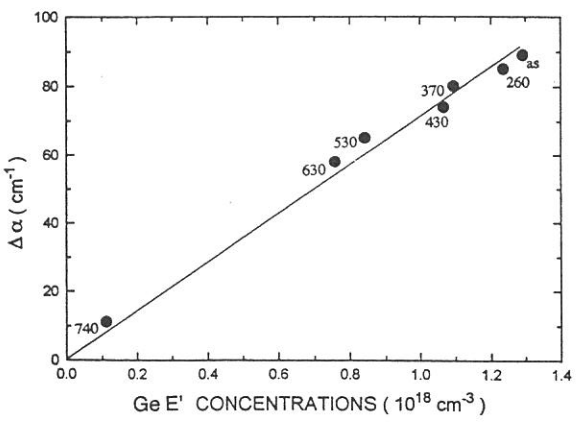

(BL1B)

# VUV absorption and photoluminescence spectroscopic studies of thermally poled germanosilicate glass

Akihiro Kameyama, Atsushi Yokotani and Kou Kurosawa

*Department of E&E Engineering, Miyazaki University, Miyazaki 889-21*

Silica glass is the most important material for optics, electronics, and also telecommunication systems. In 1991, Myers et al. have found a new function of silica glass, i.e., second-order optical nonlinearity is added to the material. Since then, the similar phenomena have been reported in naturally fused silica glass, synthetic silica glass, germanosilicate glass, and Ti-doped silica glass, although the second-order susceptibility depends on research groups and samples. We have also reported that the second-order nonlinearity or second-harmonic generation (SHG) in high-purity synthetic silica glass, when X-ray induced defects are introduced in the glass before the poling procedures.

Germanosilicate glass is one of the important materials for the current optical telecomunication systems. If second-order nonlinearity is added to the material, a big advantage must be added to the telecommunication systems. We study X-ray radiation effects to the second-order nonlinearity in germanosilicate glass, i.e., we are interested in whether X-ray induced defects enhance the second-order nonlinearity in the material as well as a high-purity synthetic silica glass or not. In order to investigate the relation between X-ray induced defects and the nonlinearity, we take absorption and photoluminescence spectra in particular in the ultraviolet to vacuum ultraviolet spectral regions.

Several samples of 1.0-mm thicknesss consisting of 3.5 mole% $GeO_2$ and 96.5 % $SiO_2$ 4.5 kV high voltage was applied between the major surfaces of the sample at 250 C for 20 min. The optical nonlinearity was estimated by measuring 532-nm green light intensity when a Nd:YAG laser beam was incident to the sample with different incident angles. In Fig. 1 are plotted the green light intensities as a functionl of the YAG laser incident angle . Comparing the intensity with the value measured for a crystal quartz, we estimated the $\chi^{(2)}_{33}$ value of the sapmle to be 0.09 pm/V. The values were in a range between 0.04 and 0.17 pm/V and thus showed large sample dependence. It is wellknown the there are two kinds of nonlinear phases in thermally poled silica glasses: one localizes near the sample surface contacted to the positive electrode during the poling and is as thin as the optical interaction length around 20 mm, and the other is in the whole bulk sample ans shows clearly Maker fringes in the angle dependence SHG curves. Fig. 1 shows that the samples have both kinds of the nonlinear phases. In Fig. 1 are also plotted the intensity data from the same sample exposed to X-ray ($\lambda$=0.152nm) radiartion for 180 min before the poling. The X-ray exposure resulted in a siginificant effect, i.e., the X-ray exposed sample did not show any optical nonlinearities.

The next interesting point is what happened in the X-ray-exposed samples. In general, X-ray radiation induces some point defect generation and/or electron rearrangement in germanosilicate glasss. In order to investigate the relationship between defects or electron rearrangement and nonlinear phase formation, we took absorption and photoluminescence spectra with the use of BL1B beam line at UVSOR. In Fig. 2 are shown the spectra taken from samples with and without the X-ray exposure before the poling procedures. The subtracted curve of the the unexposed one from the exposed one is also plotted. The X-ray radiation apparently decreases a 5-eV absorption peak which is assigned to neutral oxygen vacancy (NOV) and/or Ge lone pair center (GLPC), and further increases significantly a 6.2-eV absorption peak assigned to Ge E' centers. Fig. 3 shows the luminescence spectra taken under excitation by 240-nm radiation from the sample with and without the X-ray irradiation. The two peaks appear at 3.2 and 4.3 eV, which are assigned to GLPC and NOV, respectively. These findings imply that the X-ray radiation-induced Ge E'centers prevent the formation of optical nonlinearity in germanosilicate glass. The next interesting step is a detailed study about why and how E' centers prevent the formation optical nonlinearity in germanosilicate glass.

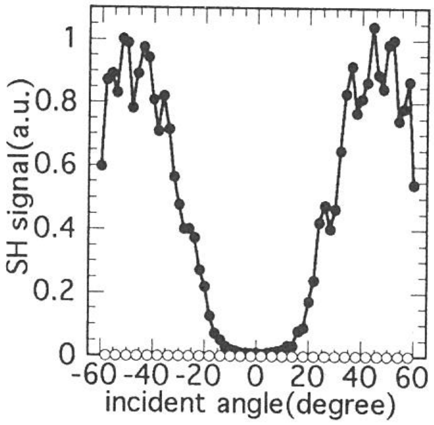

Fig. 1 SHG intensities taken from a germanosilicate glass plate with (open circles) and without (solid circles) X-ray exposure before the poling procedures as a function of the incident angle of YAG laser beam.

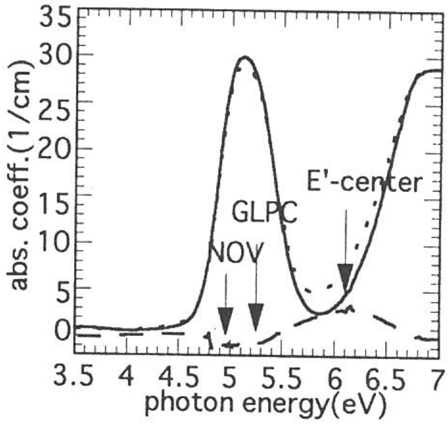

Fig. 2 Absorption spectra taken from a germanosilicate glass plate with (dotted line) and without (solid line) X-ray exposure before the poling procedures. The subtraction curve is also plotted by a broken line.

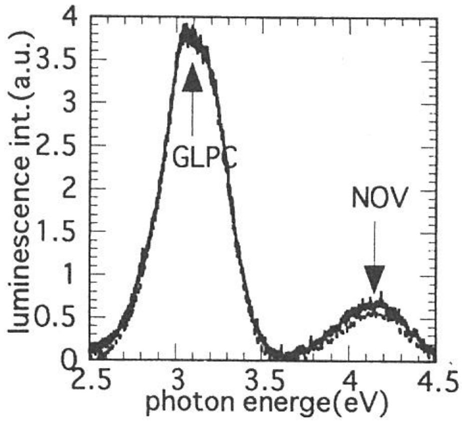

Fig. 3 Photoluminescence spectra taken from a germanosilicate glass plate with (dotted line) and without (solid line) X-ray exposure before the poling procedures.

(BL1B)

# Luminescence Spectra of Amorphous $CdI_2$ Thin Films

Kazutoshi FUKUI, Ikuto ISHIZUE, Takanobu YAMADA and Hideyuki NAKAGAWA

*Dept.Elec.Elec.Engi., Fac.Engi., Fukui Univ., FUKUI 910*

We have been studying the crystallization processes of the amorphous $CdI_2$ thin films by using both optical absorption and luminescence measurements. The main motivation of this study is to determine a means of creating the good crystalline (*c*-) $CdI_2$ thin films. However, since the properties of the amorphous (*a*-) $CdI_2$ are still not clear, the purpose of the present study is to investigate the luminescence in the *a*-phase by using visible and ultraviolet lights. The luminescence spectra in both the microcrystalline and/or two dimensional crystalline (*m*-) phase, and the *c*-phase are also measured for reference.

$CdI_2$ thin films were evaporated onto $SiO_2$ plate, which were kept at near liquid nitrogen temperature (LNT), by Pt basket evaporators with a vacuum pressurein the range of $10^{-9}$ Torr. The emission and excitation spectra of *as-deposited* films (*a*-phase) were measured at LNT just after the evaporation (*in situ* measurements). Since the luminescence lights from the film were too weak to be monochromatized, the excitation measurements were performed using band-pass optical filters. The $as-deposited$ film was then annealed *in situ* to 280 K and kept at 280 K. The film was again cooled to LNT fifteen minutes later, and both the emission and excitation spectra in the *m*-phase were measured. This was followed by annealing the film *in situ* to 380 K and keeping it at 380 K for 15 minutes before cooling it to LNT to get the luminescence data in the *c*-phase. In this way, all spectra were measured on the same sample.

Figure 1 shows the emission spectra of *a*-phase $CdI_2$ thin film under excitation with 6.22, 8.96, 9.93 and 11.8 eV. There are at least two emission bands: one around 2.2 eV (Y'-emission) and the second around 3.1 eV (V-emission). In the *c*-phase, it is known that ultraviolet (UV) and yellow (Y) emission bands are dominant. The emission mechanism in *c*-phase is explained by the $MX_6$ model [1]. In this model, both UV and Y-emission bands in *c*-phase can correspond to the allowed transitions between the $[Cd^{2+}I^{-}{}_6]^{4-}$ molecular orbitals, and there are parity forbidden transitions among these two allowed transitions. The forbidden transition in *c*-phase, which corresponds to V-emission band, becomes allowed transition in *a*-phase because *a*-phase has a lower structural symmetry than *c*-phase. It is clear that the intensity ratio between Y' and V-emission band depends on the excitation energy. The higher the excitation energy, the stronger the Y'-emission intensity, and *vice versa*. The V-emission is the dominant band at the lower excitation energy in Fig. 1. It is consistent with our previous work in which the emission spectra in the *a*-phase obtained by the excitation around the fundamental absorption edge shows that the V-emission band is quite dominant.

Figure 2 shows the excitation spectra of *a*-$CdI_2$ thin film for the Y' and V-emission bands. The baselines increase with increasing excitation photon energy. This is mainly due to the reflectance decrease with increasing photon energy. However, both Y' and V emission bands show essentially the same excitation spectrum: the threshold at around 9 eV and the peaks at 10.2 eV. The spectrum feature above 9 eV is almost similar to that of the fundamental absorption spectrum in the *a*-phase [2]. It suggests that these emission bands are intrinsic in the *a*-phase. We also found that both Y' and V-emission were quite excited at 7 to 8 eV in the *m*-phase, and the emission spectra in the *c*-phase are consistent with the previous result for the bulk single crystals [3]. The blanket emission mechanism from *a*-phase to *c*-phase via *m*-phase has yet to be established.

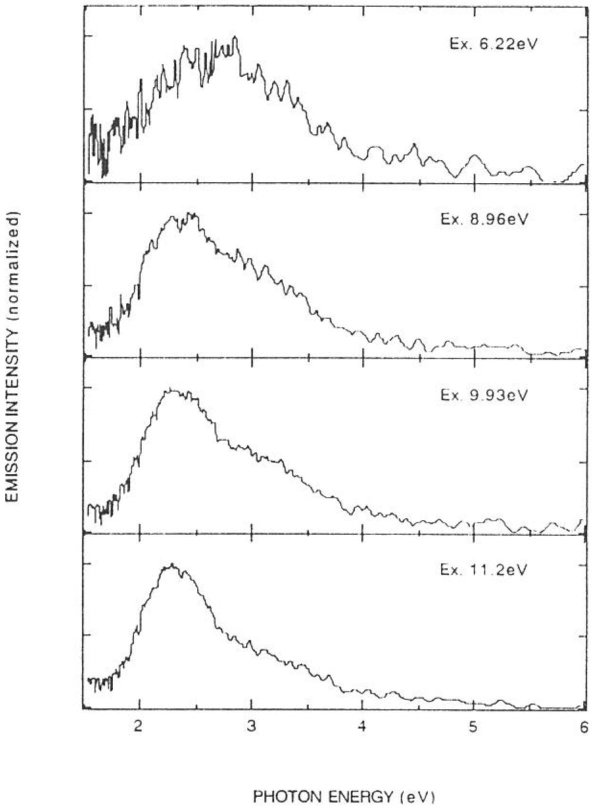

Fig. 1. Emission spectra of amorphous $CdI_2$ thin film.

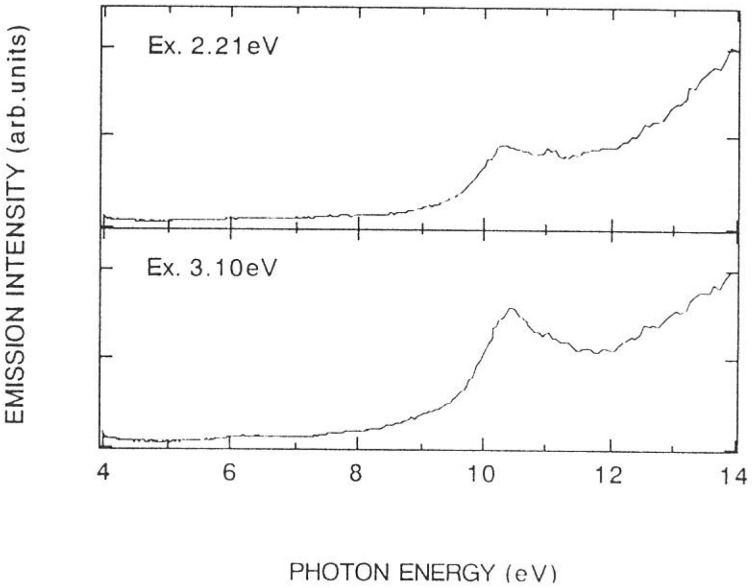

Fig. 2. Excitation spectra of amorphous $CdI_2$ thin film.

## Reference

[1] H.Matsumoto and H.Nakagawa, J. Luminescence **18/19** (1979) 19.

[2] H.Matsumoto, H.Nakagawa and S.Kondo, Mem. Fac. Engi. Fukui Univ. **31** (1983) 1.

[3] K.Fukui, K.Niimi, T.Yamada and H.Nakagawa, UVSOR Activity Report No.22 (1995) 186.

(BL2A)

# Photoabsorption and Fluorescence Cross Sections of $CF_3CN$ in the Valence Region

Toshio IBUKI and Kazumasa OKADA

*Institute for Molecular Science, Myodaiji, Okazaki 444*

A fluorinated compound has in general an ionization potential (IP) higher than its corresponding hydrocarbon because of the high IP of F atom, 17.42 eV. The first IP of $CF_3CN$ is 14.3 eV[1]) while it is 12.21 eV for $CH_3CN$.[2]) This high IP caused by the F atom substitution may give characteristic features to the photoabsorption spectrum. Little is known, however, on the spectra of the fluorinated compounds.

Figure 1 shows the absolute photoabsorption and fluorescence cross sections of $CF_3CN$ in the region 6-41 eV. Higher order light from a 1-m Seya monochromator has been suppressed by the use of a LiF window at 5.9-11.8 eV and an argon gas filter in the range 11.3-15.5 eV.[3]) The emitting species were identified as the $A^2\Pi_i \rightarrow X^2\Sigma^+$ and $B^2\Sigma^+ \rightarrow X^2\Sigma^+$ transitions of CN radical. The electronic configuration of the valence molecular orbitals (MOs) of $CF_3CN$ is given by $(3a_1)^2(4a_1)^2(2e)^4(5a_1)^2(3e)^4(1a_2)^2(4e)^4(6a_1)^2(5e)^4$.[1]) The outermost 5e and the next $6a_1$ MOs represent the $\pi_N$ and $n_N$ characters, respectively, and their IPs are accidentally degenerate at 11.4 eV.[1]) The IPs from the 4e to $3a_1$ MO are 16.3, 16.56, 17.1, 18.10, 21.6, 22.6 and 25.7 eV[1]) as shown by bars in fig. 1a. It can be seen that the electronically excited CN fragment is produced even in the ionization region, that is, especially the ionization of the $(5e)^{-1}$ and/or $(6a_1)^{-1}$, $(2e)^{-1}$ and $(4a_1)^{-1}$ MO electron enhances the CN* formation.

Figure 2 shows the photoabsorption spectrum up to 18 eV deconvoluted by Gaussian functions, and the result is shown by the while curve superimposed on the experimental data marked by the solid circles. The lowest broad band at 8.78 eV has been assigned as the $\pi^* \leftarrow \pi(5e)$ transition.[4]) The peaks at 10.37, 11.05 and 11.25 are assigned as the 3s, 3p and 3p' Rydberg transitions, respectively. In $CH_3CN$, the 3s and 3p Rydberg bands lie at 9.04 and 9.56 eV, respectively.[4]) These observations indicate that the substitution by F atoms gives a photoabsorption spectrum shifted to high energy region by ≅1.5 eV. The mean quantum defects for the ns, 3p and 3d Rydberg series in fig. 2 are deduced to be $\delta(ns)= 1.28 \pm 0.05$, $\delta(3p)=0.87 \pm 0.05$ and $\delta(3d)=-0.02 \pm 0.09$ which are comparable to those for F atom: $\delta(3s)= 1.26 \pm 0.01$, $\delta(3p)=0.82 \pm 0.04$ and $\delta(3d)=0.00 \pm 0.04$.[5])

In the 12-15 eV region the vibrational fine structures were observed as shown in fig. 3. The vibrational spacings are 320 ± 8 (CN str), 770 ± 140 (FCF bend), 970 ± 110 (CF str) and 600 ± 60 $cm^{-1}$ (FCF bend), that is, the Rydberg states are highly vibrationally excited as have been observed in the photoabsorption spectrum of $CH_3CN$.[1])

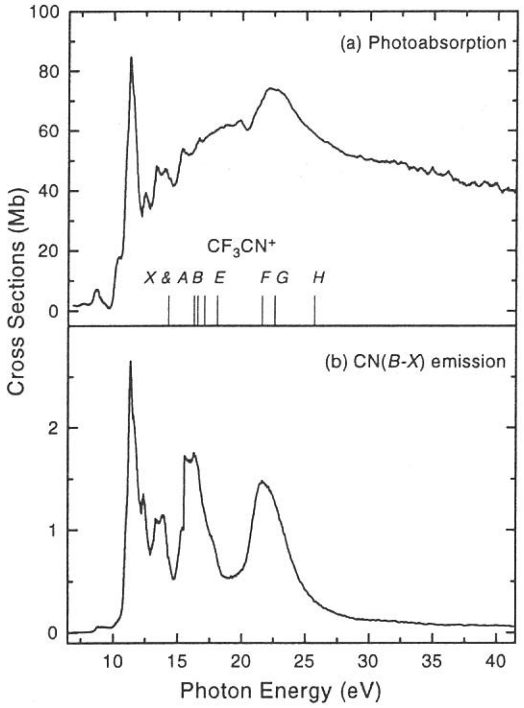

**Fig. 1. Photoabsorption and emission cross sections.**

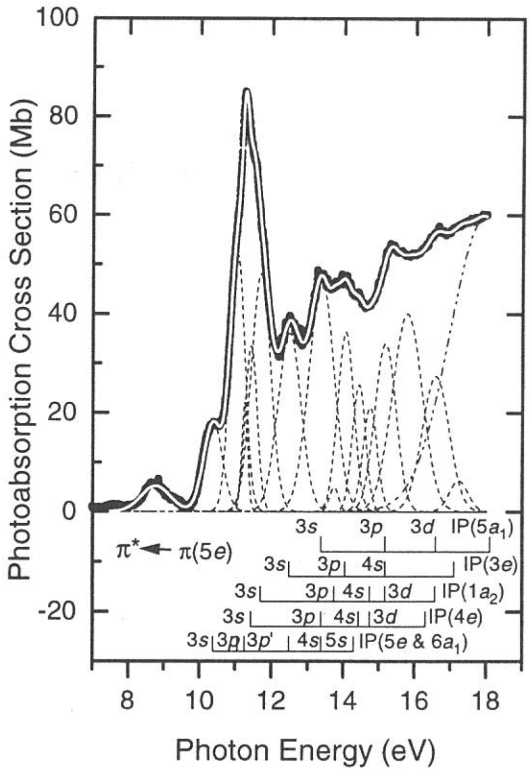

**Fig. 2. Expanded photoabsorption cross section.**

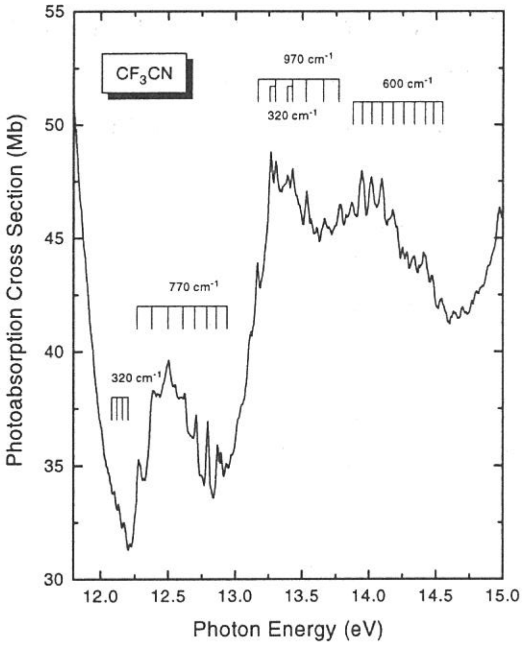

**Fig. 3. Vibrational fine structures.**

## References

[1] H. Bock, R. Dammel, and D. Lentz, Inorg. Chem. **23**, 1535 (1984).

[2] K. Kimura, S. Katsumata, Y. Achiba, T. Yamazaki, and S. Iwata, Handbook of He I photoelectron spectra of fundamental organic molecules (Jpn. Sci. Press. Tokyo, 1981) p.178.

[3] T. Ibuki, M. Kono, Y. Asari, A. Hiraya, and K. Shobatake, J. Chem. Phys. in press.

[4] M. Robin, Higher excited states of polyatomic molecules, Vol. 3 (Academic, Orlando, 1985) p.295.

[5] C. E. More, Atomic energy levels, NSRDS-NBS 35, Vol. 1 (US GPO, Washington DC, 1971) p.60.

(BL2A)

# Hydrogen Isotope Effects in the Radiative Dissociation of $CH_3CN$ and $CD_3CN$ in the Extreme UV Region

Toshio IBUKI and Kazumasa OKADA

*Institute for Molecular Science, Myodaiji, Okazaki 444*

Little information has been known on the reaction dynamics of polyatomic molecules superexcited or in the Rydberg levels. Hydrogen isotope effects were observed in the fluorescence intensities of the $A^2\Pi_i \rightarrow X^2\Sigma^+$ and $B^2\Sigma^+ \rightarrow X^2\Sigma^+$ transitions of the CN radical formed by the EUV photoexcitation of $CH_3CN$ and $CD_3CN$. This observation may give a clue to elucidate reaction mechanism of the highly excited molecules.

Figure 1 shows the total photoabsorption cross section of $CH_3CN$ and the fluorescence cross section for the $CN(B^2\Sigma^+ \rightarrow X^2\Sigma^+)$ transition. The electronic configurations of the valence electrons are given by $(6a_1)^2(1e)^4(7a_1)^2(2e)^4$. The assignments in fig. 1 were taken from Nuth and Glicker.[1)] No hydrogen isotope effects were observed in the total photoabsorption cross sections of $CH_3CN$ and $CD_3CN$. Figure 2 shows the relative emission quantum yields for the $CN(B^2\Sigma^+ \rightarrow X^2\Sigma^+)$ emission produced from $CD_3CN$ (denoted by $\sigma_{CN}(D)$) to that from $CH_3CN$ (denoted by $\sigma_{CN}(H)$). *Inverse* hydrogen isotope effect was observed in the 10-15 eV region. The ionization potentials of $CH_3CN$[2)] shown by bars seem to have no effect on the quantum yields ratio.

The thermochemical onset to generate the $CN(B^2\Sigma^+)$ radical is :

$$CH_3CN \rightarrow CH_3 + CN(B^2\Sigma^+), \quad \Delta H = 8.8\ \text{eV}. \qquad (1)$$

The $\sigma_{CN}(D)/\sigma_{CN}(H)$ ratio becomes unity at $h\nu = 9.4$ eV, and just at this energy the following channel is thermochemically possible:

$$CH_3CN \rightarrow CH + H + HCN. \qquad (2)$$

In reaction (2) the ground state HCN molecule may be formed through a three-member cyclic activated complex:

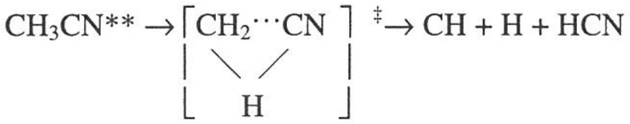

$$CH_3CN^{**} \rightarrow \left[ \begin{array}{c} CH_2 \cdots CN \\ \diagdown \quad \diagup \\ H \end{array} \right]^{\ddagger} \rightarrow CH + H + HCN \qquad (3)$$

The tunneling effect may work in the intramolecular hydrogen atom migration in reaction (3), and hence the H atom in $CH_3CN$ may migrate easier than the D atom in $CD_3CN$. That is, the $CN(B^2\Sigma^+)$ emission from the D-compound becomes stronger than that from the H-substitution since the dark reaction (3) competes with the radiative reaction (2). The $\nu_3$ (HCC bent) vibrational mode is excited in the 10.8-13 eV region (see fig. 1) where the inverse hydrogen isotope effect is strongly observed, and may promote the formation of the cyclic activated complex in reaction (3).

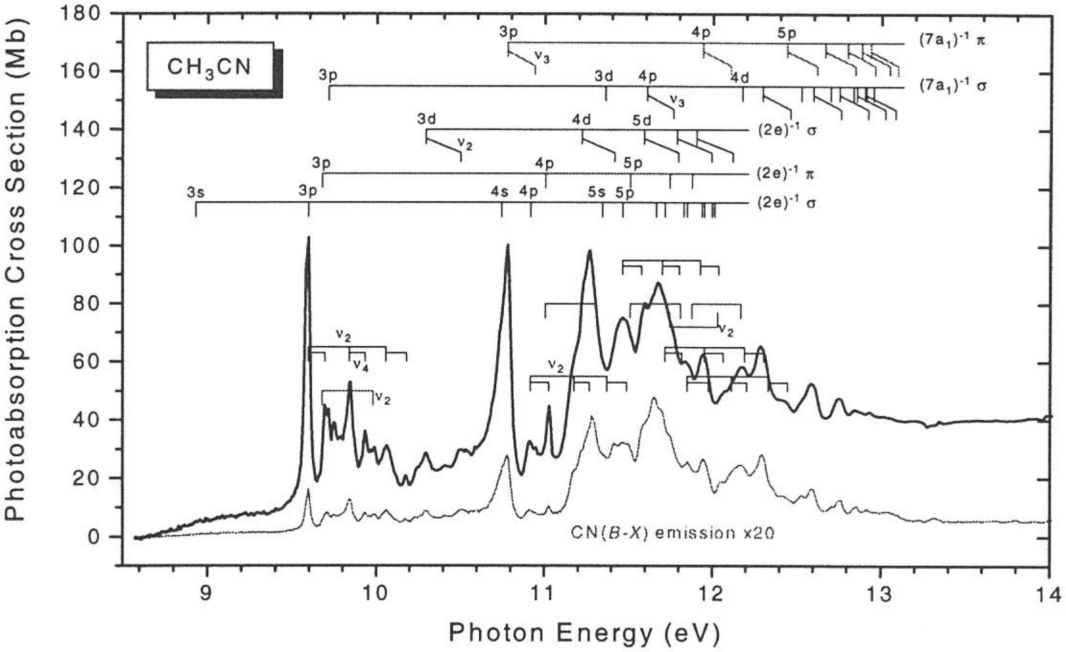

Fig. 1. Total photoabsorption and emission cross sections of CH$_3$CN in the region 8.5-14 eV.

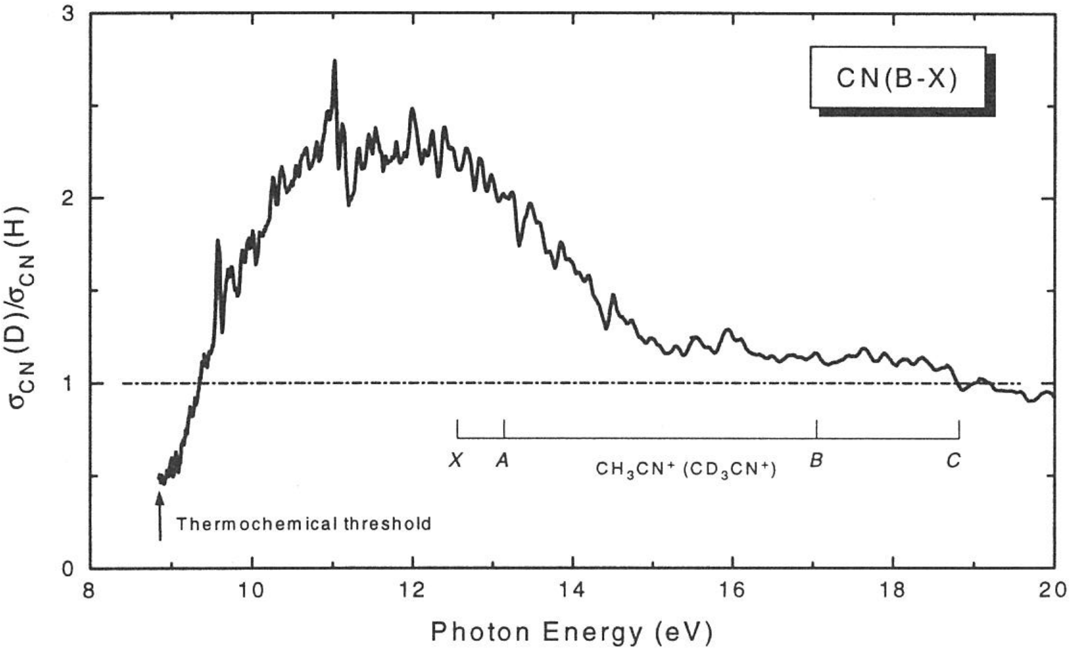

Fig. 2. Relative emission yields.

## References

[1] J. A. Nuth and S. Glicker, J. Quant. Spectrosc. Radiat. Transfer, **28**, 223 (1982).

[2] K. Kimura, S. Katsumata, Y. Achiba, T. Yamazaki, and S. Iwata, *Handbook of He I photoelectron spectra of fundamental organic molecules* (Jpn. Sci. Press, Tokyo, 1981) p.178.

(BL2A)

# Fluorescence Excitation Cross Section of Formic Acid in the VUV Energy Region.

T. HINO, K. TABAYASHI, K. SAITO,
K. OKADA*, T. IBUKI*

*Department of Chemistry, Hiroshima University,*
*Kagamiyama, Higashi-Hiroshima 739*
**Institute for Molecular Science, Myodaiji, Okazaki 444*

There have been reported several experimental works on the photo-absorption and electron impact spectra of carboxylic acids in the UV and VUV energy region, and gross features of the electronic structure and transitions in the molecules have been interpreted. However, little is known about the photochemical reaction initiated by absorption of VUV light in the gas phase. As a preliminary study to examine the fluorescent processes induced, fluorescence excitation cross section of deuterated formic acid has been measured in the excitation wavelength range 105-155 nm.

Fig.1. shows absorption and fluorescence excitation spectra of DCOOD measured in the 105-155 nm region. Each spectrum is very similar to that of ordinary HCOOH. Isotope shift of each absorption band is quite small($< \pm 0.15$ nm). The results of band assignments are also indicated in Fig.1. The vibrational progressions appeared in the absorption have average spacing of $\sim 1500$ cm$^{-1}$, and are attributed to C=O stretching vibration. The fluorescence excitation spectrum was obtained by detecting the photons in the 230-400 nm region using an optical filter. Absolute scale for the fluorescence excitation cross section was determined by comparing the photo-emission intensity with that of reference molecule, $H_2O$. Excitation band structure is found to be resolved at the excited states higher than the $3p \leftarrow 10a'$.

When HCOOH was photo-excited at 110 nm, dispersed fluorescence spectrum showed clear OH(A-X) bands in the 280-325 nm region and broad HCOO* bands [1] in the 330-500 nm region. The following dissociative excitation processes are also expected to proceed for DCOOD,

$$\begin{aligned} \mathrm{DCOOD} + h\nu &\rightarrow \mathrm{DCO} + \mathrm{OD(A)} \\ &\rightarrow \mathrm{DCOO}^* + \mathrm{D} \end{aligned}$$

Fluorescence quantum yield(QY) was calculated as the ratio of the fluorescence excitation cross section to the absorption cross section at each wavelength. In Fig.2, QY thus obtained is compared with that of HCOOH. Here, isotope enhancement of the QY(DCOOD) is prominent (by a factor of $\sim 1.2$) at excitation wavelengths below 125 nm. Detailed measurements and analysis of the product branching ratio are in progress, for the photo-dissociation of HCOOH and its deuterated analogues.

[1] M.Suto, X.Wang and L.C.Lee, J. Phys. Chem. **92**, 3764 (1988).

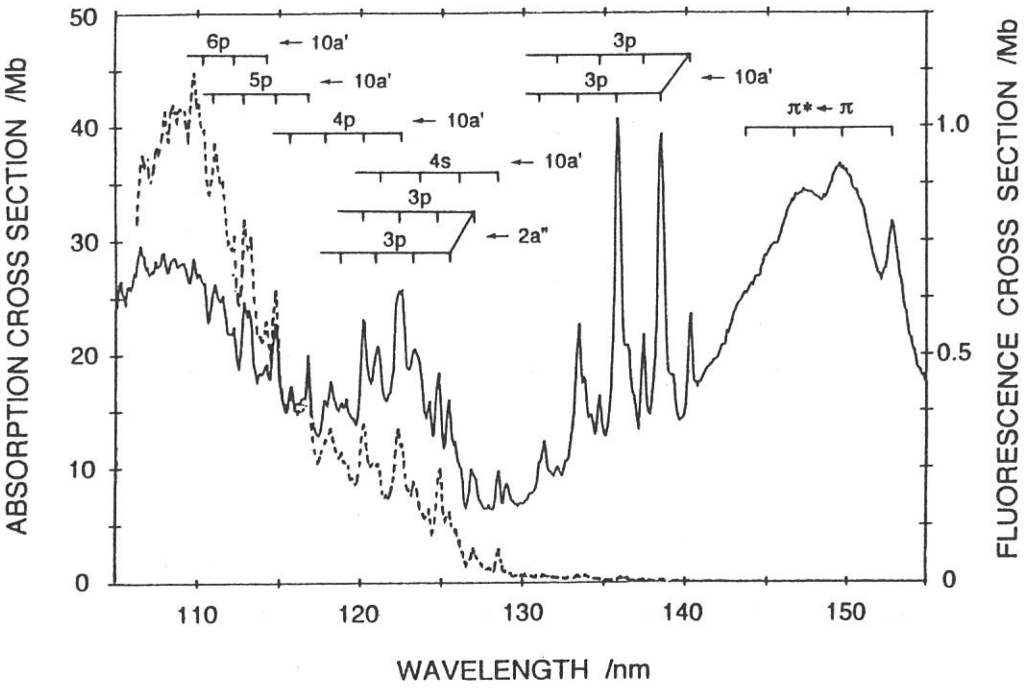

**Fig. 1.** Absorption and fluorescence excitation cross sections of DCOOD in the 105 - 155 nm region. The spectral resolution was 0.2 nm. Sample pressure was 30 mTorr.

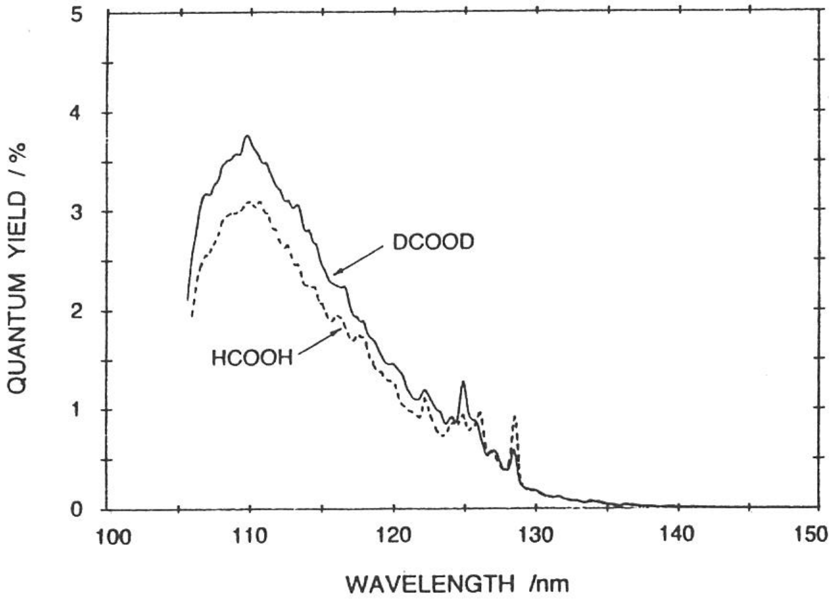

**Fig. 2.** Fluorescence quantum yields in the VUV-photodissociation of DCOOD and HCOOH.

(BL2A)

# Photochemistry of Some Simple Nitriles in the 30 - 150 nm Region

Kazuhiro KANDA, Takashi NAGATA[1], Mitsuhiko KONO[1],
Kosuke SHOBATAKE[2] and Toshio IBUKI[1]

*Department of Fundamental Science, College of Science and*
*Engineering, Iwaki Meisei University, Iwaki 970*
*[1] Institute for Molecular Science, Myodaiji, Okazaki 444*
*[2] Department of Materials Chemistry, School of Engineering,*
*Nagoya University, Chikusa-ku, Nagoya 464-01*

Photodissociation of simple nitriles, $CH_3CN$, $C_2H_5CN$, n-$C_3H_7CN$ and $C_6H_5CN$ was investigated by the measurement of the absolute cross sections for the photoabsorption of nitriles and the production of $CN(B^2\Sigma^+-X^2\Sigma^+)$ emission in the excitation wavelength range 30-150 nm. The photoabsorption spectra and photoexcitation spectra in the 30-90 nm region and the 80-120 nm region have been measured by use of the window-less configuration and the LiF window cell configuration, respectively. For the measurement in the 80-120 nm region, the argon pressure in the gas filter which was mounted in front of the absorption cell was kept constant at 270 mTorr in order to eliminate the secondary light of an incident SOR beam. The photoabsorption cross section was obtained from the ratio of the vacuum UV photon fluxes measured with the sample gas on and off. The $CN(B^2\Sigma^+-X^2\Sigma^+)$ emission in the UV and visible region was isolated by a band-pass filter (Toshiba C-39A) and detected by a photomultiplier (Hamamatsu R585). The absolute cross section for the production of $CN(B^2\Sigma^+)$ was determined by a comparison of the intensity of the $CN(B^2\Sigma^+-X^2\Sigma^+)$ emission produced in the photodissociation of $CH_3CN$ in the 105-150 nm region.[1]

Fig. 1 shows absorption (thin line) and fluorescence excitation (thick line) spectra of $CH_3CN$, $C_2H_5CN$, n-$C_3H_7CN$ and $C_6H_5CN$. In the absorption spectrum of $CH_3CN$, numerous sharp peaks were observed in the $\lambda >$ 100 nm region. On the other hand, broad structureless continua were observed in the wavelength region shorter than 100 nm. The first ionization potential (IP) of $CH_3CN$ has been reported to be 12.129 eV (102.2 nm). Therefore, these sharp peaks can be assigned to the Rydberg transitions converging to the first IP and/or intravalence transitions. The excitation function for CN(B-X) emission was almost mimic the absorption spectrum of $CH_3CN$. The quantum yield for the CN(B) production was observed to be less than 0.01. The dominant photodissociation channel may be the production of CN(X). In the absorption spectra and photoexcitation spectra of $C_2H_5CN$ and n-$C_3H_7CN$, no sharp peak was observed. Broad bands appeared in the $\lambda$ > 100 nm region were assignable to the Rydberg transitions converging to the first IP. The cross section of the $CN(B^2\Sigma^+-X^2\Sigma^+)$ emission decreases with the length of the hydrocarbon chain. The decrease in the quantum yield for the CN(B) production was also observed in the collisional dissociation of nitriles with the rare-gas metastables.[2] This decrease and broadening of the absorption band can be attributed to the dissipation of the excitation energy to the alkyl group. The absorption and fluorescence excitation spectra of $C_6H_5CN$ have numerous peaks in the wavelength region $\lambda > 100$ nm. The absorption peaks, observed in the wavelength region shorter than 128 nm which corresponds the first IP of $C_6H_5CN$ (9.71 eV), were assigned to the transitions to the super-excited states. These states are probably associated with the Rydberg series converging to the higher IPs. The cross section of the $CN(B^2\Sigma^+-X^2\Sigma^+)$ emission was larger than those of $C_2H_5CN$ and n-$C_3H_7CN$. This increase indicates that the rigid structure of phenyl group enhanced the quantum yield for the CN(B) production.

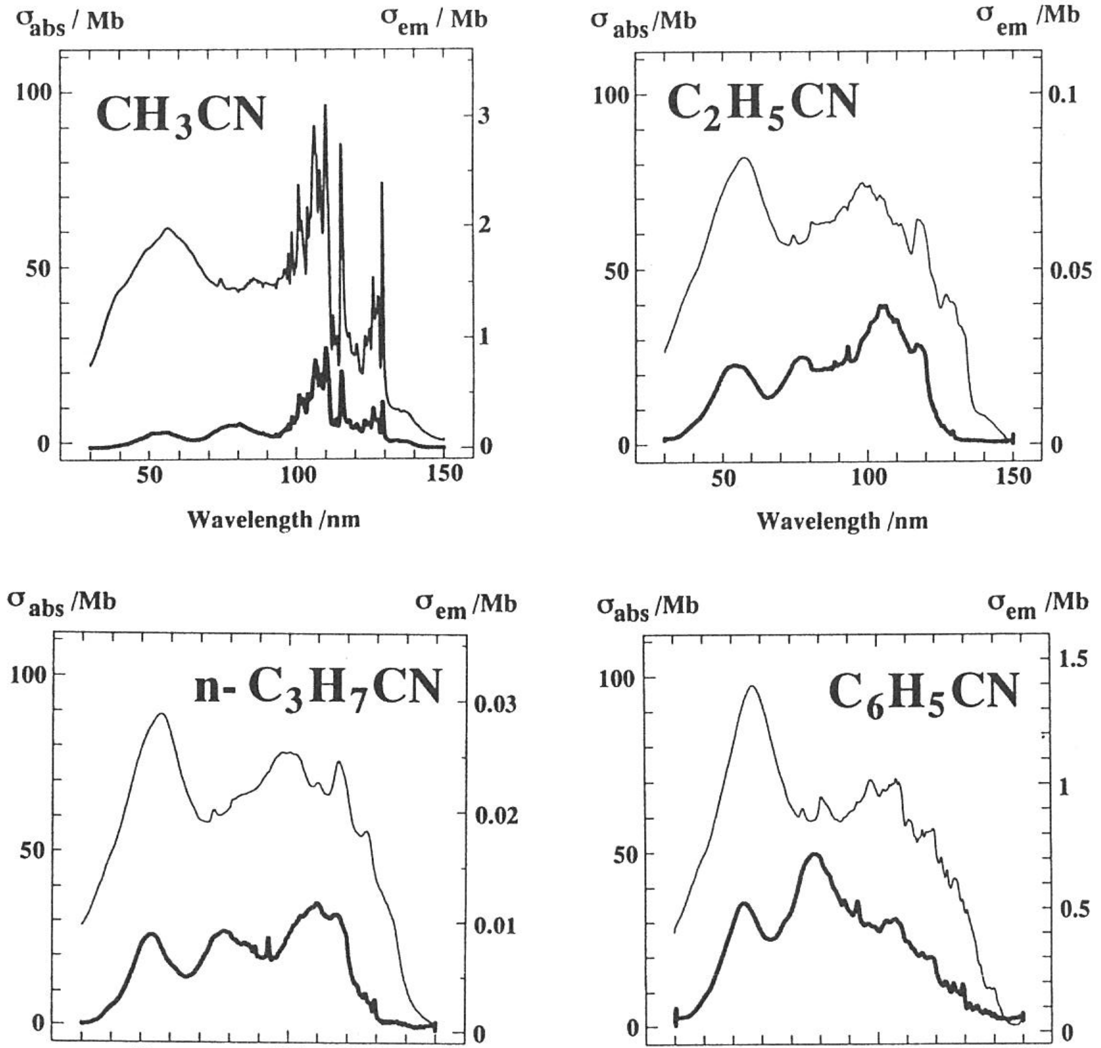

Fig. 1 The absorption and photoexcitation cross sections of $CH_3CN$, $C_2H_5CN$, n-$C_3H_7CN$ and $C_6H_5CN$ in the 30-150 nm region. The spectral resolution was 0.1 nm.

Reference

[1] M. Kono, D. Thesis, Grad. Univ. Adv. Stud., (1995).

[2] K. Kanda et al., J. Phys. Chem., 99, 5269 (1995).

(BL2A)

# Excited $C_6F_5X^{+\cdot}$ (X=H, F, Cl, Br, and I) Radical Cation Formation in the 30-160 nm Region

Takumi HIKIDA, Kazumasa OKADA* and Toshio IBUKI*
Department of Chemistry, Tokyo Institute of Technology, Tokyo 152
*Institute for Molecular Science, Okazaki 444

Far-UV absorption spectra of benzenes have been assigned to Rydberg series leading to the ionization of $\pi$ or $\sigma$ electrons. The ground state of $C_6H_6^{+\cdot}$ is $^2E_{1g}(\pi^{-1})$, and the first and the second excited states are $^2E_{2g}(\sigma^{-1})$ and $^2A_{2u}(\pi^{-1})$, respectively. The $\sigma^{-1}$ state may play an important role in the relaxation of the $\pi^{-1}$ excited states. $C_6H_6^{+\cdot}$ is a typical example of a radical cation for which emission could not be observed. The presence of the dark $\sigma^{-1}$ state near the $\pi^{-1}$ excited state probably opens a non-radiative pathway of the excited $\pi^{-1}$ state to the ground state, and the fluorescence quantum yield is lowered substantially, $<10^{-5}$. Substitution of H by F atoms in benzene increases the ionization energy of the $\sigma$ electron. One might observe the fluorescence from radical cations of which $\sigma^{-1}$ states lie above the emissive $\pi^{-1}$ states.

Absorption spectra of $C_6F_5X$(X=H, F, Cl, Br, and I) were measured in the excitation region 30-160 nm. Nearly the same absorption spectra were observed for these molecules. The main absorption band appeared between 120 nm to 30 nm and two broad peaks at around 85 nm and 60 nm with barely resolved vibrational structures were observed.

Only the emission from $C_6F_5X^{+\cdot}$ were observed by the photolysis of $C_6F_5X$ at around 90 nm. The peak positions are in reasonable agreements with $\nu_{00}$ of the allowed $\pi^{-1} \rightarrow \pi^{-1}$ transitions estimated from the adiabatic ionization energies determined by photoelectron spectroscopy as listed in Table 1. Beside the strong $\pi^{-1} \rightarrow \pi^{-1}$ transitions, $C_6F_5H^{+\cdot}$ and $C_6F_5Br^{+\cdot}$ barely showed the forbidden $\sigma^{-1} \rightarrow \pi^{-1}$ transitions at longer wavelength region. The emission from excited $C_6F_5I^{+\cdot}$ were extremely weak and the peak position could not be determined accurately.

Both $C_6F_5Br^{+\cdot}$ and $C_6F_5I^{+\cdot}$ have their $\sigma^{-1}$ states slightly below the emitting $\pi^{-1}$ states. The $\pi^{-1}$ states may take relaxation via the dark $\sigma^{-1}$ states. Accordingly the emission intensities of the $C_6F_5Br$ and $C_6F_5I$ systems were very weak compared to other systems. The intensity ratio is roughly 50:150:600:5:1 for $C_6F_5X$(X=H, F, Cl, Br, and I).

Excitation spectra of $C_6F_5X^{+\cdot}$ were measured using a long-path glass filter(>400 nm). Similarly structured emission excitation spectra were found to start at around 100 nm to about 35 nm. A typical example is shown in Fig.1 for $C_6F_5Cl$. The ionization energies determined from the threshold wavelengths of the excitation spectra are listed in Table 1. These are in good agreements with the ionization energies determined by photoelectron spectroscopy.

Weak signals appearing $\lambda$ >100 nm to 160 nm are probably due to the second order light escaped from the Ar gas filter. Excitations to other than the formation of $C_6F_5X^{+\cdot}$ are apparent for the excitation energies more than about 50 nm.

Table 1 Ionization energies (IE) and transition energies ($\nu_{00}$) of $C_6F_5X^{+\cdot}$.

| | $C_6F_5X^{+\cdot}$ | IE (eV) | | $\nu_{00}$(cm$^{-1}$) | |
|---|---|---|---|---|---|
| | | reported [a)] | observed [b)] | calculated [c)] | observed [d)] |
| $C_6F_5H$ | X $^2A_2(\pi^{-1})$ | 9.64 | | 0 | |
| | B $^2B_1(\pi^{-1})$ | 12.50 | 12.4 | 23070 | 22700 |
| | C $^2B_2(\sigma^{-1})$ | 13.71 | | 32830 | |
| $C_6F_6$ | X $^2E_{1g}(\pi^{-1})$ | 9.91 | | 0 | |
| | B $^2A_{2u}(\pi^{-1})$ | 12.58 | 12.5 | 21540 | 21700 |
| | C $^2B_{2u}(\sigma^{-1})$ | 13.85 | | 31780 | |
| $C_6F_5Cl$ | X $^2A_2(\pi^{-1})$ | 9.72 | | 0 | |
| | B $^2B_1(\pi^{-1})$ | 12.20 | 12.2 | 20000 | 20000 |
| | C $^2B_2(\sigma^{-1})$ | 12.37 | | 21370 | |
| $C_6F_5Br$ | X $^2A_2(\pi^{-1})$ | 9.67 | | 0 | |
| | B $^2B_2(\sigma^{-1})$ | 11.49 | | 14680 | |
| | C $^2B_1(\pi^{-1})$ | 11.90 | 12.0 | 17990 | 19200 |
| $C_6F_5I$ | X $^2A_2(\pi^{-1})$ | 9.5 | | 0 | |
| | B $^2B_2(\sigma^{-1})$ | 10.5 | | 8070 | |
| | C $^2B_1(\pi^{-1})$ | 11.25 | 11.2 | 14520 | 14900 |

a)References for the ionization energies(IE) are given in ref.[1]. b) $C_6F_5X^{+\cdot}$ fluorescence thresholds. c)Estimated from reported IE. d)Emission intensity maxima.

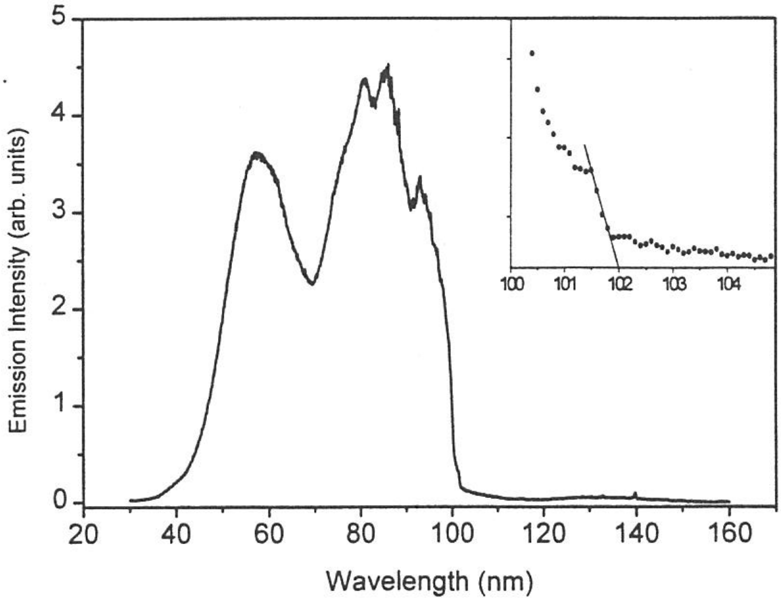

Fig.1. Excitation spectra of $C_6F_5X^{+\cdot}$
Emission intensity was measured >400 nm.

[1] Oomori and Hikida, Chemical Physic 178(1993) 477-481.

# (BL2A) Photoabsorption cross section and radiative processes of $SnCl_4$ in the valence region of 6–31 eV

Ikuo TOKUE and Toshio IBUKI*

*Department of Chemistry, Faculty of Science, Niigata University, Niigata 950-21*
**Institute for Molecular Science, Myodaiji, Okazaki 444, Japan*

In order to establish reliable Rydberg assignments for $SnCl_4$, it is necessary to measure the photoabsorption spectrum in the energy region above the first IP. In this study the absolute photoabsorption ($\sigma$) and emission cross sections of $SnCl_4$ have been measured in the 6–31 eV region. Assignments of the observed bands and radiative processes of fragments resulting from photoexcitation are discussed.

The primary photon longer than 40 nm was practically available at the beam line BL2A. Higher-order light in the 80–110 nm region was suppressed by using an Ar gas filter at a pressure of 0.3 Torr. A LiF window was used in the 105–200 nm region. The absolute emission cross section was determined by normalizing with those for the OH($A^2\Sigma^+$–$X^2\Pi$) transition from $H_2O$ measured at 117.6 and 133.6 nm.[1]

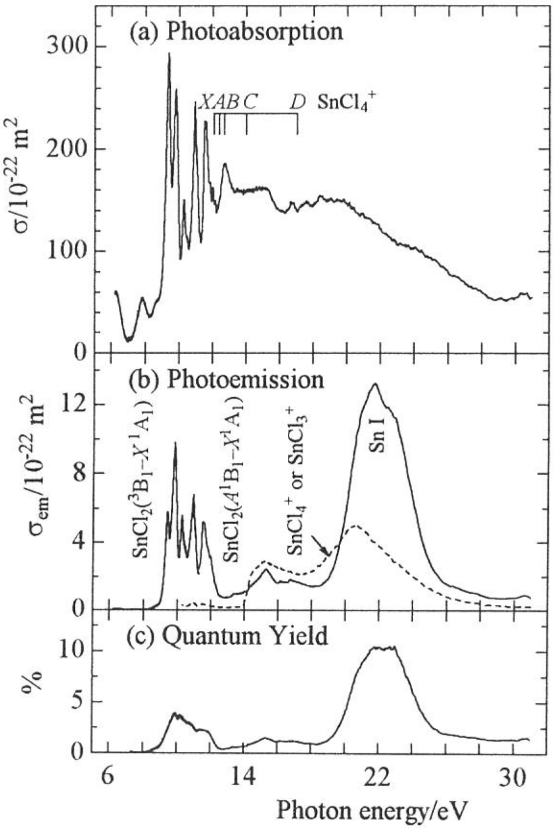

**FIG.1.** Total photoabsorption, partial emission cross sections, and fluorescence quantum yield of $SnCl_4$ in the excitation energy of 6–31 eV.

Fig. 1a shows $\sigma$'s of $SnCl_4$. The electronic configuration of $SnCl_4$ in the valence shell with $T_d$ symmetry is given by

$$(1a_1)^2(1t_2)^6(2a_1)^2(2t_2)^6(1e)^4(3t_2)^6(1t_1)^6$$

The vertical IP's were reported to be 12.10–12.13, 12.38–12.50, 12.71–12.74, 14.0–14.29, and 17.0–17.36 eV [2] for the $1t_1$, $3t_2$, $1e$, $2t_2$, and $2a_1$ orbitals, respectively. The photoabsorption spectrum of $SnCl_4$ in the 6–12 eV region was deconvoluted by Gaussian functions to 16 peaks. The assignments for 14 peaks are given in Table 1 with the quantum defects ($\delta$) and the oscillator strengths ($f$); the $f$ value was calculated from the following equation: $f = 0.02096 \int \sigma(E)dE$, where $\sigma$ is the deconvoluted Gaussian function and $E$ is the excitation energy (eV) of the incident photon. The mean $\delta$ values for the 4*s*, *np* (*n*=4–6), and 4*d* Rydberg transitions are deduced to be 2.06 ± 0.06, 1.68 ± 0.16 , and 0.29 ± 0.07, respectively. The quantum defects for the Rydberg series of $SnCl_4$ assigned in this study lie nearly those of Cl atom.

Fig. 1b shows the partial emission cross sections ($\sigma_{em}$) of $SnCl_4$; the solid curve represents $\sigma_{em}$ for the fluorescence in the 200–600 nm region and the corresponding quantum yield is shown in Fig. 1c. The uncertainty in these curve was estimated to be within 15% of the given value. The broken curve in Fig. 1b represents the relative emission cross section for the fluorescence above 540 nm; the optical sensitivity is not calibrated for the broken curve.

Fig. 2 shows dispersed fluorescence spectra of $SnCl_4$ excited at 10.9, 15.2, and 21.5 eV; a low spectral resolution of 10 or 16.5 nm was employed because of weak emission intensities. In the spectrum excited at 10.9 eV (113.3 nm), emissions peaked around 340 and 443 nm are assigned as the $A^1B_1$–$X^1A_1$ and $^3B_1$–$X^1A_1$ transitions, respectively, of the $SnCl_2$ radical by comparing with the bands observed in the chemiluminescent experiments. [3] The threshold for the $SnCl_2(^3B_1$–$X^1A_1)$ emission from $SnCl_4$ was found to be 7.21 ± 0.04 eV (172 ± 1 nm). The reaction for formation of $SnCl_2(^3B_1)$ from $SnCl_4$ is

$$SnCl_4 \rightarrow SnCl_2(^3B_1) + 2Cl,$$
$$\Delta H = 7.21 \pm 0.04 \text{ eV}.$$

This result gives $\Delta H_f^o[SnCl_2(X^1A_1)] = -3.00 \pm 0.04$ eV (- 289 ± 4 kJ/mol). The intense band peaked at 217 nm was observed in the emission spectrum excited at 15.2 eV (81.6 nm). All the emission produced by the 15.2 eV photodissociation is concluded to be due to the SnCl radical. The spectral features obtained at the 21.5 eV (57.6 nm) are attributed to Sn I lines from the similarity with those obtained by the collisions of $He(2^3S)$ with $Sn(CH_3)_4$ and $SnCl_4$.[4] The vertical lines in Fig. 4c represent the intensity and wavelength of Sn I lines observed in the $He(2^3S)$ with $Sn(CH_3)_4$ collision.

TABLE I. Rydberg assignments for $SnCl_4$ in the region of 6–14 eV.

| Peak (eV) | δ | Assignment | *f* |
|---|---|---|---|
| 6.225 | | $3a_1 \leftarrow 3t_2$ | 1.069 |
| 7.818 | | $3a_1 \leftarrow 2t_2$ | 0.866 |
| 8.743 | 2.09 | $4s \leftarrow 3t_2$ | 0.751 |
| 9.155 | 2.02 | $4s \leftarrow 1e$ | 0.519 |
| 9.375 | 1.77 | $4p \leftarrow 1t_1$ | 1.608 |
| 9.795 | 1.75 | $4p \leftarrow 3t_2$ | 1.885 |
| 10.267 | 1.64 | $4p \leftarrow 1e$ | 0.824 |
| 10.530 | 2.06 | $4s \leftarrow 2t_2$ | 0.298 |
| 10.927 | 1.62 | $5p \leftarrow 1t_1$ | 0.987 |
| | 2.05 | $5s \leftarrow 3t_2$ | |
| 11.143 | 0.26 | $4d \leftarrow 1t_1$ | 0.299 |
| | 1.82 | $5p \leftarrow 3t_2$ | |
| 11.491 | 1.67 | $6p \leftarrow 1t_1$ | 0.401 |
| | 0.31 | $4d \leftarrow 3t_2$ | |
| | 1.66 | $5p \leftarrow 1e$ | |
| 11.611 | 1.68 | $4p \leftarrow 2t_2$ | 0.479 |
| 11.832 | 1.55 | $6p \leftarrow 3t_2$ | 0.130 |
| 11.997 | 1.63 | $6p \leftarrow 1e$ | 0.083 |

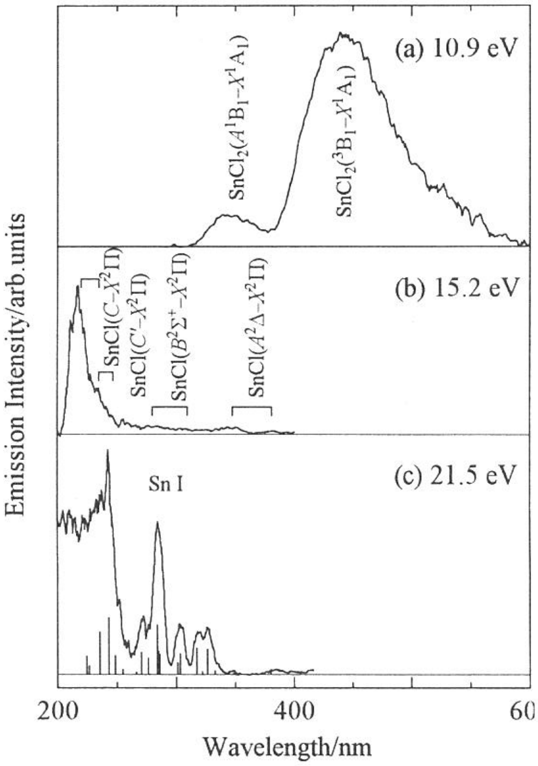

FIG.2. Dispersed emissions from $SnCl_4$ excited at (a) 10.9, (b) 15.2, and (c) 21.5 eV. The optical sensitivity is calibrated.

## References

[1] L.C.Lee *et al.*, J. Phys. B **11**, 47 (1978).
[2] (a) P. J. Bassett and D. R. Lloyd, J. Chem. Soc. A **1971**, 641. (b) J. C. Green, *et al.*, Phil. Trans. Roy. Soc. London A **268**, 111 (1970).
[3] J. H. Wang *et al.*, J. Chem. Phys. **93**, 7830 (1990).
[4] I. Tokue *et al.*, Bull. Chem. Soc. Jpn. **69**, 2815 (1996).

(BL2A)

# Potential of Site Specific Photochemical Processing Using Synchrotron Radiation

Tsuneo Urisu and Toshio Ibuki [a]   Yoshiaki Imaizumi [a] Masahiro Kawasaki [c],

[a] *Institute for Molecular Science,* [b] *The Graduate University for Advanced Studies ,*
*Myodaiji, Okazaki, 444 Japan*
[b] *Hokkaido University, Sapporo 060, Japan*

An absorption spectrum in the vacuum ultra violet region and a photoelectron spectrum for the valence-electron-states of the gas phase DMAH were measured and the energy levels of the DMAH electronic states were determined. Using this result, it was concluded that the difference of the carbon contamination in photo-stimulated Al deposition between white beam SR and Mg $K_a$ line irradiations is due to the difference of the reaction channels induced. The Mg $K_a$ line irradiation excites valence-electron-states, mainly pCH3 states, and breaks the C-H bond. On the other hand, in the case of SR irradiation, not only valence-electron-states, but also Al 2p and Al 2s core-electron-states are excited and the Al-C bond is broken. This indicates the usefulness of the photochemical *site-specific* processing. The observed absorption spectra were shown in Fig. 1.

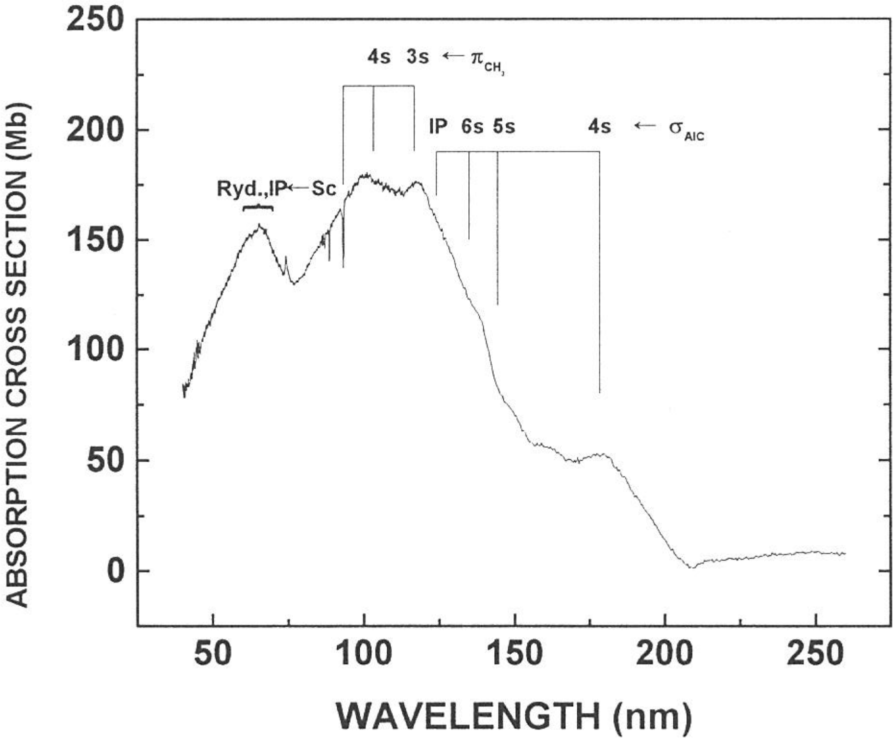

Fig. 1 Photoabsorption cross sections of DMAH observed at 1×$10^{-2}$ Torr. The spectral resolution is 0.2 nm. The Rydberg assignments are indicated.

(BL2B1)

# Photoemission study of benzene adsorbed on Si(111)(7×7)

Yukihiro TAGUCHI, Yasuaki OHTA, and Osamu AITA

*College of Engineering, Osaka Prefecture University, Gakuen-cho 1, Sakai 593*

Benzene chemisorbs on low-index Si surfaces and shows an interesting crystal-face specificity. On (100)(2×1) and (111)(7×7) surfaces $C_6H_6$ chemisorbs intact,[1] while on a cleaved (111)(2×1) surface it chemisorbs dissociatively forming $C_6H_5$ and H adsorbates.[2] In the previous study[1] we have found that vibrational spectra of benzene chemisorbed on (100)(2 × 1) and (111)(7 × 7) are qualitatively different from each other. The chemisorbed states of benzene are also different between the two surfaces. In this work we have studied the adsorbed state of benzene on the Si(111)(7 × 7) suface using photoemission (PE) and C *K*-edge near-edge x-ray absorption fine structure (NEXAFS) spectroscopies.

The sample used was a Si(111) wafer. The clean (7×7) surface was prepared by several cycles of $Ar^+$-ion bombardment and annealing. $C_6H_6$ was introduced into an analysis chamber through a variable leak valve. The spectrometer used for PE and NEXAFS measurements was a cylindrical mirror analyzer, which is normal to x-ray beam from a grass-hopper monochromater. We have assumed that a benzene exposure of 1.3 L (1 L = $1.33 \times 10^{-4}$ Pa s) at liquid nitrogen temperature (LNT) corresponds to the formation of one monolayer (ML) of physisorbed benzene on the surface.[1] The chemisorbed benzene was left on Si(111)(7 × 7) by exposing the surface to benzene at LNT and heating briefly to 250 K.

The saturation coverage of chemisorbed benzene on Si(111)(7 × 7) is estimated by comparing the PE-peak-height ratios of C 1*s* and Si 2*p* for benzene-chemisorbed and -physisorbed surfaces. The saturation coverage is $\sim 1/3$ ML, which is consistent with the previous study.[1] The fractional coverage is approximately equal to that for the rest atom of the Si(111)(7 × 7) surface. The saturation coverage on Si(111)(7 × 7) is about half as that on Si(100)(2 × 1). The valence-band PE spectrum for benzene-chemisorbed Si(111)(7×7) surface taken with excitation-photon-energy of 100 eV shows features derived from the adsorbates, which are not evident as observed for the benzene-chemisorbed Si(100)(2 × 1) surface.[3] Lower excitation energy may be appropriate to examine the electronic structure of adsorbates in the valence band region. The C 1*s* PE spectra for chemisorbed and physisorbed benzene show symmetric single peaks with almost equal widths, it follows that six C atoms of the molecule is in the same chemical environment upon chemisorption on Si(111)(7 × 7).

Figure 1 shows the C *K*-edge NEXAFS spectra of benzene chemisorbed on the Si(111)(7× 7) surface. The spectra are constant-final-state spectra with photoelectron-kinetic-energy of 262 eV, which are divided by total photoelect ric yield. There is a strong $\pi^*$ resonance at 286 eV for grazing x-ray incidence [Fig. 1(a)] while weak resonance at normal incidence [Fig. 1(c)]. Chemisorbed benzene lies nearly parallel to the surface plane.

References

[1] Y. Taguchi *et al.*, J. Chem. Phys. **95**, 6870 (1991), Y. Taguchi *et al.*, Chem. Phys. Lett. **178**, 363 (1991).

[2] M. N. Piancastelli *et al.*, Phys. Rev. B **30**, 1945 (1984).

[3] Y. Taguchi *et al.*, UVSOR Act. Rep. **1995**, 106.

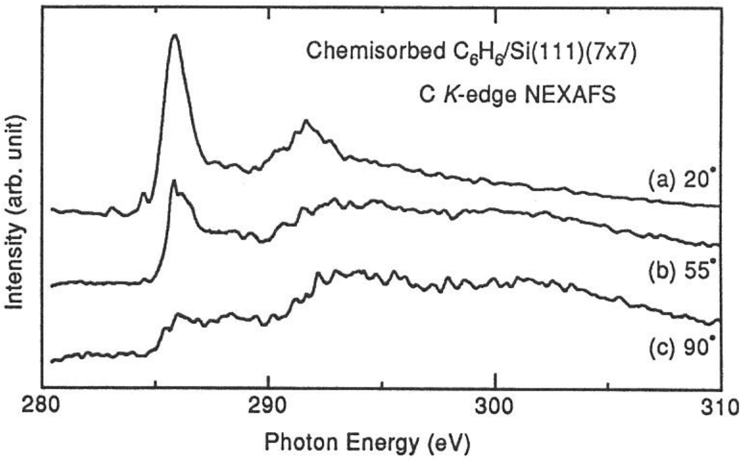

FIG. 1

(BL2B1)

# Deexcitation Electron Spectra of the $H_2O$/Si(100) Surface

Shin-ichiro Tanaka, Kazuhiko Mase, Mitsuru Nagasono, and Masao Kamada
Institute for Molecular Science, Myodaiji, Okazaki 444, Japan

The Deexcitation electron spectroscopy is rather new technique which is sometimes referred as resonant Auger spectroscopy or autoionization spectroscopy[1]. It is obtained by measuring the Auger electron spectra as a function of the photon energy corresponding to the excitation from the core level to the bound state. In such case, the initial state of the Auger decay is not a 1h ( one hole ) state as created by an excitation with an electron beam but a 1h1e ( one hole and one electron ) state which can be controlled by changing the photon energy. The Deexcitiaon spectra is a good tool for the investigation of the core excited state and its decay process. In the present report, we have observed the Deexcitaion spectra of the $H_2O$/Si(100) surface, and found the different behavior of the core-decay process for the adsorbates on the semiconductor surface from that of gaseous and condensed molecules.

The interaction of water on the semiconductor surface, particularly Si, has been extensively studied because of its importance in technology[1]. Vibrational studies ( High resolution electron energy loss spectroscopy[2] and Surface infrared spectroscopy [3] ) have shown that water dissociates into Si-OH and Si-H species on the Si(100) surface at room temperature. In contrast, Schmeisser et. al. insisted the molecularly ( non-dissociative ) adsorption using the photoelectron spectroscopy[4]. However, Ciraci et.al. and Oellig et. al. stated that the photoelectron spectra which had been assigned to molecularly chemisorbed water could be attributed to the Si-OH and Si-H species. Vibrational spectroscopy is generally more sensitive to the bonding configuration than the photoelectron spectroscopy, and thus, the dissociative adsorption of water on Si(100) surface is generally accepted although the assignments of the feature in the photoelectron spectrum are not clear yet[5]. In the present study, we report the Deexcitation electron spectra of the $H_2O$/Si(100) surface after the excitation of the O-1s core level.

All the experiments were made in the ultra-high vacuum chamber ( base pressure of 1 x$10^{-11}$ Torr) which were installed at the beamline 2B1 of the UVSOR facility in Institute for Molecular Science. The grasshopper monochromator was installed there The surface of the Si(100) wafer ( p-doped, 0.5Ωcm) were cleaned by the resistive heating. The exposure of the water vapor was 5 L ( 1L= 1x$10^{-6}$ Torr sec ) which were sufficient for the saturation coverage. Figure 1 shows the partial electron yield spectra at the O-K edge of the $H_2O$/Si(100) surface. The kinetic energy of detected electron was 510 eV and the window was about 10 eV. The spectra observed is similar to the previous results reported by Sekiguchi et.al (6) The peak at the threshold is ascribed to the excitation from the O-1s core level to the 4 $\sigma^*$ ( and probably $2\pi^*$ ) bound state, and rather broader second peak is ascribed to the shake-up ionization. The photoelectron spectra observed at the photon energies indicated in the figure 1 and shown in figure 2. The peaks are ascribed not only to the O-KVV Auger electrons but also to the directly excited phtoelectrons from the valence band and the Si-2p level which show the linear shift as a function of the photon energy. It is possible to eliminate the contribution from the directly excited photoelectrons by shifting the spectrum taken at hv=520 eV ( below the O-K edge ) according to the photon energy and subtracting it from the raw spectra. Results are shown in figure 3. There are no significant differences among the spectra of different photon energies. It contrasts with the case of the condensed $H_2O$(7) where the spectator Auger electrons were observed at the higher kinetic energy side of the normal Auger electrons. It is an emission from the 1h1e state, and the peak shift is due to the effect of the excited electron trapped near the core hole. These are not observed for $H_2O$/Si(100), which is attributed to the adsorbate-substrate interaction. The Si(100) surface should act as a "sponge" to quench the excited state of the adsorbates.

The assignments of the spectrum can be made by comparison with the gaseous H2O(8)(Fig.4). The molecular orbitals of $H_2O$ are $2a_1$, $1b_2$, $3a_1$ and $1b_1$, and they correspond to $2\sigma$, $O\sigma$, $3\sigma$ and $1\pi$ of the OH species on the Si(100) surface. The assignments are listed as follows with those for gaseous $H_2O$(8)

| Peaks in $H_2O$/Si(100) (eV) | Assignments | Peaks in $H_2O$ gas (eV) | Assignments |
|---|---|---|---|
| 468.5 | $(2\sigma)^2$ | 458 | $(2a_1 2a_1)$ |
| 479 | $(2\sigma, O\sigma)$ | 468 | $(2a_1,1b_2)^1$ |
| 483 | $(2\sigma,3\sigma),(2\sigma,1\pi),(2\sigma,1\pi)$ | 474 | $(2a_1 3a_1)^1, (2a_1 1b_1)^1,(2a_1 1b_1)^3$ |
| 490 | $(2\sigma,3\sigma),(2\sigma,1\pi)$ | 482 | $(2a_1,3a_1)^3,(2a_1,1b_1)^3$ |
| 496 | $(O\sigma)^2$ | 487 | $(1b_2 1b_2)$ |
| 501 | $(3\sigma)^2,(O\sigma,3\sigma) ,(O\sigma,1\pi)$ | 493 | $(3a_1 3a_1),(1b_2,3a_1)^1,(1b_2 1b_1)^1$ |
| 506 | $(1\pi)^2, (3\sigma,1\pi)$ | 498 | $(1b_1 1b_1),(3a_1,1b_1)^1$ |

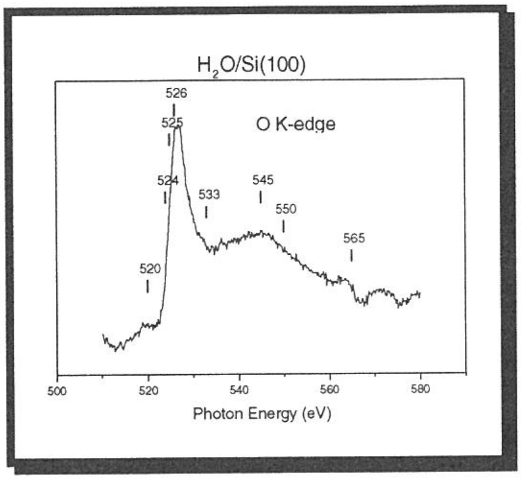

**Figure 1:**Partial electron yield spectrum at the O-K edge from the $H_2O$/Si(100) surface. Photoelectron spectra ( deexcitation spectra ) were measured at the photon energies indicated in the figure.

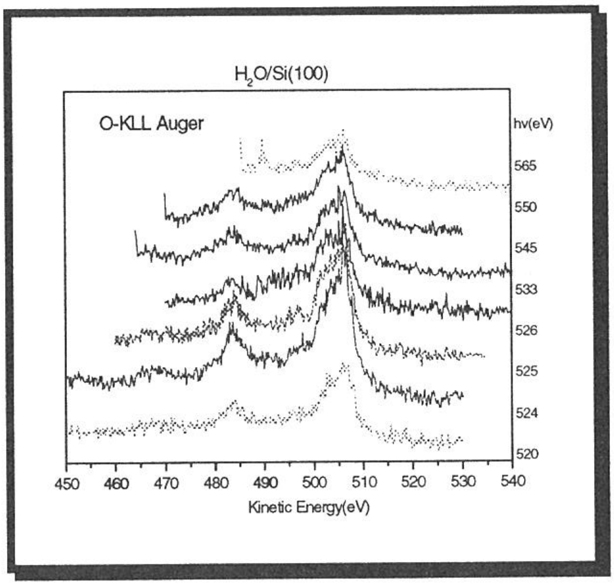

**Figure 3:**O-KVV Auger electron spectra of the $H_2O$/Si(100) surface taken at various photon energies, which are obtained by subtracting the contribution of the valence band from the spectra in figure 2 using the spectra taken at hv = 520 eV

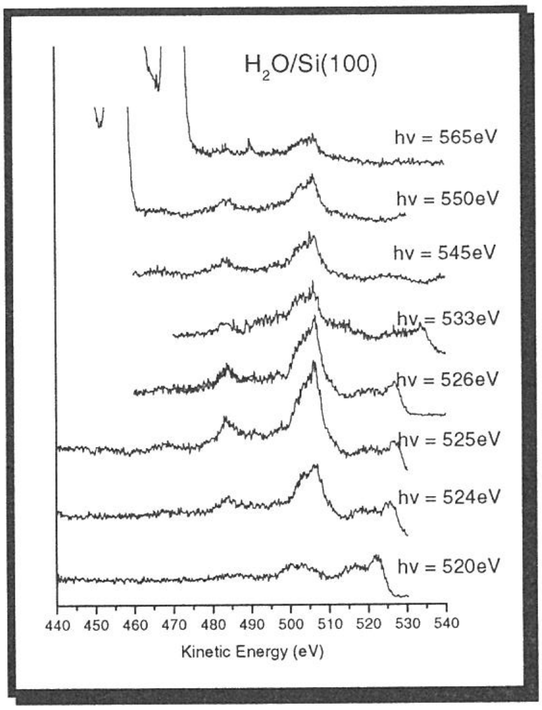

**Figure 2:**Deexcitaion spectra of the $H_2O$/Si(100) surface. Photon energies used are indicated in the figure.

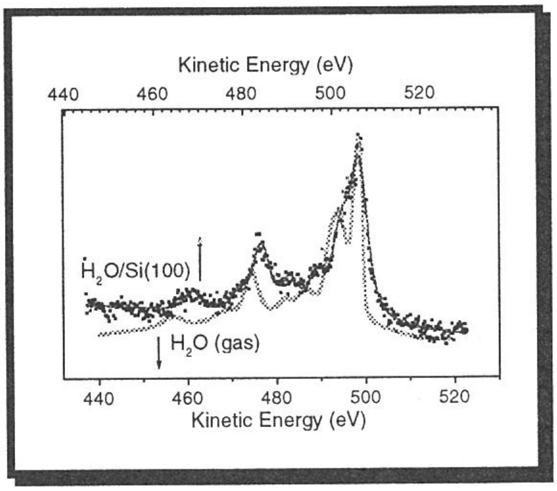

**Figure 4:**Comparison of O-KVV Auger electron spectra between $H_2O$/Si(100) and gaseous $H_2O$. The energies are shifted as the largest peaks are aligned for each other.

Reference:
1) P. E. Thiel and T.E. Madey, Surf. Sci. Rep. 7(1987) 211, and references therein.
2) H. Ibach, H. Wagner and D.Bruchmann, Solid State Commun. 42 (1982) 457.
3) Y. J. Chabal and S.B. Christman, Phys. Rev. B29(1984)6974.
4) D. Schmeisser, F.J. Himpsel and G. Hollinger, Phys. Rev. B27(1983)7813, and references therein.
5) S. Katircioglu, Surf. Sci. 187 (1987) 569
6) T. Sekiguchi, H. Ikeuram K. Tanaka, K. Obi, N. Ueno and K. Honma, J. Chem. Phys. 102(1995)1422
7) M. Nagasono, et. al, in preparation
8) H. Siegbahn, L. Asplund and P. Kelfve, Chem. Phys. Lett., 35(1975)330.

(BL2B1)

# NEXAFS Studies of Higher Fullerenes up to C100

R. Mitsumoto[a], H. Oji[a], I. Mori[a], Y. Yamamoto[a], K. Asato[a], T. Iwano[a], Y. Ouchi[a], H. Shinohara[a], K. Seki[a],
K. Umishita[b], S. Hino[b], S. Nagase[c], K. Kikuchi[c] and Y. Achiba[c]
[a]*Department of Chemistry, Nagoya University, Chikusa-ku, Nagoya 464-01, Japan*
[b]*Department of Image Science, Chiba University, Chiba 260, Japan*
[c]*Department of Chemistry, Tokyo Metropolitan University, Hachioji, Tokyo 192-03, Japan*

NEXAFS measurements for a series of higher fullerenes with increasing carbon number is expected to give spectra representing the difference of their electronic structures. We performed NEXAFS measurements of higher fullerenes C78, C84, C86, C88, C90, C92, C94, C96 and C100. Besides the carbon number dependence electronic structures should depend on their geometrical structures. We also performed NEXAFS measurements using carefully isomer-separated C78, C84 and C90 fractions, i.e.(1) a C2v' isomer of C78, (2) mixture of D2 and D2d isomers of C84, (3) a C2 isomer of C84 and (4) a C90 isomer with C2 symmetry.

Fullerene soot obtained by arc-heating of graphite was separated by high pressure liquid chromatography (HPLC) into fractions each of which consists of fullerenes with the same carbon number. These fractions were characterized by mass spectrometry and NMR measurements about their carbon numbers and symmetries. In the further separation, the chromatogram showed at least two peaks in the range corresponding to C78. The fractions corresponding to the first peaks were used for the present measurements, which was characterized as the species with C2v' symmetry. Similarly, four peaks were observed in the range corresponding to C84. The fractions corresponding to the first and the second peaks were used. They were characterized as the mixture of isomers with D2 and D2d symmetries and as the isomer with C2 symmetry, respectively. In the range corresponding to C90, at least three peaks were observed. The fraction corresponding to the dominant peak, characterized as an isomer with C2 symmetry, was used. The samples were prepared using fullerene powders as thin films by vacuum evaporation onto Cu and Ni substrates under vacuum of $10^{-5}$ Torr. Their thickness was monitored with a quartz oscillator, and was adjusted to be 10-100nm. NEXAFS measurements were performed using synchrotron radiation at the beamline 11A of Photon Factory at the National Laboratory for High Energy Physics (KEK-PF) and at the beamline 2B1 of the UVSOR facility at Institute for Molecular Science (IMS), both equipped with a Grasshopper monochromater with a grating of 2400 lines/mm. The spectra were measured in the total electron yield mode.

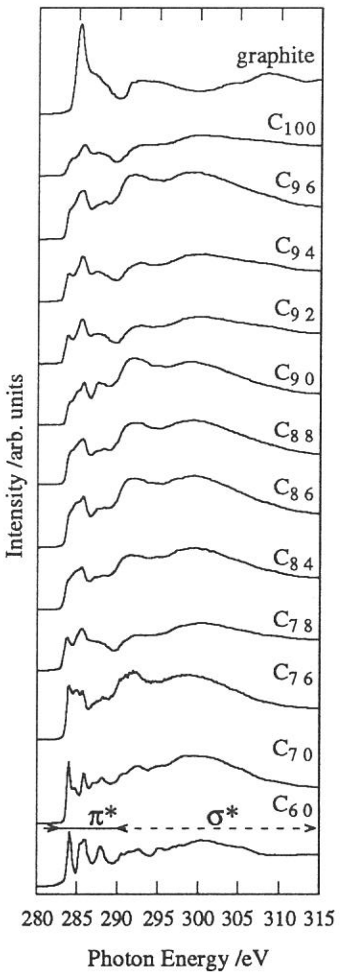

Fig 1. NEXAFS Spectra of Fullerenes

In Fig. 1, we show the NEXAFS spectra of isomer-mixed higher fullerenes up to C100, compared with the spectra of C60, C70, C76 and graphite we obtained previously under the same experimental conditions. The observed spectra of C76 and C84 are in reasonable agreement with the reported EELS spectra [1,2], except for some difference in relative peak intensities. Even the spectrum of C100 is much different from that of graphite. At lower energy region corresponding to the transitions to the π* orbitals, the spectra of smaller fullerenes C60 and C70 show several sharp peaks and that of C76 still show some fine spectral features. On the other hand, the spectra of higher fullerenes become broader with rather similar gross features with a peak at about 285.5 eV. These differences suggest that electronic and geometrical structures of fullerenes significantly change between C70 and C78. In previous report on C84 [2], such a broadening was ascribed to two origins: (a) the lower symmetry of higher fullerenes, and (b) overlap of electronic structures of mixed isomers. As for (a), smaller fullerenes with high symmetries have highly degenerated $\pi^*$ levels, which leads to sharp peaks in the NEXAFS spectra. The $\pi^*$ levels of higher fullerenes with lower symmetries are distributed in broader range, and will produce broad and complicated NEXAFS structures. However, we see sharp features still in the spectra of C86 and C90, suggesting that the spectra of each isomer may show sharper features.

This expectation was confirmed by comparison the spectra of isomer-mixed higher fullerenes with the spectra of isomer-separated C78, C84 and C90. These isomer-separated fractions were a C2v' isomer of C78, mixture of D2 and D2d isomers of C84, a C2 isomer of C84 and an isomer C90 with C2 symmetry. The spectra of isomer-separated fractions are clearly different from each other, with sharper features than those of the mixtures.

In the $\sigma^*$ excitation region, the spectra of C60 and C70 have some fine features, while the spectra of other fullerenes have two dominant broad structures at about 292 eV and 299 eV.

We also compared the observed spectra of C76 and isomer-separated C84 with the calculated densities of unoccupied states (DOUS) for C76 (D2 symmetry) and C84 (D2d symmetry) by *ab initio* method. Poor agreement was seen both about energy and intensity of the spectral features. This may arise from modification of DOUS by core excitonic effect, and/or insufficient accuracy of geometry optimization of MO calculations. These points need further theoretical studies.

**References**

[1]J. F. Armbruster, H. A. Romberg, P. Schweiss, P. Adelmann, M. Knupfer, J. Fink, R. H. Michel, J. Rockenberger, F. Hennrich, H. Schreiber and M. M. Kappes, Z. Phys. B95(1994)469

[2]R. Kuzuo, M. Terauchi, M. Tanaka, Y. Saito and Y. Achiba, Phys. Rev. B51(1995)11018

(BL2B1)

# Study of Ion Desorption Induced by Resonant Core-Level Excitations of Condensed $NH_3$ by Using Auger Electron-Photoion Coincidence (AEPICO) Spectroscopy Combined with Synchrotron Radiation

Mitsuru Nagasono, Kazuhiko Mase, Shin-ichiro Tanaka, and Tsuneo Urisu
*Institute for Molecular Science, Okazaki 444, Japan*

Photo-stimulated ion desorption (PSID) following photoexcitation of core level is one of the most interested phenomena in DIET. In the ion desorption induced by normal excitation from core level to vacuum level Auger stimulated ion desorption (ASID) is one of the most probable model for the desorption mechanism. For investigations of ASID mechanism, energy-selected electron - mass-selected ion coincidence (EICO) spectroscopy is one of the most efficient method. Recently we have reported ASID studies at normal excitation of condensed $NH_3$ using EICO spectroscopy [1]. The ASID probability at normal excitation have been found to be governed by three factors, i.e. the character of the valence orbital where electrons are emitted, the effective hole-hole Coulomb repulsion, and the reneutralization probabilities before ion desorption. In the present paper we describe a study of PSID for condensed $NH_3$ at a resonant excitation from core to unoccupied orbital by using a total ion yield spectroscopy (TIYS), a Auger electron yield spectroscopy (AEYS), a photoelectron spectroscopy (PES), and Auger-electron - photoion coincidence (AEPICO) spectroscopy.

The TIYS divided by AEYS (TIY/AEYS) exhibited a clear resonance peak at hυ = 399 eV, as shown in figure 1. The PES (B) at the resonance excitation of hυ = 399 eV was found to be different from that (D) at the valence excitation of hυ = 396 eV, and also from normal N KVV Auger electron spectrum (normal AES) (A) at the normal excitation of hυ = 419 eV. We have decomposed the resonant PES at hυ = 399 eV into three components; the first is photoelectron from valence orbital, the second is normal AES because of delocalization of excited electron, and the third is resonant AES. We ascribed the resonant AES (E) mainly to the spectator Auger transitions on the basis of the peak assignment. Furthermore, a series of AEPICO spectra at the resonant excitation was measured as a function of the Auger electron kinetic energy, as shown in figure 3. The spectrum of $H^+$ yield of AEPICO in figure 4 was also found to be greatly different from that at the normal excitation, and its peak was found to correspond to the peak in the resonant (spectator) AES. On the basis of these results we have assigned the peak of TIYS at hυ = 399 eV to the resonant transition form the N 1*s* to an antibonding $4a_1$ orbital in the topmost layer, and concluded that the main channel of PSID at the resonance excitation of hυ = 399 eV is the spectator-Auger-stimulated desorption.

[1]. M. Nagasono, K. Mase, S. Tanaka, and T. Urisu, Surf. Sci., in press.

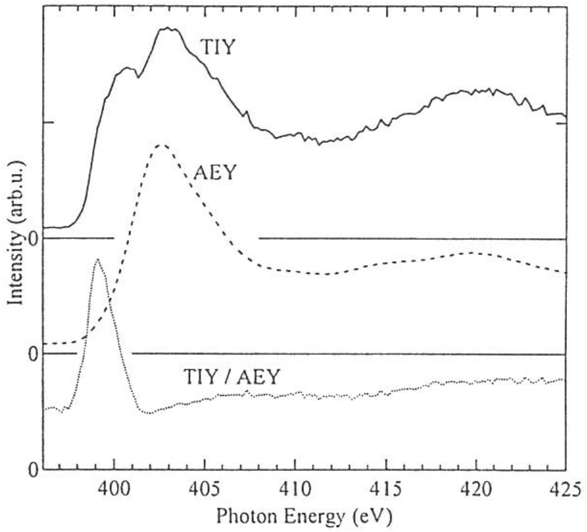

Figure 1. Total ion yield spectrum (TIYS), Auger electron yield spectrum (AEYS), and TIY/AEYS for condensed NH3. Auger electron was selected at eKE = 369 eV corresponding to N KVV Auger electron

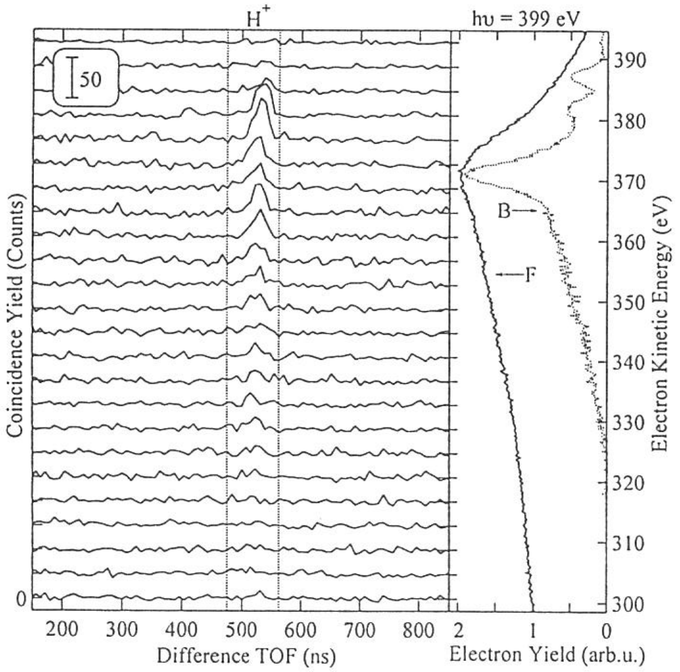

Figure 3. AEPICO spectra (left) and PES (spectra B and F) at the resonant excitation. AEPICO spectra are displayed at the corresponding eKE (right axis). The spectrum (F) is raw data measured with the single pass CMA (E/ΔE = 80) under the same condition of the AEPICO measurement

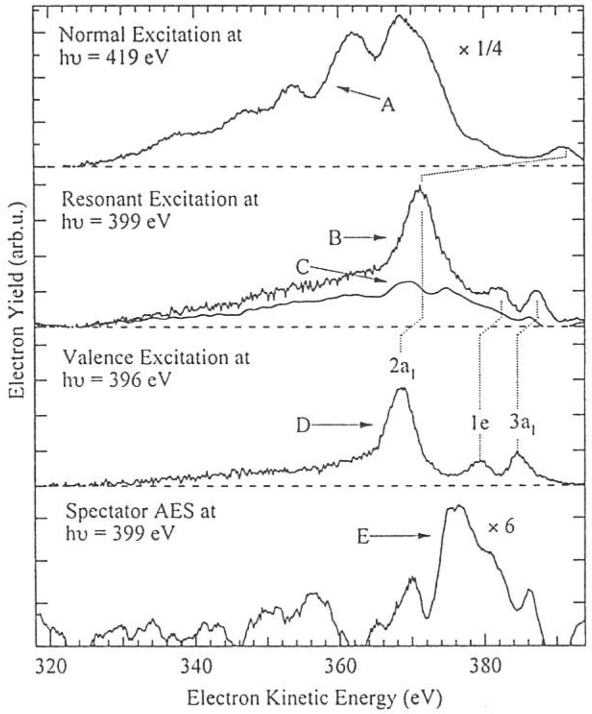

Figure 2. Photoelectron spectra (PES) at hυ = 419 (A), 399 (B), and 396 eV (D). The spectrum (C) show the difference spectrum between (B) and (D) assuming an energy shift of hυ - eKE. The spectrum (E) show the difference spectrum between (C) and (A) multiplied by an appropriate factor of 1/15

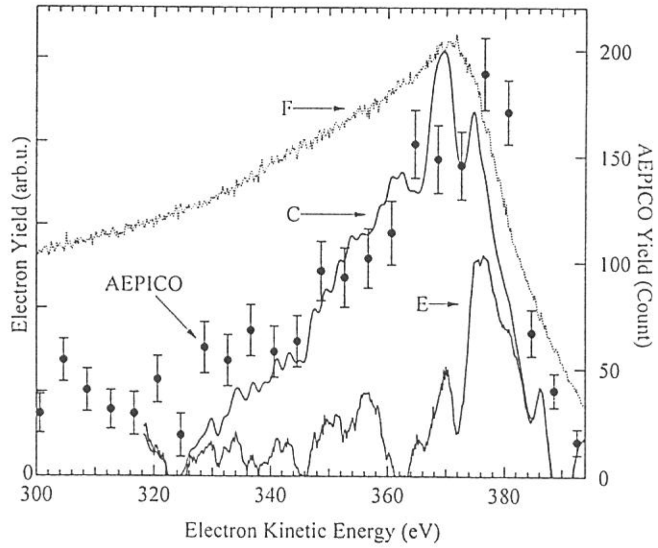

Figure 4. AEPICO yield spectrum as a function of eKE.

(BL-2B1)

# Auger-electron-photoion-coincidence study in solid benzene

Iwao Shimoyama,
Hiroki Horiuchi[1)], Yasushi Otsuki[1)], Takeshi Mochida[1)],
Sachiko Saijou[2)], Kazumichi Nakagawa[2)]
Mitsuru Nagasono[3)], Shin-ichiro Tanaka[3)], Kazuhiko Mase[3)]

Graduate School of Sci. and Tech., Kobe University, Rokkohdai, Nada-Ku, Kobe 657
[1)]Graduate School of Education, Kobe University, Tsurukabuto, Nada-Ku, Kobe 657
[2)]Faculty of Development, Kobe University, Nada-Ku, Kobe 657
[3)]Institute for Molecular Science, Okazaki, Aichi 444

Aromatic compounds are known to be strong against irradiation. However the detail in radiation damage on aromatic compounds has not be known yet. Kimura et al. [1] reported that anthracene single crystals had a strange nature, the color center formation yield $\eta$ decreased above the carbon K-edge. To investigate this problem, we measured C-H dissociation yields in solid benzene with Auger-electron-photoion-coincidence(AEPICO) technique.

Experiments were performed at BL-2B1. Benzene were adsorbed to Au surface about 100L at 80K. Cylindrical mirror electron energy analyzer(CMA) and time of flight spectrometer(TOF) were mounted on UHV chamber. Using CMA, we measured NEXAFS in the carbon K-edge region with partial electron yield(PEY) spectra. The resolution of CMA was about 50. We measured total ion yield(TIY) spectra with TOF.

Figure 1 shows PEY and TIY spectrum in the region $280<h\nu<300$eV. In the PEY spectrum, largest peak at the 285eV is assigned to $1s\rightarrow\pi^*(e_{2u})$ [2] and hatced line shows the ionization energy. TIY/PEY spectrum is also shown in Fig. 1. Most of total ion is $H^+$, so that an obvious peak near 287eV on this curve implies high C-H dissociation yield. Menzel et al. [2] called this peak $X_D$ peak. Excitation photon energy, 285eV and 287eV, are followed by resonant Auger decay. We examined AEPICO measurement for these two $h\nu$. To make a comparison between normal Auger decay and resonant Auger decay, we then measured AEPICO at $h\nu=430$eV which completely causes $1s\rightarrow$ionization transition. Figure 2 shows AEPICO spectrum for $h\nu=430$eV. We can find coincidence signals in the gate times between 420-456ns for $h\nu=430$eV and 287eV, however for $h\nu=285$eV we can't find coincidence signals. From AEPICO spectra, we estimated coincidence counts in each $h\nu$ and got AEPICO yields spectra(AEPICOYS). Figure 3 shows AEPICOYS for $h\nu=430$eV. In Fig. 3, the solid curve shows Auger electron spectrum(AES) and black circle shows coincidence counts. From fig. 3, we got maximum coincidence counts at kinetic energy(KE)=255eV. This energy is lower than AES peak energy about 5eV. So, we founds coincidence yield Y(coincidence counts / Auger electron counts) for each $h\nu$ at KE=255eV. The results was that $Y(430\text{eV})=2\times10^{-6}$, $Y(287\text{eV})=2.5\times10^{-6}$ and $Y(285\text{eV})\leqq10^{-7}$. This result implies that the C-H dissociation yields for $1s\rightarrow\pi^*(e_{2u})$ transition is about ten times smaller than those for $1s\rightarrow X_D$ and $1s\rightarrow$

ionization transition, which may means that the validity of spectator electron effects suggested by Mase et al.[3] is appropriate. The small value of C-H dissociation yield for 1s→$\pi^*(e_{2u})$ may suggests to cause decrease of $\eta$.

Reference
[1]A.Kimura et al., NIM B 91(1994) [2]Menzel et al., JCP. 96,3(1992)
[3]Mass et al., Phys. Soc. of Jap. 50th annual meeting 3a-PS-14

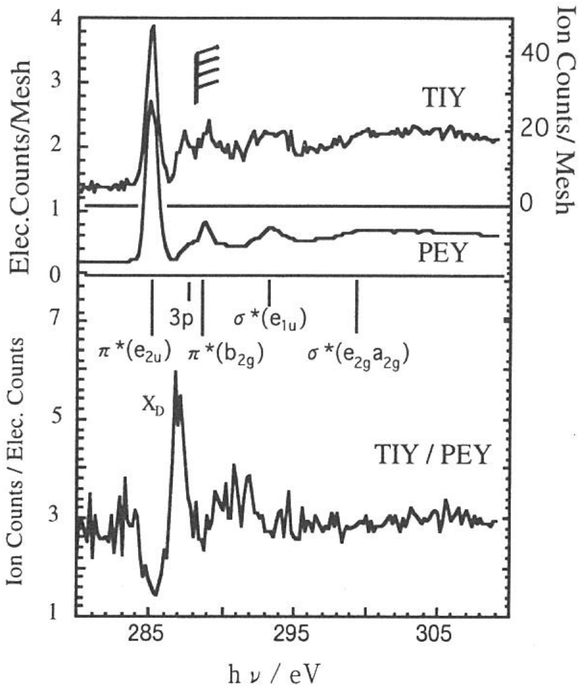

Figure 1. NEXAFS spectra of solid benzene.

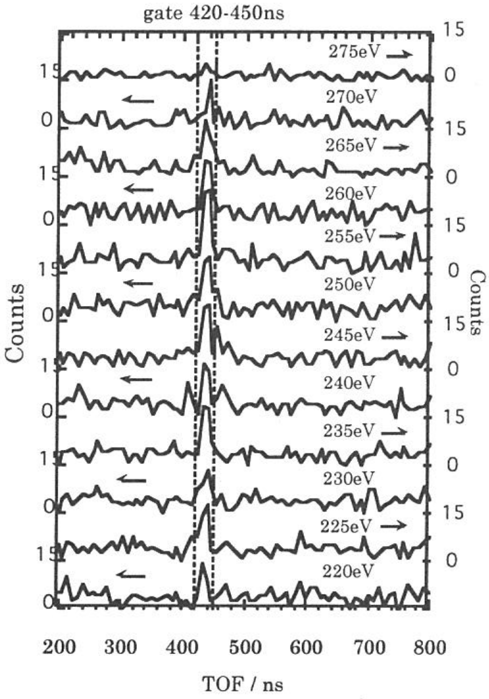

Figure2. AEPICO spectrum for h ν=430eV.

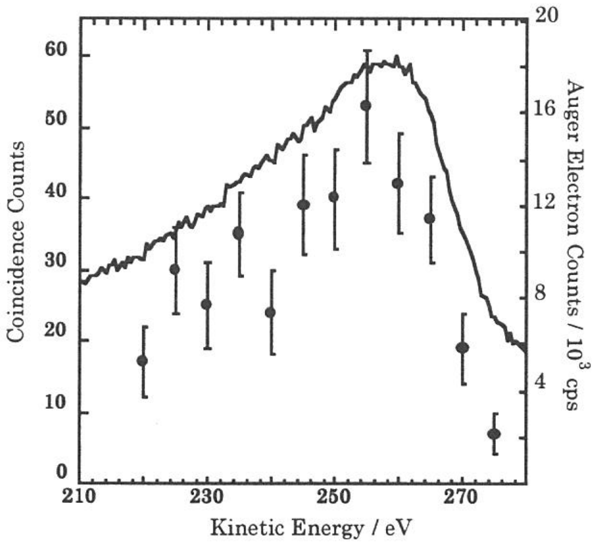

Figure 3.
AEPICO yield spectrum and Auger electron spectrum for h ν=430eV.
Solids curve:AES
● :Coincidence counts

(BL2B1)

# Site-Specific Fragmentation Following Si:2p Core-Level Photoionization of $F_3Si(CH_2)_2Si(CH_3)_3$ Condensed on Au Surface

Shin-ichi NAGAOKA, Kazuhiko MASE,* Mitsuru NAGASONO,*
Shin-ichiro TANAKA,* Tsuneo URISU,* and Joji OHSHITA**

Department of Chemistry, Faculty of Science, Ehime University,
Matsuyama 790-77
*Institute for Molecular Science, Okazaki 444
**Department of Applied Chemistry, Faculty of Engineering,
Hiroshima University, Higashi-Hiroshima 739

In recent years, relaxation processes following core ionization in molecules have been a topic of much interest. We have investigated site-specific fragmentation following Si:2p photoionization of (trifluorosilyl)(trimethylsilyl)ethane ($F_3Si(CH_2)_2Si(CH_3)_3$, FSMSE) condensed on Au surface.

The experiments were performed using a cylindrical mirror electron-analyzer and a time-of-flight ion detection assembly coupled to a grasshopper monochromator (Mark XV) installed on the BL2B1 beamline of the UVSOR synchrotron radiation facility in Okazaki.[1]

Figure 1 (a) shows the total electron yield (TEY) spectrum of FSMSE condensed on Au. The TEY spectrum is similar to the total photon-stimulated-ion-desorption (PSID) spectrum of FSMSE [Fig. 1 (b)]. By using TOF mass spectroscopy under single-bunch-mode operation of synchrotron radiation, $H^+$ and $F^+$ were found to be the only products desorbed in significant quantities from condensed FSMSE at the photon energy of 270 eV. Accordingly, the total PSID spectrum is likely to correspond to the yield spectrum of $H^+$ and $F^+$. Assignments of peaks in the spectra, which were made by comparison with the photoabsorption spectra of condensed

$SiF_4$ and $Si(CH_3)_4$ vapor, are given in the figure. The TEY and total PSID spectra of condensed FSMSE [Figs. 1 (a) and (b)] are very close to the total photoionization efficiency curve of FSMSE vapor as in the cases of $SiF_4$ and $SiCl_4$. The TEY and total PSID spectra of FSMSE are considered to be made up of the superposition of those of $Si(CH_3)_4$ and $SiF_4$. This result shows that the site-specific excitation indeed occurs in FSMSE.

In the yield spectrum of the Si(LVV) Auger electrons [Fig. 1 (c)], one can see a shoulder around 105 eV (Si[Me]:2*p* -> $\sigma^*$) and a peak at 106.5 eV (Si[F]:2*p* -> $\sigma^*$), which originate from the Si(LVV) resonant-Auger electrons; the peaks at 95 and 118 eV are due to the valence-electron emission.

The site-specific fragmentation pattern of FSMSE condensed on Au surface is quite different from that in the vapor phase. In contrast to the case in the vapor phase, $H^+$ and $F^+$ ions are predominantly desorbed coincidentally with the Si[Me]:2*p* and Si[F]:2*p* electrons, respectively, on Au surface;[2] the TEY and PSID spectra of FSMSE are close to those of (trifluorosilyl)(trimethylsilyl)methane ($F_3SiCH_2Si(CH_3)_3$).

1. K. Mase et al. Surf. Sci., in press.
2. S. Nagaoka et al. Phys. Rev. Lett., submitted.

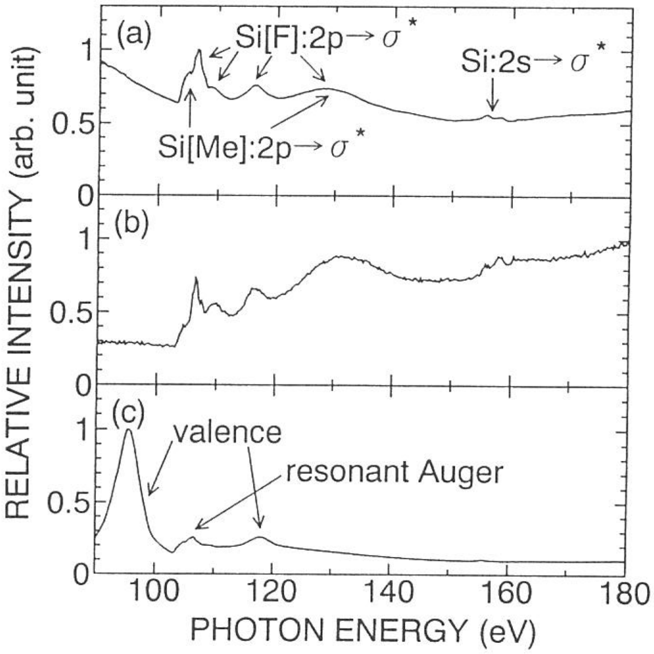

**Fig. 1** (a) TEY spectrum of FSMSE. (b) Total PSID spectrum of FSMSE. (c) Yield spectrum of Si(LVV) Auger electron of FSMSE. Each channel was measured for 3 s at the step of 0.25 eV.

(BL2B1)

# Study of Ion Desorption Induced by Resonant Core–level Excitations of Condensed $H_2O$ by Using Auger–Electron Photoion Coincidence (AEPICO) Spectroscopy Combined with Synchrotron Radiation

Kazuhiko MASE, Mitsuru NAGASONO, Shin–ichiro TANAKA, and Tsuneo URISU
*Institute for Molecular Science, Okazaki 444, Japan*
Eiji IKENAGA, Tetsuji SEKITANI, and Ken–ichiro TANAKA
*Department of Materials Science, Faculty of Science, Hiroshima University, Higashi Hiroshima 739, Japan*

Dynamics induced by resonant core–level excitations of molecules on a surface is one of the most prospective fields in synchrotron radiation (SR) researches, because the details of the nature involved are scarcely explored. Recently, Auger–electron photoion coincidence (AEPICO) spectroscopy combined with SR has been developed as a novel method for study of ion desorption induced by core–level excitations [1]. Previously we have studied $H^+$ desorption following O 1*s* photoemission of condensed $H_2O$ at hν = 670 eV, and reported that the Auger–stimulated ion desorption (ASID) mechanism is responsible for the $H^+$ desorption [2]. In the present article, we describe an ion desorption study in the region of resonant excitations from O 1*s* to the unoccupied states of condensed $H_2O$ studied by total ion and total electron yield spectroscopy (TIYS and TEYS), non–derivative Auger–electron spectroscopy (AES), and AEPICO spectroscopy.

Figure 1 shows a TIYS, a TEYS, and a spectrum of the total ion yield divided by the total electron yield (TIY/TEYS) for condensed $H_2O$ in the region of hν = 530–546 eV. The TIY/TEYS has exhibited a characteristic peak at *hν* = 533.4 eV. Figure 2 shows a typical AEPICO spectrum of condensed $H_2O$ at hν = 534 eV in coincidence with the electron at the kinetic energy (Ek) of 510 eV. Figure 3 shows the AEPICO spectra of condensed $H_2O$ measured at *hν* = 533.5, 535, 534, 537, 540, and 560 eV for Ek of 440–530 eV corresponding to the O(KVV) Auger transitions. $H^+$ was found to be the only ion species desorbed in all the cases. The AEPICO yield is greatly enhanced at *hν* = 533.5 and 534 eV while suppressed at *hν* = 537 and 540 eV as compared with that at *hν* = 560 eV. Furthermore, the Ek dependence of the AEPICO yield is greatly different among *hν* = 533.5–534, 537–540, and 560 eV as shown in figure 4. On the basis of these results, we have concluded as follows: (1) The spectator–Auger–stimulated ion desorption (spectator–ASID) mechanism following the resonant electronic transition from the O 1*s* to the $4a_1$ is responsible for the $H^+$ desorption at *hν* = 533.5 and 534 eV. The enhancement of the $H^+$ yield is ascribed to the anti–bonding character of the $4a_1$ orbital. (2) The spectator–ASID following the resonant transition from the O 1*s* to a non–bonding orbital is responsible for the $H^+$ desorption at *hν* = 537 and 540 eV. The suppression of the $H^+$ yield is ascribed to the reduction of the hole–hole interaction due to the shield effect of the electron in the non–bonding orbital. (3) The normal–ASID mechanism following the O 1*s* photoelectron emission is responsible for the $H^+$ desorption at *hν* = 560 eV.

References

[1] K. Mase, M. Nagasono, S. Tanaka, M. Kamada, T. Urisu, and Y. Murata, Rev. Sci. Inst., in press.
[2] M. Nagasono, K. Mase, S. Tanaka, and T. Urisu, UVSOR Activity Report 23, 100 (1996).

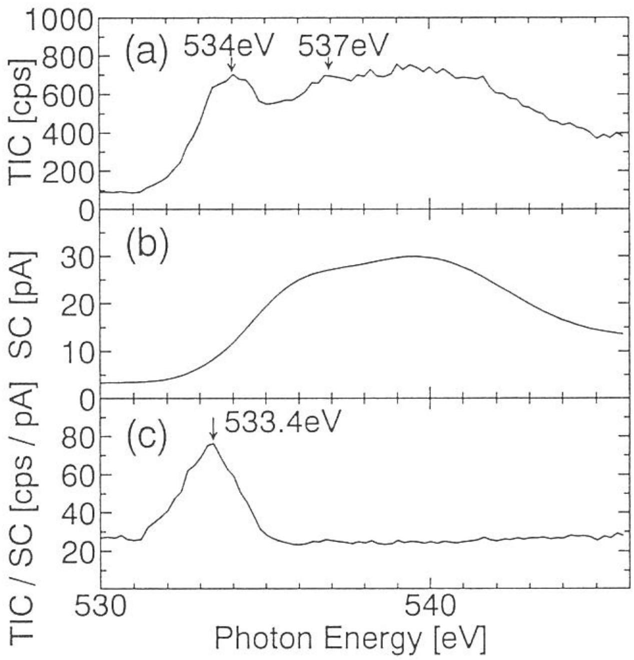

Figure 1. (a) TIYS, (b) TEYS, and (c) TIY/TEYS for condensed $H_2O$ in the region of hν = 530–546 eV.

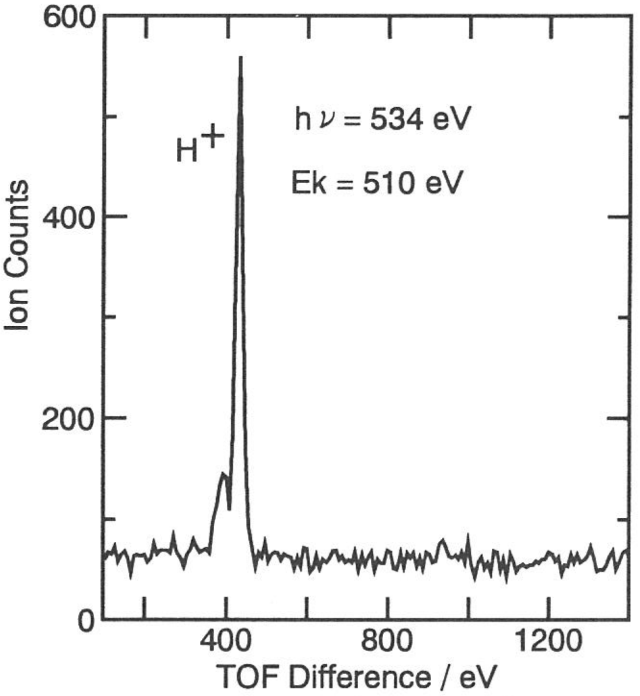

Figure 2. Typical AEPICO spectrum of condensed $H_2O$ at hν = 534 eV in coincidence with the electron at Ek of 510 eV.

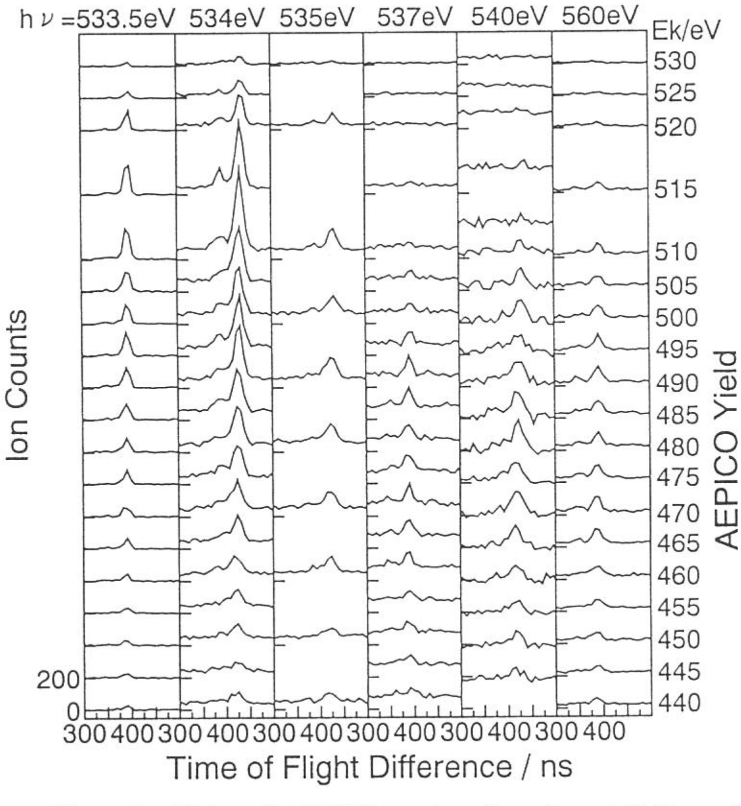

Figure 3. Series of AEPICO spectra of condensed $H_2O$ at hν = 533.5, 534, 535, 537, 540, and 560 eV measured for the electron kinetic energies (Ek) of 440–530 eV.

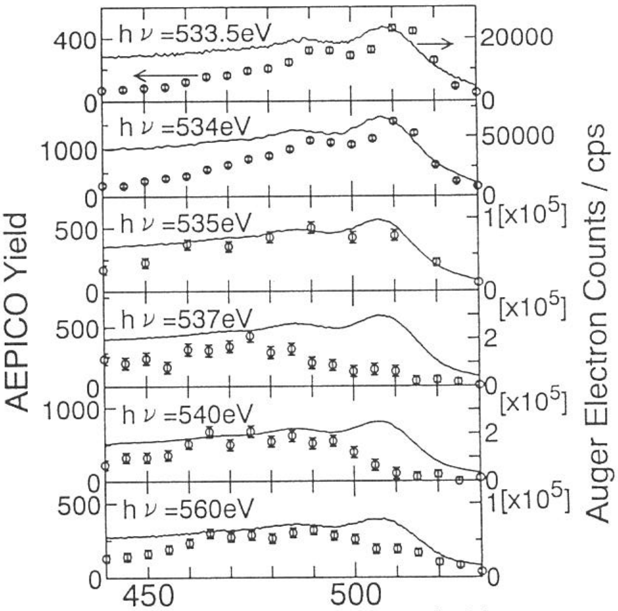

Figure 4. AEPICO $H^+$ signal intensities as a function of Ek at hν = 533.5–560 eV. The solid lines show typical AES.

## (BL2B1)

# 4d-4f Resonant Photoemission of Tm Compounds

Y.Ufuktepe*, S. Kimura, K.G. Nath** and T. Kinoshita
** Physics Department, University of Cukurova, 01330 Adana, Turkey*
*UVSOR Facility, Institute for Molecular Science, Okazaki 444, Japan*
***Department of Structural Molecular Science, The Graduate University for Advanced Studies, Okazaki 444, Japan*
H. Kumigashira, T. Takahashi, T. Matsumura and T. Suzuki
*Department of Physics, Tohoku University, Sendai 980-77, Japan*
H. Ogasawara
*Institute for Solid State Physics, University of Tokyo, Tokyo 103, Japan*

Photoemission spectroscopy and its resonance process provide important information to investigate the electronic properties of rare earth based materials [1]. In this report, we have studied electronic structure of several thulium monochalcogenides (TmX ; X=S, Se, Te) by resonant photoemission in photon energy ranges of 4d-4f (100-190 eV) excitations. Comparison with the theoretical calculations has also been carried out.

Experiments were performed at the beam line, BL2B1 with a Grasshopper monochromator. Emitted electrons from the sample were analyzed with a double-pass cylindrical mirror analyzer (DCMA) and computer controlled data acquisition systems . The total energy resolution was about 0.5 eV. A clean surface was prepared by scraping the sample with a diamond file in situ. The Fermi level was determined by measuring an Au layer which was evaporated on the sample.

Figure 1 shows the valence band photoemission energy distribution curves (EDC) of TmSe with different photon energies both on and off resonance at the Tm 4d threshold. Excitation photon energies were determined from the total yield spectrum which is also shown in the figure.

The divalent part (4f$^{12}$ final state) of the TmSe spectrum was estimated to be situated from 0 to 5.6 eV binding energy (BE) and Tm 4f$^{11}$ trivalent state between (5.6 -14) eV B.E. range. Intensities of the 4f$^{11}$ and 4f$^{12}$ photoelectron peaks did not show a big difference which agreed with previous results ; namely Tm ions in TmSe show mixed valent character [2-4]. We have observed large resonant photoemission intensity enhancement from both divalent and trivalent part of Tm 4f final state multiplets respectively. A comparison of our results with a previous study [2] shows that our photoemission spectra has sharper features with higher resolution in the 4f final state multiplets. From the other results of photoemission spectra near Fermi edge, we can conclude that TmS and TmSe are metallic while TmTe is semiconducting.

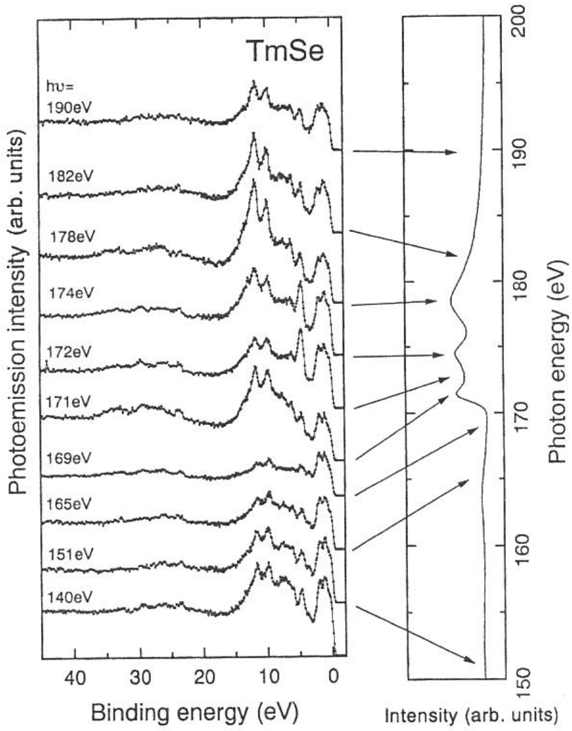

**Figure 1:** *Photoelectron spectra of TmSe from the valence band with different (140-190) eV photon energies and the total yield spectrum of TmSe from the 4d region.*

We have calculated Constant Initial State (CIS) spectra for each photoemission peak in Fig. 1. The two of the representative ones both for trivalent and divalent components of Tm ions are shown in Fig. 2(a). The upper CIS spectrum shows the typical behavior of the trivalent nature of Tm, namely three resonant peaks. The lower CIS spectrum shows single resonant peak originating from divalent components. The calculated 4d-4f absorption spectra also show similar features. Considering the allowed photoabsorption for $4f^{12}$ and $4f^{13}$ initial state configurations derives three intermediate states ($^3H_6$, $^3H_5$, $^3G_5$) for trivalent components and single intermediate state ($^2D_{5/2}$) for divalent components. These are reflected in the shape of CIS spectra in Fig.1(a).

For comparison, we show the experimental CIS spectra for TmSe and TmTe in Figs 2(b) and (c). These CIS spectra are corresponding ones to those calculated in Fig. 2(a). As described above, the 9.9 eV BE photoemission peak of TmSe originates from trivalent component of Tm. The corresponding CIS spectrum in Fig. 2(b) also shows trivalent behavior. In the same manner, the 4.5 eV photoemission peak of TmSe is due to divalent part and the CIS as well. We have compared every CIS spectrum for each photoemission peak with those calculated (not shown here). The accordance of experimental results with calculation was quite well. From these comparisons, we can also conclude that the divalent photoemission peaks are located in (0-5.6) eV while the trivalent ones in (5.6-14) eV.

The CIS spectrum for 5.2 eV BE peak of TmTe (Fig. 2(c) lower) is also understood as above, which also shows the typical behavior of divalent component. The upper CIS spectrum in Fig. 2(c) behaves in the other way. This shows strong resonance at 174 eV photon energy. The 11.2 eV BE photoemission peak is to be trivalent one. Since TmTe is mostly divalent compound, we could observe just weak peaks in the photoemission from trivalent part. The electrons at 11.2 eV BE might mostly come from the secondary parts from divalent component peaks in lower BE. Therefore, the CIS spectrum seems to behave almost as divalent features but with weaker trivalent structures.

The absorption (TY) spectra in Fig. 1 and others not shown here for TmS and TmTe are understood as superposition of the divalent and trivalent absorption peaks. We performed curve fitting to estimate the mean valency by changing the relative intensity of theoretical absorption spectra for each divalent and trivalent component. The results are 2.84 for TmS, 2.71 for TmSe and 2.15 for TmTe. These values are almost consistent with those obtained at previous studies [2,5].

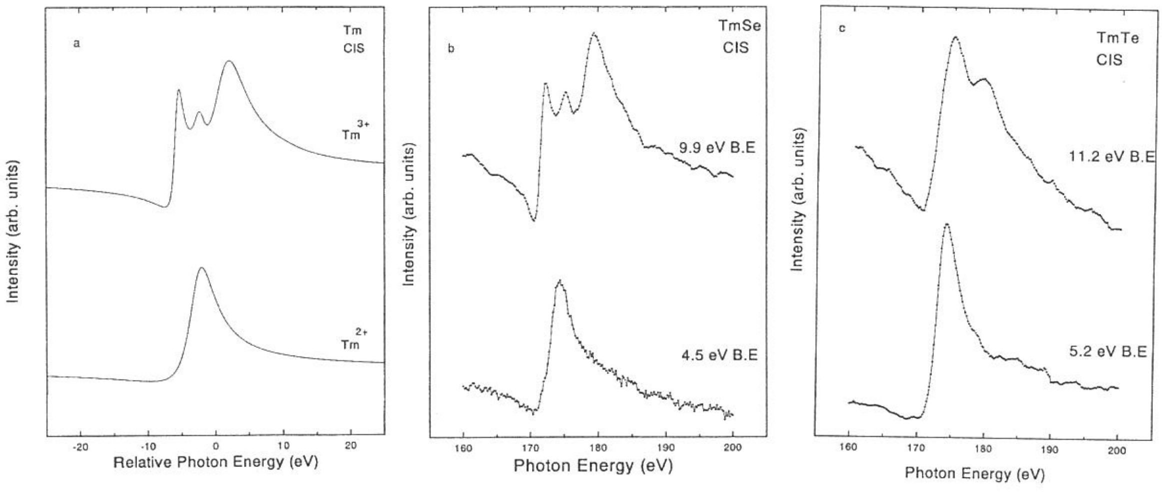

**Figure 2:** *Experimental and calculated results of CIS.*

## References

**[1]**. *"Giant Resonances in Atoms, Molecules and Solids"*, edited by J.P. Connerade, J.M. Esteva, and R.C. Kartanak (Plenum Press, New York, 1987).

**[2]**. S. J. Oh, J.W. Allen and I. Lindau, Phys. Rev. B. **30**, 1937 (1984)

**[3]**. G. Kaindl, C. Laubschat, B. Reihl, R.A. Pollak, N. Martensson , F. Holtzberg, and D.E. Estman, Phys. Rev. B. **26**, 1713 (1982)

**[4]**. G. K. Wertheim, W. Eib, E. Kaldis, and M. Campagna, Phys. Rew. B., **22**, 6240 (1980).

**[5]**. H. R. Ott, F. Hulliger, Z. Phys. B Condensed Matter **49**, 323 (1983)

(BL2B1)

# Photoemission spectra of $La_{2-x}M_xCoO_4$ ($M$=Ca, Sr, Ba) and $(SrO)\{(La_{1-x}Sr_xMnO_3\}_n$ ($n$=1, 2, ∞) with layered perovskite structure

Minoru TAKEMOTO, Tatsuya MIYAJIMA, Michio YAMASHIRO, Takeshi OGAWA, Hiroyuki IKAWA,
Hiroshi MIZOGUCHI[1] and Takahisa OMATA[2]

*Kanagawa Institute of Technology, Shimo-Ogino, Atsugi, Kanagawa 243-02, Japan*
[1]*Osaka National Research Institute, Midorigaoka, Ikeda, Osaka 563, Japan*
[2]*Dept. of Mater. Science and Processing, Faculty of Eng., Osaka Univ., Yamada-Oka, Suita, Osaka 565, Japan*

One of cuprate superconductors, $La_{2-x}Sr_xCuO_4$ has $K_2NiF_4$-type structure which is recognized as layered (or two dimensional) perovskite structure. Many transition metal (Ti ~ Ni) oxides also have the same structure and they show semiconductive behavior, except heavily doped $La_{2-x}Sr_xNiO_4$ ($x$>1.0)[1]. However, there are many conductive transition metal oxides which have perovskite-type (three dimensional) structure. Cuprate with perovskite structure, on the other hand, no longer shows superconductivity[2]. Low dimension of crystal structure is one of the most important factors to understand properties of transition metal oxides. In the present work, the photoelectron spectra were measured for cobaltites of $La_{2-x}M_xCoO_4$ ($M$=Ca, Sr, Ba) with $K_2NiF_4$-type structure and for manganates of $(SrO)\{(La_{1-x}Sr_x)MnO_3\}_n$ which have higher dimensional structure with increasing $n$; $K_2NiF_4$-type structure (two dimensional) for $n$=1, $Sr_3Ti_2O_7$-type structure (pseudo-two dimensional) for $n$=2 and perovskite-type structure (three dimensional) for $n$=∞, respectively[3].

The samples were prepared by a solid state reaction method. For the cobaltites of $La_{1.4}M_{0.6}CoO_4$ ($x$=0.6; $M$=Ca, Sr, Ba), appropriate mixtures of $La_2O_3$, $CaCO_3$, $SrCO_3$, $BaCO_3$ and CoO were sintered at 1100 ~ 1400 °C for 72h in $O_2$ gas ($M$=Ba) or $N_2$ gas ($M$=Ca, Sr) with intermediate grindings[4]. For the manganates of $(SrO)\{(La_{0.6}Sr_{0.4})MnO_3\}_n$ ($x$=0.4),appropriate mixtures of $La_2O_3$, $SrCO_3$, $Mn_3O_4$ were sintered at 1400 ~ 1500°C for 24h in $N_2$ gas ($n$=1 and 2 samples) or $O_2$ ($n$=∞ sample) gas with intermediate grindings. Photoelectron spectra were measured in BL2B1 at room temperature or low temperature (~100 K; for only the $n$=∞ manganate sample) using liquid $N_2$ in vacuum of ~ $10^{-10}$ Torr, after scrapping on sample surface with diamond file in vacuum of ~$10^{-9}$ Torr.

We present firstly the results for the Ca-substituted and Ba-substituted cobaltites for easy comparison. Figure 1 shows the photoelectron spectra of Ca-substituted sample $La_{1.4}Ca_{0.6}CoO_4$ in the vicinity of Fermi level. The spectra mainly consisted of three features A, B and C. When energy of incident photon increased from 100 eV to 200 eV, intensity of the feature A increased by comparison with the feature B. Photoionization cross section of O 2$p$ is reduced more rapidly than that of Co 3$d$ emission with the energy of incident photon[5]. Therefore, the feature A is mainly contributed by the emission from Co 3$d$ orbital and the feature B is mainly contributed by the emission from O 2$p$ orbital.

Figure 2 shows the photoelectron spectra of Ba-substituted sample $La_{1.4}Ba_{0.6}CoO_4$ in the vicinity of Fermi level. The spectra also mainly consisted of three features A, B and C and the relative intensity of the feature A increased with increasing energy of incident photon. So, the valence band structure also consitsts of the emission mainly from Co 3*d* (feature A) and the one mainly from O 2*p* (feature B) in $La_{1.4}Ba_{0.6}CoO_4$.

From comparison between fig. 1 and fig. 2, relative intensity of the feature A to the feature B increased by change substituted ion from Ca to Ba, *i.e.*, 0.3 for *M*=Ca and 0.4 for *M*=Ba when energy of incident photon is 100 eV. Electric conductivity of the samples increased from $2\times10^{-4}$ Ωm for *M*=Ca to $6\times10^{-1}$ Ωm for *M*=Ba. Therefore, the change in spectral weight from the feature B to A is related to the improvement of electric properties.

The photoelectron spectra in the vicinity of Fermi level are shown for the manganate samples in figure 3. Intensity of peak at 3 eV increased relatively with increasing *n*, *i.e.*, increasing dimension of crystal structure from 2 to 3. The *n*=1 and 2 samples were confirmed to be semiconductors near room temperature and the *n*=∞ sample was confirmed to be metal below room temperature from measurement of electrical resistivity. The *n*=1 sample had the resistivity of 5 Ωcm and the *n*=2 sample had the resistivity of $8\times10^{-1}$ Ωcm. Therefore, the relative increase in intensity of the 3 eV peak also corresponds to the improvement of electrical conduction with increasing *n* in $(SrO)\{(La_{0.6}Sr_{0.4})MnO_3\}_n$.

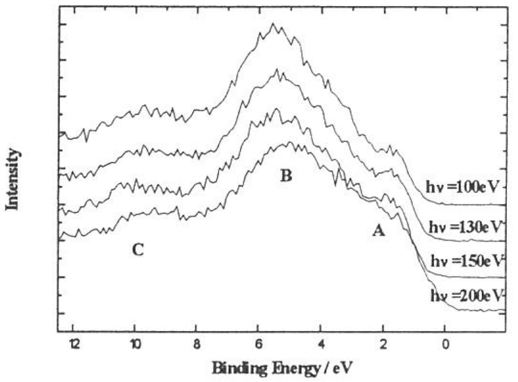

**Figure 1** Photoelectron spectra of $La_{1.4}Ca_{0.6}CoO_4$.

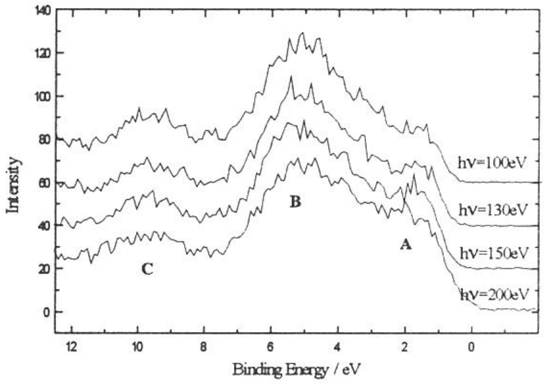

**Figure 2** Photoelectron spectra of $La_{1.4}Ba_{0.6}CoO_4$.

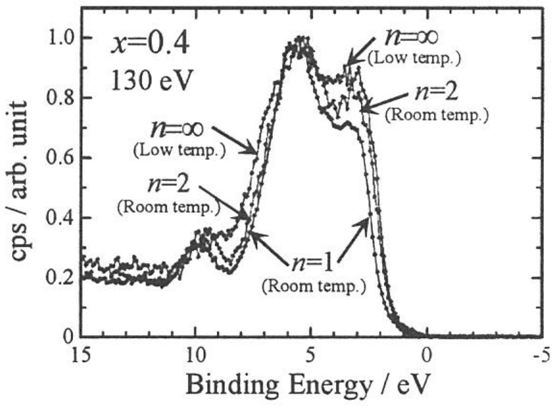

**Figure 3** Photoelectron spectra of $(SrO)\{(La_{1-x}Sr_x)MnO_3\}_n$ ($n$=1, 2, ∞).

**References**

[1]H.Eisaki *et al.*, Phys.Rev. B**45**, 12513 (1992).
[2]G.Demazeau *et al.*, Mater. Res. Bull. **7**, 913 (1972).
[3]R.A.M. Ram *et al.*, J. Solid State Chem. **70**, 82 (1987).
[4]T.Omata *et al.*, UVSOR Activity Report, (1995).
[5]J.J.Yeh and I.Lindau, At. Data Nucl. Data Tables **32**, 1 (1985).

(BL2B1)

# Desorption of the H ions from water chemisorbed on Si(100) by the O-1s excitation - Auger electron-photoion coincidence spectroscopy study

S. Tanaka*, K. Mase, M. Nagasono and M. Kamada
Institute for Molecular Science, Okazaki 444, Japan

The desorption of ions induced by the core-level excitation is one of the subjects which have been extensively studied in the field of DIET. We have applied the AEPICO technique to the Si(100) surface exposed to $H_2O$ [denoted as $H_2O$/Si(100), hereafter]. The chemisorbed states of the $H_2O$/Si(100) surface has been well-studied, and it was shown that water is dissociated into H and OH species and covalently bonded to the dangling bonds on the Si(100) surface. On the other hand, the ion desorption from $H_2O$ /Si(100) induce by the O-1s excitation was recently studied by Sekiguchi et.al.[12], and it was was found that H+ is predominant ions to desorb from the $H_2O$/Si(100) surface at photon energy of 530 - 570eV, and the ion desorption was enhanced by multiple ionization.

The experiments were carried out in the UHV chamber at BL2B1 with a grasshopper monochromator of the synchrotron radiation facility (UVSOR) at the Institute for Molecular Science. The Si(100) wafer was cleaned by resistive heating, and exposed to 3L ( 1L = 10-6 Torr sec ) of $H_2O$. It was enough for the saturation coverage. The detail of the home-made AEPICO apparatus, which consists of a cylindrical mirror analyzer for electrons and a time-of-flight (TOF) mass analyzer for ions, has been described elsewhere. The partial electron yield (PEY) spectrum, which yielded the surface NEXAFS ( near-edge X-ray absorption fine structure ), was obtained by the use of the CMA with Ek = 505eV, which corresponds to the O-KVV Auger electron. All the ion and electron signals were normalized for the incident photon flux by the simultaneously measured photocurrent which was emitted from the Au-mesh ( 90% of transmission ) installed near the sample. All measurements were carried out at room temperature.

A partial electron yield (PEY) spectrum and a total ion yield (TIY) spectrum of $H_2O$/Si(100) near the O-K edge ( O-1s excitation ) are shown in the upper and lower left-hand panels, respectively, of figure 1. Yields are shown in counts per second (cps) normalized by the photocurrent from the Au-mesh. Ion fragments in the TIY spectrum are predominantly H+ produced by breaking of the O-H bond of the OH species on the Si(100) surface [12]. The near-edge peaks at 535 eV and the broad features around 555 eV are ascribed to the excitation from the O-1s to the OH-4$\sigma$* ( and probably OH-2$\pi$* ) bound state and to the shake-up ionization ( and possibly the doubly ionization and the shake-off ionization ), respectively. A comparison between the TIY and SEY spectra indicates that there is no resonant enhancement of the ion desorption yield at the edge peak. It indicates that the fast relaxation of the excited state with a core-hole and an excited electron takes place before the core-hole decay on the Si(100) surface, and was confirmed by our detailed investigation in the Auger electron spectroscopy of this system. Meanwhile, the feature around 555 eV in the TIY spectrum is enhanced compared to the PEY spectrum[13]. It indicates that the efficiency of the ion desorption is increased when the initial state of the Auger decay has an extra hole at a valence band as a result of the shake-up excitation.

The photoelectron spectra of $H_2O$/Si(100) taken at the photon energies of (a) -(d) in the PEY and TIY spectra are shown in the right-hand panel of fig. 1. The photon energies of (a) - (c) correspond to the core-to-bound excitation, and that of (d) corresponds to the shake-off excitation discussed above. We have measured the H+ yield desorbing in coincidence with the O-KVV Auger electron emission indicated in the right-hand panel of fig. 1. Figure 2 shows the AEPICO spectra ( open circles with error bars ) and the O-KVV Auger electron spectra ( dots ) of $H_2O$/Si(100). The Auger electron spectra in figs. 2 (a) - (d) were obatined by subtracting the background ( mainly the tails of the large Si-2p peaks ) from the photoelectron spectra (a) - (d) in figs. 1. We also made curve-fitting calculations to use voigt functions for the Auger electron spectra ( solid lines in figs. 2 ). The results show that the spectra consist of four [figs. 2 (a)- (c)] or five [fig. 2(d)] components. It is noted that the width of each peak is 17 eV, which is partly determined by the resolution of the AEPICO instruments. Three components at 469, 486 and 503 eV appeared in all spectra are ascribed to the O-KVV Auger electron emission, and the others to the directly excited photoelectron emission from the valence band[13]. There is no significant difference among the shapes of the AEPICO ( and also the Auger electron ) spectra [figs. 2(a) -(d)].

For a further discussion on the mechanism of the Auger stimulated ion desorption for the adsorbate system, the final-state-selected relative cross sections of ion desorption induced by the Auger transition were calculated as follows: we made curve-fitting calculations by changing only the intensities of the three components appeared in the Auger electron spectra [figs. 2(a)-(d)], and then, got the peak height ratio of each component in the AEPICO spectra to corresponding one in the Auger electron spectra. The data (open circles) and the results of the curve fitting ( solid lines ) of the AEPICO spectra are shown in the left-hand panel of the figures 3(a)-(d). The relative cross sections of the Auger stimulated ion desorption calculated for the peaks at 469, 486 and 503 eV are plotted in logarithmic scale in the right-hand panel of fig.3. They are obviously increased when the kinetic energies of the Auger electrons are decreased. In other words, the cross section of the Auger stimulated desorption increases as the holes are created at the deeper levels of the valence bands as the final state of the Auger decay. Cross sections for the 469 eV component are about 10 times large as for the 503eV component in each spectrum. It is noted that the AEPICO yield of H+ from condensed $H_2O$ increases when holes were created at the orbital with O-H bonding character. Meanwhile, the main Auger peak associated with the O-H bonding orbital ( OH-3$\sigma$ ) is expected to be at 503 eV for $H_2O$/Si(100), and no such enhancement is observed (the right panel of fig.3). It is considered that the adsorbate-substrate interaction effects is responsible to this significant difference. The desorption cross section to correspond to the shake-off excitation [dots (d) in the right-hand panel of fig.3 ] are larger by a factor of about 5 than that to the core-to-bound excitation [ dots (a), (b) and (c) in the right-hand panel of fig.3] for each component. This is consistent with the TIY and PEY spectra ( the upper and lower left-hand panels in fig. 1) as discussed above.

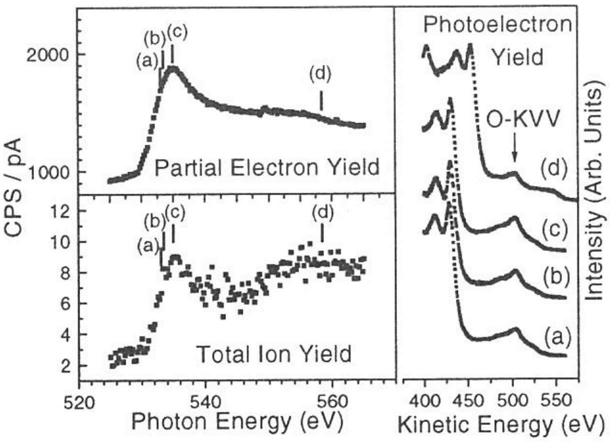

Fig. 1. Left: comparison of the total ion yield (TIY) (the lower left-hand panel) and the partial electron yield (PEY) (the upper left-hand panel) spectra near the O-K edge of the Si(100) surface exposed to $H_2O$. Right: photoelectron spectra taken at several photon energies which correspond to (a) - (d) shown in the TIY and PEY spectra.

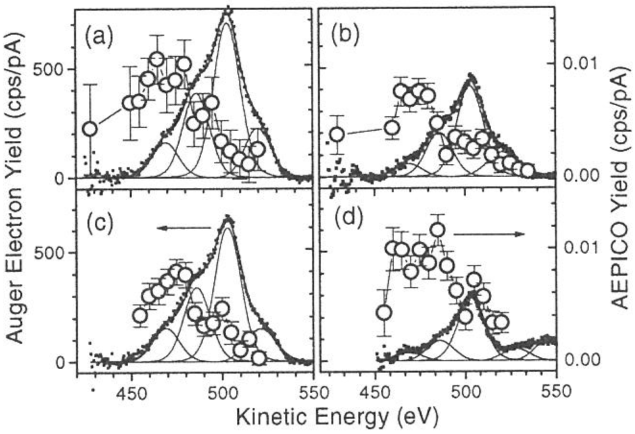

Fig. 2. AEPICO spectra (open circles with error bars ) and O-KVV Auger electron spectra ( dots ) with the results of the peak-fitting calculations ( solid lines ). To obtain the Auger electron spectra, the backgrounds were subtracted from curves in the right-hand panel of the figure 1. Spectra of (a) - (d) were taken at the photon energies which correspond to (a) - (d) in the fig. 1, respectively.

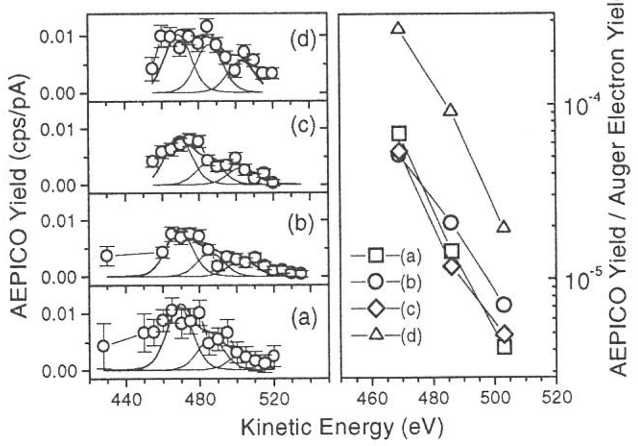

Fig. 3. Left: The AEPICO spectra (open circles with error bars), same as in figure 2, with the results of the peak-fitting calculation. The spectra (a) - (d) were taken at the photon energies which correspond to (a) - (d) in figs. 1 and figs.2, respectively. Right: The ratio of the AEPICO yield to the Auger electron yield calculated for the peaks at 469, 486 and 503 eV. The photon energies for (a) - (d) were same as (a) - (d) in figs.1 and figs. 2

(BL2B1)

# Photon stimulated ion desorption of condensed acetonitrile by Auger -electron photo-ion coincidence spectroscopy

Eiji IKENAGA, Tetsuji SEKITANI, Kenichiro TANAKA
*Department of Materials Science, Hiroshima University, Higashi-Hiroshima 739, Japan*
Kazuhiko MASE, Mitsuru NAGASONO, Shin-ichiro TANAKA, Tsuneo URISU
*Institute for Molecular Science, Okazaki 444, Japan*

A study of surface photochemical reaction induced by core excitation has been developed with the advance of synchrotron radiation technique. In particular, site-specific reaction has been found in photon stimulated ion desorption(PSID) following core electron excitation [1]. Auger stimulated ion desorption (ASID) mechanism is widely proposed as a model of PSID. As the Auger final state is directly related to the ion desorption in ASID model, it is essential for the elucidation of the PSID mechanism to get the information about the Auger final state.

In the present study, we have performed Auger-electron photo-ion coincidence (AEPICO) experiments for acetonitrile condensed on a gold foil at 80 K to study the desorption mechanism related to the Auger process. We have used AEPICO apparatus,which was recently developed by Mase et al [2]. This apparatus detects the energy selected electron and the ion produced simultaneously by a single excitation event.

Fig. 1(a) and 1(b) shows a total ion yield (Yion) spectrum and a total ion yield divided by total electron yield (Yion / Yelectron) spectrum, respectively. Assignment of the structure in the Yion spectrum is also shown in Fig. 1 (a) [3]. Yion / Yelectron spectrum shows that the desorption efficiency is largely increased at resonant excitation to C-H* (h $\nu$ =288.1eV) [Fig. 1(b)]. We have also measured Auger-electron spectrum (AES) and AEPICO yield spectrum at C-H* excitation. We have detected only $H^+$ ion in AEPICO spectrum. Fig. 2 shows an AES as a function of the electron kinetic energy around C(KVV) Auger-electron energy range (200 ~ 285eV) and an AEPICO yield spectrum for $H^+$ desorption at C-H* excitation. The Auger spectrum is quite different in comparison with normal Auger spectrum. At present we can't descibe in detail, however, we consider that the Auger spectrum is mixture of spectator resonant Auger (2 hole 1 electron state) and normal Auger. Further, the feature of the AEPICO yield spectrum is different from that of AES. AEPICO yield spectum shows enhancement at 245 ~ 250eV electron energy. It is considered that the spectator resonant Auger stimulates ion desorption (spectator-ASID). That is, $H^+$ desorption is much enhanced due to 2 hole 1 electron state in which one electron exists anti-bonding C-H* orbital and two holes may exist in 1 $\pi$ bonding orbital which is localized at -$CH_3$ group. We conclude that the PSID seems to proceed strongly depending on the bonding/anti-bonding character and localization character of the excited state.

[1] K. Tanaka et al. Rev. Sci. Instrum. 66, 1474 (1995)

[2] K. Mase et al. UVSOR Activity Report. 94 (1995)

[3] P. A. Stevens et al. J. Chem. Phys. 91, 4338 (1989)

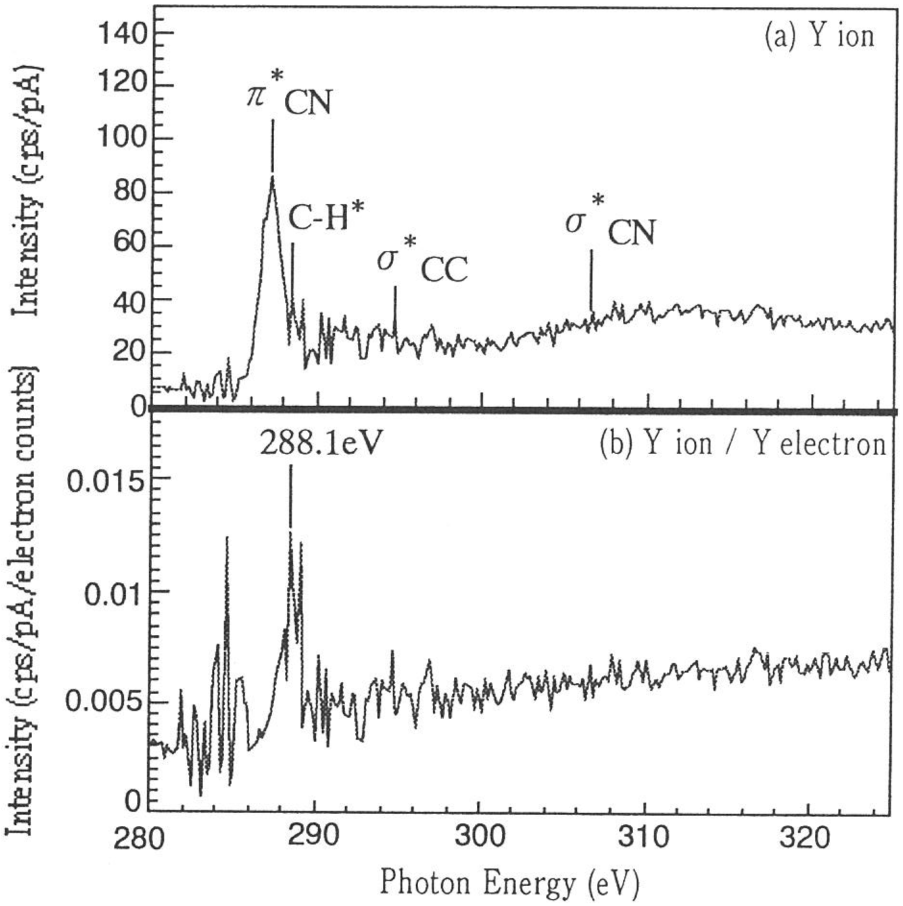

Fig. 1. total ion yield (TIY) spectrum (a) and TIY divided by total electron yield (TEY) spectrum (b).

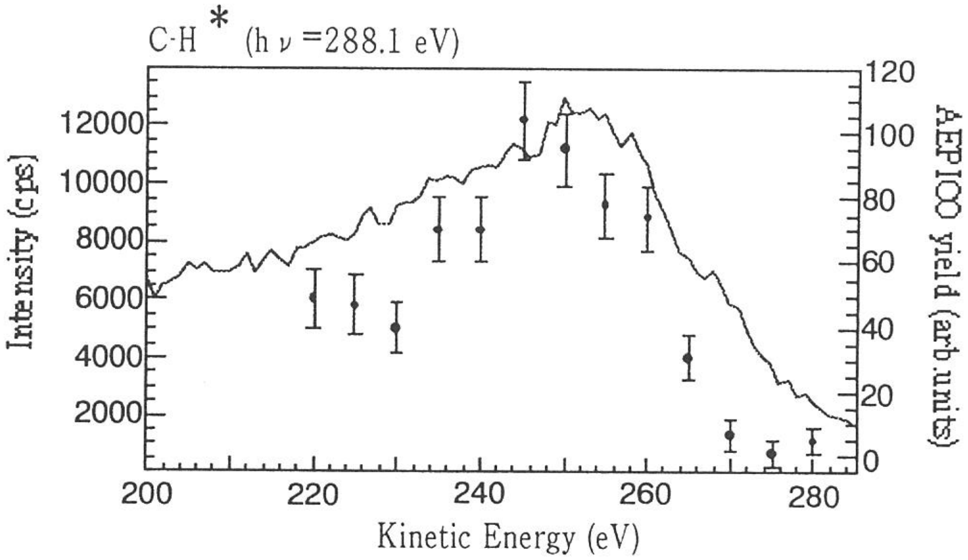

Fig. 2. Auger-electron photo-ion coincidence yield spectrum (closed circles) and Auger-electron spectrum (solid line) as a function of C (KVV) Auger-electron kinetic energy.

(BL 2B1)

# Na adsorption process on a ZrC(100) surface

Kenichi OZAWA, Takeshi IWASAKI, Kazuyuki EDAMOTO, Shinichiro TANAKA* and Shigeki OTANI**
*Department of Chemistry, Tokyo Institute of Technology, Ookayama, Meguro-ku, Tokyo 152, Japan*
* *Institute for Molecular Science, Myodaiji, Okazaki-shi, Aichi 444, Japan*
** *National Institute for Research in Inorganic Materials, Tsukuba-shi, Ibaraki 305, Japan*

The group IV and V transition metal carbides (TMCs) are of considerable interest because of their interesting combination of physical properties and a number of useful applications. Especially, they have been used as very stable field electron emitters. On the other hand, alkali-metal adsorption is well known to promote electron emission from the surface because of the large decrease of the work function. Therefore, the adsorption process of alkali-metals and their effects on the electronic structure of TMC surfaces are of particular interest. Recently, we have investigated the potassium adsorption process on the polar (111) and the neutral (100) surfaces of NbC and have found that the adsorption mechanisms are totally different from each other on these surfaces [1, 2]. The former proceeds via a polarization-depolarization transition with increasing K coverage, while the latter proceeds via an island formation from the initial stage of adsorption.

Such a clear face-dependence of the adsorption mechanism on the NbC surfaces is considered to be due to a pure surface effect, thus farther investigation of alkali-metal adsorption on the TMC is motivated from a scientific view point. In this work, we have studied the Na adsorption process on the ZrC(100) surfaces with core-level photoemission spectroscopy and Auger electron spectroscopy.

The photoemission and Auger electron spectroscopy measurements using synchrotron radiation were performed at BL 2B1. The photoelectrons and the Auger electrons were collected by a double-pass cylindrical mirror analyzer. The ZrC(100) surface was cleaned by flashing to ~ 1800 K in the vacuum chamber. The ZrC(100) clean surface thus prepared showed a sharp (1×1) LEED pattern. The Na atoms were deposited on the surface at room temperature using a well-degassed SAES dispenser. The base pressure in the UHV system was less than $2\times10^{-8}$ Pa.

Fig. 1a shows the change in the photoemission spectrum in the Na 2p core-level region for the Na/ZrC(100) system as a function of Na coverage ($\theta_{Na}$). The LEED shows only a (1×1) pattern for all coverages with the increase of the background intensity as $\theta_{Na}$ increases. The Na 2p peak is observed at 32.3 eV at $\theta_{Na}$ = 0.13 ML and shifts continuously to the lower binding energy side by 1.5 eV up to ~ 0.7 ML (Fig. 1c). At coverages larger than 0.7 ML, the Na 2p peak does not show a substantial shift. The large shift of the Na 2p core-level peak suggests that the chemical environment of adsorbed Na atoms changes substantially between 0.13 and 1 ML.

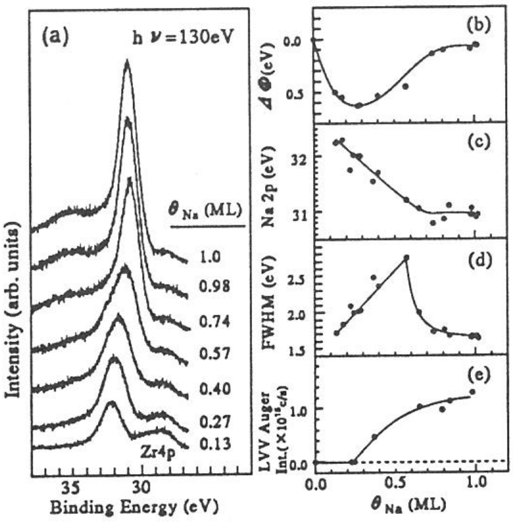

Figure 1: (a) Change in the photoemission spectra of the Na 2p core-level region as a function of $\theta_{Na}$. The $\theta_{Na}$ dependence of (b) the work function change ($\Delta\Phi$), (c) the Na 2p peak position, (d) the Na 2p FWHM and (e) the Na LVV Auger intensity.

The work function change ($\Delta\Phi$) for the Na/ZrC(100) system as a function of $\theta_{Na}$ is shown in Fig. 1b. The overall shape of the $\Delta\Phi$ curve is characteristic to alkali adsorption system; the work function ($\Phi$) drastically decreases in the initial stage and reaches a minimum (~ 0.3 ML) and then increases in the successive region. $\Phi$ does not change at $\theta_{Na} > 0.7$ ML, which coincides with the coverages where the Na 2p peak position doesn't show the shift (Fig. 1c), implying that the nature of the Na overlayer does not change at $\theta_{Na} >$ 0.7 ML. In the initial stage of adsorption, the adsorbed Na is considered to be polarized on the surface, which is suggested from the rapid decrease of $\Phi$ in the initial stage. The Na 2p peak in the low coverage region (< 0.3 ML) is thus attributed to the emission from Na adatoms in the polarized phase. On the other hand, the Na 2p peak in the high coverage region (0.7 – 1.0 ML) at 31 eV is attributed to the emission from depolarized metallic Na layer. The metallic layer formation in this region is well confirmed from the observation of Na LVV Auger electron emission (Fig. 1e) since the transition requires two valence electrons in one site, which is possible only when the atom is in a metallic state.

It is obvious from Fig. 1a that the line shape of the Na 2p core-level peak is dependent on $\theta_{Na}$; the peak observed at 32.3 eV in the initial stage is broadened to be a rather asymmetric peak up to 0.57 ML and turns to the more symmetric and sharp peak in the successive region. The full width at half maximum (FWHM) of the Na 2p peak are plotted in Fig. 1d as a function of $\theta_{Na}$. Such a unique $\theta_{Na}$ dependence of the FWHM could be explained if the peak is composed of two components overlapping each other at the coverage region of $0.3 < \theta_{Na} < 0.7$ ML. Thus, we deconvoluted the Na 2p peaks using two Gaussian-convoluted Doniach-Šunjić functions. The result of the deconvolution is shown in Fig. 2, where the Na peaks are shown after the inelastic background is subtracted to facilitate a comparison of the line shape. At $\theta_{Na} = 0.13$ and 1 ML, the observed peaks are well reproduced with only one function. However, two functions are required for the 0.57 ML peak. The peak at lower binding energy side is attributed to the emission form the Na adatoms in the condensed metallic patches, and the peak at higher binding energy side is formed by the emission from the dispersive Na adatoms.

From the discussions as above, the analysis of the Na 2p spectra suggests that Na adsorption proceeds via the following steps: (i) In the initial stage ($\theta_{Na} < 0.3$ ML), the polarized adsorbed layer is formed. (ii) In the second stage ($0.3 < \theta_{Na} < 0.7$ ML), adsorbed Na atoms in the polarized phase and metallic phase coexist. The existence of the metallic adsorbed layer from the early stage (~ 0.3ML) is confirmed by the observation of the Na LVV Auger signal (Fig. 1e). The adsorbed Na atoms in the polarized phase should be dispersive due to the Coulomb repulsion. On the other hand, the adsorbed Na atoms in the metallic phase should be condensed in order to form a metallic band through the orbital-orbital interaction. The coexistence of the two phase results in a broad and asymmetric line shape of the Na 2p spectra in this region (Fig. 2). (iii) In the high coverage region ($\theta_{Na} > 0.7$ ML), all the observed Na atoms form a metallic overlayer, which results in a sharp and more symmetric peak accompanied by the Na 3s plasmon loss satellite in the Na 2p spectra.

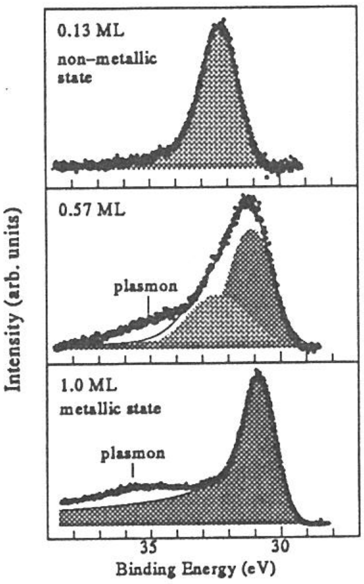

Figure 2: Na 2p photoemission peaks at various coverages.

Recently, we performed photoemission studies on K adsorption on NbC(111) [1] and NbC(100) [2], and have proposed that the adsorption mechanism on these surfaces are different from each other because of the difference in surface electronic structures. On the NbC(100) surface, adsorbed K atoms are in metallic phase due to the island formation from the very initial stage of adsorption. On the NbC(111) surface, on the other hand, the adsorption process is characterized by a polarization-depolarization transition of the whole adsorbates, and the island patches are not formed in the submonolayer region. For the Na/ZrC(100) system, the polarized layer is formed in the initial stage, indicating that the interaction between Na and ZrC(100) is rather strong relative to that between K and NbC(100). However, the metallic patches are formed from early stage of adsorption (~ 0.3 ML) as in the case for the K/NbC(100) system, suggesting that the island formation is characteristic to the (100) surface of transition metal carbides.

## References

[1] K. Ozawa, S. Tokumitsu, R. Sekine, E. Miyazaki, K. Edamoto, H. Kato and S. Otani, Surf. Sci. **357/358** (1996) 350.

[2] K. Ozawa, T. Anazawa, S. Tokumitsu, R. Sekine, E. Miyazaki, K. Edamoto, S. Tanaka and S. Otani, Surf. Sci. **336** (1995) 93.

(BL2B1)

# Total Yield Spectra of the group III Nitride Thin Films

Kazutoshi FUKUI, Masatake ICHIKAWA and Akio YAMAMOTO

*Dept.Elec.Elec.Engi., Fac.Engi., Fukui Univ., FUKUI 910*

Recently, good quality group III nitride (GaN, AlN and InN) crystalline thin films have been fabricated, and they have potential for many opto-electronic device applications. However, the investigations on the optical properties of the group III nitride are mainly performed at around the fundamental absorption edge region. The core absorption spectra of Carbon 1*s*, Nitrogen 1*s*, Indium 3*d* and Oxygen 1*s* were measured using total photoelectron yield (TY) method [1].

Thin films were made by the MOCVD method at Nichia Chemical (GaN), Riken (AlN) and Fukui University (InN). GaN thin film is 4 μm thickness on $\alpha$-$Al_2O_3$ substrate, AlN thin film is 1 μm on SiC, and InN thin film is 0.1 μm on GaAs(111). All films were cleaned with organic solvents just before the installation in the vacuum chamber, and the measurement was performed at room temperature in the range of $10^{-10}$ Torr. The photon energy calibration was carried out by using the binding energy of indium 4*d* core level of InN as 18.1 eV.

Figure 1 shows the TY spectrum of InN thin film from 275 to 580 eV. The structures around 280, 400, 450 and 530 eV correspond to carbon 1s, nitrogen 1s, indium 3d and oxygen 1s core absorptions, respectively. The spectrum feature of the carbon 1s core absorptions in fig.1 is similar to that of thin hydrogenated amorphous carbon film. From the depth profile of our Auger electron spectrum measurement, we found that the carbon is mainly located on the films. Therefore, it is concluded that carbon atoms mainly contaminate the film surface, and their structure is amorphous. Nitrogen 1s absorption which has a threshold at 396 eV shows a sharp peak at 401 eV and a clear XANES feature up to 447 eV. Indium 3*d* absorption with doublet which reflects the spin-orbit splitting of the indium 3*d* level (7.5 eV), is observed at above 447 eV. The huge broad peak with superimposed oscillatory structure can be seen above the indium 3*d* doublet. The small peaks at about 534 eV and above may be due to the transition from the oxygen 1*s* core level. However, it is very difficult to separate the oxygen 1*s* spectrum from the background structure.

Figure 2 shows the Nitrogen 1*s* absorption of GaN, AlN and InN. The resolution in fig.2 is lower than fig.1. The increase in the TY spectrum of InN above 470 eV is the huge peak as mentioned above. This huge peak is interpreted to be due to the transition from indium 3*d* levels to the continuum *f* states, because there are no such huge peak in GaN and AlN spectra. The threshold energy of Nitrogen 1*s* absorption which corresponds to the chemical shift is lower, in the order of InN $<$ GaN $<$ AlN. The strong first peak within 10 eV from the threshold, where the 1*s* absorption spectrum reflects the *p*-like final state structures, are the common feature of those three spectra. However, the spectra in XANES region show the difference among these materials. Further study with high resolution measurement is now in progress.

## Reference

[1] K.Fukui, M.Ichikawa, A.Yamamoto and M.Kamada, Solid State Electronics 41 (1997) 299.

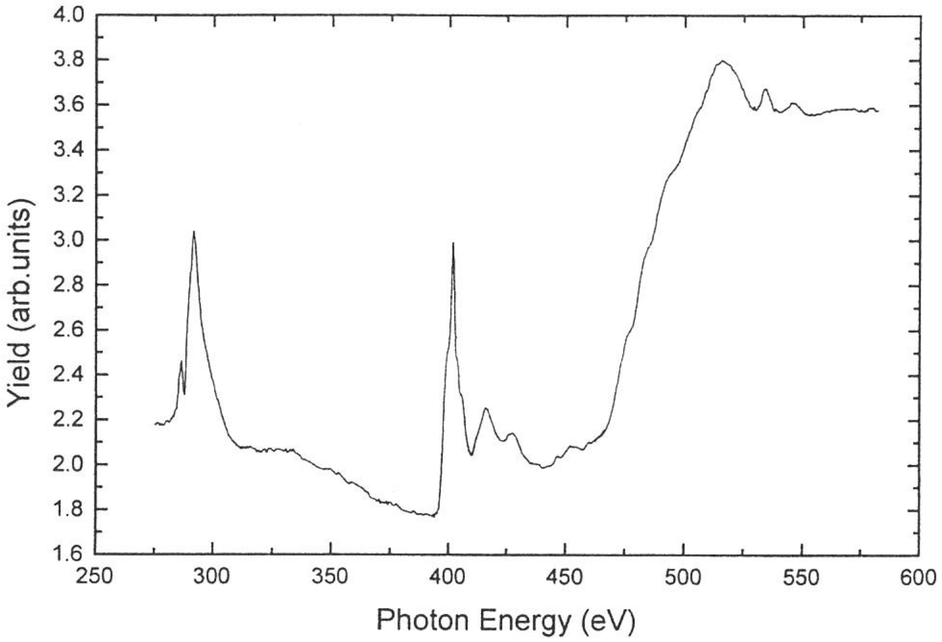

Fig. 1. Total photoelectron yield spectrum of InN thin film.

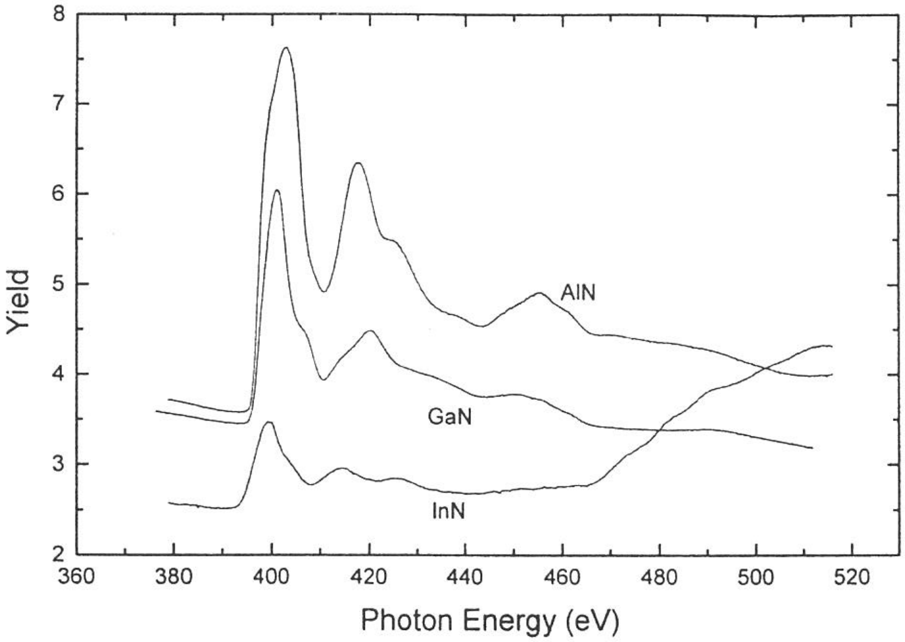

Fig. 2. Nitrogen 1s absorption spectra of AlN, GaN and InN thin films.

(BL2B2)

# Main Parameters of Renewed Beamline 2B2 with an 18m Spherical Grating Monochromator

Hiroaki YOSHIDA and Koichiro MITSUKE

*Department of Vacuum UV Photoscience, Institute for Molecular Science,*
*Myodaiji, Okazaki 444*

An 18m spherical grating monochromator (SGM) with high resolution and high flux is now manufactured and will be installed in March 1997 at the bending-magnet beamline 2B2 of the UVSOR. The basic design of the beamline was previously described [1]. The monochromator is designed to cover the energy range of 20–200 eV with a resolving power (E/ΔE) of more than 5000 and photon flux of more than $10^{10}$ photons/s/100mA. Main parameters of the 18m SGM beamline are presented in Table 1. The schematic side view of the beamline is shown in Fig. 1.

Table 1 Main parameters of 18m SGM beamline

| Optical element Mirrors(M) & Gratings(G) | | Radii R × ρ (mm) | Material | Coating | Reflective area L × W (mm) | Grazing angle (° ) |
|---|---|---|---|---|---|---|
| Elliptic cylinder | M0 | 28914 | quartz | Au | 500×20 | 6.5 |
| Spherical | M1 | 22580 | quartz | Au | 400×34 | 5.0 |
| Spherical | G1 | 18000 | quartz | Au | 130×20 | 10.0 (0th order) |
| | G2 | 18000 | quartz | Au | 130×20 | 10.0 (0th order) |
| | G3 | 9250 | quartz | Au | 130×20 | 20.0 (0th order) |
| Plane | M2 | | quartz | Al | 250×24 | 15.0 |
| Plane | M3 | | quartz | Al | 600×24 | 5.0 |
| Troidal | M4 | 18358×202 | quartz | Au | 300×50 | 5.0 |

Reference

[1] H. YOSHIDA and K. MITSUKE, UVSOR ACTIVITY REPORT 1995, p.112 (1996).

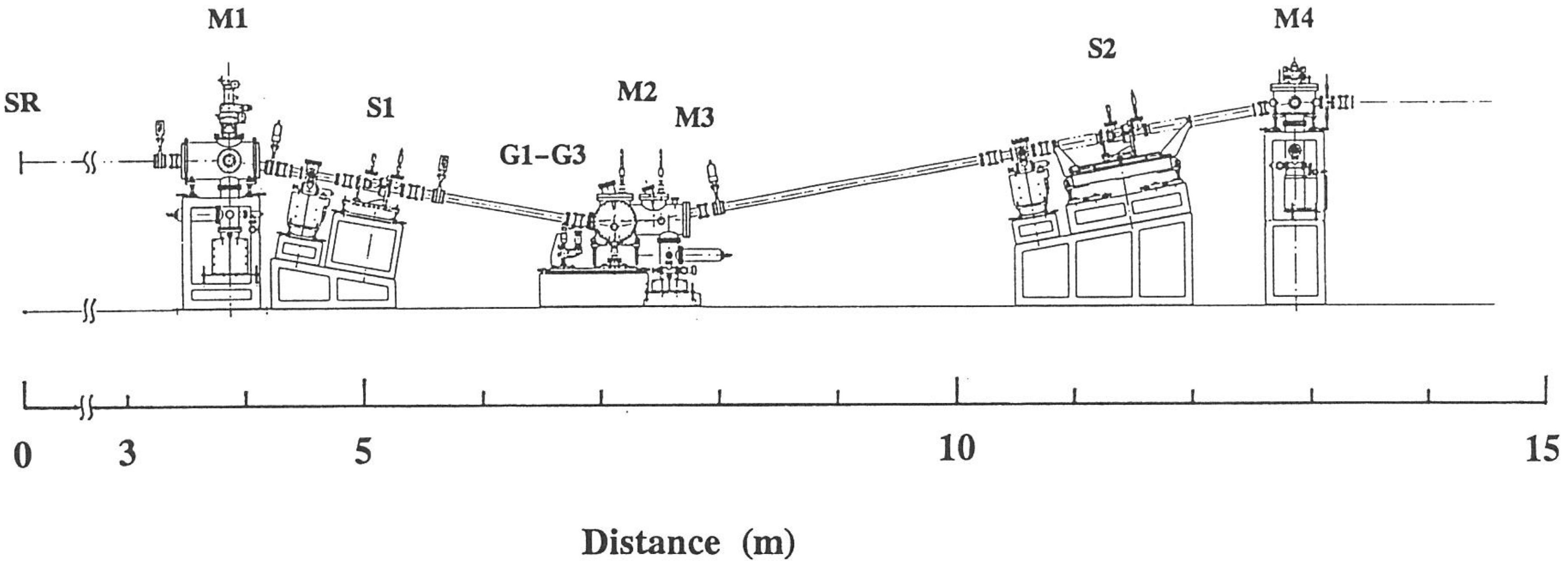

Fig. 1. Schematic side view of the 18m SGM beamline from the second prefocus mirror (M1) chamber to the refocus mirror (M4) chamber. SR, synchrotron radiation source; M1, spherical mirror; S1, entrance slit; G1–G3, spherical gratings; M2 and M3, plane mirrors; S2, exit slit; M4, toroidal mirror.

(BL3A1)

# Photocurrent in Amorphous Arsenic Trisulfide by Undulator Radiation

Koji HAYASHI, Atsushi HIRAI* and Koich Shimakawa*

*Center for Cooperative Research, Gifu University, Gifu 501-11*
**Department of Electronics and Computer Engineering, Gifu University, Gifu 501-11*

The time-dependent change (decrease) in photocurrent during and after bandgap illumination has been observed in amorphous chalcogenides[1] and hydrogenated amorphous silicon (a-Si:H)[2]. This effect is usually called photodegradation and is explained in terms of light-induced metastable defects (LIMD). In the device application of these materials, LIMD creation is a serious problem. Although a number of models have been proposed for LIMD creation[3], details of the mechanism underlying LIMD creation in these materials are still not clear. Understanding the physical mechanism underlying metastability is one of the important fundamental problems related to these materials. To obtain a wide knowledge of the photoinduced effects, it is necessary to investigate photoinduced effects on wide energy range. In the previous reports[4-7], we reported the photodarkening in amorphous arsenic trisulfide (a-$As_2S_3$) by the vacuum ultra-violet (VUV) light. In this report, we study the time-dependent change in photocurrent during illumination of the VUV light.

Thin films of a-$As_2S_3$ used for the measurements of photoconductivity were prepared onto quartz substrates by conventional evaporation technique. The thickness of the films was around 6000Å. For the measurements of the photoconductivity, coplanar gap-cell electrodes using Al contacts were fabricated on the samples (gap spacing=0.1 mm). The experiments were performed at a BL3A1 beam line of the UVSOR facility of the Institute for Molecular Science in Okazaki. VUV light that is filtered through an Al film from undulator radiation was used to measure the photoconductivity. Before illumination, the samples were annealed at 443K (near the glass transition temperature) for two hours in a vacuum. To eliminate visible lights of synchrotron radiation and higher harmonics of undulator radiation, Al film was inserted between undulator and samples. The samples were fixed in sample chamber which were evacuated below $10^{-8}$ Torr. The photon flux of undulator radiation through Al film was estimated from the total photoelectric yield of gold mesh.

Figure 1 shows the change in the photocurrent as a function of number of photons for a-$As_2S_3$ at room temperature. This figure is obtained by normalizing the photocurrent to the photon flux. As shown in the figure, the photocurrent is decreased at the first stage. At the second stage, the photocurrent is gradually increased and the photocurrent seems to be finally saturated. This change also depends on the illumination energy of the photon. It seems that the decrease and the increase in the photocurrent are related with the LIMD creation and photodarkening , respectively.

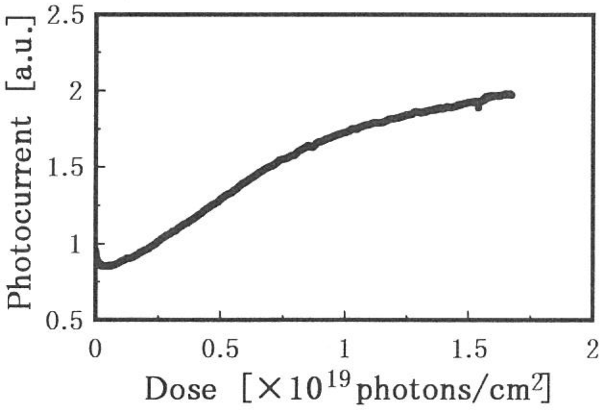

Fig.1 Change in the photocurrent measured at room temperature for a-$As_2S_3$. The illumination energy of the photon is 44 eV.

## REFFERENCES

[1] K. Shimakawa, S. Inami, and S. R. Elliott, Phys. Rev. B, 42(1990)11857.
[2] D. L. Staebler and C. R. Wronski, Appl. Phys. Lett., 31(1977)292.
[3] K. Shimakawa, A. Kolobov, and S. R. Elliott, Adv. Phys., 44(1995)475.
[4] K. Hayashi, D. Kato, S. Takeda, K. Shimakawa, and A. Yoshida UVSOR Activity Report 1993, p173.
[5] K. Hayashi, D. Kato, and K. Shimakawa, UVSOR Activity Report 1994, p82.
[6] K. Hayashi, A. Hirai, and K. Shimakawa, UVSOR Activity Report 1995, p128.
[7] K. Hayashi, D. Kato, and K. Shimakawa, J. Non-Cryst. Solids., 198-200(1996)696.

(BL3A1)

# Spectroscopic Search for $CH_5^+$ in solid parahydrogen

Takamasa MOMOSE, Tomonari WAKABAYASHI, and Tadamasa SHIDA

Division of Chemistry, Graduate School of Science, Kyoto University

Recently, we have found that solid parahydrogen is a useful substance for the matrix isolation spectroscopy of both stable and unstable molecules(1-4). In solid parahydrogen, high resolution spectroscopy is feasible with the spectral resolution as high as that of molecules in gas phase. In addition, since there is no appreciable "cage effect" in this matrix, various chemical reactions such as photodissociation can be studied with a high resolution.

When molecules are ionized in solid parahydrogen, the production of protonated ions can be expected as a result of ion-molecule reaction. The purpose of this study is to observe $CH_5^+$ in solid parahydrogen. The protonated methane is known as a prototype of the "non-classical" carbonium ion. It attracts attention in various field such as organic chemistry, theoretical chemistry, and interstellar chemistry. There are, however, very few spectroscopic observations of this ion. In solid parahydrogen, there is a possibility of the production of the ion by use of the intense VUV light from the undulators of UVSOR. Once the ion is produced, we can obtain information on the molecular structure, the electronic structure, the chemical reactivity and so on through the high resolution spectroscopy.

The expected mechanism of the production of $CH_5^+$ is as follows; first we ionize methyl iodide isolated in solid parahydrogen using the VUV light of the energy above the ionization potential of the iodide (9.54eV) ($CH_3I + VUV \rightarrow CH_3I^+$). The radical cation of methyl iodide is then photodissociated by the UV light from a mercury lamp to produce $CH_3^+$ ($CH_3I^+ + UV \rightarrow CH_3^+ + I$). The $CH_3^+$ thus obtained reacts with the neighboring hydrogen molecule to produce $CH_5^+$ ($CH_3^+ + H_2 \rightarrow CH_5^+$).

The hydrogen crystal was grown in a Cu optical cell sealed with $MgF_2$ windows as described in our previous paper [1]. The temperature of the sample was about 4.5K. The methyl iodide isolated in solid parahydrogen was irradiated by the undulator light from the BL3A1 beam line. The irradiation dose was high enough to quench most of the neutral methyl iodide which was confirmed by the disappearance of the infrared absorption spectrum of the iodide. Several experiments were performed by changing the photon energy from 10.2eV to 11.5eV. However, no new infrared absorption was observed except those of methyl radical and methane after the VUV irradiation. The UV irradiation followed by the synchrotron irradiation caused no effect. Since the ionization potential of methyl radical is 9.8eV, we also tried to ionize the methyl radical directly by the VUV light. In this experiment, the methyl radical was first produced by the UV irradiation of methyl iodide in solid parahydrogen. Then the sample was irradiated by synchrotron radiation. However, again no new spectrum was observed.

Accordingly, it is concluded that direct ionization of both methyl iodide and methyl radical does not occur in solid parahydrogen. Although the photon energy of the light was higher by a few eV than the ionization potential of these molecules, the quantum yield of ionization seems to be very small. Thus, at the moment, we consider that under the experimental conditions superexcitation dominates over direct ionization of both methyl iodide and methyl radical. The branching ratio between the superexcitation and the direct ionization was well studied in the gas phase, but there are essentially no studies in condensed phase.

Although we failed to detect the protonated methane in this experiment, we believe that the one photon ionization using the shorter wavelength undulator light is prospective to study protonated ions. We are planning to continue the experiment.

(1) T. Momose et al. J. Chem. Phys. 103, 1400 (1995). T. Momose et al. Chem. Phys. Lett. 246, 583 (1995).
(2) M. Miki et al. J. Phys. Chem. 100, 12135 (1996).
(3) N. Sogoshi et al. J. Phys. Chem. in press.
(4) T. Momose, Bunko Kenkyu 45, 125 (1996).

**(3A1)**

# Nano-Second Desorption of Ground-State K Atoms from KCl and KBr Studied by a Laser-Induced Fluorescence Method

Sayumi Hirose and Masao Kamada

*UVSOR Facility, Institute for Molecular Science*

Bombardment of solids by energetic electrons and photons induces the desorption of ions and neutral atoms from the surface. There have been many reports on electron-stimulated desorption (ESD) and photon-stimulated desorption (PSD) from alkali halides [1]. However, the desorption phenomenon is complex and the detail mechanism still remains to be clarified. The time dependence is one of the important information to know the desorption mechanism. There are several studies of the time response of ground-state halogen and alkali desorption from alkali halides. Kanzaki and Mori [2] have measured PSD of ground-state halogen and alkali atoms from RbBr and KI by using a mass spectrometer. They derived the response time of halogen and alkali desorption to be in the submilli-second range from the frequency dependence of the intensity obtained with a mechanical chopper. They proposed that the desorption process of ground-state alkali atoms is related to the diffusion of $V_K$ centers (the $V_K$ center is a halogen$_2^-$ molecular ion located in two halogen sites with reduced interatomic distance) and the surface reaction of F centers (the F center is an electron trapped in a halogen vacancy) and alkali ions. Loubriel *et al.* [3] and Green *et al.* [4] have studied the time dependence of ground-state Li desorption from LiF by using a pulsed electron beam, and found a response time in the range from μs to ms. They suggested that the persistence of the Li desorption is due to the slow diffusion of bulk F centers and their reaction with alkali ions in the surface layer.

The nano-second desorption of ground-state K atoms from KCl and KBr was investigated for the first time by the present laser-induced fluorescence method with synchrotron radiation and laser pulses. The experiments were carried out with synchrotron radiation (SR) at a undulator beam line 3A1 of UVSOR Facility. Intense quasimonochromatic radiation of 36 eV from the undulator was used as an excitation light source. The desorption of ground-state alkali atoms was observed by means of a LIF method. Ground-state alkali atoms desorbed from the alkali halide surface were excited with a laser, and then the fluorescence from the excited state of the alkali atoms was observed with an image-intensified CCD detector (Princeton Instruments Inc. ICCD-576) A laser diode (LD) (HAMAMATSU PLP-02) was used to excite the desorbed ground-state K atoms, because of its high repetition (2 MHz). The peak power and the pulse width of LD were about 250 mW and about 29 ps, respectively. The full with at half maximum (FWHM) of the LD spectrum was about 8 nm and the peak position was tuned to the transition from the ground state (4s) to the excited state (4p) of K atoms by using a potassium-gas cell. The time response of the desorption was investigated by means of a pump-probe method with SR and LD pulses under a single bunch operation. The interval between successive SR pulses was 178 ns and the time width of the pulses was about 480 ps. The RF signal (5.6 MHz) from the UVSOR electron storage ring was divided into 1/3 in order to control LD under the external mode. The delay time between SR and LD was changed with a ns-delay circuit, and the real value of each delay time was confirmed by observing scattered lights of SR and LD with a time-correlated single photon counting method.

Figures 1 shows the time responses of ground-state K desorption from KCl at 374K. The zero value on the abscissa means that SR and LD pulses coincide in time scale. It shoud be noted that the desorption consists of a nano-second component and a slow one more than 178 ns. The fast desorption is several orders of magnitude faster than the existing results of the time response of ground-state alkali desorption. Therefore, the fast desorption of ground-state alkali atoms can not be interpreted with the existing mechanisms and requires a new desorption model. We suggest that the lattice instability due to the electronic excitation in the surface layer may play an important role on the fast desorption of ground-state alkali atoms.

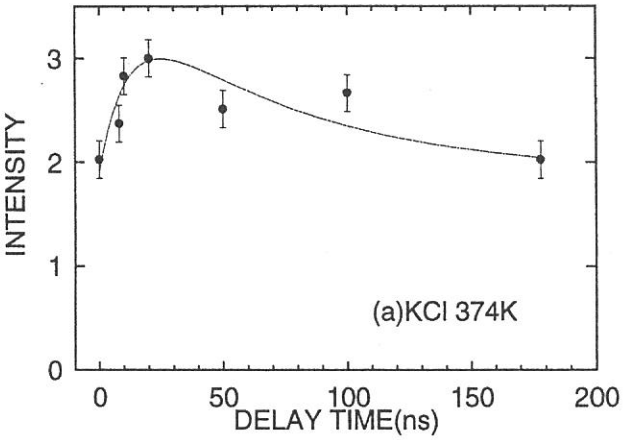

Fig. 1 The time response of ground-state K desorption from KCl.

References

[1] DESORPTION INDUCED BY ELECTRONIC TRANSITIONS (DIET-6) (North-Holland, 1995).
[2] H. Kanzaki and T. Mori, Phys. Rev. B 29, 3573 (1984).
[3] G. M. Loubriel etc, Phys. Rev. Lett. 57, 1781 (1986).
[4]T. A. Green etc., Phys. Rev. B 35, 781 (1987).

(BL3A1)

# Initial Stages of Undulator Lifig..ght-induced Surface Reaction Using Scanning Tunneling Microscope

O.Hosokawa and A.Yoshida
*Toyohashi University of Technology, Toyohashi 441*

Recently, synchrotron radiation sources are opening up a new prospect in a semiconductor processing technology. The effect on the semiconductor surface with vacuum ultra violet light must be clarified. Though it is of importance to investigate the defect creation and an atomic behavior on the semiconductor surfaces, only a few techniques are available for the surface analyzes. Scanning tunneling microscopy (STM) can give much information not only the local electron density , but also the surface structure with extremely high spatial resolution.

In this work, we study an initial stage of Undulator Radiation (UR)-induced surface reaction on molybdenum disulfide ($MoS_2$) surface in vacuum and oxygen atmosphere by using STM.

The experiments were performed in ultrahigh vacuum chamber equipped with UHV- STM. $MoS_2$ substrates were cleaved in air at room temperature just before it was loaded into the preparation chamber. UR irradiation, oxygen exposure, and heating up were performed inside a reaction chamber with a base pressure below $1\times10^{-8}$Torr. STM images were obtained in the constant-height mode at the sample bias of 150mV and -150mV.

Figure 1 shows the STM image of the $MoS_2$ clean surface on 80Å scale with the sample bias of -150mV and the tunneling current of 1nA. The atomic structure in the top layer of sulfur atoms was clearly seen. STM images of $MoS_2$ surface irradiated for 300 and 500mAmin by Undulator Radiation in vacuum on 500Å scale are shown in figures 2 and 3 , respectively. All images were taken with the negative sample bias. From these images, the depression region and the ring structure were found at the initial stages of irradiation. The depression region became grater and the number of the ring structure increased with increasing the irradiation dose. Similar results were also seen at the positive sample bias. It means that these reactions are mainly due to a topographical, not electronic structure. After irradiated samples were heated up at 150℃ for an hour, dotted ring structure partially disappeared. In the samples irradiated in oxygen atmosphere, there were no particularly different patterns on the $MoS_2$ surface. But surface reactions were promoted under the same irradiation dose. These patterns did not exist on the heated sample surface without irradiation in vacuum or oxygen atmosphere.

From these results, the surface reaction induced by undulator radiation light was mainly accelerated in the oxygen atmosphere.

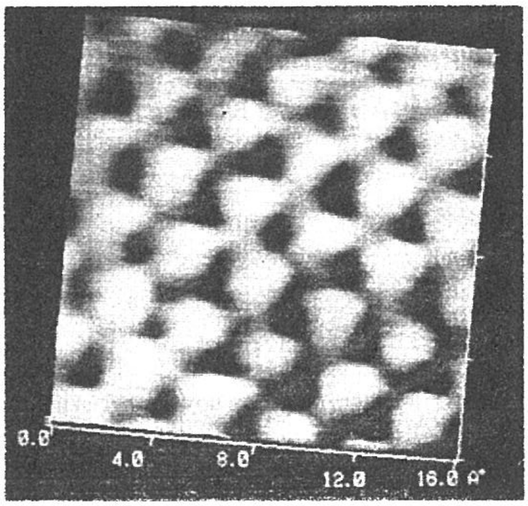

Fig1. MoS$_2$ clean surface

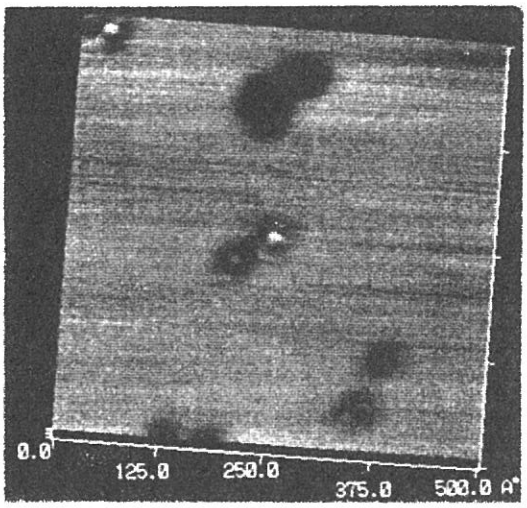

Fig.2 MoS$_2$ surface irradiated
for 300mA・min in vacuum

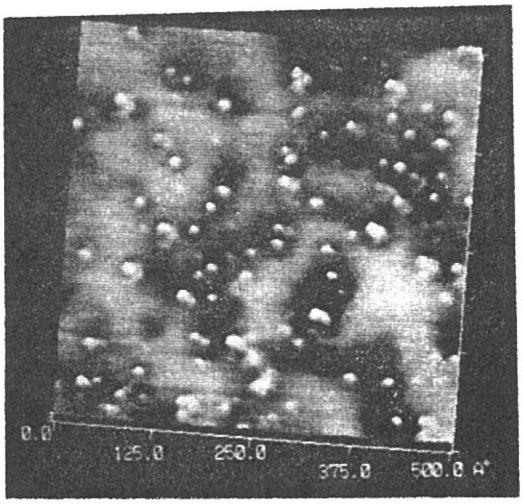

Fig3. MoS$_2$ surface irradiated
for 500mA・min in vacuum

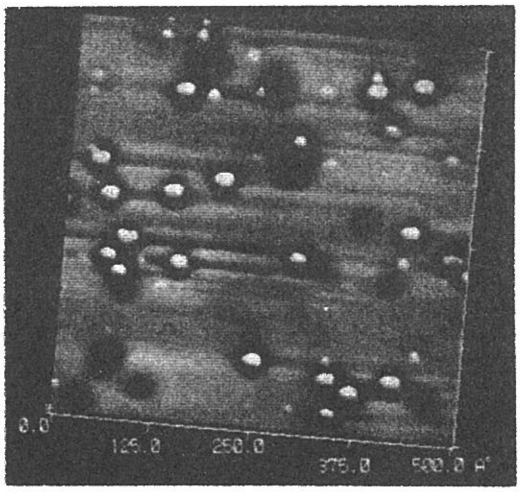

Fig.4 MoS$_2$ surface heated at 150℃ for 1h
irradiated for 500mA・min in vacuum

## (BL3A2)

# Vacuum UV Spectroscopy Making Use of the Combination of Synchrotron Radiation and Laser — Synchronization of UV Laser with the Undulator Radiation

Masakazu MIZUTANI, Manabu TOKESHI[a] , Atsunari HIRAYA[b] and Koichiro MITSUKE

*Institute for Molecular Science, Myodaiji, Okazaki 444*
[a]*Department of Molecular Science and Technology, Kyushu University, Kasuga 816*
[b]*Faculty of Science, Hiroshima University, Kagamiyama, Higashi-Hiroshima 739*

For time-resolved two-photon excitation spectroscopy, we have developed a novel laser-synchrotron radiation (SR) combination system in which precise synchronization of the photon pulses has been realized between the third harmonic (TH) of a mode-locked Ti:sapphire laser and the undulator radiation emitted from the UVSOR storage ring.

The typical repetition rate of the mode-locked laser was changed from 82 MHz (standard version) to 90.115 MHz to match the frequency of the master oscillator of the storage ring. The duration time of the SR and laser pulse is 400 ps and 1.8 ps, respectively. Any phase difference between the phase of the train of the laser output pulse and that of the reference signal, the 90.115 MHz synchronous output from the master oscillator, is converted into an error voltage by a phase detector. This voltage controls the servo electronics of a cavity mirror holder and changes the pulse repetition frequency. By this electronics, the repetition rate of the laser is exactly same as the frequency of the master oscillator. The adjustment for pulse timing is performed by the phase shifter.

Detection of photon pulses *in situ* using a high bandwidth photosensitive device is essential for attaining precise synchronization between the laser light and SR. For this purpose we monitor fluorescence at ~ 340 nm from *p*-terphenyl ($C_{18}H_{14}$) excited by the laser and Auger-free luminescence at ~ 220 nm from $BaF_2$[1)] excited by the undulator radiation. The observed lifetimes of the fluorescence from two compounds are of the same order of 900 ps. Both lights are simultaneously detected with a metal package photomultiplier tube. A Cu block, having a triangular prism shape, is inserted across the photon been axis at a point 44 mm from the center of the ionization cell, as shown in Fig. 1. The laser light impinges on one of the rectangular sides covered by a thick film of *p*-terphenyl with an incident angle of 45°, while a piece of $BaF_2$ crystal glued on the other side is illuminated by the undulator radiation. To examine the temporal and spatial overlap, the output current of the photomultiplier is amplified by a preamplifier and fed into a digital oscilloscope. The Cu block is connected to the rod of a linear-motion feedthrough so it can be easily put in and out of the path of the photon beams without breaking the system vacuum.

Figure 2 shows the traces of the photomultiplier signal for two different cases of the timing. The reference signal from the master oscillator is supplied to the trigger input of the oscilloscope. If the timing of the photon pulses between the laser and SR is different, two pulse trains with the same interval of 11 ns are observed in separate positions, as indicated in Fig. 2(a). Here, the SR pulse arrives at the Cu block 3.4 ns earlier than the laser pulse. In Fig. 2(b) the phase shifter is so adjusted that the two pulse trains are almost overlapped in time. A precise value of the delay can be estimated to be 0.3 ns from Fig. 2(c), in which the laser and SR pulses are individually recorded by blocking the two beams alternatively. This 0.3 ns delay at the Cu block corresponds to that of (0 ± 0.1) ns at the center of the ionization cell, which is 44 mm from the block. Thus, the pulses of the laser and SR are expected to be definitely overlapped in time at the ionization region. Viewing the signal on the oscilloscope permits the delay time between the laser and SR pulses to be measured with a precision of ± 100 ps. The whole system operates stably at a fixed delay within this resolution limit for 2 - 3 h without readjustment of the timing.

**Reference**

1) M. Itoh, S. Hashimoto, S. Sakuragi and S. Kubota, Solid State Commun. 65, 523 (1988).

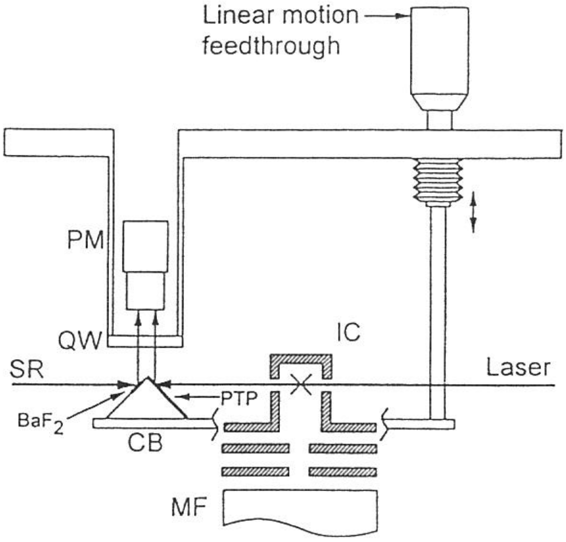

Fig. 1. Schematic diagram of the detector of the photon pulse. The luminescence emitted from the surface of a Cu block (CB) passes through a vacuum-sealed quartz window (QW) and is admitted to a photomultiplier tube (PM). The adopted luminescing substances are *p*-terphenyl (PTP) and BaF$_2$ for the laser and SR, respectively. All materials except an ionization cell (IC) and a quadrupole mass filter (MF) are mounted on a vacuum flange of diameter 8".

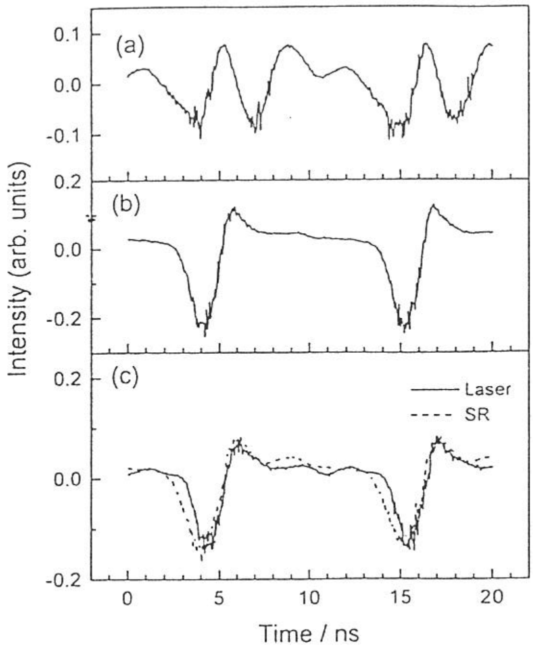

Fig. 2. Traces of the photomultiplier signal on a digital oscilloscope for two different cases of the timing between the laser and SR. The delay of the laser pulse at the Cu block with respect to the SR pulse is 3.4 ns in (a) and 0.3 ns in (b) and (c). At the 0.3 ns delay, the two photon pulses are considered to be definitely overlapped in time at the ionization cell. They are monitored either simultaneously in (a) and (b) or individually in (c).

(BL3A2)

# Dissociative Photoionization of $Cr(CO)_6$ in the Cr:3p Inner-Valence Region.

Yusuke Tamenori and Inosuke Koyano
*Department of Material Science, Himeji Institute of Technology,*
*Kamigohri, 678-12*

Over the last several years, we have been performing a series of detailed studies of dissociative photoionization of transition-metal carbonyls in the inner-valence region by use of TOF mass spectrometry and photoion-photoion coincidence (PIPICO) technique.[1) In the present work, the dissociative photoionization of $Cr(CO)_6$ is studied in the range 37-100eV with a special emphasis in the vicinity of the Cr;3p ionization threshold (51.1eV).

Shown in Figure 1 is the incident photon energy dependence of the partial photoion yields of all observed ions. The yields are obtained by multiplying the total photoionization efficiencies by the values of the PEPICO branching ratio. We can see a large broad resonance in each curve at about 50eV corresponding to the Cr;3p ionization threshold. The dissociation channels can be classified into two categories; one is that of the channels including only the simple CO elimination and the other that at the channels involving additional cleavage of the C-O covalent bond. The prominent dissociation channels belonging to the former categories are mostly those of doubly charged ions. Typical examples are channels producing $Cr(CO)_n^{2+}$ (n=1,2), whose yield curves show a pronounced increase in the above energy region. The PIPICO yield curves (not shown) are found also to show the same trend: the partial yields of various ion-pairs also rapidly increase in this energy region with the increase of the incident photon energy.

$$Cr(CO)_6 + h\nu \rightarrow Cr(CO)_6^{2+} + 2e^-$$

$$Cr(CO)_6^{2+} \rightarrow Cr(CO)_n^{2+} + n.p. \qquad (n=0\text{-}5) \qquad (1)$$

$$\rightarrow Cr(CO)_n^{+} + CO^{+} + n.p. \qquad (n=0,1) \qquad (2)$$

Cooper *et al.* have shown that the Cr:3d cross section is strongly enhanced near the Cr:3p ionization threshold and interpreted this fact in terms of the Cr 3p-3d resonance photoabsorption followed by Super-Coster-Kronig decay with associated emission of a metal d electron ($t_{2g}^{-1}$). The eliminated $t_{2g}$ electron is well-known to largely contribute to the π-back donation interaction and characterizes the strong Cr-CO bonding orbital. Then it can be assumed that the loss of the $t_{2g}$ electron enhances the neutral or ionic CO elimination. The singly charged ions ( $Cr(CO)_n^+$ ) also show large enhancement similar to the doubly charged ions in the PEPICO measurement. However, the subtraction of the ion-pair contributions from the partial yield of those ions reveals that the observed increment is not caused by the single ionization but is due to the charge separative dissociation of doubly charged ions.(scheme 2).

Dissociation channels that result in the cleavage of a C-O bond on the metal atom (the second category) are also enhanced in the same energy region .

$$Cr(CO)_6^{+} \rightarrow CrC^{+} + n.p. \qquad (3)$$

$$Cr(CO)_6^{2+} \rightarrow CrC(CO)^{2+} + n.p. \qquad (4)$$

Among the ions produced by pure single ionization, the $CrC^+$ ion is the only species that shows a resonant enhancement at the Cr 3p-3d resonance absorption. This indicates that the disintegration of the ligand on the metal atom is also a significant decay process following 3p-3d excitation, although the bond strength of C-O is much stronger than that of Cr-CO bond.

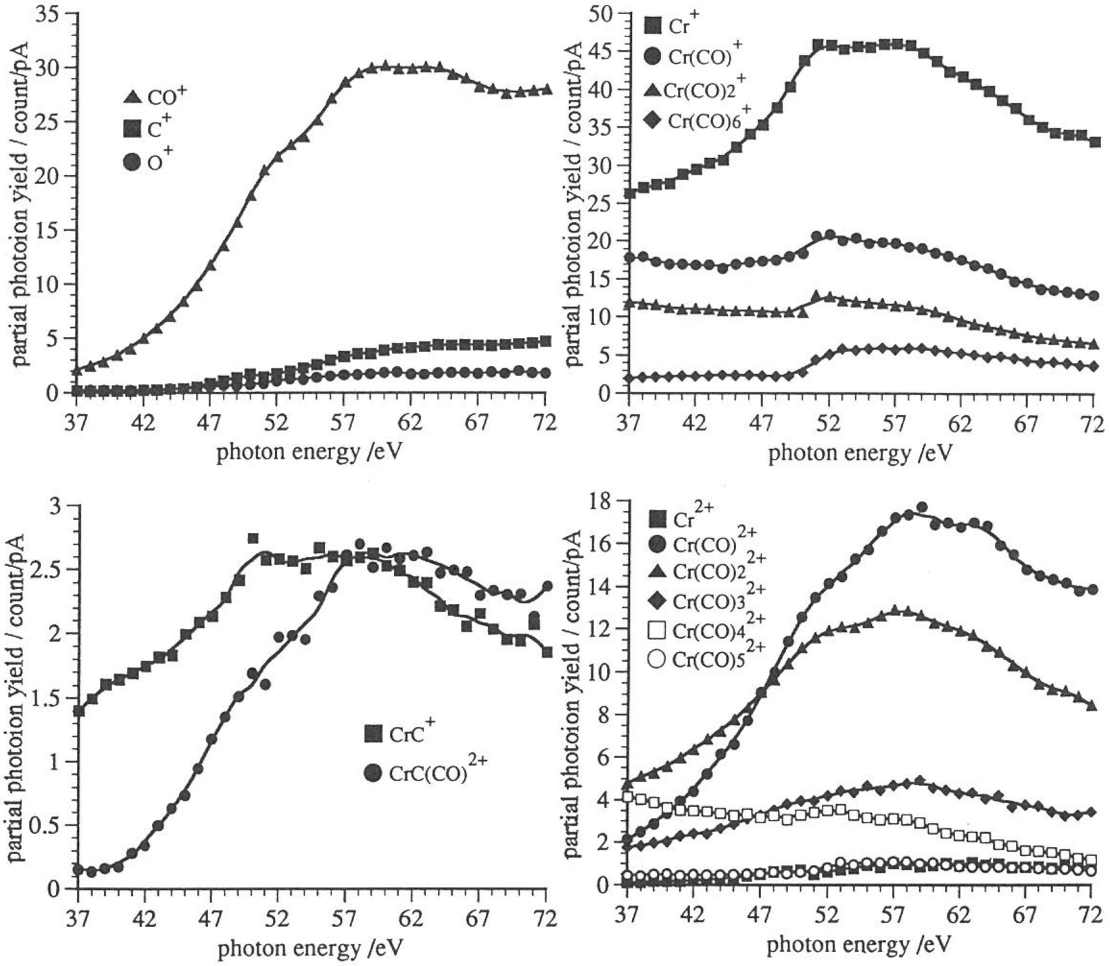

**Figure 1**, The incident photon energy dependence of partial photoion yield for various product ions in the range 37-72eV.

**Reference** 1, Y. Tamenori, K. Inaoka, and I.Koyano, J. Electron. Spectros. Rela. Phenom. 79, 503 (1996)
Y. Tamenori and I.Koyano, UVSOR Activity Report, (1994), p92
Y. Tamenori, K. Inaoka, and I.Koyano, UVSOR Activity Report, (1995), p138

## (BL3A2)

# Vacuum UV Spectroscopy Making Use of the Combination of Synchrotron Radiation and Laser — Time-Resolved Spectroscopy of He$^*(1s2p\ ^1P)$

Masakazu MIZUTANI, Manabu TOKESHI[a], Atsunari HIRAYA[b] and Koichiro MITSUKE

*Institute for Molecular Science, Myodaiji, Okazaki 444*
[a]*Department of Molecular Science and Technology, Kyushu University, Kasuga 816*
[b]*Faculty of Science, Hiroshima University, Kagamiyama, Higashi-Hiroshima 739*

Time-resolved spectroscopy of He$^*(1s2p\ ^1P)$ state has been carried out to obtain direct evidence supporting the precise synchronization of the photon pulses between the third harmonic (TH) of a mode-locked Ti:sapphire laser and the undulator radiation emitted from the UVSOR storage ring and to check the performance of the adjustment mechanism for pulse timing. The details of the apparatus is described elsewhere.[1)] The third harmonic of the laser is introduced coaxially with the fundamental of the undulator light (U1) supplied from BL3A2. A sample gas is expanded from a nozzle. The molecular beam intersects the two photon beam at 90° at a cylindrical ionization cell. Photoions are analyzed by a quadrupole mass filter placed perpendicularly to the photon beams and the molecular beam. The synchronizing system is described in another report in this journal.

The lifetime of He$^*(1s2p\ ^1P)$ state is measured with two-photon ionization of He. The scheme is expressed as

$$\mathrm{He} + h\nu_1\,(E_{SR} = 21.218\ \mathrm{eV}) \rightarrow \mathrm{He}^*(1s2p\ ^1P)$$
$$\mathrm{He}^*(1s2p\ ^1P) + h\nu_2\,(E_{laser} \sim 4.8\ \mathrm{eV}) \rightarrow \mathrm{He}^+ + e^-.$$

The primary excitation with U1 produces a resonant state He$^*(1s2p\ ^1P)$ whose lifetime is 0.555 ns. After specific lapse of time the excited atom is photoionized by absorbing another photon, TH at 260 nm. Consequently, the ion counts measured as a function of the delay between the laser and synchrotron radiation (SR) exhibit a decay curve associated with the lifetime of He$^*(1s2p\ ^1P)$. The overall temporal resolution is determined theoretically from the temporal profile of the SR pulse, *i.e.* the FWHM of 400 ps.

The fundamental light of the undulator is monochromatized by a grazing incidence monochromator. Two 100 nm-thick Sb foils are prerequisite to suppressing the second and higher order lights from a grating which produce a serious background noise of He$^+$ resulting from single-photon ionization.

Figure 1 shows the ratio between the He$^+$ signal counts, with and without the laser, as a function of the delay of the laser pulse with respect to the SR pulse. At 1 ns or longer delays the ratio is almost constant at 0.95, though the data points show some scatter. Accordingly, we assume that this value corresponds to the background level. Its deviation from unity probably arises from the uncertainty with regard to the effective gate time of a gated photon counter operating with an optical chopper. The ratio in Fig. 1 is found to be greater than the background level within a narrow time window from - 100 to + 400 ps. This enhancement can be accounted for by He$^+$ signal counts due to the two-photon ionization by way of He$^*(1s2p\ ^1P)$.

**Reference**

1) M. Mizutani, M. Tokeshi, A. Hiraya and K. Mitsuke, J. Synchrotron Rad. (1997), in press.

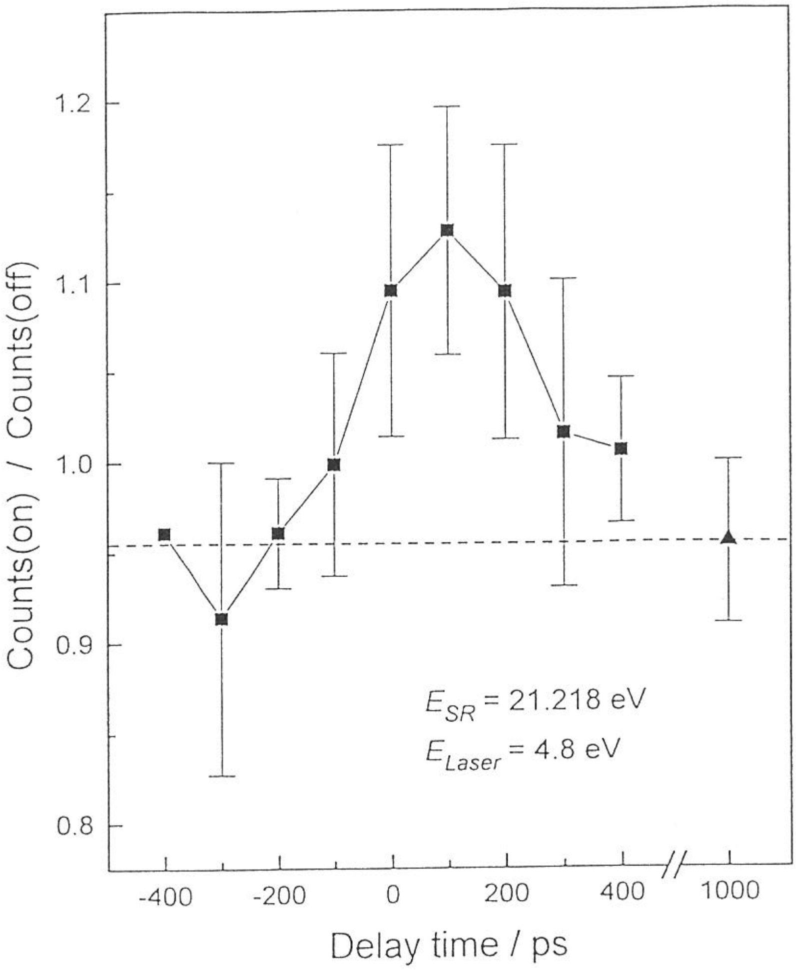

Fig. 1. Time-dependent signal of He$^+$ produced by two-photon ionization of He. The ratio between the ion counts with and without the laser is plotted as a function of the delay of the laser pulse with respect to the undulator pulse. The dashed line represents the background level which is determined from the ratio at 1 ns or longer delays. A broad peak centered around 100 ps results from the pump-probe signal counts due to the two-step transition: the SR excitation from He$(1s^2\ ^1S)$ to He$^*(1s2p\ ^1P)$ followed by the laser photoionization. The spectral resolution of SR is set to ~15 meV.

## BL3A2

# Single- and double-photoionization cross sections of sulfur dioxide ($SO_2$) and ionic fragmentation of $SO_2^+$ and $SO_2^{2+}$

Toshio MASUOKA

*Department of Applied Physics, Faculty of Engineering, Osaka City University, Sugimoto 3, Sumiyoshi-ku, Osaka 558*

Doubly charged molecular ions are produced in abundance at high energies. However, since molecular double ionization ($m^{2+}$) is usually followed by the production of an ion pair ($m_1^+ + m_2^+$, dissociative double ionization) doubly charged molecular ions are rare or non-existent in the mass spectra of many molecules. In the determination of double-photoionization cross section ($\sigma^{2+}$), it is essential to include both the stable $m^{2+}$ ions (if they exist) and the $m_1^+ + m_2^+$ ion pairs. Another problem is that the $m_1^+$ ion is produced from $m^+$ and/or $m^{2+}$ at excitation energies where dissociative single and double photoionization take place concomitantly. It is desirable to determine how many $m_1^+$ ions are produced respectively from $m^+$ and $m^{2+}$.

In the present study, molecular and dissociative single- and double-photoionization processes of sulfur dioxide ($SO_2$) are examined in the photon energy region of 37-120 eV by use of time-of-flight (TOF) mass spectrometry and the photoion-photoion-coincidence (PIPICO) method together with synchrotron radiation. The TOF mass spectra and the PIPICO spectra were measured at an angle of 55° with respect to the polarization vector where the second-order Legendre polynomial is close to zero. Under these conditions, the effects of anisotropic angular distributions of fragment ions are minimized [1].

The ratio of double to single photoionization is shown in Fig. 1. Above 100 eV, the ratio exceeds 0.4. This ratio may be regarded as the lower limit of $\sigma^{2+}/\sigma^+$ because the $O^+ + O^+ + S$ channel of $SO_2^{2+}$ is not included in the evaluation of $\sigma^{2+}$ and discrimination effects against energetic ions produced in dissociative double photoionization has not been corrected. The absolute cross sections for the single and double photoionization shown in Fig. 2 were obtained from the total cross section $\sigma_t$ [2,3] assuming that $\sigma_t = \sigma^+ + \sigma^{2+}$. The ion branching ratios for the precursor $SO_2^+$ determined separately from those for $SO_2^{2+}$ are shown in Fig. 3. The production of the molecular $SO_2^+$ ion is less than 50% so that the dissociation of the parent $SO_2^+$ ion is the dominant process throughout the energy region examined. It is interesting to note that the ion branching ratios of the molecular $SO_2^+$ and $SO^+$ ions increase at high excitation energies, whereas those of atomic $O^+$ and $S^+$ ions decrease. The ion branching ratios for the precursor $SO_2^{2+}$ separately determined from those for $SO_2^+$ are shown in Fig. 4. The thresholds of the dissociation of $SO_2^{2+}$ into $O^+ + SO^+$ and $O^+ + S^+ + O$ are found to be 35.0 ± 0.5 eV and 37.7 ± 0.5 eV, respectively; the former is in agreement with 34.1 ± 0.4 eV reported by Dujardin *et al.*[4]. Whether the parent $SO_2^{2+}$ ions are produced or not is not clear because the $SO_2^{2+}$ mass peak, if it exists, overlaps with those of $S^+$ ($O_2^+$). The charge-localized dissociation of $SO_2^{2+}$, forming $O^{2+}$, becomes appreciable at higher excitation energies above about 80 eV.

## REFERENCES

[1] T. Masuoka, I. Koyano, and N. Saito, J. Chem. Phys. **97**, 2392 (1992).

[2] C. Y. R. Wu and D. L. Judge, J. Chem. Phys. **74**, 3804 (1981).

[3] J. A. R. Samson (unpublished data).

[4] G. Dujardin, S. Leach, O. Dutuit, P.-M. Guyon, and M. Richard-Viard, Chem. Phys. **88**, 339 (1984).

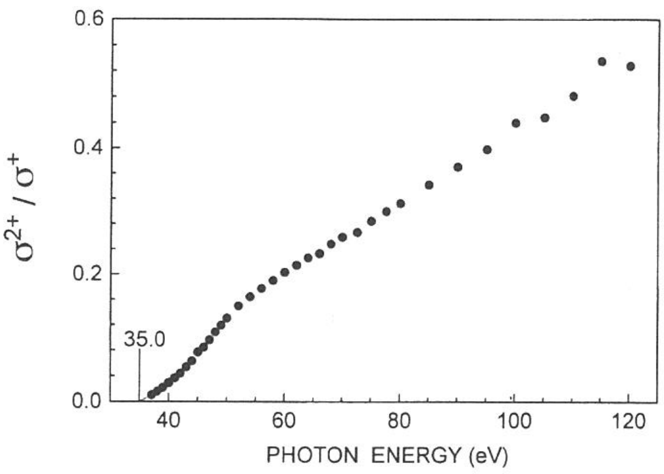

FIG. 1. Ratios of double- to single-photoionization cross section of $SO_2$.

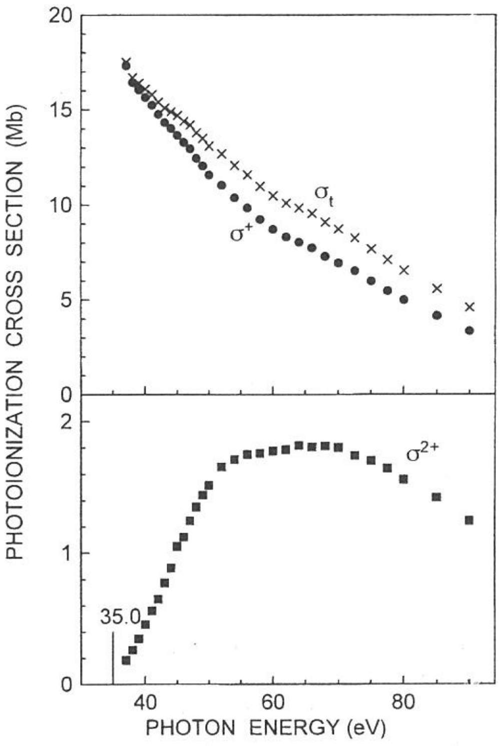

FIG. 2. Cross sections for single- and double-photoionization of $SO_2$. The total cross section is from Refs. [2] and [3].

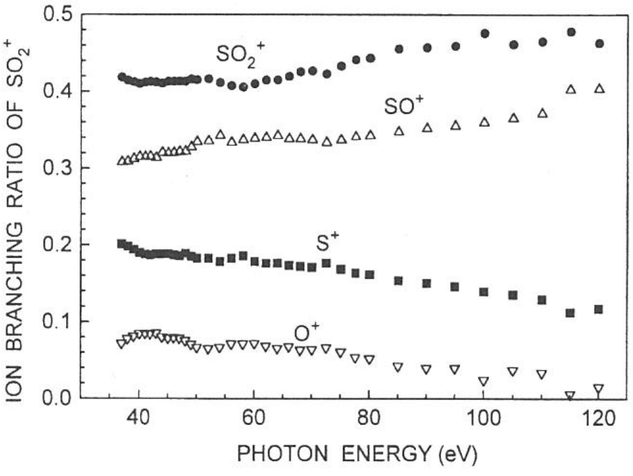

FIG. 3. Ion branching ratios of single photoionization of $SO_2$.

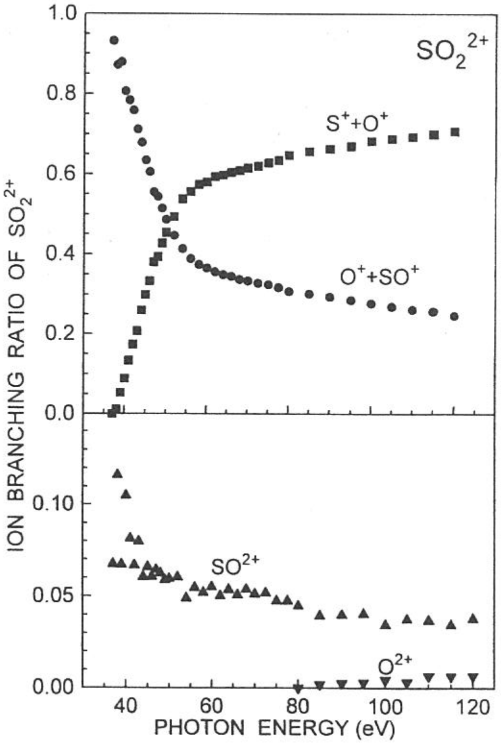

FIG. 4. Ion branching ratios of double photoionization of $SO_2$.

**(BL3B)**

# Production of Autoionizing Sulfur Atoms from Superexcited States of OCS

Yasumasa HIKOSAKA, Hideo HATTORI*, Takumi HIKIDA, and Koichiro MITSUKE*

*Department of Chemistry, Tokyo Institute of Technology, Ohokayama, Meguro 152, Japan*
**Department of Vacuum UV Photoscience, Institute for Molecular Science, Okazaki 444 Japan*

Photodissociation of OCS followed by autoionization of an atomic fragment is studied by two-dimensional photoelectron spectroscopy using synchrotron radiation. Figure 1(a) shows a two-dimensional photoelectron spectrum (2D-PES) of OCS at photon energies from 14.2 to 16.8 eV. The vertical axis corresponds to the incident photon energy $E_{h\nu}$ and horizontal axis to the kinetic energy $E_k$ of the ejected electron. The energy difference $\Delta E \equiv E_{h\nu} - E_k$ is essentially equal to the ionization energy $I_E$, and a set of lines with various $\Delta E$ values is indicated on the top of the figure. The electron counts are plotted on a linear scale and the intense structures are truncated. Figure 1(b) represents the curve obtained by summing electron counts over the whole range of $E_k$ as a function of $E_{h\nu}$. This curve resembles photoabsorption and photoionization spectra, and the most peaks can be assigned to the Rydberg states OCS*($R_B$) whose converging limit is OCS$^+$($\tilde{B}\,^2\Sigma^+$) lying at 16.04 eV. Patterns due to direct photoionization of OCS into vibronic states of OCS$^+$ appear as diagonal stripes with a slope of unity on Fig. 1(a), since the ionization energy $I_E$ for the OCS$^+$ state is equal to $\Delta E$. Vibrational excitation of OCS$^+$($\tilde{X}\,^2\Pi$) is more extensive at photon energies of the OCS*($R_B$) resonances than in a He I photoelectron spectrum ($E_{h\nu}$ = 21.22 eV), which is interpreted in terms of conversion of OCS*($R_B$) to other superexcited states.

If a superexcited molecule dissociates without autoionization and one of the produced fragments still has enough internal energy, autoionization of this fragment can subsequently occur. The kinetic energy of the electron ejected from the fragment is definitely determined by the energy difference between two particular states. As a result, the electron yield due to the fragment autoionization generates a vertical pattern running parallel to the $E_{h\nu}$ axis in 2D-PES. Figure 1(a) shows several vertical stripes at $E_{h\nu}$ = 15 - 16.8 eV which are confined within the region of $E_k$ < 1.8 eV. These patterns are considered to result from autoionization of S* converging to S$^+$($^2D^o$) into S$^+$($^4S^o$). The electron yield shows enhancement at excitation energies for OCS*($R_B$), especially at those for the $s\sigma$ states. This suggests that S* is produced by conversion of OCS*($R_B$) to a dissociative state OCS*($D$) correlating with S* + CO. The electronic state of the counter CO molecule is expected to be $\tilde{X}\,^1\Sigma^+$ from an energetical relation between $\Delta E$ and a dissociation limit for the final product S$^+$ + CO. We thus propose the following mechanism for the formation and autoionization of S*:

$$\mathrm{OCS}(\tilde{X}\,^1\Sigma^+) + h\nu \rightarrow \mathrm{OCS}^*(R_B) \rightarrow \mathrm{OCS}^*(D)$$
$$\mathrm{OCS}^*(D) \rightarrow \mathrm{S}^*[\text{converging to } \mathrm{S}^+(^2D^o)] + \mathrm{CO}(\tilde{X}\,^1\Sigma^+)$$
$$\mathrm{S}^*[\text{converging to } \mathrm{S}^+(^2D^o)] \rightarrow \mathrm{S}^+(^4S^o) + e^- .$$

If principal quantum number $n$ is unchanged after the conversion of OCS*($R_B$) to OCS*($D$), autoionization of S* results in a diagonal stripe with a slope of unity on 2D-PES. This is because, as long as the core ion model is pertinent to the binding energy of the Rydberg electron, the term values of OCS*($R_B$) and S* are nearly the same if their $n$ values are the same. The diagonal stripe is expected to be restricted within a region of $E_{h\nu}$ below the ionization threshold for OCS$^+$($\tilde{B}\,^2\Sigma^+$) and $E_k$ below the difference in the atomic levels between S$^+$($^4S^o$) and S$^+$($^2D^o$): $E_{h\nu}$ < 16.04 eV and $E_k$ < 1.84 eV. In Fig. 1(a), a diagonal pattern at $\Delta E \sim 14.2$ eV is considered to be formed by autoionization of S* atoms from high-Rydberg OCS*($R_B$) states whose $n$ values are conserved throughout the conversion to OCS*($D$) states and their dissociation. To examine the intensity change of the diagonal pattern at $\Delta E \sim 14.2$ eV, electron counts are summed at every $E_{h\nu}$ over a range of $\Delta E$ = 14.1 - 14.3 eV along the $E_k$ direction. The summation in Fig. 2 thus obtained gradually increases with $E_{h\nu}$, reaches a maximum at ~ 16 eV, and greatly diminishes above $I_E$ [OCS($\tilde{B}\,^2\Sigma^+$)] = 16.04 eV.

We will now simulate the photon energy dependence of the cross section σ(S*) for the formation of S* fragment in order to compare with the curve of Fig. 2. If OCS*($R_B$) with high-$n_{\mathrm{OCS}}$ is converted to OCS*($D$) with the same $n$, and if the transition rates for other decay channels are supposed to be proportional to $n_{\mathrm{OCS}}^{-3}$, σ(S*) can be given as

$$\sigma(\mathrm{S}^*) \propto \frac{1}{(a_2/a_1)\, n_{ocs}^{x} + n_{ocs}^{3}},$$

where $a_1$ and $a_2$ represent proportional constants for conversion to OCS*($D$) and for other channels, respectively. We assume that the rate for conversion to OCS*($D$) with the same $n$ has a form of $a_1 n_{\mathrm{OCS}}^{-x}$ using a fitting parameter $x$. The calculations deal only with the $s\sigma$ states ($\delta$ = 1.12) of OCS*($R_B$), S* being produced most efficiently from these states. A curve is plotted at energy intervals of 30 meV, in accordance with our experimental resolution, by summing $\sigma(S^*)$ for neighboring Rydberg states lying in each width of 30 meV. Figure 3 shows the curve obtained by setting the adjustable parameters to $x = 0$ and $a_2/a_1 = 12500$ and by taking account of $n_{OCS}$ up to 10000. This curve closely resembles that of the experimental spectrum in Fig. 2. In this simulation, the $x$ value is somewhat arbitrary in the region of $x < 2$, because we can accordingly choose an $a_2/a_1$ value to reproduce the curve in Fig. 3. Though some ambiguities still remain, the present simulation certifies that the diagonal stripe at $\Delta E \sim 14.2$ eV in Fig. 1(a) is attributed to conversion of OCS*($R_B$) with $n_{OCS}$ to OCS*($D$) with $n \sim n_{OCS}$, and that the rate for the conversion depends weakly on $n_{OCS}$.

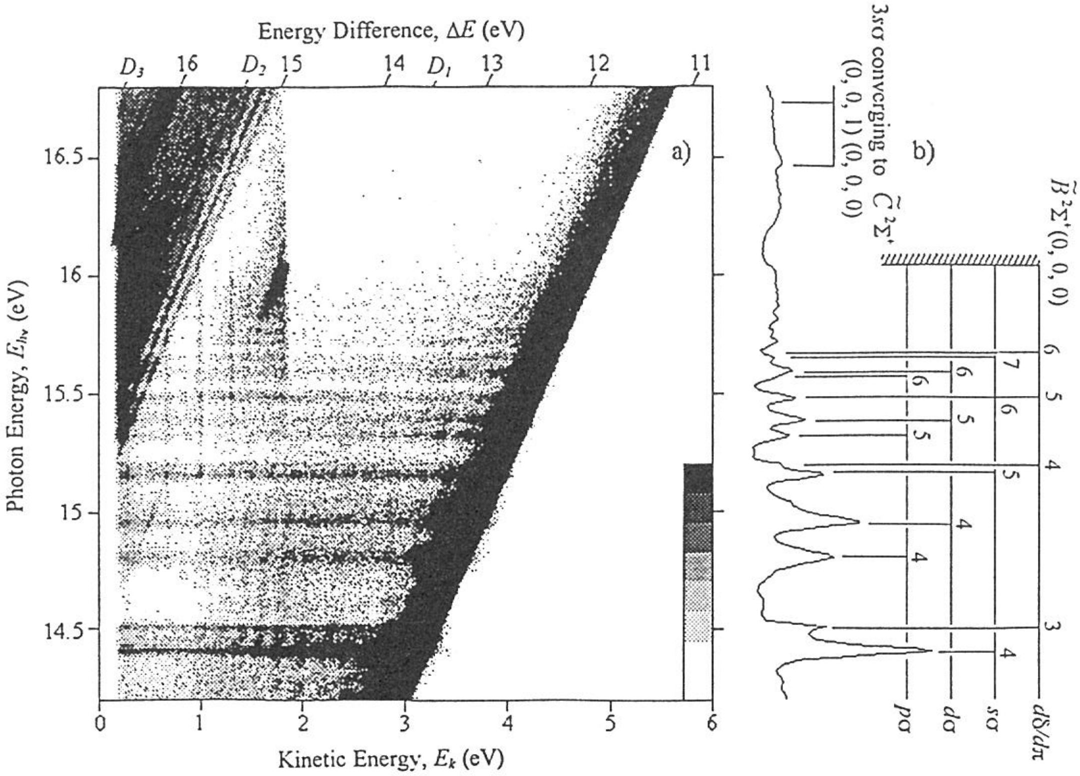

**Figure 1(a)** Two-dimensional photoelectron spectrum of OCS in the photon energy range of 14.2 - 16.8 eV. The electron yield is presented by the plots with eight tones from light to dark on a linear scale. **(b)** The curve obtained by summing electron counts over the whole range of $E_k$ as a function of $E_{h\nu}$.

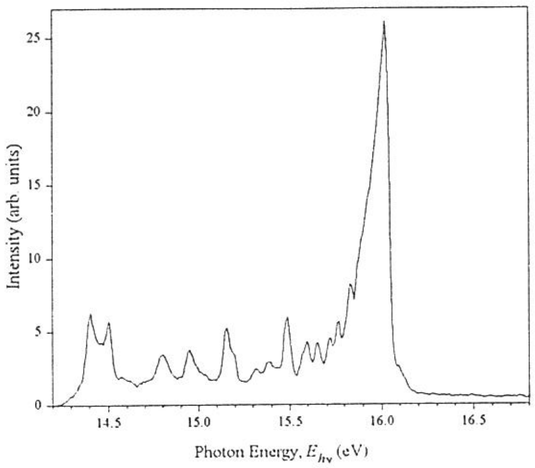

**Figure 2** The curve obtained by summing the electron counts in Fig. 1(a) over a range of $\Delta E$ = 14.1 - 14.3 eV along the $E_{h\nu}$ direction.

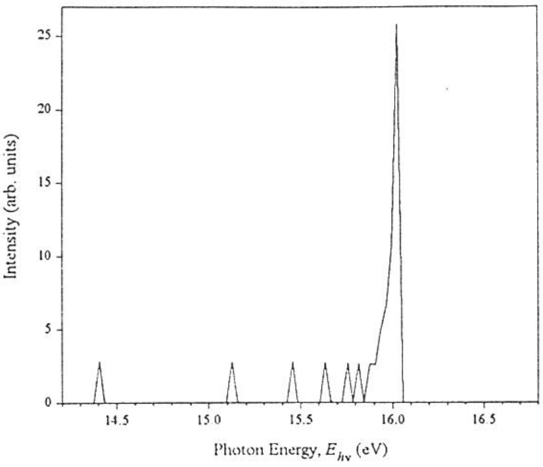

**Figure 3** The calculated curve of the relative partial cross section for the formation of S* from OCS through predissociation of high-Rydberg OCS*($R_B$) states.

(BL3B)

# Two-dimensional photoelectron spectroscopy of acetylene : Rydberg-valence interaction between the $(3\sigma_g)^{-1}(3p\sigma_u)^1$ and $(3\sigma_g)^{-1}(3\sigma_u)^1$ states.

Hideo Hattori[a], Yasumasa Hikosaka[b], Takumi Hikida[b], and Koichiro Mitsuke[a]

[a] *Department of Vacuum UV Photoscience, Institute for Molecular Science, Myodaiji, Okazaki 444*
[b] *Department of Chemistry, Tokyo Institute of Technology, Ohokayama, Meguro 152*

A two-dimensional photoelectron spectrum is measured for studying autoionization of acetylene in the Franck-Condon gap between the $X\ ^2\Pi_u$ and $A\ ^2A_g$ states of $C_2H_2^+$.[1] In Fig. 1, pronounced vertical stripes correspond to vibrational levels of the $X\ ^2\Pi_u$ state. Exclusive vibrational excitation of the symmetric C-H stretching mode $\nu_1$ of $C_2H_2^+(X\ ^2\Pi_u)$ in the photon energy range $E_{h\nu}$ = 12.5 - 13.6 eV results from autoionization of the valence state $(3\sigma_g)^{-1}(3\sigma_u)^1$. A least-squares fit of the ionization energies of the observed vibrational levels to a second order expansion provides vibrational constants for the $\nu_1$ and $\nu_2$ modes of $\omega_1 = 0.410 \pm 0.002$, $\omega_2 = 0.228 \pm 0.002$, $\chi_{11} = -0.0072 \pm 0.0004$, $\chi_{22} = -0.0009 \pm 0.0005$, and $\chi_{12} = -0.0013 \pm 0.0005$ eV. Here, $\nu_2$ denotes the C-C stretching mode.

At $E_{h\nu}$ = 14.120 eV, autoionization of the Rydberg state $(3\sigma_g)^{-1}(3p\pi_u)^1$ leads to a complicated photoelectron spectrum where the *trans*-bending mode $\nu_4$ of $C_2H_2^+(X\ ^2\Pi_u)$ as well as $\nu_1$ is excited, reflecting a substantial geometrical change during autoionization.

In the $E_{h\nu} \approx 13.8$ eV region in Fig. 1, irregularity in the vertical stripes is observed. Positions of the vibrational levels of $C_2H_2^+(X\ ^2\Pi_u)$ are in good agreement between the spectra at $E_{h\nu} \sim 13.8$ and 14.120 eV. This suggests the presence of a Rydberg state at ~ 13.8 eV on the basis of the core ion model. We assign this state to the $(3\sigma_g)^{-1}(3p\sigma_u)^1$ state which has been predicted to exist around 13.7 eV by several theoretical authors[2,3] but has not been identified previously in the photoabsorption or photoionization cross section curves.

The constant-ionic-state spectra for the $\nu_1$ = 0 - 4 levels of $C_2H_2^+(X\ ^2\Pi_u)$ are shown in Fig. 2. Some differences among the five spectra are observed at $E_{h\nu} \sim 13.8$ and 14.1 eV. In the range of $E_{h\nu}$ = 14.0 - 14.4 eV, all spectra display two groups of peaks corresponding to vibrational levels of the $(3\sigma_g)^{-1}(3p\pi_u)^1$ state. At $E_{h\nu}$ = 13.8 eV, where the $(3\sigma_g)^{-1}(3p\sigma_u)^1$ state is observed, the CIS spectra show a small maximum for $\nu_1$ = 1 - 4 and only a faint shoulder for the $\nu_1$ = 0 level. This large difference in the vibrational distribution, resulting from autoionization, between the two Rydberg states cannot be interpreted in terms of the core ion model.

It is well known that the C-H bond distances in the equilibrium geometry are larger in $C_2H_2^+(A\ ^2A_g)$ than in $C_2H_2^+(X\ ^2\Pi_u)$, and that $C_2H_2^+(X\ ^2\Pi_u)$ has the same C-H bond distances as those of $C_2H_2(X\ ^1\Sigma_g)$. On the basis of the core ion model, it is likely that $C_2H_2$ in the Rydberg state converging to $C_2H_2^+(A\ ^2A_g)$ autoionize at its larger C-H bond distances to the $\nu_1 > 0$ levels of $C_2H_2^+(X\ ^2\Pi_u)$ and autoionize to the $\nu_1$ = 0 level at the C-H bond distances corresponding to the Franck-Condon region for the primary photoexcitation.

Lack of the 13.8 eV peak structure in the $\nu_1$ = 0 spectra in Fig. 2 reflects depression of the Franck-Condon factor between the primary excited vibrational level of the $(3\sigma_g)^{-1}(3p\sigma_u)^1$ state and the $\nu_1$ = 0 level of $C_2H_2^+(X\ ^2\Pi_u)$. Such depression probably results from the distortion of the potential energy surface of the $(3\sigma_g)^{-1}(3p\sigma_u)^1$ state in the vicinity of the Franck-Condon region for photoexcitation. An avoided crossing of the potential energy surfaces between the $(3\sigma_g)^{-1}(3p\sigma_u)^1$ state and the valence state $(3\sigma_g)^{-1}(3\sigma_u)^1$ with the same symmetry is considered to be responsible for the distortion.

## References

1. H.Hattori, Y.Hikosaka, T.Hikida, and K.Mitsuke, J. Chem. Phys. (in press).
2. T.Hayaishi, S.Iwata, M.Sasanuma, E.Ishiguro, Y.Morioka, Y.Iida, and M.Nakamura, J. Phys. B **15**, 79 (1982).
3. P.W.Langhoff, B.V.McCoy, R.Unwin, and A.M.Bradshaw, Chem. Phys. Lett. **83**, 270 (1981).

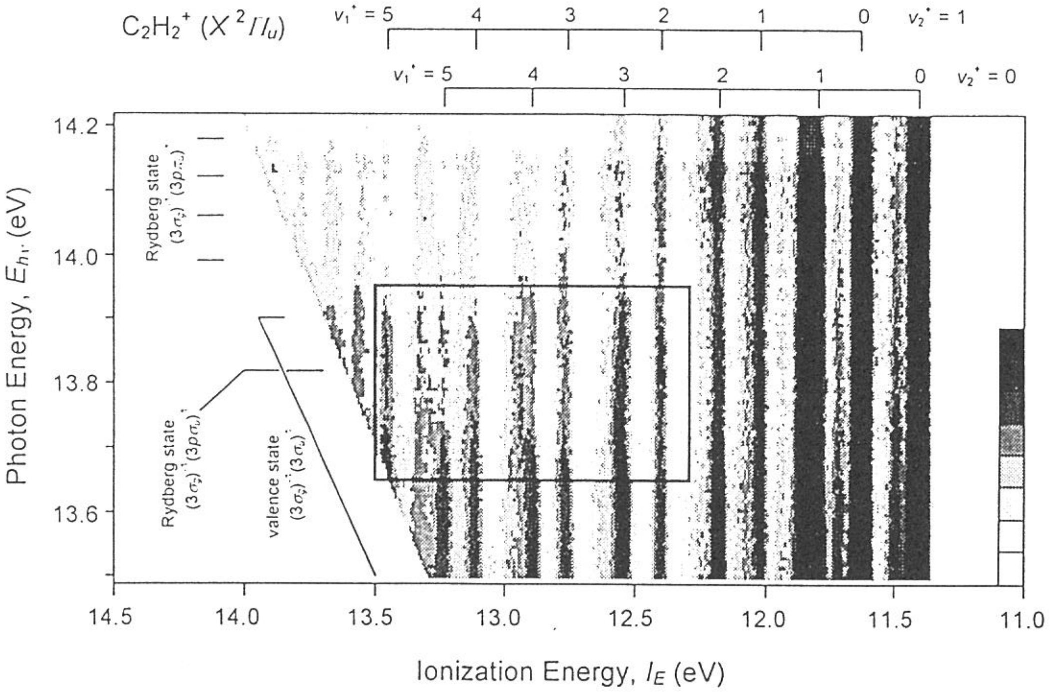

**Figure 1.** Two-dimensional photoelectron spectrum of $C_2H_2$, taken at the electron energy resolution of 50 meV. The electron yields are presented by the plots with eight tones from light to dark on a logarithmic scale. For clarity, higher electron yields are truncated. A rectangular frame indicates the region characterized by irregularity in the vertical stripes.

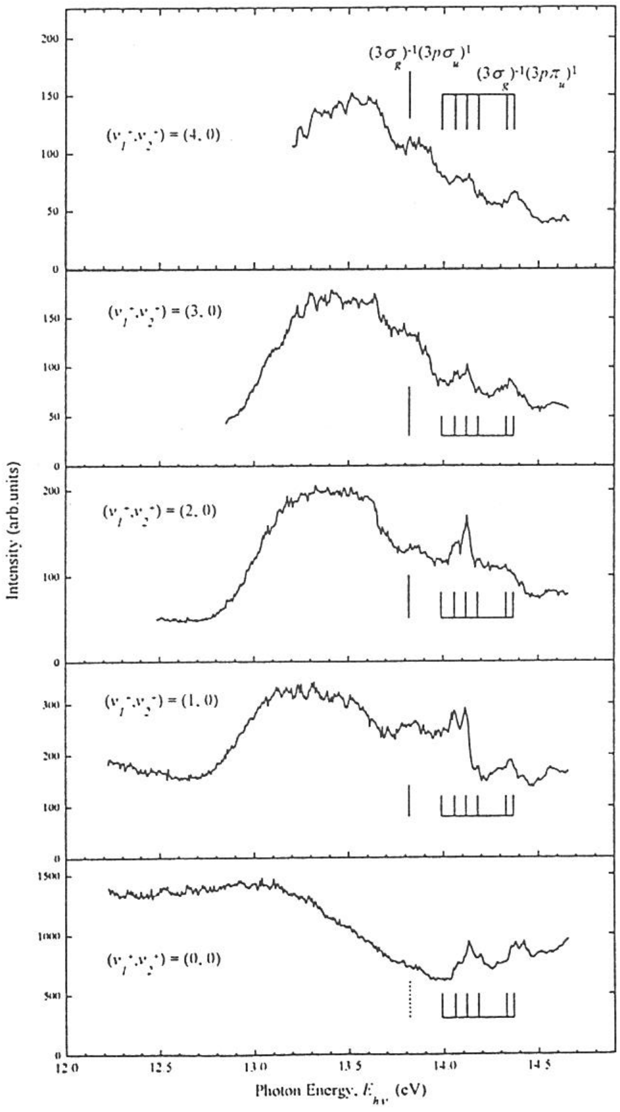

**Figure 2.** Constant-ionic-state (CIS) spectra for $v_1 = 0 - 4$ levels of $C_2H_2^+$ ($X\ ^2\Pi_u$).

(BL4A1)

# Double Multi-Layered-Mirror Monochromator Beam-line for Synchrotron Radiation Stimulated Processing Study

Harutaka Mekaru[a], Yoshiaki Imaizumi[a], Yoshiyuki Tsusaka[b], Eiken Nakamura[c],
Toyohiko Kinoshita[c] and Tsuneo Urisu[c]

[a]*The Graduate University for Advanced Studies, Institute for Molecular Science, Myodaiji, Okazaki 444*
[b]*Department of Material Science, Himeji Institute of Technology, Kamigori-cho, Akou-gun 678-12*
[c]*Institute for Molecular Science, Myodaiji, Okazaki 444*

It is not so easy to clear up the mechanism of the chemical reaction process stimulated by a synchrotron radiation due to a difficulty of preparing monochromatic light with a sufficient photon flux covering vacuum ultra violet (VUV) wavelength regions. Therefore, we developed a new type of monochromator to get high photon flux and to scan wide wavelength regions. The new monochromator is based on the double multi-layered-mirror type and set up at beam line BL-4A1 of UVSOR.

Figure 1 shows the drawings of BL-4A1, which consists of a pre-mirror chamber , a double mirror monochromator, a white beam chamber, a differential pumping chamber, a filter box, a current monitor and an X-ray photoelectron spectrometer (XPS). When the multi-layered-mirror is not used, the SR beam is reflected by a pairs of Pt coated plain mirrors with grazing incident angle of 2 degrees in the white beam chamber to keep the output beam at the same height as that of the multi-layered-mirror monochromator output. The pre-mirror is a elliptically-bent cylindrical mirror which is set at a distance of 2345.4 mm from the light source point and focuses the beam at the point of 6100mm down stream from the center of the pre-mirror.

Figure 2 shows the mirror folder and the driving mechanism of the double multi-layered-mirror monochromator. This driving mechanism changes the linear motion parallel to the SR beam of the first mirror mount stage to the translational and rotational motion of the double multi-layered-mirror keeping them parallel with each other.[1] This mechanism can sweep the incident angle of the SR beam to the multi-layered-mirror from 10 to 80 degrees continuously without changing the entrance and exit beam positions of the monochromator. Two mirrors can be set on one mirror holder, and the two pairs of the multi-layered-mirrors can be mounted and exchanged with each other by the rotation of the mirror holder by the super sonic motor driving without breaking the high vacuum ( $10^{-10}$ torr ) of the monochromator chamber.

Figure 3 shows the calculated spectrum distribution of the output beam of the monochromator when using Mo/C multi-layered-mirror together with a 1000Å thick C filter. The thickness of the Mo and C layers is 37.5Å and the layer number is 50. Serious problem of the multi-layered-mirror monochromator in the soft X-ray region is to reduce the high back ground level which appears at the lower energy side of monochromatized peak. The C filter is effective to reduce the back ground.

## Reference

1) J.A.Golovchenko, R.A.Levesgue and P.L.Cowan : Rev.Sci.Instrum.52 (1981) 509-516.

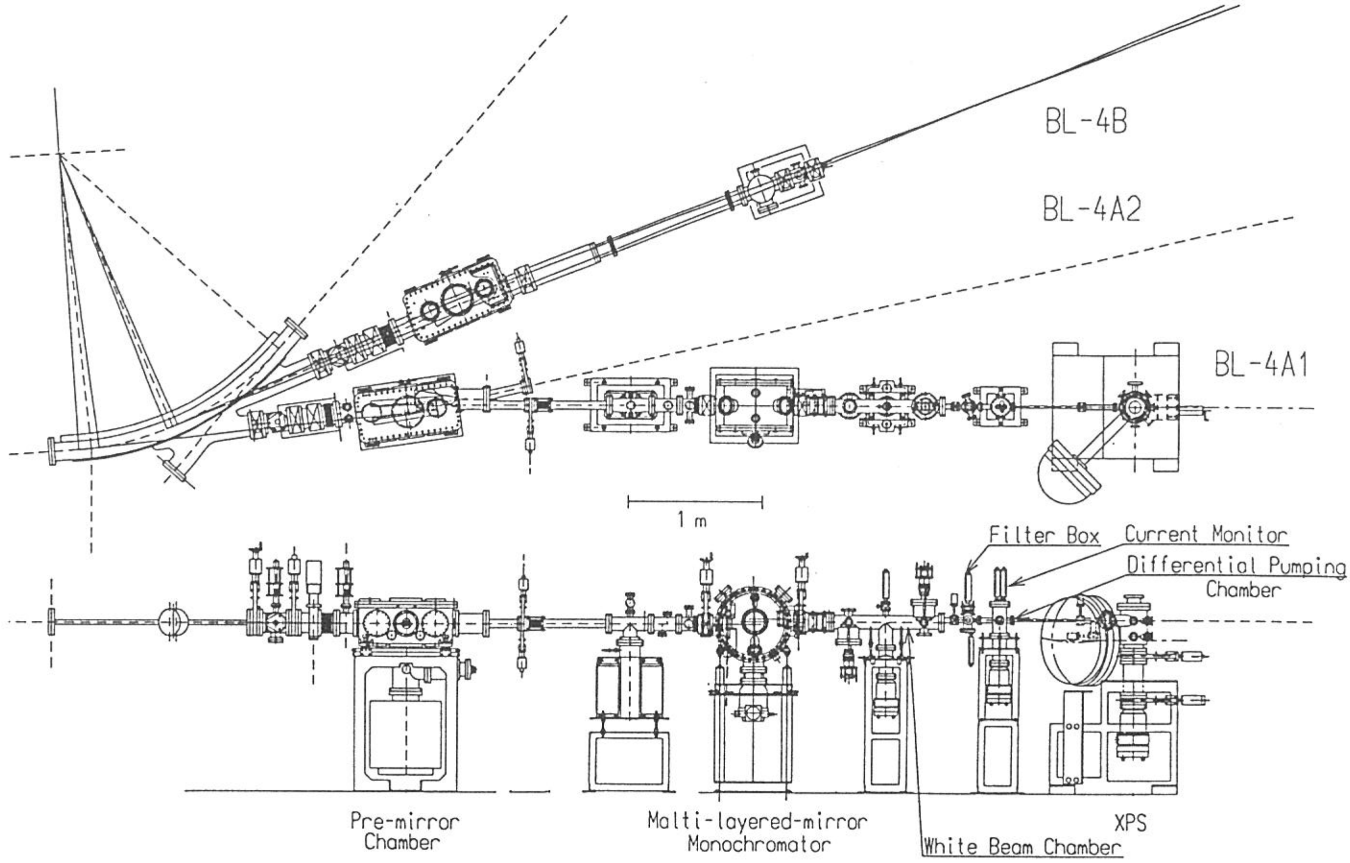

Figure 1. Drawings of BL-4A1 in UVSOR.

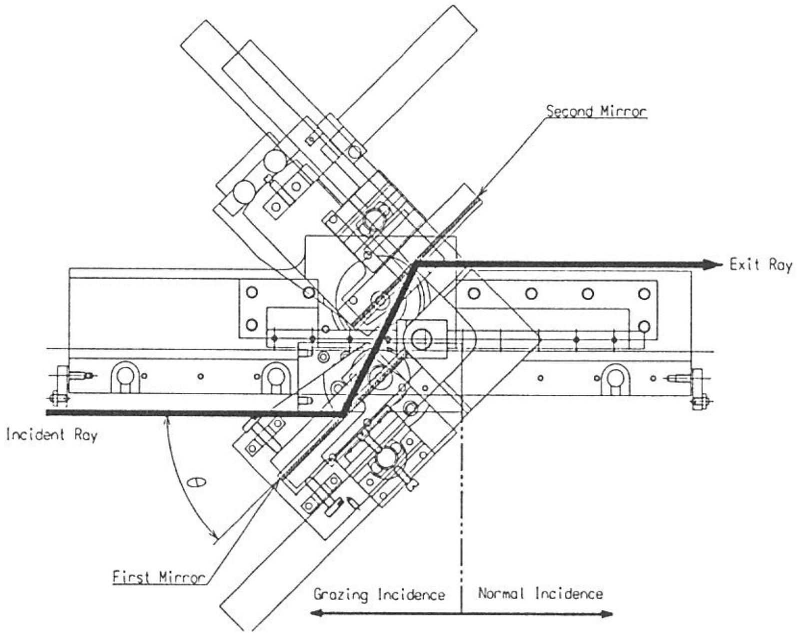

Figure 2.Mirror holders and driving mechanisms of the double multi-layered-mirror monochromator.

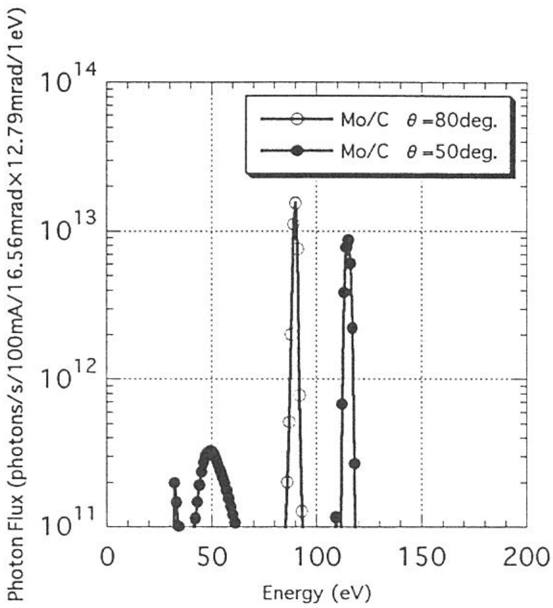

Figure 3.The calculated spectrum distribution of the monochromatized beams. C filter (1000 Å thick) is used.

(BL4A)

# Carbon Contamination in Synchrotron-Radiation-Stimulated Al Deposition Using a Low Temperature Condensed Layer of Dimethyl Aluminum Hydride

Yoshiaki Imaizumi [a], Yoshiyuki Tsusaka [b], Tsuneo Urisu [b]

[a] *The Graduate University for Advanced Studies and* [b] *Institute for Molecular Science,*
*Myodaiji, Okazaki, 444 Japan*

The carbon contamination in photochemically deposited Al films fabricated using non-monochromatized synchrotron radiation (SR) and Mg $K_\alpha$ line (1253.6 eV) irradiation were compared by X-ray photoelectron spectroscopy (XPS) analysis. The excitation energy dependence of the carbon contamination, especially the effects of core electron excitations, in the photo-CVD of Al using a low-temperature condensed layer of dimethyl aluminum hydride was determined using XPS spectra and gas-phase photo absorption cross section spectra. A significant decrease of the carbon contaminations was observed in the films fabricated using SR irradiation, which can excite Al 2s and Al 2p core electrons as well as the valence electrons, while no change was observed in the films fabricated using Mg $K_\alpha$ line irradiation. This is explained by the fact that core electron excitation breaks the Al-C bonds *site-specifically*. The aborption spectra of DMAH were measured in the range of 5 eV to 30 eV, and calculated for 80 to 1500 eV as shown in Fig. 1.

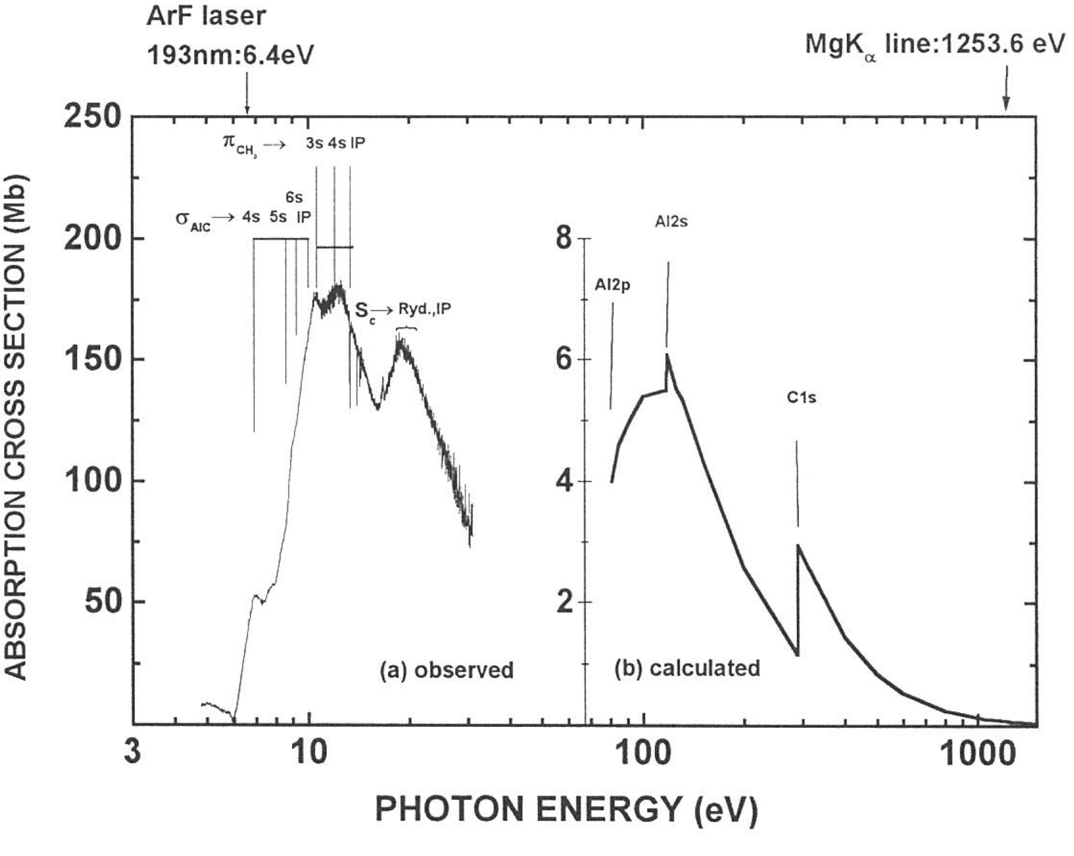

Fig. 1 The observed (5 - 30 eV) and calculated (80 - 1500 eV) photo absorption cross section spectra of gas phase DMAH. The calculation was carried out using data in ref. 1.

References

1. J.J. Yeh and I. Lindau : *Atomic Data and Nuclear Data Tables* 5 (1973) 51.

(BL4B)

# Mechanism of synchrotron radiation-assisted Si epitaxial growth using $Si_2H_6$

A. Yoshigoe, S. Hirano* , T. Urisu**

Toyohashi University of Technology, Tempaku-cho, Toyohashi 441
*The Graduate University for Advanced Studies, 38 Myodaiji, Okazaki 444
**Institute for Molecular Science, Myodaiji, Okazaki 444

Mechanism of synchrotron radiation-assisted Si epitaxial growth using $Si_2H_6$ (SR-SEG) at 140℃ was investigated by an infrared reflection absorption spectroscopy using the $CoSi_2$ buried metal layer substrate (BML-IRAS). In our previous works[1,2], the behavior of $SiH_n$ on a Si(001) surface during SR-SEG as a function of substrate temperature have been investigated by BML-IRAS. In the case of high substrate temperature around 400℃, it has been clear that SiH is dominant species on the Si(001) surface during film deposition. On the other hand, with decreasing substrate temperature (275℃→140℃→50℃), $SiH_2$ and $SiH_3$ species increase during SR-SEG. It has been also noticed that $SiH_3$ and $SiH_2$ are easily decomposed to SiH by SR irradiation and SiH isn't decomposed by SR irradiation. In spite of this result, the bulk network SiH has not been observed after SR-SEG. This result indicates that the deposition mechanism based on the SR-stimulated desorption of the surface hydrogen and the following chemisorption of $Si_2H_6$ molecules are incorrect, and there exists another types of hydrogen removal process essentially important in the process of the epitaxial growth.

Figure 1 shows that the change of IRAS spectra after SR-SEG on the Si(001) surface terminated with deuterium. The assigned peaks are indicated by arrows. In this figure, up and down peaks indicate the increase and the decrease of the species, respectively. The $SiD_n$ disappear and $SiH_n$ increase on the surface after SR-SEG. The replacement reaction between H and D was not observed when only exposing the Si(001) surface terminated with deuterium to the $Si_2H_6$ gas without SR irradiation. After 3000mA・min film deposition, deuterium was completely replaced by hydrogen. This results indicate that the SR irradiation to the gas phase, that is, the generation of active species such as H and $SiH_n$ including their ions in the gas phase by SR irradiation, is essentially important for the progress of the film deposition. It is concluded that the epitaxial growth proceeds through the desorption of the surface hydrogen by the reaction with gas phase reactive species.

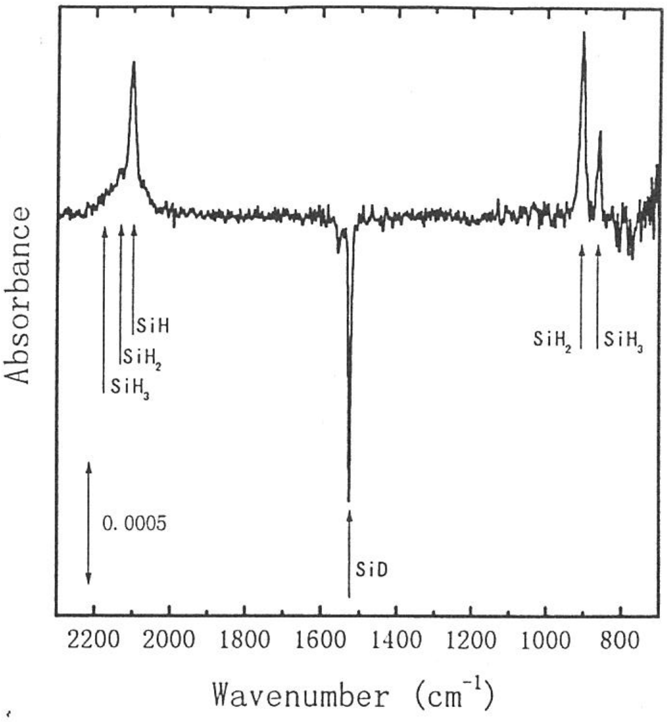

Fig. 1. IRAS spectra during the SR-SEG on the Si(001) surface terminated with deuterium atoms. The substrate temperature is 140℃. The $Si_2H_6$ gas was $1.0\times10^{-3}$ Torr. The up and down side peaks indicate the increase and the decrease of the surface species, respectively.

References
1) A. Yoshigoe, K. Mase, Y. Tsusaka, Y. Kobayashi, T. Ogino, and T. Urisu, Appl. Phys. Lett. 67, 2364 (1995).
2) A. Yoshigoe, M. Nagasono, K. Mase, and T. Urisu, Jpn. J. Appl. Phys. 34, 6894 (1995).

(BL4B)

# Synchrotron Radiation-excited Etching of Si(100)/XeF$_2$ Studied by Measuring the Velocity Distributions of the Desorbed Neutral Species

Haruhiko Ohashi[a] and Kosuke Shobatake[b]

[a] *Institute for Molecular Science, Myodaiji, Okazaki 444, Japan*

[b] *Department of Molecular Design and Engineering, Graduate School of Engineering, Nagoya University, Furo-cho, Chikusa-ku, Nagoya 464-01, Japan*

We have been studying etching reactions of semiconductor material and diamond surfaces induced by synchrotron radiation (SR) in the environment of an etchant such as $SF_6$, $XeF_2$, and $O_2$.[1] However in most of the cases one carries out experiments without knowing what kind of product species are desorbed from the surface, except few cases in which desorbed ions are detected.

In this report are presented some results obtained for SR-excited etching of Si(100) with $XeF_2$ by measuring the velocity distributions of the neutral species desorbed from the surface under the conditions that etching reaction is proceeding. This reaction system of Si + $XeF_2$ has been extensively studied at IBM Almaden Research Center.[2] Houle has measured the velocity distributions of the desorbed species and has found that the system is extremely complicated. However we have chosen this particular system since even at low $XeF_2$ pressures ($< 1 \times 10^{-4}$ Torr) many enough F atoms are supplied to the Si surface to observe etching reaction products.

The details of the apparatus has been described previously. Briefly the velocity distributions of the desorbed species from the surface are measured using a quadrupole mass spectrometer equipped with an electron bombardment ionizer and a time-of-flight (TOF) technique. A pseudorandom correlation chopper with N = 255 elements was employed to modulate the incoming beam into the detector. The neutral flight length from the chopper to the ionizer was 31 cm. Synchrotron radiation was shone on the surface at an incident angle of 45 degrees and the products desorbing normal to the surface was detected. In this report only the results obtained using the focused synchrotron radiation from the bending magnet field of the UVSOR facility are presented.

The desorbed species from the dark reaction which were detected at ion masses, m/e = 85 ($SiF_3^+$) and = 47 ($SiF^+$) are considered to be $SiF_4$ and $Si_2F_6$, respectively, and exhibit velocity distributions which are well fitted to a Maxwell-Boltzmann (MB) form with a translational temperature approximately identical to the surface temperature. Figure 1 shows the time variation of the TOF spectra after the radiation of synchrotron light and dosing of $XeF_2$ to the Si(100) surface are started at the same time. It is immediately clear that the for 30 minute or so, one observes only the slow velocity component which is well represented by the MB form. However, a fast component starts to grow after about 30 minutes of illumination. After about two hours of illumination the relative intensity of the fast component to the light intensity levels off. It is noted that the fast component has a sharper velocity distribution than a MB distribution and thus the fast product molecules are formed via direct process. Although not shown in this report the fast component disappears when the synchrotron light is turned off and the fast component reappears when the light is turned on. However it is noted that the surface temperature varies when the SR is shown on the surface. From other experiment it is shown that the temperature can go up to 365 K after the SR is illuminated on the surface. Therefore in order to make sure that the temperature is kept almost the identical, the surface was heated with a heater immediately after the SR is turned off. Then the fast component stays on for as long as some forty minutes. This result means that the fast products are formed via thermal reaction, even when the SR is turned off but the temperature should stay at the same level as that when the SR is illuminated. The fast component dies away as the thermal reaction proceeds. The "memory" of the photoexcitation, which is represented by the appearance of the fast component, remains for up to 40 minutes. This means that conversion of the thick fluorosilyl layer is induced by SR.

**[References]**

1. H. Ohashi, A. Yoshida, and K. Shobatake, Appl. Surf. Sci., **69**, 20 (1993).
2. H. F. Winters and J. W. Coburn, Surf. Sci. Report. 14, 161(1992).
3. H. Ohashi and K. Shobatake, J. Electron Spec. and Related Phenomena 80, 73 (1996).

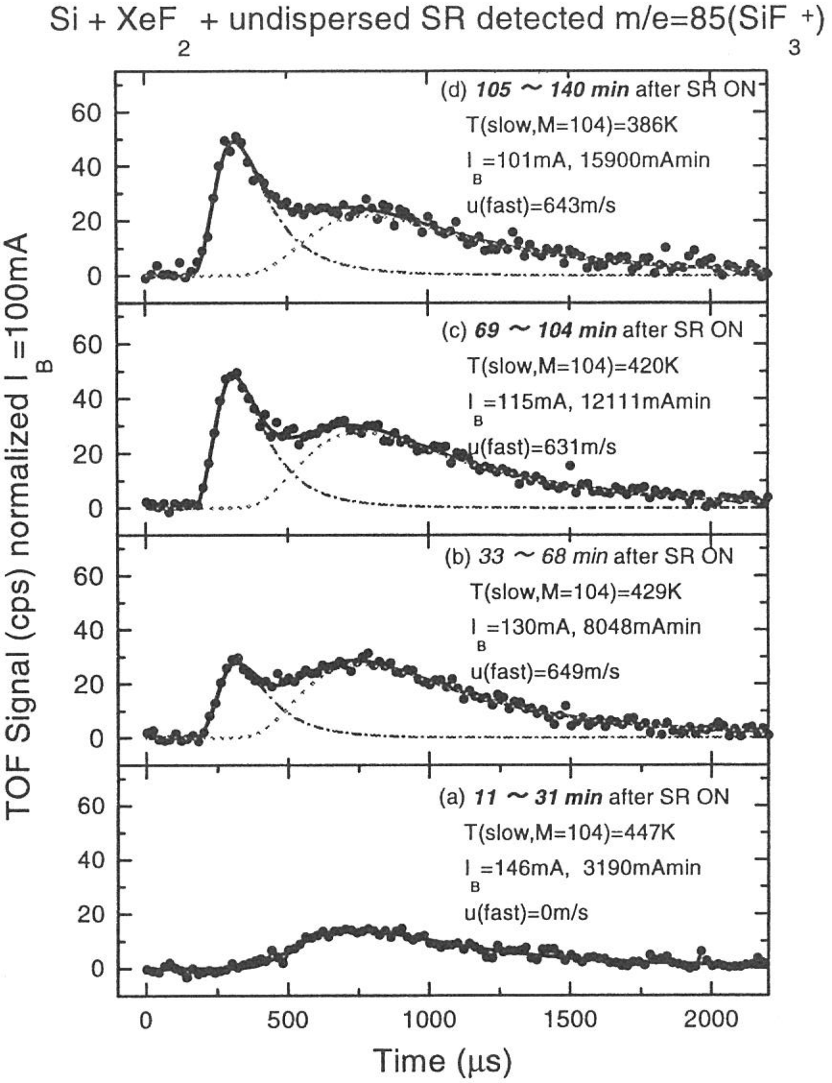

**Figure 1.** Variation of time-of-flight spectra of the desorbed product detected at mass 85 ($SiF_3^+$) with time after the dosing of $XeF_2$ and illumination of SR from the bending magnet were started simultaneously. The spectra (a)~(d) were observed during the period 11~31 min, 33~68 min, 69~104 min, 105~140 min, respectively. Dotted, dot-dashed, and solid curves are the MB and shifted MB components and the sum of the two after deconvolution analysis. The numbers shown in each figure are $T$(slow, $M$=104) (translational temperature of the low component assuming that neutral species is $SiF_4$), $I_B$ (average beam current during the measurement), the accumulated beam current at the end of the measurement, and $u$(fast) (the drift velocity for the fast component). The intensity is normalized to the beam current at 100 mA.

(BL4B)

# Infrared Reflection Absorption Spectrum of Silicon Deuterides on Si(100)Surfaces

## — Thermal and Synchrotron Radiation Irradiation Effects —

Shinya Hirano [a], Akitaka Yoshigoe [b], Shed.Irfan.Gheyas [c], Kazuhiko Mase [c] and Tsuneo Urisu [c]
[a] The Graduate University for Advanced Studies, Myodaiji, Okazaki 444
[b] Department of Electronics Engineering, Toyohashi University of Technology, Toyohashi 441
[c] Institute for Molecular Science, Myodaiji, Okazaki 444

The behavior of hydrogen on Si (100) surfaces is one of the most fundamentally important subject of semiconductor process technologies. In this work, in order to understand the behavior of deuterium on Si (100) surfaces during annealing and irradiation of the synchrotron-radiation (SR), the relation between the surface adsorbed hydrides and the surface reconstruction structure and their chemical reactivity have been investigated by using the infrared reflection absorption spectroscopy using the buried metal layer substrate (BML-IRAS)$^{1)}$ and reflection high energy electron diffraction (RHEED). Here we used deuterium gasses ($D_2$) instead of hydrogen gasses ($H_2$) to easily identify the effects of residual $H_2$ in the reaction chamber. A hot tungsten spiral filament was used to dissociate $D_2$ molecules.

Figure 1 shows the change of the BML-IRAS spectrum of surface SiDn as a function of deuterium exposure in the stretching vibration region, at the substrate temperature of 140°C. In this figure, the dose ($1L=10^{-6}$ Torr × sec) is defined as a $D_2$ pressure times exposure time.

The deuterium saturation coverage is obtained at about 6000L and RHEED pattern shows that the surface is (1 × 1) reconstruction structure at the saturation coverage, and IRAS peaks are observed at 1525cm$^{-1}$, 1544cm$^{-1}$, and 1554cm$^{-1}$.

Figure.2 shows the effect of SR irradiation on the deuterium adsorbed Si (100) surfaces at the saturation coverage. Spectrum B is after SR irradiation of 20000mA・min on spectrum A, which was obtained after $D_2$ 10000L exposure. The difference spectrum between A and B indicates that peaks of 1544cm$^{-1}$ and 1554cm$^{-1}$ decrease and 1525cm$^{-1}$ increases by SR irradiation.

It is known that $SiH_2$ and $SiH_3$ are decomposed to SiH by SR irradiation, and SiH is hardly decomposed $^{1)}$. So, the 1525cm$^{-1}$ peak in Fig.2 is assigned to SiDn symmetric stretching mode. This agrees with the reported value 1527.8cm$^{-1}$ .The $SiD_2$ symmetric and asymmetric stretching vibrations are reported to be observed 1517.5cm$^{-1}$ and 1539cm$^{-1}$ ,respectively$^{2)}$.

In the present case, $SiD_2$ asymmetric stretching vibrations is a forbidden mode from the surface selection rule. So only the $SiD_2$ symmetric stretching should be observed in the present case. The absorption peak at around 1517cm$^{-1}$ is observed weakly as the lower frequency side tail of the 1525cm$^{-1}$ peak in Fig.1. Therefore, the peaks at 1544cm$^{-1}$ and 1554cm$^{-1}$ are possibly assigned to the $SiD_3$ symmetric and asymmetric stretching vibration modes, respectively.

To make this assignment more clear, the change of the IRAS spectrum from the saturation coverage with increasing substrate temperature was measured. It was observed that 1544cm$^{-1}$ and 1554cm$^{-1}$ peaks start to decrease at around 300°C and 1525cm$^{-1}$ peak at around 450°C respectively. These temperature values well agree with the onset temperature of the $SiD_3^+$ peak and $D_2^+\beta_1$ peak in the temperature programmed desorption spectrum with deuterium adsorbed Si (100) surface$^{3)}$.

## REFERENCES

(1)A.Yoshigoe, M. Nagasono, K. Mase, and T. Urisu, Jpn. J. Appl. Phys. **34**, 6894 (1995).
(2)Y. J. Chabal and K. Raghavachari, Phys. Rev. Lett. **53**, 282 (1984)
(3)S. M. Gates, P. R. Kunz, and C. M. Greenlief, Surf. Sci. **207**, 364 (1989)

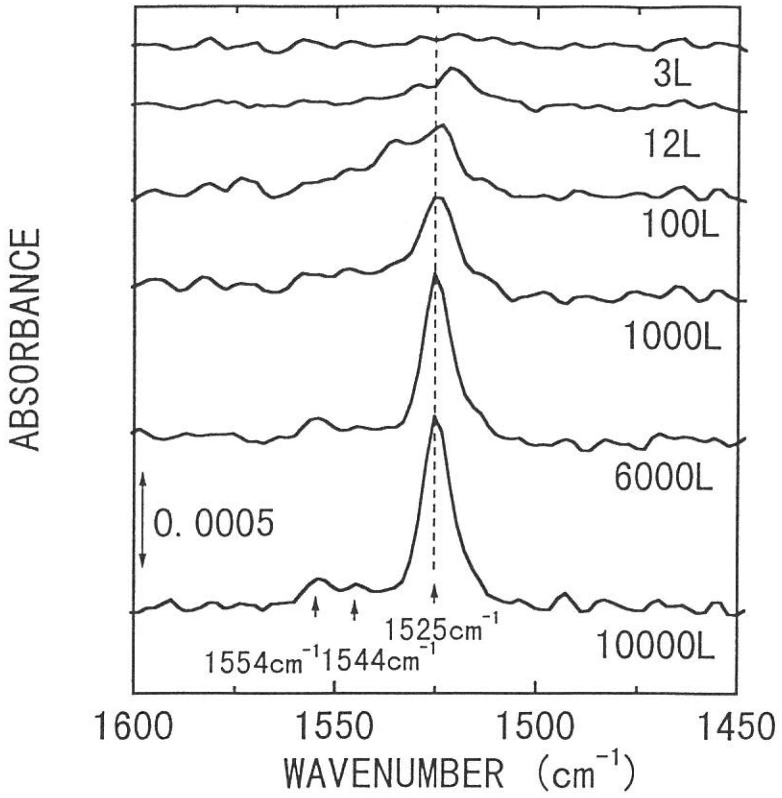

Fig.1 BML-IRAS spectrum of the deuterium adsorbed Si(100) surfaces as a function of deuterium exposure in the stretching vibration regions at the substrate temperature of 140℃.

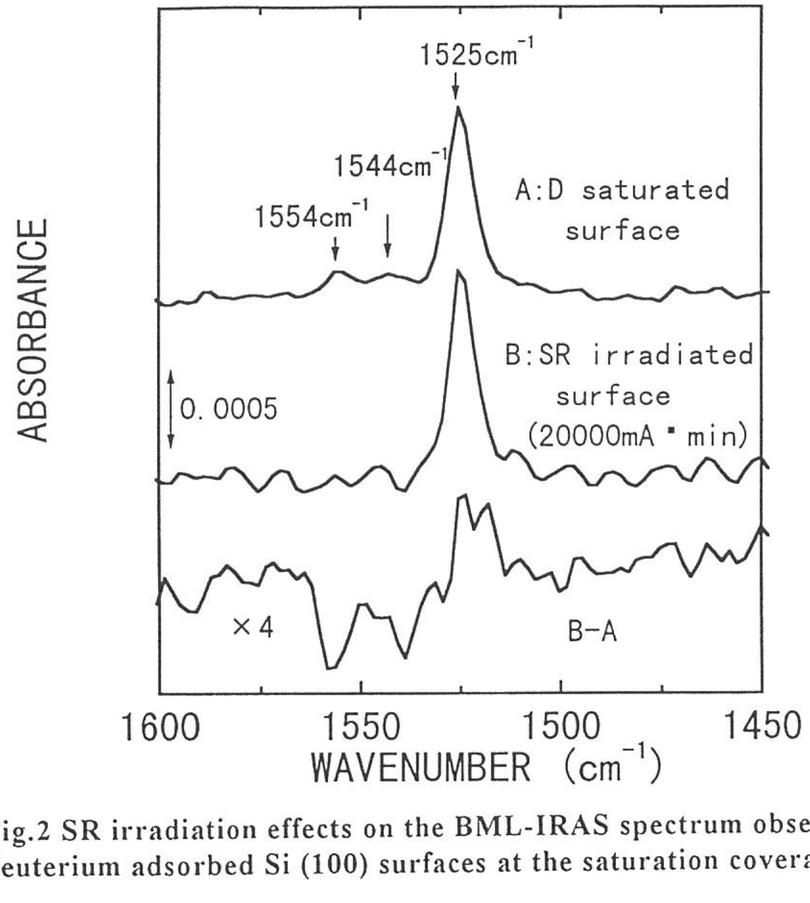

Fig.2 SR irradiation effects on the BML-IRAS spectrum observed for deuterium adsorbed Si (100) surfaces at the saturation coverage.

(BL4B)

# Atomic deuterium adsorption on ultrathin Ge film deposited over Si(100)−2×1

Syed Irfan Gheyas[a], Tsuneo Urisu[b], Shinya Hirano[c], Mitsuhiro Nishio[d] and Hiroshi Ogawa[e]

[a−c]Chemical Dynamics Laboratory, Institute for Molecular Science, Okazaki National Research Institute, Nishigonaka − 38, Myodaiji Machi, Okazaki − 444, Japan

[d,e]Department of Electronic Engineering, Saga University, Honjo−1, Saga−840, Japan

Deuterium and hydrogen adsorption, especially hydrogen adsorption, on Si(100) and also on Ge(100) have been studied quite extensively in the recent past. These studies reveal some fundamental differences between the way hydrogen reacts with these two surfaces. Different hydride phases have been found to form on Si(100) by hydrogen adsorption at different temperatures, i.e., chemisorption at 630 K yields only monohydride phase (2×1 phase), at 400±10 K, formation of both the monohydride and dihydride phases (3×1 phase) occur and at <400 K, the surface is a mixture of monohydride, dihydride and trihydride species (1×1 phase).[1] Since (1×1) phase involves trihydrides ie. $SiH_3(a)$, which requires Si−Si bond breaking, substantial surface reconstruction and disordering become inevitable. Heating this phase results in $SiH_4$ desorption along with $H_2$, whereas almost only $H_2$ desorbs from both the (2×1) and (3×1) phases when heated. Hydrogen chemisorption on the Ge(100) surface, on the other hand, has widely been reported to yield only monohydrides (2x1 phase).[2,3] Also only hydrogen has been found to desorb from the hydrogen−covered−Ge surface during temperature programmed desorption measurements. It, however, would be interesting to study the effect of hydrogen or deuterium on ultrathin Ge deposited over Si(100), a system of intense current research, where strains resulting from lattice mismatch between Si and Ge can open up new possibilities.

In this work, Infrared Reflection Absorption Spectroscopy (IRAS) and Reflection High Energy Electron Diffraction (RHEED) measurements are used to show clearly that atomic deuterium has an etching effect on thin Ge (100) deposited over Si(100) 2×1. The etching reaction seems to proceed even under a 2×1 : D phase and low temperature. Also the etching rate has been found to be at least an order faster compared to the etching rate observed in the case of Si.

All the experiments were carried out in a ultrahigh vacuum reaction chamber (base pressure about $2.0\times10^{-10}$ Torr) equipped with facilities for RHEED and IRAS measurements. Buried metal layer Si(100) substrates which were used in all experiments were cleaned by conventional wet method followed by annealing in the UHV chamber. Si layer, about 10 nm thick, is then deposited on the BML substrate followed by the growth of an ultrathin layer of Ge, roughly 1.5 monolayer thick, This resulted in a sharp 2×1 pattern. An incandescent W spiral filament was used to produce atomic deuterium during $D_2$ exposure. The exposures quoted here will refer to molecular deuterium uptake.

Fig. 1 shows the effect of atomic deuterium adsorption on ultrathin Ge at a low temperature of about 85 °C. At a low exposure of about 300 L, Ge − D stretching vibration mode at about 1440 $cm^{-1}$ can be observed clearly. Notably no Si related peak was detected. A deuterium exposure of 1200 L, on the other hand, visibly weakens the Ge–D peak intensity. This points at a certain etching of the Ge surface by atomic deuterium. Ge–D peak, on the other hand, disappears completely and strong silicon related peaks become visible under an exposure of about 2.4×$10^6$ L which should establish that atomic deuterium has an etching effect on ultrathin Ge deposited over Si (100).

Fig. 2 shows the effect of temperature on the deuterium covered Ge / Si (100). A deuterium dose of about 80 L at 127 °C (fig. 2a), an exposure low enough to keep the RHEED 2×1 pattern fully intact, results in a strong absorption line at about 1440 $cm^{-1}$ due to the Ge–D stretching mode. No traces of the substrate could be visible in this spectra. Now heating the surface up to about 280 °C results in the complete disappearance of the Ge–D absorption line (fig. 2e). Interestingly the absorption lines due to silicon monodeuteride and dideuteride, at about 1521 $cm^{-1}$ and 1558 $cm^{-1}$ respectively, pop out clearly in the process which should indicate that deuterium forces a part of the Ge to desorb from the surface when heated. It should also indicate that a part of the surface deuterium moves to the bare Si atoms to form bonds with it. Further evidence of the etching of the Ge layers can be found in the fact that exposing the deuterium desorbed surface once more to 80 L at 127 °C results in a intensity decrease of the Ge–D absorption feature by about 25% (fig. 2f) as compared to its intensity in the case of similar exposure just after Ge deposition. This result is interesting because 2×1 : D adsorbed phase on bulk Ge or Si is supposed not to result in etching of these materials even when heated. Now deuterium not only etches away Ge but also does it with remarkable efficiency. The etching rate about an order higher than that was generally observed in the case of Si.

## References

[1] C. C. Cheng and J. T. Yates, Jr., Phys. Rev. Lett. 43, 4041 (1991).

[2] Y. J. Chabal, Surf. Sci. 168, 594 (1986).

[3] Y. M. Wu, J. Baker, P. Hamilton and R. M. Nix, Surf. Sci. 295, 133 (1993).

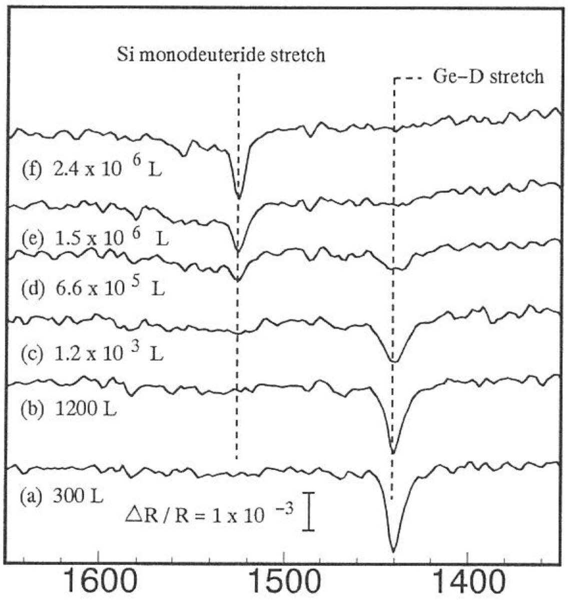

Fig. 1. IR spectra taken at 85 ℃ after a series of deuterium exposure of ultrathin Ge deposited over Si(100).

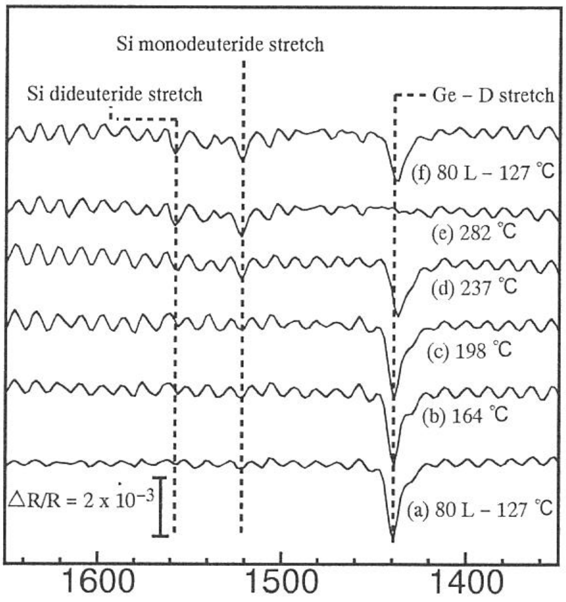

Fig. 2. IR spectra taken after (a) exposing Ge / Si (100) to D and then [ (b) – (e) ] heating it to successive higher temperatures and then (f) exposing the surface to D once again.

(BL5A)

# Performance Test of SGM-TRAIN at BL5A

M. Kamada, M. Hasumoto, S. Kimura, N. Mizutani, T. Horigome, S. Hirose, K. Sakai,
and K. Fukui[a]
UVSOR, Institute for Molecular Science, Myodaiji, Okazaki 444
[a]College of Engineering, Fukui Univ., Fukui 910

A new monochromator called SGM-TRAIN ( Spherical Grating Monochromator with Tranlational and Rotational Assemblies Including Normal-incident-mount (1) ) designed for the use of circularly polarized lights from a new helical undulator (2) has been constructed at BL 5A. In the followings, a part of the performance testing results of the SGM-TRAIN is given, although the SGM-TRAIN was tentatively aligned along a beam line with 152° in horizontal direction.

The SGM-TRAIN is an improved version of the constant deviation and constant length monochromator (CDCL-SGM) designed by Ishiguro et al. (3) and a 15-m glancing-incidence monochromator at BL8B1 (4). The main improved points are the followings; (1) the SGM-TRAIN has a large constant length of 3500mm between entrance and exit slits to achieve a high resolving power, (2) the length between entrance and exit slits can be changed within 40 mm to get best focus, (3) a new driving system enables us to translate a grating-and-mirror chamber and rotate gratings independently in order to get better resolving power and easier driving mechanism, (4) three gratings can be used to cover photon energy range from 5 to 250 eV.

Figure 1 shows the photocurrent from a Si diode with slits of 0.1 mm. The output of the SGM-TRAIN obtained with a comnination of a Grating #2 and a plane mirror #2 is about 6x1011 phs/s, which is comparable to the expected one ( 7x1011 phs/s). Any dip due to Si-L edges is not appreciable around 240 A, indicating that the second order lights are well suppressed.

Figure 2 shows the ion-current from an Kr-ionization chamber, which was obtained with slits of 0.01mm and the pressure of 50 mTorr. This spectrum is almost the same as those obtained by SX-700 in BESSY. It should be noted that the Kr M4,5 spectrum shows a lot of Rydberg lines up to n=10 and the spectral widths of each lines are determined by natural widths, but not by the resolving power of the monochromator.

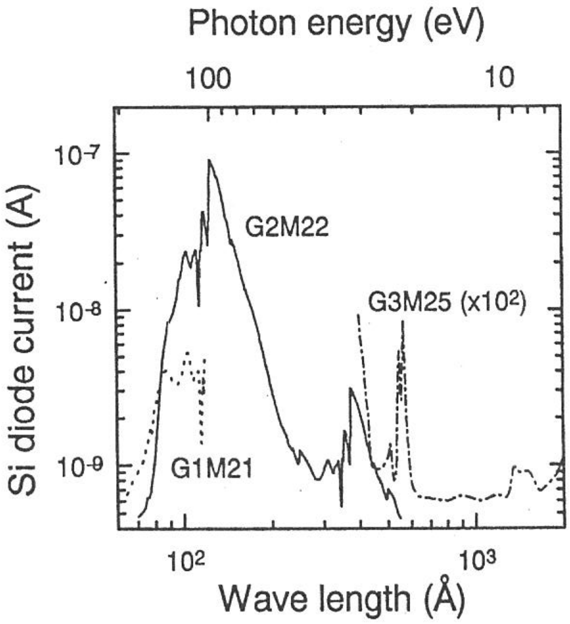

Fig. 1 Output spectra obtained with a Si-diode from SGM-TRAIN with slits of 0.1 mm

Figure 3 shows the He-photoionization spectrum with slits of 0.01mm and the pressure of 50 mTorr. We can find many Rydberg lines up to n=11. From this result, we can estimate a resolving power of about 4,000 at 200 A. This is close to the expected value of 5,000.

In conclusion, the SGM-TRAIN showed good performance enough to compare with calculated values in photon flux and a resolving power. The SGM-TRAIN is going to move to a new line, where circularly polarized lights from a new helical undulator are available. The further test of the performance will be conducted at this line soon.

References
(1) M. Kamada, K. Sakai, S. Tanaka, S. Ohara, S. Kimura, A. Hiraya, M. Hasumoto, K. Nakagawa, K. Ichikawa, K. Soda, K. Fukui, Y. Fujii, and E. Ishiguro, Rev. Sci. Instrum. 66, 1537 (1995).

(2) S. Kimura, M. Kamada, H. Hama, X. M. Marechal. T. Tanaka, and H. Kitamura, J. Elec. Spec. & Relat. Phenom, 80, 437 (1996).

(3) E. Ishiguro, M. Suzui, J. Yamazaki, E. Nakamura, K. Sakai, O. Matsudo, N. Mizutani, F. Fukui, and M. Watanabe, Rev. Sci. Instrum. 60, 2105 (1989).

(4) A. Hiraya, E. Nakamura, M. Hasumoto, T. Kinoshita, E. Ishiguro, and M. Watanabe, Rev. Sci. Instrum. 66, 2104 (1995).

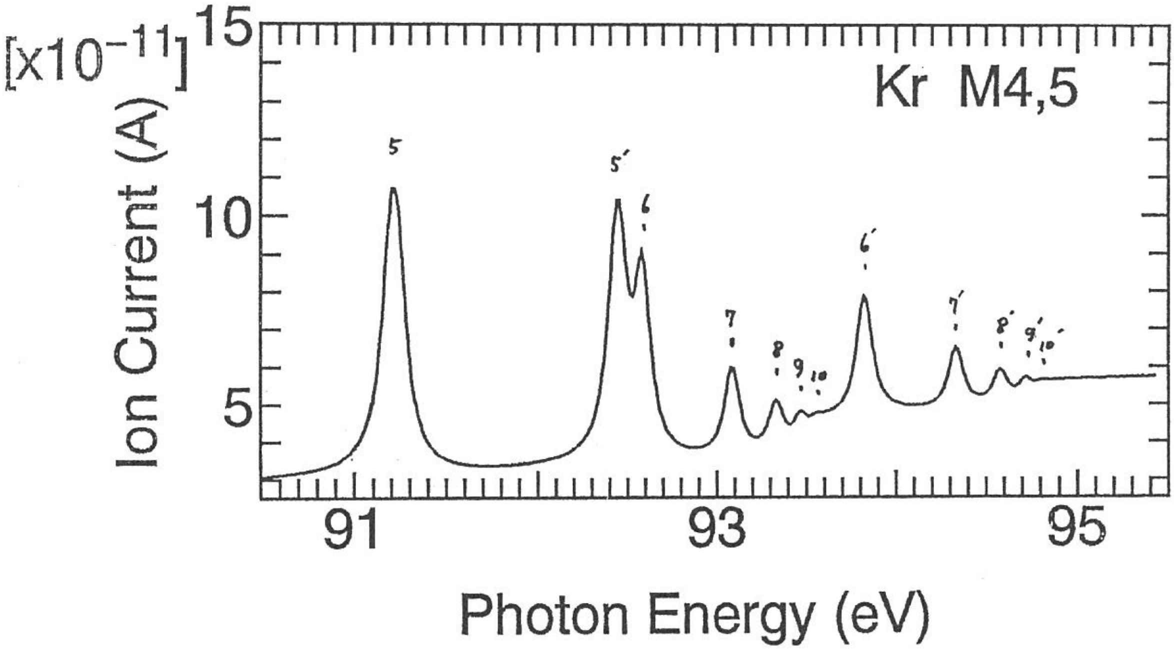

Fig. 2. Kr ionization spectrum obtained with slits of 0.01mm

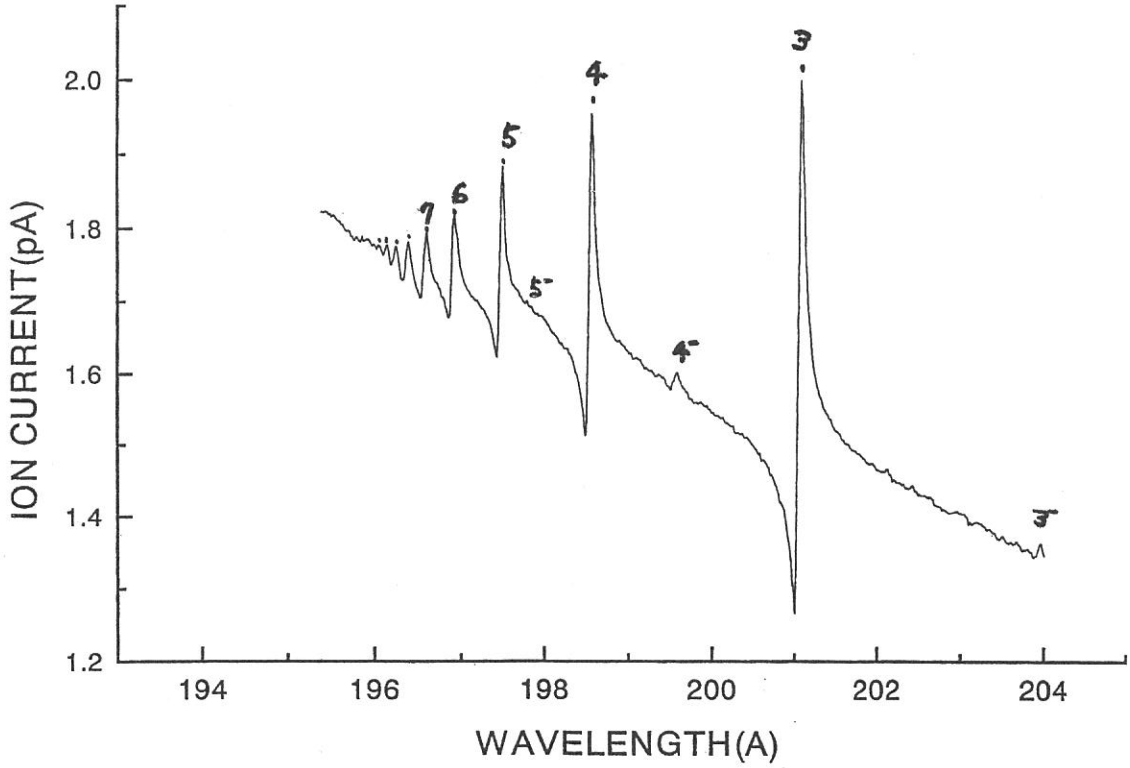

Fig. 3. He ionization spectrum obtained with slits of 0.01mm

**(BL5A)**

# Construction of a Spin- and Angle-Resolved Photoelectron Spectrometer

Naoshi TAKAHASHI[1,2], Masatake ICHIKAWA[3], Koichi NAKANISHI[4], Yasuo FUJII[4],
Shigeo OHARA[5], Shin-ichiro TANAKA[1] and Masao KAMADA[1]

[1]*Institute for Molecular Science, Myodaiji, Okazaki 444*
[2]*The Graduate University for Advanced Studies*
[3]*College of Engineering, Fukui University, Fukui 910*
[4]*Osaka City University, Osaka 558*
[5]*Nagoya Institute of Technology, Nagoya 466*

Photoelectron spectroscopy is one of the established techniques in the study of electronic structures of solids and surfaces. Energy distribution curves (EDCs) of photoelectrons indicate the binding energy of the electronic states, and angle-resolved photoelectron spectroscopy enables the electronic band structure to be mapped on the momentum and the energy axes. Moreover, spin-resolved photoelectron spectroscopy has been required in recent years for investigation of not only magnetic but also non-magnetic materials, since the electronic structures can be completely determined by energy, momentum and spin. However, the Mott detector, which has been widely used to measure the spin polarization of electrons inconvenient for angle-resolved photoelectron spectroscopy because it is large (typically several cubic meters) owing to the high-energy accelerating optics and the safety region which isolates the device. This is a serious problem in a limited experimental area, and several kinds of smaller spin detector have been proposed and constructed, e.g. SPLEED[1)] and low-energy diffuse scattering[2)] detector. We prefer the low-energy diffuse scattering detector, because the SPLEED demands frequent cleaning of the target crystal under ultra-high vacuum. We constructed it in order to install to BL5A, because this type of detector is very small (about $10^{-3}$ $m^3$), and does not need higher voltage than several hundred volts. In this paper, we will describe about the construction of new electron spectrometer and its performance.[3)]

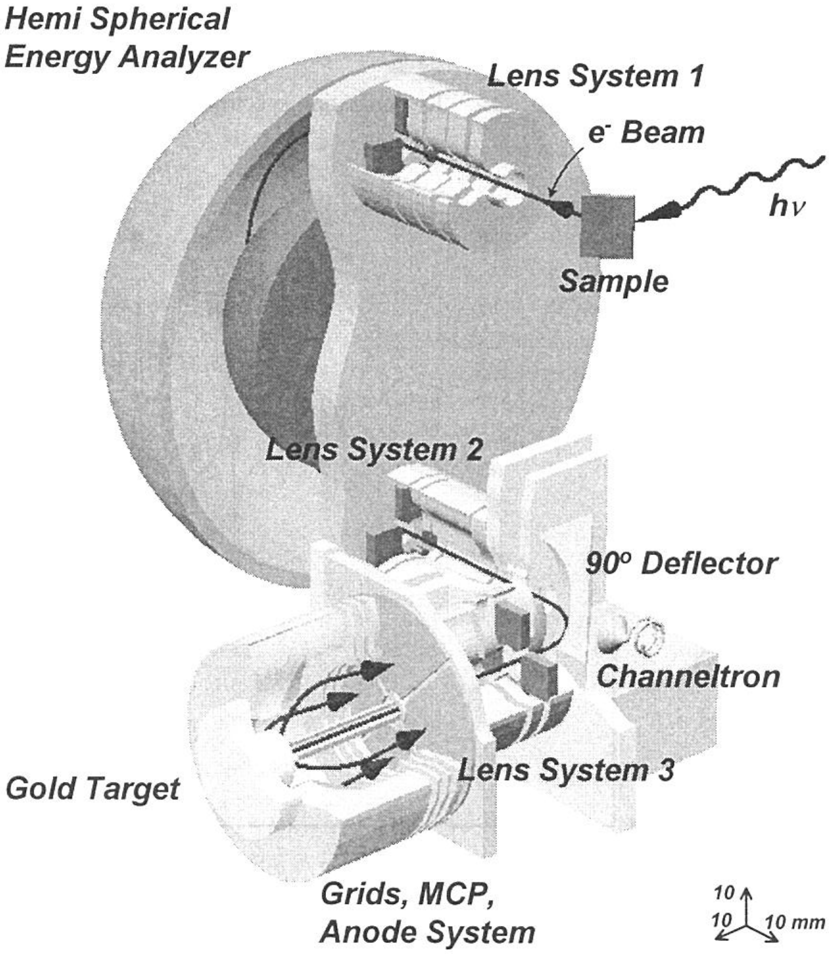

Figure 1 Schematic view of a spin- and angle-resolved photoelectron spectrometer

The low-energy diffuse scattering detector is based on the spin-orbit interaction between an incident electron and a target. According to the *ls* term of the spin-orbit interaction,[4)] the spin analyzer is sensitive to the transverse component of the spin polarization which is normal to the scattering plane, while the longitudinal component along the incident electron direction cannot be observed. On the other hand, normal emission of photoelectrons is widely observed to determine the momentum perpendicular to the sample surface. Thus, we have designed a spin- and angle-resolved photoelectron spectrometer in which a 90° deflector is installed between a hemispherical analyzer and a spin detector, as shown in Figure 1. The 90° deflector changes the direction of the electron beam but not the spin direction, and then the transverse configuration of the spin polarization, which is necessary for the spin detector based on the spin-orbit interaction, is satisfied. The parallel and perpendicular components of spin polarization with respect to the sample surface can be simultaneously observed with the present detector system. As depicted in Fig. 1, the present electron optical system consists of three sets of cylindrical lenses with four deflection plates, a hemispherical energy analyzer and a 90° section of a spherical deflector. The hemispherical energy analyzer is a commercial one having a mean radius of 50 mm (VSW HA-54), while the other components are home-made. All optical elements are designed to overlap adjoining elements so that there is no line of sight for the electron beam to detect an insulating surface and be affected by charging. The 90° deflector has a pinhole 1 mm in diameter, through which a straight electron beam can be observed by a channeltron. The spin detector consists of a drift tube, a gold scattering target, guard electrodes, two retarding grids to reject secondary electrons, a micro-channel plate (MCP), and a four-section anode assembly. The figure of merit of a low-energy diffuse scattering detector has already been reported to be about $1 \times 10^{-4}$, which is comparable to that of the traditional Mott detector.[2)]

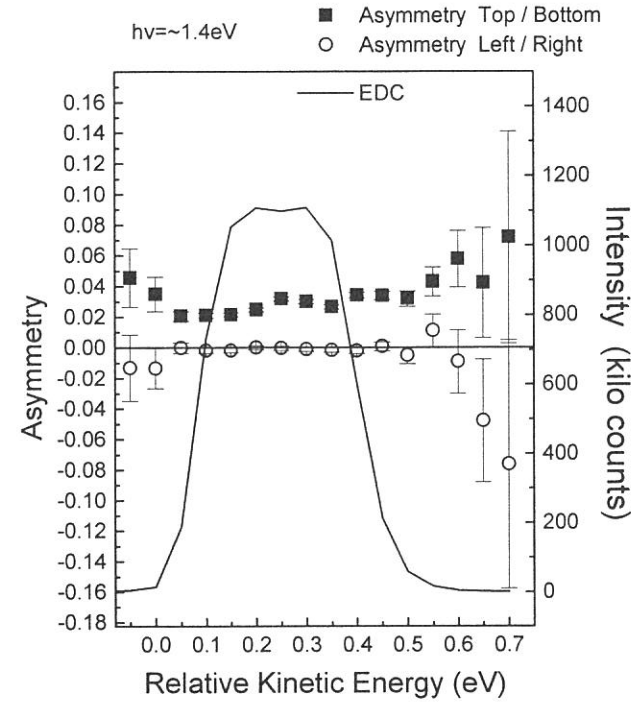

Figure 2 Asymmetry and EDC (solid curve) of the spin-polarized photoelectrons from O/Cs/GaAs(100). Solid cubes and open circles show the asymmetry for top/bottom anodes and for left/right anodes, respectively.

The parameters of optical elements have been adjusted by using emitted electrons from GaAs(100) surface excited with the He-I (or Ne-I) line. We optimized parameters by maximizing the intensity, and all parameters were fixed like this way. It is important to compare the experimentally determined parameters of optical elements with the calculated ones, and it should be noted that the lens parameters determined in the experiment are in good agreement with the results of ray tracing.

Negative electron affinity (NEA) surface of GaAs(100) which activated by coadsorption of Cs and oxygen on GaAs(100) is well known standard spin polarized electron source. Photoelectrons from this surface exited by circularly polarized lights from a Ti-sapphire laser were used as spin polarized electrons. Figure 2 shows the EDC (solid curve), asymmetry observed with top/bottom anodes (solid cubes) and that observed with left/right anodes (open circles). The value of asymmetry is about 2.7 % for top and bottom anodes, but is almost zero for left and right anodes. This result indicates that the spin-polarization of the photoelectrons is parallel to the <100> direction of the sample. This is in good agreement with the selection rules of optical transition at the Γ point of GaAs.[4)] The spin polarization of photoelectrons from GaAs is expected to be 50 % in principle, but a typical observed value for O/Cs/GaAs(100) is about 36 %.[5)] Using this typical value, the Sherman function of the present analyzer is estimated to be about 8 %, which is slightly smaller than the expected one (11 %).[2)] This may be due to the contamination of the surface of the gold target.

It is concluded that the present compact spin- and angle-resolved photoelectron spectrometer works well, although further improvement in order to obtain a better value of the effective Sherman function is still required. It is expected that the present spectrometer will be useful with circularly polarized light in the vacuum-ultra violet region which is provided from a helical undulator[6)] with a new monochrometer SGM-TRAIN.[7)]

## References

**1)** See for example, J. Kirschner: *Polarized Electrons at Surfaces* (Springer, Berlin, 1985).
**2)** J. Unguris, D. T. Pierce and R. J. Celotta: Rev. Sci. Instrum. **57** (1986) 1314.
**3)** N. Takahashi *et al.* : Jpn. J. Appl. Phys. **35** (1996) 6314.
**4)** J. Kessler: *Polarized Electrons* (Springer, Berlin, 1985) 2nd ed.
**5)** I. Hirose *et al.*: Genshikaku Kenkyu **30** (1985) 97 [in Japanese].
**6)** S. Kimura *et al.*: J. Photoelectrospectrosc. & Relat. Phenom. **80** (1996) 437.
**7)** M. Kamada *et al.*: Rev. Sci. Instrum. **66** (2) (1995) 1537.

**(BL5B)**

# Absolute desorption yield of metastable atoms from the surface of solid rare gases induced by exciton creation

T. Hirayama, A. Hayama, T. Koike, T. Kuninobu, and I. Arakawa.
*Department of Physics, Gakushuin University, Mejiro, Toshima, Tokyo 171 JAPAN.*

K. Mitsuke.
*Institute for Molecular Science, Myodaiji, Okazaki 444 JAPAN.*

M. Sakurai.
*Department of Physics, Kobe University, Nada, Kobe 657 JAPAN.*

E.V. Savchenko
*Verkin Institute for Low Temperature Physics and Engineering, Kharkov 310164 UKRAINE.*

When an exciton is created in the bulk or on the surface of the rare gas solids (RGS), a desorption may occur after various relaxation processes. The desorbed particle can be the atoms in the ground or excited states, singly and multiply charged ions, neutral and ionic clusters, etc. As to the neutral atom desorption, two mechanisms, excimer dissociation (ED) and cavity ejection (CE), were proposed[1] and have been confirmed experimentally. The desorption via ED process is due to a dissociation of a molecular type self-trapped exciton (m-STE) similar to the dissociation of an excited dimer (excimer) in the gas phase. Negative electron affinity of the matrix is known to be essential for the CE process to have a repulsive interaction between the excited atom and the surrounding ground state atoms, so that desorbed atoms via CE mechanism are essentially in excited states. We have measured for the first time the absolute desorption yield of metastable excited atoms via cavity ejection (CE) mechanism from the surface of RGSs by photon impact in excitonic excitation region.

Experiments have been done using an UHV chamber ($P \leq 10^{-8}$Pa) at a beam line BL5B in UVSOR, Institute for Molecular Science. Detail of the experimental setup has been described elsewhere[2, 3]. Briefly, the Pt substrate is attached to the head of a liquid He cryostat which is cooled down to 6K or less. Monochromatized synchrotron radiation is pulsed using a mechanical chopper whose width and interval are 15$\mu$sec and 2.5msec, respectively. The photon beam is incident at 20 deg. from the normal direction of the sample surface. Thickness of the RGS is 500 atomic layers or more. The desorbed metastable atoms (Ne*, $2p^5 3s\ ^3P_{0,2}$) are detected by an open electron multiplier tube (EMT, HAMAMATSU, R595) with a CuBe dynode as a first electrode. The diameter of the EMT opening is 8mm which corresponds to the detection solid angle of $3.1\times10^{-5}$sr. Charged particles are rejected by applying suitable potentials on the first dynode of the EMT and the retarding grids in front of the EMT. The detector is fixed at the distance of 360mm from the sample in the normal direction of the sample.

Figure 1 shows the time-of-flight (TOF) spectra of desorbed particles measured at 72.3nm, 70.7nm, 65.4 nm, and 61.1nm, which corresponds to the excitation energies of the 1st order surface (S1) and bulk (B1) excitons, $2p^5 3p$ type surface exciton (S'), and the 2nd order bulk exciton, respectively. Detailed analysis of these spectra has already been given in ref [4].

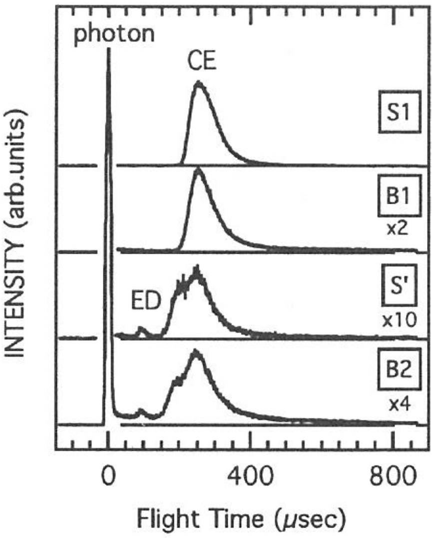

Fig.1. Time of flight spectra of desorbed particles from the surface of solid Ne at the excitation of 72.3nm (S1), 70.7nm (B1), 65.4nm (S'), and 61.1nm (B2).

In order to obtain the absolute yield, we have to know the efficiency of the metastable atom detector, absolute intensity of the incident photon beam, and the angular distribution of the desorbed atoms. Absolute detection efficiency of EMT for the metastable rare gas atoms with thermal energy has been reported by several authors[5, 6] to be 0.12, 0.035, 0.020, and 0.0050 for Ne*, Ar*, Kr* and Xe*, respectively. The intensity of the incident

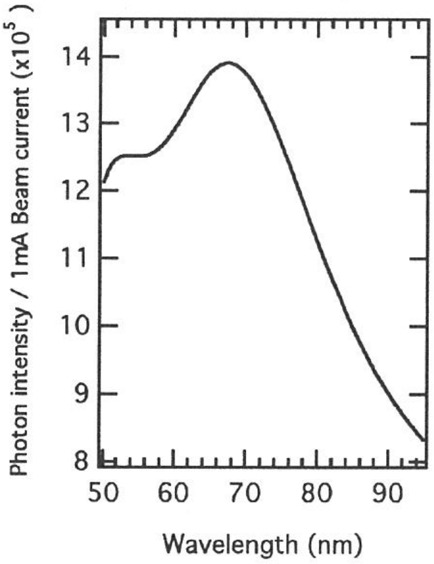

Fig.2. Absolute photon intensity normalized by the ring current (mA) as a function of the wavelength. Photon beam is pulsed using a mechanical chopper. The width and the interval of the pulsed light is 15$\mu$sec and 2.5sec, respectively.

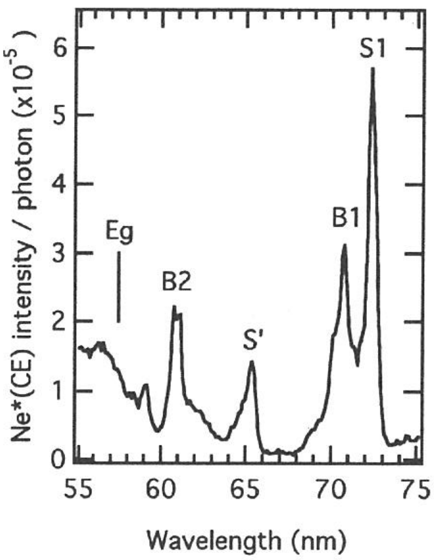

Fig.3. Absolute Ne* intensity desorbed from the surface of solid Ne normalized by the number of incident photon as a function of the wavelength. The assignments for each peaks and the position of the band gap energy (Eg) are shown.

photon beam is estimated by measuring the current of photoelectron emitted from a thick Au plate[7]. Typical result for the absolute intensity of the incident photon normalized by the ring current (mA) as a function of wavelength is shown in Fig.2. This spectrum has been measured using grating No.3 and mirror No.4, and with the width of the monochromator slit, 300$\mu$m, and the diameter of the beam defining aperture, 3mm. It should be noted that the intensity of the *pulsed* photon beam is plotted in the figure. The duty ratio of the pulse is about 0.5%, i.e., the photon intensity in DC mode is about 200 times higher.

Figure 3 shows the absolute Ne* intensity normalized by the number of incident photon as a function of wavelength. The assignment of the each peaks and the position of the band gap energy (Eg) are shown in the figure. Total desorption yield is then determined absolutely taking the desorption angular distribution[3] and the geometrical condition into account. Absolute yield for Ne* from pure solid Ne by the creation of the 1st order surface (S1) and the 1st order bulk (B1) exciton by photon excitation are found to be $1.3\times10^{-3}$ and $8.2\times10^{-4}$ (Ne*/photon), respectively.

## REFERENCES.

1 T. Kloiber and G. Zimmerer, Radiat. Eff. Def. Solids **109**, (1989) 219.
2 T. Hirayama, T. Nagai, M. Abo, I. Arakawa, K. Mitsuke and M. Sakurai, J. Electr. Spectr. Rel. Phen. **80**, (1996) 101.
3 M. Sakurai, T. Nagai, M. Abo, T. Hirayama and I. Arakawa, J. Vac. Soc. Jpn. **38**, (1995) 298.
4 I. Arakawa, D. E. Weibel, T. Nagai, M. Abo, T. Hirayama, M. Kanno, K. Mitsuke and M. Sakurai, Nucl. Instrum. Meth. Phys. Res. B**101**, (1995) 195.
5 Borst, Rev. Sci. Instrum. **42**, (1971) 1543.
6 J. M. Alvariño, C. Hepp, M. Kreiensen, B. Staudenmayer, F. Vecchiocattivi and V. Kempter, J. Chem. Phys. **80**, (1984) 765.
7 J. A. R. Samson, J. Opt. Soc. Am. **54**, (1964) 6.

(BL5B)

# Soft-X-Ray Reflectances of Oxide Multilayers for Free Electron Lasers

Hiroshi Kumagai and Koichi Toyoda

*Laser Science Research Group,*
*The Institute of Physical and Chemical Research (RIKEN),*
*2-1 Hirosawa, Wako, Saitama 351-01, Japan*

Since Barbee et al. successfully demonstrated normal-incidence soft-X-ray reflectors with high reflectances of over 50% at 13.8 nm using 50-layer Mo/Si multilayers deposited by magnetron sputtering,[1] there have been various studies on the fabrication of soft-X-ray multilayer reflectors using electron beam evaporation and ion beam, RF and DC magnetron sputtering deposition. In particular, development of high-performance normal-incidence multilayer optics for the *water-window* wavelength region between the oxygen and carbon K absorption edges at 2.33 and 4.36 nm, respectively, where water is relatively transmissive and organic materials are absorptive, has been a technical challenge of great interest. The extremely small periods (1.2-2.2 nm) of soft-X-ray reflectors require very rigorous specifications to be met with respect to interface roughness and interlayer mixing, because interface roughness on an atomic scale has a substantial effect on soft-X-ray reflectance. Therefore, the highest reflectance achieved at *water-window* wavelengths has been 3.3%,[2] in spite of the various efforts which have been made in this field. The reason that the reflectances achieved at these wavelengths are so low is that the Fresnel coefficients of materials are so small at these wavelengths that a large number of bilayers must be used, which means that the problems of interface roughness and imperfect interfaces due to interlayer mixing become serious.

The authors have proposed the use of a novel metal oxide multilayer, whose material combination is the same as that used in free electron lasers, for soft-X-ray reflectors at *water-window* wavelengths,[3] because an oxide multilayer can prevent the forming of an alloy at the interface, and the absorption of oxygen in oxides is negligible at the *water-window* wavelengths; moreover, the metal oxide multilayer can be fabricated by the atomic layer deposition or atomic layer epitaxy technique. These techniques can be used to control surfaces on an atomic scale by sequentially dosing the surface with appropriate chemical precursors and then promoting surface chemical reactions which are inherently self-limiting. We have found that the self-limiting adsorption mechanism works in the fabrication of oxide thin films such as aluminum oxide and titanium oxide.[4-6]

We report here that we could experimentally demonstrated high reflectance of over 30% of novel metal oxide multilayers of titanium oxide and aluminum oxide using monochromatized synchrotron radiation (SR) from the beamline 5B of the 750-MeV electron storage ring located at the Ultraviolet Synchrotron Radiation Facility (UVSOR).

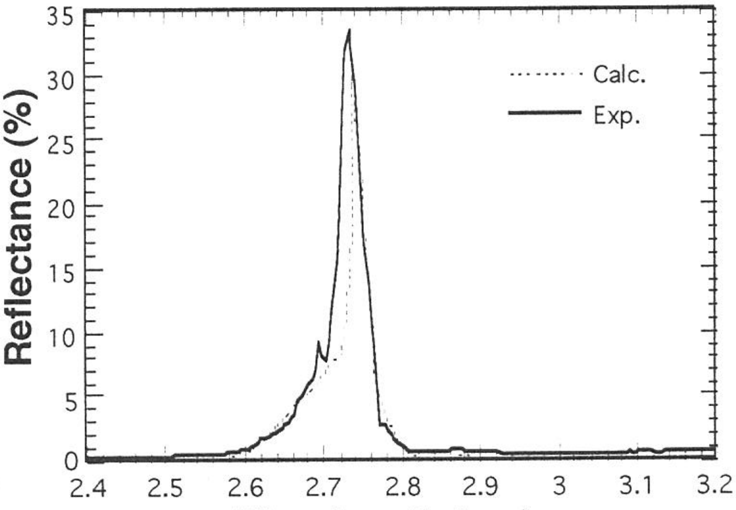

*Figure 1 Experimental and calculated reflectances of the aluminum oxide/titanium oxide multilayer.*

Figure 1 shows the experimental and calculated reflectances of the aluminum oxide/titanium oxide multilayer fabricated by the atomic layer deposition method of controlled growth with sequential surface chemical reactions. A high reflectance (s-polarization) of 33.4% at the wavelength of 2.734 nm and an incident angle of 71.8° from the normal incidence are demonstrated in the experimental data (solid curve), which were obtained using the monochromatized SR. The calculated reflectance (dashed line) shows almost the same reflectance of around 32% as the experimental one. However, the full width at half-maximum of the experimental reflectance at 2.734 nm is 0.0381 nm, 1.8 times larger than the calculated value of 0.0212 nm. This is because the interpolative approximation of complex atomic scattering factors using the atomic data tables formulated by Henke et al.7) is not accurate around the titanium L absorption edge. The reflectance of 33.4% in the experimental results is almost the same as that in the calculation, based on the hypothesis that the compositions and densities of the binary layers should be the same as those in rutile $TiO_2$ and $\alpha$- $Al_2O_3$. Further reduction of the surface and interface roughnesses will lead to the fabrication of normal-incidence reflectors at these wavelengths.

This work was supported by the Joint Studies Program (1996-1997) of the Institute for Molecular Science.

**References**

1) T. W. Barbee, Jr., S. Morowka and M. C. Hettrick, Appl. Opt. **24**, 883 (1985).
2) I. V. Kozhevnikov, A. I. Fedorenko, V. V. Kondratenko, Yu. P. Pershin, S. A. Yulin, E. N. Zubarev, H. A. Padmore, K. C. Cheung, G. E. van Dorssen, M. Roper, L. L. Balakireva, R. V. Serov and A. V. Vinogradov, Nuclear Instruments and Methods in Physics Research **A 345**, 594 (1994).
3) H. Kumagai, M. Matsumoto, Y. Kawamura, K. Toyoda and M. Obara, Jpn. J. Appl. Phys. **33**, 7086 (1994).
4) H. Kumagai, K. Toyoda, M. Matsumoto and M. Obara, Jpn. J. Appl. Phys. **32**, 6137 (1993).
5) H. Kumagai and K. Toyoda, Appl. Surf. Sci. **82/83**, 481 (1994).
6) H. Kumagai, M. Matsumoto, K. Toyoda, M. Obara and M. Suzuki, Thin Solid Films **263**, 47 (1995).
7) B. L. Henke, E.M. Gullikson and J.C. Davis, Atomic Data and Nuclear Data Tables **54**, 181(1993).

(BL5B)

# Higher performance X-ray multilayer mirror fabrication by using surface smoothing effect of atomic layer epitaxy

Yoshinobu AOYAGI, Sohachi IWAI, Masashi ISHII

*The Institute of Physical and Chemical Research (RIKEN)*

In recent years, atomic layer epitaxy (ALE) of III-V compound semiconductors [1,2] has been extensively studied, and is considered to be a powerful technique for the fabrication of quantum devices with superlattice structures. In ALE, source gases are alternatively introduced into the growth chamber, and according to a self-limiting mechanism, the epitaxial growth is automatically stopped at strictly 1 monolayer (ML) in one alternative gas supply. This self-limiting mechanism may be also valuable for fabrication of other functional multilayer structures, such as X-ray multilayer mirrors [3-7]. In previous report, AlP and GaP ALE were primarily applied to fabrication of X-ray multilayer mirror, and according to the layer-by-layer growth nature of ALE, the wavelength of multilayer mirror was proved to be exactly controlled by ALE cycle number [8]. Moreover, we proposed a new soft X-ray mirror with a multi-periodic structure [9], in which the X-ray phase was compensated for via layer-by-layer controlled films. By contrast with these single crystal optics grown by ALE, multilayer mirrors deposited by sputtering are amorphous or polycrystal. In this report, we discuss an effect of single crystal growth characteristic on optical property, and its advantage for fabrication of short period X-ray optics.

ALE were performed in a metalorganic vapor-phase epitaxy (MOVPE) system with a horizontal quartz reactor. [10] The metalorganic gas sources for group-III elements were dimethylaluminum hydride (DMAH) for AlP, and trimethylgallium (TMG) for GaP. Phosphine ($PH_3$) was used as a group-V gas source. The temperature of DMAH and TMG liquid gas source was kept at 40 ℃ and -4 ℃, respectively, and these source gases were carried into the reactor by $H_2$ bubbling. The $H_2$ flow rate through DMAH and TMG was varied from 10 to 20 sccm. $PH_3$ diluted with $H_2$ to 20 % was fed into the reactor at a flow rate of 150 sccm. Hydrogen carrier gas was continuously introduced and the total gas pressure in the reactor was fixed at $6\times 10^2$ Pa. The substrate was (100) oriented non-doped GaP which was chemically etched in $HCl:HNO_3:H_2O$ = 2:1:2 solution at room temperature prior to experiments. The X-ray reflectivity of multilayer mirrors fabricated by ALE was measured using monochromatized synchrotron radiation (SR) from the 750 MeV electron storage ring located at the Ultraviolet Synchrotron Radiation Facility (UVSOR), Institute for Molecular Science, Okazaki, Japan.

Figure 1 shows AFM observations of surface morphology of (a) GaP wafer just before the growth, and (b) the typical AlP/GaP multilayer structure grown by ALE. The ALE conditions are same as previous experiments [8]. As shown in Fig. 1(a), there are a lot of spikes on the initial GaP surface. The surface roughness is estimated at ~0.6 nm, root mean square (rms.). By contrast, the surface of the multilayer mirror is smoother than that of the initial wafer; the substrate surface is smoothed by ALE. Note that the vertical axis of Fig 1 (b) is expanded; the

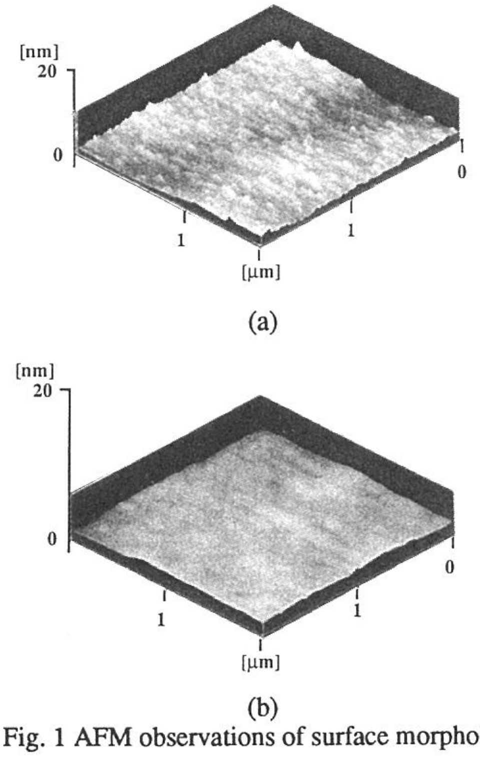

(a)

(b)

Fig. 1 AFM observations of surface morphology of (a) GaP wafer, and (b)AlP/GaP multilayer.

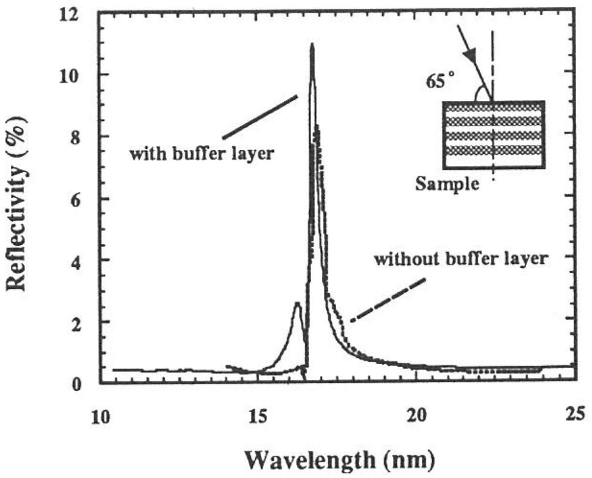

Fig. 2 Comparison of a reflectivity between multilayer mirrors with and without buffer layer.

surface roughness is emphasized. The roughness of the multilayer structure surface is estimated at ~0.3 nm, rms. The detailed mechanism of this smoothing by ALE is not understood at this time, but the cause will certainly be related to the enhanced reaction induced by dangling bonds in the spokes and the surface steps.

It is well known that interface roughness decreases the reflectivity of the multilayer mirror according to the Debye-Waller factor. Therefore, the X-ray reflectivity measurement of the multilayers structure provide evidence for the degree to which the surface roughness is smoothed during ALE growth. Figure 2 shows a comparison of the reflectivity between multilayer mirrors with and without a buffer layer of 1000 ML. The reflectivity of these structures was estimated from the reflected X-ray intensity divided by direct incidence beam into an electron multiplier. The incident angle of X-ray is fixed at 65° . Though the structure of both mirrors is the same, 50 bilayers of $(AlP)_{22}(GaP)_{11}$, the reflectivity of the mirror without the buffer layer is less than that of another mirror with the buffer layer. This difference is obviously caused by the surface smoothing effect by ALE; in the case of the direct mirror construction on the GaP substrate without the buffer layer, more serious AlP/GaP interface fluctuation will be introduced, resulting in an attenuation of the reflectivity. Since the Debye-Waller factor becomes more significant with shortening X-ray wavelength, this smoothing by ALE will be effective in the fabrication of the X-ray mirror at short wavelength regions such as a few nm.

In summary, surface smoothing effect in atomic layer epitaxy (ALE) is found. The initial substrate surface roughness is improved by ALE growth. By using this surface smoothing effect, the interface roughness of the X-ray multilayer mirror is improved, resulting that the reflectivity is increased.

References

[1] J. Nishizawa, J. Electrochem. Soc. 132, 1197 (1985).
[2] Y. Aoyagi, J. Vac. Sci. Technol. B5, 1460 (1987).
[3] T. W. Barbee, J. Mrowka, Stanley and M. C. Hettrick, Appl. Opt. 24, 883 (1985).
[4] C. Montcalm, B. T. Sullivan, M. Ranger, J. M. Slaughter, A. Kearney, C. M. Falco and M. Chaker, Opt. Lett. 19, 1004 (1994).
[5] C. Sella, K. Youn and R. Krishnan, Appl. Surf. Sci. 33/34, 1208 (1988).
[6] J. F. Seely, G. Gutman, J. Wood, G. S. Herman, M. P. Kowalski, J. C. Rife and W. R. Hunter, Appl. Opt. 32, 3541 (1993).
[7] I. V. Kozhevnikov, A. I. Fedorenko, V. V. Kondratenko, Y. P. Pershin, S. A. Yulin, E. N. Zubarev, H. A. Padmore, K. C. Cheung, G. E. van Dorssen, M. Roper, L. L. Balakireva, R. V. Serov and A. V. Vinogradov, Nucl. Instr. and Meth. in Phys. Res. A345, 594 (1994).
[8] Y. Aoyagi, S. Iwai, M. Ishii and K. Hirofumi, UVSOR activity report 1995 UVSOR-23, 170 (1996).
[9] M. Ishii, S. Iwai, T. Ueki and Y. Aoyagi, Appl. Opt. (1996).
[10] H. Isshiki, Y. Aoyagi, T. Sugano, S. Iwai and T. Meguro, Appl. Phys. Lett. 63, 1528 (1993).

# (BL5B & BL7A)

# Photoelectron Spectro-Microscopy Experiments at UVSOR Facility: -Application to Imaging of Magnetic Domains-

Toyohiko KINOSHITA, Krishna G. NATH[1], Masamitsu WATANABE*, Shinya YAGI**,
Shinichi KIMURA and Andreas FANELSA[2]

UVSOR Facility, Institute for Molecular Science, Okazaki 444, Japan
[1] Department of Structural Molecular Science, Graduate University for Advanced Studies, Okazaki 444, Japan
[2] Institut für Angewandte Physik, Heinrich-Heine -Universität Düsseldorf, Düsseldorf D-40225, Germany

In order to investigate the surfaces and interfaces of solids and to study electronic structures of small samples and small area of surfaces, the photoelectron spectro-microscopy experiments have been started at the UVSOR. The ESCALAB 220i-XL (Fisons Instruments) has been connected to the UVSOR beamlines BL5B and BL7A, which cover the photon energy range from 5 eV to 5 keV. The outline of the equipment was described last year [1]. Briefly, it consists of a hemispherical electron analyzer with 150 mm radius, an electrostatic lens system, a magnetic lens system for further magnification of the photoelectron image, an X-ray tube (Mg K$\alpha$, Al K$\alpha$) for photoexcitation, a sputtering gun, and so on. It is expected that spatial resolution of 2 $\mu$m for the imaging mode and 20 $\mu$m for the spectroscopic mode respectively, can be achieved. The studies with X-ray tube have also been performed. To impinge the SR light in oblique incidence angle, we set up the whole system on the rotatable stand and connect the port to the end port of the beamline via a bellow tube. The maximum rotation angle is 7.5 degree, which is limited by inner bore radius of the port for SR incidence in analyzer chamber. Figure 1 shows the photograph of the system installed at the end station of BL5B.

As a demonstration of our apparatus, we show the magnetic domain image of Fe(110) surface with magnetic dichroism at the Fe 2p3/2 core level photoemission by linearly polarized light and by unpolarized light.

So far, most of the magnetic domain imaging experiments used magnetic circular dichroism effect for absorption edge or (energy resolved) photoemission or Auger signals [2]. Recently, the possibility to observe the magnetic domain by using linearly polarized light has been suggested [3]. Magnetic domain imaging of Fe (001) surface by linearly polarized light is shown in Ref. 4, where PEEM (photoelectron emission microscope) system is used for imaging of secondary electrons. We have used the magnetic linear dichroism in angular distribution (MLDAD) and/or MLD effects of Fe 2p3/2 photoemission signal. Figure 2 shows magnetic domain image taken with MLD(AD) effect of Fe 2p 3/2 at BL7A. The photon energy was 1758eV. The linearly polarized light was impinged from the bottom. The Fe 2p electrons at Ek=1046.2eV and at Ek=1044.6eV were corrected. After subtraction and normalization of the two sets of data, we got the magnetic domain image, in which the directions of the magnetic moments are indicated. The contrast between up magnetized area and down one is apparent.

Very recently, the domain imaging by unpolarized light has been also suggested [5]. Since the unpolarized X-ray light can be considered as the incoherent superposition of s- and p-polarized lights, it is also possible to observe the MLDAD effect by using conventional X-ray tube. The example of the MLDAD effect by unpolarized light is shown in Figure 3, where the small area (50 $\mu$m) Fe 2p photoemission spectra from two different regions were measured. The MLDAD signal can be clearly observed reflecting the magnetic domain information. We have also succeeded to take the magnetic domain image by the X-ray tube, which is similar image as Figure 2 (not shown here).

In summary, we have started the photoelectron spectro-microscopy experiments at the UVSOR facility. In 1997, the sample preparation chamber equipped with LEED and evaporation systems will be attached to the system. We will proceed further studies related to surface and bulk electronic structures from micro-area.

## Acknowledgements

The authors thank to Prof. Kronmüller for lending them a Fe(110) single crystal. They also would like to express their gratitude to Prof. E. Kisker and Dr. F. U. Hillebrecht for their encouragement and discussion. The staff members of the UVSOR facility are acknowledged for their experimental support.

## References

* Present address: Photon Factory, National Laboratory for High Energy Physics, Oho 1-1, Tsukuba 305, Japan.

** Present address: Department of Material Science, Faculty of Science, Hiroshima University, Kagamiyama 1-3, Higashi-Hiroshima 724, Japan.

[1] T. Kinoshita, S. Yagi and S. Kimura, *UVSOR activity report*, 1995, p.47.

[2] See, for example, B.P.Tonner et al., *J. Electron Spectrosc. Relat. Phenom.* 75 309 (1995).

[3] Ch. Roth, F. U. Hillebrecht, H. B. Rose and E. Kisker, *Phys. Rev. Lett.* 70, 3479 (1993).

[4] D. Spanke, J. Dresselhaus, T. Kinoshita, Ch. Roth, H. B. Rose, F. U. Hillebrecht and E. Kisker, *J. Electro. Spectrosc. Relat. Phenom.* 78 (1996) 299: F. U. Hillebrecht, T. Kinoshita, D. Spanke, J. Dresselhaus, Ch. Roth, H. B. Rose and E. Kisker, *Phys. Rev. Lett.* 75 (1995) 2224.

[5]A. Fanelsa, PhD thesis (**Düsseldorf Univ.*), 1996: F. U. Hillebrecht and W. D. Herberg, *Z. Phys.* B93, 299 (1994).

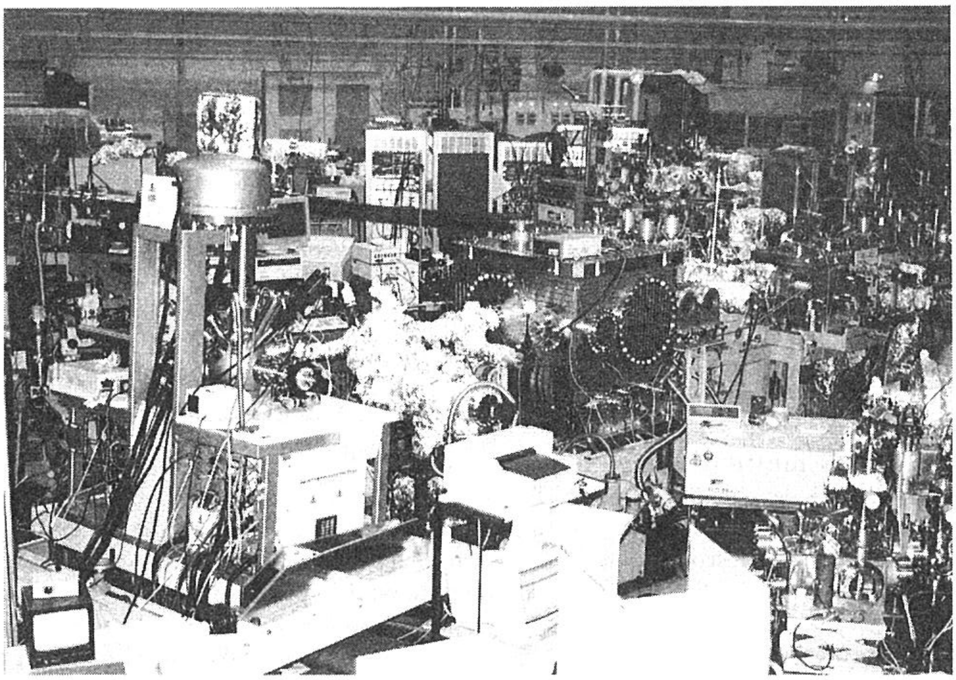

**Figure 1.** Photograph of the equipments connected to the beamline BL5B at the UVSOR.

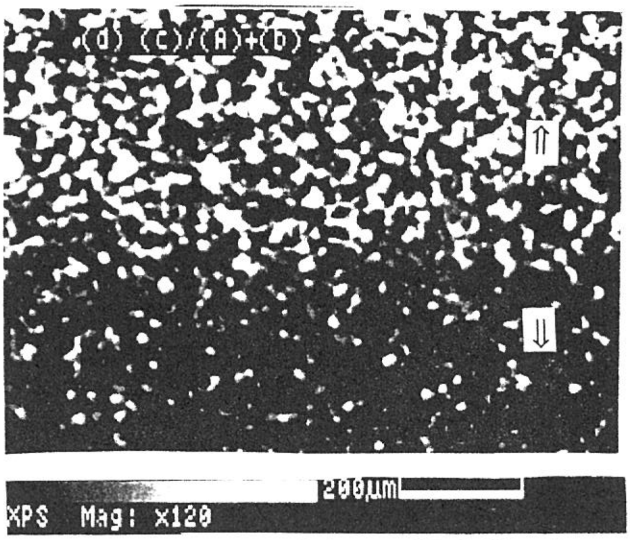

**Figure 2.** Magnetic domain image of Fe(110) surface. Magnetic dichroism effect of Fe 2p3/2 photoelectrons excited by linearly polarized light (h ν =1758eV) was used.

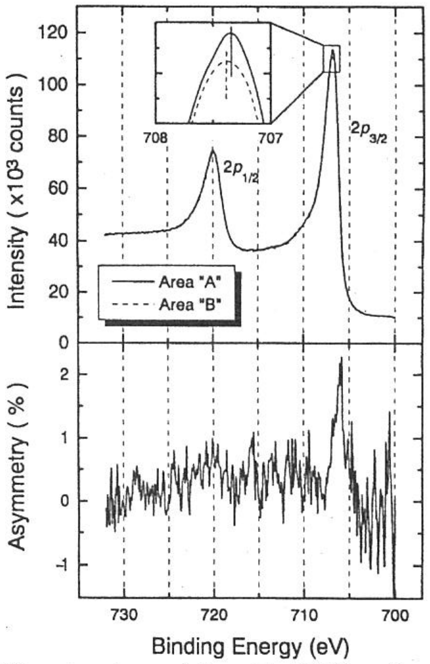

**Figure 3.** Small area (50 μm) photoemission spectra from two different regions of the Fe (110) surface excited by Al K α line. The MLDAD signal can be observed reflecting the magnetic domain information.

*(BL5B)*

# High Wavelength Resolution XUV Multilayer Mirror for XUV Doppler Telescope Aboard Sounding Rocket

Saku TSUNETA, Taro SAKAO, Hirohisa HARA, Toshifumi SHIMIZU[1],
Ryouhei KANO[1], Tsuyoshi YOSHIDA[1], Shin'ichi NAGATA[1]

*National Astronomical Observatory, 2-21-1 Osawa, Mitaka, Tokyo, 181, Japan*
[1] *Department of Astronomy, School of Science, The University of Tokyo, Bunkyo-ku, Tokyo, 113, Japan*

**SiC/Al high wavelength resolution multilayer mirror:** Multilayer mirror with system wavelength resolution ($\lambda/\Delta\lambda$) as high as $30 \sim 50$ is required for the diagnostics of the cosmic plasma with temperature 1–20 MK. Such a high wavelength resolution can be realized by increasing the number of the layer pairs contributing to the reflectance, *ie* by selecting less-absorbing materials for both the reflector and the spacer, and by decreasing the thickness of the reflector. We fabricated the multilayer mirror with silicon carbide reflector (20 % thickness of the layer period) and aluminum spacer, and found $\lambda/\Delta\lambda \sim 26.8$, and the peak reflectivity ~13.0 %. This wavelength resolution is close to the value obtained with the numerical simulation, and is considerably higher than the value obtained with the conventional Mo/Si multilayer. The design, fabrication, and characterization of the SiC/Al mirror is reported by Nagata et al. (1997).

**SiC/Al and MoSi/Si multilayer with light trap for XUV Doppler Telescope:** Based on these promising results, we are developing the XUV Doppler Telescope aboard ISAS sounding rocket (Sakao et al. 1996, Yoshida et al. 1997). In this project, the entire solar corona is observed at Fe XIV line (211.3Å) with two normal incidence telescopes, whose peak wavelengths are slightly (about 2Å) shifted toward red and blue from the wavelength of the line. The line moves in between the blue and red windows of the multilayer telescopes due to the motion of the plasma (Doppler effect), and the velocity map of the 1.8MK plasma is obtained by subtracting the blue from the red images. We can also obtain the images of the 1.8MK plasma by summing the blue and red images. The velocity maps together with the X-ray images allow us to obtain the information on the dynamics of the coronal plasma. In order to improve the detection limit of the velocity field, and to avoid the contamination from the nearby emission lines, we need to develop the high-wavelength resolution mirror tuned for the 211Åline. We have characterized two sets of multilayer mirrors; (1) SiC/Al, and (2) MoSi/Si (Sakao et al. 1996). The wavelength resolution of both the mirrors (Fig. 1) satisfies the requirement($\lambda/\Delta\lambda \sim 24$ for MoSi/Si, and 36 for SiC/Al). We have added the anti-reflection layer (light-trap) to the MoSi/Si mirror for the intense ($X100$) HeII line at 304Å(Ishiyama et al. 1997). Fig. 1 also shows the sharp peak at 211Å, and the anti-peak near 304Å.

**Large-area multilayer mirror with high uniformity:** The mulitlayer coated on the large-area mirror inherently has large non-uniformity in the wavelength of the reflectivity peak owing to the radius-dependent distance from the sputtering source. This must be corrected with an accuracy of a few times 0.1Åover 15 cm diameter. We have measured the non-uniformity of the large-area sample mirror and then made the uniform mirror with the correcting mask designed on the basis of the measurement. The uniformity is within 0.5Åpp over the distance (Fig. 2), and satisfies the requirement for the flight mirror (Nagata, 1997) .

## References:

High wavelength resolution XUV multilayer mirror, Nagata, S., et al., Applied Optics, in press (1997)
Japanese sounding rocket experiment with the solar XUV Doppler telescope, Sakao, T., et al., Proc. SPIE, 2804, 153 (1996)
Development of XUV telescope aboard sounding rocket, Nagata, S., Master Thesis, University of Tokyo (1997)
Solar XUV Doppler Telescope, Yoshida, T., et al., Proc. Observational Plasma Astrophysics, Kluwer, in press (1997)
Mulitlayer light-trap, Ishiyama et al., JJAP, to be submitted (1997)

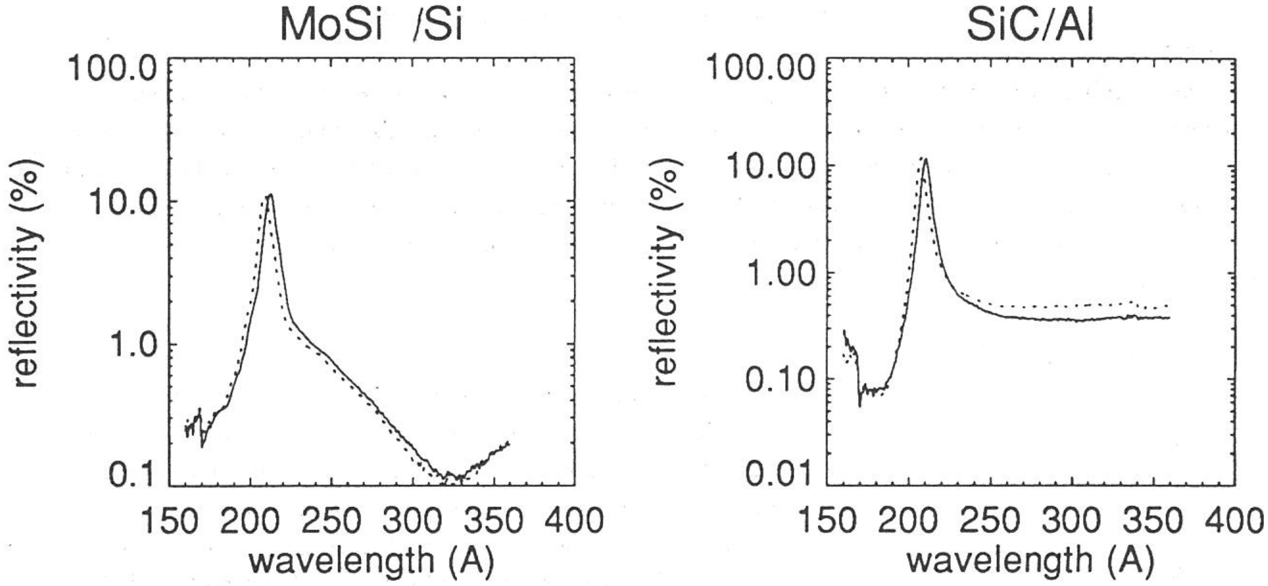

Figure 1: Measured reflectivity profile of the MoSi/Si ($\Gamma$ =0.2) and SiC/Al($\Gamma$ =0.25) multilayer mirror. Solid lines: measurement, Dotted lines: numerical simulation. The angle of incidence is 89 degree. The anti-peak around 304Åis due to the light-trap (single Si layer) to absorb the intense HeII line at 304Å, which is hazardous for the observation.

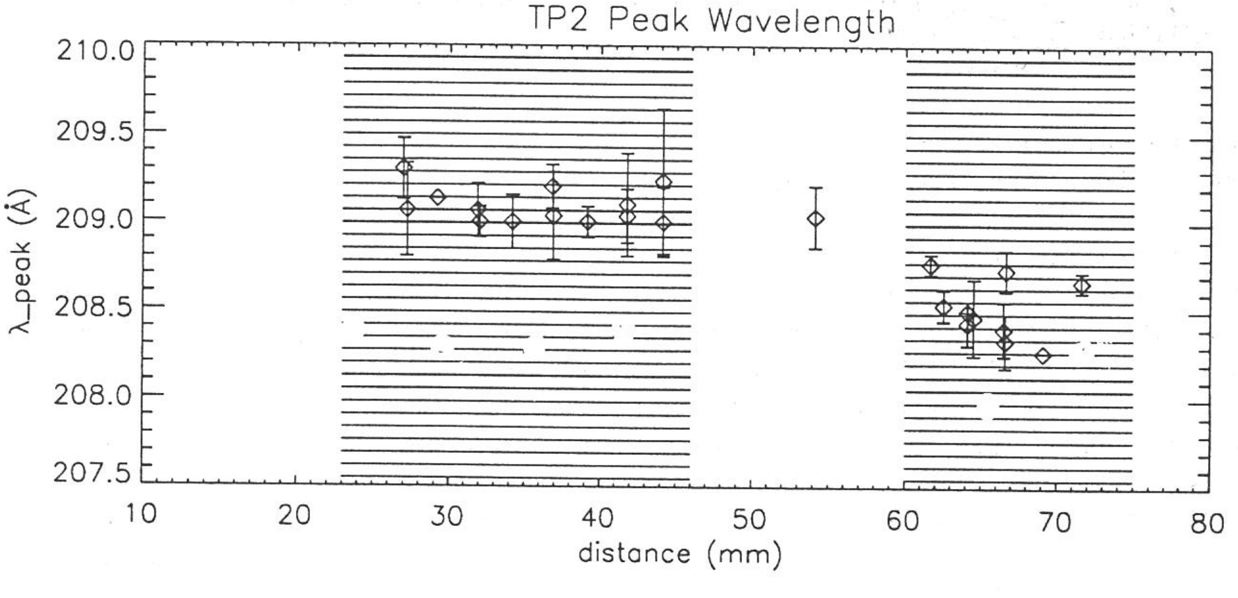

Figure 2: The wavelength of the peak reflectivity over 15 cm. Inner shaded region corresponds to the secondary mirror, and the outer shaded region to the primary mirror. The design peak wavelength of the primary mirror is 0.4Åshorter than 210.4Åowing to the different incidence angles. The uniformity of the primary and secondary mirrors are within 0.5Å, and the wavelength match of the primary and secondary mirrors are excellent.

(BL5B)

# Development and Calibration of extreme ultraviolet telescope onboard Mars orbiter

Masato Nakamura, Ichiro Yoshikawa, Yoshiyuki Takizawa,
Atsushi Yamazaki, and Kei Shiomi
Earth and Planetary Science, University of Tokyo

## 1. Our Scientific Aim

We have calibrated the ultraviolet telescope (XUV) onboard the first Japanese Mars orbiter which will be launched on July 1998. In this mission, we will measure the abundance and distribution of neutral and singly ionized helium in the Martian atmosphere. The XUV is adjusted to detect He I (58.4 nm) and He II (30.4 nm) emissions which are solar resonance scattering lines of neutral and ionized helium, respectively. The imagery of the Martian atmosphere with these emission lines will provide us important progress in planetary and magnetospheric physics.

## 2. Description of XUV

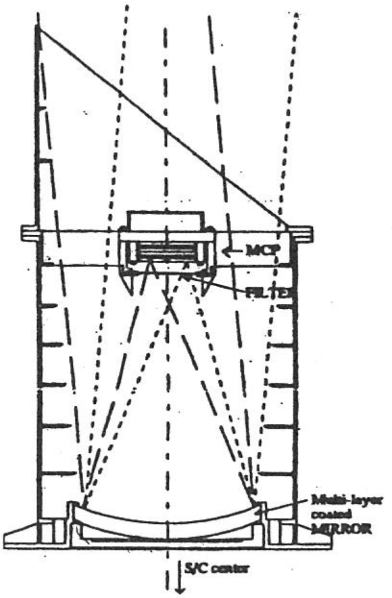

Fig. 1. The cross sectional diagram of EUV telescope onboard first Japanese Mars orbiter

The XUV consists of a spherical mirror to focus EUV lights, an Al/C filter to eliminate longer wavelength lights, and microchannel plate (MCP) to amplify the signal. The cross sectional diagram of XUV is shown in Fig. 1. The field of view is 2 degrees. The mirror's surface is multi-coated with 20 alternating pairs of Mo and Si to reflect He II (30.4 nm) and He I (58.4 nm) lights preferentially and also to reduce the contamination from shorter wavelength lights such as star lights. The Al/C filter is used to reduce longer wavelength lights such as O II (83.4 nm), H I (105.4 nm), and H I (121.6 nm) which are major strong emissions in earth's plasmasphere. The filter is separated into 2 parts. One half of it transmits He II (30.4 nm) and the other part passes He II (30.4 nm) and He I (58.4 nm).

In this year, we have calibrated the mirror, the filter, and MCP separately. The results are shown in next sections.

## 3. Optical item calibrations

At first, we measured the reflectivity of the spherical mirror and the transmittance of the Al/C metal-thin filters which had various Carbon thickness. The results are shown in Fig. 2 and 3 together with the theoretical calculations. As shown in Fig. 2, the reflectivity was above our expectation except around the 1st Bragg peak. On the other hand, the transmittances of the filters were below our calculations as shown in Fig.3. One of the probable reasons is considered to be the contamination of higher-order lights. If the differences between the results and calculations in Fig. 2 are ascribed to the contamination of higher-order lights, the EUV direct beam should be about 50% contaminated by them. Furthermore, the edge at 34 nm, which is attributed to Aluminum edge (17nm × 2), is found. If there was no contamination of higher-order lights, the edge at 34nm couldn't be found. Another possibility is in broad EUV beam from orbital radiation. The 2D image of the direct beam by the MCP with a position sensitive anode is shown in Fig. 4. The broad EUV beam is also considered to affect our results.

As a result, we qualitatively have confirmed the mirror's layer construction and filter's characteristic, because the reflective peak was found around 33nm in both calibration and theoretical data and the transmittance rapidly increased at the Aluminum edge of 17nm.

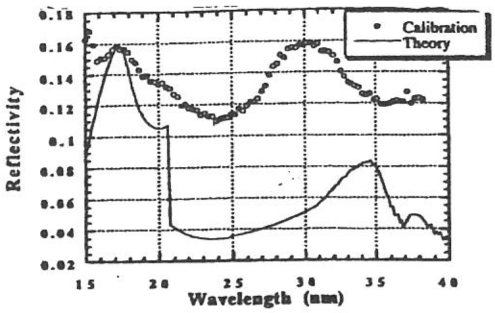

Fig. 2. The reflectivity of Mo/Si multi-layer coated mirror and theoretical calculation. Except around the 1st Bragg peak, the reflectivity is above theoretical calculation. Possible reasons are

1) contamination from higher-order lights is not negligibly small.

2) the direct EUV beam broadens rapidly after entering to the space chamber.

This problem still remains unsolved.

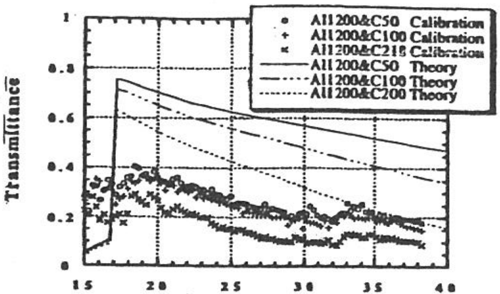

Fig. 3. The transmittance of Al/C filters. The thickness of Aluminum is 150nm, and Carbon are 5, 10, and 21.8 nm. The transmittance of three filters are all below the theoretical calculations. There is considered to be non-negligible contamination of higher-order lights, because the double edges are found at 17 (Aluminum edge) and 34 nm. If there was no contamination, the edge at 34nm couldn't be found.

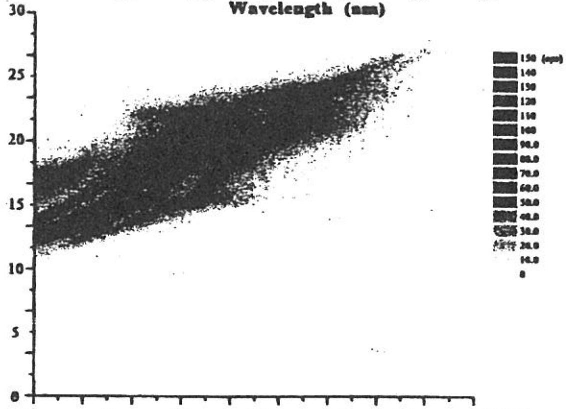

Fig. 4. The 2D image of direct beam at 30.4 nm with G3 and M4. Although we placed the pinhole of 0.5mm diameter at the entrance of chamber, direct EUV beam broadened at the center of the chamber.

Next, we have tested the MCP and high sensitive charge-amplifier onboard the satellite. We made a comparison of the characteristics between MCP with CsI coated and uncoated. Uncoated MCP was previously calibrated by using ion beam in another facilities. The pulse height of MCP-multiplied electrons for 30.4 nm lights are shown in Fig. 5 (Upper panel). As the pulse height with CsI uncoated is extremely below that with CsI coated, we confirmed the necessity of CsI coating and also determined the threshold level of charge-amplifier.

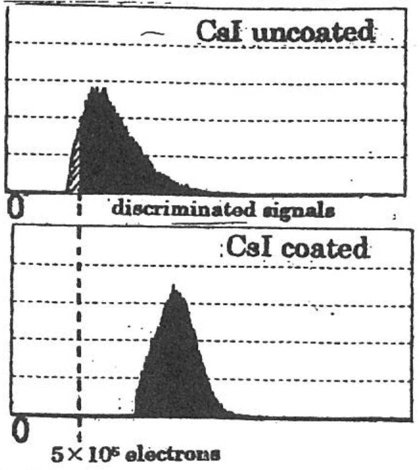

Fig. 5. The pulse height profile of MCP-multiplied electrons when injecting of 30.4nm beam and applying of 2.0kV voltage. The upper panel represents the data of MCP with CsI coated. On the other hand, the lower panel shows CsI uncoated data calibrated in another facilities. The signals in shadow area were discriminated by charge-amplifier.

## 4. Summary and Future plan

This year, we have calibrated the EUV telescope onboard the Mars orbiter. The optical items such as multi-layer coated mirrors, metal-thin filters, and MCP were calibrated separately and qualitatively. We consider it necessary to make a plan in next year based on this information. Next year, we will measure quantitatively the precise efficiency of MCP with CsI coated, and the total sensitivity of XUV. In order to measure the precise characteristics quantitatively, we will use the pinholes with suitable size, the spectroscope, and absolutely calibrated photo-diode.

The schedule in UVSOR provides us a quite important and unique opportunity for calibrating our newly developed EUV telescope.

(BL6A1) & (BL5B)

# Anisotropic optical reflection of CePdSb and LaPdSb

Raniero Pittini [a], H. Okumura, Mikihiko Ikezawa [a], Akira Ochiai [b] and Takashi Suzuki [c]

[a] *Research Institute for Scientific Measurements, Tohoku University, Sendai 980-77, Japan*
[b] *Department of Material Science and Technology, Niigata University, Niigata950-21, Japan*
[c] *Department of Physics, Faculty of Science, Tohoku University, Sendai 980-77, Japan*

CePdSb presents two main interests. On the one hand it is a low–carrier Kondo system, with a carrier concentration even lower than CeSb, because the presence of the 4d band formed from Pd states inhibits the radial overlap of the valence 5p states, originating from the 5p orbitals of the anion Sb, and therefore limits the dispersion of the valence 5p band, which overlaps only weakly with the conduction 5d band. On the other hand, CePdSb orders ferromagnetically below 17 K. We are dealing with a ferromagnet growing out from a Kondo system. In addition, this material is anisotropic, since it crystallizes in the hexagonal $CaIn_2$–type structure. In this structure, the Sb ions are alternated to Pd ions along the crystallographic axis ***c***, limiting the formation of a valence 5p band along ***c***. In fact, the electrical resistivity is strongly anisotropic and it is, yet metallic, about 3 times higher along ***c*** than in on the plane *ab*. Instead, in the reference material LaPdSb, the electrical resistivity along the ***c*** direction shows a semiconducting behavior.

We have carried out anisotropic reflectivity measurements over a wide energy range (from 0.001 to 100 eV) at several temperatures down to 15 K on CePdSb and LaPdSb using three spectrometers equipped with monochromators in Tohoku University and two IR interferometers of the types Martin–Puplett (constructed by Specac) and Michelson (made by Bruker) installed at the beam line BL6A1, as well as a VUV monochromator at BL5B of the synchrotron radiation facility of UVSOR. The obtained reflectivity spectra were then extrapolated in the IR with a Hagen–Rubens law using the values of the DC conductivity at the corresponding temperatures and on the UV side with a $\omega^{-4}$ law. Successively, the anisotropic optical functions of CePdSb and LaPdSb could be determined by a Kramers–Kronig transformation of the extrapolated reflectivity curves. These measurements were particularly difficult due to the low size of the samples and the severe light intensity losses arising from the use of a wire grid polarizer, which was used to insure a high degree of polarization of better than 99%. Only in the FIR measurements carried out at UVSOR using the Martin Puplett interferometer, no additional wire grid polarizer was used, because the degree of polarization of the synchrotron radiation was sufficient for our experiment.

The reflectivity of CePdSb shows in the plasma edge an anisotropy of factor 2 between the direction *c* and the plane *ab*. This is equivalent to a factor 4 larger ration $N/m^*$ on the *ab* plane than in ***c*** direction and compares well with the anisotropy detected in the electrical resistivity. Two TO phonons could be clearly recognized in the IR signal of CePdSb and LaPdSb, while some additional far IR absorptions still need to be clarified. Furthermore, the optical conductivity shows the signal of the interband transitions 5p (Sb) → 5d (Ce) in the visible range, as well as 5p (Ce) → 5d (Ce), 4p (Pd) → 5d (Ce) in the VUV. Also visible is the weak transition 4d (Pd) → 5p (Sb), which does not appear in LaPdSb for ***E*** // ***c***, confirming the semiconducting character of LaPdSb in ***c*** direction.

(BL6A1)

# Optical study of the $Yb_4(As_{1-x}Sb_x)_3$ system

Raniero Pittini [a], Mikihiko Ikezawa [a], Akira Ochiai [b], Hidekazu Aoki [c] and Takashi Suzuki [c]

[a] *Research Institute for Scientific Measurements, Tohoku University, Sendai 980-77, Japan*
[b] *Department of Material Science and Technology, Niigata University, Niigata950-21, Japan*
[c] *Department of Physics, Faculty of Science, Tohoku University, Sendai 980-77, Japan*

A great experimental and theoretical effort has been devoted recently to the still puzzling 'novel' heavy fermion system $Yb_4As_3$ on the borderline between insulator and semimetal. The Sb substitution for As strongly suppresses the charge ordering temperature from room temperature (for $Yb_4As_3$) to 230 K in the $Yb_4(As_{0.88}Sb_{0.12})_3$ sample, while for the $Yb_4(As_{0.71}Sb_{0.29})_3$ sample the charge ordering appears to be completely suppressed, even though a weak maximum in the resistivity at low temperatures is indicative for a charge ordering below 60 K, which takes place at least in clusters of this sample.

To achieve a deeper insight into the electronic structure of this compound and the related $Yb_4X_3$ materials, we have carried out optical reflectivity measurements over a wide energy range (from FIR to VUV) at several temperatures down to 15 K on $Yb_4(As_{0.88}Sb_{0.12})_3$ and $Yb_4(As_{0.71}Sb_{0.29})_3$ using three spectrometers equipped with monochromators in Tohoku University and two IR interferometers of the types Martin–Puplett (constructed by Specac) and Michelson (made by Bruker) installed at the beam line BL6A1 of the synchrotron radiation facility of UVSOR. The obtained reflectivity spectra were then extrapolated in the IR with a Hagen–Rubens law using the values of the DC conductivity at the corresponding temperature and on the UV side with a $\omega^{-2}$ law up to 20 eV and a $\omega^{-4}$ law for higher photon energies, following the standard procedure. Successively, the optical functions of $Yb_4(As_{0.88}Sb_{0.12})_3$ and $Yb_4(As_{0.71}Sb_{0.29})_3$ could be determined by a Kramers–Kronig transformation of the extrapolated reflectivity curves.

In the optical conductivity, the signal of the phonons is strong and a comparison with the optical conductivity of $Yb_4As_3$ allows to separate the contributions of the As-Yb-As and the Sb-Yb-Sb vibrating systems, while the mixed components As-Yb-Sb are visible but weaker. Due to the low carrier densities of these materials, the intraband contributions vanish in the background of the TO phonons. In the real space, this picture is equivalent with a free–carrier cloud screened by the vibrating polar ionic environment, leading to a partial localization of the carriers. This is just the opposite of what one usually observes in metals and semimetals, where the conduction electrons screen several physical quantities, among others the phonons. Furthermore, the interband transitions $4f^{14} \rightarrow 5d^1 4f^{13}$ can be recognized in the optical conductivity, as well as the signal from the 4p (As), 5p (Sb) and 5d (Yb) bands. This study allows to draw a preliminary picture of the energy level scheme and it is thought to yield essential information for the theories to be written for these still puzzling materials.

(BL6A1)

# Infrared and far-infrared studies of strongly correlated electronic systems: NiS and $YbB_{12}$

H. Okamura, H. Shinozaki, T. Nanba, M. Nishioka*, S. Anzai*, and F. Iga**[1]

Department of Physics, Kobe University, Kobe 657, Japan
* Faculty of Science and Technology, Keio University, Hiyoshi, Yokohama 223, Japan
** Electrotechnical Laboratory, Tsukuba, Japan.

We are currelntly studying the reflectivity spectra of NiS and $YbB_{12}$ in infrared (IR) and far-infrared (FIR) regions using BL6A1 at UVSOR, in order to obtain information about gap formations due to strong electron correlation in these materials.

NiS undergoes a metal-semiconductor (M-S) transition upon cooling through $T_c$=263 K. The resistivity increases by a factor of about 50 at the transition, and the semiconducting phase is also antiferromagnetic. The M-S transition in NiS has been studied by many workers. While early works suggested the S phase to be a Mott insulator, recent photoemission study by Fujimori *et al*[1] suggested that it is a charge transfer-type insulator. Their high-resolution photoemission study showed a small energy gap of the order of 10 meV, while earlier infrared studies by Barker and Remeika[2] showed a gap of about 120 meV. As shown in Fig. 1, our reflection spectra in IR exhibited a dip below $T_c$, which was similar to that observed by Barker and Remeika. We did not observe any significant structure in the FIR region which might correspond to the gap energy implied by photoelectron studies. This is not necessarily a contradiction, since photoemission detects a shift in the Fermi energy, while the optical study detects the total magnitude of the gap. Currently we are attempting to account for our spectra based on a charge transfer-type picture.

$YbB_{12}$ is one of the compounds known as "Kondo insulators". In $YbB_{12}$ at low temperatures, an energy gap of about 10 meV is formed near Fermi energy, due to strong correlation between the conduction and 4f electrons. In the optical study by Wachter and Travaglini [3] on polycrystalline samples, the gap formation was clearly identified as a strong suppression in the reflectivity in FIR region ($\leq 200$ cm$^{-1}$). The fact that the gap is not a conventional band gap was shown by magnetization study [4], where the gap was closed by a field of 50 T. We plan to study high-field behaviors of the gap using FIR spectroscopy. As a preliminary study, we have measured the reflectivity spectra of polycrystalline $YbB_{12}$ in FIR at zero-field. Fig. 2 shows the obtained reflection spectra at T=8, 30, 50, 78 K, divided by that at room temperature. The 8 K spectrum is very similar to that by Wachter and Travaglini[3] on a polycrystalline sample at 4.2 K. Our spectra between 8 K and 78 K show, however, that the suppression in the reflectivity occurs in two stages. Namely, as T is lowered from 78 K to 30 K, the reflectivity above 40 cm$^{-1}$ is first suppressed, then that below 40 cm$^{-1}$ is suppressed rapidly as T is furthur lowered to 8 K. This temperature dependence may imply that there are two gaps with different magnitudes, as presiously suggested.[4] Recently, single crystals of $YbB_{12}$ have become available[5], and we expect to evaluate the temperature and magnetic field dependencies of the gap more quantitatively using single crystals.

---

[1] Present address: Department of Physics, Hiroshima University, Higashi-Hiroshima 724, Japan.

# References

[1] A. Fujimori *et al.* Phys. Rev. **B42**, 620 (1990); M. Nakamura *et al.* Phys. Rev. Lett. **73**, 2891 (1994).

[2] A.S. Barker, Jr and J.P. Remeika, Phys. Rev. **B10**, 987 (1974).

[3] P. Wachter and G. Travaglini, J. Mag. Mag. Mat. **47&48**, 423 (1985).

[4] K. Sugiyama *et al*, J. Phys. Soc. Jpn. **57**, 3946 (1988).

[5] F. Iga *et al*, in preparation.

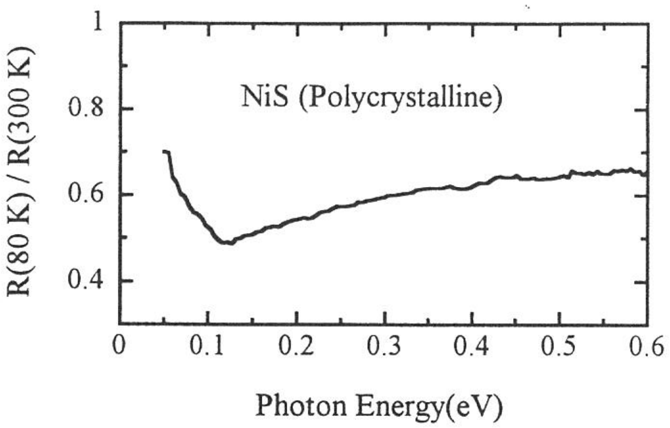

Fig. 1. Reflection spectrum of NiS at 80 K divided by that at room temperature. The dip around 0.1 eV is due to the gap formation in the semiconducting phase of NiS.

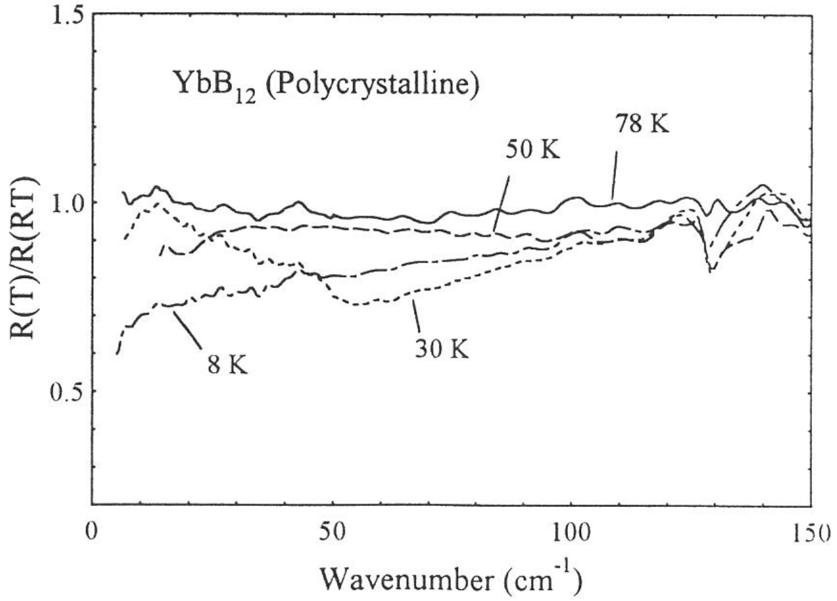

Fig. 2. Reflection spectra of YbB$_{12}$ (polycrystalline) at 8 K, 30 K, 50 K, and 78 K, divided by that at room temperature. The reflectivity below 150 cm-1 is suppressed as the temperature is lowered, which is a result of gap formation.

# Time-Resolved Infrared Spectroscopy at BL6A1

H. Okamura, S. Kimura*, T. Nanba, and M. Kamada*

Department of Physics, Kobe University, Kobe 657, Japan
* UVSOR, Institute for Moleculer Science, Okazaki 444, Japan

BL6A1, one of the two infrared beamlines at UVSOR, has recently gone through a major upgrading, with the intention of (1) extending the measurement range and (2) carrying out such experiments as time-resolved IR spectroscopy and surface IR spectroscopy, which take advantage of unique characteristics of the SR (pulsed broad-band IR source, high brilliance).[1] The upgrade included the introduction of a rapid-scan FT-IR spectrometer (Bruker IFS66v), which can record a time-resolved (TR) IR spectrum with a time-resolution of 5 nsec. As a test for the TR feature, we tried to record the temporal profile of the SR in IR region. The detector was a photovoltaic MCT (HgCdTe) detector (Broward Inc.) combined with an AC-coupled pre-amplifier (Broward Inc.).

Measurements were done in step-scan mode. While scanning the position of the movable mirror, the temporal profile of the signal through the interferrometer was recorded at each scanning position. After completing a scan, the data (the intensity as functions of time and mirror position ) were re-organized and FFT was performed at each time slice. An example of the resulting data is shown in Fig. 1. The time needed to record the spectra was approximately 8 min (for the acquisition parameters, see the figure caption), and the signal-to-noise ratio can be improved by taking more scans and averaging them.

Figure 2 shows the temporal response at $\nu = 1400$ cm$^{-1}$. The actual temporal width of the SR pulse is about 0.4 nsec, hence from Fig. 2 the overall response of the system is estimated to be about 20 nsec (limited by the response of MCT.).

Future plans for time-resolved IR spectroscopies also include pump-probe experiments (pumping a sample by an external source such as pulsed lasers synchronized with SR, then probing it with the IR pulses from SR).

## References

[1] M. Sakurai, H. Okamura, K. Watanabe, N Hiraoka, T. Nanba, S. Kimura, and M. Kamada, UVSOR Annual Report 1995, p174.

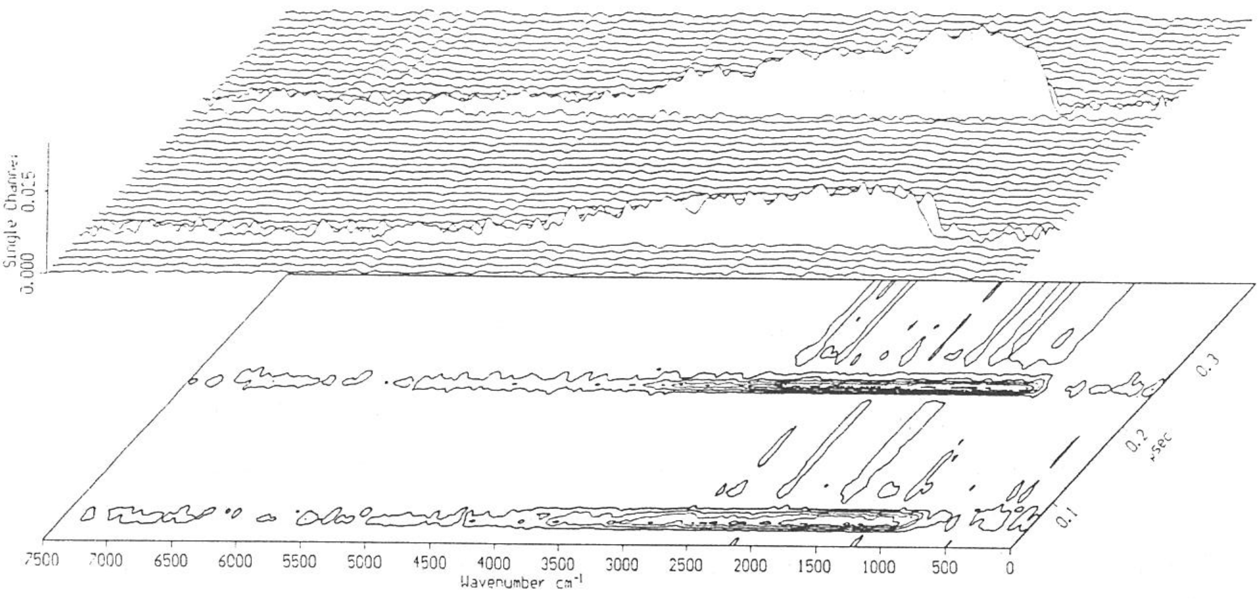

Fig. 1. Time-resolved infrared spectra of SR measured at BL6A1, UVSOR, under a single-bunch operation (25 mA beam current). The time interval between two consecutive spectra is 10 nsec. A KBr beam-splitter was used in the spectrometer, and a photovoltaic MCT detector was used to record the signal.

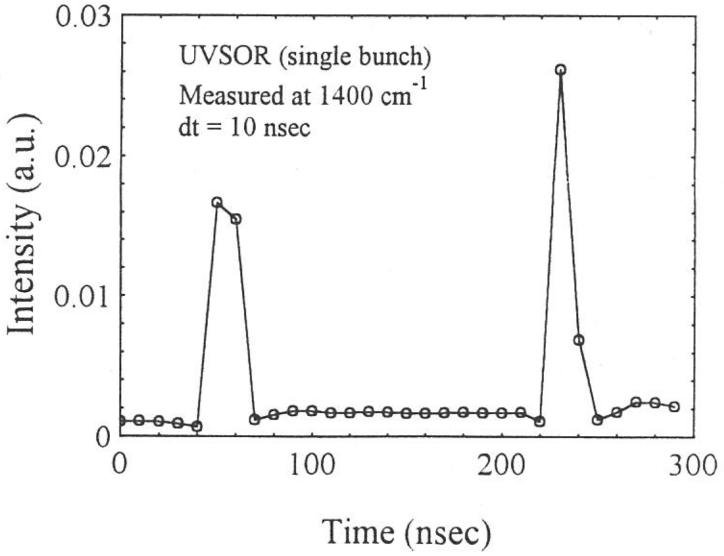

Fig. 2. Temporal profile of SR at 1400 cm-1, which is taken from Fig. 1.

(BL6A1)

# Development of Far-infrared reflection measurement system under high pressure using diamond anvil cell

Takao NANBA, Nozomu HIRAOKA and Shuhji KAGA

*Department of Physics, Faculty of Science,*
*Kobe University, Kobe 657*

Far infrared spectroscopy under high pressure in the range of several GPa requires a photon beam with very low *etendue* because the small aperture in a diamond anvil cell. The advantage of synchrotron radiation (SR) with high brilliance makes them possible to perform. A few years ago, we started the development of the transmission measurement system at the BL6A1 and successfully demonstrated the clear results on the change in the phonon spectrum of microcrystals with pressure[1]. This year we started another project to develop a reflection measurement system on solids under high pressure using a diamond anvil cell. In the optical configuration of reflection measurement, the high brilliance of the SR is required to detect the signal from the small sample surface in the pressure cell.

Fig.1 shows the reflection spectrum of KCl single crystal; KCl in DAC (*a*) and a large single crystal (*b*) at atmospheric pressure at room temperature. A large peak in both spectra corresponds to a *TO* phonon mode. In a DAC the continuous background of the spectrum is superposed on the reflection spectrum of KCl in contrast to that of a large KCl. This is due to the direct reflection of the incident photon beam from the surface of the diamond window of the DAC. We obtained the “true” reflection spectrum of KCl in DAC by separately measuring the reflected photon intensity of the DAC only filled with a pressure transmitting material (Apiezon grease ) and by subtracting it from the observed spectral intensity of KCl in DAC. The result is shown in Fig.2. The dielectric constant $\varepsilon$ ($\varepsilon$ 1, $\varepsilon$ 2) of Kcl under pressure was reduced from the K-K transformation of the reflection spectra and shown in Fig.3. The peak positions of the TO and LO phonon are plotted with pressure in Fig.4. The energy position of the LO phonon is given by the condition of $\varepsilon_1(\omega_{\mathrm{LO}}) = 0$. The TO phonon energy showed a blue shift with pressure up to 2.2 GPa and a sudden decrease at the pressure of 3.3 GPa. This sudden decrease in energy corresponds to the occurrence of the structural phase transition (B1-B2 transition) of KCl.

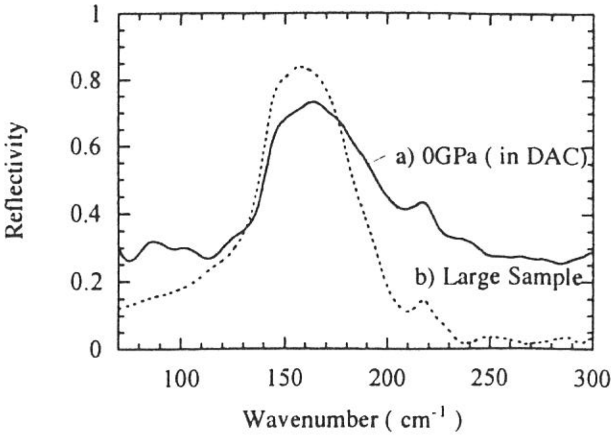

Fig.1

The reflection spectrum of KCl single crystal; KCl in DAC (*a*) and a large single crystal (*b*) at atmospheric pressure at RT.

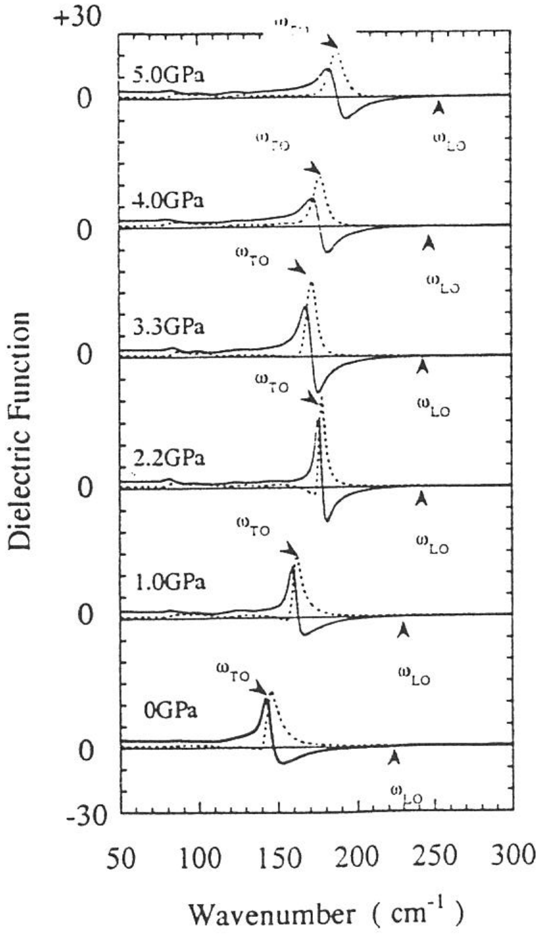

Fig.3

Dielectric function of KCl under pressure.

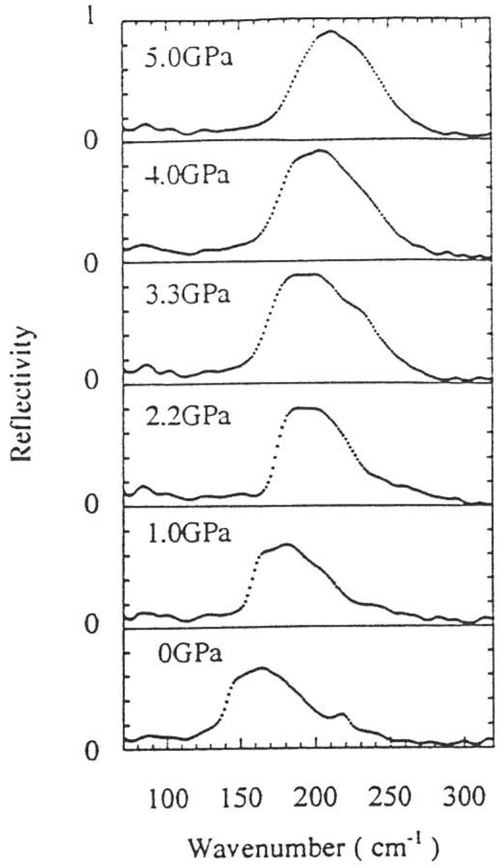

Fig.2

Development of the reflection spectra of KCl with pressure at RT in DAC.

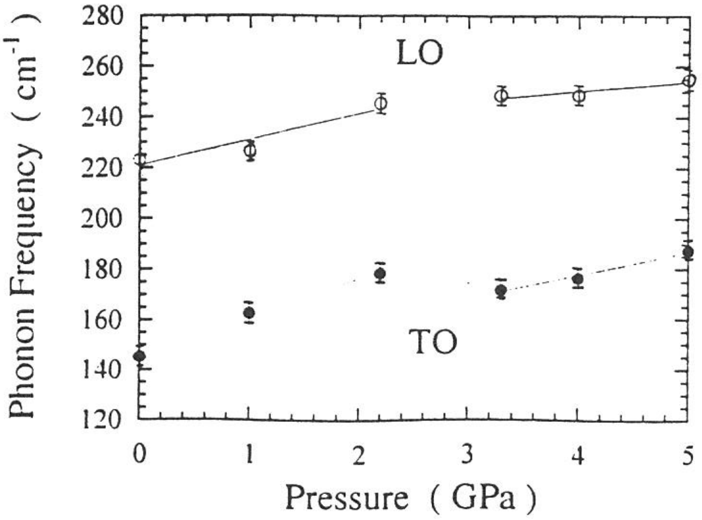

Fig.4

Plotting of the energy positions of TO and LO phonons with pressure.

(BL6A1)

# Metal-insulator Transition of SmTe crystal under high pressure

Nozomu HIRAOKA, Takao NANBA, and Shuhji KAGA

*Department of Physics, Faculty of Science,*
*Kobe University, Kobe 657*

SmTe is a divalent compound. The electronic configuration is $Sm^{2+}$: $(4f)^6(5d)^0(6s)^0$ and $Te^{2-}$:$(5s)^2$,$(5p)^6$ . The conduction band is composed of Sm6s and 5d electrons and the valence band is of Sm 4f and Te 5p. In conduction band the Sm 5d state suffers from a crystal field splitting into $t_{2g}$ and $e_g$ which are separated by 10Dq. Then, SmTe is non-magnetic and shows a semiconductor-like properties which possesses a energy band gap of about 0.6 eV[1,2]. According the volume compression data[3], SmTe undergoes the valence transformation from $Sm^{2+}$ to $Sm^{3+}$ in the pressure range of P=3-5 GPa which change SmTe to a metal and finally exhibits a structural phase transition from the NaCl to the CsCl type at 11 GPa. The change of the electric resistivity of SmTe with temperature as function of pressure was measured by Kwon *et al*[4].

We measured the far-infrared transmission and reflection spectrum of SmTe under pressure in order to directly observe the closing of the band gap. Pressure works to enlarge the crystal splitting which leads to the enhancement of the mixing between the 4f and 5d state. Fig.1 shows the transmission spectra of SmTe under pressure at room temperature. The intensity of the transmission light in the energy range of 90-160 cm-1 is almost zero because of the strong absorption by the TO phonon. At 3 GPa, the transmission intensity almost zero in the whole region. This means the closing of the energy gap. We measured also the reflection spectrum under pressure. Fig.2 shows the development of the reflection spectra of SmTe with pressure. The peak in each spectrum corresponds to the reststrahlen band of SmTe which means SmTe to be semiconductor. With pressure the peak structure becomes weak and at P=5.0 GPa the structureless continuous spectrum appeared instead of the reststrahlen band. This metallic reflectivity means that SmTe turned to be metallic.

**References**

[1] A.Jayaraman et al; P.R.B9(6)(1974)2513.
[2] B.Batlog et al; P.R.B14(12)(1976)5503.
[3] Y.S.Kwon et al; Physica B206&207(1995)389.

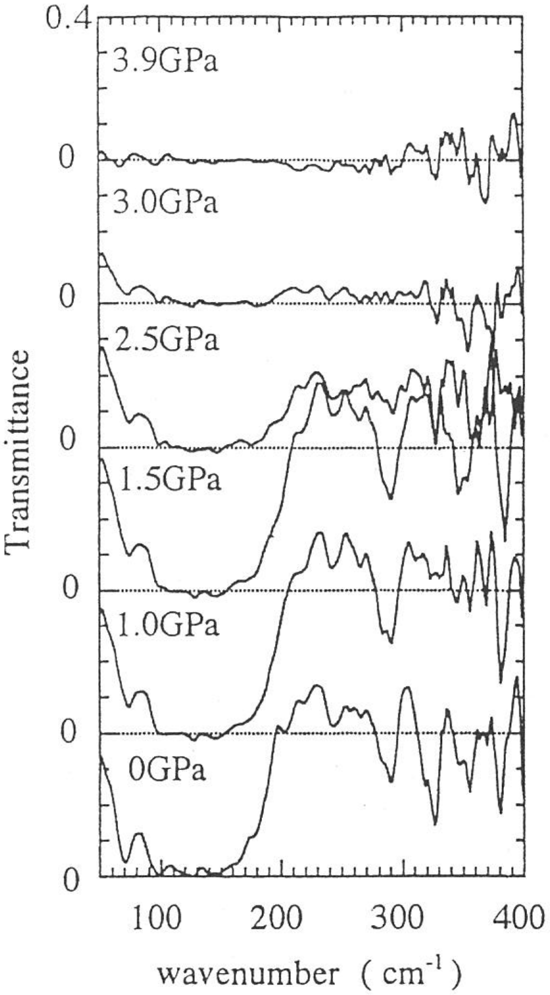

Fig.1

Development of transmission spectra of SmTe at room temperature with pressure.

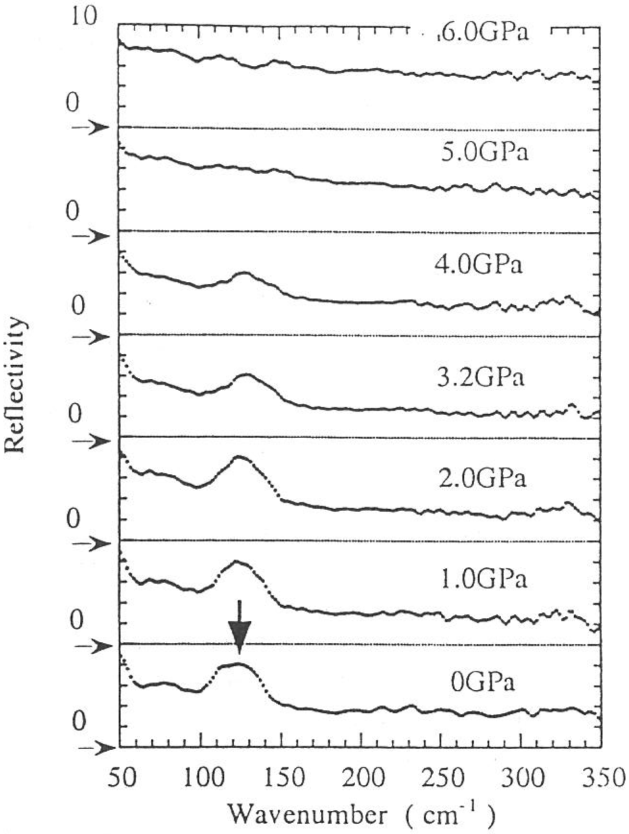

Fig.2

Development of reflection spectra of SmTe with pressure.

(BL6A1)

# Magneto-Optical Apparatus in Infrared Region

Shin-ichi KIMURA

*UVSOR Facility, Institute for Molecular Science, Okazaki 444*

Correlation between magnetic moments and carriers is one of most important problems in solid state physics. Materials with strongly correlated electrons are investigated by using several experimental methods in the world. Up to now, we have been studying electronic structure which is made by many body effect near the Fermi level. For instance, CeAs [1] and $Yb_4As_3$ [2], which show heavy fermion like character in spite of the low carrier density, were observed to have conduction with long relaxation time. On the other hand, Carriers of $Gd_{3-x}\square_xS_4$ ($\square$ denotes vacancy and $x \approx 1/3$) are known to become magnetic polarons which are trapped by potential walls due to defects at low temperature. The trapped state was directly observed as an energy gap by optical measurement [3]. The energy gap is collapsed by magnetic field of 3 T, i. e., the material shows nonmetal-to-metal transition by magnetic field. The collapse process was observed by optical measurement [4].

Infrared magneto-optical (IRMO) apparatus was constructed in an infrared beam line, BL6A1, for the measurement of electronic structures with magnetic moments near the Fermi level. The main purpose is to measure infrared magnetic circular dichroism (IRMCD) using circularly polarized synchrotron radiation (SR). Circularly polarized light can be obtained from off-axis SR from a bending magnet. According to my calculation, circularly polarized infrared light with the helicity of 60 % or higher can be obtained in the energy range of 1 meV - 1 eV in BL6A1.

Before the measurement of IRMCD, temperature and magnetic field dependence of reflectivity spectra can be measured by using the IRMO apparatus. Until now, our reflectivity measurements were temperature dependence at 0 T in the energy range of 1 meV - 40 eV and magnetic field dependence at 14 K in the energy range of 1 - 30 meV. I combined these measurements in IRMO apparatus. The first experimental result is presented in a separate paper [5].

A top view of the constructed IRMO apparatus is shown in Figure and the parameter is written in Table. I will continue to measure temperature and magnetic field dependence of optical spectra and IRMCD of strongly correlated electron systems.

I would like to thank Prof. Ikezawa and technical staff of Research Institute for Scientific Measurements, Tohoku University for making parabolic mirrors and also UVSOR staff for their technical support.

## References

[1] S. Kimura, F. Arai, T. Suzuki, Y. Haga and M. Ikezawa, Physica B **206&207** (1995) 780.

[2] S. Kimura, M. Ikezawa, A. Ochiai and T. Suzuki, J. Phys. Soc. Jpn. **65** (1996) 3591.

[3] S. Kimura, F. Arai, T. Suzuki and M. Ikezawa, J. Phys. Soc. Jpn. **62** (1993) 4331.

[4] S. Kimura. Y. Sato, T. Suzuki and M. Ikezawa, J. Phys. Soc. Jpn. **64** (1995) 200.

[5] S. Kimura, D. X. Li, Y. Haga and T. Suzuki, in this report.

| Superconducting magnet | (Oxford SM1000-8S) |
|---|---|
| Magnetic field | 8T (at magnet temp. of 2K)<br>6T (at magnet temp. of 4.2K) |
| Bore diameter at R.T. | ϕ 78mm |
| Cryostat | Liquid He continuous flow type |
| Temperature range | 10 - 300K |
| Temperature controller<br>(SI-9650-7) | $RuO_2$ diode sensor<br>Manganin wire heater |
| Sample size | ϕ 2, 3, 4 mm |
| Vacuum level around sample | $< 5\times10^{-8}$ mbar |

**Table.** Parameters of IRMO apparatus.

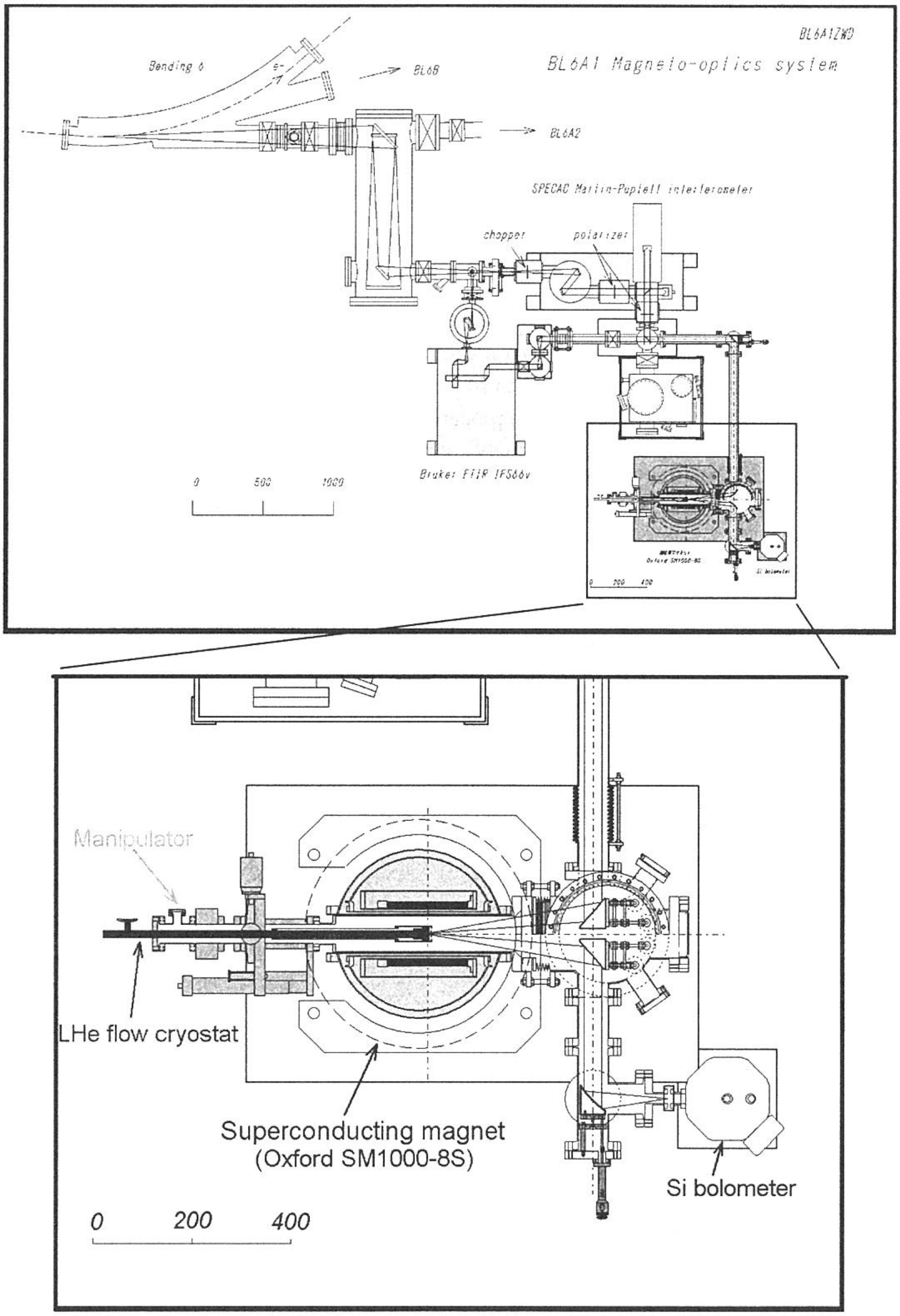

**Figure.** Top view of BL6A1 after installation of IRMO apparatus (upper figure) and magnified IRMO apparatus (lower one).

(BL6A1)

# Magnetic Field and Temperature Dependences of Low Energy Excitation in GdAs

Shin-ichi KIMURA, Dexin LI [1], Yoshinori HAGA [2] and Takashi SUZUKI [3]

*UVSOR Facility, Institute for Molecular Science, Okazaki 444*
[1] *Oarai Branch, Institute for Material Research, Tohoku University, Oarai 311-13*
[2] *Advanced Science Research Center, Japan Atomic Energy Research Institute, Tokai 319-11*
[3] *Department of Physics, Tohoku University, Sendai 980-77*

Stoichiometric and nonstoichiometric GdAs also have different physical properties from each other [1]. Stoichiometric GdAs is an antiferromagnetic material with the Néel temperature of 18.7 K. However nonstoichiometric GdAs is a ferromagnetic material with the Curie temperature of -11.5 K. The origin of the ferromagnetic is explained to be the creation of a magnetic polaron in which carriers are trapped by defects. On the contrary, stoichiometric GdAs is thought to be a self-trapped magnetic polaron but the evidence has not been observed. The physical properties are thought to come from the electronic structure near the Fermi level. So we measured reflectivity spectra of stoichiometric GdAs with parameters of temperature and magnetic field in the infrared region.

The temperature and magnetic field dependences of reflectivity spectra were measured in the photon energy range of 0.005 - 0.8 eV in BL6A1. The experiment was done by using an infrared magneto-optical apparatus which has been recently constructed [2]. The temperature range was 16 - 400 K at 0 T and the magnetic field was applied up to 6 T below 80 K.

The obtained reflectivity spectra with temperature dependence at 0 T is shown in Fig. 1. An absorption due to carriers appears below 20 meV. The shape can be almost explained by a Drude model using the results of the resistivity and the Hall effect. A shoulder and a peak appear at 0.3 eV and 0.4 eV, respectively. The peak at 0.4 eV shows strong temperature dependence.

The temperature dependence of optical conductivity spectra, which are derived from the Kramers-Kronig transformation of the reflectivity spectrum, in the energy range of 0.3 - 0.54 eV are shown in Fig. 2 (a). The intensity (effective electron number; $N_{eff}$) and the width are plotted in Fig. 2 (b). $N_{eff}$ can be estimated by the integration of an optical conductivity spectrum. The intensity linearly decreases as the temperature increases. The intensity at 400 K is less than half of that at 0 K. If an absorption originates from a normal band-to-band transition, the intensity should not change. Therefore the electronic state is considered to become large as the temperature decreases.

The width of the peak at 0.4 eV also changes linearly with the temperature. The coefficient of the fitted function is $0.31k$, where $k$ is the Boltzman constant of $8.62\times10^{-5}$ eV / K. If thermal broadening occurs, the coefficient should be $2k$ or higher. Therefore the broadening of 0.4 eV peak is much less than thermal one.

The spectrum at 16 K is in the antiferromagnetic phase. However the transition effect does not appear.

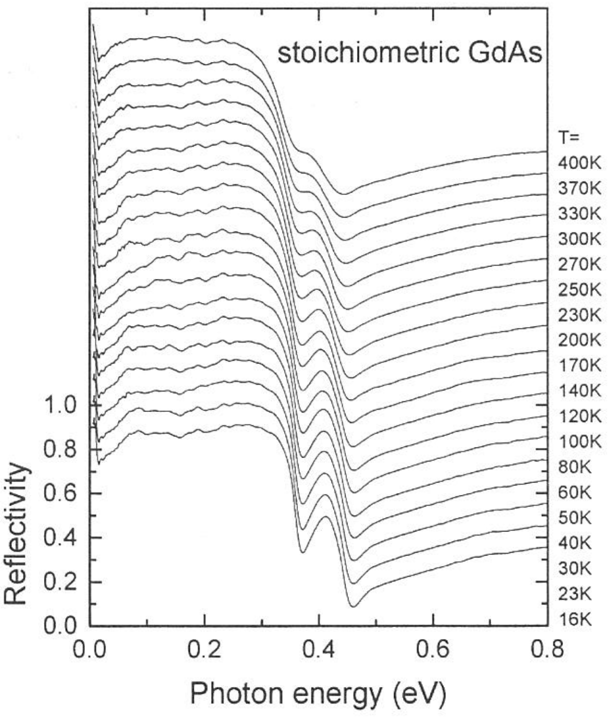

**Fig. 1.** Temperature dependence of reflectivity spectra of GdAs.

The magnetic field dependence of the peak at 0.4 eV at several temperatures is shown in Fig. 3 (a). The peak is reduced by magnetic field. The $N_{eff}$ of the peak is plotted as the functions of temperature and magnetic field in Fig. 3 (b). The $N_{eff}$ decreases almost linearly as the temperature increases below 2 T. However, a dip structure appears around 30 K above 3 T. The origin of the dip is unknown but the peak has strong magnetic field dependence. Anyway this result indicates that the electronic structure which makes the peak has magnetic moments and the magnetic field dependence of the electronic structure changes with the temperature.

## References

[1] D. X. Li, Y. Haga, H. Shida, T. Suzuki, T. Koide and G. Kido, Phys. Rev. B **53** (1996) 8473.

[2] S. Kimura, in this issue.

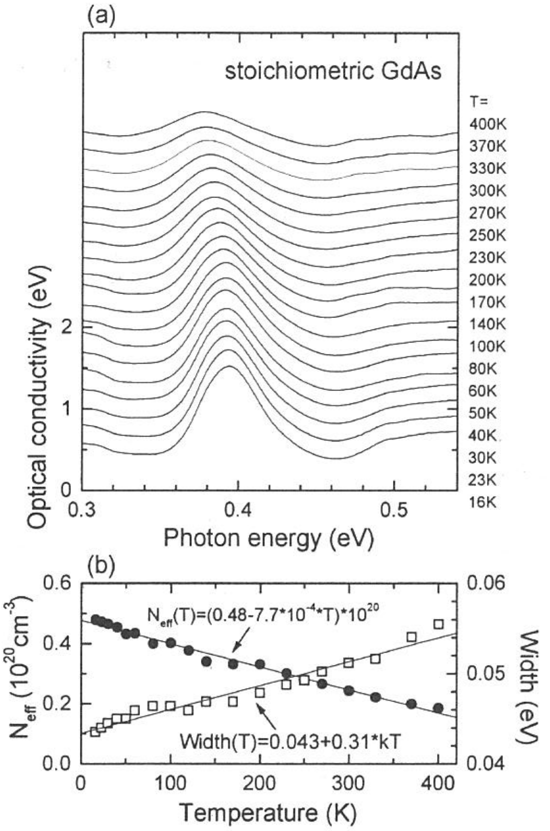

**Fig. 2.** (a) Temperature dependence of optical conductivity spectra of 0.4 eV peak of GdAs. (b) Effective electron number and the peak width of 0.4 eV absorption as the function of temperature. *k* means the Boltzman constant.

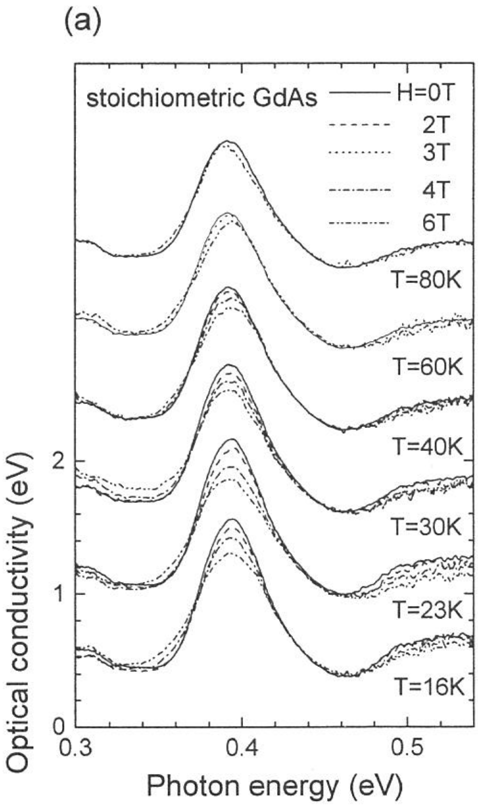

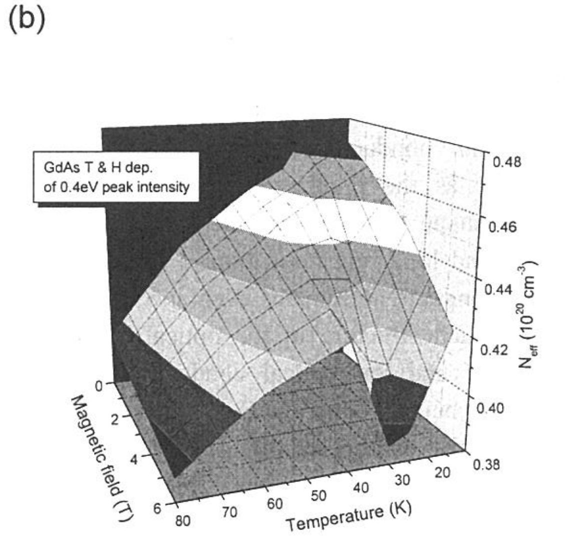

**Fig. 3.** (a) Temperature and magnetic field dependences of optical conductivity of the peak at 0.4 eV of GdAs. (b) Effective electron number ($N_{eff}$) as the functions of temperature and magnetic field.

(BL6A1)

# Low Energy Excitation of $Yb_4As_3$

Shin-ichi KIMURA, Akira OCHIAI[1], and Takashi SUZUKI[2]

*UVSOR Facility, Institute for Molecular Science, Okazaki 444*
*[1]Department of Material Science and Technology, Niigata University, Niigata 950-21*
*[2]Department of Physics, Tohoku University, Sendai 980-77*

Physical properties of $Yb_4As_3$ have been investigated by many experiments [1] and theories [2] over a past decade. $Yb_4As_3$ is considered to be not only a mixed valence material with the mean valence of 2.25 but also a heavy fermion with low carrier density. The unique temperature dependences of the resistivity and the Hall coefficient are explained by a four-band model proposed by Ochiai *et al.* [1] and by a two-band model by Kasuya. [2] There are considered to be a hole band which consists of As 4p and a high density band of Yb 4f states which is made by a large $\gamma$ value of the specific heat in both of these models.

Our purpose is to understand the electronic structure which makes anomalous physical properties as mentioned above. We measure the reflectivity spectra in wide photon energy range from far-infrared to vacuum-ultraviolet and get the information of the electronic structure.

In this study, we measured the reflectivity spectra of $Yb_4As_3$ in the photon energy range from 2 meV to 50 eV at several temperatures of 39 - 320 K and observed an absorption band which strongly changes with the temperature at 0.4 eV. The measurement below 1 eV was done using BL6A1. The sample was polished by emery papers and soft leather with rouge in He gas atmosphere to avoid surface oxidation. Since the sample surface becomes a little rough after polishing, a correction for the reflectivity was made by an Au film evaporated to the $Yb_4As_3$ sample. The size of the sample surface was 4 mm diameter.

The electronic structure is analyzed using the optical conductivity spectra, which were derived from the Kramers-Kronig transformation of reflectivity spectra, shown in Fig. 1. A peak appears at 1.1 eV. The origin is considered to be due to the transition of $Yb^{2+}$-$4f^{14}$ $5d^0$ + $h\upsilon \rightarrow$ $Yb^{2+}$-$4f^{13}$ $5d^1$ because the similar structure is observed in other Yb-compounds. [3] Several peaks around 0.02 eV come from optical phonons.

The absorption below 0.8 eV strongly changes with the temperature. At 39 K, a peak is not only observed at 0.4 eV but also a Drude-like optical conductivity appears below 10 meV. The intensity of optical conductivity of a Drude function decreases as the photon energy increases. The spectral shape indicates that the carrier has a little density and long relaxation time. The Drude like optical conductivity remains even at 85 K. Above 140 K, such structure in the optical conductivity disappears and the optical conductivity becomes almost flat below 10 meV. From the spectral shape at 39 K, the carrier density is very low and the relaxation time is very long. The situation is similar to the other heavy fermion materials. [4]

On the other hand, it is observed that the spectral weight at 0.4 eV moves to the lower energy side as the temperature increases in Fig. 1. At 39 K, a peak is located at 0.4 eV. The peak shifts to the lower energy part and also becomes broad as the temperature increases. The peak energy and the

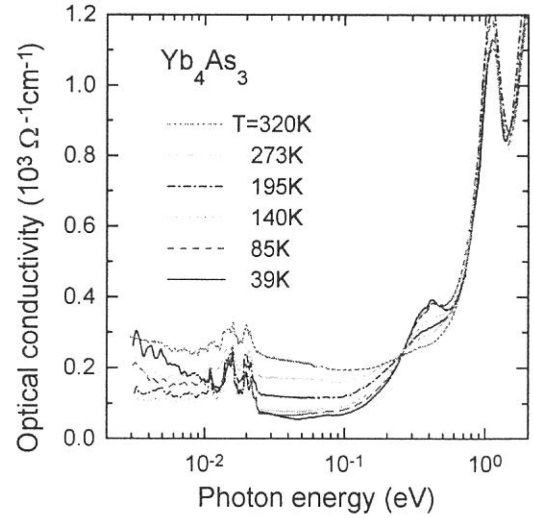

**Fig. 1.** Temperature dependence of optical conductivity spectrum of $Yb_4As_3$ in the photon energy range of 2 meV - 2 eV at temperatures of 39, 85, 140, 195, 273 and 320 K.

half width are plotted in Fig. 2. Below 100 K, both of the peak energy and the half width change little with the temperature, but the peak energy goes down and the half width becomes large as the temperature increases above 100 K. The absorption band crosses the zero photon energy around the temperature of 200 K because the peak energy becomes equal to the half width at the temperature. This means that the electronic state which makes the peak at 0.4 eV crosses the Fermi level around 200 K.

The background intensity of the optical conductivity around 0.1 eV does not change below 140 K. Above 140 K, the back ground intensity increases rapidly and seems to become a part of absorption due to carriers. According to the effective electron number spectrum as the function of the photon energy in Fig. 3, the sum rule of the optical absorption almost completes at 0.6 eV. This means that the absorption band at 0.4 eV at 39 K only moves to the low energy side as the temperature increases.

The origin of the absorption band at 0.4 eV should be considered. From a high resolution photoemission measurement of $Yb_4As_3$ by Suga *et al.*, the corresponding peak is not observed below the binding energy of $Yb^{2+}$-$4f_{7/2}$ peak. [5] Therefore the absorption band is considered to come from the unoccupied state. The most plausible origin is a mixing band of $Yb^{3+}$-4f and Yb-5d. The mixing band is considered to have a strong temperature dependence. The situation is considered to be an opposite case to strongly correlated Ce compounds. Therefore it is thought that the mixing band is important to understand the anomalous temperature dependence of the physical properties.

## References

[1] A. Ochiai, T. Suzuki and T. Kasuya, J. Phys. Soc. Jpn. **59** (1990) 4129.
[2] T. Kasuya, J. Phys. Soc. Jpn. **63** (1994) 843.
[3] S. Kimura, T. Nanba, S. Kunii and T. Kasuya, J. Phys. Soc. Jpn. **61** (1992) 371.
[4] S. Kimura, F. Arai, Y. Haga, T. Suzuki and M. Ikezawa, Physica B **206&207** (1995) 780.
[5] S. Suga et al., unpublished data.

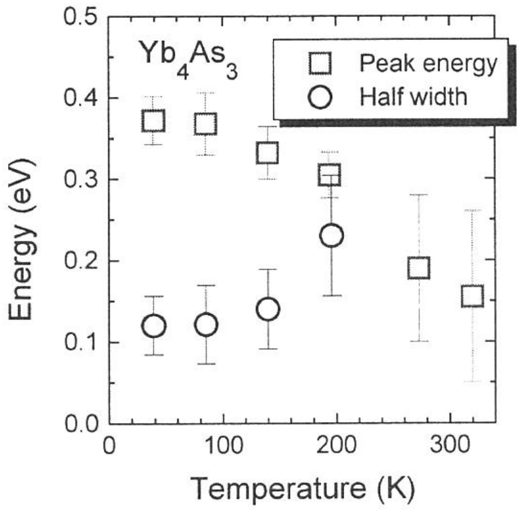

**Fig. 2.** Temperature dependence of the peak energy and the half width of the absorption band at the photon energy of 0.4 eV.

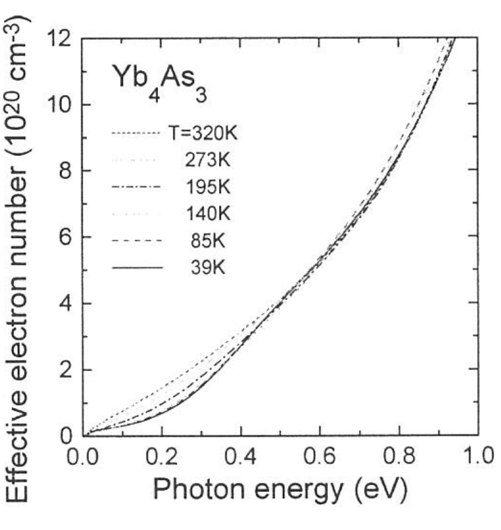

**Fig. 3.** Temperature dependence of the effective electron number spectrum of $Yb_4As_3$ as the function of photon energy.

(BL6A1)

# Optical Properties of $LaTe_2$ and $CeTe_2$

M. H. Jung, Y. S. Kwon, T. Kinoshita[a)] and S. Kimura[a)]

*Department of Physics, Sung Kyun Kwan University, Suwon 440-746, South Korea*
*[a)]Institute of Molecular Science, Myodaiji, Okazaki 444, Japan*

The near normal reflectivity spectra for the single crystals of $LaTe_2$ and $CeTe_2$, which is shown in Fig. 1 and Fig.2, are measured at several temperatures in the photon energy range from 2meV to 10.78eV. The optical conductivity spectra, which is shown in Fig. 3 and Fig.4, are obtained by the Kramers-Kronig transformation of the reflectivity spectra.

As shown in Fig. 3 and Fig. 4, all of the resolved peaks denoted *A* to *I* are nearly similar each other except the *J* and *K* peaks around 2eV and 5.8eV in $CeTe_2$. Note that because the intensity of the peaks *A* and *C* is very weak, these peaks seem to be masked by the intense peaks *J* and *K* in $CeTe_2$. Let us consider at first the common peak structures in the interband transition range. The peak positions are at about 3eV for *A*-peak, 4eV for *B*-peak, 7eV for *C*-peak, 7.6eV for *D*-peak, 9eV for *E*-peak, 0.46eV for *F*-peak and 0.75eV for *G*-peak. The broad-peak structures labelled *A* to *E* are thought to be related to the crystal field splitting of 5d band. This is reasonable in the following several facts. The 5d band in the rare-earth monotellurides such as LaTe, CeTe and so on is well known to be splitted into the double bands, $d(t_{2g})$ and $d(e_g)$, of which splitting is about 2eV, and the transitions from the valence p-band to the 5d-bands are shown above 5eV[1]. In $LaTe_2$ and $CeTe_2$, however, the crystal field splitting is expected to be more than two because the structure of these materials has the tetragonal symmetry. Here, there is a puzzling question that the splitted energy range becomes broader from 3 to 10eV. According to the results of transport properties, $CeTe_2$ is an extremely low carrier system, which leads the weak screening effect and the large splitting of crystal field[2]. On this respect, the peaks *A*, *B*, *C*, *D* and *E* are thought to be due to the interband transitions from the valence p-band to the conduction d-bands splitted through the strong crystal field with the bad symmetry.

Next, it is thought that the peaks *F* and *G* are due to the p-d transition mentioned above, or may be a virtual exciton because these materials are extremely low carrier systems. The peaks due to excitons, however, are known to become stronger while these peaks become weaker as the temperature decreases. To clarify this mechanism, more experimental and theoretical research is needed.

In the spectrum of $CeTe_2$, the intense peaks named *J* and *K* which do not be shown in $LaTe_2$ are observed at about 2eV and 5.6eV, respectively. Since $LaTe_2$ has no 4f electron, these peaks are thought to be related to the 4f electron. However, we cannot know where the occupied 4f level of $CeTe_2$ is located below the Fermi level because of no detail experimental measurements such as XPS, UPS and so on. The Ce-ion of $CeTe_2$ is trivalent according to the slope of magnetic susceptibility[3]. This means that $CeTe_2$ has no valence fluctuation and the 4f level is not located on the Fermi level. The occupied 4f level in almost all of the rare-earth compounds such as the monopnictides is observed at about 1eV below the Fermi level[4]. It means that the peaks due to the interband transition from the occupied 4f state to the conduction 5d band shoud be shown above 1eV. Therefore, the peaks *J* and *K* in $CeTe_2$ seem to be due to the f-d transition.

In Fig. 4, it is important to notice a hump around 0.2eV which does not be shown in $LaTe_2$. This hump is thought to be due to the transition from the trivalent 4f level to the exciton which is due to the f-d transition, or be due to the absorption which is due to the scattering between the conduction electrons and the localized 4f magnetic moments similar to the rare-earth monopnictides[5]. In the spectra of Fig. 4, the two additional peaks denoted *H* and *I* seem to be due to the phonon. To clarify this phenomenon, we need a theoretical calculation and the experimental measurements such as neutron scattering and so on.

References

[1] Y.S.Kwon, T.Suzuki and T.Kasuya : Jpn.J.Appl.Phys, 8 (1993) 104.
[2] M.H.Jung, Y.S.Kwon and T.Suzuki : Physica B to be published.
[3] Y.S.Kwon, T.S.Park, K.R.Lee, J.M.Kim, Y.Haga and T.Suzuki : J.Magn.Magn.Mater, 140-144 (1995) 1117.
[4] H.Takahash and T.Kasuya : J.Phys.C, 18 (1985) 2697.
[5] Y. S.Kwon, M.H.Jung, K.R.Lee, S.Kimura and T.Suzuki : Physica B to be published.

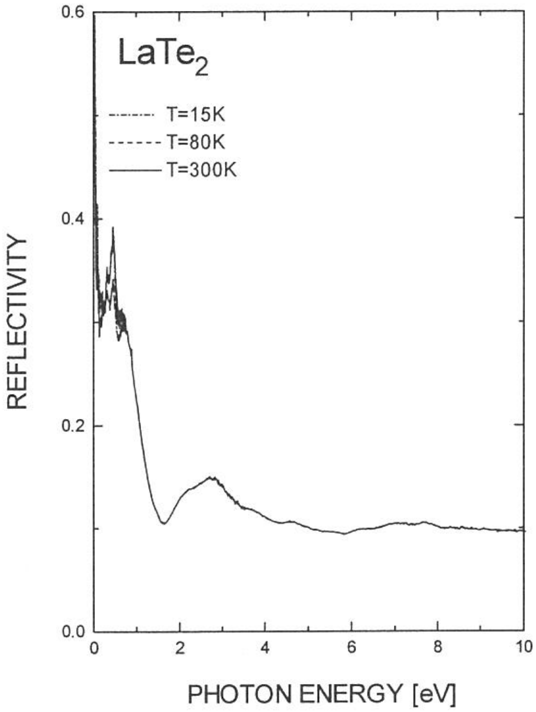

Fig. 1. Energy dependence of reflectivities R under several temperatures for $LaTe_2$ : R above 1eV is plotted at 300K.

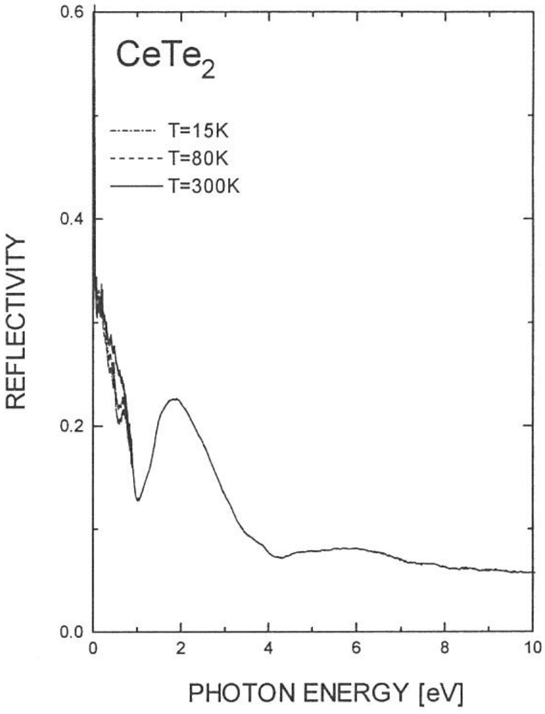

Fig. 2. Energy dependence of reflectivities R under several temperatures for $CeTe_2$ : R above 1eV is plotted at 300K

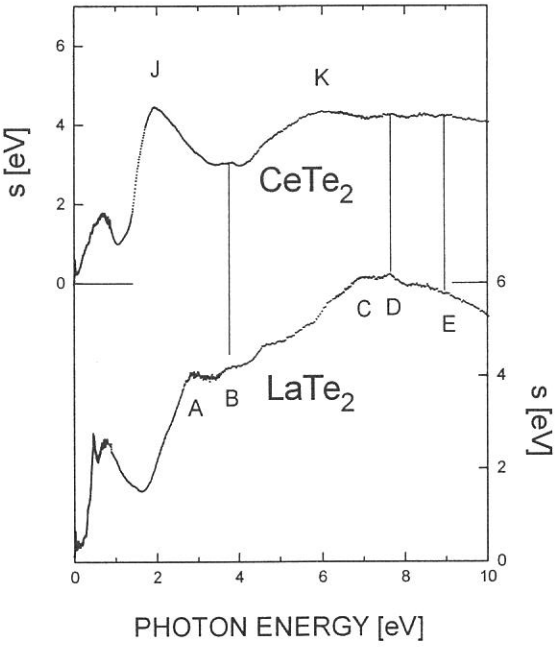

Fig. 3. Optical conductivities σ of $LaTe_2$ and $CeTe_2$ in higher energy region at 300K.

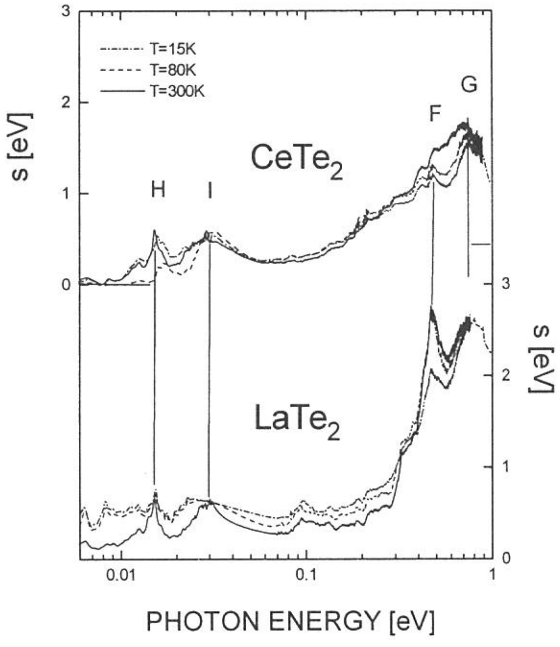

Fig. 4. Optical conductivities σ of $LaTe_2$ and $CeTe_2$ in lower energy region at several temperatures on the logarithmic scale of photon energy.

(BL6A1)

# Reflection spectra of $Ca_{1-x}Y_xTiO_3$ single crystals in the IR region

K.Ueda, H. Yanagi, M.Mizuguchi and H.Kawazoe
Research Laboratory of Engineering Materials, Tokyo Institute of Technology
4259 Nagatsuta, Midori-ku, Yokohama 226, Japan

N.Ueda and H.Hosono
Institute for Molecular Science
Myodaiji, Okazaki 444, Japan

Understanding of chemical states of dopants in oxide semiconductors is very important because the chemical states significantly influence on the electrical properties. In addition, understanding of states of the matrix substances such as electronic structure or lattice vibration is also important because they are closely correlated with the chemical states of the dopants.

Optical spectra of oxide semiconductors in the IR or FIR region give us useful information about energy levels of dopants, carrier densities and lattice vibrations of the matrix substance. The energy levels of dopants are directly observed in the FIR region. The plasma oscillation of the carriers results in the optical absorption or reflection in the FIR-IR region. The changes in the lattice vibrations by doping are also observed in the FIR-IR region. In order to obtain these observations for a typical doped semiconductor, reflection spectra of $Ca_{1-x}Y_xTiO_3$ ( $x=0$, $10^{-3}$, $10^{-2}$ ) single crystals were measured at BL6A1 in UVSOR.

Single crystals were grown by the FZ method using an infrared radiation furnace. The crystals were cut in the shape of a plate and the surfaces were polished using diamond slurry. The plate shaped single crystals were set so that the incident angle of light was about 10 degrees in order to simulate the normal incident reflection. The direction of the incident light to $Ca_{1-x}Y_xTiO_3$ crystals was normal to (100) planes. The reflection spectra were measured at liquid nitrogen temperature in two regions, FIR and IR regions. The FIR reflection spectra were measured in the range from 50 to 250cm$^{-1}$ and the IR reflection spectra were done from 450 to 5000cm$^{-1}$. The radiation light from UVSOR was used as light source for the FIR reflection measurement and the globar lamp in the conventional spectrometer installed in the beam line was used with a polarization filter for the IR reflection measurement.

Figure 1 shows the IR reflection spectra of dopant-free $CaTiO_3$. Wide band due to the Ti-O stretching vibration appeared in the range from 550 to 800cm$^{-1}$ in both polarization directions. Two small bands appeared at 500 and 540cm$^{-1}$ under the $E \perp c$(electric field normal to the c axis) configuration. Factor group analysis predicts that $CaTiO_3$ has 15 IR active modes ($9B_{1u}+7B_{2u}+9B_{3u}$). More detailed examinations are necessary for the assignment of the observed bands.

Figure 2 shows the IR reflection spectra of $Ca_{1-x}Y_xTiO_3$ under the $E \perp c$ configuration. With the increase of x, two small bands at 500 and 540cm$^{-1}$ became smaller and the edge of the wide band at 800cm$^{-1}$ became smooth. These results indicate that the dopant ion disturbed the periodicity in the crystal and depressed some modes of the lattice vibrations in spite of the small doping amount.

Figure 3 shows reflection and transmission spectra of $Ca_{1-x}Y_xTiO_3$ for $x=10^{-2}$ in the wide range. Transmission spectrum and reflection spectrum in the VIS region were obtained using a conventional spectrometer and the crystal thickness was about 200μm. The sample of $x=10^{-2}$ was conductive and its carrier density was about $2x10^{18}cm^3$. The absorption due to the conduction electrons distinctly appeared in the transmission spectrum. On the other hand, no remarkable reflections due to the conduction electrons were observed because of the small carrier densities.

Unfortunately, the reliable reflection spectra in the FIR region could not be obtained in this measurement. The FIR reflection spectra of $BaTiO_3$$^{1)}$ and $SrTiO_3$$^{2)}$ were used as guides for our measurement. These spectra shows that these titanates keep high and almost constant reflectance in the FIR region except a sharp drop at about 180cm$^{-1}$. Our spectra obtained for $CaTiO_3$ surely showed the high and almost constant reflectance, about 0.9, but the sharp drop was not observed and slight structure in the spectra was not reproducible. More experiments are needed for the reliable FIR spectra.

In these measurements, although we observed the doping effects on the lattice vibrations, but we could not succeed in detecting the donor levels for yttrium ion in $CaTiO_3$. Even though there might be some problems in the FIR reflection measurement, the detection of the donor levels would be very difficult in $Ca_{1-x}Y_xTiO_3$ because their reflectance is very high in the FIR region. Therefore, it was concluded that another measurements such as ESR measurement or resistivity measurement are suitable for the estimation of the donor levels in $Ca_{1-x}Y_xTiO_3$.

References
1) W.G. Spitzer, R.C. Miller, D.A. Kleinman and L.E. Howarth, Phys. Rev. 126 (1962) 1710
2) A.S. Baker Jr., Phys. Rev. 145 (1966) 391

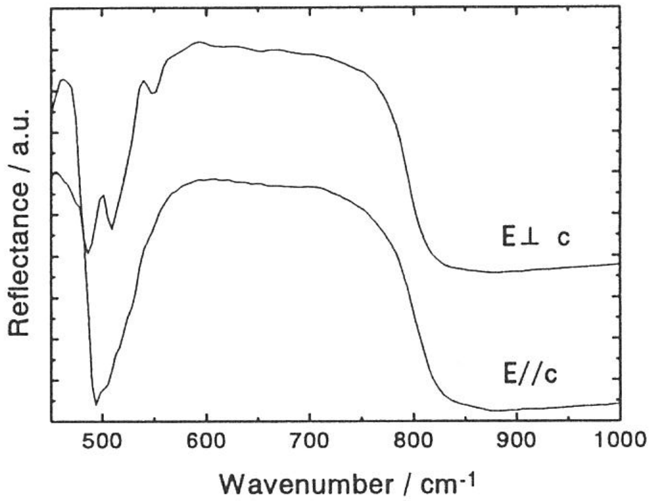

Fig. 1 IR reflection spectra of $CaTiO_3$

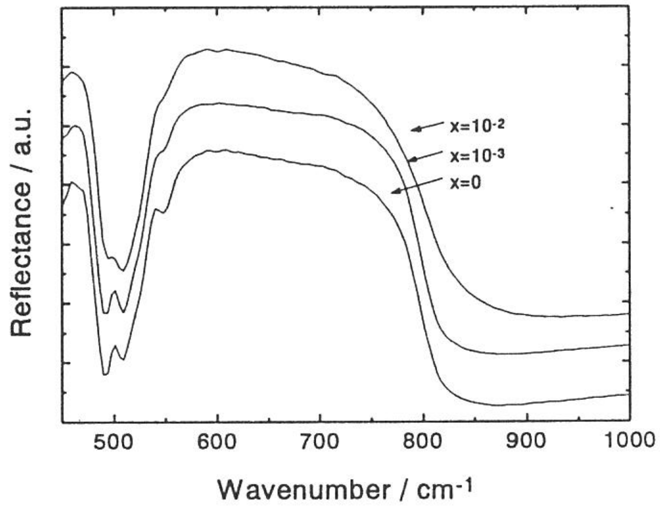

Fig. 2 IR reflection spectra of $Ca_{1-x}Y_xTiO_3$

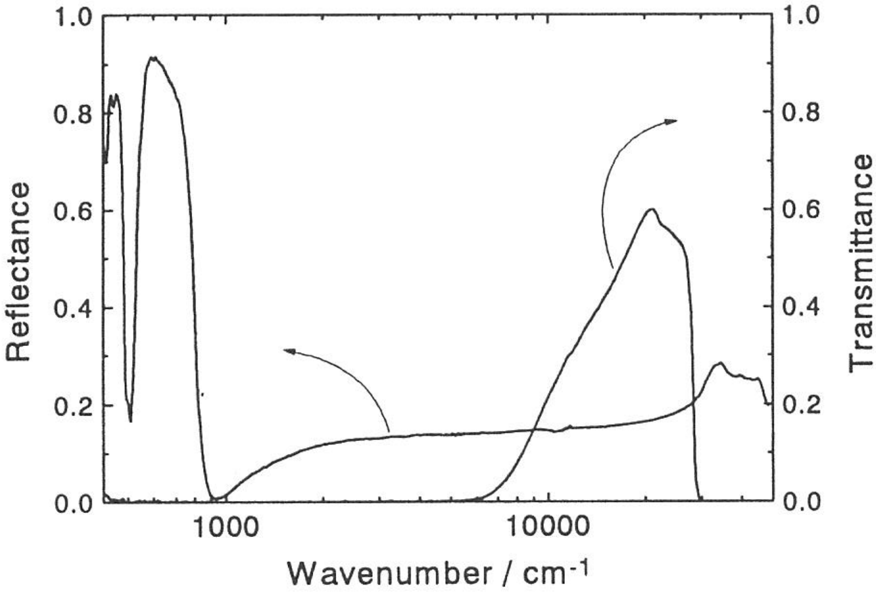

Fig. 3 Reflection and transmission spectra of $Ca_{0.99}Y_{0.01}TiO_3$

(BL6A1)

# Pressure Dependence of Phonon Frequencies in Ice Ⅷ

Michihiro Kobayashi

*Faculty of Engineering Science, Osaka University, Toyonaka, Osaka 560*

So far, more than ten stable phases of ice have been reported. Various types of optical measurements have been performed in ice. However, the far-infrared spectroscopy has never been applied to high pressure phases of ice. This is because the sample area provided with a diamond anvil cell (DAC) is very small, the transmission light is too weak to be detected. We have used therefore the synchrotron radiation as the light source. As the result, we have succeeded to measure far-infrared absorption spectra in ice Ⅶ, Ⅷ and XI for the first time [1].

Figure 1 shows the pressure dependence of phonon frequencies in ice Ⅷ. The open circles denote the infrared active lattice mode which was measured under high pressure at 260K by using UVSOR light and DAC. The data expressed by a hexagon shows the infrared active mode for pressure retrieved sample measured by Tay et al. [2] at 100K. In the figure, the data of the open circles were corrected as if it were taken at 100K by shifting the frequency up by 8.3 cm$^{-1}$, using a temperature coefficient of 0.052 cm$^{-1}$/kelvin. Closed circles express the data for the Raman active lattice mode measured at 260K. A straight line in Fig.1 is obtained by fitting and we have ensured that the line fits to experimental data beyond of the figure up to 10 GPa. A broken line was drawn by assuming that the pressure coefficient of the infrared active phonon mode should be same to that of the Raman active mode, since both the frequencies are near to each other. A dotted line was drawn to be a guide for the eye. The experimental points show a remarkable deviation from the expected dependence given by the broken line below 2.5 GPa.

Ice Ⅷ is stable at pressures higher than 2 GPa near 270K. At low temperature like as 100 K, it exists below 2 GPa as a metastable phase. So far, the metastable phase has been believed to be the same structure as ice Ⅷ. Anomalous pressure dependence of the lattice mode shown in Fig.1 indicates that the metastable phase has a different structure to ice Ⅷ.

Recently, Besson et al. [3] measured the neutron diffraction and found that there is an isostructural phase transformation below 2 GPa. This finding coincides with the anomalous pressure dependence of the phonon frequency.

[1] M. Kobayashi, Solid State Physics (Japan) 31, 127 (1996).

[2] S. P. Tay, D. D. Klug and E. Whalley, J. Chem. Phys. 83, 2708 (1985).

[3] J. M. Besson, S. Klotz, G. Hamel, W. G. Marshall, R. J. Nelmes and J. S. Loveday, under submission.

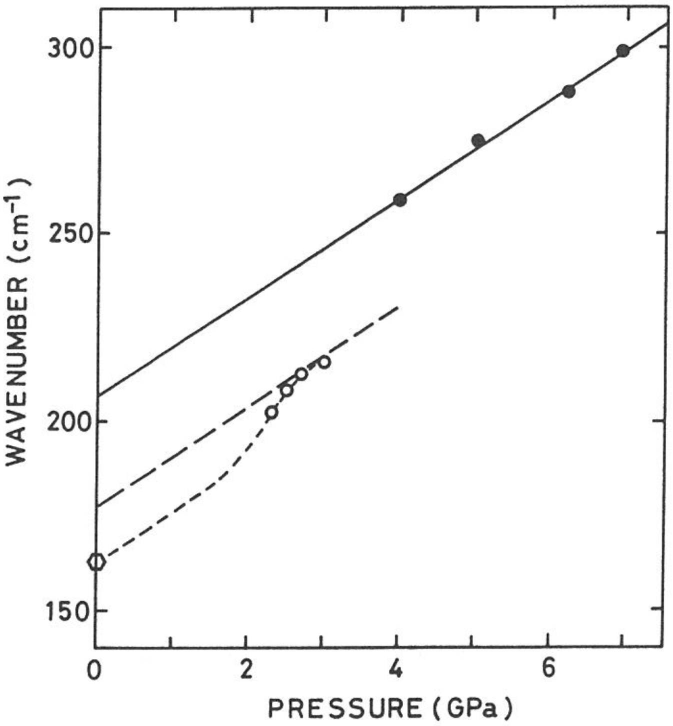

Fig. 1 Pressure dependence of the phonon frequencies for the lattice modes in ice Ⅷ. Open circles correspond to the infrared active mode measured at UVSOR at 260K. Closed circles express the Raman active mode measured at 100 K.

(BL6A1)

# Millimeter Wave Reflection Measurement of Superionic Conductor $LiNiO_2$

Hitoshi OHTA, Hideki SHINOZAKI, Takao NANBA, Atushi HIRANO* and Ryoji KANNO*

*Department of Physics, Faculty of Science, Kobe University, 1-1 Rokkodai, Nada, Kobe 657*
**Department of Chemistry, Faculty of Science, Kobe University, 1-1 Rokkodai, Nada, Kobe 657*

$LiNiO_2$ has been studied intensively due to its two interesting aspects. One is its magnetic properties which have attracted much interest since the suggestion by Hirakawa *et al.* Their suggestion was that it may be the model substance for the two dimensional quantum liquid-like state or resonating valence bond (RVB) state.[1)] Another interesting aspect is that of a super-ionic conductor and it is promising for an electrode material in secondary Li batteries, especially when it is stoichiometric, because it is light weight and economical than $LiCoO_2$.[2)] Although we have done some studies on its magnetic properties by our submillimeter wave ESR previously,[3)] we extended our studies to investigate the properties of $LiNiO_2$ as a super-ionic conductor using the millimeter wave spectrometer at BL6A1.

The composition of $LiNiO_2$ is very sensitive to the synthesis condition, especially the sintered temperature, and it can be easily lead to a decomposition to $Li_{1-x}Ni_{1+x}O_2$. The non-stoichiometry degrades the charge and discharge characteristics significantly. However, Kanno *et al.* succeeded in synthesizing nearly stoichiometric $LiNiO_2$.[2)] Therefore $LiNiO_2$ became promising candidate to replace $LiCoO_2$ as an electrode material in secondary Li batteries and has attracted much attention. Both $Li^+$ ions and electrons contribute to the conductivity in $LiNiO_2$. Therefore our aim is to obtain the information about the diffusive motion of $Li^+$ ions separately by observing "ionic plasmon" whose existence can be proved as a definite increase in a reflectivity towards a low energy side in the millimeter wave region because the mass of $Li^+$ ion is much larger than that of electron. The first observation of ionic plasmon has been performed for alkali silver iodide super-ionic conductors $MAg_4I_5$ (M=Rb, K and $NH_4$) by Awano *et al.*[4)] They observed ionic plasmon at wave number from 26 to 85 $cm^{-1}$ depending on M above $T_c$ (=122 K (Rb), 139 K (K) and 135 K($NH_4$)). There is no contribution of electrons in these systems and the ionic conductivity of these substances becomes high above $T_c$. The idea of our investigation is to obtain separate information about the diffusive motion of $Li^+$ ion by observing ionic plasmon of $LiNiO_2$ in the millimeter wave region.

The reflection measurements have been performed for the first time at 11 K, 79 K and 300 K in the spectral region from 10 to 50 $cm^{-1}$ using the beam line BL6A1 of UVSOR. Two samples are measured. One is nearly stoichiometric $LiNiO_2$ sintered at 650°C (sample A), and the other is $Li_{1-x}Ni_{1+x}O_2$ (x=0.05) sample sintered at 850°C (sample B). Figure 1 (a) and (b) show the results for both samples. Almost the same flat reflectivity was obtained at 11 K and 79 K for both samples. However, the rise of the reflectivity was observed at 300 K for both samples. It suggests that the diffusive motion of $Li^+$ ions is present at 300 K but not at 11 K or 79 K. As the reflectivity is higher at 300 K for sample B than sample A, we can expect that there is much more diffusive motion of $Li^+$ ions in sample B but its origin needs further investigation. As more diffusive motion of $Li^+$ ions are expected above 300 K, the measurement at higher temperature is required.

References

[1] K. Hirakawa *et al.*: J. Phys. Soc. Jpn. **54** (1985) 3526.

[2] R. Kanno *et al.*: J. Solid State Chem. **110** (1994) 216.

[3] H. Ohta *et al.*: Physica B **211** (1995) 217.

[4] T. Awano *et al.*: Solid State Ionics **53-56** (1992) 1269.

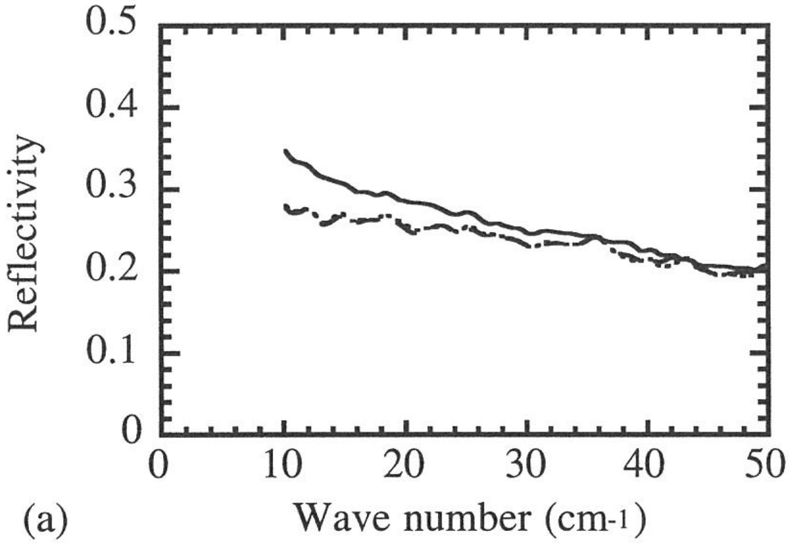

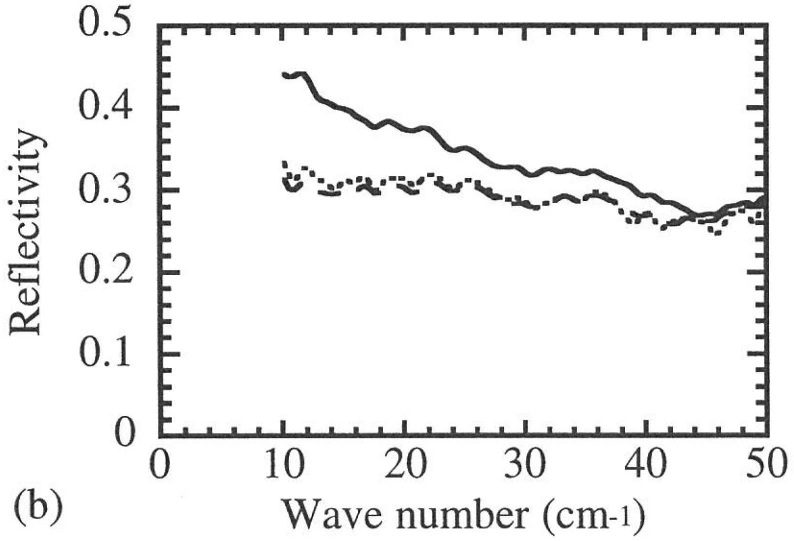

Fig. 1 Reflectivity spectra of samples A (a) and B (b). Solid, dashed and dotted lines correspond to room temperature, 79 K and 11 K, respectively.

(BL6A1)

# Far-infrared and Millimeter Wave Spectroscopy of Silver Conducting Organic-Inorganic Glasses

Naotake SASAKI, Katsuyoshi HANDA and Teruyoshi AWANO

*Department of Applied Physics, Tohoku Gakuin University, Tagajo 985*

Superionic glasses have high ionic conductivity even at room temperature. This is different from superionic crystals. The dynamics of mobile ions in disordered structure in these glasses has been investigated recently. Some conductivity measurements from DC to microwave region of a few of these glasses have been executed and power law has been observed commonly$^{1)}$. However, their spectroscopic behavior in the spectral region between microwave and far-infrared has not been investigated in detail.

We measured reflectivity spectra and transmission spectra of $(AgI)_x(AgPO_3)_{1-x}$ (x=0, 0.25, 0.5), $(CuI)_{0.25}(CuPO_3)_{0.75}$ and $((CH_3)_4NI)_{0.1}((C_2H_5)_4NI)_{0.1}(AgI)_{0.8}$ glasses in FIR and MW region$^{2,3)}$. There were two broad peaks around 90 cm$^{-1}$ and 15 cm$^{-1}$ commonly in the reflectivity spectra of the $(AgI)_x(AgPO_3)_{1-x}$. The low energy tail below 9 cm$^{-1}$ slightly increased in the superionic conducting glasses (x=0.5) in energy loss function spectra. However, this structure of the "ionic plasmon" was not so clear as in $AM_4X_5$ crystals. This seems to be due to a large scattering of the mobile ion by the non-periodic structure of the glass. The temperature dependence of the intensity of this longitudinal motion of conduction ion was not so drastic as that in $AM_4X_5$ crystal. This seems to be due to the random and coarse network of the $AgI_4$ tetrahedron.

The network structure of glass does not exist, and each ion of $Ag^+$, $I^-$, $(CH_3)_4N^+$ and $(C_2H_5)_4N^+$ disperses randomly in $((CH_3)_4NI)_{0.1}((C_2H_5)_4NI)_{0.1}(AgI)_{0.8}$. Absorption bands were observed at 7 cm$^{-1}$, 100 cm$^{-1}$ and 220 cm$^{-1}$. In this glass, the Drude like structure was not clear even at the room temperature. The attempt mode as observed in $(AgI)_x(AgPO_3)_{1-x}$ was not seen in this glass.

We expected a shift of the plasma frequency by the substitution of conduction ion from $Ag^+$ to $Cu^+$. The apparent "ionic plasmon" was observed clearly in $(CuI)_{0.25}(CuPO_3)_{0.75}$. It seems to be, however, a mixture spectrum of ionic motion and hole absorption which is doped from $Cu^{2+}$ impurity.

In this study, we measured reflectivity spectra (and transmission spectra if it was possible) of $(AgI)_{0.75}(Ag_2MoO_4)_{0.25}$, $((CH_3)_4NI)_{0.1}(CsI)_{0.2}(AgI)_{0.7}$ and $((CH_3)_4NI)_{0.07}((C_2H_5)_4NI)_{0.1}((C_3H_7)_4NI)_{0.03}(AgI)_{0.8}$ glass in spectral region from 3 to 250 cm$^{-1}$. $(AgI)_x(Ag_2MoO_4)_{1-x}$ is different from $(AgI)_x(AgPO_3)_{1-x}$ in the glass network structure. The former has no network connection between $MoO_4$ tetrahedrons. The latter has long chains of $PO_4$ tetrahedrons. $((CH_3)_4NI)_{0.1}(CsI)_{0.2}(AgI)_{0.7}$ and $((CH_3)_4NI)_{0.07}((C_2H_5)_4NI)_{0.1}((C_3H_7)_4NI)_{0.03}(AgI)_{0.8}$ are derivatives from the $((CH_3)_4NI)_{0.1}((C_2H_5)_4NI)_{0.1}(AgI)_{0.8}$. $(C_3H_7)_4N^+$ ion seems to cut conduction path of $Ag^+$ ion. CsI seems to increase ionicity of glass matrix.

Fig. 1 shows absorption, dielectric constants, energy loss function and conductivity spectra of $(AgI)_{0.75}(Ag_2MoO_4)_{025}$ glass. The 90 cm$^{-1}$ peak by vibrational mode was almost the same as that in $AgI$-$AgPO_3$ glasses. There was not attempt mode but "boson peak" around 22 cm$^{-1}$. There was a weak absorption around 8 cm$^{-1}$. Fig. 2 shows absorption, dielectric constants, energy loss function and conductivity spectra of $((CH_3)_4NI)_{0.07}((C_2H_5)_4NI)_{0.1}((C_3H_7)_4NI)_{0.03}(AgI)_{0.8}$ glass. These spectra were almost the same as those in $((CH_3)_4NI)_{0.1}((C_2H_5)_4NI)_{0.1}(AgI)_{0.8}$. This is consistent with the results in microwave region$^{4)}$. Fig. 3 shows absorption, dielectric constants, energy loss function and conductivity spectra of $((CH_3)_4NI)_{0.1}(CsI)_{0.2}(AgI)_{0.7}$ glass. These spectra were also similar to those in $((CH_3)_4NI)_{0.1}((C_2H_5)_4NI)_{0.1}(AgI)_{0.8}$. However, all absorption bands were shift to lower energy.

**References**

1) C. Cramer et al., Solid State Ionics, 86-88 (1996) 481.
2) T. Awano and T. Nanba, UVSOR activity report 1994, 146.
3) T. Awano and T. Nanba, UVSOR activity report 1995, 180.
4) J. Kawamura, private communication.

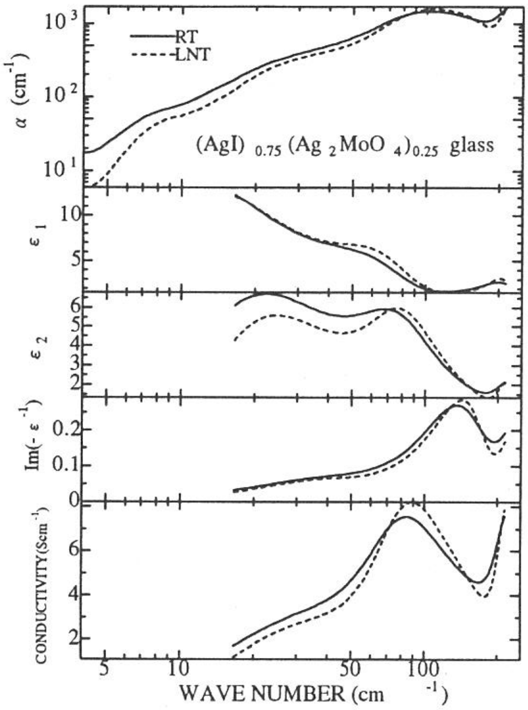

Fig. 1. Optical spectra of $(AgI)_{0.75}(Ag_2MoO_4)_{0.75}$ glass.

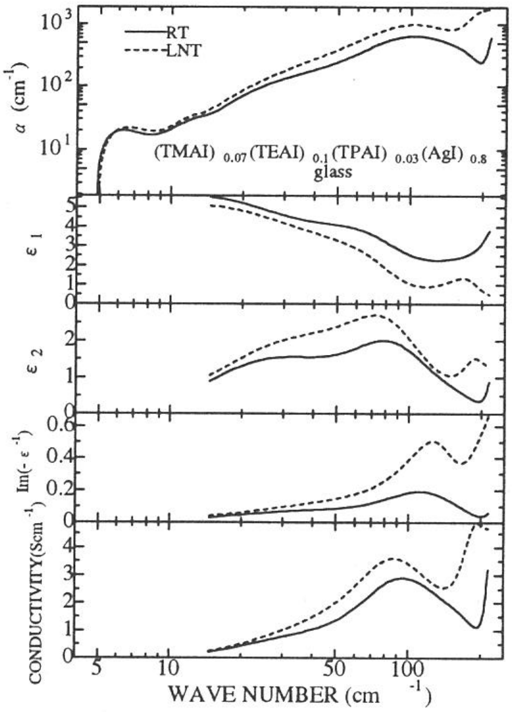

Fig. 2. Optical spectra of $((CH_3)_4NI)_{0.07}((C_2H_5)_4NI)_{0.1}((C_3H_7)_4NI)_{0.03}(AgI)_{0.8}$ glass.

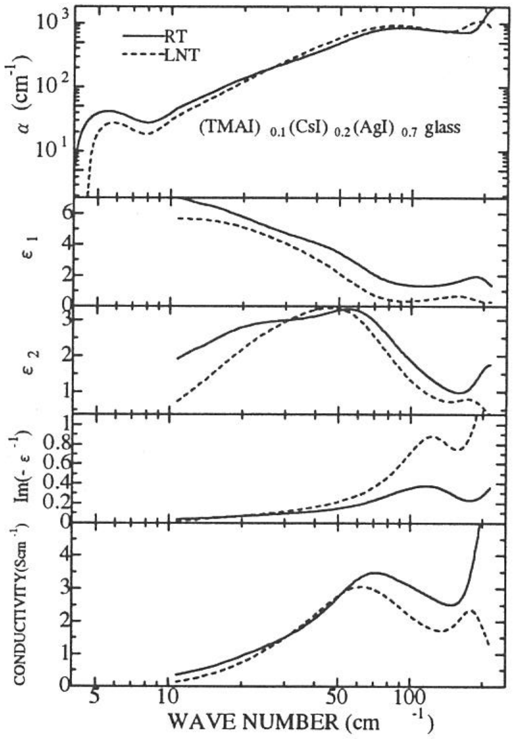

Fig. 3. Optical spectra of $((CH_3)_4NI)_{0.1}(CsI)_{0.2}(AgI)_{0.7}$ glass.

## (BL6A2)

# Creation of Secondary Electronic Excitations by Hot Photoelectrons in RbCl

Masao Kamada and Aleksandr Lushchik*

*UVSOR, Institute for Molecular Science, Okazaki 444, Japan*

*Permanent address: *Tartu Universiry, Tähe 4, Tartu EE2400, Estonia*

Using photoelectric and luminescent methods the processes of multiplication of electronic excitations (MEE) have been investigated in detail in pure and doped KCl, KBr and KI crystals under irradiation by photons with energies up to 30 eV (see, e.g., [1-3]). An inelastic scattering of hot photoelectrons, created by radiation, on valence electrons leads to the formation of secondary electron-hole pairs [1-3] or secondary excitons [3].

The purpose of this study is to investigate the role of hot photoelectrons in MEE processes in RbCl. The salt was previously purified by manifold recrystallization from the melt. The photoelectrons from RbCl evaporated thin film (thickness ~ 100 Å) were analysed using an angle-integrated cylindric-retarding field analyzer. The intensity of incident light was monitored by a gold mesh located between a past-mirror and a sample. All spectra are normalised by using photoelectric yield of this gold mesh.

The energy distribution curves (EDC) of emitted electrons have been measured on the excitation of RbCl by 13-30 eV photons at 295 K. Figure 1 presents some of these EDC. The kinetic energy is given relative to the vacuum level. It is easy to separate two groups of emitted electrons: slow electrons with kinetic energy $E_{kin} < 2$ eV and hot photoelectrons with $E_{kin}$ linearly increasing with the increase of exciting photon energy $h\nu_{exc}$. Photons with $h\nu_{exc} =$ 8.4-16.0 eV cause the ionization of chlorine ions with the formation of hot photoelectrons. The effective mass of simultaneously formed photoholes in RbCl is by ten times larger than that of photoelectrons [4], so a photohole gains only a small part of the photon energy.

Figure 2 shows the dependence of a number of emitted electrons with definite kinetic energy on the exciting photon energy. The energy of conduction electrons inside a crystal is higher by a value of an electron affinity ( for RbCl $\chi = 0.5$ eV [2]). There are two maxima for every value of $E_{kin}$: at 13-19 eV and 21-28 eV. The low-energy peak is caused by the ionization of chlorine ions, while the ionization of $Rb^+$ ions takes place in RbCl at $h\nu_{exc} \geq 17$ eV. Spin-orbit splitting of $Rb^+$ (0.9 eV) is significantly higher than for $Cl^-$ (0.1 eV). This is one of the reasons of peak broadening at $h\nu_{exc} > 21$ eV in comparison with the peaks at $h\nu_{exc} < 16$ eV. An inelastic scattering of 8.0-8.5 eV photoelectrons on valence electrons leads to the creation of secondary electron-hole pairs, while 7.0-7.5 eV photoelectrons form at room temperature secondary excitons. As a result of these processes, the number of hot photoelectron decreases and the number of slow ones increases (see Figure 2).

The intensity of $Tl^+$ center recombination luminescence significantly increases in RbCl:Tl in the regions $h\nu_{exc} \geq 18$ eV and $h\nu_{exc} \geq 26$ eV, where secondary electron-hole pairs are formed [4]. In the same energy regions the value of photoelectric yield decreases [2]. The intensity of self-trapped exciton luminescence sharply increases at $h\nu_{exc} \geq 25$ eV, where secondary excitons are produced [4]. It is of special interest to reveal in RbCl:Tl a direct excitation of $Tl^+$ ions by hot photoelectrons. Electron transitions ${}^1S_0 \rightarrow {}^3P_1$ and ${}^1S_0 \rightarrow {}^1P_1$ occur in $Tl^+$ on a crystal excitation by 14-15 and 15.0-15.7 eV, respectively [4]. According to Figure 2 such photons form hot photoelectrons with energies of 5 and 6 eV inside a crystal. These energies are sufficient enough for ${}^1S_0 \rightarrow {}^3P_1$ and ${}^1S_0 \rightarrow {}^1P_1$ transitions in $Tl^+$ ions. ${}^1S_0 \rightarrow {}^3P_1$

transitions occur on the excitation by photons of $h\nu_{exc} > 22$ eV also. Such photons cause the ionization of $Rb^+$ ions and the formation of conduction electrons with 5 eV energy.

References

[1]D.Blechschmidt, M.Skibovski and W.Steinman. *Phys. Status Solidi* **42** 61 (1970).

[2]A.Ejiri, A.Hatano and K.Nakagawa. *J. Phys. Soc. Jap.* **63** 314 (1994).

[3]A.Lushchik, E.Feldbach, R.Kink, Ch.Lushchik, M.Kirm and I.Martinson.. *Phys. Rev. B* **53**, 5379-5387 (1996).

[4]E.Feldbach, M.Kamada, M.Kirm, A.Lushchik, Ch.Lushchik and I.Martinson, to be submitted in *Phys. Rev. B*.

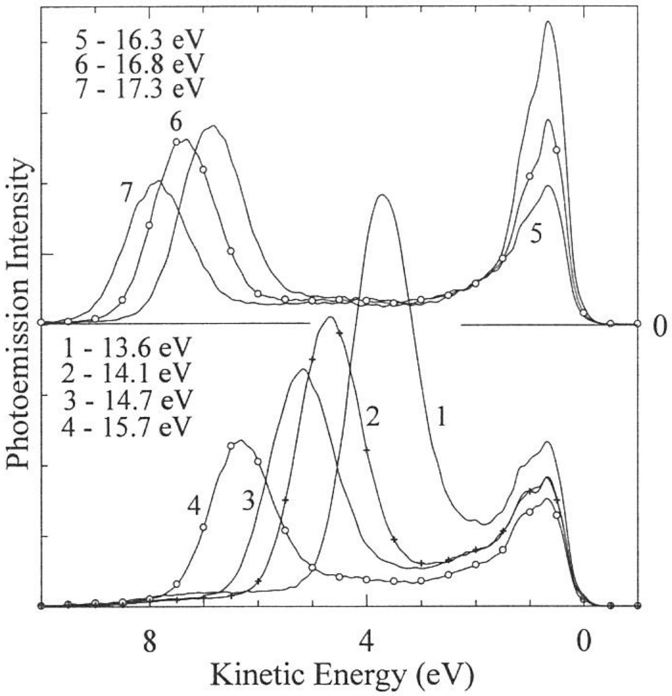

Figure 1. EDC of RbCl for various exciting photon energies. Kinetic energy of emitted electrons is measured relative to the vacuum level. T = 295 K.

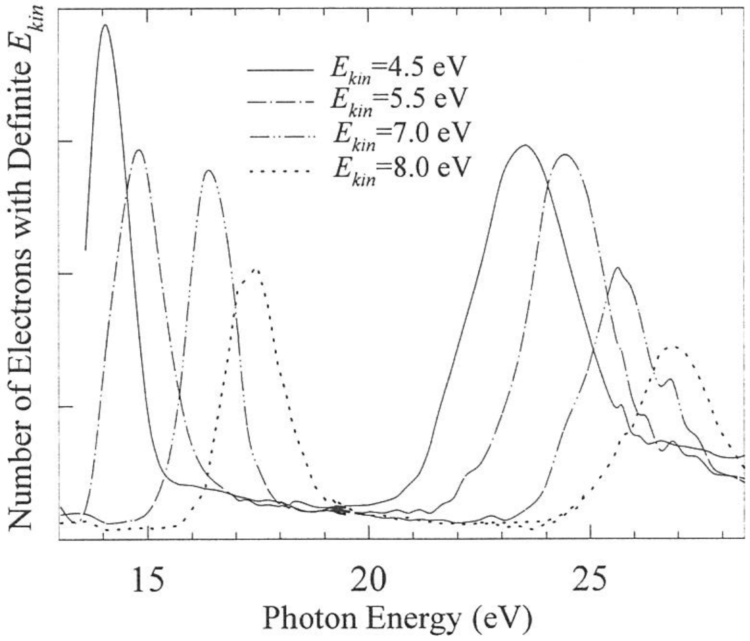

Figure 2. Number of emitted electrons with definite kinetic energy ($E_{kin}$) as a function of exciting photon energy in RbCl.
T = 295 K.

(6A2)

# Photoelectron and Luminescence Spectra of $CsTaF_6$

M. Kamada, N. Takahashi, S. Hirose, S. Ohara, and [a] M. A. Terekhin

Institute for Molecular Science, Myodaiji, Okazaki 444, Japan
[a]Nagoya Institute of Technology, Nagoya 466, Japan
[b]Russian Research Center "Kurchatov Institute", Moscow 123182, Russia

Fluorides have attracted much interest in recent years, because they show a variety of luminescence. For examples, the Auger-free luminescence due to the transition between the valence and the core level is observed in $BaF_2$ and CsF. [1] Moreover, BaFCl and BaFBr including rare-earth elements show the strong recombination luminescence band. These luminescence have been applied to a fast scintilation and a resistration of x-rays. However, the detailed mechanism of the luminescence under VUV and soft x-ray excitations is still not clear, and systematical studies are required. The purpose of the present work is to understand the electronic structures of $CsTaF_6$ and to investigate the luminescence properties in the energy regions corresponding to the Cs-4d excitation.

Experiments were carried out at beam line 6A2 of UVSOR facility, Institute for Molecular Science. The monochromatized synchrotron radiation through a plane grating monochromator was used as an light source. Absorption spectra were obtained by measuring total electron yields from samples. Photoelectron spectra were measured with a cylindrical energy analyser. The overall resolution was about 0.35 eV around 100 eV.

Excitation spectra were obtained by using an interference filter, since the luminescence intensity from evaporated films was too weak. Decay curves of the luminescence was obtained with a correlated single-photon counting method under a single-bunch operation of the storage ring. The duration and repetition of the synchrotron radiation pulses were 0.4 and 180 ns, respectively.

Samples were prepared by in-situ evaporation on gold substrates in a preparation chamber, and were transfered into an analysing chamber, the pressure of which was about $2x10^{-8}$ Pa. Thickness of the samples were about 10 and 100 nm for photoelectron and luminescence spectroscopies, respectively.

Figure 1 shows the photoelectron spectrum of $CsTaF_6$ excited with 100 eV. The valence band is observed at about 5 eV. The Cs-$5p_{3/2}$, Cs-$5p_{1/2}$,Cs-5s, Cs-$4d_{5/2}$, and Cs-$4d_{3/2}$ levels are seen at 7.1, 8.7, 20, 72, and 74.2eV, respectively, while the Ta-$5p_{3/2}$ and Ta-$5p_{1/2}$ levels are observed at 26.4 and 28 eV, respectively. Broad bands denoted by A1 and A2 are attributed to the $N_{4,5}$-$O_{2,3}$V and $N_{4,5}$-$O_{2,3}O_{2,3}$ Auger electrons, respectively. It should be noted that the energy difference between the peaks of the valence band and the Cs-$5p_{3/2}$ level in $CsTaF_6$ is about 2.2 eV, which is smaller than that in CsF (4.8 eV). [2] This indicates that the valence band in $CsTaF_6$ originates from the mixing of the F-2p level with the Cs-5p level as well as the Cs-6s, Ta-6s, and Ta-6p levels.

Figure 2 shows the excitation spectrum of 360 nm emission band and the absorption spectrum. The absorption spectrum is similar to that of CsF and is a little bit obscure in comparison with those of CsCl and CsBr.[3] According to the existing reports about the absorption spectra of cesium halides [4,5], the absorption peaks a and b are attributed to the transitions from Cs-4d level to Cs-6p level and f levels, respectively, while the other structures may be due to the collapsed f wave function associated with $4d^94f$ and $4d^9\varepsilon f$ giant resonance and/or double excitation by a single photon. The excitation spectrum shows structures in this Cs-4d region, but the enhancement due to the Cs-4d excitation is not so large and the correspondence in structures between the excitation and absorption spectra is a fairy good.

By assuming that the luminescence intensity due to the Cs-4d excitation, Ic, superposes the intensity due to the valence excitation, Iv, and that the energy dependence of Iv is negligible in the energy region of the Cs-4d excitation, the ratio of the quantum efficiencies between the Cs-4d and the valence excitations is given by $\eta c/\eta v = (Ic\mu v)/(Iv\mu c)$.

The ratio in the quantum efficiency between the Cs-4d and the other excitations, which was carried out by using the formula (1), is about 0.2 for the peak a. This estimation indicates that secondary processes do not effectively produce electrons and holes near the luminescence centers. As mentioned above, the valence band of $CsTaF_6$ consists of mixing states originated from Cs, Ta, and F elements. Therefore, it is supposed that the valence holes induced by the decay of the Cs-4d holes are not well localized near the luminescence center, and then the center may be similar to a $[TaF_6]^{-5}$ center.

The decay curves of the 360 nm luminescence were observed with the excitation photon energies at 20 and 100 eV. The decay curves consist of three components at least, a fast one with about 2.5 ns, a slow one with a decay time more than 180 ns, and a middle one between them. It is worthwhile to note that the decay curves are almost the same between 20 and 100 eV. This result indicates that the effect induced by core excitation such as the quenching effect observed in $BaF_2$ [6] is not appreciable in $CsTaF_6$. Valence holes induced by secondary processes following the decay of the Cs-4d hole may recombine with electrons, producing the luminescence. In conclusion, $CsTaF_6$ is not a good candidate for a scintillating material around 100 eV, because of the low quantum efficiency and the slow response time.

## Ackowledgements

The authors would like to express their sincere thanks to S. S. Galaktionov of Mendeleev University and S. S. Galaktionov of NPO "Simplex" in Moscow, Russia for their kind supply of samples.

## References

1] S. Kubota, M. Itoh, J. Ruan(Gen), S. Sakuragi, and S. Hashimoto, Phys. Rev. Lett. 60 (1988) 2319.
2] M. Kamada, O. Aita, K. Ichikawa, M. Okusawa, and K. Tsutsumi, Phys. Rev. B45 (1992) 12725.
3] K. Radler and B. Sonntag, Chem. Phys. Lett. 39 (1976) 371.
4] J. P. Connerade and M. W. D. Mansfield, Phys. Rev. Lett. 48 (1982) 131.
5] M. A. Terekhin, A. N. Vasil'ev, M. Kamada, E. Nakamura, and S. Kubota, Phys. Rev. B52 (1995) in press.

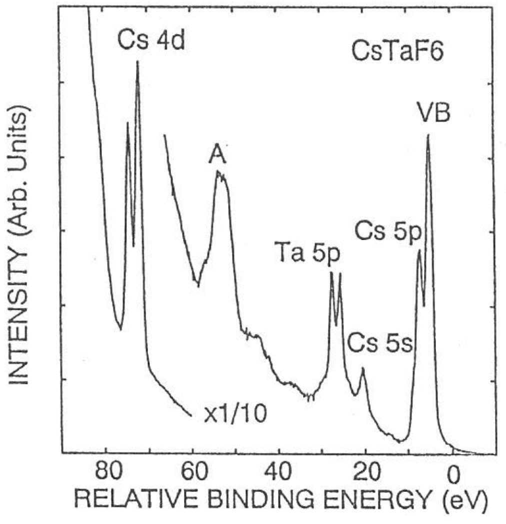

Fig. 1 Photoelectron spectrum of $CsTaF_6$.

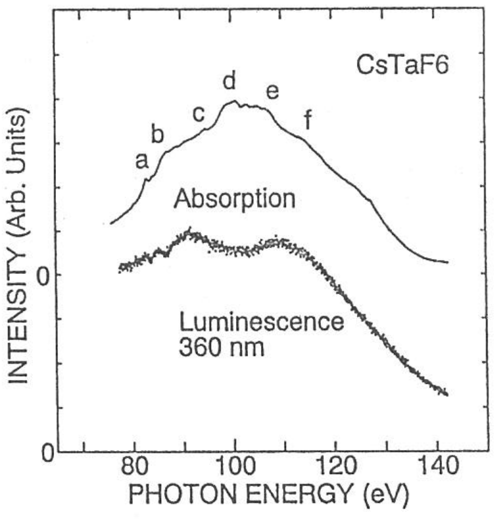

Fig. 2 Absorption and Excitation spectra of the 360 nm band.

# (BL6A2) Angle resolved photoelectron spectroscopy of the CuCl(100) surface

Shin-ichiro Tanaka and Masao Kamada
Institute for Molecular Science, Myodaiji, Okazaki 444, Japan

CuCl is known as a material for nonlinear optics, and has been extensively studied for several decades(1). To summarize the previous studies, CuCl has a direct band gap of 3.4eV at the Brillouin zone center, and the top of the valence band is derived primarily from Cu 3d states, while the conduction band is predominantly from Cu 4s state. There is a lower lying band about 5eV below the valence band maximum which is mainly derived from Cl 3p state with some Cu 3d admixtures. Although the photoelectron spectroscopy(3) has been one of most powerful tools for investigating such an electronic structure, the sample used in the photoelectron measurements was not a single crystal but an evaporated policrystalline film except a few studies(3) due to a charge-up problem. Recently, it was shown that the CuCl film of single crystal can be produced by the evaporation on the well defined surface whose lattice constant fits that of CuCl(4).By the use of the single-crystalline thin film, the photoelectron spectroscopy can be carried out without the charge-up problem. In this report, we made a CuCl single crystalline film on the Si(100) surface, and measured the angel-resolved photoelectron spectroscopy.

Experiments were made at BL6A2.The LEED pattern for the CuCl(100) surface produced on the Si(100) surface is shown in figure 1. Only the integral spots are observed without any extra spots which indicates that there is no surface reconstruction. The CuCl has a zinc blend structure and its (100) surface is so called polar surface. It means there can be two kinds of surfaces, one has a Cu top layer and the other has a Cl top layer. In this stage, it is difficult to tell which surface ( or both ) is observed.

The angle resolved photoelectron spectra measured in a (010) plane are shown in figure 2. The energies are referred to the Fermi energy measured with the Ta sample holder. Features observed among -8 and -5 eV are ascribed to the bands which is predominantly derived from the Cl-3p and features observed among -5 and -2 eV to the bands from the Cu-3d. For a detailed investigation, we made fitting calculations by the use of the voigt function and one of the results is shown in figure 3. Peaks A-G are separated. In figure 4 (-5 to 0 eV) and figure 5 (-5 to -15 eV), the dispersions in the Brillouin zone are plotted by calculating the $k_{||}$ with the kinetic energy and the angle of the detection. One gray tape in figure 4 and 5 indicate one curve in figure 1, and intensities of the curves is presented as a gray scale on tapes. Dots in figure 4 and 5 correspond to peaks as shown in figure 3, where the size of the dots indicate the relative area intensities of peaks. Photon energy dependence of the spectra with a condition of the normal emission was also measured ( not shown in this report) , and changes in the peak intensities were observed, however, no changes in peak position were observed. It is generally accepted that the change of peak position depending on the photon energy reflects the dispersion of the band along $k_{\perp}$ , and the results here can be interpreted as the $k_{\perp}$ is not still a good quantum number in the case of thin film because the number of the lattice in the film along the surface normal is not large enough.

Peaks A and D are ascribed to the surface states, since (1) Peaks A and D have not been observed in the study of polycristalline CuCl, (2) The peak A has drastically changed in intensity by changing an angle of the incident light ( not shown ) , which suggests that the symmetry of the electronic state associated with the peak A is different from the other peaks. It is noted that it was not clearly observed whether there is such dependence on the peak D. (3) The measurement of the photon energy dependence ( not shown ) have shown that the state associated with the peak A is not derived from Cu-3d as the peaks B-D but from Cl-3p. Thus, if it were a bulk state, the state of the valence band top would be Cl-3p, which is not consistent with the previous results. It is noted that the peak D is ascribed to the Cu-3d. (4) After the exposure to CO gas, the peak D was shifted in energy and increased in intensity ( not shown ), which indicate that the charge transfer from the CO 5$\sigma$ molecular orbital occurs through the bonding between the chemisorbed CO and the Cu atom at the surface. The peak A is not affected by the CO adsorption and it is due to the Cl atom dose not interact with the CO molecule. This conclusion is consistent with the previous results(3) where the He-lump was used as an excitation source.

In conclusion, we measured the dispersion of the surface state on the CuCl(100) surface produced on the Si(100) surface, observed a band dispersion of CuCl(100) surface.

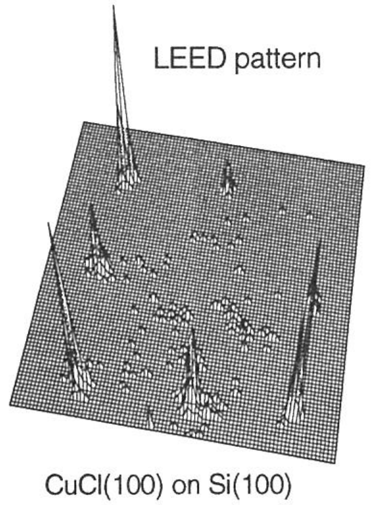

**Figure 1**

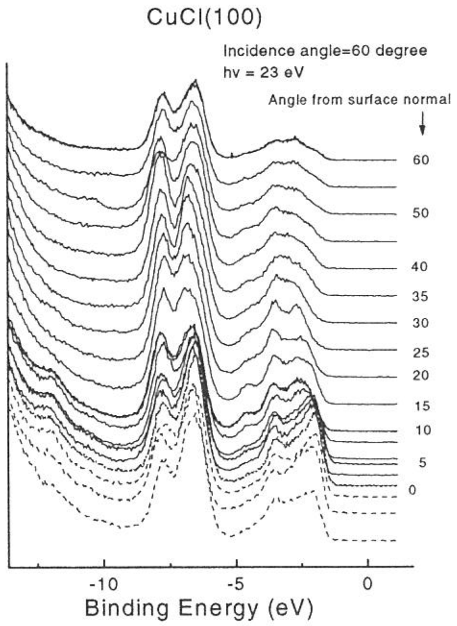

**Figure 2**

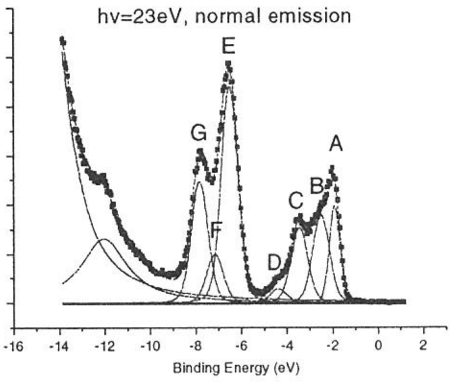

**Figure 3**

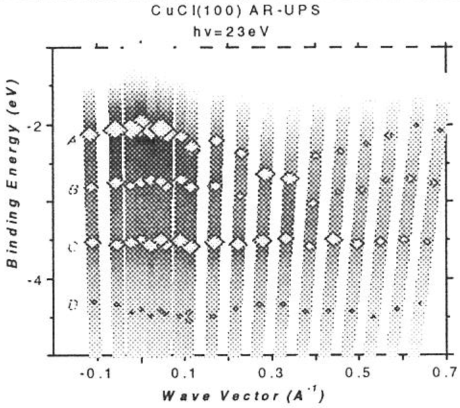

**Figure 4**

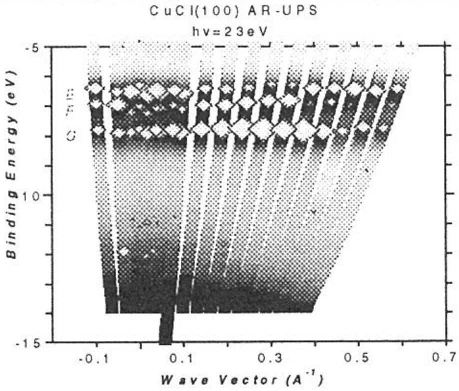

**Figure 5**

References
(1)A. Goldman, Phys. Sta. Ol. 81(1977) 9, and references therein
(2)S. Kono, T.Ishii, T.Sagawa and T.Kobayashi, Phys. Rev. B 8 (1973) 795
(3)D. Westphal and A.Goldman, Solid State Commun. 35 (1980) 441, J. Phys. C, 15 (1982) 6661
(4)N. Nishida, K. Saiki, A. Koma, Surf. Sci. 324 (1995) 149

(BL6A2)

# Photoelectron Spectroscopic Study of Coadsorbed States of Cs and O on GaAs(100)

Naoshi TAKAHASHI[1,2], Shin-ichiro TANAKA[1], Masatake ICHIKAWA[3],
Yong Q. CAI[1,*] and Masao KAMADA[1]

[1]*Institute for Molecular Science, Myodaiji, Okazaki 444, Japan*
[2]*The Graduate University for Advanced Studies*
[3]*College of Engineering, Fukui University, Fukui 910, Japan*

It[1)] is known that coadsorption of Cs and O on GaAs makes the vacuum level lie below the conduction band minimum. This negative electron affinity (NEA) surface has been applied to make efficient photocathodes in the long wavelength region, and the NEA surface of O/Cs/GaAs(100) is known as an useful emitter for spin-polarized electrons with high degrees of polarization and efficiency. Although extensive studies have been reported on NEA surfaces, the coadsorption kinetics of Cs and O on the GaAs surface is not yet well understood. The purpose of the present study is to investigate the electronic states of O/Cs/GaAs(100) by using the ultraviolet photoelectron spectroscopy (UPS) in order to understand the coadsorption kinetics of the NEA formation.

Experiments were carried out in an ultrahigh vacuum chamber with the base pressure less than 2∋$10^{-10}$ Torr of BL-6A2, and all UPS spectra were obtained by using synchrotron radiation as a light source. The UPS spectra were taken at the angle of 45° from the surface normal, and the measurements of the work function were taken in normal emission. In this paper, we will describe about the Ga-rich c(8∋2) surface assigned by LEED pattern.

Figure 1 shows EDCs at $h\nu = 110$ eV. The EDCs were measured after heating (a), the first Cs deposition (b), subsequent oxygen exposure of 3.6 L (c) and so on (d-h). The Cs coverage is estimated to be about 1.0, 1.5, 1.8 and 2.2 monolayers for EDCs (b), (d), (f) and (h), respectively, by referring the mean free path of the Ga-3d photoelectrons.[2,3)] The intensity ratio of the As-3d peak to the Ga-3d peak decreases during the Cs and oxygen treatments. On the other hand, another As-3d peak originated from oxidized As atoms increases.[4)] Total intensity of the As-3d and oxidized As-3d peaks during multiple treatments is almost constant. Figure 2 shows energy positions of Cs-4d$_{5/2}$, Ga-3d and As-3d photoelectrons observed after the treatments. The changes in energy position of the Ga-3d and As-3d peaks are classified into two stages; the first treatment stage (b) and (c), and the higher treatment stage (f), (g) and so on.

At the first treatment stage, the deposition of Cs causes the Ga-3d and As-3d peaks to shift to the lower binding energy side, and the first exposure of oxygen makes these peaks to shift to the higher energy side. These energy shifts are in good agreement with the chemical shift of core-levels by metallic atoms or halogen atoms adsorbed on semiconductors. It is suggested that

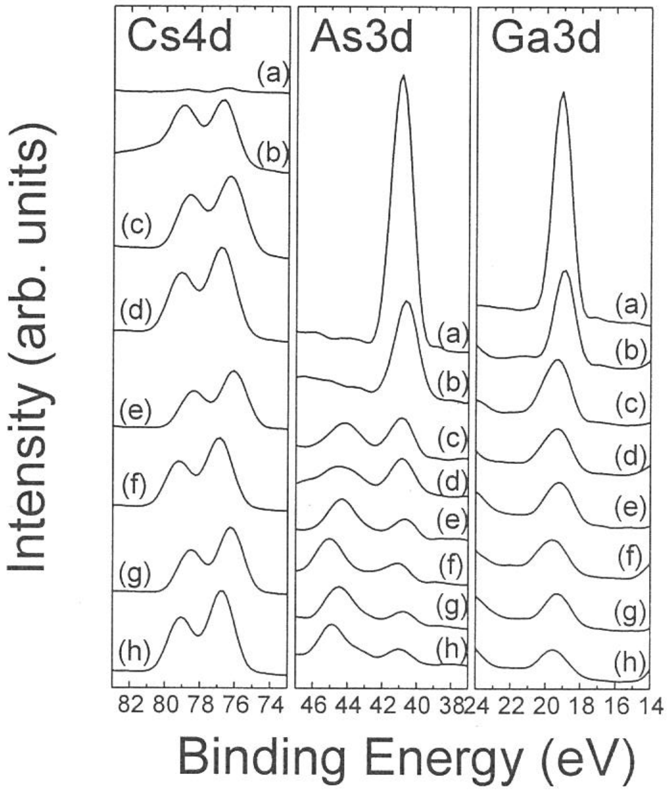

Figure 1 The EDCs observed at $h\nu = 110$ eV. The EDCs were measured after heating (a), the first Cs deposition (b), the subsequent $O_2$ exposure of 3.6 L (c), the second Cs deposition (d), the second $O_2$ exposure (e), the third Cs deposition (f), the third $O_2$ exposure (g) and the fourth Cs deposition (h). The Cs coverage in each deposition is estimated to be about 1.0, 1.5, 1.8 and 2.2 monolayers for EDCs (b), (d), (f) and (h), respectively. The differences in work function relative to the clean surface were -0.99, -3.47, -2.12, -3.31, -2.29, -3.11, -2.37 and -2.84 eV for (a)-(h), respectively.

---

[*] Present address: Fritz-Haber-Institut der Max-Planck-Gesellschaft, Faradayweg 4-6, D-14195, Berlin (Dahlem), Germany.

cesium atoms donate electrons to Ga and As atoms, which results in the shift to the lower energy side, while oxygen atoms attract electrons from Ga and As atoms to cause the shift to the higher energy side. The Cs-4d peak also shifts to the lower binding energy side by the first oxygen exposure. According to the simple relation between the chemical shift and the net charge of atoms, the experimental results indicate that the average number of electrons in Cs increases by the oxygen exposure. This is not easily understood from the view point of the simple direct reaction between Cs and oxygen atoms. The present results may be explained by taking account of the complex reaction including As segregation and the resurfacing of Cs atoms. It is supposed that As atoms segregate and Cs atoms move inside during the Cs deposition, which results in the situation where Cs atoms are located in the mid of the As atoms and the GaAs substrate. After the oxygen exposure, it is also supposed that Cs atoms move toward the surface, and it causes the increase of the intensities of Cs-4d peak, while oxygen atoms go inside to react with As and Ga atoms. It is noted that the oxidation of As and Ga atoms is enhanced by the existence of Cs atoms.[5] The broadening of the Ga-3d and Cs-4d peaks and the appearance of the oxidized As-3d peak after the first oxygen exposure support this complex reaction which produces oxides of As, Ga and Cs.

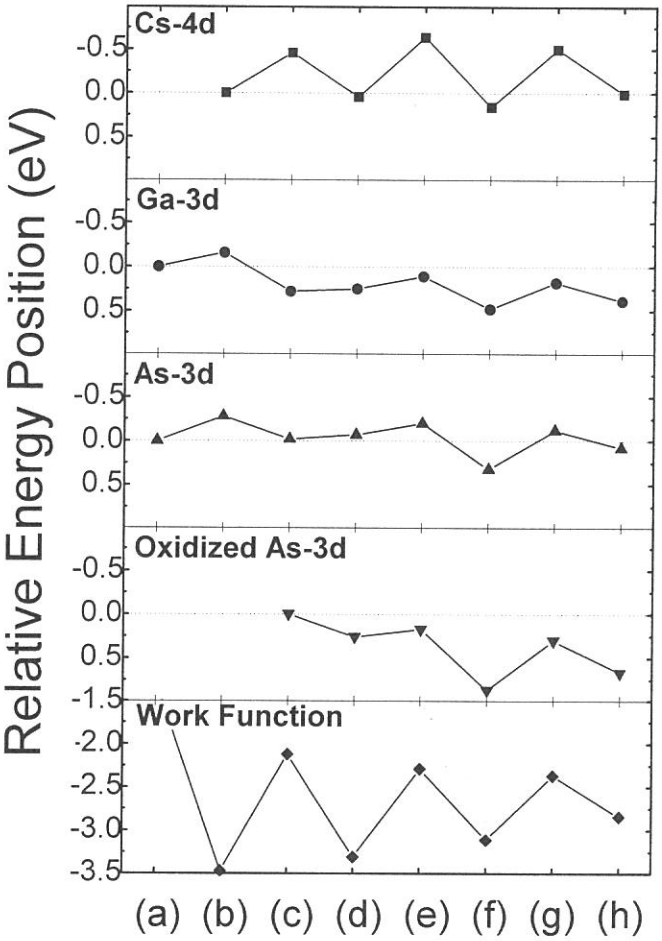

Figure 2 The energy positions of Cs-4d$_{5/2}$, Ga-3d and As-3d photoelectrons observed after the treatments. The + and - signs of the energy positions mean the decrease and the increase of the binding energy, respectively. The change in the work function relative to the clean surface is also shown in the figure. The treatments (a)-(h) correspond to those shown in Fig. 1.

At the higher treatment stage, the deposition of Cs causes the Ga-3d and As-3d peaks to shift to the higher energy side, and the exposure of oxygen makes the shift of these peaks to the lower energy side. On the other hand, the energy positions of Cs-4d and oxidized As-3d peaks are shifted to the higher energy side by the Cs deposition and to the lower energy side by the oxygen exposure. As shown in Figs. 2, the reaction dynamics at the higher treatment stage is very different from those at the first treatment stage mentioned above. The energy positions of all photoelectrons including Ga-3d, As-3d, Cs-4d and oxidized As-3d are shifted to the lower and higher binding energy sides by n-th oxygen exposure and Cs deposition, respectively. The enhancement of Cs-4d peak in intensity is not observed at the higher treatment stage. The intensity of As-3d peak decreases with the treatment, but the total sum of the As-3d and the oxidized As-3d peaks is almost constant. These results indicate that the reaction among GaAs, Cs and oxygen at higher treatment stage leads to the formation of stable layers or clusters consisting of Cs, O, As and Ga on the GaAs(100) surface. The change in the energy positions of all photoelectrons at the higher treatment stage may be interpreted in terms of the change in band bending, since photoelectron peaks and the work function make parallel shifts in energy.[6]

## References

1 ) W. E. Spicer: Appl. Phys., **12** (1977) 115.

2 ) T. Balasubramanian, J. Cao and Y. Gao: J. Vac. Sci. Technol. A **10** (1992) 3158.

3 ) P. K. Larsen, J. H. Neave, J. F. van der Veen, P. J. Dobson and B. A. Joyce: Phys. Rev. B **27** (1983) 4966

4 ) M. Besancon, R. Landers and J. Jupille: J. Vac. Sci. Technol. **A5** (1987) 2025.

5 ) R. Miranda: *Physics and Chemistry of Alkali Metal Adsorption*, (Elsevier Science Publishers B. V., Amsterdam, 1989), p. 425.

6 ) F. J. Himpsel *et al.*: *Photoemission and Absorption Spectroscopy of Solids and Interfaces with Synchrotron Radiation*, (Elsevier Science Publication B. V., Amsterdam, 1990), p. 203.

(BL6A2)

# The effect of valence hole self-trapping on fast luminescence in $BaF_2$

M.A.Terekhin, S.Fujiwara, M.Kamada

UVSOR Facility, Institute for Molecular Science, Okazaki 444 Japan

The emission and excitation spectra have been measured for impurity and intrinsic luminescence for pure $BaF_2$ and mixed crystal $BaF_2$(70%) - $LaF_3$(30%) in the region 80-130 eV using beamline BL6A2 [1].

The figure 1 (insert) shows the emission spectra of $BaF_2$ and $BaF_2$-$LaF_3$ measured at room temperature. The spectrum of $BaF_2$ consists of one nanosecond band at 5.6 eV (called cross or Auger-free luminescence (AFL)) and self-trapped exciton (STE) luminescence at 4.2 eV. The emission for $BaF_2$-$LaF_3$ is composed from two nanosecond bands at 4.6 and 5.4 eV and peak at 3.8 eV which could be assigned to rear-earth impurity in the crystal .

We have found that the excitation spectrum for $BaF_2$ near (Ba,4d) absorption edge decreases with the energy excitation (figure 1, curve 1), while the spectrum for $BaF_2$-$LaF_3$ increases (curve 2), showing the same features as the absorption coefficient in region 90 -107 eV (curve 3) measured in [2]. One of the explanation of the different behavior in excitation spectra of AFL is the thermal quenching of STE in $BaF_2$-$LaF_3$. In pure $BaF_2$ the local concentration of STEs created in the same absorption process near (Ba,4d) should be more than in $BaF_2$-$LaF_3$ and so the secondary electron excitation quenching [3,4,5] due to interaction of (Ba,5p) core hole and STE in the former crystal is more pronounced. It seems that the important role in this process plays the self-trapping of the valence hole which sufficiently decreases the distance between core hole and secondary excitation created at the same absorption process.

References

[1] UVSOR Activity Report **1995** (1996) 21.

[2] C.Tarrio, D.E.Husk, and S.E.Schnatterly, J.Opt.Soc.Am. B **8**, 1588 (1991).

[3] M.A.Terekhin, A.N.Vasil'ev, M.Kamada, E.Nakamura, and S.Kubota, Phys.Rev.B 52 (1995) 3117.

[4] M.A.Terekhin, I.A.Kamenskikh, V.N.Makhov, V.A.Kozlov, I.H.Munro, D.A.Shaw, C.M.Gregory, and M.A.Hayes, J.Phys.:Condens.Matter **8** (1996) 497.

[5] A.N.Belsky, R.A.Glukhov, I.A.Kamenskikh, P.Martin, V.V.Mikhailin, I.H.Munro, C.Pedrini, D.A.Shaw, I.H.Shpin'kov, and A.N.Vasil'ev, Journal of Electron Spectroscopy and Related Phenomena **79** (1996) 147.

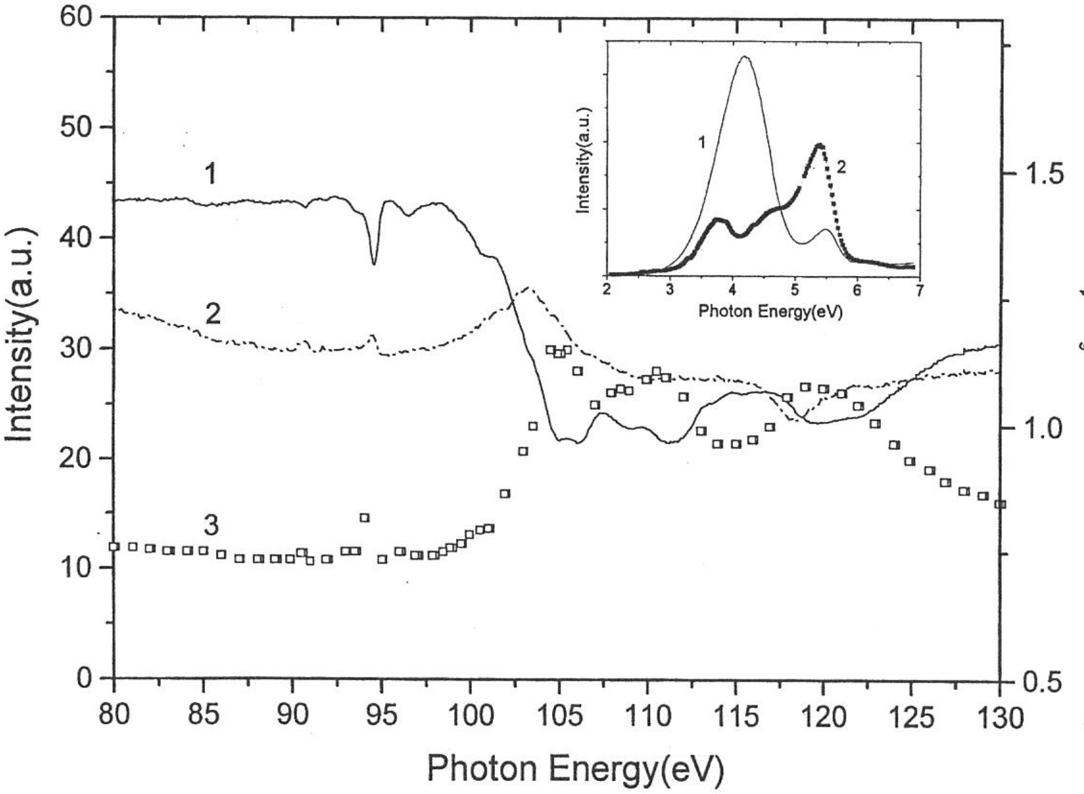

Figure 1. The excitation spectra of 5.6 eV emission band in $BaF_2$ (1), and 5.4 eV in $BaF_2$ - $LaF_3$ (30%) (2) and for comparison the absorption spectrum of $BaF_2$ at T=295 K (3) [5]. (the insert shows the emission spectra for $BaF_2$ and mixed $BaF_2$ - $LaF_3$(30%) crystals) .

(BL6B)

# Synchronization between Picosecond Mode-locked Laser and Synchrotron Radiation for Time-resolved Measurement in Far-infrared Region

Tahei TAHARA, Misa KAYAMA, Akito UGAWA and Kyuya YAKUSHI
Institute for Molecular Science, Myodaiji, Okazaki 444

It is well known that far-infrared spectra contain much information about low-frequency motions in materials, including intermolecular vibrations in liquids and phonons in solids. It is highly desirable to develop time-resolved far-infrared spectroscopy (TRFIR), since it is expected to shed new light on the dynamics of materials from the viewpoint of low-frequency vibrations. However, in spite of recent rapid advances of the laser and detector technologies, it is still difficult to carry out TRFIR spectroscopy because (1) the lack of suitable crystals makes it difficult to generate short FIR pulses with the nonlinear optical process, and (2) the response of ordinary far-infrared detectors is quite slow. Synchrotron radiation (SR) affords picosecond optical pulses ranging from X-ray to far-infrared, and hence it gives us a unique chance to carry out picosecond TRFIR spectroscopy [1]. In the UVSOR facility, there exist two beamlines (BL6A1 and BL6B) designed for the infrared and/or far-infrared experiments, which are now equipped with Fourier-transform-type spectrometers and bolometers. At present, far-infrared spectra of *static* samples are measured at these beamlines using *picosecond SR pulses* which automatically collect spectral information through a picosecond time window. If we can induce a detectable change in the sample by irradiation of the picosecond laser pulses which are synchronized to SR, we can accomplish TRFIR measurement without any change in the detection system already available at UVSOR. Based on this idea, we are now constructing a setup for the trial of TRFIR measurements at beamline 6B (Fig. 1).

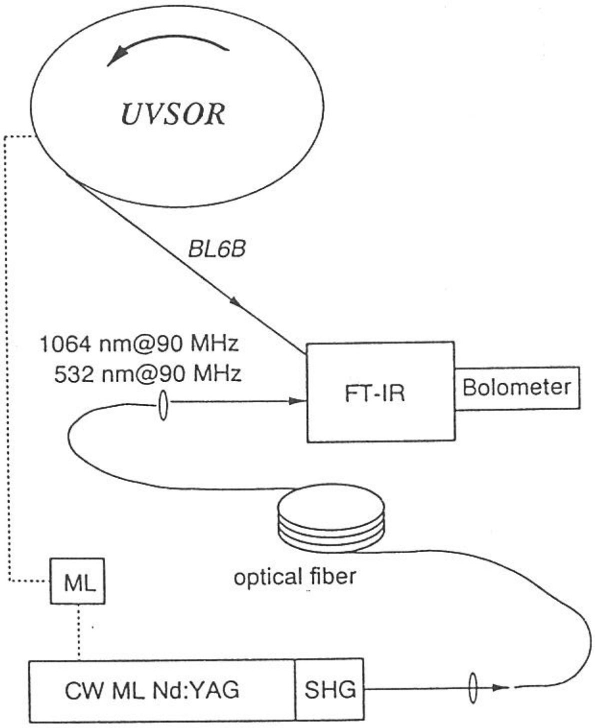

Fig. 1 An experimental setup for TRFIR measurement at BL6B.

A key technology for this type of pump (laser) - probe (SR) spectroscopy is synchronization between picosecond lasers and SR. One of the practical advantages of the SR at UVSOR is that its frequency (90 MHz) matches the repetition rate of ordinary mode-locked lasers, which allows us to achieve full one-to-one synchronization between laser pulses and SR pulses without reducing the number of the electron bunches in the storage ring. We applied the RF signal given from the storage ring to a cw mode-locked Nd:YAG laser (Quantronix 416) whose cavity length is optimized for the 90-MHz operation, and achieved full synchronization between the laser and SR. The synchronization based on this scheme was fistly demonstrated and reported by Mitani and coworkers [2]. The laser pulses were transported to the beamline with use of single-mode optical fibers, and the timing between the laser pulse and the SR was measured with single photon counting technique. Figure 2 shows a typical temporal profiles of picosecond laser pulses and SR pulses. The timing were controlled by a phase shifter which changes the phase of the RF signal applied to the mode-locker of the laser.

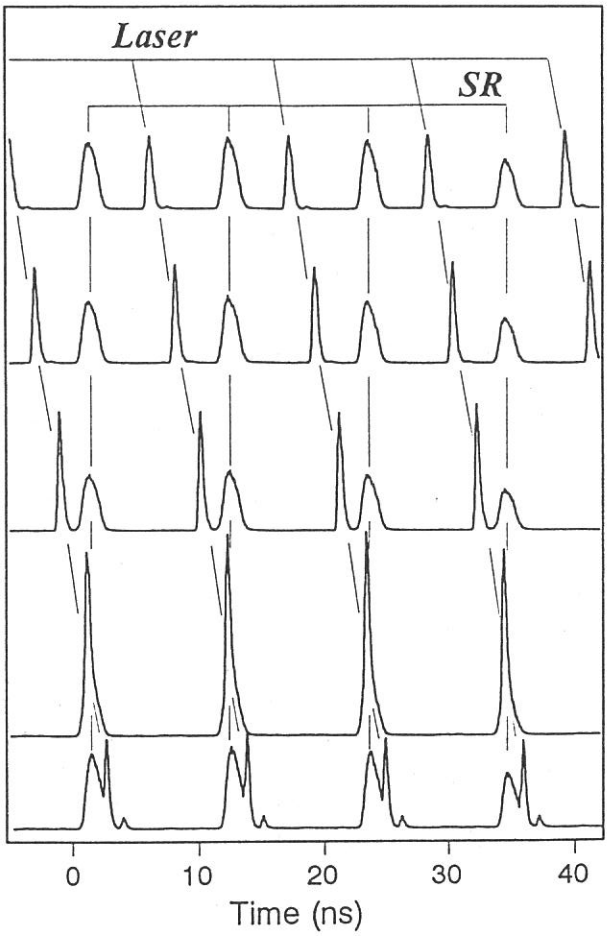

Fig. 2 Synchronization between synchrotron radiation and a picosecond mode-locked laser.

References

1. J. Long, *Synchrotron Radiation News*, 7 , 20 (1994).
2. T. Mitani, H. Okamato, Y. Takagi, M. Watanabe, K. Fukui, S. Koshihara and C. Ito, *Rev. Sci. Instr.*, 60, 1569 (1989).

## (BL7A)

# Performance of YB66 Soft X-ray Monochromator Crystal at the Wiggler Beamline of UVSOR Facility

Toyohiko KINOSHITA, Yasutaka TAKATA, Tokuo MATSUKAWA[1], Hirofumi ARITANI[2],
Shigehiro MATSUO[2], Takashi YAMAMOTO[2], Masao TAKAHASHI[3], Hisao YOSHIDA[4],
Tomoko YOSHIDA[5] and Yoshinori KITAJIMA[6]

Institute for Molecular Science, Myodaiji, Okazaki 444, Japan
[1]Department of Physics, Naruto University of Education, Naruto 772-01, Japan
[2]Department of Molecular Engineering, Kyoto University, Kyoto 606-01, Japan
[3]The Institute of Scientific and Industrial Research, Osaka University, Mihogaoka 8-1, Ibaraki, Osaka 567, Japan
[4]Department of Applied Chemistry, School of Engineering, Nagoya University, Nagoya University, Furo-cho, Chikusa-ku, Nagoya 464-01
[5]Division of Energy Science, Center for Integrated Research in Scinece and Engineering, Nagoya University, Furo-cho, Chikusa-ku, Nagoya 464-01
[6]Photon Factory, National Laboratory for High Energy Physics, Oho 1-1, Tsukuba 305, Japan

We have succeeded to measure soft X-ray spectra by using YB66 monochromator crystal at the double crystal monochromator beamline BL7A of the UVSOR facility, where the 4T wiggler radiation is provided. The YB66 is known to be one of the best monochromator crystals which cover soft X-ray region from 1.1 to 2keV with higher performance1), for example, higher energy resolution, no absorption structures originating from the elements of crystal in the photon energy range, toughness against radiation and so on. So far only the SSRL (Stanford synchrotron radiation laboratory) group employed the YB66 crystal2), since the crystal is easily deformed by higher heat load from synchrotron radiation from higher energy storage ring. The storage ring of the UVSOR facility is operated at rather lower energy (750 MeV) which produce rather lower heat load. At the crystal position, the value of less than 0.03W/mm$^2$ is estimated, which is 2 order lower than those for the double crystal monochromator beamlines at the Photon Factory. Further, the 4T wiggler to provide higher photon flux in the region of soft X-ray is installed at the UVSOR. These are the motivations why we tried to make a performance check of the YB66 monochromator crystal at the UVSOR facility. The crystal is commercial one and made by Crystal Systems Inc., Yamanashi, Japan.

Figure 1 shows the throughput of the monochromator with the use of YB66 (400). We have also measured the XAFS spectra for Mg and Al compounds as shown in Figures 2 and 3. The deviation originated from deformation effect by heat load to the crystal is less than 0.01 degree which corresponds to the energy shifts of about 0.1eV. It is concluded that the effect of heat load is almost negligible for spectroscopy measurements.These results show that the YB66 crystal can be enough to use as the monochromator crystal. In Figs. 1and 2, two positive glitches at 1385.6 and 1438 eV are observed. These two glitches are known to be due to the 600 reflection light corresponding to the Y $L_{2,3}$ absorption edges whose original (400 reflection light) peaks are also shown in Figure 1 at 2080 and 2156 eV, respectively3). In order to take more precise XAFS data especially for the Mg compounds, the reduction of the higher energy component of the light is necessary for the next step of the improvement of the beamline.

We have tried to measure the rocking curves of YB66 crystal in order to estimate energy resolution (not shown here). The rocking curves showed some multi-structures and wider width than those reported before2). We have also observed the image of output light by using fluorescence screen. The image was not homogeneous. These results mean that the surface of the crystal is not ideal single crystal, instead, consists of multi-domains.

The use of the YB66 crystal might be very powerful and valuable for the future studies of the soft X-ray spectroscopy at the UVSOR. The YB66 crystal has already been used in some beam times. As shown in the part of this activity report by Y. Ufuktepe et al., photoelectron spectroscopy in such photon energy region also became possible.

## Acknowledgements

Authors would like to thank to the staff members of the UVSOR facility for the support. T.K. and Y. T. thank to Dr. T. Tanaka and Dr. J. Wong for the invaluable discussions.

## References

1) J. Wong, G. Shimkaveg, W. Goldstein, M. Eckart, T. Tanaka, Z. U. Rek and H. Tompkins, *Nucl. Instr. and Meth.* **A195**, 243 (1990).
2) M. Rowen, Z. U. Rek, J. Wong, T. Tanaka, G. N. George, I. J. Pickering, G. H. Via and G. E. Brown Jr., *Synchrotron Radiation News* **6**, 25 (1993).
3) T. Tanaka, T. Aizawa, M. Rowen, Z. U. Rek, Y. Kitajima, I. Higashi, J. Wong and Y. Ishizawa, submitted to *J. Appl. Crystallography* .

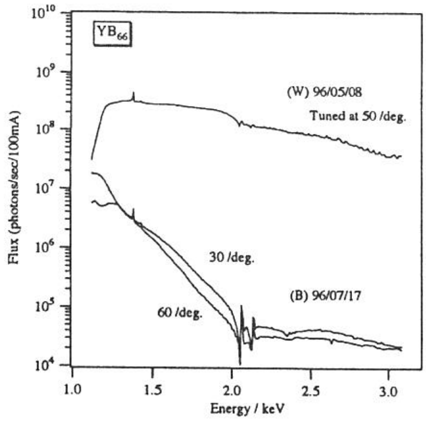

**Figure 1.** Throughput from the double crystal monochromator with YB66(400). Radiations from the 4T wiggler (W) and the bending magnet (B) are used respectively. The position of the 2nd crystal of the monochromator was tuned at 50, 30 and 60 degrees, respectively.

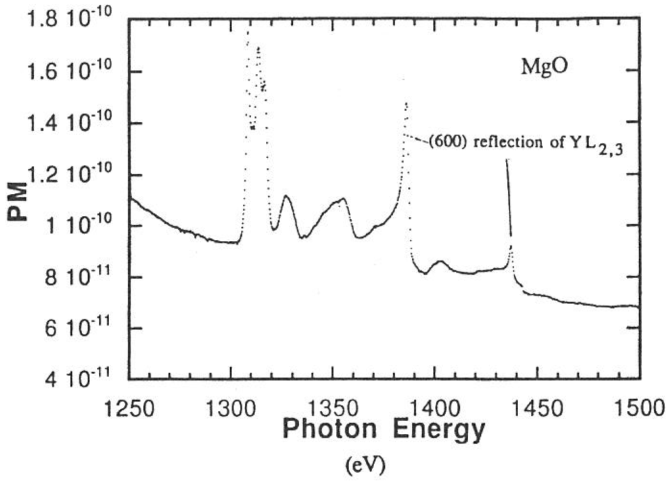

**Figure 2.** Absorption spectrum of MgO at Mg *K* edge. It is noticed that two glitches originating from 600 reflection overlap with EXAFS structures.

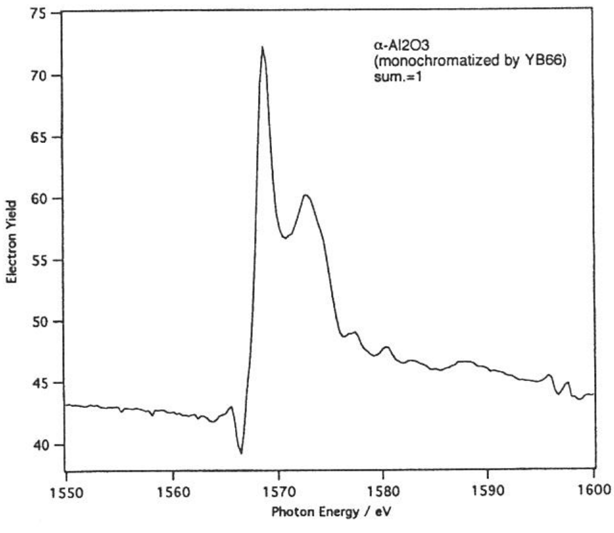

**Figure 3.** Absorption spectrum of α -$Al_2O_3$ at Al *K* edge

(BL7A)

# 3d-4f Resonant Photoemission of Tm Compounds

Y.Ufuktepe*, S. Kimura, K.G. Nath** and T. Kinoshita
** Physics Department, University of Cukurova, 01330 Adana, Turkey*
*UVSOR Facility, Institute for Molecular Science, Okazaki 444, Japan*
***Department of Structural Molecular Science, The Graduate University for Advanced Studies, Okazaki 444, Japan*
H. Kumigashira, T. Takahashi, T. Matsumura and T. Suzuki
*Department of Physics, Tohoku University, Sendai 980-77, Japan*
H. Ogasawara
*Institute for Solid State Physics, University of Tokyo, Tokyo 103, Japan*

The electronic structure study of rare earth element and their compounds is an area of increasing interest. The majority of recent studies has focused on resonant photoemission [1]. In order to obtain information about resonant behavior of core excited states, we have studied several thulium monochalcogenides (TmX ; X=S, Se, Te) in photon energy ranges of 3d-4f (1450-1550 eV) excitations followed by 4d-4f resonant photoemission which is described in detail elsewhere [2].

The advantages to perform 3d-4f resonant photoemission study are as follows. First of all, the kinetic energy of the photoelectrons is higher and results should reflect bulk sensitive information. Second, as shown in Ref. 3, the absorption peaks of Tm 3d core level are very sharp and show well separated multiplet structures . This will enable us to separate the different excitation and decay channels and 4f photoemission from different valences more easily than when using 4d-4f resonant excitation.

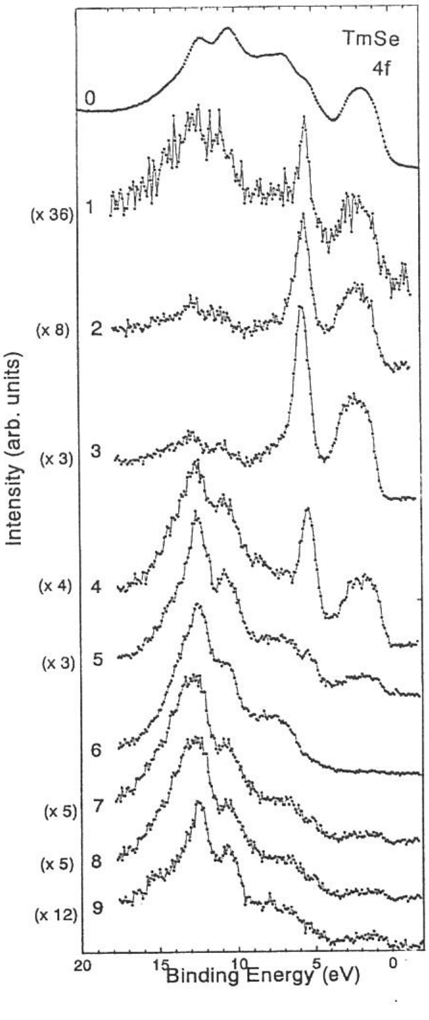

(a)

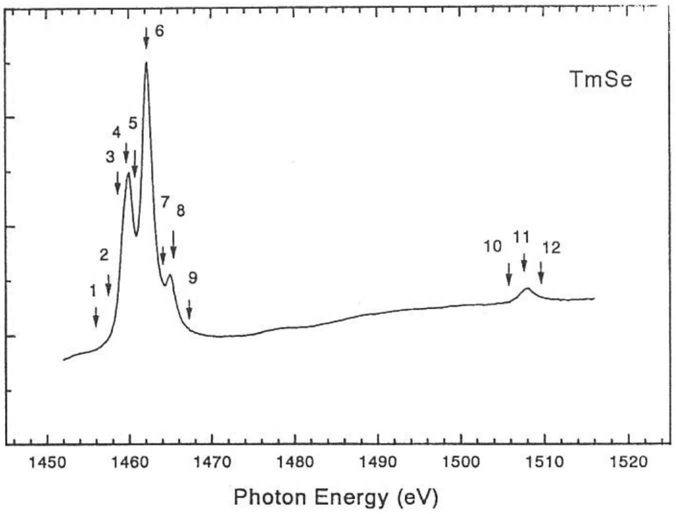

(b)

**Figure 1:** **(a)** *Photoemission spectra of TmSe in the excitation energies of 1456- 1467 eV and XPS spectrum with MgKα excitation shown at the top most of the Figure.* ***(b)*** *Total yield spectrum of TmSe from the Tm 3d region. Selected excitation photon energies for photoemission spectra are marked by arrows.*

Further the contrast of on and off resonant intensities should be larger in the 3d-4f excitation process. This might be suitable for resolving photoemission features of such a mixed valent compounds. However it is not easy to perform photoemission experiments in such high binding energy of 3d core level region of heavy rare earth compounds. The main difficulties are due to relatively lower photon flux and energy resolution in this photon energy region. By this reason, most of the 3d-4f resonant experiments have been performed only by absorption spectroscopy and very little photoemission study has been done with tunable light source so far.

Experiments were performed at the double crystal monochromator (DXM) beam line BL7A. The monochromator crystal of $YB_{66}$ was used [4]. The photon energy was calibrated by using MgK$\alpha$ and AlK$\alpha$ X-ray photoemission spectra, which was incorporated with our experimental system. In order to perform photoemission measurements, the VG ESCA LAB 220i-XL system whose base pressure was less than $2\mathrm{x}10^{-10}$ torr was connected to the beam line. A clean surface was prepared by cycles of $Ar^+$ ion bombardment. Sample cleanliness was monitored by the oxygen 1s photoemission peak. Overall energy resolution was expected to be less than 1 eV.

Figure 1 (a) shows the valence band photoemission spectra of TmSe in the 3d-4f resonance region. The total yield (TY) spectrum which corresponds to 3d-4f absorption spectrum is also shown in Fig. 1(b). Excitation photon energy of the resonant photoemission measurements were chosen from the position of the TY spectrum indicated by arrows. Total yield spectrum shows two groups of peaks, which are assign to be $3d_{5/2}$ and $3d_{3/2}$ . The $3d_{5/2}$ peaks show multiplet structures mainly from trivalent component. It has been reported that $3d_{5/2}$ absorption peaks consist of three peaks for trivalent component and single peak for divalent Tm ions due to their final state multiplets [3,5]. TmSe is a mixed valent material [6,7]. Therfore, our TY spectrum can be understood as a superposition of divalent and trivalent components. Actually around 1459 eV photon energy we can observe a little shoulder structure in the spectrum. Further, near this photon energy the photoemission spectra show big resonant enhancement mostly from divalent components located between (0-6) eV binding energy (BE) . On the other hand, only the trivalent peaks located between (6-14) eV BE were enhanced around 1462 eV which is a position of most dominant absorption peak of trivalent ions.

We can clearly observe and distinguish the divalent and trivalent parts of photoemission spectrum as explained above . The 3d-4f resonant photoemission results indicate that the ratio of on and off resonance intensity much higher than the 4d-4f. We conclude that 3d-4f resonant photoemission is a very powerful technique to investigate the 4f emission process and excitation and decay channel mechanisms in mixed valent systems the different valencies can be clearly observed. We have calculated EDC's and constant initial state spectra (CIS's) of $Tm^{3+}$ and $Tm^{2+}$ when the excitation photon energy was tuned near the Tm 3d core level binding energy. Our calculated spectra support the interpretation of the experiments.

## References

[1] "Synchrotron Radiation Research: Advances in Surface and Interface Science, Volume 1; Techniques" , edited by R. Z. Bacharach, (Plenum Press, New York, 1992).

[2] Y. Ufuktepe et al., in this issue.

[3] B.T. Thole, G. van der Laan, J. C. Fuggle, G. A. Sawatzky, R. C. Kartanak, and J. M. Estava, Phys. Rev. B, **32**, 5107 (1985).

[4] T. Kinoshita et al., in this issue.

[5] A. B. Belhassan, R. C. Kartanak, N. Spector, and C. Bonnelle, Phys. Lett. **82A**, 174 (1981)

[6] G. Kaindl, C. Laubschat, B. Reihl, R.A. Pollak, N. Martensson , F. Holtzberg, and D.E. Estman, Phys. Rev. B. **26**, 1713 (1982)

[7] G. K. Wertheim, W. Eib, E. Kaldis, and M. Campagna, Phys. Rew. B., **22,** 6240 (1980).

(BL7A)

# Na and Mg K-edge XANES of silicate minerals and glasses

Dien Li [a,c], Tatatoshi Murata [b] and Mingsheng Peng [c]

[a] Department of Surface Chemistry, National Institute of Materials and
Chemical Research, Tsukuba, Ibaraki 305, Japan
[b] Department of Physics, Kyoto University of Education, Kyoto 612, Japan
[c] Department of Geology, Zhongshan University, Guangzhou, 510275, P.R. China

Na and Mg act as network modifiers in silicate glasses. The local structure and coordination of Na and Mg are closely related to the physical properties of the silicate glasses and melts, and have been studied using x-ray scattering analysis, IR and Raman, magic angle spinning (MAS) NMR. However, the results from different techniques are inconsistent. In this work, Na and Mg K-edge x-ray near-edge structure (XANES) has been applied to study their local structure and coordination in silicate glasses.

The preparations of diopside (Di)-albite (Ab), $Na_2O$-$SiO_2$ and $Na_2O$-$SiO_2$-$P_2O_5$ glasses are referred in literature[1-3]. The Na and Mg K-edge XANES of powder samples were measured on the BL7A beamline that used beryl as the monochromator crystal, and recorded by Total Electron Yield (TEY) in the chamber of about $\sim 10^{-7}$ torr.

Fig. 1 shows the Mg K-edge XANES of spinel, diopside and pyrope (upward) (A) and diopside (Di)-albite (Ab) glasses. The coordination of Mg in spinel, diopside and pyrope is 4, 6 and 8, respectively. The spectral profiles of these minerals are different, and the Mg K-edge shifts towards higher energy with increase in the coordination number of Mg, the former may be related to the coordination geometry, and the latter to the Mg-O bond distance. By comparison, the Mg K-edge XANES of the Di-Ab glasses are very different from that of diopside, and more resemble to the profile of the pyrope spectrum, but the energy position of the Mg K-edge is similar to that of spinel. Thus, it is speculated that Mg in the Di-Ab glasses is eight-fold coordinated with oxygen, but the Mg-O bond distance is shorter than that of the eight-fold coordinated Mg in normal silicate minerals.

Fig. 2 shows Na K-edge XANES of $Na_2O$-$SiO_2$ (A) and $Na_2O$-$SiO_2$-$P_2O_5$ glasses (B). The Na K-edge XANES show little change with increase in the content of $Na_2O$ in $Na_2O$-$SiO_2$ glasses (A). However, the addition of P into the $Na_2O$-$SiO_2$ system causes dramatic change of the Na K-edge XANES, and the Na K-edge spectra of $Na_2O$-$SiO_2$-$P_2O_5$ glasses also change with the increase of $P_2O_5$ content (B). The correlation between the Na K-edge XANES features and its coordination geometry remains unclear at this stage.

This work is also partially supported by The Natural Science Foundation of China.

## References

[1] Keppler, H. (1992), Amer. Mineral. 77, 62-75.
[2] Henderson, G.S. (1995), J. Non-Cryst. Solids, 196, 43-50.
[3] Li, Dien, Bancroft, G.M. and Fleet, M.E. (1996), Amer. Mineral., 81, 111-118.

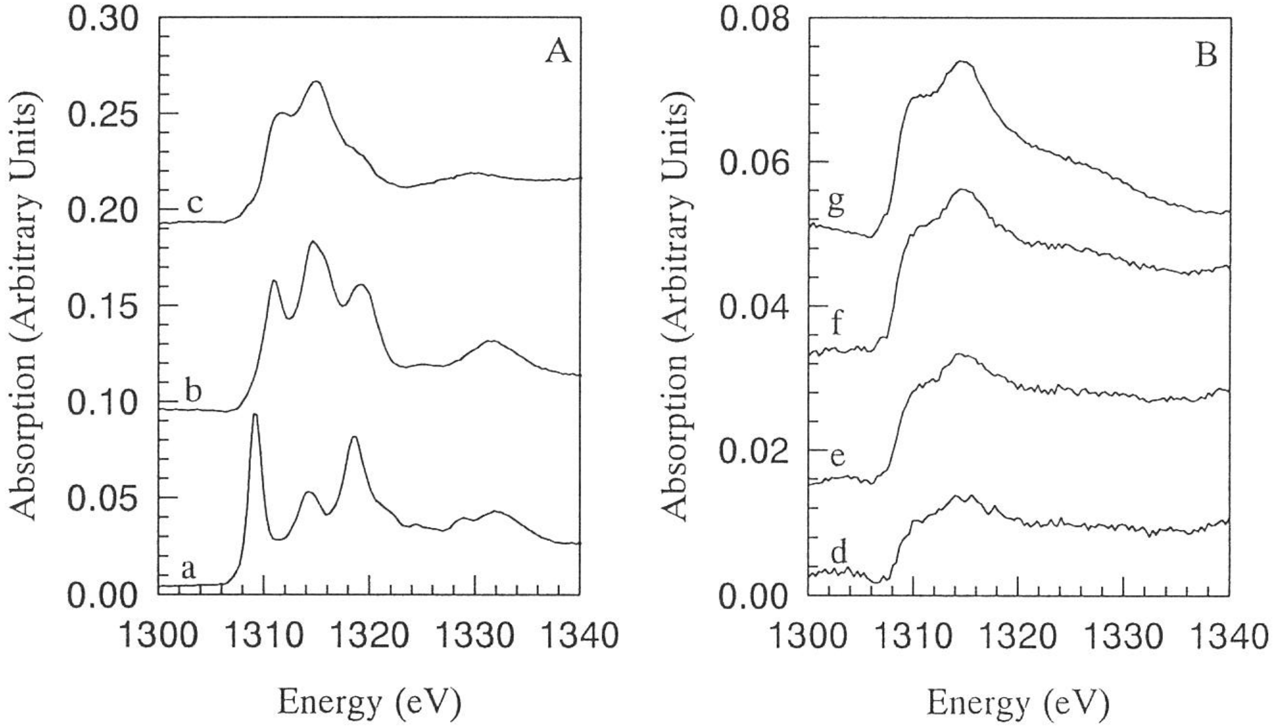

Fig. 1 Mg K-edge XANES of some minerals (A) and diopside (Di)-albite (Ab) glasses (B). a. Spinel; b. Diopside; c. Pyrope; d. $Di_{10}Ab_{90}$; e. $Di_{20}Ab_{80}$; f. $Di_{50}Ab_{50}$; g. $Di_{100}$ glass.

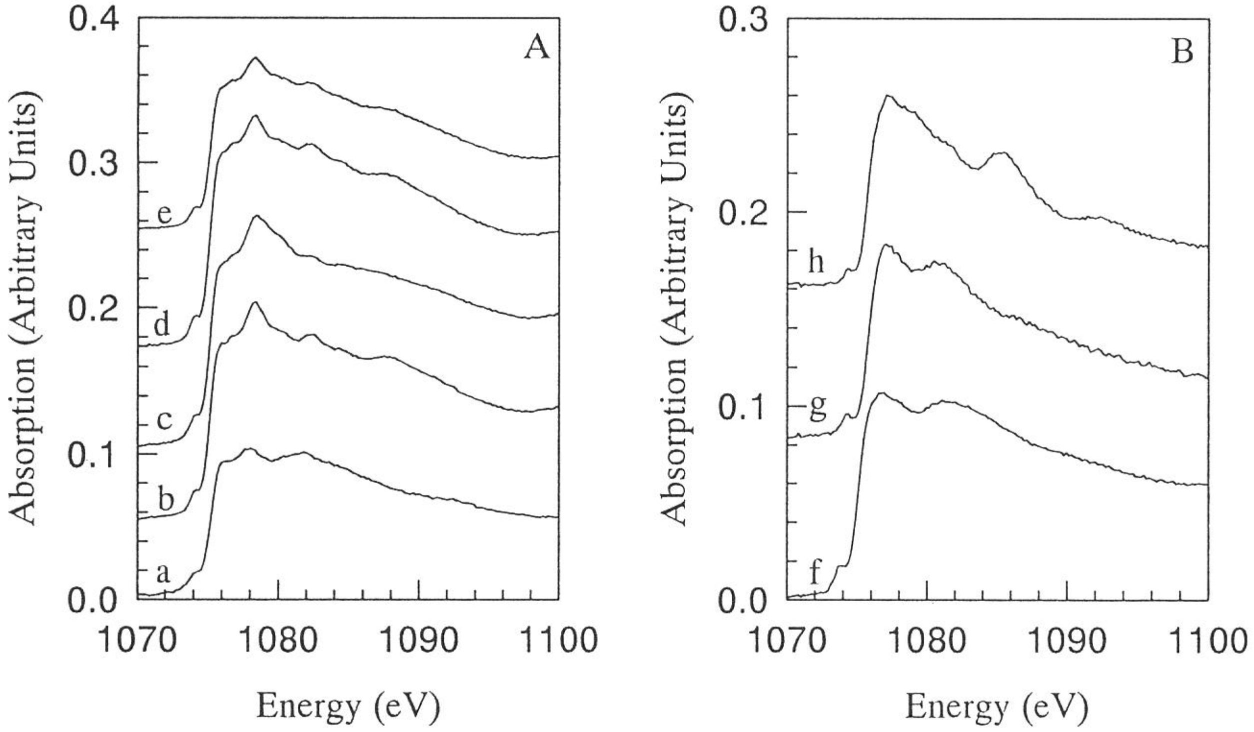

Fig. 2 Na K-edge XANES of $Na_2O$-$SiO_2$ (A) and $Na_2O$-$SiO_2$-$P_2O_5$ (B) glasses.
(A). From a to e, the content of $Na_2O$ is 15, 20, 25, 30 and 35 mol%, respectively;
(B). From f to h, the content of $P_2O_5$ is 15.6, 31.7 and 58.3 mol%, respectively.

(BL7A)

# Photo-luminescence yield spectra of porous Si in the Si-K excitation energy.

Tokuo MATSUKAWA, Yosifumi HARA, Hiroaki OKUTANI,
Makoto HONDA, Kouzou ATOBE and Noboru FUKUOKA
*Department of Physics, Naruto University of Education, Naruto, Tokusima 772*

Visible light emission from electrochemically etched surface of crystalline silicon has been attracting much attention. An origin of the light emission has been attributed to nano-scale porous structures formed by anodizing process, while the other possibilities have been proposed. Although extensive studies have been carried out, the scheme is controversial.

We have measured the photo-luminescence spectra of porous silicon as excited with Si-K soft x-ray as well as the total photoelectron yield spectra. The experiments were carried out at the soft x-ray beam line, BL-7A, in the Institute of the Molecular Science, Okazaki. The visible light from the porous Si were detected by photomultiplier tube through focusing lens , as well as the drain current of the sample owing to the photoelectron was measured. Thus, the photo-luminescence yield and the total electron yield spectrum were measured simultaneously. Porous Si samples were prepared by a standard anodizing method. Visible light emission spectra were measured before and after the experiment. One of the porous sample was anodized on site, and immediately evacuated in the sample chamber just after holding onto the sample holder. Thus the spectra should be considered to be with fresh surface which has not covered with no extra-chemical compound layer.

Figure 1. show the results obtained with typical porous Si samples with different surface conditions. In the bottom of the figure, the result of crystal Si is shown for comparison. The bold curves show the photo-luminescence yield spectra (PLY), and the thin curves show the total electron yield spectra (TEY). The PLY curve show abrupt step-like rise in intensity at the Si-K edge, while no signal was detected from crystal Si except dark current noises. Thus, the porous Si emits visible light under the excitation of the soft x-ray, and the photo-luminescence yield jump arises at Si-K edge. Sham *et al.* had reported the same results and discussed the surface condition of the porous Si (1). We have measured on the porous Si which may be regard to be with fresh surface. In the figure, the spectrum of porous Si designated as P-PS was obtained just after the anodizing procedure. For comparison, the result on the thermally oxidized porous Si sample is shown in the figure designated as SO-PS. The both photo-luminescence spectra show only step like simple structure, while the photoelectron yield spectra show differences. The total-electron yield spectrum of the fresh porous Si is different from that of crystal Si. They show no oxide related structure, and the details of the structures appear different among the porous and the crystalline Si structures. The XPS analysis also supported the results. Thus the visible light

emission is originated in the porous structure itself.

The top spectra (WP-PS) were obtained on the porous Si kept in pure water. The total-electron yield spectrum shows the distinct absorption peek at 1844 eV, which may be due to Si-O bondings. At the absorption edge the other structures, a week peak and shoulder, are observed. The photoluminescence yield spectrum shows the similar features at the edge, whereas the other porous Si show no structures. The energy positions of the structures seem to correspond to each other between the photoluminescence and spectra. Such features were poor in the oxidized sample (SO-PS). The spectral feature may be attributed to chemical compounds layer which cover the porous structures

Fig.1. Photo-luminescence spectra (PLY) and total photo-electron yield spectra (TEY) of porous Si and crystal Si.

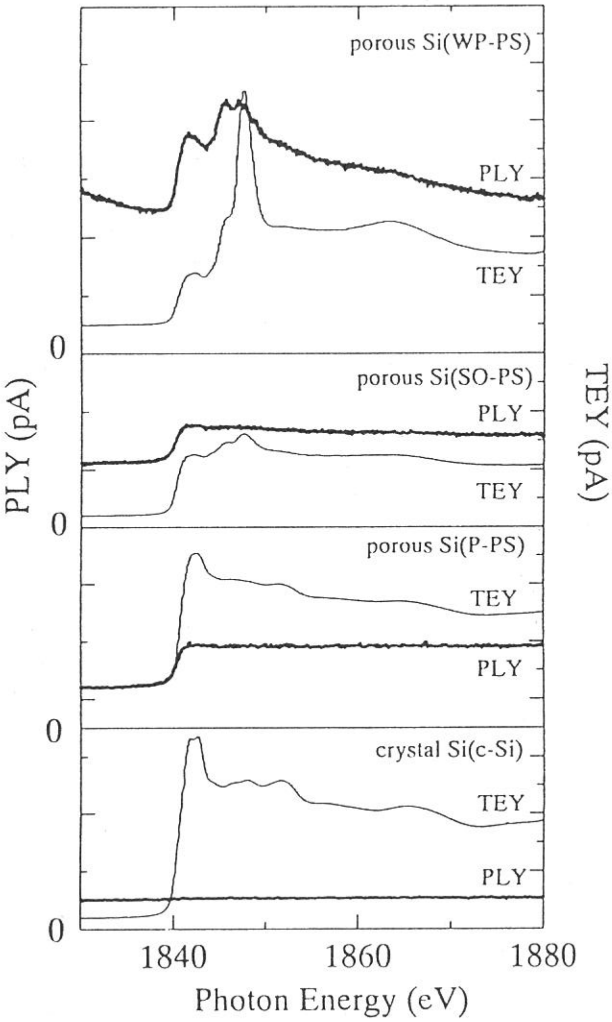

Refefrence

(1) T.K.Sham, D.T.Jiang, I.Coulthard, J.W.Lorimer, X.H.Feng, K.H.Tan, S.P.Ftigo, R.A.Rosenberg, D.C.Houghton and B.Bryskiewcz, Nature,363(1993),331

(BL7A)

# Mg K-edge XANES Study of Silica-Magnesia

Hisao YOSHIDA, Tomoko YOSHIDA,* Tsunehiro TANAKA,* Takuzo FUNABIKI,*
Satohiro YOSHIDA,* Tatsuya ABE, Koichi KIMURA, Tadashi HATTORI

Department of Applied Chemistry, School of Engineering, Nagoya University, Nagoya 464-01
*Department of Molecular Engineering, School of Engineering, Kyoto University, Kyoto 606-01

Silica-magnesia is one of the acid-base bifunctional catalysts. To control the function sophisticatedly, it is important to know the status of component ions, especially the local structure of Mg ion; *e.g.* Mg ion in MgO is octahedrally coordinated, while it is believed that Mg ion located in silica matrix is tetrahedral coordinated [1,2]. In this study [3], Mg K-edge XANES was employed to obtain information of the local structure of the Mg ions in silica-magnesia samples.

Silica-magnesia samples were prepared in following four ways. MgO content of each sample was 15 mass% as standard. (I) Supported sample $MgO/SiO_2$(W) was prepared by impregnation of silica with an aqueous solution of $Mg(NO_3)_2$ followed by evaporation to dryness and calcination in air at 773 K. Silica support was prepared from $Si(OC_2H_5)_4$, ethanol and water by sol-gel method. (II) Another supported sample $MgO/SiO_2$(M) was prepared in the same manner with a methanol solution of $Mg(OCH_3)_2$ instead of the aqueous solution [3]. The solution was prepared by reaction of magnesium metal with refluxed methanol. (III) Binary oxide sample $MgO$-$SiO_2$(W) was synthesized from $Si(OC_2H_5)_4$, ethanol and an aqueous solution of $Mg(NO_3)_2$ by sol-gel method followed by drying and calcination. (IV) Another binary oxide sample $MgO$-$SiO_2$(M) was synthesized in the same way with a methanol solution of $Mg(OCH_3)_2$ instead of the aqueous solution. In addition to these four samples, a reference catalyst JRC-SM-1 (MgO contents was 29 mass%, the Catalysis Society of Japan) was also employed, which was synthesized hydrothermally from MgO and $SiO_2$. X-ray absorption experiments were carried out on the BL-7A at UVSOR. Spectra were recorded at room temperature, using a beryl two-crystal monochromator in a total electron yield mode. The sample was mixed with active carbon in dry hexane and was put on the first photocathode made of Cu-Be of the electron multiplier.

Fig. 1 shows XANES spectra of the silica-magnesia samples a) - e) and reference compounds f) - k). Reference spectra f) - k) seem to be dominantly composed of three peaks, though the energy position, intensity and sharpness are different from each other. The spectra of the prepared silica-magnesia samples a) - d) are classified into three types, indicating that the local structures around Mg atom are obviously distinguishable.

The XANES of $MgO/SiO_2$(M) b) is obviously identical with that of MgO f) of typical rock salt structure, indicating Mg ion exists as MgO particle, *i.e.* the Mg ion is octahedrally surrounded by 6-oxygen atoms [4]. $Mg(OCH_3)_2$ easily reacts with water. In methanol solution, $Mg(OCH_3)_2$ reacts with surface hydroxyl groups on silica and/or reacts with $H_2O$ and $Mg(OCH_3)_2$ molecules in methanol. Each reactions leads to dispersed Mg species and MgO particle, respectively. Since MgO particle was produced in this sample, the latter reaction would be dominant;

$$2\ Mg(OCH_3)_2 + H_2O \rightarrow Mg(OCH_3)\text{-}O\text{-}Mg(OCH_3) + 2\ CH_3OH. \qquad (1)$$

The XANES of $MgO$-$SiO_2$(M) d) is essentially identical to that of JRC-SM-1 e) and a magnesium silicate, $Mg_2Si_3O_8$ i). Sol-gel method and hydrothermal synthesis are known to be suitable for preparing binary oxide whose components are well mixed at an atomic level, *i.e.*, Mg ions would be completely in the silica tetrahedral matrix. Therefore this spectra would be assigned to the tetrahedrally coordinated Mg ion. Through hydrolysis and condensation between $Mg(OCH_3)_2$ and $Si(OC_2H_5)_4$, Mg-O-Si network would be constructed, and high dispersion of Mg ion in silica matrix would be achieved;

$$Mg(OR)_2 + Si(OR)_4 + H_2O \rightarrow Mg(OR)\text{-}O\text{-}Si(OR)_3 + 2\ ROH\ (R = H,\ CH_3,\ C_2H_5). \quad (2)$$

$MgO/SiO_2$(W) a) shows another type of XANES which has twin broad peaks at 1310 and 1315 eV. There are no identical spectrum of the references. Generally in the supported catalysts, metal oxide loaded is classified into alternative structures; particle or dispersed species on the surface. The XANES of $MgO/SiO_2$(W) is clearly different from that of the former, therefore this is assigned to the latter species. Since the species on the silica surface would be affected by silica matrix structurally or electronically, we tentatively propose that it is surface tetrahedral species. The difference between the spectra a) and d) would be explained by the location of Mg species; on the surface or in the bulk. This sample, $MgO/SiO_2$(W) a), was prepared by using aqueous solution of $Mg(NO_3)_2$; under the preparation, it is suggested that Mg ion in aqueous solution adsorbed on the negative charge points of silica surface so that Mg oxide species produced are dispersed and strongly affected by silica surface.

The sample $MgO\text{-}SiO_2$(W) were also prepared by using aqueous solution of $Mg(NO_3)_2$. The spectrum c) is identical to that of $MgO/SiO_2$(W) a), suggesting that the magnesium species are mainly located on the surface of silica. While Mg ion exists as a hydrate cation in aqueous solution, silica-gel network was constructed through the hydrolysis and condensation,

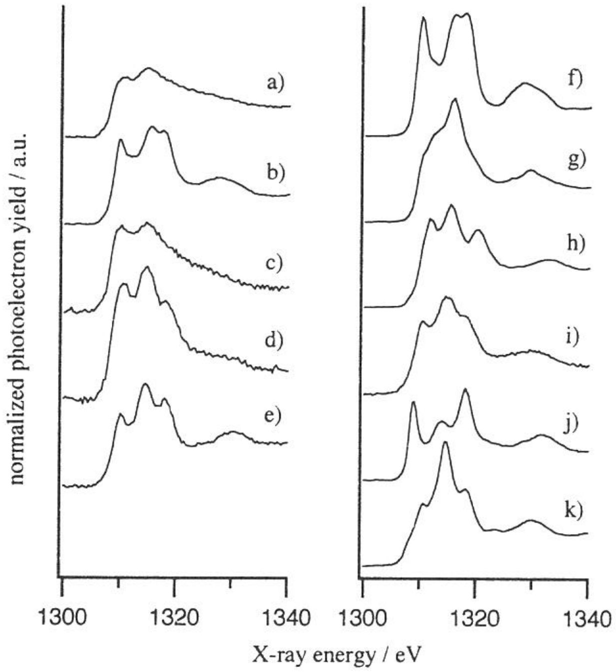

Fig. 1 XANES spectra of the silica-magnesia samples and reference compounds.
a) $MgO/SiO_2$(W), b) $MgO/SiO_2$(M),
c) $MgO\text{-}SiO_2$(W), d) $MgO\text{-}SiO_2$(M), e) JRC-SM-1,
f) MgO, g) $Mg_2SiO_4$ [4], h) $MgSiO_3$ [4],
i) $Mg_2Si_3O_8$, j) $MgAl_2O_4$, k) $Mg(OH)_2$.

$$2\ Si(OR)_4 + H_2O \rightarrow Si(OR)_3\text{-}O\text{-}Si(OR)_3 + 2\ ROH \quad (R = H,\ C_2H_5). \qquad (3)$$

Mg ion would not react with $Si(OC_2H_5)_4$ but only adsorb on silica gel, resulting in the dispersed Mg oxide species like that of $MgO/SiO_2$(W).

In conclusion, it is clarified that three types of magnesium oxide species in silica-magnesia systems are respectively prepared by each suitable method; (i) MgO particle on silica, where Mg ion is located octahedral site, (ii) dispersed magnesium oxide species on the silica surface, which is interacted with surface silica matrix, (iii) dispersed Mg species in the silica matrix, which is tetrahedral.

## References

[1] M. Kermarec, M. Briend-Faure and D. Delafosse, *J. Chem. Soc. Faraday Trans. 1,* **70** (1974) 2180-2188.
[2] H. Yoshida, T. Tanaka, A. Satauma, T. Hattori, T. Funabiki and S. Yoshida, *Chem. Commun.,* (1996) 1153-1154.
[3] H. Yoshida, T. Yoshida, T. Tanaka, T. Funabiki, S. Yoshida, T. Abe, K. Kimura, T. Hattori, *J. de Physique IV, in press.*
[4] H. Yoshida, T. Tanaka, K. Nakatsuka, T. Funabiki and S. Yoshida, *Stud. Surf. Sci. Catal.,* **90** (1994) 473-478.

(BL7A)

# Zr $L_3$-Edge XANES Studies of MgO doped $ZrO_2$

K.Nagashima, T.Ohnari, M.Takagi and S.Hasegawa

*Department of Chemistry, Tokyo Gakugei University, Koganei, Tokyo 184*

## 1. Introduction

It is well established that certain mixedoxide systems have high rates of oxygen anion transport. One classic example of this is when $ZrO_2$ is stabilized in the fluorite structure (cubic) by the addition of a lower valency cation, usually $Ca^{2+}$ or $Y^{3+}$ .1) 2) However, for these results we have another results that $Mg^{2+}$ doped $ZrO_2$ formed tetragonal, not cubic. And also, MgO crystal is important from the view point of heterogeneous catalysis, in spite of it's simple lattice and electronic structure. Base catalyzed reactions occur on MgO at the produced regions such as edge and/or corner of the MgO crystal, and the localized electronic states are considered to be associated with the catalytic behaviors.3)

In the present study, the electronic states of $ZrO_2$ influenced by addition of $Mg^{2+}$ were investigated by Zr $L_3$-edge XANES spectra.

## 2. Experimental

Ziruconium oxychloride was dissolved in water at R.T., then stirring and slowly added aqueous ammonia of 25% to obtain $Zr(OH)_4$ until the solution change into pH8. After $Zr(OH)_4$ was washed by a large quantity water, dried at 383K for 24h. Catalysts were prepared by impregnation with an aqueous solution of $MgCl_2$ of suitable concentration. After impregnation the samples were dried at 393K for 24h, finally catalysts were calcined at 1073K.

The measurements Zr $L_3$-edge XANES spectra were carried out on a facility of BL-7A station of soft X-ray beamline. Each sample was prepared for measurement by grinding with hexane, and then spread on a beryllium-copper dinode which was attached to a first position of electron multiplier into the beamline chamber. After the chamber had been evacuated, the spectrum was recorded in a total electron yield mode at room temperature, using a Ge(111) double crystal monochromator.

## 3. Result and discussion

Figure 1 shows Zr $L_3$-edge XANES spectra of $ZrO_2$ and Mg doped $ZrO_2$ samples. This spectra have two absorbance peak as follows : the first peak($I_A$) corresponds to $2p_{3/2} \rightarrow t_{2g}$ transition and the second one($I_B$) to $2p_{3/2} \rightarrow e_g$ transition. In the case of 15mol% MgO doped $ZrO_2$, intensity ratio($I_B/I_A$) is maximum. This is explained by the changes of electron density that localization to oxygen side or ziruconium side. On the other hand, as shown in Figure 2, crystal systems of these samples moved from monoclinic to tetragonal, increasing with MgO contents. Lattice constant of tetragonal is smaller than that of monoclinic. So, it is presumed that electron density localized to the lattice oxygen. High basic strength was shown on 15mol% MgO doped $ZrO_2$, as shown in Figure 3. This catalyst had much greater activity than another samples in this study. As a result of isomerization of 1-butene, $CO_2$-TPD and XANES, it is presumed that lattice oxygen of 15mol% MgO doped $ZrO_2$ acts as active species exhibited basicity.

Table 1 reported that the energy gap between two absorbance peak of XANES spectra is different between $ZrO_2$ monoclinic and 15mol% MgO doped $ZrO_2$ tetragonal. It is suggested that coordination number is decreased by moving tetragonal. These results are consistent with the initial observations reported by Bare et. al..4)

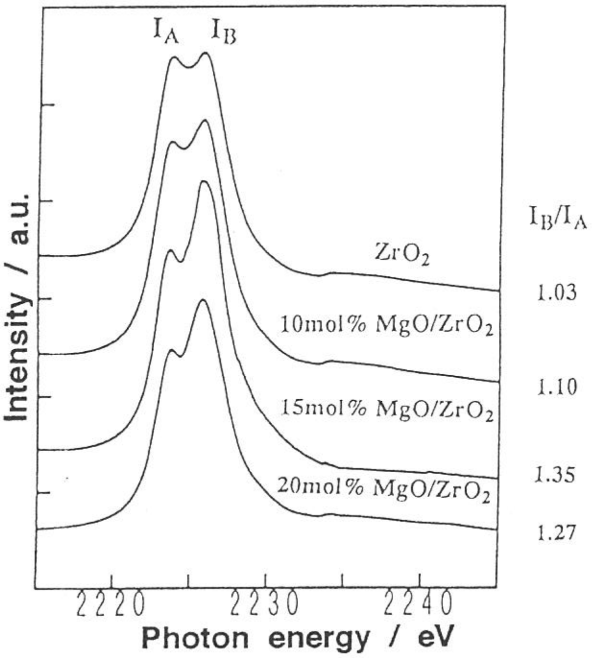

Fig.1 Zr $L_3$-edge XANES patterns of $ZrO_2$ and $MgO/ZrO_2$.

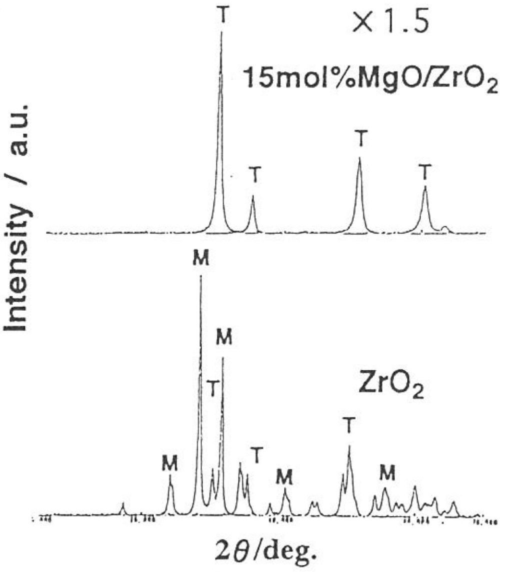

Fig.2 XRD patterns of $ZrO_2$ and 15mol% $MgO/ZrO_2$.
T : $ZrO_2$ tetragonal
M: $ZrO_2$ monoclinic

Table 1. Value of d-orbital splitting.

| samples | symmetry | d-d spritting / eV |
|---|---|---|
| $ZrO_2$ | monoclinic | 2.26 |
| 10mol% $MgO / ZrO_2$ | tetragonal | 2.10 |
| 15mol% $MgO / ZrO_2$ | tetragonal | 2.09 |
| 20mol%$MgO / ZrO_2$ | tetragonal | 2.09 |

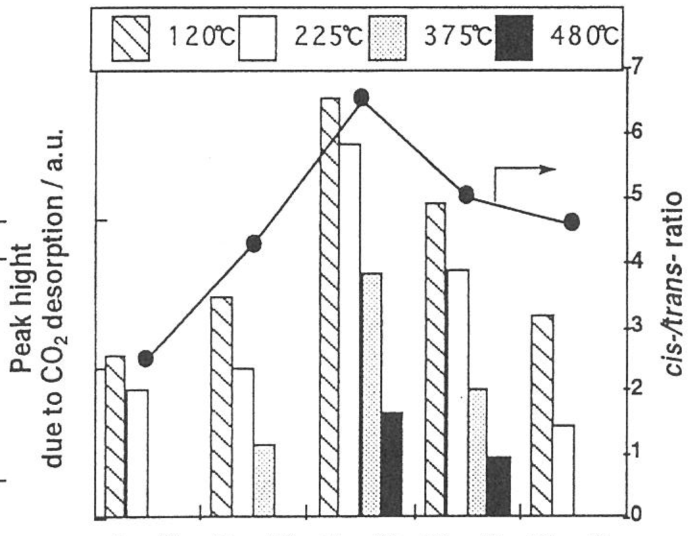

Fig.3 Desorption hight and temperature of $CO_2$ and cis-/trans- ratio for isomerization of 1-butene over $MgO/ZrO_2$ samples.

References
1)L. Ketron, *Ceram. Bull.* **68**, 860 (1989)
2)M. Coile, C. R. A. Catlow and J.P.Dragun, *J. Phys. Chem. Solids.*, **53**, No2, 233. (1992)
3)H. Hattori, Mater. *Chem. Phys.*, **18**, 533 (1988).
4)S. R. Bare, G. E. Mitchell, J. J. Maj; G. E. Vieland and J. L. Gland, *J. Phys. Chem.*, **97**, 6048 (1993) .

(BL7A)

# Mo $L_3$-edge XANES of Molybdenum Bronzes

Hirofumi ARITANI, Tsunehiro TANAKA, Takuzo FUNABIKI,
Satohiro YOSHIDA, Sadao HASEGAWA,* and Noriyuki SOTANI**

*Division of Molecular Engineering, Graduate School of Engineering, Kyoto University,*
*Kyoto 606-01*
* *Department of Chemistry, Tokyo Gakugei University, Koganei, Tokyo 184*
** *Department of Chemistry,Graduate School of Science, Kobe University, Nada, Kobe 657*

## Introduction

Hydrogen molybdenum bronze, $H_xMoO_3$, is classified to four phases depending on included hydrogen[1]; type I (orthorhombic) $0.21 < x < 0.42$, type II (monoclinic) $0.85 < x < 1.04$, type III (monoclinic) $1.55 < x < 1.72$ and type IV (monoclinic) $x = 2$. Type I has a layered structure in which a layer consists of two $MoO_x$ sheets. The $MoO_6$ units connecting to each other with vertices (corner) sharing in the sheet have been proposed to be in an axially symmetric moiety deduced from the result of FT-IR[2] and $^1$H-NMR[3] studies. The other monoclinic phases are not fully characterized. From the results of Mo K-edge XAFS studies, it is proposed that the $MoO_x$ sheet in type I is similar to $MoO_3$ while in type II, a $MoO_x$ sheet is similar to that in rutile $MoO_2$ in which $MoO_6$ is conneced to form a chain by sharing the edges of opposite sides.[4] The present report is devoted to analysis of the local structure of hydrogen molybdenum bronzes by means of Mo $L_3$-edge XANES spectroscopy to clarify more distinct structure around Mo ions.

## Experimental

The hydrogen molybdenum bronze samples, type I and type II, were prepared by a method as reported by Sotani *et al.*[2] The authentic samples were used for the reference of XANES information. The Mo $L_3$-edge XANES data were collected on a facility of BL-7A station of soft X-ray beam line at UVSOR, IMS, with a ring energy, 750 MeV and stored current, 80 - 220 mA. The measurements were carried out in a total electron yield mode at room temperature. The photon energy was calibrated by the Mo $L_3$-edge of a Mo-metal sample (2520.63 eV), and this energy is set as a standard reference one.

## Results and Discussion

For H-bronzes, $MoO_6$ octahedra of $(MoO_6)_n$ sheets cause minor rearrangements in Mo-O framework by insertion of hydrogen into $MoO_3$ interlayers, and the octahedra are axially symmetric $MoO_6$ units and six Mo-O bonds whose distances are almost the same as those of $MoO_3$. Hydrogen atoms are intercalated into the $(MoO_6)_n$ layers and stabilized by linking to oxygen atoms, resulting in OH or $OH_2$ groups located between the intra- and inter-layers. Thus, the insertion of hydrogen atoms result in a structural change in $MoO_6$ octahedra, however, it is naturally accepted that formation of reduced Mo ions such as $Mo^{5+}$ and/or $Mo^{4+}$ are brought about by insertion of hydrogen atoms. The $L_3$-edge XANES spectra of H-bronze samples and their second derivatives are shown in Fig. 1. For these samples, the amount of hydrogen atoms of type I is lower than type II. The peaks in the XANES spectrum of H-bronzes are positioned at lower energy than those of other samples with $Mo^{6+}$-octahedra such as $MoO_3$, indicating that reduced Mo ions exist in H-bronzes. Thus, it is clearly shown that intercalated hydrogen atoms in H-bronzes bring about not only formation of axially symmetric $MoO_6$ octahedra but also reduction of Mo ions. For these spectra, the peak in the lower energy side is positioned at 3.2

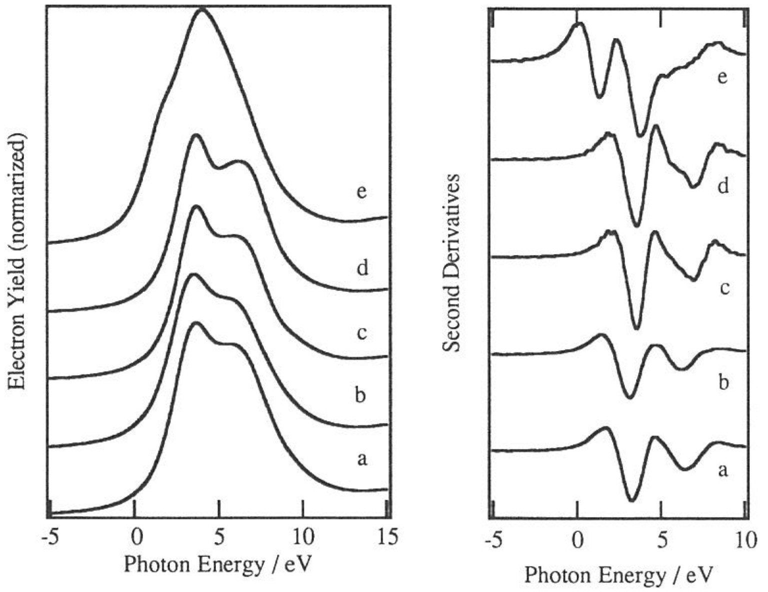

**Fig. 1** Mo $L_3$-edge XANES spectra (left hand) and their second derivatives (right hand) of H-bronzes and reference samples.
(a) H-bronze TYPE I; (b) H-bronze TYPE II; (c) $MoO_3$; (d) $MoO_2(acac)_2$; (e) $MoO_2$.

- 3.3 eV, which is independent of hydrogen amount. Furthermore, the energy gap of the splitting is also similar to each other. These results show that intercalation of hydrogen atoms brings about formation of axially symmetric $MoO_6$ octahedra in $(MoO_6)_n$ sheets even in $x \geq 0.3$ (type I) as $H_xMoO_3$, and an increase in hydrogen amount does not cause more reduction of surface Mo ions but affect the bulk Mo ions. The results of type II that hydrogen atoms intercalate into $(MoO_6)_n$ sheets as similarly as those of type I, and elongate the lattice spacings between these sheets. When the bronzes are assumed to have only a $Mo^{6+}$ ion, the energy gap between two white lines is expected to be larger than that of $MoO_3$ and white line at higher energy side should be narrower, because the $MoO_6$ unit in H-bronze is closer to the regular octahedron than that in $MoO_3$. However, the energy gaps of splitting of H-bronzes are smaller than that of $MoO_3$. It suggests that the reduction of Mo ions in bronzes gives the decrease of the energy gap between $t_{2g}$ and $e_g$ in 4*d*-state of Mo. Thus, the spectrum of $MoO_2$ is also collected. The $Mo^{4+}$ ions in $MoO_2$ exist in almost symmetric $MoO_6$ $O_h$ structure. For the $MoO_6$ octahedron in $MoO_2$, the threefold-degenerate $t_{2g}$ manifold of octahedral symmetry is split into a $d_{\parallel}$ orbital and two $d_{\perp}$ orbitals, and form Mo($d_{\perp}$)-O($p_{\pi}$)-Mo($d_{\perp}$) bonding whose interactions bring about a quasidegenerate pair of $\pi^*$ bands. A pair of Mo 4*d* electrons in $t_{2g}$ state occupies molecular orbitals of Mo($d_{\perp}$)-O($p_{\pi}$) and the orbitals in $e_g$ state are vacant. The energy gap between $t_{2g}$ and $e_g$ in $MoO_2$ having $Mo^{4+}$ ions should be smaller than that of the sample having $Mo^{6+}$ ions because of the less effect of perturbation by the ligand field of six O ions. In the XANES spectrum of $MoO_2$, a shoulder peak at 1.4 eV due to the electron transition to the $\pi^*$ band is seen. The intensity of this peak is weaker than that of the samples including $Mo^{6+}$ ions because of a decrease in transition cross sections. The broad peak maximized at 3.8 eV is due to the transition to $e_g$ state. The splitting of these peaks can be clearly seen in the second derivative spectrum. The 2.4 eV of energy gap is much smaller than that of $MoO_3$ although the Mo ions in $MoO_2$ exist in a symmetric $MoO_6$ octahedron. This result strongly explains that the reduction of Mo ions brings about the condensation of a total 4*d*-state, and it reflects the $L_3$-edge XANES spectrum directly.[5] The reduction of Mo ions from $Mo^{6+}$ gives the lower absorption edge, and narrower splitting of energy gap regardless of the symmetry of $MoO_6$ octahedra.

## References

(1) Birtill, J. J., Dickens, P. C., *Mater. Res. Bull.* **13** (1978) 311.
(2) Sotani, N., Eda, K., Sadamatsu, M., Takagi, S., *Bull. Chem. Soc. Jpn.* **62** (1989) 903.
(3) Sotani, N., Eda, K., Kunimoto, M., J. Chem. Soc. Faraday Trans. **86** (1990) 1583.
(4) Tanaka, T., Aritani, H., Yoshida, S., Eda, K., Sotani, N., Hasegawa, S., *J. Phys.* (*colloque*), in press.
(5) Aritani, H., Tanaka, T., Funabiki, T., Yoshida, S., Eda, K., Sotani, N., Kudo, M., Hasegawa, S., *J. Phys. Chem.*, in press.

(BL7A)

# Soft X-ray Study of Mixed Valence Compounds TlS

M. MORI, S. KASHIDA[‡] and T. OGAWA

School of Informatics and Sciences, Nagoya University, Nagoya 464-01
[‡] Faculty of Science, Niigata University, Ikarashi, Niigata, 950-21

The ternary thallium chalcogenides $TlMX_2$ (M=Ga,In, X=S,Se,Te) crystallize in two different structures. The first is the tetragonal TlSe type. The structure is characterized by a linear chains formed of edge connected $MX_4$ tetrahedra. Monovalent Tl ions are located between the chains and have eightfold coordination of chalcogen ions. The second is the monoclinic $TlGaSe_2$ type. This structure is characterized by layers formed of corner connected $MX_4$ tetrahedra. Monovalent Tl ions are located between the layers and have sixfold coordination of chalcogen ions.

The layer type thallium compounds, such as $TlGaSe_2$ and $TlInS_2$, undergo successive phase transitions. The lowest temperature phase is ferroelectric and the intermediate phase is incommensurate. The origin of the ferroelectricity is discussed on the basis of the stereochemical instability of the 6s lone pair electrons, that is, the distortion around a Tl ion would cause Tl 6p orbitals to mix into the filled Tl 6s orbital and stabilizes the ferroelectric structure. Thallium monosulfide will belong to this family. It is considered as a mixed valence compound containing monovalent and trivalent thallium ions ($Tl^{1+}Tl^{3+}S_2$). Recent studies have shown that TlS crystallizes both in the chain (TlSe) and layer ($TlGaSe_2$) type structures. Like the ternary thallium compounds, the layer type TlS crystal undergoes successive ferroelectric phase transitions. The microscopic origin of the phase transition is ascribed to small displacements of Tl ions relative to the S ions. Although TlS is known as a good photoconductor, its electronic structure is not well known. We have measured the photoemission spectra in order to investigate the electronic structure of TlS.

As the photoemission experiments, the most prominent peaks in the measured energy range of 0-20 eV, are those of Tl 5d 3/2 and 5/2 core levels$^{1)}$. The positions of these 5d core levels of both chain and layer typesTlS specimens agree within the experimental error. As the average valence of Tl atoms increases, the levels shift to higher binding energies. The shifts measure the charge transfer from the cations to the anions. However, the splitting of the 5d levels was not observed for different valences of $Tl^{+}$ and $Tl^{3+}$ ions present in TlS. A qualitative interpretation can be made by the shift of the Madelung energy at the $Tl^{3+}$ site, since the anions are in closer distances compared with the case of $Tl^{3+}$ ions.

Single crystal samples were grown from sulfur rich melts$^{2),3)}$. When the melts were cooled slowly we obtained needle like crystals having the tetragonal TlSe type structure, while when the melts were cooled rapidly we obtained platy crystals having the monoclinic $TlGaSe_2$ type structure. The electrical conductivity of the TlS samples was measured by the two terminal dc method. It was found that the conductivity of the layer type TlS is about two order lower than that of the chain type TlS. For comparison, the samples of Tl metal and TlS crystal were also prepared and used for this study.

The soft x-ray electron yield experiments were performed at beam line BL7A by using synchrotron radiation from UVSOR at the Institute for Molecular Science. A combination of a modified Double germanium monochrometor system was used to measure the soft x-ray electron yield spectra near sulpher K absorpsion edge. The overall energy resolution was about 0.5 eV. The experimental results were normalized with respect to synchrotron electron current. Clean surfaces were obtained by scraping using a diamond file. The experiments were done at room temperature in the vacuum of $1x10^{-8}$ Torr. The surfaces of the samples were fairly stable.

In the photoemission experiment, the splitting of the 5d levels was not observed for different valences of $Tl^{+}$ and $Tl^{3+}$ ions present in TlS. As two sites exist in Tl ions on good authority of crystallography, It is possible for two sites to exist in S ions substitute for Tl ions. But the results shown as Fig. 1 is that the sulpher is only one site and the peak position of the absorption edge is same as the $S^{2-}$ ions. Therefore, $TlS(Tl^{1+}Tl^{3+}S_2)$seems to be a material, $Tl^{2+}S^{2-}$. It is strange for the spectroscopy.

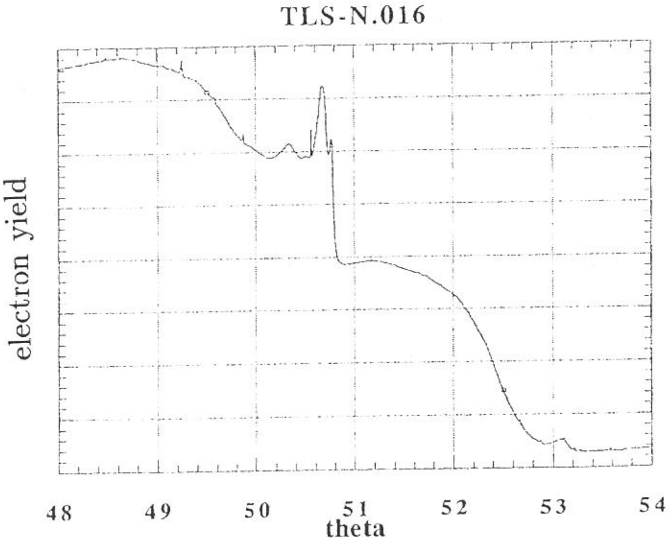

Fig. 1. Electron yield emission spectrum of the chain type TlS.

1) S. Kashida, T. Saito and M. Mori: in preparation.

2) S. Kashida, K. Nakamura and S. Katayama: Solid State Commun. 82 (1992) 127.

3) K. Nakamura and S. Kashida: J. Phys. Soc. Jpn. 62 (1993) 3135.

(BL7B)

# Time-Resolved Fluorescence Spectroscopy of tryptophan powders

Mieko TANIGUCHI, Kouji. TANI and Masaya KATOU

*Division of Material Science, School of Science,*
*Nagoya University, Chikusa-Ku, Nagoya, 464-01 Japan*

Tryptophan is an aromatic amino acid and play a significant role in dynamical structure and regulation. n proteins. The purpose of this experiments is to clarify the temperature-induced conformational changes of tryptophan powders. The static and dynamical aspects of tryptophan powders at various temperatures have been studied by fluorescence spectroscopy using synchrotron radiation at UVSOR. The fluorescence spectra and lifetimes of the powders were measured at the multi- and single-bunch modes , respectively.

The excitation spectrum at room temperature has three bands peaks at 184, 245 and 309 nm for the fluorescence emission at 330 nm. The later two excitation band peaks change to 258 nm (red shift) and to 304 nm (blue shift), respectively, at 88.9 K. For the emission spectrum excited at 250 nm, the wavelength of maximum emission shifts from 332.1 nm at room temperature to 326.4 nm at 90 K with the blue shift occurring between 150 and 220 K. The inverse temperature dependence of the emission intensity is biphasic with inflection around 160 K The fluorescence intensity tends to zero, it is almost same as the melting point (562 K) of tryptophan. The fluorescence decays emitted at 330 nm were analyzed by the nonlinear least-squares method. The result was fitted by two decay components. The inverse temperature dependence of the inverse long lifetime is also biphasic with inflection around 160 K. The emission intensity is closely related to the long lifetime.

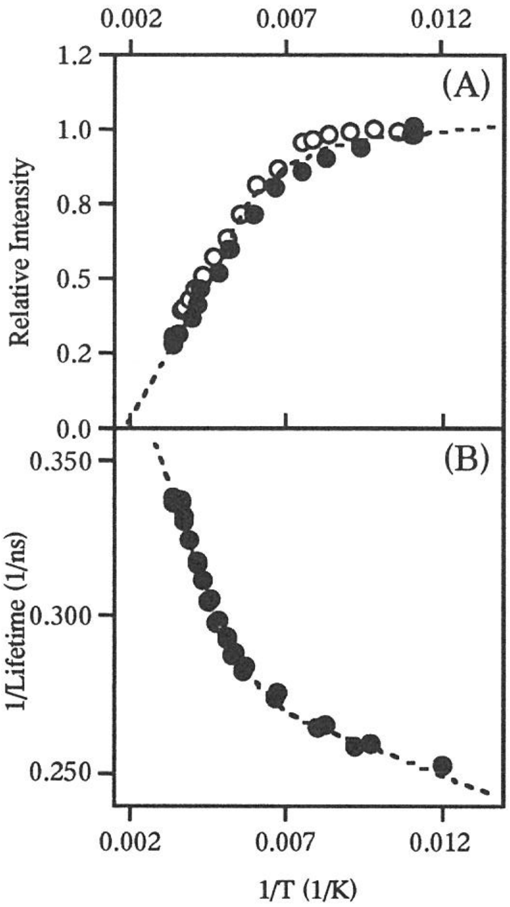

Fig. 1 (A) Inverse temperature dependence of relative intensity excited 250 nm, (●) is from high to low temperature and (○) is the reverse process. (B) Inverse temperature dependence versus inverse lifetime. Excitation at 250 nm. Emission at 330 nm. The arrow point shows the melting temperature of tryptophan.

References

1. M. Taniguchi, K. Tani and M. Katou ; Spectroscopic and dynamic aspects on luminescence of tryptophan powders. J. Electron. Spectroscopy and . Related Phenomena 78 (1996) 427-430.

(BL-7B)

# Optical properties of densified metaphosphate glasses

N. Kitamura, J. Nishii and K. Fukumi
*Department of Optical Materials, Osaka National Research Institute, AIST*
1-8-31 Midorigaoka, Ikeda, Osaka 563, JAPAN

When glasses are submitted to very high pressure and temperature, glass structure changes to a high density state. The glass structure is frozen by cooling the glass to a room temperature, so that a high density state is realized even after the release of pressure. Densification of glass by high pressure is a useful method to obtain a new glass with high refractive index. However, only few attempts have so far been made at densification of phosphate glass as compared with silicate glasses. In the present investigation, some alkaline-earth metaphosphate glasses were densified by a multi-anvil type high pressure apparatus. Structural changes of the glass with increasing density and change in optical properties such as reflectivity or transmittance are discussed.

The densification of $50MO{\bullet}50P_2O_5$ (M=Ca, Sr and Ba) glasses was carried out with a 6-8 multi-anvil-type high-pressure apparatus[1]. The experimental procedure of densification has been described in detail elsewhere[1,2]. The sample was submitted to a high pressure of 6 GPa. Then, it was heated at 400 °C under the pressure for 1 min. The density of the dense and undensified glasses were measured by Archmedes' method with distilled water. Density increased by 4.6%, 3.5% and 2.0% for $Ca(PO_3)_2$, $Sr(PO_3)_2$ and $Ba(PO_3)_2$ glasses after densification, respectively. The vacuum ultraviolet (<200 nm) reflectance and transmittance spectra were measured. The incident angle for the reflectance measurement was kept at about 10°. The measurement was performed at room temperature.

The vacuum-uv reflection spectra of the $Ca(PO_3)_2$, $Sr(PO_3)_2$ and $Ba(PO_3)_2$ glasses, shown in figure 1, contain a strong broad band centered at about 10 eV and a weak shoulder at 14 eV. As some oxide glasses give reflection bands arising from interband transitions in oxygen atoms at almost the same energies[2], these bands may be due to the interband transitions. The peak position of the strong band varied toward lower energies with replacing cation ion from calcium (10.0eV) to barium (9.6eV) as seen in the figure. The difference in peak positions is not clear yet. Width of both bands broaden slightly with the increase in density, while the band peak positions do not shift. The broadening of reflection bands corresponds to that of Raman bands, that is, it means that electronic states of oxygen was modified by the distortion of the $PO_4$ tetrahedra and then the distribution of bandgap energy increased[3]. These broadening of the 10 eV band should bring about low energy shift of intrinsic cut-off wavelength because the absorption coefficient increases in the low energy side of band tail.

Figure 2 shows transmission spectra of the $Ca(PO_3)_2$, $Sr(PO_3)_2$ and $Ba(PO_3)_2$ glasses in the vacuum-uv region. Few weak absorption bands are found near the cut-off wavelength for all undensified glasses. These absorption bands may be due to impurities in the glass. However these glasses have a good transparency in the uv region. The relationship between cut-off wavelengths (energies) for three glasses is well correspond to the case of peak positions on the reflection band. After the densification of these glasses, the cut-off wavelength shifted toward longer wavelengths by about 10, 15 and 20 nm for M=Ca, Sr and Ba, respectively. It is not consistent with the broadening behavior of the 10 eV band in the reflection spectra. The increase of the band width is in the order of 0.1 eV, so that the long energy shift of the cut-off wavelength expected from the broadening is a few nano-meters at most. This anomalous large shift may belong to a high pressure effect on the electronic state of impurity ions. Because the absorption coefficient around cut-off wavelength do not obey the Urbach law, that is, the absorption around this region is not intrinsic. If many structural defects are created in the glass by applying high pressures, new characteristic absorption band may appear between the bandgap. Therefore the origin of the anomalous extinction of transmittance around cut-off cannot be specified in this experiment.

## REFERENCES

[1] N. Kawai and M. Togaya and A. Onodera, Proc. Jpn. Acad., 49(1973)623.

[2] N. Kitamura, K. Fukumi, K. Kadono, H. Yamashita and K. Suito, Phys. Rev. B50(1994)132.

[3] N. Kitamura, K. Fukumi, M. Makihara, T. Sasaki and N. Ohno, Proceedings of the 2nd Internatinal Meeting of Paciffic Rim Ceramic Societies, 1996, in press.

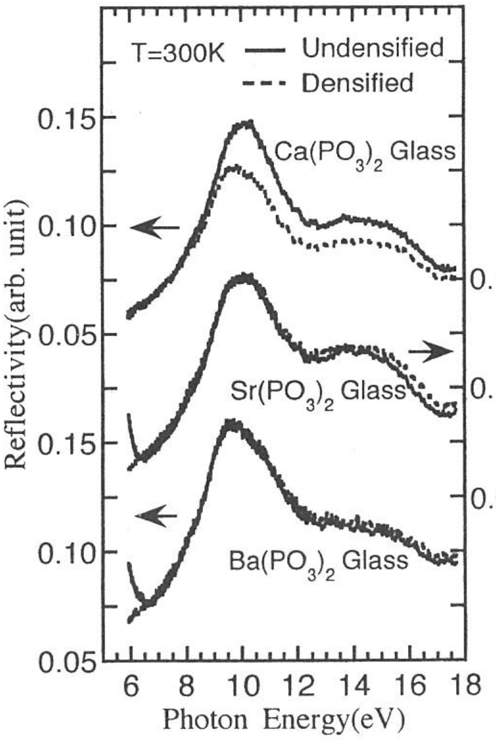

Fig.1 Reflection spectra for MO-$P_2O_5$ (M=Ca, Sr and Ba) glasses before and after densification

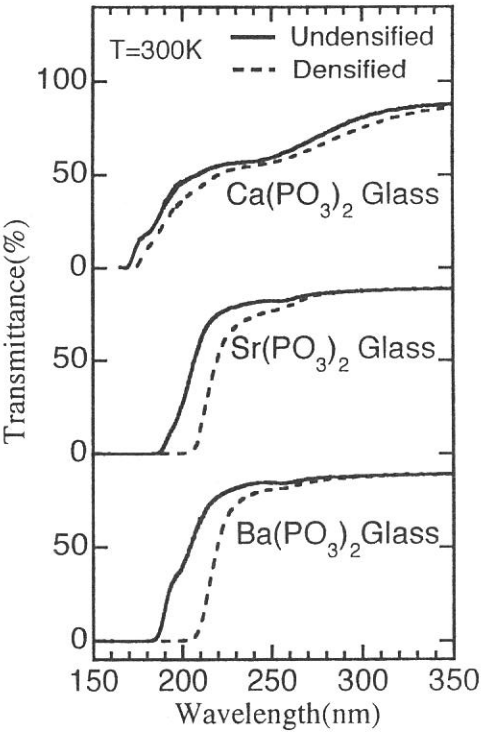

Fig.2 Transmission spectra for MO-$P_2O_5$ (M=Ca, Sr and Ba) glasses before and after densification

(BL7B)

# Quantum Yield of $S_1$ Exciton Formation in Anthracene Single Crystal

H.Horiuchi, I. Shimoyama[1)], Y. Otsuki and K.Nakagawa[2)]

Graduate school of Education, Kobe University, Tsurukabuto, Nada-Ku, Kobe 657
[1)]Graduate school of Science and Technology, Kobe University, Rokkohdai, Nada-Ku, Kobe 657
[2)]Faculty of Human Development, Kobe University, Tsurukabuto, Nada-Ku, Kobe 657

We measured absolute values of quantum yield $\phi(h\nu)$ of singlet exciton formation in anthracene single crystals as a function of the incident photon energy $h\nu$, in an attempt to study an multiplication mechanism of excitons in molecular crystals.

Anthracene single crystals were grown by a sublimation method from the scintillation grade anthracene of Merck Company. Anthracene crystals were attached to a sample holder which was cooled to 210K in order to avoid sample evaporation in the vacuum sample chamber which was evacuated up to the pressure of about $2.1\times10^{-6}$Pa.

Experiments were performed at the beam line BL-7B of the UVSOR. The sample was irradiated by monochromatized synchrotron radiation with the energies of $3 < h\nu < 17$eV. We measured $S_1$ emission intensity($I_F(h\nu)$) together with the incident light intensity $I_x(h\nu)$. Values of quantum yield $\phi(h\nu)$ was calculated by an equation; $\phi(h\nu)=I_F(h\nu)/I_x(h\nu)$. The absolute value of $\phi(h\nu)$ was determined on the basis of the experimental result that luminescence efficiency of the $S_1$ exciton was unity[1]. So we determined that $\phi(3.6\text{eV})=1$. Obtained values of $\phi(h\nu)$ is plotted in Fig. 1 for the case of excitation by b-axis polarized light beams.

As seen from Fig.1, values of $\phi(h\nu)$ are nearly constant around 1 with several peaks and dips in the energy range from 3.1 to 10eV, and $\phi(h\nu)$ shows a clear increase above 10 eV.

We examined carefully the energy positions of peaks and dips in $\phi(h\nu)$ curve with those in the optical absorption spectrum and the reflection spectrum reported by A. Bree and L. E. Lyons[2]. We found that peaks in $\phi(h\nu)$ curve correspond to dips in the reflection spectrum and dips in $\phi(h\nu)$ curve correspond to peaks in the reflection spectrum. On this observation, we concluded that the structures in the energy range from 3.1 to 5.6 eV are originated from the reflection instead of absorption.

The clear increase in $\phi$ ($h\nu$) above 10 eV seems to show the beginning of multiplication of $S_1$ excitons. As shown in the figure, this energy is nearly equal with Eg+2$E_{S1}$, where Eg(=3.9eV[1]) is the band gap energy and $E_{S1}$ (=3.1eV[1]) is the formation energy of a $S_1$ exciton. In order to initiate the multiplication of exciton at this energy, a secondary electron and a secondary hole have to carry the energy ≧ $E_{S1}$ each other. This situation is possible only when both the electron band and the hole band has the band width greater than $E_{S1}$ (=3.1eV). For anthracene crystals, it is known that these bands are not so wide[1]. On this view point, we are examining the possible mechanisms from which exciton multiplication occurs.

[1]M. Pope and C. E. Swemberg, "Electronic Processes in Organic Crystals", Oxford University Press, 1982.
[2]A. Bree and L. E. Lyons, J. Chem. Soc. 1956, pp. 2662-2670.

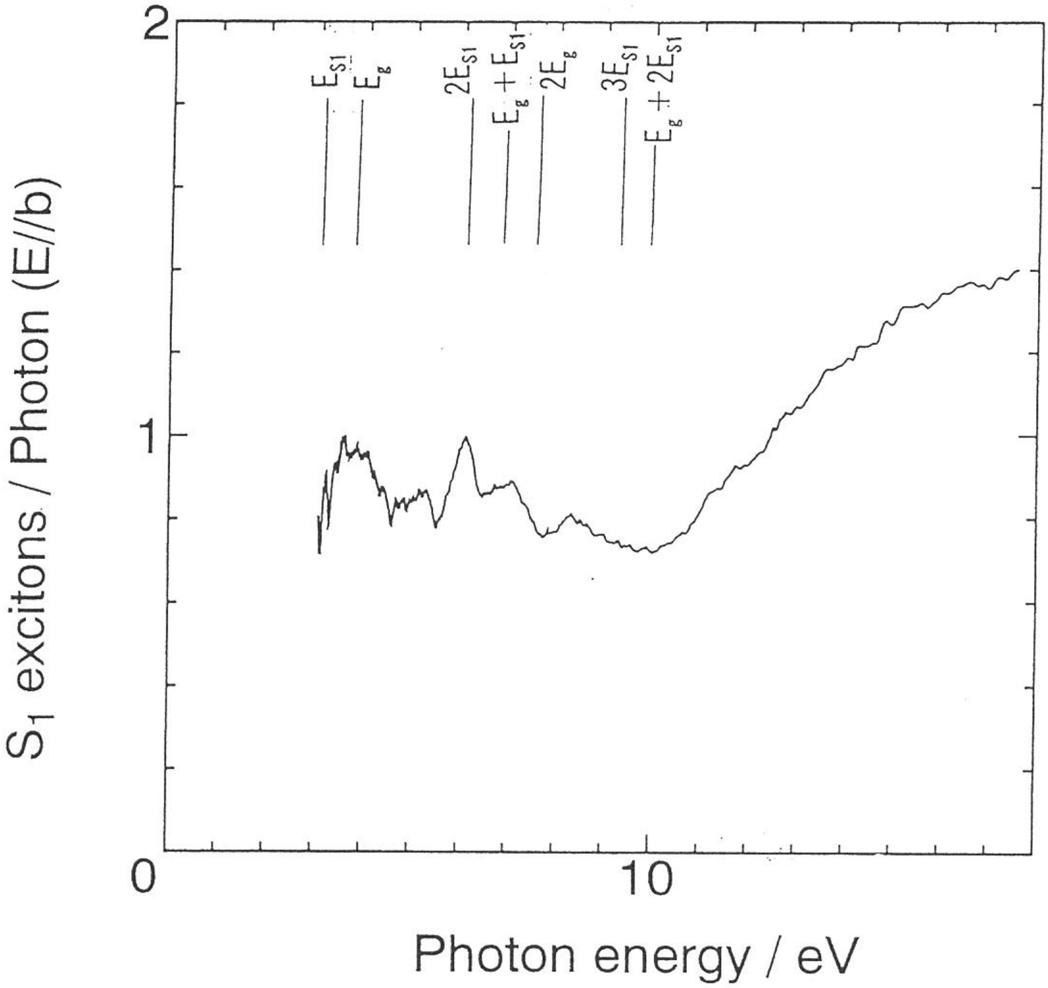

Fig. 1 Quantum yield of $S_1$ exciton formation in anthracene single crystal at 210 K.

(BL7B)

# Density dependence of photoionization potential of anthracene in supercritical ethane : A role of dynamic cluster

Yasushi Otsuki, Iwao Shimoyama[1], Takeshi Mochida, and Kazumichi Nakagawa[2]

Graduate school of Education, Kobe University, Tsurukabuto, Nada-Ku, Kobe 657

[1]Graduate school of Sciensce and Technology, Kobe University, Rokkoudaityou, Nada-Ku, Kobe 657

[2]Faculty of Human Development, Kobe University, Tsurukabuto, Nada-Ku, Kobe 657

We measured ionization potentials of anthracene doped in ethane as a function of ethane density N from gas to liquid through supercritical states, in an attempt to study microscopic mechanisms of ionization phenomena in dense media.

After introducing anthracene in a high pressure photocurrent cell, we poured ethane and measured photocurrent spectra i(h $\nu$ ;N) in the range of N; $0.001< N/(10^{21}\text{molecules/cm}^3)<8.61$, by changing the temperature and pressure.

Values of Ip(N) were obtained by analyzing each spectrum with the threshold law : $\eta$ (h $\nu$ ) = (h $\nu$ -Ip)$^{5/2}$[1], where $\eta$ (h $\nu$ ) is the quantum yield obtained by dividing the observed photocurrent spectra i(h $\nu$ ;N) by incidence intensity. Values of Ip(N) at each densities are shown by □ in Fig.1.

We examined the density dependence of Ip(N) on the basis of a relation; Ip(N)=Ig+P(N)+ $V_0$(N)[1], where Ig is the gas-phase ionization potential of anthracene, P(N) is a polarization energy of ethane induced by anthracene positive ion, and $V_0$(N) is the conduction band energy of an electron in ethane fluids. Values of Ig and $V_0$ were taken from literature[2]. We calculated P(N) by two models, namely, the continuum model and the cluster model[3]. In the continuum model, values of P(N) were calculated with the Born formula; $P(N)=-e^2(1-1/\varepsilon)/2R$[1], which regarded ethane fluid as a uniform medium with dielectric constant $\varepsilon$ . In Fig.1, we shown Ip(N) values calculated with the continuum model by dotted lines A and B (A is a result at an anthracene ion radius R=0.325nm, B is R=0.300nm). An anthracene ion radius of 0.325nm is known to reproduce values of P in many liquids of nonpolar hydrocarbon molecules. As seen from Fig.1, the continuum model cannot reproduce experimental results even using the too small value of R(=0.300nm). In the cluster model, values of P(N) were calculated taking the Langmuir-equilibrium between association and evaporation of ethane into account; $P(N)=(\Delta p \cdot n_{max} \cdot N)/(N_1(n_{max}-1)+N)$, namely, $\Delta p$ is the decrement of P by association of an ethane molecule to anthracene molecule, $n_{max}$ is the maximum association number of ethane to an anthracene, and $N_1$ is the bulk density under which an ethane molecule associates to an anthracene molecule. The curve C in Fig.1 shows a result of calculation of Ip(N) via the cluster model . The best fit parameter is $n_{max}=6$, $N_1=0.563 \times 10^{21}$molecules/cm$^3$, and $\Delta p=-0.18$eV, respectively. From this result, we concluded that the cluster model can reproduce measured results.

[1]R.A.Holroyd et.al., J.Chem.Phys.79(1983)483.
[2]Y.Yamaguchi et.al., J.Chem.Phys.71(1979)550.
[3]K.Nakagawa et.al., J.Electron Spectrosc.Relat.Phenom.78(1996)415.

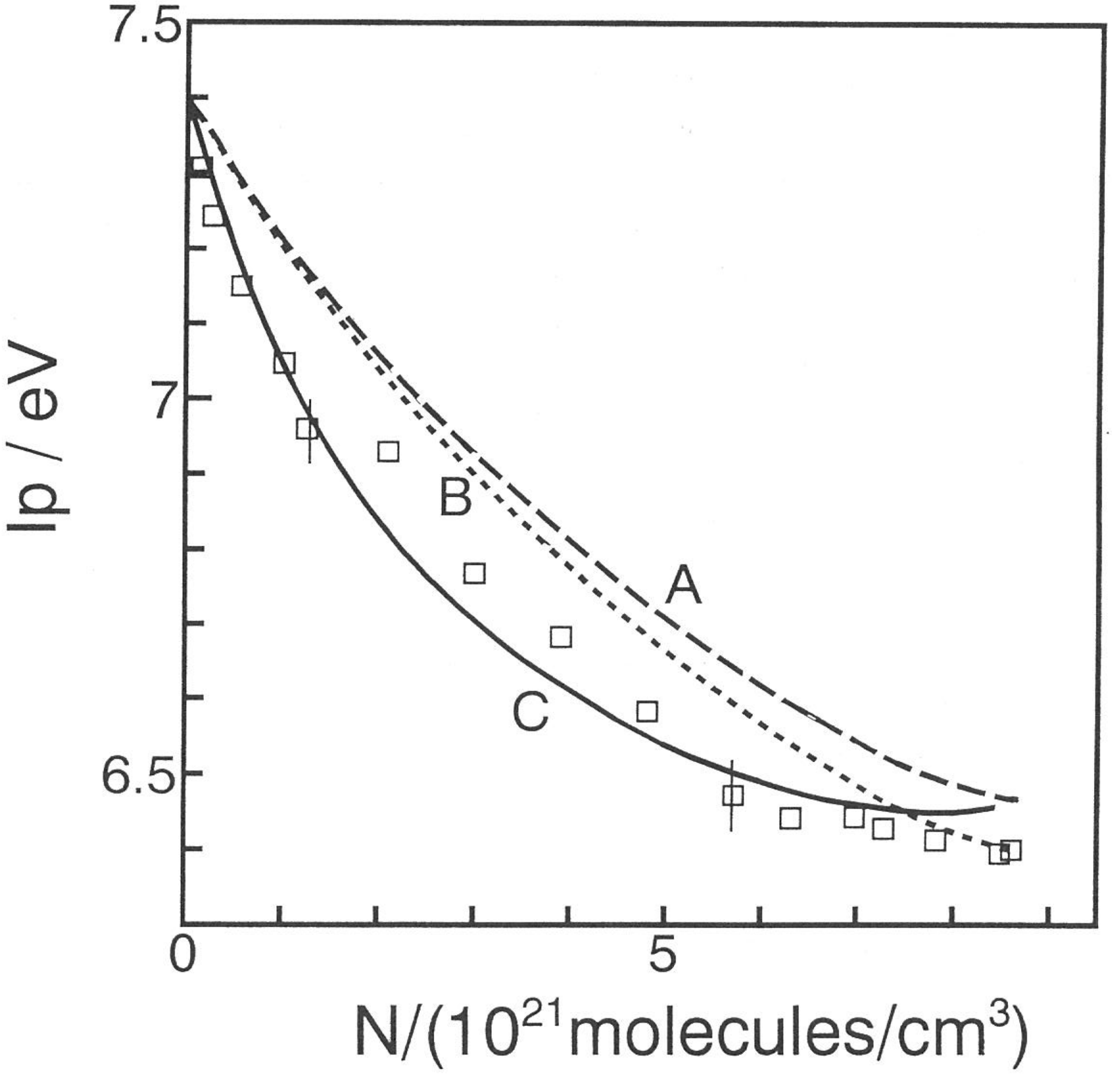

Fig.1 Density dependence of photoionization potential of anthracene in ethane

(BL7B)

# Energy states of Ge-doped $SiO_2$ glass estimated through absorption and photoluminescence

Makoto Fujimaki and Yoshimichi Ohki

Department of Electrical, Electronics and Computer Engineering, Waseda University,
3-4-1 Okubo, Shinjuku-ku, Tokyo 169, Japan

Germanium-doped $SiO_2$ glass is widely used as a material not only for a conventional optical fiber but also for fiber-type functional elements such as a Bragg grating [1] which utilizes refractive-index change induced by the irradiation of ultraviolet (UV) photons. It has been reported that germanium oxygen-deficient centers (GODCs) existing in the oxygen-deficient type glass are thought to be responsible for the structural change which causes the refractive-index change. [2] Two types of GODCs, neutral oxygen vacancy (NOV) and germanium lone pair center (GLPC), have been reported. [2] The NOV has an absorption band at 5.06 eV and is known to become the E' center by the irradiation of UV photons, while the GLPC has an absorption band at 5.16 eV and two photoluminescence (PL) bands at 4.3 eV and 3.1 eV. Recently, PL intensity changes associated with the structural change which causes the refractive-index change were reported. [3,4] Therefore, it is very important to know the optical property of GLPC for investigating the structural change.

While the properties of the absorption and PL bands of GLPC in the range of visible to UV have been intensively examined, [2,4,5] there still remain debatable points in the electronic transition process under VUV excitation. For example, some has assigned a large absorption above 6 eV to the electronic excitation from the ground state ($S_0$) to the second-lowest excited singlet state ($S_2$) at GLPC, [5] while the other has assigned it to that from the valence band to the lowest excited singlet state ($S_1$). [4]

In this research, in order to give a clue to the energy state of GLPC in the VUV region, the electronic transition processes under VUV excitation are discussed through the measurements of optical absorption, PL excitation (PLE) spectra, and PL decay profiles in the UV and VUV region.

Figure 1 shows absorption spectra of the oxygen-deficient sample (solid line) and the oxygen-rich sample (dotted line). The oxygen-rich sample shows absorption above 6.7 eV, which is assigned to the interband transition since the band gap of Ge-doped $SiO_2$ glass is 7.1 eV. [6] The oxygen-deficient sample has a large absorption band at 5.1 eV and an absorption tail above 6 eV. While the 5.1 eV absorption is a combination of the 5.06 eV absorption due to the NOV and the 5.16 eV absorption due to the GLPC, [2] the assignment of the absorption tail above 6 eV is unclear. Note that all the data hereafter were taken for the oxygen-deficient sample.

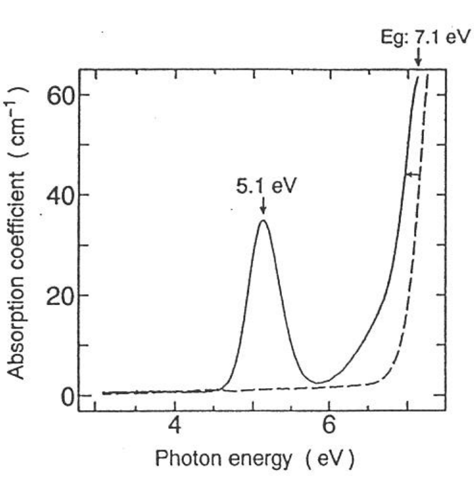

Fig. 1. Absorption spectra of the oxygen-deficient sample (solid line) and the oxygen-rich sample ( dotted line).

Figure 2 shows the PLE spectra of the 4.3 eV and the 3.1 eV PL bands measured at room temperature (solid lines) and 89 K (dotted lines). From Fig. 2(A), it is observed that the 4.3 eV PL has PLE bands at 5.1 eV and above 6.0 eV, although the PLE spectra above 6.5 eV is believed to be distorted by the strong absorption ( $\alpha \sim$ 60 $cm^{-1}$) above 6.5 eV seen in Fig. 1. The peak seen around 4.3 eV is not a PLE band but a scattered excitation light through the interference filter. From this figure, it is understood that the 4.3 eV PL is stronger at 89 K than at room temperature for both PLE bands. The 3.1 eV PL has similar two PLE bands at 5.1 eV and above 6.0 eV, and an additional small PLE band at 3.7 eV. When the PLE band at 5.1 eV is excited, the 3.1 eV PL is stronger at room temperature, but it rather becomes weaker at room temperature when it is excited by the PLE bands at 3.7 eV and above 6 eV.

Figures 3(A) and 3(B) show the decay of the 3.1 eV PL and that of the 4.3 eV PL, respectively. For the 3.1 eV PL, the lifetime of 113 μs, which is similar to the reported value, [5] is seen irrespective of the excitation photon energy being 5.0 eV or 6.4 eV. For the 4.3 eV PL, the lifetime is 9 ns irrespective of the excitation photon energy being 5.0 eV or 7.0 eV. The same lifetime was observed for the 4.3 eV PL with four other different excitation photon energies of 4.8, 5.5, 6.5, and 7.2 eV.

From the above-mentioned results, we propose that the absorption band and the PLE band above 6 eV in the oxygen-deficient sample are due to the electronic excitation from $S_0$ of GLPC to the conduction band.

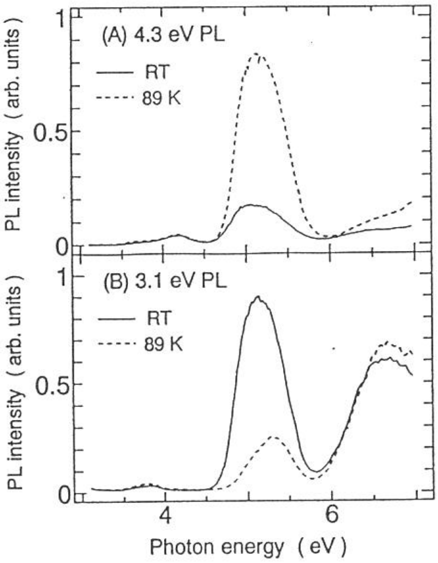

Fig. 2. PLE spectra of the 4.3 eV PL (A) and those of the 3.1 eV PL (B), at room temperature (solid lines) and at 89 K (dotted lines).

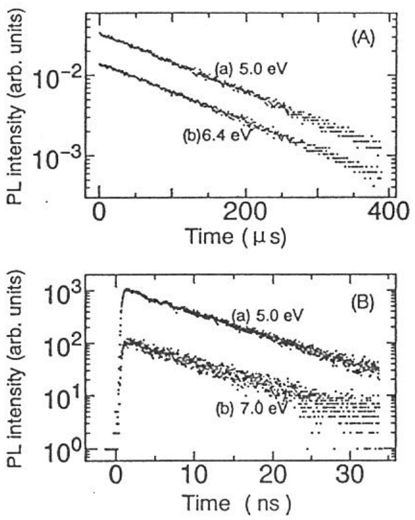

Fig. 3. Decay profiles of the 3.1 eV PL (A) and those of the 4.3 eV PL (B), excited by 5.0 eV photons (a) and 6.4 eV or 7.0 eV photons (b) at 89 K. As for the 4.3 eV PL, similar results were obtained at four other excitation photon energies (4.8, 5.5, 6.5, and 7.2 eV).

## References

[1]K. O. Hill, Y. Fujii, D. C. Johnson, and B. S. Kawasaki, Appl. Phys. Lett. **32**, 647 (1978).

[2]H. Hosono, Y. Abe, D. L. Kinser, R. A. Weeks, K. Muta, and H. Kawazoe, Phys. Rev. B **46**, 11445 (1992).

[3]E. M. Dianov, D. S. Starodubov, and A. A. Frolov, Electron. Lett. **32**, 246 (1996).

[4]M. Gallagher and U. Osterberg, J. Appl. Phys. **74**, 2771 (1993).

[5]L. Skuja, J. Non-Cryst. Solids **149**, 77 (1992).

[6]J. Nishii, N. Kitamura, H. Yamanaka, H. Hosono, and H. Kawazoe, Opt. Lett. **20**, 1184 (1995).

(BL7B)

# Refractive Index Dispersion and Vacuum Ultraviolet Reflection of Oxide Glasses

Hiromichi Takebe, Shigeru Fujino, and Kenji Morinaga
Department of Materials Science and Technology, Graduate School of Engineering Sciences, Kyushu University, Fukuoka 816

Refractive indexes as a function of wavelength are important properties for optical and optoelectronic glasses such as laser hosts, fibers for communications and photonic switches. We measured accurate refractive indexes of various oxide glass systemses in the wavelength range from ultraviolet to infrared region using the minimum-deviation method[1]. Our previous study concluded that the values of refractive indexes were mainly affected by the various oscillators such as bridging oxygens, nonbridging oxygens and cations in oxide glasses in the vacuum ultraviolet region[2].

In this work we measured the reflection spectra of potassium tantalum gallate (KTG) glasses in a series of $30K_2O$-$xTa_2O_5$-$(70-x)Ga_2O_3$, where x=0,10,20,30, 35, and 37 in the spectral range of 2 to 10 eV using the synchrotron radiation. KTG glasses are of interest as host of infrared-to-visible upconverstion and infrared lasers. We determined the resonance energies of the oscillators in oxide glasses. Figure 1 shows the reflection spectra of KTG glasses:(a)x=0, (b)x=10, (c)x=20, (d)x=30, (e)x=35, and (f)x=37. The resonance energy of (a)x=0 are attributed to nonbridging oxygens combined with $Ga^{3+}$ or $K^+$. A new band of (b)x=10 appears at 6.2 eV with $Ta_2O_5$ addtion. This band is attributed to nonbridging oxygens combined with $Ta^{5+}$. The peak energies of these band ((b)-(e)) remain constant, but the resonance energy of (f)x=37 appears at 5.2 ev, which are attributed to nonbridging oxygens combined with $Ta^{5+}$. Our results suggests that the variation of resonance peaks is related to the mixed anions structure of $Ga_2O_3$ and $Ta_2O_5$.

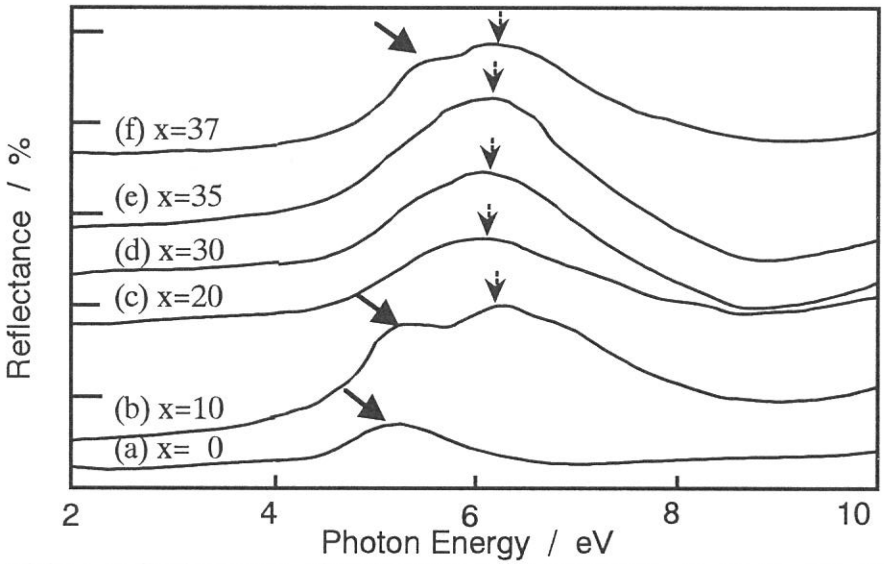

Figire 1 Reflection spectra of KTG glasses in a series of $30K_2O$-$xTa_2O_5$-$(70-x)Ga_2O_3$, where (a)x=0, (b)x=10, (c)x=20, (d)x=30, (e)x=35, and (f)x=37.

[1] S. Fujino, H. Takebe and K. Morinaga, *J. Am. Ceram. Soc.* , [78]5,1179-84(1995).
[2] S. Fujino, H. Takebe and K. Morinaga, *Proc. XVII Int. Cong. on Glass,*[3]163-68(1995).

(BL8A)

# Synchrotron Radiation-excited Etching of Diamond Surface. Temperature Dependence

Haruhiko Ohashi[a], Eiji Ishiguro[b], Tomohiko Sasano[c], Takahiro Oguri[d], and Kosuke Shobatake[d, e]

[a] *Institute for Molecular Science, Myodaiji, Okazaki 444, Japan*
[b] *Department of Education, University of Ryukyus, Nishihara, Okinawa 903-1, Japan*
[c] *Department of Applied Physics, Osaka City University, Sumiyoshi-ku, Osaka 558, Japan*
[d] *Department of Molecular Design and Engineering, Graduate School of Engineering, Nagoya University, Furo-cho, Chikusa-ku, Nagoya 464-01, Japan*

We have been studying etching reactions of semiconductor material and diamond surfaces induced by synchrotron radiation (SR) in the environment of an etchant such as $SF_6$, $XeF_2$, and $O_2$.[1] In this report we present the results obtained for the temperature dependence of SR-excited etching rate of diamond surface.[2] The light illuminated on the diamond surface is focused SR from the bending magnet field deflected by 4 degrees. The pressure dependence of the etch rate is found to have a maximum at an $O_2$ pressure of 0.1 Torr and thus the etching experiment was carried out at an $O_2$ pressure of 0.1 Torr. Figure 1 and 2 illustrate the temperature dependence of the etch rate as a function of the surface temperature for the two diamond samples, CVD diamond and crystalline diamond synthesized at high pressures, respectively. The depth profiles were measured using a stylus gauge.

From these figures one finds that the etch rate remains almost constant in the low temperature region ranging from -140 to about 300 ℃ and abruptly increases with temperature above 300 ℃ for CVD diamond. Considering the facts that micron size of diamond crystallites start to be oxidized around 400 ~ 500℃, these results show that the etching reaction proceeds via non-thermal processes in the low temperature region.

**[References]**

1. H. Ohashi, A. Yoshida, and K. Shobatake, Appl. Surf. Sci., **69**, 20 (1993).
2. H. Ohashi, E. Ishiguro, T. Sasano, and Kosuke Shobatake, Appl. Phys. Lett. **68**, 3713 (1996).

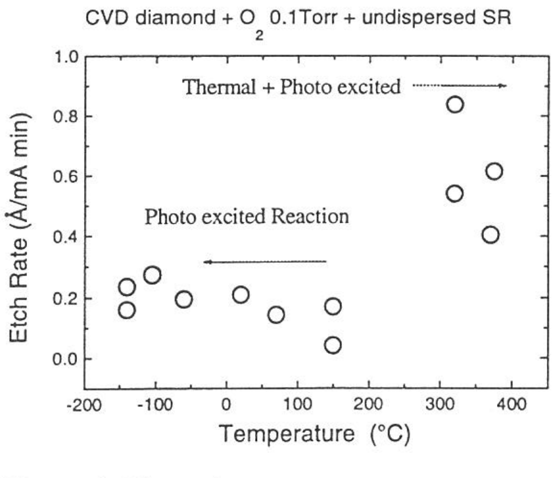

**Figure 1.** The etch rate vs. surface temperature for the SR-excited etching of CVD diamond at $O_2$ pressure of 0.1 Torr using focused SR from a bending magnet field.

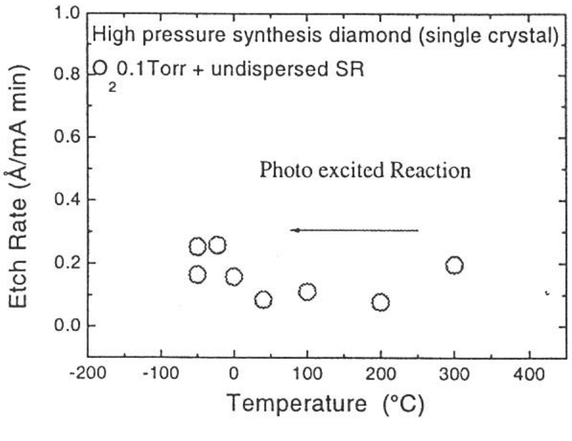

**Figure 2.** The etch rate vs. surface temperature of the SR-excited etching of high pressure synthesied diamond at $O_2$ pressure of 0.1 Torr using focused SR from a bending magnet field.

---

[a] Present Address: JASRI(SPring-8), Kamigori, Ako-gun, Hyugo 678-12, Japan.
[e] Adjunct Professor of Institute for Molecular Science from April, 1994 through Mar. 1996.

(BL8A)

# Synchrotron Radiation-excited Etching of Diamond Surface. Wavelength Dependence

Haruhiko OHASHI[a], Eiji ISHIGURO[b], Takahiro OGURI[c], Morimichi WATANABE[c],
and Kosuke SHOBATAKE[c, d]

[a] *Institute for Molecular Science, Myodaiji, Okazaki 444, Japan*
[b] *Department of Education, University of Ryukyus, Nishihara, Okinawa 903-1, Japan*
[c] *Department of Molecular Design and Engineering, Graduate School of Engineering, Nagoya University, Furo-cho, Chikusa-ku, Nagoya 464-01, Japan*

We have been studying etching reactions of diamond surfaces induced by synchrotron radiation (SR) in the environment of an $O_2$ etchant.[1] In this report we present the results on the wavelength dependence of etch rate. The spectra of the SR illuminated on the diamond surface is shown in Figure 1. The solid curve represents the focused SR by a Pt-coated mirror with a deflection angle of four degrees. The light with this spectrum provides with photons with photon energies from about 2 keV down to 1 eV. The dotted curve represents the filtered SR of the focused SR shown with the solid curve through a carbon filter 100 nm thick which was used to filter out the longer wavelengths of photons. The dot-dashed curve represents that reflected by a SiC mirror with a deflection angle of 25 degrees which removes the high energy photons leaving only long wavelength light. The last one is a pseudomonochromatic undulator radiation peaked at 34.5 nm (36 eV).

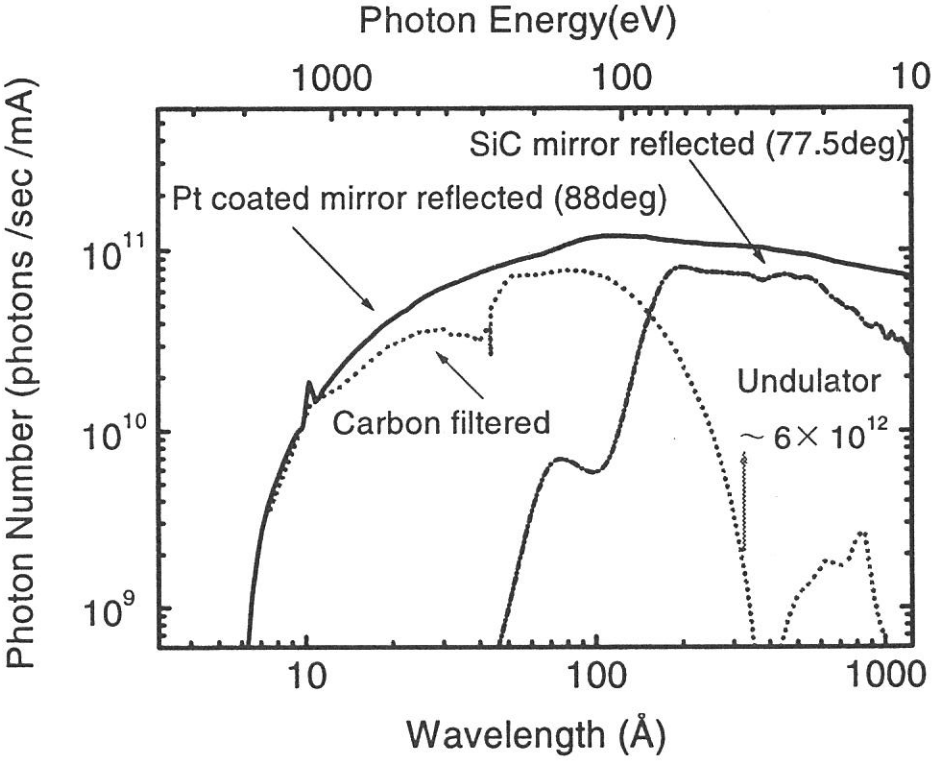

**Figure 1.** Spectra of the synchrotron light illuminated on the diamond surface for the study of wavelength dependence of etch rate. For the details see the text above.

---

[a] Present Address: JASRI(SPring-8), Kamigori, Ako-gun, Hyugo 678-12, Japan.
[d] Adjunct professor at IMS from April 1994 till March, 1996.

The etching reaction was carried out at an etchant pressure of 0.10 Torr and at room temperature. The etch rates obtained by illuminating four types of synchrotoron light upon the crystalline diamond synthesized at high pressures are summarized in Figure 2. The crosses are the experimental numbers of carbon atoms removed per mA of stored current per second. It is noted that the etching does not proceed at all if etchant gas ($O_2$) is not present, which means that only the illunination of synchrotron light does not induce etching reaction with an observable rate. It is concluded that the presence of etchant gas is important. The etch rates are about 0.02 % of the photons illuminated upon the surface except case when the light reflected with a SiC mirror is used (0.004 %). Since surface atom excitation is considered to be important in SR-excited etching, the following calculation was carried out to compare the experimental results with the model calculation. In the model calculation it was assumed that a) excitation of surface layer atoms (1.54 A thick) is essential, and b) K shell excitation is 100 % effective in inducing etching reaction but only 1.6 % effective for other types of excitation. The open circles are the effective numbers of photons absorbed by a 1.54 A thick diamond layer. The correlation of the observed etch rate and the estimated effective numbers of photons absorbed is very good. One is tempted to conclude that only inner core excitation is important in the diamond etching reaction. However, further experiment should be carried to clarify the reaction mechanism.

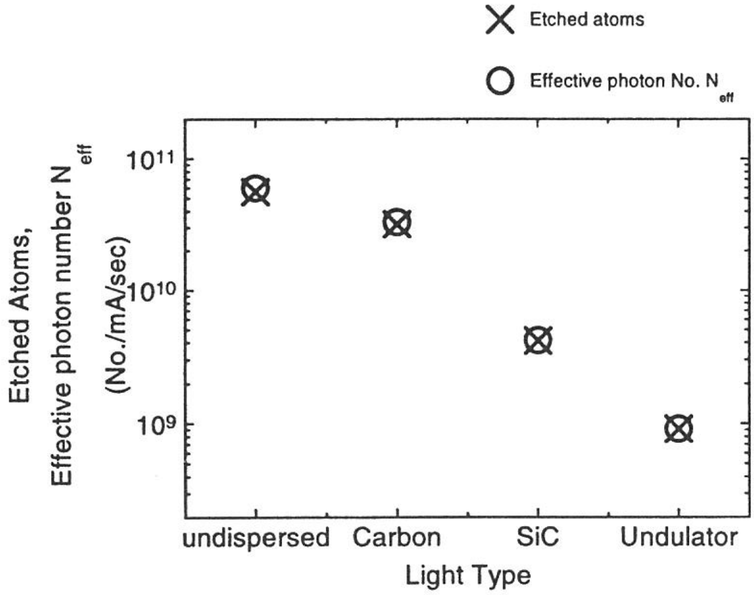

**Figure 2.** Crosses are the etch rates of crystalline diamond measured for four types of SR used; 1) undispersed, focused SR, 2) undispersed, focused SR through a cabon filter 100 nm thick, 3) undispersed focused light which was reflected with a SiC mirror, and 4) undulator radiation peaked at 34.5 nm. The circles are the calculated effected photon numbers absorbed by the surface layer 1.54 A thick. See the test for details.

# Temperature-dependent dephasing characteristics of Aniline and Phenol doped in hosts

H. Itoh[1], S. Nakanishi[1], T.Fuji[2], T.Kashiwagi[2]
N. Tsurumachi[2], M.Furuichi[2], H. Nakatsuka[2], and M. Kamada[3]

[1] *Department of Physics, Kagawa University, Takamatsu 760*
[2] *Institute of Applied Physics, University of Tsukuba, Tsukuba 305*
[3] *UVSOR, Institute for Molecular Science, Okazaki 444*

We have applied synchrotron radiation ( SR ) to investigate incoherent accumulated photon echo signals of simple aromatic molecules ( Aniline and Phenol) doped in Polyvinyl Alcohol( PVA ) and Polymethel Methacryrate ( PMMA ) in ultraviolet wavelength (UV) region. In this paper, we show that different types of temperature dependent phase relaxation could exist in both samples, Aniline and Phenol doped in PVA and PMMA. In this experiment, we have attempted to understand the dephasing mechanism of simple aromatic molecules, in particular Aniline, doped in PVA.

The experiment was performed at BL-8A of the UVSOR. The output beam from the quartz window of the BL-8A was filtered by the bandpass filters with each center wavelength of 310 nm and 289 nm and corresponding bandwidth of about 10.5 nm and 12 nm, respectively. The SR beam was split into two beams, pump and probe beam, by the plate beam splitter (PBS), which center wavelength was 248 nm and thickness was 3mm and the beams were temporally delayed to the other with micrometer and harmonic gear motor system. One pump beam was phase modulated with a piezoelectric transducer at the frequency of f=5.0 kHz. The two beams collinearly overlapped were focused onto the samples in the cryostat. Transmitted beam through the sample was detected with p-i-n photodiode whose output was fed into a lock-in amplifier. The echo signal was obtained in the 2f component of the output of the photodiode.

The temporal width of field autocorrelation was measured as 34 fs and 25 fs, respectively, corresponding to each bandpass filter used. To compensate the dispersion of the system, we tuned the angle of 3 mm thick quartz plate, located between the PBS and one of the corner cube prism of the interferometer. Figure 1 shows temperature dependennt dephasing time of the Aniline doped in PVA and PMMA as a function of inverse temperature. No particular change of dephasing time has been investigated in spite of the host molecule was removed from PVA to PMMA. Moreover, decreasing tendency of dephasing did not show drastic change as the sample temperature was increased from 4 K to 50 K.

On the other hand, we show the dephasing time of the Phenol doped in PVA vs. inverse of temperature in Fig. 2. The dephasing time of Phenol is longer as orders than that of the Aniline at the temperature 4.3 K. This behavior of the dephasing times would be originated from the interaction between the host and the guest molecules, i.e.electron-lattice interaction. It is thought that the dephasing mechanism for the Aniline/PVA would be different from that of the Phenol/PVA system. We imply that charge transfer or resonant excitation transfer would become candidates to explain these fast dephasing characteristics. In particularly, it is important that the molecular conformation of the Aniline is more planar in the first excited state than in the ground state. The plane of the $NH_2$ group is twisted away from the phenyl plane by about 46° in the electronic ground state [1]. This angular change could cause strong interaction between the Aniline and the hosts when the molecule is excited.

## Reference

[1] S.K.Sarakar and G.S.Kastha, Spectrochimica, 48A,1611(1992)

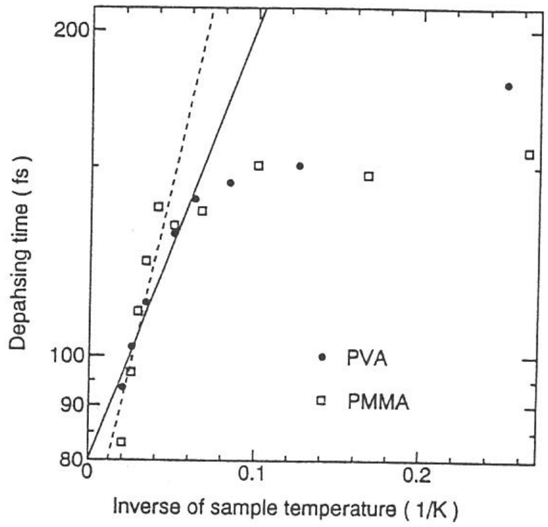

**Fig. 1:** Accumulated photon echo decay of Phenol doped in PVA at the temperature of 4.3 K. The excitation wavelength is 289 nm and the band width is about 12 nm. The dephasing time is 9.04 ps

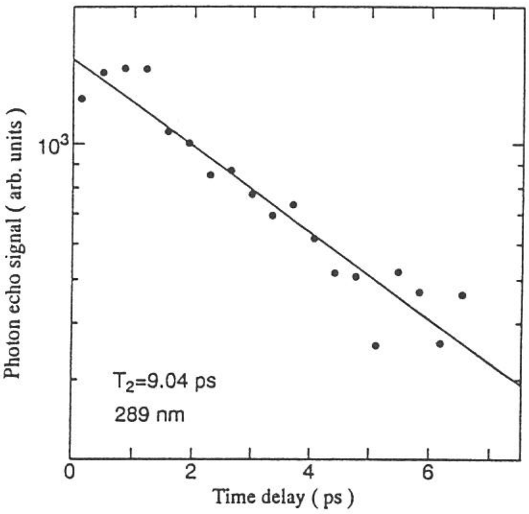

**Fig. 2:** Dephasing time of the Aniline doped in PVA and PMMA as a function of inverse of temperature. Circle denotes the case of doped in PVA and square corresponds to of PMMA.

(BL8A)

# Clarification of High-Rate and Anisotropic Ablation Mechanism of Polytetrafluoroethylene Using Synchrotron Radiation Ablation Process

Muneto INAYOSHI, Masafumi ITO, Mineo HIRAMATSU*, Masaru HORI and Toshio GOTO

*Department of Quantum Engineering, Nagoya University,*
*Chikusa-ku, Nagoya 464-01, Japan*
**Department of Electrical and Electronic Engineering, Meijo University,*
*Tempaku-ku, Nagoya 468, Japan*

## I. INTRODUCTION

Polytetrafluoroethylene (PTFE) has been expected as the parts for production of micromachine because of its low dielectric constant, high mechanical strength, and chemical and thermal stability.

Recently, We proposed the PTFE fabrication process using SR irradiation, that is, the SR ablation process, and reported that the extremely deep microstructures of 100 μm- square hole pattern and 2 μm hole pattern was successfully created in a PTFE sheet of 5 mm thickness using the SR ablation process.[1] However, the mechanism of PTFE ablation using the SR ablation process was not clarified.

In this report , we performed the experiments for clarifying the mechanism of PTFE ablation in SR ablation process.

## II. EXPERIMENTAL

The experiments were carried out at beam line BL-8A. Figure 1 shows a schematic diagram of the experimental apparatus used in this study. The experimental apparatus consists of the SR beam, a reaction chamber, a pumping system. The PTFE target was set perpendicularly to the SR beam. A 200-mesh of nickel (Ni) (a square pattern of 100 mm) was used for the contact mask. SR beam irradiated the masked PTFE target at room temperature.

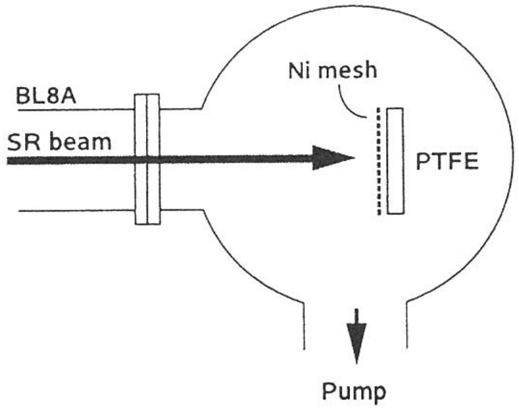

Fig. 1 A schematic diagram of the experimental apparatus used in this study.

## III. RESULTS AND DISCUSSION

The ablation of PTFE was carried out in Ar atmosphere. Ar gas pressure was varied in the range from 1 to 100 mTorr. Figure 2 shows the ablation rate of PTFE as a function of Ar gas pressure. The ablation rate decreased with increasing of Ar gas pressure. This result suggests that the ablation rate of PTFE irradiated by SR beam is dependent on the vapor pressure of the fragments generated by decomposition of PTFE .

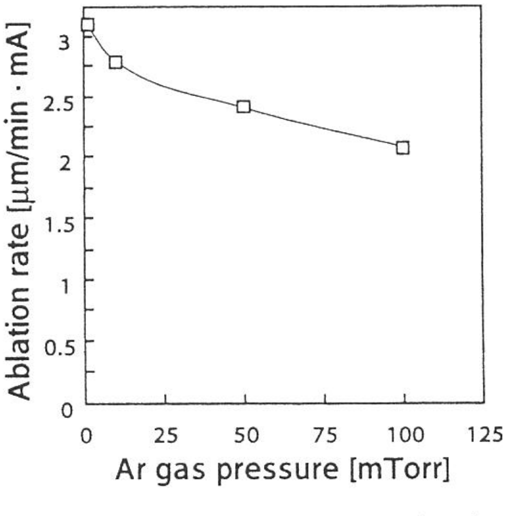

Fig. 2 The ablation rate of PTFE as a function of Ar gas pressure.

Figure 3 shows the ablation rate of PTFE as a function of beam current using a 200-mesh of Ni as a contact mask. It was found that ablation of PTFE started at beam current of 70-90 mA, and the ablation rate increased rapidly with increasing of beam current up to 120 mA and than increased linearly with increasing of beam currents more than 120 mA. This fact suggests that PTFE is ablated over surface temperature of PTFE correspond to beam current of 70-80 mA. So, in order to investigate the effect of infrared (IR) light on the PTFE ablation by SR beam, PTFE was irradiated by CO2 laser beam (wavelength of 10.6 μm). As a result, PTFE was not ablated anisotropically, although it was ablated at high rate by CO2 laser beam. This fact indicates that IR light does not contribute to anisotropic ablation of PTFE by SR irradiation. However, IR light contributes to high rate ablation of PTFE by SR irradiation.

The ablation of fluorinated ethylene propylene (FEP) and perfluoroalkoxy (PFA) was carried out by using SR ablation process. Both FEP and PFA were ablated at high rate with high aspect ratio like PTFE. The molecular weight of FEP and PFA are lower than that of PTFE. And the molecular weight of FEP are lower than that of PFA. Figure 4 shows the ablation rates of FEP, PFA and PTFE as a function of the pattern width. In all samples, the ablation rate was increased with increasing pattern width. This fact suggests that the ablation rates of FEP, PFA and PTFE irradiated by SR beam are dependent on the vapor pressure of the fragments generated by decomposition of FEP, PFA and PTFE. Moreover, in any pattern width, the ablation rate of FEP was the highest compared with those of PFA and PTFE. This fact indicates that material with lower molecular weight is ablated at higher rate in SR ablation process. Therefore, it is suggested that C-C bonds of PTFE are decomposed at high rate by photon absorption of ultraviolet - X-ray.

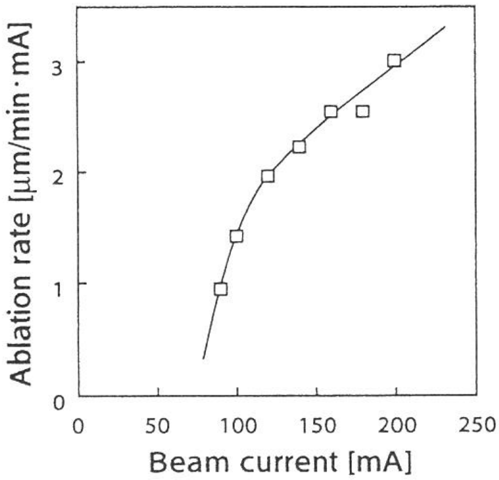

Fig. 3 the ablation rate of PTFE as a function of beam current using a 200-mesh of Ni as a contact mask.

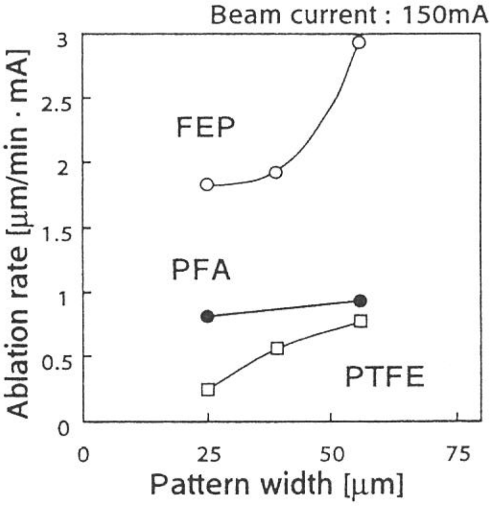

Fig. 4 The ablation rates of FEP, PFA and PTFE as a function of the patern width.

## IV. CONCLUSION

In order to clarify the mechanism of PTFE ablation using SR ablation process, We performed PTFE ablation by variation of pressure, beam current and molecular weight. As a result, It was suggested that PTFE ablation rate by SR irradiation is dependent on the vapor pressure of the fragments generated by decomposition of PTFE. Moreover, it was found that IR light dose not contribute to anisotropic ablation of PTFE by SR irradiation, and photon absorption of ultraviolet - X-ray contributes to the anisotropic ablation of PTFE at high rate by SR irradiation.

[1] M. Inayoshi, M. Ikeda, M. Hori, T. Goto, M. Hiramatsu and A. Hiraya: Jpn. J. Appl. Phys. **34** (1995) L1675

(BL8A)

# SOR Excited Etching of Si Wafer in $CF_4$ Gas Atmosphere

Ryoichi Inanami, Tomoya Yamada and Shinzo Morita
Center for Cooperative Research in Advanced Science and Technology,
Nagoya University,
Furo-cho, Chikusa-ku, Nagoya 464-01, JAPAN

Previously, it was reported that etching of Si wafer in $CF_4$ gas under SOR irradiation was observed at a negatively biased voltage. Therefore, Si wafer etching will be referred to positive ions[1]. In this experiment, the positive ions were analyzed by a mass spectrometry during the etching, and a 50 nm pattern etching through an electron-beam resist pattern was examined experimentally.

A reaction chamber was equipped along the beam line of BL8A from UVSOR through two or three differential evacuating pumps. The $CF_4$ gas was introduced into the reaction chamber through a mass flow controller and the focused SOR beam was irradiated to the substrate perpendicularly. Si wafers used as a substrate were P doped n-type with (100) orientation. After removing native oxide by dipping into HF solution, the Si wafer was mounted on a sample holder which was isolated electrically and a bias voltage was applied on the holder. For the observation of mass spectra of positive ions, a quadrupole mass analyzer, MODEL MSQ-400, ULVAC Co., Inc., was set at the third differential evacuated chamber. For the fine pattern etching of Si wafer, two differential evacuation pumps were used to decrease the SOR energy loss in the $CF_4$ gas.

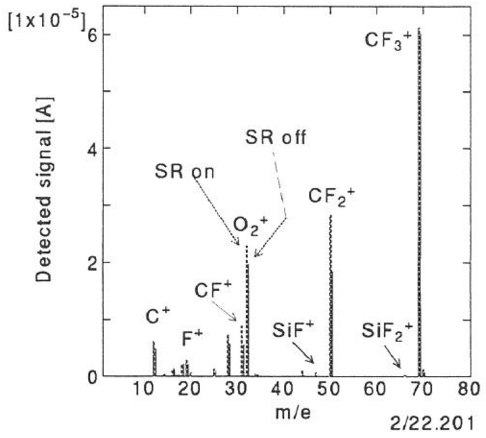

Figure 1: Detected ions by mass spectrometry with and without SOR exposure

Detected positive ions by the mass analyzer are shown in Fig.1. Introduced gas was composed with $CF_4$ and oxygen, where the partial pressure of oxygen was 4% and the total pressure was 0.100 Torr. The analysis chamber for the mass spectrometry was equipped at upper side of the reaction chamber and the pressure was

$5.2 \times 10^{-4}$ Torr. The detected positive ions were $CF_3^+$, $CF_2^+$, $CF^+$, $F^+$ and $C^+$, and etching products, $SiF^+$ and $SiF_2^+$ under an applied voltage of $-300$ V. Among these species, $CF_x^+$ signals were relatively large, but the effective species was not specified from the experiment. Detected $SiF^+$ and $SiF_2^+$ suggested $F^+$ was contributed for the etching evenif $F^+$ density was small at the sampled place. However, $CF_x^+$ contribution was not distinguished from the experiment.

For a fine pattern etching, a resist pattern was fabricated by an electron-beam exposure technique. A negative tone chemically amplified resist SAL-601 (Shipley Far East Ltd.) was spin-coated on a Si wafer with a thickness of 55 nm and pre-baked in oven. A 50 nm line and space pattern was delineated on the resist by an electron-beam exposure system, JBX-6000SG (JOEL Co., Ltd.). Then, the patterned resist was developed by dipping into a developer, after post-exposure-bake on a hot plate.

Si wafer etching through the electron-beam resist was performed at a $CF_4$ pressure of $6 \times 10^{-4}$ Torr and a dc bias voltage of $-287$ V. The substrate currents were about 190 $\mu$A during exposure to SOR and the total dose was 5000 mA·min. The etched pattern was shown in Fig.2. It was observed that a 50 nm width line structure was successfully etched by SOR excited plasma.

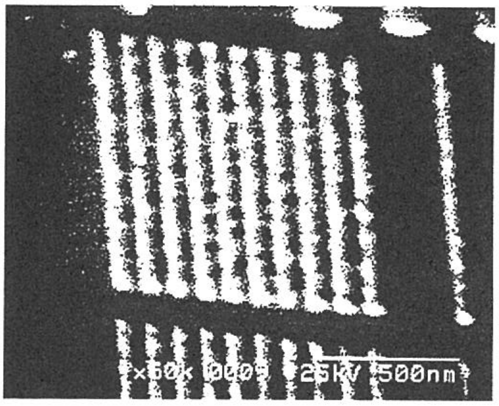

Figure 2: SEM photograph of etched Si wafer surface with 50 nm line structure

From the present experiments, it was confirmed that the etching was promoted by an ionized $CF_x$ species. However, the effect of SOR irradiation on the etching process was not distinguished experimentally. For the fine pattern fabrication with a high aspect ratio, the irradiation of collimated SOR is expected to be important compared to the positive ions of $CF_x^+$. Therefore, the effect of SOR irradiation on the etching will be studied in the future experiment.

## References

[1] R.Inanami, T.Uchida and S.Morita: *J. Electrochem. Soc.*, **143** (1996) 3752 (now printing)

(BL8A)

# Homoepitaxial growth of ZnTe by synchrotron radiation using metalorganic sources

**Hiroshi OGAWA, Mitsuhiro NISHIO, Qixin GUO, Yoshiaki MITSUISHI, Shin TAKUNO, Kazuhiko SATO and Shinji TANAKA**

Department of Electronic Engineering, Faculty of Science and Engineering, Saga University, 1 Honjo, Saga 840, Japan

Synchrotron radiation (SR) excited growth of compound semiconductors using metalorganic sources is attracting much attention for the purpose of low-temperature growth. We have already demonstrated that the deposition of ZnTe occurs epitaxially in the SR irradiation part of a (100) GaAs substrate at room temperature[1]. This fact suggests that SR is a powerful light source for the low temperature growth of ZnTe. Thus, it is very desirable to study systematically the epitaxial growth.

This report describes the effect of the transport rate of source materials upon the homoepitaxial growth of ZnTe using diethylzinc(DEZn) and diethyltelluride(DETe). The (100) oriented ZnTe was used as a substrate. The source materials were independently fed into the reaction chamber using hydrogen carrier gas. The growth was carried out at very low pressures such as $-10^{-4}$ Torr in the reaction chamber using the SR beam line, BL-8A. The substrate was located about 5.5m away from the source point of the bending magnet. The incident SR beam irradiated the sample surface perpendicularly. All the growth experiments were carried out at room temperature.

The formation of film was recognized only in the region exposed to SR illumination, as well as in the case of GaAs substrate[1]. It was confirmed by RHEED measurement that ZnTe film grows epitaxially on the ZnTe substrate. Figure 1 shows the relationship between the growth rate and DEZn transport rate when DETe transport rate is kept at 1 $\mu$m/min. The growth rate shows a value of about 1.3Å$\mathrm{mA}^{-1}\mathrm{min}^{-1}$ at DEZn transport rate of 0.6$\mu$mol/min. The growth rate is almost independent of DEZn transport rate under the condition of more than 0.1$\mu$mol/min. When DETe transport rate is varied keeping DEZn transport rate constant at 0.5 $\mu$mol/min, on the other hand, the growth rate increases monotonically and then saturates when the transport rate of DETe exceeds 1$\mu$mol/min, as shown in Fig.2. Thus, the growth rate is governed by the supply of DETe, implying that the process associated with the adsorption of DETe molecules followed by the decomposition due to SR irradiation will be essential in the ZnTe deposition. The tendency of saturation indicates that the rate-limiting step is due to the number of photons. If the wavelength region between 5 and 1500Å has a possibility of contribution for the growth, the calculated quantum yield for forming ZnTe molecules by photon can be estimated to be as high as about 1%. It is found that the surface morphology of the film depends upon the transport rate ratio of DETe to DEZn. The film with the relatively smooth surface can be obtained only at the high transport rate ratio of 10 or 15. The photoluminescence from the crystal grown by SR illumination can be observed in all the samples. This fact is very interesting because little research has so far dealt with such luminescence. The photoluminescence spectrum of the film is dominated by strong deep level emission located at 2.1 eV, as shown in Fig.3.

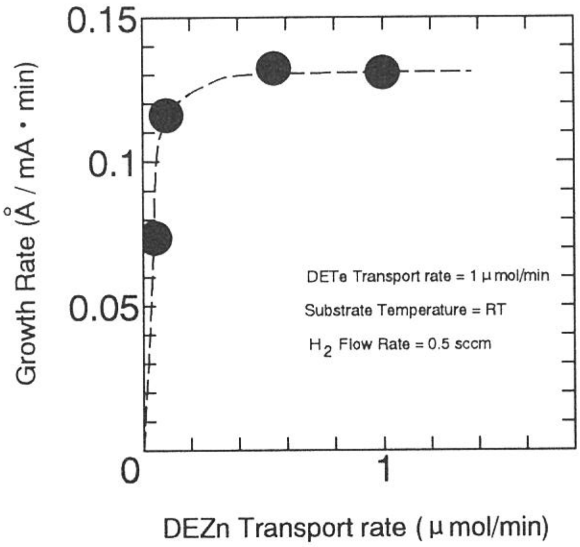

Fig.1 Growth rate versus DEZn transport rate

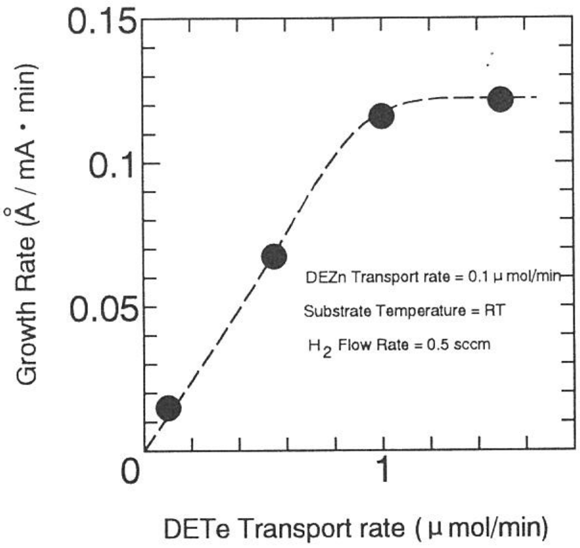

Fig.2 Growth rate versus DETe transport rate

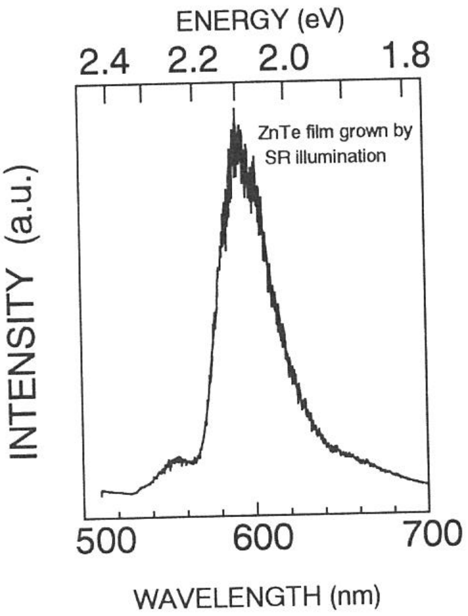

Fig.3 Typical photoluminescence spectrum of ZnTe film

**Reference**

1)M.Ikejiri, T.Ogata, H.Ogawa, M.Nishio and A.Yoshida,J. Vac. Sci. & Technol. 12, 278 (1994).

T.Ogata, S.I. Gheyas, M.Ikejiri, H. Ogawa and M.Nishio,J.Crystal Growth 146, 587 (1995).

T.Ogata, S.I. Gheyas, M.Ikejiri, H. Ogawa and M.Nishio,Thin Solid Films 266, 168 (1995).

(BL8B1)

# State selective photo-fragmentation of acetonitrile in gas-phase by core excitation

Hidenobu TAKESHITA, Yasunori SENBA, Hideki MATSUO, Kazumasa OKADA*
Tatsuo GEJO*, Atsunari HIRAYA, Ken-ichirou TANAKA

*Department of Materials Science, Hiroshima University, Higashi-hiroshima 739*
**UVSOR, Institute for Molecular Science, Okazaki 444*

Ionic photo-fragmentation process of 1s-core (C and/or N) excited acetonitrile ($CH_3CN$, $CD_3CN$) in gas phase was studied with using Synchrotron Radiation (SR) as a soft X-ray source. Branching ratio of fragment ions as well as kinetic-energy distribution of fragment ions for several core-excited states were investigated in order to elucidate the state dependence of dissociation processes after core excitations.

Experiments were carried out at BL8B1 of UVSOR. Fragment ions created in photodissociation processes were detected by a time-of-flight (TOF) mass spectrometer. By selecting excitation energy, C1s and N1s electron of acetonitrile was excited to the $\pi^*$ state and above the ionization threshold (IP), respectively. In order to subtract the contribution from valence bands excitation, mass spectra were also measured below the 1s excitation threshold (pre-edge). The detection axis of TOF mass spectrometer was perpendicular to the plane of polarization of SR.

Figure. 1 shows mass spectrum obtained for the resonant excitation N1s→ $\pi^*$ of acetonitrile-d3 ($CD_3CN$). In the present measurements, singly charged fragment ions $D^+$, $D_2^+$, $CD_X^+$(X=0～3), $C_2D_X^+$(X=0～3), $D_XCN^+$(X=0～2), and $CD_XCN^+$(X=0～3) were obserbed. Only one doubly charged ion was observed at mass number 21 that can be assigned as $CD_2CN^{2+}$. In this

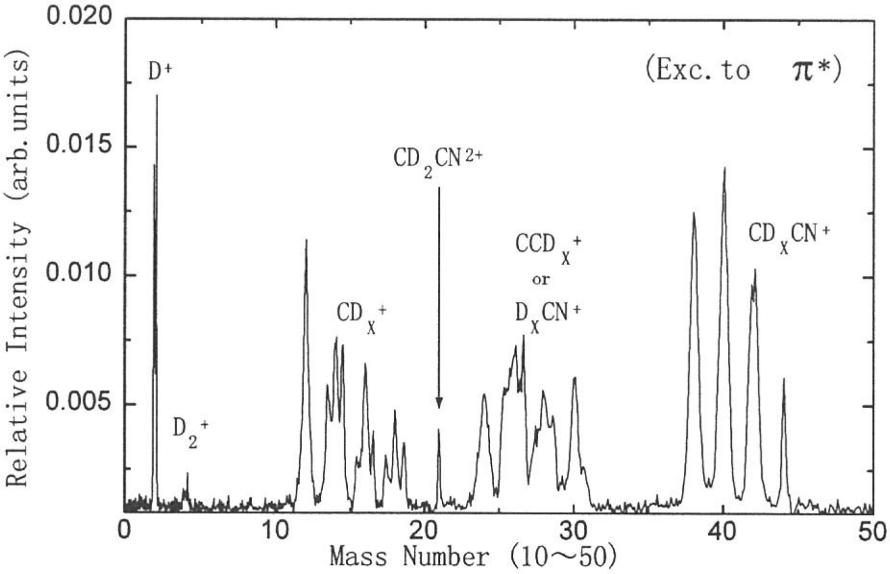

Fig.1 Mass spectrum of photofragments of $CD_3CN$ after N1s→ $\pi^*$ excitation.

spectrum, characteristic triad features are observed at mass 14, 16, 18, 26, 28 and 30. The triad features consist of a sharp central peak (K.E.=0 or low) and broad wings (K.E.≠0). Where K.E. is kinetic energy of ions released in dissociation process following excitation by SR. The central peak and the wings corresponds to different dissociation processes.

Figure. 2 shows the spectra obtained for excitation at pre-edge, N1s→$\pi$* and N1s→IP of $CD_3CN$. Relative intensity of triad feature was changed by the difference of excited state. Especially, the most remarkable change are observed at mass 16 and 18. Only the central peak of triad feature is observed in the spectrum of pre-edge excitation. Conversely, only the wings of triad feature are observed in the spectrum of IP excitation. Both the central peak and wings of triad feature are observed in the spectrum of the $\pi$* excitation. Change in these spectra is caused by the difference in photodissociation process for each excited state. Auger decay of core excited states is well-known as the dominant decay process prior to dissociation. Thus, difference of these spectra can be attributed to the difference in the final state of Auger decay. Each component of the triad feature were assigned as follows. The central peak in pre-edge excitation corresponds to the ionic fragmentation of valence one-hole states. The wings in IP excitation correspond to that of two-hole states after normal Auger decay. Finally, in the $\pi$* excitation, the central peak and wings correspond to the ionic fragmentation of one-hole states after resonant participator Auger decay and that of two-hole one-electron state after resonant spectator Auger decay, respectively.

In addition to the state selectivity found in kinetic energy resolved mass spectra, the most remarkable state selectivity was found for $CD_2CN^{2+}$ that appears only in the $\pi$* excitation. The decay process responsible to the formation of this doubly charged ion is tentatively assigned as autoionization after resonant spectator Auger decay.

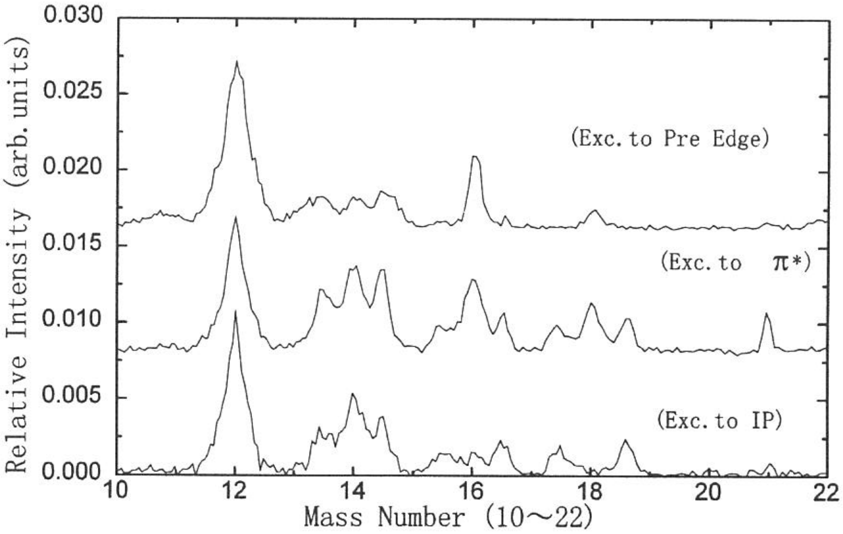

Fig.2 Comparison of mass spectra obtained for different excitation energies.
Top ; below N1s-excitation threshold (pre-edge), middle ; N1s to $\pi$*,
bottom ; above N1s ionization threshold (IP).

(BL8B1)

# Site-Dependent and Angle-Resolved Fragmentations of *K*-Shell Excited $CF_3CN$

Toshio IBUKI, Kazumasa OKADA, Tatsuo GEJO, and Eiji ISHIGURO [a]
*Institute for Molecular Science, Myodaiji, Okazaki 444*
[a] *College of Education, University of Ryukyus, Nishihara-cho, Okinawa 903-01*

Site-specific fragmentations of polyatomic molecules were studied for $(CH_3)_2CO$ and $CF_3CH_3$ in the early 1980s,[1,2] which showed the *K*-shell excited molecules memorize the initial site of energy deposition. Since then *K*-shell excitation has been expected to be a scalpel-like tool to cut a chemical bond around certain selected atoms (C, N, O, etc.) within a polyatomic molecule.

In the present work we measured photofragmentations of $CF_3CN$ by exciting *K*-shell electrons of the F, two C, and N atoms. In addition angle-resolved TOF mass spectra were measured by locating the TOF tube at the perpendicular and parallel positions with respect to the linearly polarized electric vector of synchrotron radiation. Fig. 1 shows the typical TOF spectra at $h\nu$=766 and 406 eV which are the direct $F(1s)^{-1}$ ionization and the Rydberg←N(1s) transition, respectively. The site-dependent fragmentations are clearly observed. That is, the large $CF_2CN^+$, $CF_3^+$, and $CF_2^+$ ions are the dominant fragments at the F(1s) electrons excitation while the small $C^+$, $N^+$, $F^+$, $CN^+$, and $CF^+$ ions are the main ionic remainders at the N(1s) edge excitation. Figure 2 shows the angle-resolved TOF mass spectra at the $\pi^*$←N(1s) resonant excitation at 397 eV. In the perpendicular experiment the $CF_3^+$, $CF_2^+$, and $CN^+$ fragment ions are split into three peaks because of the energetic components or the anisotropic distributions. On the other hand, the $C^+$ and $CF^+$ ions, which are generated by four and three bonds dissociation, respectively, are approximated by a single Gaussian function in both the parallel and perpendicular spectra. These ions should be produced via isotropic fragmentations.

The total ion yield spectrum at the carbon edges is shown in fig. 3. In the fluorinated C(1s) excitation (denoted by $C_F$ in fig. 3), the small fragment $C^+$, $N^+$, $F^+$, $CN^+$, and $CF^+$ ions were mainly produced similar to fig. 1a. When the C(1s) electrons of the CN group (denoted by $C_N$) are excited, the *KVV* Auger decay leads to the small fragments formation similar to fig. 1b. These observations suggest fragmentations occur locally around the carbon atom initially energized. The excess energy in the resonant process such as $\sigma^*$ or Rydberg←N(1s) is redistributed within the molecule simultaneously or just before the Auger decay.

## References

[1] W. Eberhardt, T. K. Sham. R. Carr, S. Krummacher, M. Strongin, S. L. Weng, and D.Wesner, Phys. Rev. Lett. **58**, 1038 (1983).
[2] K. Müller-Dethefs, M. Leslie, L. A. Chewter, and E. W. Schlag, J. Phys. Chem. **88**, 6098 (1984).

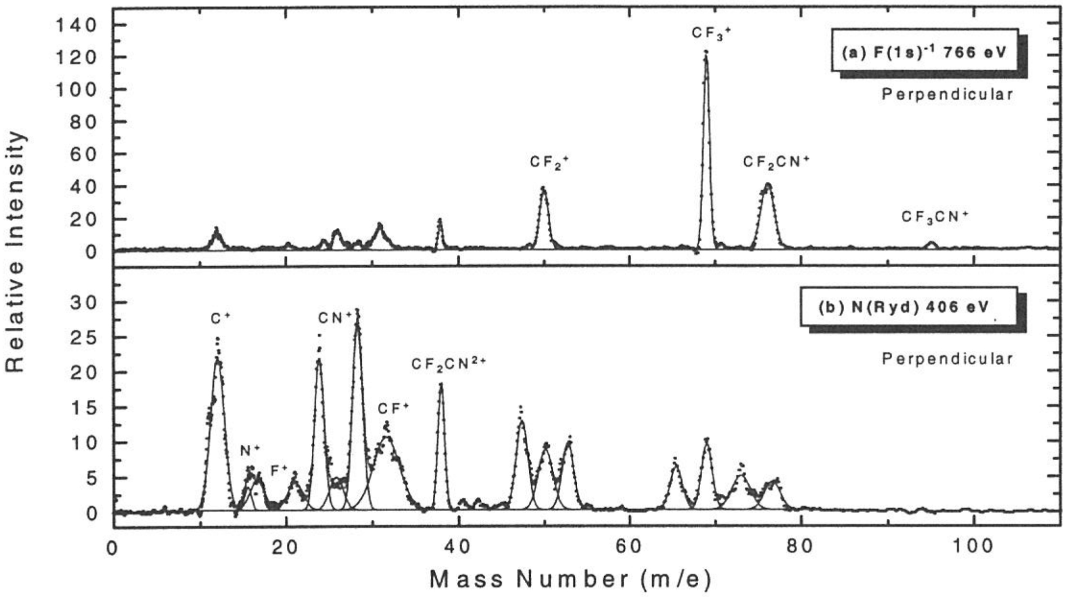

Fig. 1. TOF mass spectra at 766 and 406 eV.

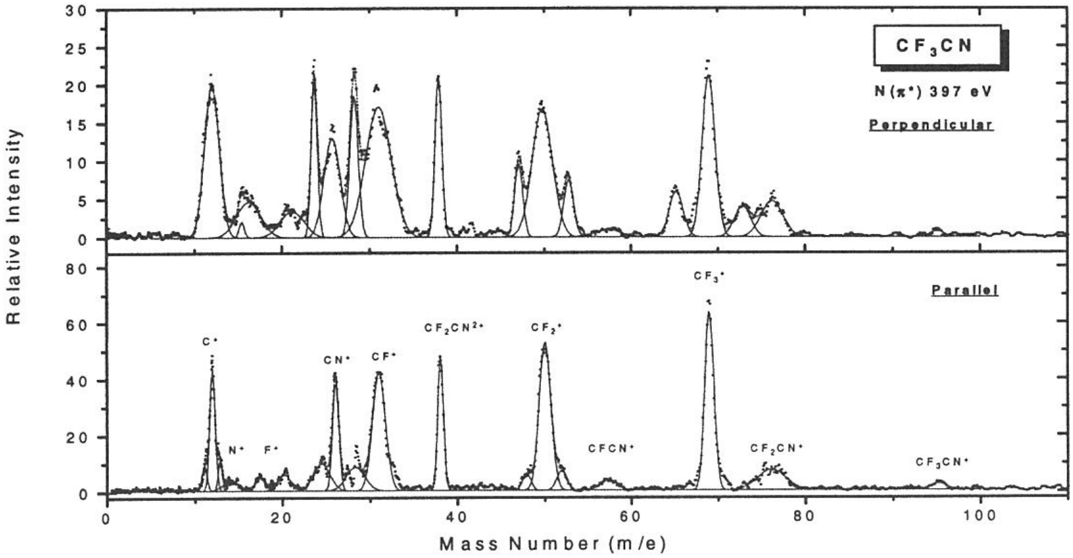

Fig. 2. Anisotropic fragmentations at 397 eV.

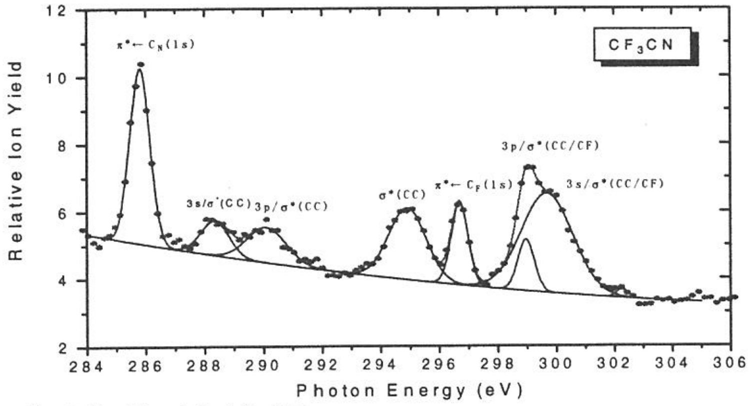

Fig. 3. Total ion yield at C edges.

(BL-8B1)

# Measurement of Quantum Efficiency of the CCD Camera Systems

Atsuhiko Hirai[1], Kuniko Takemoto[2], Norio Watanabe[3], Hidekazu Takano[3],
Sadao. Aoki[3], Yasuyuki Nakayama[1] and Hiroshi Kihara[2]

[1] *Department of Physics, Ritsumeikan University, Kusatsu, Shiga 525-77*
[2] *Physics Laboratory, Kansai Medical University, Hirakata 573*
[3] *Institute of Applied Physics, Tsukuba University, Tsukuba 305*

Recently, the CCD camera system is used as a detector for soft X-ray microscopy at BESSY[1] and ALS[2]. We also used the CCD camera system at UVSOR BL-8A[3], Rits SR center BL-12[4], and Tsukuba University[5].

The spatial resolution and image field of the CCD camera system matched to a detector for a soft X-ray microscope. The quantum efficiency of the CCD camera system at wavelength 1.0-5.0nm is an important factor for soft X-ray microscope[6][7]. Using synchrotron radiation at BL-8B1 of UVSOR at wavelength 1.0-5.0nm[8], we measured the quantum efficiency of two CCD camera systems.

Each CCD camera system consists of a CCD chip (back illuminated), Astrocam CCD camera 4200(liquid nitrogen cooling) and personal computer for camera controlling and data acquisition. The two CCD camera systems use CCD chips of SITe SI502A (512 x 512 pixel, each 24μm x 24μm) and EEV CCD 02-03 (385 x 578 pixel, each 22μm x 22μm).

The scheme of the experimental arrangement is shown in Fig. 1. It consists of a Au mesh(open area 90%), a silicon photodiode (IRD AXUV-100) and the CCD camera system.

The absolute number of incident photons $N_{ph}$ was measured by drain current of Au mesh, which is calibrated by silicon photodiode. The quantum efficiency of silicon photodiode can be approximately predicted in most of the XUV region by the theoretical expression $E_{ph}$ / 3.63, where $E_{ph}$ is photon energy in electron-volts[9].

The number of detected photoelectrons $N_{pe}$ was measured by the CCD image (Fig. 2). For majority of XUV photons, about 3.63eV energy is required to generate one electron-hole pair. The average number of photoelectrons per photon detected in an ideal detector is $N_{max} = E_{ph} / 3.63$.

The quantum efficiency QE is defined as the number of detected photoelectrons per incident photon $N_{pe} / N_{ph}$ divided by the maximum number $N_{max}$, and is given by

$$QE = \frac{N_{pe} / N_{ph}}{N_{max}} = \frac{N_{pe} / N_{ph}}{E_{ph} / 3.63} \quad .$$

The quantum efficiency of EEV CCD 02-03 is shown in Fig. 3, obtained more than 20% at wavelength 2.0-5.0nm. Peak at wavelength 4.3nm were due to low accuracy of the value of incident photons.

The quantum efficiency of SITe SI502A was a few percent at wavelength 2.0-5.0nm. This was considerably worse compared with other experiments[6][7]. We consider this is due to the coating of the chip with antireflection material.

## Acknowledgment

The authors are grateful for the help and encouragements from Prof. T. Kinoshita, Dr. T. Gejoh, Mr. E. Nakamura and other staffs of the Institute for Molecular Science.

## References

[1] B. Niemann et al., **X-ray Microscopy IV,** eds. A. G. Michette et al. (Springer-Verlag, Berlin), 66 (1995).
[2] W. Meyer-Ilse et al., Synch. Rad. News **8,** No.3 29 (1995).
[3] A. Hirai et al., UVSOR Activity Report **1995**, 230 (1996).
[4] A. Hirai et al., **X-ray Microscopy V,** eds. J. Thieme et al. (Springer-Verlag, Berlin), (in press).
[5] S. Aoki et al., **X-ray Microscopy V,** eds. J. Thieme et al. (Springer-Verlag, Berlin), (in press).
[6] H. Aritome et al., SPIE **1741**, 276 (1992).
[7] T. Wilhein et al., **X-ray Microscopy IV,** eds. A. G. Michette et al. (Springer-Verlag, Berlin), 470 (1995).
[8] A. Hiraya et al., Rev. Sci. Instrum. **66**, 2104 (1995).
[9] R. Korde et al., IEEE Trans. Nucl. Sci. **NS-16**, 1655 (1993).

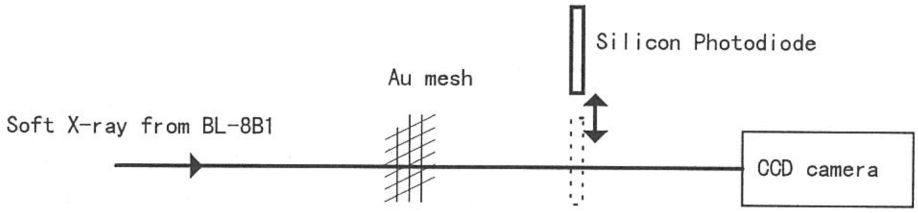

Fig. 1. The scheme of the experimental arrangement for quantum efficiency of the CCD camera system.

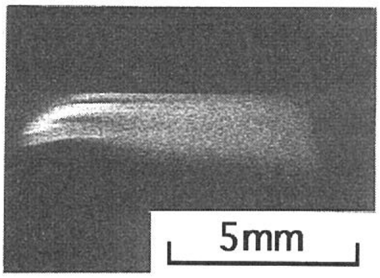

Fig. 2. Image of beam profile at BL-8B1 by CCD camera.

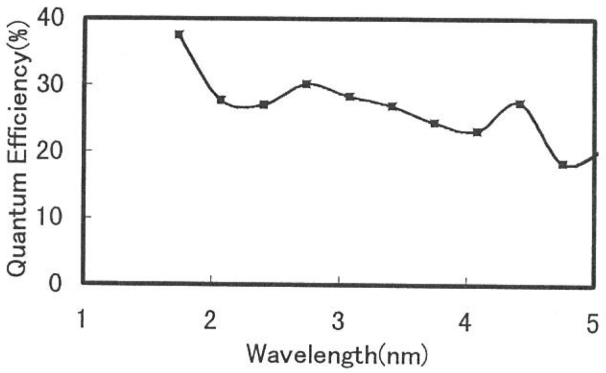

Fig. 3. Quantum efficiency of the CCD(EEV CCD02-03).

(BL-8B1)

# Core Absorption Spectra of Thin Polyester Films in the Soft X-ray Region

Isuke OUCHI, Ikuo NAKAI, Masao KAMADA*, Shin-ichiro TANAKA* and Atsunari HIRAYA**

Faculty of Engineering, Tottori University, Tottori 680
*UVSOR, Institute for Molecular Science, Okazaki 444
** Faculty of Science, Hiroshima University, Higashi Hiroshima, 739

We studied the core absorption spectra of thin polyester films for the past few years by the total electron yield methods; we made assignments for some of the fine structures of the absorption peaks of them utilizing the published literature data of the low molecular weight carbonaceous compounds and by our observed results on the dependence of the spectrum shape on the change of the incidence angle.[1, 2] Prior to these experiments, we made measurements by transmission mode but did not obtain well resolved spectra. In this study, we made second trials for transmission mode utilizing the beam line 8B1, which is equipped with a constant-deviation constant-length spherical grating monochromator.[3] Samples for transmission measurements were same as those used for total electron yield method; isotropic amorphous films were formed on a glass plate by dipping and, after dried, were stripped off from the plate in water. Uniaxially oriented films were made by drawing the amorphous films by use of a tensile tester at the temperatures a little higher than their glass transition temperatures. Biaxially oriented films 0.7$\mu$m thick were made at the pilot plant of the Film Research Laboratories of Teijin Limited.[1]

In the most, but not all, measurements, the G2 grating and the entrance and exit slits both of 20$\mu$m width were utilized. The incident beam was monitored by an Au mesh placed in front of the sample and the transmitted beam was detected by a similar Au mesh. The optical density was determined as the ratio of the normalized transmitted intensity through the sample and that without sample. These measurements were not carried out alternatively at each wavelength; the sample run and the reference run were made separately so that there could have been some error involved due to the change of dark current etc, although usually the dark current was relatively stable. The most concerned error comes from the fact that any monochromator is contaminated more or less by carbonaceous materials and oxydized ones at the mirrors, gratings, slits etc, while the absorption edges we concern are carbon and oxygen. Hence, a slightest play in the movement of the grating could cause a significant error in the ratio oflog(Io/I) of the sample and the blank, because Io (intensity monitored by the front Au) and I (intensity obtained by the Au mesh after transmission) of both the sample film and the blank sharply change with the wavelength near at the carbon and oxygen edges. This is to be carefully checked for each data and corrected if necessary.

Examples of the absorption spectra taken by transmission mode are shown in Fig. 1 and 2, where the ordinates are taken for log(Io/I) of the sample before divided by that of the blank, their unit being arbitrary; Fig. 1 shows the spectrum of a uniaxially drawn PET film and Fig. 2 represents that of a biaxially drawn one, both by normal incident light. The details of the peaks are not so well displayed as those by total electron yield mode taken with a grating of 2400 lines/mm in the grasshopper monochromator in the BL-2B1, but are nearly comparable to those with 1200 lines/mm. The spectra taken by an oblique incident beam did not conform to those taken by total electron yield mode; the intensity of the peaks corresponding to the 1s ---> $\pi^*$ transitions did not grow when the film plane made a larger angle with the film normal. This may have been due to a misalignment of the sample rotating axis which was brought about during setting the sample holder in the chamber; this point should be clarified in the next trial.

The spectra at the oxygen K-edge are similarly resolved as in the total electron yield mode with a grating of 1200 lines/mm at BL-2B1. The absorption spectra should be better taken because the concentration of oxygen in the PET and PEN films is much lower than that of carbon; the optical density of the biaxialy drawn PEN films shown in Fig. 3 is reasonable.

Some more measurements are to be made for further analysis.

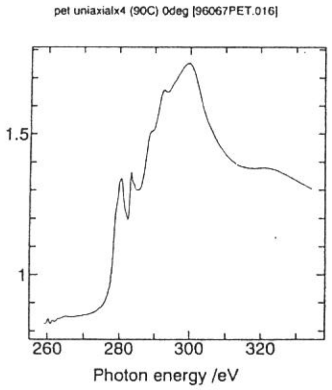

Fig. 1. Absorption spectra of a uniaxially oriented PET film at carbon K-edge for normal incidence by transmission mode.

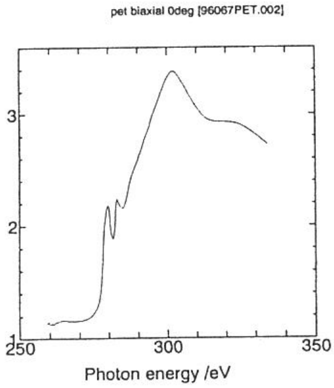

Fig. 2. Absorption spectra of a biaxially oriented PET film at carbon K-edge for normal incidence by transmission mode.

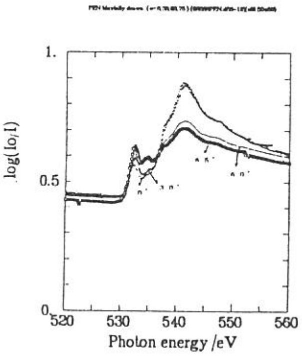

Fig. 3. Absorption spectra of a biaxially oriented PEN film at oxygen K-edge for incident angles of 0, 30 and 60° by transmission mode.

1) I. Ouchi, I. Nakai, M. Kamada, S. Tanaka & T. Hagiwara; Polym. J., 27 (1995) 127.

2) I. Ouchi, I. Nakai, M. Kamada & S. Tanaka; J. Electr. Spectrsc. Rel. Phenom., 78 (1996) 363.

3) A. Hiraya, E. Nakamura, M. Hasumoto, T. Kinoshita, K. Sakai, E. Ishiguro & M. Watanabe; Rev. Sci. Instrum., 66 (1959) 2104.

(BL8B1)

# Si-L Absorption Spectra of $CaF_2/Si/CaF_2$ Multilayers

Takeo EJIMA, Katsumi OUCHI and Makoto WATANABE

*Research Inst. for Scientific Measurements, Tohoku Univ., Sendai 980-77, JAPAN*

In the previous Si-L absorption measurements on LiF/Si/LiF multilayers, it was suggested that the structure of Si layer is anisotropic, that is, the structure parallel to the LiF layer is similar to that of porous Si, but the structure perpendicular to the LiF layer is similar to that of bulk crystalline Si [1]. In this study, we measured Si-L absorption spectra of the different system of $CaF_2/Si/CaF_2$ multilayers, which were grown epitaxially on Si(111) surfaces at 750℃ and checked by RHEED, in order to investigate the crystallinity of the Si layers. The Si-L absorption were obtained by total photoelectron yield measurements changing the incidence of angle with the electric vector of the monochromatized light parallel to the plane of incidence, as before.

Figure 1 shows the spectra on $CaF_2$ 15Å /Si 420Å/$CaF_2$ 70Å multilayers. For the angles of incidence between 0° and 55° the spectral shapes are similar to that of the bulk crystalline Si, but different above 60°. The difference becomes more prominent with increase in the angle of incidence. That is, the intensity just above the L edge decrease in comparison with that below the L edge. This tendency could not found in bulk crystalline Si (Si wafer of which surface is cleaned by chemical etching and terminated by oxygen). Therefore, it is suggested that the structure parallel to the surface is similar to that of the bulk crystalline Si, but the structure perpendicular to the surface is quite different with that of the bulk crystalline Si. It is quite interesting that this tendency is different with that in LiF/Si/LiF system.

Detailed analysis in terms of optical constants is now underway.

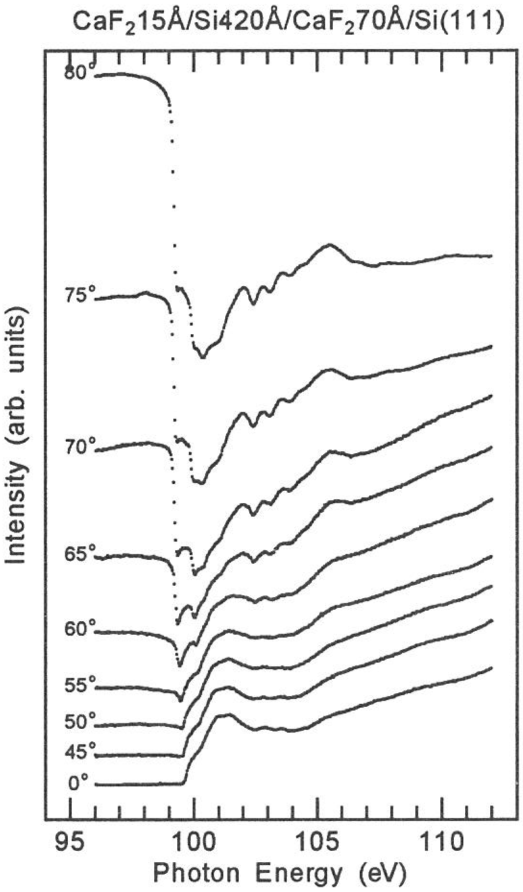

FIGURE 1. Si-L total photoelectron yield spectra of $CaF_2$ 15Å /Si 420Å/$CaF_2$ 70Å multilayer as a function of angle of incidence.

## Reference

[1] T.Ejima, K. Ouchi and M.Watanabe, UVSOR Activity Report 1995, p238.

BL8B2

# Resonant photoemission study of ladder compound $Sr_{14}Cu_{24}O_{41}$

O. Akaki, A. Chainani, and T. Takahashi
Department of Physics, Tohoku University, Sendai 980-77

There is increasing interest in one-dimensional cuprates, because of their peculiar electronic and magnetic properties as well as its relation to the superconducting mechanism in two-dimensional cuprates. In this report, we present results of resonant photoemission spectroscopy (PES) on $Sr_{14}Cu_{24}O_{41}$, which was recently found to show superconductivity below 12K under high pressure (3.5-4 GPa) by replacing Sr with Ca atoms [1]. $Sr_{14}Cu_{24}O_{41}$ consists of $Cu_2O_3$ planes with two-leg ladders and $CuO_2$ chains (Fig. 1). Sr, $Ca)_{14}Cu_{24}O_{41}$ is regarded as a "self-doped" ladder material with the Cu formal valence of 2.25. However, it is experimentally established that $Sr_{14}Cu_{24}O_{41}$ is an insulator and the replacement of Sr atoms with Ca gradually increases its metallic conductivity. The superconductivity is observed in a heavily replaced sample $Sr_{0.4}Ca_{13.6}Cu_{24}O_{41}$ under high pressure of 3.5 - 4 GPa [1]. It is still unknown at present where doped holes are and what role the Ca replacement plays in the crystal. In order to study the charge distribution in $Sr_{14}Cu_{24}O_{41}$, we have performed a resonant photoemission spectroscopy.

Photoemission measurements were performed at BL8B2 with $Sr_{14}Cu_{24}O_{41}$ single crystals at room temperature. Samples were repeatedly scraped by a diamond file to obtain a fresh and clean surface. Figure 2 shows PES spectra of $Sr_{14}Cu_{24}O_{41}$ measured at various photon energies across the Cu3p-3d core threshold (about 74 eV). We find that a new structure emerges around 13 eV binding energy at the core-threshold excitation (~ 74 eV). This new structure in the PES spectrum is ascribed to a so-called two-hole bound state, which is known to resonantly enhanced at the photon energy of Cu 3p-3d core excitation. The appearance of two hole-bound state in the resonant PES spectrum indicates that there is a substantial number of $Cu^{2+}$ ions with $Cu3d^9$ configuration in the compound. At the present stage, it is unknown whether these $Cu^{2+}$ ions are located on ladders or chains in the crystal. However, it is at least obvious that both (ladder and chain) are not doped and either of them should have almost no holes. This finding establishes the starting point to elucidate the electronic structure of "doped" superconducting $(Sr, Ca)_{14}Cu_{24}O_{41}$.

We thank Prof. Akimitsu at Aoyama-Gakuin University for providing $Sr_{14}Cu_{24}O_{41}$ single crystals.

[1] M. Uehara et al., J. Phys. Soc. Jpn.,65, 2764 (1996).

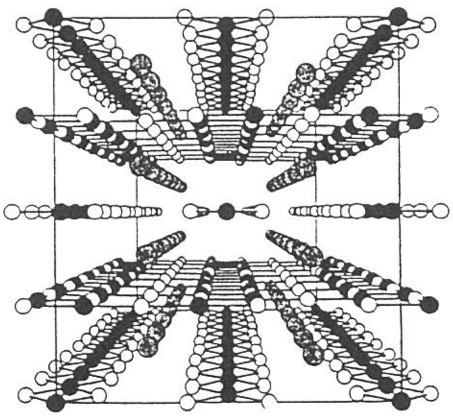

**Fig. 1** Crystal structure of $Sr_{14}Cu_{24}O_{41}$

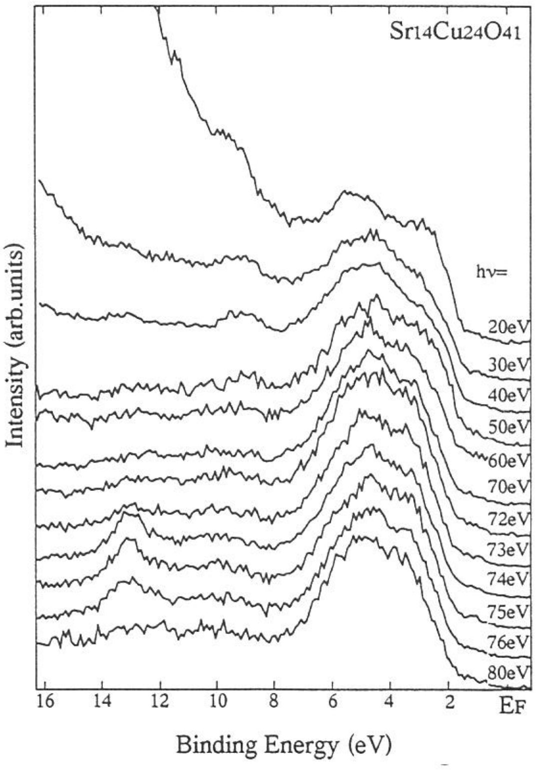

**Fig. 2** Photoemission spectra of $Sr_{14}Cu_{24}O_{41}$ at various photon energies across the Cu3p-3d core threshold (~74 eV).

(BL8B2)

# Ultraviolet Photoelectron Spectra of $C_{86}$ and $C_{90}$

Shojun Hino, Kazunori Umishita, and Kentaro Iwasaki, Takafumi Miyazaki*,

and Koichi Kikuchi** and Yohji Achiba**

*Faculty of Engineering, Chiba University, Inage-ku, Chiba 263*
** Institute for Molecular Science, Okazaki 444 Japan*
***Faculty of Science, Tokyo Metropolitan University, Hachioji, Tokyo 192-03 Japan*

Figure 1 shows the photoelectron spectra of $C_{86}$ obtained with the excitation photon energy described at the right side of each spectrum. The spectral onset is 1.1 eV below the Fermi level ($E_F$), which is very close to that of $C_{82}$ [1]. There are seven bands denoted by A - G in the spectra. Broken lines indicate their approximate peak positions. Band A is consisted of two structures; a shoulder at around 1.9 eV and a peak at 2.2 eV. Band B is consisted of a single peak component of which peak position shifts with the incident photon energy change. The peak of band C also moves its position from 5.1 eV in the hν = 50 eV spectrum to 5.3 eV in the hν = 40 eV one. Bands D - G are neither sharp nor distinct so that their peak positions cannot be located exactly, but comparison among the spectra reveals their peak shift upon the incident photon energy change as bands A - C exhibit.

Figure 2 shows the incident photon energy dependence of the photoelectron spectra of $C_{90}$. The spectral onset is 1.3 eV below the Fermi level, which is exceptionally large from the comparison of those of other higher fullerenes [1-6]. This relates to the difference in the absorption spectral edge of corresponding fullerenes [7]. There are six distinct structures labeled A - F in the spectra. Broken lines indicate their approximate peak positions. Band A seems to be consisted of more than three peak components. While it shows one peak at 2.05 eV in the hν = 40 and 45 eV spectra, two humps emerge at 1.95 and 2.25 eV in the hν = 15, 30 and 35 eV spectra. Band B is obviously consisted of two peak components, $b_1$ and $b_2$. This is noteworthy, since the most spectral bands of other higher fullerenes are consisted of a single envelope that occasionally accompanies the shoulder structure(s). This splitting is characteristic so that it is helpful to consider the geometry of this $C_2$-$C_{90}$ isomer by the theoretical calculation. The positions of components $b_1$ and $b_2$ shift slightly upon the change of the excitation photon energy, but they remain mainly at 3.25 and 3.7 eV. The peak position of the other bands also shift their peak position slightly upon the incident photon energy change.

The intensity of the bands of $C_{86}$ and $C_{90}$ oscillates when the incident photon energy is changed as that of other fullerenes shows. From present results and the results of other fullerenes, we propose the photoelectron excitation process itself as one of the reasons of the incident photon energy induced intensity oscillation including the interference effect among the wave functions of out going photoelectrons [8.9]. The wavelength of the de Broglie wave of the photoelectrons measured in our UPS measurements ranges approximately from 0.4 nm to 1.2 nm that is shorter than or close to the diameter of the fullerene cage. The photoelectrons generated from the carbon atoms situated at the bottom of the fullerene cage must travel through the cage and they are eventually scattered by the other carbon atoms. As in the case of EXAFS the interference effect between the outgoing photoelectrons with and without scattering might play an important role in the intensity oscillation.

This work has been published in Phys. Rev. B 53 (1996) 7496. TM's present address is Faculty of Science, Toyama University, Toyama Japan.

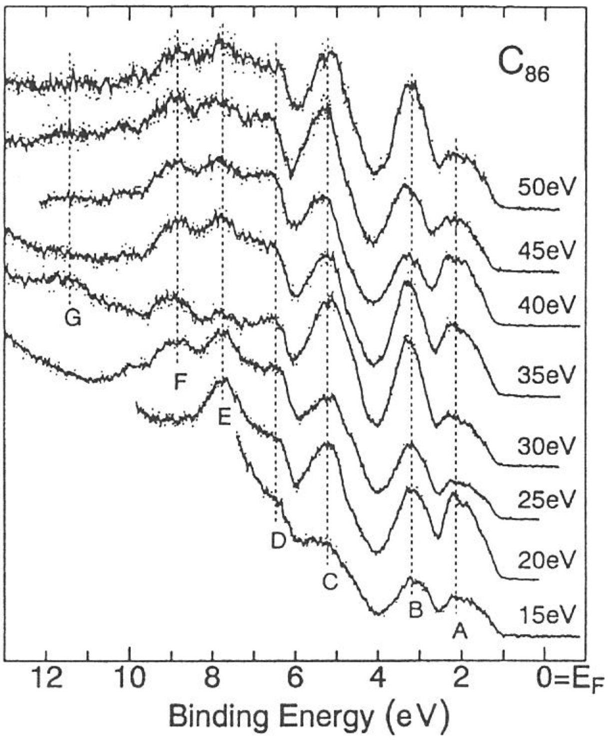

Figure 1
The incident photon energy dependence of of $C_2$-$C_{86}$.

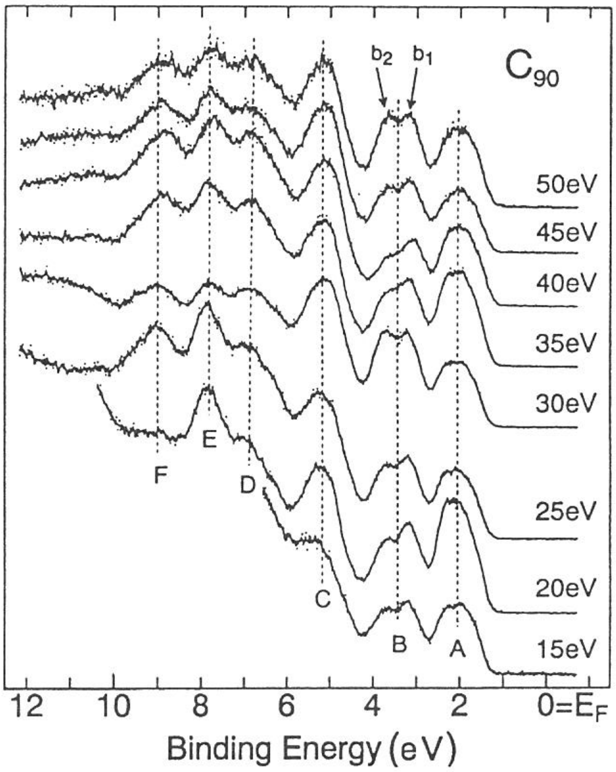

Figure 2
The incident photon energy dependence of $C_2$-$C_{90}$.

References
1). S. Hino et al., Phys. Rev. B **48** (1993) 8418.
2). S. Hino et al., Chem. Phys. Letters **190** (1992) 169.
3) S. Hino et al., Chem. Phys. Letters **197** (1992) 38.
4) S. Hino et al., Chem. Phys. Letters **230** (1994) 165.
5) J. W. Weaver et al.,, Phys. Rev. Letters **66** (1991) 1741.
6) P. J. Benning et al., Phys. Rev. B **44** (1991) 1962.
7) K. Kikuchi et al., Chem. Phys. Letters **188** (1992) 177.
8) T. Liebsch et al., Phys. Rev. A **52** (1995) 457.
9) Y. Xu et al., Phys Rev. Letters **76** (1996) 3538.

(BL8B2)

# Ultraviolet Photoelectron Spectra of Potassium-Oxygen-Graphite Intercalation Compounds

T. Yamashita, T. Enoki, T. Miyamae[a, b] and T. Miyazaki[a, *]

*Department of Chemistry, Tokyo Institute of Technology, Meguro-ku, Tokyo 152*
*[a]Institute for Molecular Science, Okazaki National Research Institutes, Okazaki 444*
*[b]Department of materials Science, Chiba University, Inage-ku, Chiba 263*

Potassium-oxygen-graphite intercalation compounds ($C_{4n}KO_x$; stage number $n$=1, 2, $x$~2) attract much interest from the view point of magnetism due to the similarity of chemical composition of intercalate to that of pristine $KO_2$ having the magnetic moment $S$=1/2.[1, 2] However, the temperature dependence of magnetic susceptibilies reveals the absence of localized magnetic moments, which is 0.1% of the stoichiometric amount of localized moment.[2] At present the absence of magnetic moments is considered to arise from the delocalized nature of intercalate oxygen, which is suggested from the self-consistent band calculation[3] and the considerations for the electronic structure based on the charge transfer per carbon atom.[2] It, therefore, is important to clarify the contribution of intercalate to the electronic structure around the Fermi level. In this report we present the results of the ultraviolet photoelectron spectra for 1st and 2nd stage potassium-oxygen-graphite intercalation compounds ($KO_x$-GICs).

Ultraviolet photoelectron spectra (UPS) were measured using synchrotron radiation at room temperature over the incident photon energy range from 25 eV to 60 eV for 1st and 2nd stage compounds. The Fermi energy of the instrument was determined by the Fermi edge of gold film. The samples were cleaved under a vacuum of $10^{-10}$ Torr by using adhesive tape to obtain the fresh surface.

The dependence of photoemission spectra on the binding energy are shown in Fig.1 for 1st and 2nd stage $KO_x$-GICs. The two peaks at 6 eV and 9.5 eV are assigned to the graphitic π and σ bands, and σ bands, respectively,[4, 5] whose peaks are shifted to the deeper binding energy compared with those of the pristine graphite due to the charge transfer to the graphitic π bands. As for 1st stage compound the additional broad peak between 6 and 12 eV obscures the obvious two peaks, which are observed for 2nd stage compound. Around the binding energy region 6 - 12 eV, the oxygen 2*p* states are suggested by the self-consistent band calculation of $KO_x$-GICs.[3] This broad peak, therefore, is assigned to the oxygen 2*p* bands. The peak around the binding energy 18 eV originates from the potassium 3*p* states, whose intensity increases rapidly with decreasing the incident photon energy due to the photon energy dependence of the photoionization cross-section for the potassium 3*p* states. The dependence of the ultraviolet photoelectron spectra around the Fermi level upon the incident photon energy is shown in Fig.2 for 1st stage compounds. The minima around 1 eV are considered to be the degenerate point of the two-dimensional graphitic bands, which is the same as the Fermi level of the pristine graphite. The apparent Fermi edge, which is not clearly observed in the pristine graphite spectrum, and the presence of the minimum around 1 eV for both 1st and 2nd stage compounds prove the donor-type feature of metallic compounds $KO_x$-GICs. The relative intensities above the minimum to the intensity at the deeper binding energy decrease with decreasing the photon energy except the incident photon energy 34.8 eV. Since the photoelectron intensity primarily depends on the photoionization cross-section and the density of the initial states, the photon energy dependence of the photoelectron intensity suggests that the electronic structure around $E_F$ consists of at least two components with the different energy dependence of the photoionization cross-sections. We, here, mention the incident photon energy dependence of the photoionization cross-section σ(C-2p) and σ(O-2p), for carbon 2*p* and oxygen 2*p* states, respectively, in order to reveal the electronic structure around $E_F$. Both σ(C-2p) and σ(O-2p) decrease with increasing the incident photon energy, and σ(C-2p) decreases more rapidly with increasing the photon energy than σ(O-2p).[6] Taking the photon energy dependence of σ(C-2p) and σ(O-2p) into account, the photoemission spectra are emphasized in the region including the oxygen 2*p* states with increasing the photon energy. Therefore, we conclude that the oxygen 2*p* states are superimposed on the graphitic π bands above the minimum. This conclusion for the electronic structure is in good agreement with the result of the band calculation for $KO_x$-GICs.[3] As for the enhancement of the photoemission intensity at 34.8 eV it is considered to be associated with the final-state effect or the resonant photoemission effect.[7] We need the further experiment to reveal the origin of the enhancement.

**Refereneces**

1) V. Z. Mordkovich, Y. Ohki, S. Yoshimura, S. Hino, T. Yamashita and T. Enoki, *Synth. Met.* **68** (1994) 79.

2) T. Yamashita, V. Z. Mordkovich, Y. Murakami, H. Suematsu and T. Enoki, *J. Phys. Chem. Solids* **57** (1996) 765.

3) S. Higai, S. Mizuno and K. Nakao, *J. Phys. Chem. Solids* **57** (1996) 689.

4) F. R. McFeely, S. P. Kowalczyk, L. Ley, R. G. Cavell, R. A. Pollak and D. A. Shirley, *Phys. Rev. B* **9** (1974) 5268.

5) A. Bianconi, S. B. M. Hagström and R. Z. Bachrach, *Phys. Rev. B* **16** (1974) 5268.

6) D. A. Verner, D. G. Yakovlev, I. M. Band and M. B. Trzhaskovskaya, *At. Data and Nucl. Data Tables* **55** (1993) 233.

7) C. Guillot, Y. Ballu, J.Paigné, J. Lecante, K. P. Jain, P. Thiry, R. Pinchaux, Y. Pétroff and L. M. Falicov, *Phys. Rev. Lett.* **39** (1977) 1632.

* Present address: Department of Chemistry, Toyama University, Toyama 930.

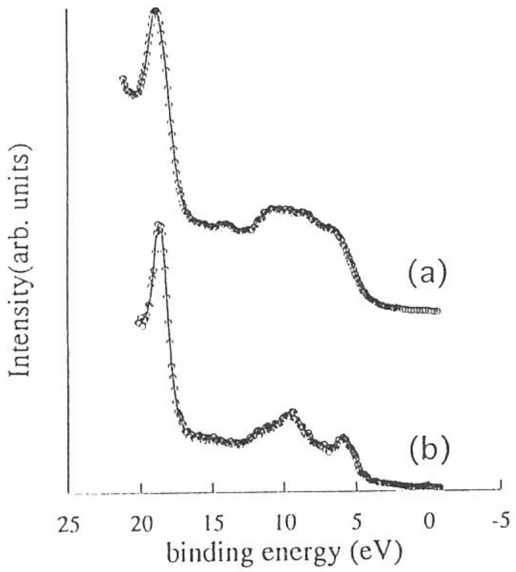

Fig.1 The photoemission spectra at the incident photon energy 30 eV for (a) 1st and (b) 2nd stage compounds.

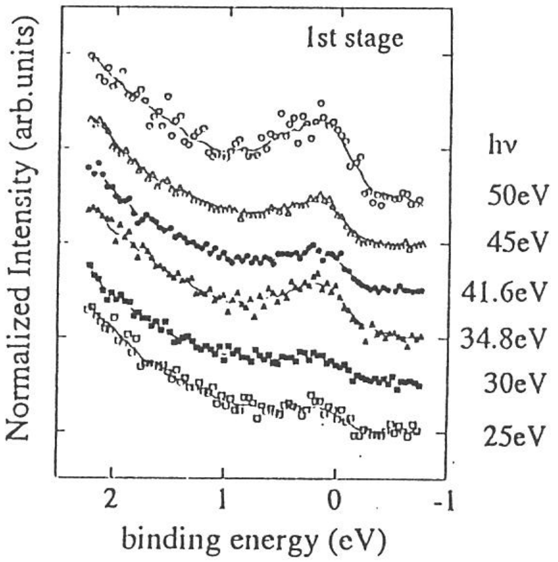

Fig.2 The incident photon energy dependence of photoemission spectra around $E_F$ for 1st stage compounds.

(BL8B2)

# ELECTRONIC STRUCTURES OF SILICON-BASED ORGANIC COMPOUNDS STUDIED BY UV PHOTOEMISSION

H. Ishii[1], A. Yuyama[2], S. Narioka[2], S. Hasegawa[1], T. Miyamae[1], M. Fujino[3], H. Isaka[3], M. Fujiki[3], K. Furukawa[3], N. Matsumoto[3], and K. Seki[2]

[1]Institute for Molecular Science, Myodaiji, Okazaki 444, Japan

[2]Department of Chemistry, Faculty of Science, Nagoya University, Chikusa-ku, Nagoya 464-01, Japan

[3]Basic Research Laboratories, Nippon Telegraph and Telephone Corporation, Morinosato, Atsugi 243-01, Japan

Silicon-based organic materials, whose electronic structure is characterized by $\sigma$-conjugation along the Si backbone instead of $\pi$-conjugation in carbon-based materials, have attracted much attention as a class of organic-inorganic hybrid system[1,2]. Especially, polysilanes and silacubanes which have silicon backbone with lower dimension than 3- dimensional crystalline silicon, are expected to have new function in relation to quantum wire and dot. For increasing the possibility of the application of such compounds to a device material, suitable substitution of side-group is necessary to make it soluble in device-fabrication process. Thus the elucidation of the electronic structures and their change by side-group substitution is indispensable for basic understanding and application of such compounds. As far as polysilanes, several studies have been made on the valence electronic structure using ultraviolet photoemission spectroscopy (UPS)[3-5]. In a part of the spectra, however, fine structures were smeared out probably due to sample degradation by air exposure or due to charging effect.

In the present study, we investigated the whole valence electronic structure of three polyalkylsilanes, two polyarylsilanes, and octa(*t*-butyl)octasilacubane(OTBOSC), using ultraviolet photoemission spectroscopy (UPS). By careful sample preparation in nitrogen environment, we could successfully measured the UPS spectra with fine structures. The spectral features were assigned by comparison with those of the constituents parts. The effect of substitution of side-group to the electronic structure was discussed.

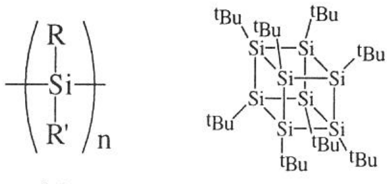

(a) (b)

Figure 1. The chemical structure of polysilane (Fig.1a) and OTBOSC (Fig.1b).

The UPS spectra were measured by using angle-resolved UPS system at the beamline 8B2 of UVSOR at IMS[6]. All the sample were synthesized at NTT. Their chemical structures are shown in figure 1. The sample films were prepared by spin-coating of 0.4 weight % toluene solution of each compounds onto Cu substrates in a glove bag under nitrogen gas flow.

**[Polyalkylsilanes]** The UPS spectrum (hν=40eV) of poly(methylpropylsilane) [PMPS, $(SiMePr)_n$] is shown in figure 2(a). The abscissa is the binding energy relative to the vacuum level. In order to assign the spectral features, we also show the UPS and XPS gas-phase spectra of $CH_4$[7,8], $C_3H_8$[8,9], and $Si_4(CH_3)_{10}$[10] as model compounds of the side group and the Si backbone in fig 2.(b)-(f). The spectrum has better quality than the reported one[3] and enables detailed analysis of the spectrum. As seen in the figure, the spectrum of $(SiMePr)_n$ corresponds well to the superposition of those of model compounds. This indicates that the valence electronic structure can be regarded as an overlap of those of the constituent parts.

Similar results were obtained for poly(dibutylsilane) and poly(dihexylsilane). It should be noted that the bands from alkyl group does not overlap with those of Si 3p derived states. This result indicates that the states of alkyl side group scarcely contribute to the uppermost valence electronic structure which mainly dominates the various properties of polysilanes.

**[Polyarylsilanes]** The UPS spectrum of poly(methylphenylsilane), [PM$\phi$S, $(SiMe\phi)_n$] is shown in figure 3(a) with the UPS and XPS spectra of $Si_4(CH_3)_{10}$[10], $C_6H_6$[11] and $CH_4$[7,8] in Fig.3(b)-(e). The spectrum has better quality than the reported one again[3]. All bands of $(SiMe\phi)_n$ except those in the uppermost energy region correspond one by one to each band in the spectra of the substituents. Similar result was obtained in the case of poly(di(4-ethylpheyl)silane). This indicates that the valence electronic structures of polyarylsilanes in higher binding energy region can be regarded mostly as an overlap of those of their constituents as in the case of polyalkylsilanes. The deviation of the spectral features in uppermost energy region from those of the constituents suggests $\sigma-\pi$ interaction between the $\pi$HOMO states of benzene and the Si $\sigma$HOVB states of the Si backbone. This results correspond to that of previous theoretical band calculation[4] .

**[Octa(*t*-butyl)octasilacubane]** TBOSC is a unique molecule consisting of silicon cube which can be regarded as a quantum dot. The UPS spectrum is shown in figure 4(a). By comparison with the UPS spectra of $Si_4(CH_3)_{10}$[10], i-$C_4H_{10}$[12] in Fig.4(b) and (c), the spectral features of OTBOSC could be assigned as follows; The topmost structures in the region of 5 to 9 eV are due to Si 3p derived states of cubic silicon backbone and C 2p derived states of i-$C_4H_{10}$ due to 9 to 15 eV. The features in higher binding energy region than 15 eV are ascribed to C 2s derived states. The ionization potential determined by the onset energy of UPS was 5.4 eV. Such a small value comparative to that of crystalline silicon (5.35 eV) can be explained by effective interaction between Si atoms due to 3-dimensional configuration and inductive effect by *t*-butyl groups.

In conclusion, UV photoemission spectra of three polyalkylsilanes, two polyarylsilanes, and ocata(*t*-butyl)octasilacubane with Si backbone were measured. Their valence electronic structure can be mostly regarded as an overlap of those of their constituents. However, the substitution of side-group induces the change of the topmost valence electronic structure, in the case of polyarylsilanes and silacubane.

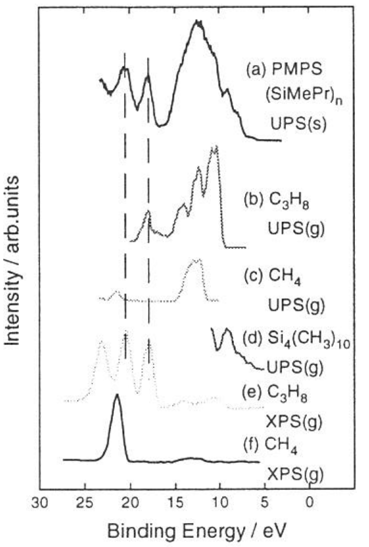

Figure 2. UPS and XPS spectra of $(SiMePr)_n$ and related compounds. (s) and (g) stand for solid and gaseous states, respectively. The gas-phase spectra are aligned to (a) at the C2s peaks as shown by vertical lines.

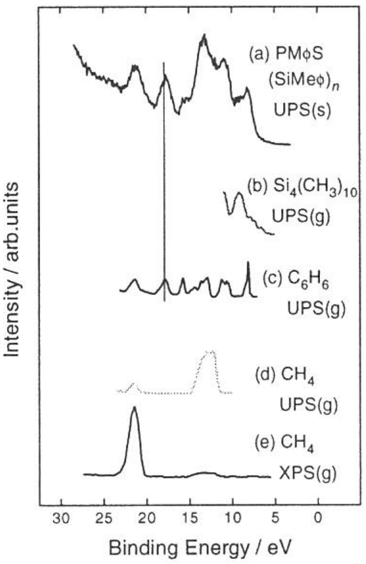

Figure 3. UPS and XPS spectra of $(SiMe\phi)_n$ and related compounds. (s) and (g) stand for solid and gaseous states, respectively. The gas-phase spectra are aligned to (a) at the C2s peaks as shown by a vertical line.

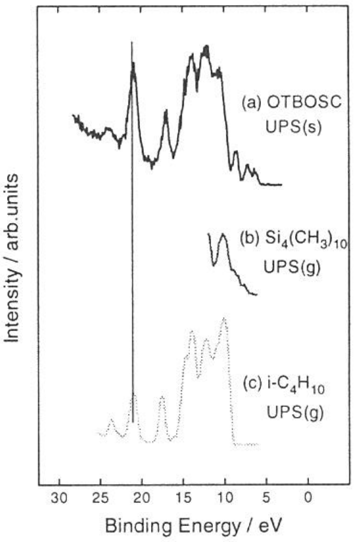

Figure 4. UPS spectra of octa(*t*-butyl)octasilacubane and related compounds. (s) and (g) stand for solid and gaseous states, respectively. The gas-phase spectra are aligned to (a) at the C2s peaks as shown by a vertical line.

## REFERENCES

1. J.M. Zeigler and F.W.G. Fearon (eds.), Silicon-Based Polymer Science: A Comprehensive Resource (ACS, Washington, 1990).
2. R.D.Miller and J.Michl, Chem. Rev., 89, 1359(1989).
3. G.Loubriel, and J.Zeigler, Phys. Rev., B33, 4203(1986).
4. K.Takeda, M.Fujimoto, K. Seki, and H.Inokuchi, Phys. Rev., B36, 8129(1987).
5. K.Seki, T.Mori, H.Inokuchi, and K.Murano, Bull. Chem. Soc. Jpn., 61, 351(1988).
6. K.Seki, H.Nakagawa, K.Fukui, E.Ishiguro, R.Kato, T.Mori, K.Sakai, and M.Watanabe, Nucl. Instrum.Methods, A246, 264(1986).
7. A.W.Potts, T.A.Williams, and W.C.Price, Faraday Disc. Chem. Soc., 54, 104(1972).
8. J.J.Pireaux, S.Svenson, E.Basilier, P.A.Malmqvist, U.Gelius, R.Caudano, and K.Siegbahn, Phys. Rev., A14, 2133(1976).
9. K.Kimura, S.Katsumata, Y.Achiba, T.Yamazaki, and S.Iwata, Handbook of He I Photoelectron Spectra of Fundamental Organic Molecules(Japan Scientific Societies Press, Tokyo, 1988).
10. H.Bock, and W. Ensslin, Angrew.Chem.Internat. Ed., 10, 404(1971).
11. L.Asbrink, O.Edqvist, E.Lindholm, and L.E.Selin, Chem. Phys. Lett., 5, 192(1970).
12. C. Sebenne, D. Bolmont, G. Gichar, and M. Balkanski, Phys. Rev., B12, 3238(1975).

(BL8B2)

# ELECTRONIC STRUCTURE OF ORGANIC CARRIER TRANSPORTING MATERIAL / METAL INTERFACES AS A MODEL INTERFACE OF ELECTRONLUMINESCENT DEVICE STUDIED BY UV PHOTOEMISSION

H. Ishii[1], D. Yoshimura[2], K. Sugiyama[2], T. Miyamae[1], T. Miyazaki[1], Y. Ouchi[2], and K. Seki[2]
[1]Institute for Molecular Science, Myodaij, Okazaki 444, Japan.
[2]Department of Chemistry, Faculty of Science, Nagoya University, Furo-cho, Chikusa-ku, Nagoya 464-01, Japan

Recently organic electroluminescent (EL) devices have attracted much attention in relation to their possible application to flat, large area displays. In order to make EL devices practical and efficient, the understanding of its mechanism is indispensable. Especially, the mechanism of carrier-injection process from an electrode to organic layer is crucial for the improvement of the life time, since the lowering of the applied voltage can decrease the eventual degradation of the device performance.

In most studies on organic EL devices, the mechanism has been discussed on the basis of the estimated interfacial electronic structure as shown in Fig.1(a). In this type of estimation, the interfacial electronic structure is deduced by lining up the separately observed electronic structures of an organic material and an electrode metal with the assumption of a common vacuum level at the interface: for example, the barrier height for hole injection, $\varepsilon_v^F$ is assumed as the difference between the work function of the electrode and ionization potential of the organic material. In this scheme, a common vacuum level has been assumed at organic/metal interface without serious discussion, naively employing the definition of vacuum level as the energy of the rest electron in vacuum. However, vacuum level in this definition is not at a microscopic (atomic scale) distance from the surface but at a macroscopic (comparable to the surface size) distance from the surface. Therefore, vacuum level cannot be energy reference at the interface where the spacing between the two components is of atomic scale. Strictly speaking, the vacuum level itself cannot be defined at the interface.

In the present study, we have investigated the electronic structure of model interfaces of organic EL devices by UV photoemission spectroscopy (UPS). On the basis of the observed electronic structure, we examined the validity of *"a common vacuum level"* and discussed the relation between the observed barrier height and the injecting nature of the interfaces.

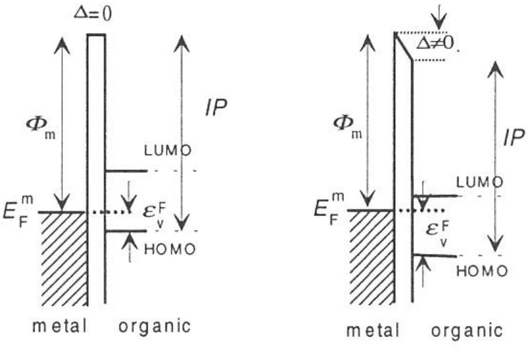

(a) (b)

Fig.1 Models for the electronic structure of an organic /metal interface. (a) Traditional method of estimation where a common vacuum level is assumed. (b) Presently observed electronic structure at the organic / metal interfaces.

Samples materials for the model interfaces of organic EL devices, tris(8-hydroxyquinolino) aluminum (Alq$_3$), *N,N'*-diphenyl-*N,N'*-(3-methylphenyl)-1,1'-biphenyl-4,4'-diamine (TPD), and *N,N'*-diphenyl-1,4,5,8-naphtyltetracarboxylimide (DP-NTCI) shown in Fig.2 were supplied from Toshiba R&D Center, and purified by vacuum sublimation. UPS spectra were measured by using angle-resolving UPS system at the beamline 8B2 of the UVSOR facility at Institute for Molecular Science.

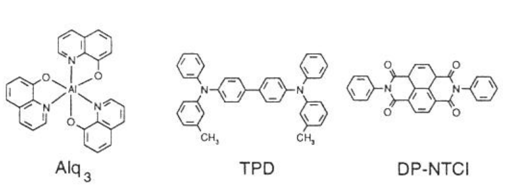

Fig.2 The chemical structures of organic EL device materials studied in this study.

Figure 3 shows the energy diagrams of the Alq$_3$ / Au, Al interface obtained from the UPS spectra of 1nm thick Alq$_3$ film on the metal substrate. The observed ionization potential $I_{th}^s$ of Alq$_3$ was $5.6\pm0.1$ eV. The energy position of the lowest unoccupied molecular orbital (LUMO) was estimated by taking the observed optical gap of 2.9 eV as the HOMO-LUMO band gap. Since we neglect the excitonic effect in this estimation, the actual band gap may be slightly larger. One can see that the vacuum level of Alq$_3$ does not coincide with that of the substrate metal; the vacuum level of Alq$_3$ is located ca. 1 eV below the vacuum level of the clean metal substrate.

Now let us examine the correlation between the electronic structure of the model interfaces and the injecting nature of the real interfaces. In Fig.3, LUMO is very close to the Fermi level of Al substrate at the Alq$_3$/Al interface, and we can expect good electron-injecting nature of the interface. On the other hand, at Alq$_3$/ Au interface, the Fermi level of the Au substrate is around the center of the band gap. Thus we cannot expect effective carrier-injecting character for both carriers. These expectations are consistent with the observations that

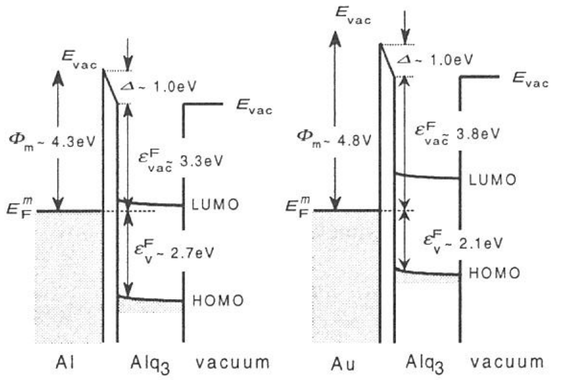

Fig.3 The interfacial energy diagrams of Alq$_3$/Al(left) and Alq$_3$/Au(right) interfaces obtained from UPS results.

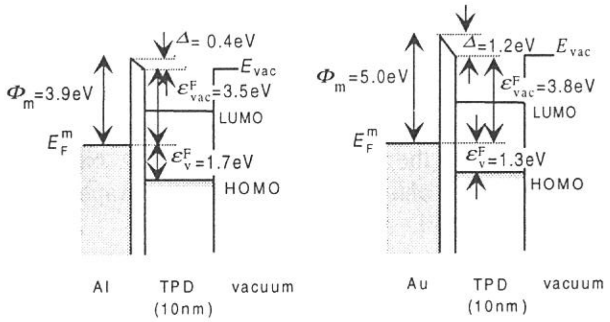

Fig.4 The interfacial energy diagrams of TPD/Al(a) and TPD/Au(b) interfaces obtained from UPS results.

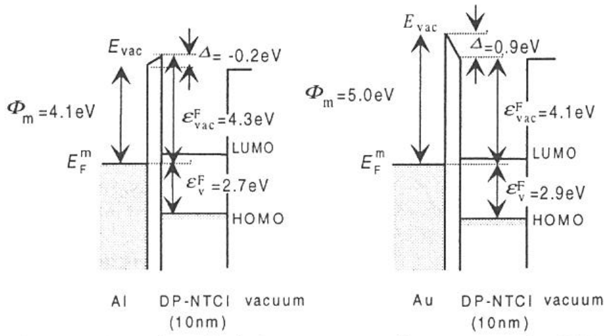

Fig.5 The interfacial energy diagrams of DP-NTCI/Al(a) and DP-NTCI/Au(b) interfaces obtained from UPS results.

(i)Alq$_3$ is widely used as both emitting and electron-injecting layer and (ii)insertion of a hole transport layer between Alq$_3$ layer and ITO substrate improves the performance of the EL devices.

It should be noted that the traditional estimation by assuming a common vacuum level leads to poor electron-injecting nature for the Alq$_3$/Al interface: this assumption locates the Fermi level of Al substrate at around the center of the gap of Alq$_3$. These findings clearly indicate that the traditional assumption of a common vacuum level at the interface is not valid.

Similar results were obtained for TPD/Al,Au and DP-NTCI/Al,Au interfaces. The energy diagrams obtained from UPS are shown in Fig.4 and 5. The film thickness of the organic layer was 10nm. Although the measurements for thinner film is desired for discussing the vacuum level shift at the interface, this was hindered since the high energy onset of UPS of the organic layer was often smeared out due to the overlap with the strong emission from the metal substrate. So we discuss here on $\Delta$ using the results of the thick film. The preliminary measurements on the thickness dependence by another spectrometer for TPD/Au interface did not show notable dependence of the energy position on the film thickness in the range from 1 to 10nm, indicating that the problem in measuring thin films does not affect the following discussion. The observed ionization potentials were 5.0±0.1 and 7.0 ±0.1 eV for TPD and DP-NTCI, respectively. At the TPD/Au interface, the Fermi level of the gold is closer to the HOMO of TPD than to the LUMO, qualitatively corresponding to the hole-injecting nature of the interface[1]. At DP-NTCI/Au interface, on the other hand, the Fermi level of gold is much closer to the LUMO than to the HOMO, corresponding to the electron-injecting character of the interface[2].

It is interesting to see that the vacuum level is slightly shifted upwards at DP-NTCI/Al interface, in contrast to other interfaces where downward shifts were observed. Usually, low work function metals are used as cathode materials to lower the barrier for electron-injection. According to the traditional estimation, we can expect lower barrier height for Al interface than Au interface. However, this is not the case due to the negative $\Delta$ at the Al interface, as seen in Fig.5. The negative sign of $\Delta$ suggests the occurrence of the charge-transfer from Al to DP-NTCI. Thus the barrier height seems not to be a monotonic function of $\Phi_m$, but there may be a minimum using an optimum electrode material. These findings strongly indicate the necessity of the direct observation of the electronic structure at the organic/metal interface.

In conclusion, we have experimentally examined the validity of the traditional methods estimating the interfacial electronic structure in organic/metal interfaces. Abrupt shifts of the vacuum level were observed at all the interfaces between metals and various organic-semiconductors ranging from donor to acceptor. These findings have clearly demonstrating the invalidity of the assumption of the alignment of the vacuum levels at organic/metal interface formed in ultrahigh vacuum. The above results imply that the neglect of vacuum level shift at the interface $\Delta$ has possibility to lead to an incorrect prediction of carrier-injecting nature of the interfaces.

References
[1]S. Egusa, N. Gemma, A. Miura, K. Mizushima, and M. Azuma, J. Appl. Phys., 71, 2042 (1992).
[2] S. Egusa, and T. Sasaki, private communication.

BL8B2

# Angle-resolved UPS on thin films of perylene tetracarboxylicdianhydride (PTCDA) on $MoS_2$ surfaces

N. Ueno[a,b], K. K. Okudaira[a], Y. Azuma[a], M. Tsutsui[b], T. Hasebe[b], T. Miyamae[b,c] and Y. Harada[a,b]

[a]*Department of Materials Science, Faculty of Engineering, Chiba University, Chiba 263*
[b]*Graduate School of Science and Technology, Chiba University, Chiba 263*
[c]*Institute for Molecular Science, Okazaki 444*

The angle-resolved ultraviolet photoelectron spectroscopy (ARUPS) using synchrotron radiation is useful to investigate the geometrical structure of the ultrathin films as well as the electronic structure. For the study of the geometrical structure of the thin films of functional organic molecules, ARUPS is very powerful, since it introduces much less radiation damages into organic thin films.

We recently developed the analysis method of the ARUPS intensity from thin films of large organic molecules using the independent-atomic-center and single-scattering approximations combined with molecular orbital calculation (IAC/MO and SS/MO), and succeeded to determine the molecular orientation of bis(1,2,5-thiadiazolo)-*p*-quinobis (1,3-dithiole) ($C_4H_4S_6N_4$) (BTQBT) and some phthalocyanines on HOPG graphite and $MoS_2$ surfaces as well as the origin of the observed ARUPS features [1-5].

In the present study, we performed ARUPS and LEED measurements on thin films of perylene tetracarboxylicdianhydride (PTCDA) deposited on cleaved $MoS_2$ surfaces. We here report the results of the quantitative analysis of the $\theta$ dependence of the spectra using the SS/MO approximation [4,5].

ARUPS measurements were carried out at the beam line BL8B2 of the UVSOR at Institute for Molecular Science. The take-off angle ($\theta$) dependence of photoelectrons were measured at normal incidence [incidence angle of photon $\alpha=0°$] and at hv=40 eV. The angle $\phi$ of the sample was measured from one of the three equivalent surface crystal axes of $MoS_2$.

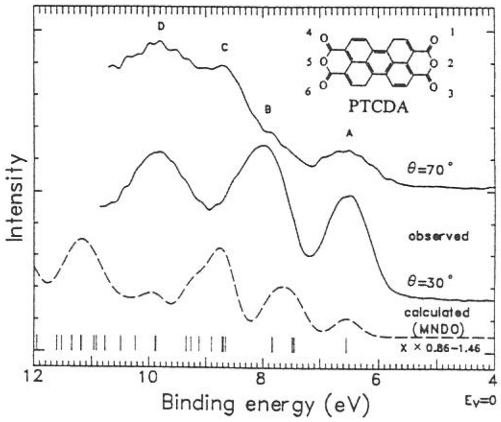

Fig.1 Comparison of the observed ARUPS spectra with MNDO/MO results.The observed spectra are shown for $\theta$= 30° and 70° at $\phi$= - 10.5° (rotational angle of a surface crystal axis of $MoS_2$ with respect to the electric vector of the photon). The calculated density-of-states (- - -) with the gaussian broadening of about 0.5 eV. The energy scale of the calculated results is contracted by 0.86 times and shifted by -1.46eV.

Figure 1 compares the observed spectra ($\theta$=30 and 70°) with the energy levels calculated with MNDO/MO. The observed feature A originates from the HOMO ($\pi$). The spectrum at $\theta$=70° gives feature C which is not observed at $\theta$=30°. As discussed later, feature C originates mainly from the photoelectron from $n_O$ (O2p non-bonding) band localized at C=O.

Figure 2 shows the $\theta$ dependence of the ARUPS spectrum of a PTCDA thin film (1.4Å) on the $MoS_2$ substrate for binding energy range from 4 to 11 eV, where four features A-D are clearly seen. With increase in $\theta$, the intensities of features A, B and D first increase, reach a maximum at about 32-34° and then decrease at larger $\theta$, while the intensity of feature C increases monotonically in this $\theta$ range. The difference of these $\theta$ dependencies reflects that of the wave functions of the initial states. Figure 3 shows the comparison between the observed and calculated $\theta$ dependencies of the photoelectron intensities at feature A and C, where the calculation were carried out with the SS/MNDO method for the HOMO and the $n_O$ state for a flat-lie PTCDA molecule. The calculated angular distributions for the HOMO state and the $n_O$ state correspond well with those of the band A and C, respectively. From these comparison, we can conclude that (i) the molecules lie flat and (ii) the observed feature C originates from the $n_O$ state at C=O.

The observed ϕ dependence and its analysis will be published near future.

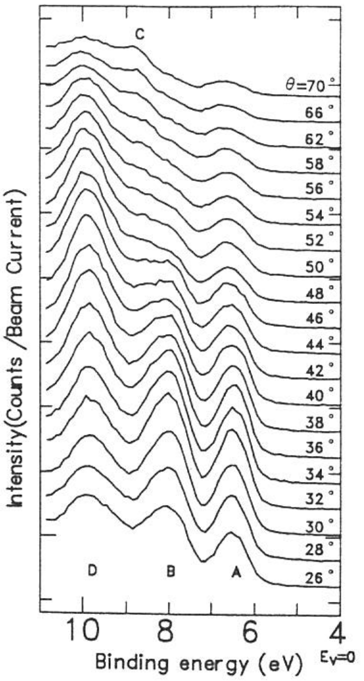

Fig. 2 The take-off angle (θ) dependence of ARUPS spectrum of a PTCDA film (1.4 Å thick) on $MoS_2$ at hv = 40 eV and at normal incidence (incidence angle of photon α=0°).

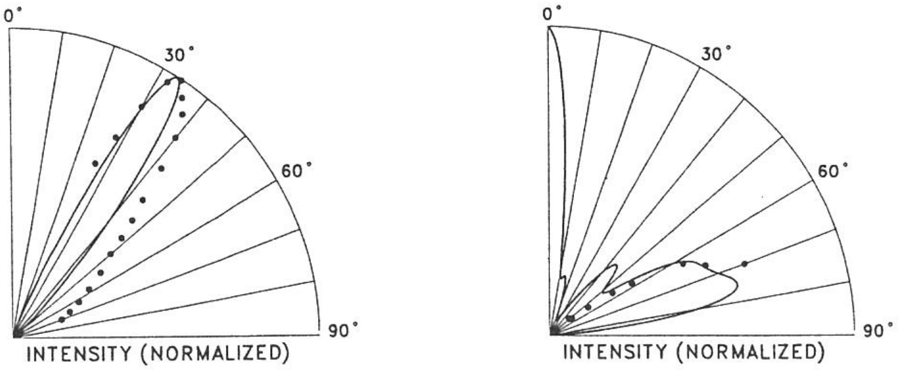

Fig. 3 Comparison between the observed (●)and The calculated (—) θ dependencies of the photoelectron intensity for the HOMO (π) (left panel) and $n_O$ (C=O) (right panel) bands of flat-lie PTCDA molecule by the SS/MNDO approximation. The calculations were performed for flat-lie molecular orientation with rotational disorder.

## REFERENCES

1. S. Hasegawa, S. Tanaka, Y. Yamashita, H. Inokuchi, H. Fujimoto, K. Kamiya, K. Seki, and N.Ueno, Phys. Rev. B, **48**, 2596 (1993).
2. N. Ueno, K. Suzuki, S. Hasegawa, K. Kamiya, K. Seki, and H. Inokuchi, J. Chem. Phys., **99**, 7169 (1993).
3. K. Kamiya, M. Momose, A. Kitamura, Y. Harada, N. Ueno, S. Hasegawa, T. Miyazaki, H. Inokuchi, S. Narioka, H. Ishii and K. Seki, J. Electron Spectr. Relat. Phenom.**76**, 213 (1995).
4. S. Hasegawa, H. Inokuchi, K. Seki and N. Ueno, J. Electron Spectr. Relat. Phenom. **78**, 391 (1996).
5. N. Ueno, J. Electron Spectr. Relat. Phenom. **78**, 345 (1996) .